



**HAL**  
open science

# Thermo-chemical-mechanical modeling of nuclear fuel behavior: Impact of oxygen transport in the fuel on Pellet Cladding Interaction

Piotr Konarski

► **To cite this version:**

Piotr Konarski. Thermo-chemical-mechanical modeling of nuclear fuel behavior: Impact of oxygen transport in the fuel on Pellet Cladding Interaction. Materials. Université de Lyon, 2019. English. NNT: 2019LYSEI080 . tel-02570386

**HAL Id: tel-02570386**

**<https://theses.hal.science/tel-02570386>**

Submitted on 12 May 2020

**HAL** is a multi-disciplinary open access archive for the deposit and dissemination of scientific research documents, whether they are published or not. The documents may come from teaching and research institutions in France or abroad, or from public or private research centers.

L'archive ouverte pluridisciplinaire **HAL**, est destinée au dépôt et à la diffusion de documents scientifiques de niveau recherche, publiés ou non, émanant des établissements d'enseignement et de recherche français ou étrangers, des laboratoires publics ou privés.



N°d'ordre NNT : 2019LYSEI080

**THESE de DOCTORAT DE L'UNIVERSITE DE LYON**  
opérée au sein de  
**l'Institut National des Sciences Appliquées de Lyon**

**Ecole Doctorale 34**  
**Matériaux de Lyon**

**Spécialité/ discipline de doctorat :**  
**Matériaux**

Soutenue publiquement le 10/10/2019, par :  
**Piotr Konarski**

---

**THERMO-CHEMICAL-MECHANICAL  
MODELING OF NUCLEAR FUEL  
BEHAVIOR. IMPACT OF OXYGEN  
TRANSPORT IN THE FUEL ON PELLET  
CLADDING INTERACTION**

---

Devant le jury composé de :

PIRO, Markus	Prof. Ontario Tech University	Rapporteur
GALLIERO, Guillaume	Prof. Université de Pau	Rapporteur
SERCOMBE, Jérôme	Dr. CEA Cadarache	Examineur
LUZZI, Leilo	Prof. Politecnico di Milano	Examineur
FREGONESE, Marion	Prof. INSA de Lyon	Directrice de thèse
CHANTRENNE, Patrice	Prof. INSA de Lyon	Co-directeur de thèse
GARNIER, Christophe	Dr. Framatome	Invité
RIGLET-MARTIAL, Chantal	Dr. CEA Cadarache	Invitée
BAURENS, Bertrand	Dr. EDF	Invité



**Département FEDORA – INSA Lyon - Ecoles Doctorales – Quinquennal 2016-2020**

<b>SIGLE</b>	<b>ECOLE DOCTORALE</b>	<b>NOM ET COORDONNEES DU RESPONSABLE</b>
<b>CHIMIE</b>	<b>CHIMIE DE LYON</b> <a href="http://www.edchimie-lyon.fr">http://www.edchimie-lyon.fr</a> Sec. : Renée EL MELHEM Bât. Blaise PASCAL, 3e étage <a href="mailto:secretariat@edchimie-lyon.fr">secretariat@edchimie-lyon.fr</a> INSA : R. GOURDON	<b>M. Stéphane DANIELE</b> Institut de recherches sur la catalyse et l'environnement de Lyon IRCELYON-UMR 5256 Équipe CDFA 2 Avenue Albert EINSTEIN 69 626 Villeurbanne CEDEX <a href="mailto:directeur@edchimie-lyon.fr">directeur@edchimie-lyon.fr</a>
<b>E.E.A.</b>	<b>ÉLECTRONIQUE, ÉLECTROTECHNIQUE, AUTOMATIQUE</b> <a href="http://edeea.ec-lyon.fr">http://edeea.ec-lyon.fr</a> Sec. : M.C. HAVGOUDOUKIAN <a href="mailto:ecole-doctorale.eea@ec-lyon.fr">ecole-doctorale.eea@ec-lyon.fr</a>	<b>M. Gérard SCORLETTI</b> École Centrale de Lyon 36 Avenue Guy DE COLLONGUE 69 134 Écully Tél : 04.72.18.60.97 Fax 04.78.43.37.17 <a href="mailto:gerard.scorletti@ec-lyon.fr">gerard.scorletti@ec-lyon.fr</a>
<b>E2M2</b>	<b>ÉVOLUTION, ÉCOSYSTÈME, MICROBIOLOGIE, MODÉLISATION</b> <a href="http://e2m2.universite-lyon.fr">http://e2m2.universite-lyon.fr</a> Sec. : Sylvie ROBERJOT Bât. Atrium, UCB Lyon 1 Tél : 04.72.44.83.62 INSA : H. CHARLES <a href="mailto:secretariat.e2m2@univ-lyon1.fr">secretariat.e2m2@univ-lyon1.fr</a>	<b>M. Philippe NORMAND</b> UMR 5557 Lab. d'Ecologie Microbienne Université Claude Bernard Lyon 1 Bâtiment Mendel 43, boulevard du 11 Novembre 1918 69 622 Villeurbanne CEDEX <a href="mailto:philippe.normand@univ-lyon1.fr">philippe.normand@univ-lyon1.fr</a>
<b>EDISS</b>	<b>INTERDISCIPLINAIRE SCIENCES-SANTÉ</b> <a href="http://www.ediss-lyon.fr">http://www.ediss-lyon.fr</a> Sec. : Sylvie ROBERJOT Bât. Atrium, UCB Lyon 1 Tél : 04.72.44.83.62 INSA : M. LAGARDE <a href="mailto:secretariat.ediss@univ-lyon1.fr">secretariat.ediss@univ-lyon1.fr</a>	<b>Mme Emmanuelle CANET-SOULAS</b> INSERM U1060, CarMeN lab, Univ. Lyon 1 Bâtiment IMBL 11 Avenue Jean CAPELLE INSA de Lyon 69 621 Villeurbanne Tél : 04.72.68.49.09 Fax : 04.72.68.49.16 <a href="mailto:emmanuelle.canet@univ-lyon1.fr">emmanuelle.canet@univ-lyon1.fr</a>
<b>INFOMATHS</b>	<b>INFORMATIQUE ET MATHÉMATIQUES</b> <a href="http://edinfomaths.universite-lyon.fr">http://edinfomaths.universite-lyon.fr</a> Sec. : Renée EL MELHEM Bât. Blaise PASCAL, 3e étage Tél : 04.72.43.80.46 <a href="mailto:infomaths@univ-lyon1.fr">infomaths@univ-lyon1.fr</a>	<b>M. Luca ZAMBONI</b> Bât. Braconnier 43 Boulevard du 11 novembre 1918 69 622 Villeurbanne CEDEX Tél : 04.26.23.45.52 <a href="mailto:zamboni@maths.univ-lyon1.fr">zamboni@maths.univ-lyon1.fr</a>
<b>Matériaux</b>	<b>MATÉRIAUX DE LYON</b> <a href="http://ed34.universite-lyon.fr">http://ed34.universite-lyon.fr</a> Sec. : Stéphanie CAUVIN Tél : 04.72.43.71.70 Bât. Direction <a href="mailto:ed.materiaux@insa-lyon.fr">ed.materiaux@insa-lyon.fr</a>	<b>M. Jean-Yves BUFFIÈRE</b> INSA de Lyon MATEIS - Bât. Saint-Exupéry 7 Avenue Jean CAPELLE 69 621 Villeurbanne CEDEX Tél : 04.72.43.71.70 Fax : 04.72.43.85.28 <a href="mailto:jean-yves.buffiere@insa-lyon.fr">jean-yves.buffiere@insa-lyon.fr</a>
<b>MEGA</b>	<b>MÉCANIQUE, ÉNERGÉTIQUE, GÉNIE CIVIL, ACOUSTIQUE</b> <a href="http://edmega.universite-lyon.fr">http://edmega.universite-lyon.fr</a> Sec. : Stéphanie CAUVIN Tél : 04.72.43.71.70 Bât. Direction <a href="mailto:mega@insa-lyon.fr">mega@insa-lyon.fr</a>	<b>M. Jocelyn BONJOUR</b> INSA de Lyon Laboratoire CETHIL Bâtiment Sadi-Carnot 9, rue de la Physique 69 621 Villeurbanne CEDEX <a href="mailto:jocelyn.bonjour@insa-lyon.fr">jocelyn.bonjour@insa-lyon.fr</a>
<b>ScSo</b>	<b>ScSo*</b> <a href="http://ed483.univ-lyon2.fr">http://ed483.univ-lyon2.fr</a> Sec. : Véronique GUICHARD INSA : J.Y. TOUSSAINT Tél : 04.78.69.72.76 <a href="mailto:veronique.cervantes@univ-lyon2.fr">veronique.cervantes@univ-lyon2.fr</a>	<b>M. Christian MONTES</b> Université Lyon 2 86 Rue Pasteur 69 365 Lyon CEDEX 07 <a href="mailto:christian.montes@univ-lyon2.fr">christian.montes@univ-lyon2.fr</a>

Cette thèse est accessible à l'adresse : <http://theses.insa-lyon.fr/publication/2019LYSEI080/these.pdf>



# Contents

<b>List of Figures</b>	<b>vii</b>
<b>List of Tables</b>	<b>ix</b>
<b>Acronyms</b>	<b>xi</b>
<b>Acknowledgements</b>	<b>xiii</b>
<b>1 Introduction on nuclear fuel</b>	<b>1</b>
1.1 Nuclear fuel behavior . . . . .	1
1.1.1 General aspects of nuclear fuel . . . . .	1
1.1.2 Fission Products . . . . .	5
1.1.3 Fuel thermomechanics . . . . .	11
1.1.4 Fission Gas Release . . . . .	12
1.1.5 Pellet-Cladding Interaction Failure . . . . .	15
1.2 Modeling nuclear fuel behavior . . . . .	18
1.2.1 Main phenomena . . . . .	20
1.2.1.1 Neutronics . . . . .	20
1.2.1.2 Thermal calculations . . . . .	20
1.2.1.3 Mechanics . . . . .	21
1.2.1.4 Fission gas release . . . . .	21
1.2.2 Advanced thermo-mechanical modeling of PCI . . . . .	22
1.3 Conclusions . . . . .	24
<b>2 Literature Review</b>	<b>25</b>
2.1 Thermochemistry of irradiated nuclear fuel . . . . .	25
2.1.1 Introduction . . . . .	25
2.1.2 Oxygen potential . . . . .	27
2.1.3 Chemical state of fission products in irradiated fuel . . . . .	31
2.1.3.1 Fission products dissolved in the fluorite solid solution . . . . .	31
2.1.3.2 Fission products and dopants precipitates at the pellet center . . . . .	33
2.1.3.3 Volatile fission products at the pellet-clad interface . . . . .	38
2.1.4 Oxygen potential measurements in irradiated fuel . . . . .	43
2.1.4.1 SIMulated irradiated FUEL (SIMFUEL) . . . . .	44
2.1.4.2 Irradiated fuel in normal operating conditions . . . . .	44
2.1.4.3 Irradiated fuel in power ramps . . . . .	49
2.1.5 Conclusions . . . . .	52

2.2	Oxygen transport in the fuel . . . . .	53
2.2.1	Theory . . . . .	53
2.2.1.1	Introduction . . . . .	53
2.2.1.2	Thermal diffusion in hypostoichiometric fuels . . . . .	54
2.2.1.3	Thermal diffusion in hyperstoichiometric fuels . . . . .	55
2.2.2	Chemical diffusion coefficient of oxygen . . . . .	57
2.2.2.1	Self-diffusion coefficient (or tracer diffusion coefficient) . . . . .	58
2.2.2.2	Chemical diffusion coefficient of oxygen . . . . .	62
2.2.3	Heat of oxygen transport . . . . .	66
2.2.4	Conclusions . . . . .	69
2.3	PCI failure by I-SCC . . . . .	69
2.3.1	I-SCC mechanisms . . . . .	70
2.3.1.1	Introduction . . . . .	70
2.3.1.2	Zirconium iodides . . . . .	70
2.3.1.3	Van Arkel reaction . . . . .	72
2.3.2	Iodine thresholds for I-SCC . . . . .	73
2.3.3	Origin of iodine in reactor . . . . .	76
2.3.4	Modelling of I-SCC . . . . .	78
2.3.4.1	Crack propagation in the cladding . . . . .	78
2.3.4.2	Iodine chemistry and transport model . . . . .	82
2.3.5	Conclusions . . . . .	85
2.4	Thermochemistry and oxygen transport in nuclear fuel simulations . . . . .	86
2.4.1	Thermochemical database . . . . .	86
2.4.2	MFPR . . . . .	87
2.4.3	THERMOCHIMICA . . . . .	88
2.4.4	ALCYONE and ANGE . . . . .	92
2.4.5	Conclusions . . . . .	94
2.5	Goal of the work . . . . .	94
<b>3</b>	<b>Thermochemical modeling of nuclear fuel</b> . . . . .	<b>97</b>
3.1	Neutronics model PRODHEL . . . . .	97
3.1.1	Fission Products isotopes in irradiated fuel . . . . .	97
3.1.2	Evolution of iodine isotopes . . . . .	99
3.1.3	Validation on a low burnup fuel . . . . .	102
3.1.4	Validation on a high burnup fuel . . . . .	105
3.2	Thermochemical solver ANGE . . . . .	113
3.2.1	Gibbs energy minimization method . . . . .	113
3.2.2	Thermodynamic database . . . . .	118
3.2.3	The Fluorite solid solution phase . . . . .	119
3.2.3.1	U-O system . . . . .	119
3.2.3.2	U-Pu-O system . . . . .	122
3.2.3.3	U-Gd-O and U-La-O systems . . . . .	124
3.2.3.4	U-Ce-O system . . . . .	126
3.2.3.5	U-Eu-O system . . . . .	127
3.2.3.6	U-Zr-O system . . . . .	128
3.2.3.7	Chromium solubility model . . . . .	129
3.2.3.8	Validation on SIMFUELS . . . . .	131

3.3	Thermochemical modeling of irradiated fuels . . . . .	132
3.3.1	General aspects . . . . .	132
3.3.1.1	Oxygen potential and stoichiometry deviation . . . . .	132
3.3.1.2	Gas phase . . . . .	136
3.3.2	Oxygen potential measurements in irradiated fuel . . . . .	137
3.3.2.1	Irradiated BWR fuels . . . . .	137
3.3.2.2	Irradiated PWR fuels . . . . .	140
3.3.2.3	High burnup irradiated PWR fuel . . . . .	146
3.4	Summary . . . . .	150
<b>4</b>	<b>Oxygen thermal diffusion</b>	<b>152</b>
4.1	Numerical solutions in 1D radial . . . . .	152
4.1.1	Steady-state temperature profile . . . . .	152
4.1.2	Steady-state solution (OXIRED) . . . . .	153
4.1.3	Transient solution (OXITRAN) . . . . .	158
4.2	Numerical solution in 2D and 3D . . . . .	163
4.2.1	Transient solution . . . . .	163
4.2.2	Cross-comparison of 1D and 2D/3D solutions . . . . .	168
4.2.3	Coupled heat and oxygen transport in 2D/3D . . . . .	169
4.2.3.1	COMSOL based solution . . . . .	169
4.2.3.2	Cast3M solution . . . . .	174
4.3	Parameters of oxygen transport in irradiated fuel . . . . .	179
4.3.1	Heat of transport . . . . .	179
4.3.1.1	Experimental observations . . . . .	179
4.3.1.2	Oxygen potential reached at the pellet center . . . . .	184
4.3.1.3	O/M ratios reached at the pellet center . . . . .	186
4.3.1.4	Heat of oxygen transport fitting . . . . .	189
4.3.2	Chemical diffusion coefficient of oxygen . . . . .	192
4.3.2.1	Concentration of point defects . . . . .	193
4.3.2.2	Self-diffusion coefficient of oxygen . . . . .	195
4.3.2.3	Thermodynamic factor . . . . .	197
4.3.2.4	Chemical diffusion coefficient of oxygen . . . . .	201
4.3.2.5	Impact of stoichiometry deviation on thermal diffusion kinetics . . . . .	202
4.3.3	Summary . . . . .	204
<b>5</b>	<b>Thermochemistry–oxygen transport coupling in ALCYONE</b>	<b>206</b>
5.1	Coupling procedure . . . . .	206
5.1.1	ALCYONE algorithm . . . . .	206
5.1.2	Thermochemical calculations at prescribed O/M ratio . . . . .	209
5.1.3	Evolution of oxygen content with O/M ratio . . . . .	210
5.1.3.1	Standard UO <sub>2</sub> fuel . . . . .	211
5.1.3.2	Cr-doped fuel . . . . .	213
5.1.4	Verification of the proposed coupled solution . . . . .	215
5.1.5	Coupling strategy in power ramps . . . . .	218
5.1.6	Validation in 1D . . . . .	219
5.1.7	Validation in 3D . . . . .	223

5.1.7.1	Characteristics of the power ramp . . . . .	223
5.1.7.2	Evolution of the O/M ratio and of the oxygen potential . . . . .	224
5.1.7.3	Impact of oxygen transport on metallic oxides . . . . .	227
5.1.7.4	Noble Fission Gas Release . . . . .	232
5.1.7.5	Iodine release and speciation . . . . .	233
5.1.7.6	Cesium release and speciation . . . . .	235
5.1.7.7	FGR from the fuel pellet fragment . . . . .	237
5.2	3D simulation of PCI-SCC . . . . .	238
5.2.1	Characteristics of the power ramp . . . . .	239
5.2.2	Temperature and pressure . . . . .	240
5.2.3	O/M ratio and oxygen potential . . . . .	242
5.2.4	Fission Gas Release . . . . .	243
5.2.5	Burnup and pre-ramp elemental composition . . . . .	245
5.2.6	Post-ramp elemental composition . . . . .	247
5.2.7	Thermochemistry of I, Cs and Te . . . . .	250
5.2.7.1	Iodine . . . . .	250
5.2.7.2	Cesium . . . . .	252
5.2.7.3	Tellurium . . . . .	255
5.2.8	I-SCC modeling . . . . .	258
5.2.8.1	Initiation criteria . . . . .	258
5.2.8.2	Crack propagation model . . . . .	263
5.2.9	Sensitivity studies on the I-SCC model . . . . .	265
5.2.9.1	Initial crack depth . . . . .	265
5.2.9.2	Iodine partial pressure threshold . . . . .	266
5.2.9.3	Iodine from CsI radiolysis . . . . .	267
5.2.9.4	Crack opening . . . . .	269
5.3	Summary . . . . .	269
<b>6</b>	<b>Conclusions and perspectives</b>	<b>272</b>
6.1	Irradiated fuel thermochemistry . . . . .	272
6.2	Oxygen thermal diffusion . . . . .	273
6.3	Fuel performance simulations including oxygen transport . . . . .	275
6.4	PCI-SCC . . . . .	277
<b>A</b>	<b>Theoretical derivation of the oxygen transport equation</b>	<b>279</b>
<b>B</b>	<b>Concentration of point defects in UO<sub>2</sub></b>	<b>288</b>
<b>C</b>	<b>Isotopic composition after 3 months</b>	<b>290</b>
<b>D</b>	<b>Thomas algorithm for solving tridiagonal systems of equations</b>	<b>296</b>
<b>E</b>	<b>Thermal diffusion problem solved by the finite element method</b>	<b>298</b>

# List of Figures

1.1	Schematic representation of a fuel pellet, a fuel rod and an assembly. . . .	2
1.2	A cross section of a fuel rod of a light water reactor. . . . .	2
1.3	”Temperature profile in light water reactor fuel during base irradiation.” .	4
1.4	Schematic representation of a PWR nuclear power plant. . . . .	5
1.5	Weight fraction of neodymium (left axis) and burnup (right axis) as a function of the relative radius. Measurements come from a UO <sub>2</sub> sample with a very high average burnup of 102 GWd/tHM. . . . .	6
1.6	Fission product yields of <sup>235</sup> U (blue) and <sup>239</sup> Pu (red) for thermal neutrons. Horizontal axis expresses the mass number and the vertical one presents the fractional cumulative fission yield. . . . .	7
1.7	The predicted evolution of fission and activation products integrated across the pellet. . . . .	9
1.8	”Chemical state of the fission products in the light water reactor fuel.” . .	11
1.9	Hour-glassing of a fuel pellet. . . . .	12
1.10	”Evolution of the gap between the cladding and the fuel during irradiation. a) fresh fuel, b) first cycle and start of second irradiation cycle, c) second half of second cycle: first cladding–pellet contact and appearance of primary ridges, d) in the case of power ramp: appearance of secondary ridges.” . . . . .	12
1.11	Schematic illustration of the grain structure of nuclear fuel with distinction of intragranular and intergranular bubbles. . . . .	13
1.12	Micrograph showing tunnels on the grain face of fuel irradiated up to 22 GWd/tHM. Sample power ramped in the Halden Reactor. Maximum temperature 1800 °C, holding time 1800 s. . . . .	14
1.13	Comparison of fractional fission gas release as a function of power for different types of fuel irradiated in different reactors. The average burnup of samples is 20-40 GWd/tHM. . . . .	15
1.14	Left figure: 3D model showing the pellet cladding interaction. Right figure: Image of the crack propagation in the cladding and of its localization in front of a fuel pellet radial crack. . . . .	15
1.15	Schematic representation of of PCI in 2D. . . . .	16
1.16	PCI technological limit. . . . .	17
1.17	Schematic illustration of a power ramp test. . . . .	17
1.18	Typical fuel rod and fuel pellet discretization in the 1.5D scheme of AL-CYONE. . . . .	19
1.19	Main phenomena that need to be taken into account in fuel behavior modeling. . . . .	19

1.20	Mesh and mechanical boundary conditions used in the 3D scheme of ALCYONE (left figure) and the calculated pellet deformation (right figure) with the triple point marked in red. . . . .	22
1.21	Images of 3D simulation performed in ALCYONE. Colors correspond to inelastic strains in the fuel pellet. 1. 1 <sup>st</sup> cycle, full power, 2. 2 <sup>nd</sup> cycle, full power, 3. End of the 2 <sup>nd</sup> cycle, pellet-cladding gap is closed, 4. End of the base irradiation, 5. Beginning of the power ramp, 6. Maximum linear heat rate of the power ramp, 7. Holding period of the power ramp, filling of the dishes by fuel creep, 8. Holding period of the power ramp, development of the cladding ridges. . . . .	23
2.1	Schematic of irradiated fuel. . . . .	26
2.2	Relative partial molar Gibbs free energies of oxygen of the fission product oxides and of UO <sub>2+x</sub> . . . . .	28
2.3	Phase diagram of the binary system U-O. . . . .	29
2.4	Oxygen partial pressure as a function of O/U. Symbols correspond to selected experimental data and curves present calculated values. . . . .	30
2.5	Radial EPMA profiles of Cs and Nd measured in the fuel sample irradiated to 32 GWd/tHM and power ramped at the linear heat rate of 463 W/cm during 12 h. . . . .	33
2.6	Diametrical weight fractions of Cs, Mo and Zr and of Xe bonded in the fuel rod studied by Kleykamp. . . . .	34
2.7	X-ray maps of Cr, O, Mo and Ru in the fuel studied by Riglet-Martial et al. Brighter color corresponds to a higher concentration. . . . .	35
2.8	Radial profiles of the EPMA measures of Cr and Mo (left axis) and of the temperature (right axis) in the fuel studied by Riglet-Martial et al. . . . .	36
2.9	Relation between chromium mole fraction in UO <sub>2</sub> (i.e., chromium solubility) and oxygen partial pressure for various temperatures. One may notice the stability areas for Cr <sub>(s)</sub> , CrO <sub>(l)</sub> and CrO <sub>3/2(s)</sub> . . . . .	37
2.10	Zirconia layer on the cladding inner wall observed in a UO <sub>2</sub> fuel rod after 5 cycles. . . . .	39
2.11	SIMS measurements presenting radial distribution of Xe, Cs, I and Te along the mid-pellet plane. NHT–no holding time, SHT–short holding time. . . . .	41
2.12	SIMS images presenting <sup>129</sup> I, <sup>130</sup> Te and <sup>137</sup> Cs near the pellet periphery. Dark blue corresponds to the lowest concentration and red to the highest concentration. . . . .	42
2.13	Cs-I-O-Te gas phase diagram at 600 °C with the assumption that $0 < \frac{I}{I+Te} < \frac{2}{3}$ . The red and blue points refer to the experiments studied by Desgranges et al. . . . .	43
2.14	Oxygen potential of SIMFUELS of increasing burnups (2, 5 and 10 at%) as a function of the O/M ratio at 1000 and 1300 °C. . . . .	44
2.15	Oxygen potential measured in irradiated UO <sub>2</sub> (a) and gadolinium-doped fuel (b). . . . .	45
2.16	Oxygen potential measurements of samples with burnups of 28.9 GWd/tHM (top left), 34.5 GWd/tHM (bottom left) and 58 GWd/tHM (top right). . . . .	46
2.17	Oxygen potential at the center compared to oxygen potential from the rim region. Specimens 1, 2 and 3 were sampled from the rim of the fuel pellet. . . . .	47

2.18	Comparison of oxygen potentials at different temperatures. . . . .	48
2.19	"Fuel and stoichiometric O/M ratios and the quantity of free oxygen as a function of radial position in the high burnup fuel." Adapted from Walker et al. . . . .	49
2.20	Oxygen potential measured in the fuel rods LIT-2/3 and LIT-B/4 studied by Adamson et al. . . . .	50
2.21	Evidence of the strong reduction of oxygen potential during the power ramp. Calculations performed with the Factsage software. The blue and purple points show the equilibrium state after two power ramps studied by Riglet-Martial et al. . . . .	51
2.22	Oxygen potential calculated at 750 °C without and with oxygen loss due to cladding oxidation. . . . .	52
2.23	Figure from Berthinier et al. Comparison of the self-diffusion coefficient of oxygen proposed by the author with the experimental data. Values for the hyperstoichiometric domain. . . . .	59
2.24	Figure from Berthinier et al. Comparison of the self-diffusion coefficient of oxygen proposed by the author with the experimental data. Values for the hypostoichiometric domain. . . . .	60
2.25	Calculated values of oxygen self-diffusion compared to experimental data. . . . .	62
2.26	Oxygen partial pressure as a function of the logarithm of the stoichiometry deviation. Different curves correspond to different temperatures. Calculations done by Berthinier et al. . . . .	65
2.27	Oxygen chemical diffusion coefficient as a function of O/U. Comparison of calculations with experiments. . . . .	66
2.28	Heat of transport as a function of O/M. Data comes from Sari and other authors. Different symbols correspond to different concentration of plutonium in samples. . . . .	67
2.29	Heat of transport calculated by Timm and Janek (solid line) compared to the experimental data from Sari, Evans and Adamson. . . . .	69
2.30	Pressure of iodine and species that it forms with zirconium as a function of temperature. $\Theta$ is the amount of iodine needed to form a monolayer. . . . .	71
2.31	Mechanism of SCC assuming presence of gaseous iodine. . . . .	72
2.32	Expanding mandrel sample configuration for I-SCC investigations of irradiated fuel cladding materials, the alumina insert with 4 longitudinal slits and the pure Zr mandrel in the central part and a cross section of a cladding sample after mandrel testing. . . . .	74
2.33	Total diametral strain to failure (blue points) and time to failure (yellow points) as a function of $I_2$ partial pressure. . . . .	75
2.34	Concentration of some chemically reactive species as a function of the O/M ratio calculated at 2000 °C. . . . .	77
2.35	Impact of temperature on the evolution of the time to failure as a function of the hoop stress during internal pressurization tests on smooth, non irradiated specimens. Results obtained under inert and iodine environments. . . . .	78
2.36	Comparison between experimental data and the model proposed by Le Boulch et al. Irradiated and non irradiated samples are compared at 350 °C. . . . .	79
2.37	Stress corrosion crack growth rate as a function of the applied stress intensity factor during internal pressurization tests on pre-cracked, non irradiated specimens. . . . .	80

2.38	Schematic representation of the I-SCC process. . . . .	82
2.39	Comparison of results obtained by Ozrin with experimental work done by Walker et al. . . . .	88
2.40	Comparison of the oxygen potential calculated by Piro et al. with experimental data from Walker et al. . . . .	89
2.41	O/M ratio predicted by Piro et al. (line) compared to the values estimated by Walker et al. (points). . . . .	90
2.42	Oxygen potential during in-reactor operation. Calculated by Piro et al. .	91
2.43	Schematic representation of the thermochemical solver ANGE implementation into the fuel performance code ALCYONE. . . . .	93
2.44	TeI <sub>2(g)</sub> at different times during the power ramp simulated by Baurens et al. . . . .	93
3.1	Schematic representation of the power sequence used in the simulation of iodine isotopic evolution. . . . .	100
3.2	Concentrations of iodine isotopes calculated in PRODHEL plotted as a function of time at zero power. The plot starts at the end of base irradiation.	100
3.3	Schematic representation of the power sequence used in the iodine isotopic evolution during the conditioning period. . . . .	101
3.4	Concentrations of iodine isotopes considered in PRODHEL plotted as a function of time during a pre-ramp conditioning period. The plot starts after 3 months at zero power. . . . .	102
3.5	Schematic representation of PR1. The conditioning period lasts until "t0 ramp". The maximum LHR is reached at "t0 HP". Durations of power transients are marked. . . . .	103
3.6	Weight fractions of some FPs calculated with PRODHEL (thick lines) and with CESAR (dashed lines) compared to EPMA measurements (thin lines) after the PR1 test. . . . .	104
3.7	Calculated burnup radial profile of PR1. . . . .	105
3.8	PRODHEL calculations of the integral weight fractions of chemical elements after 1, 3 or 5 years of cooling. . . . .	106
3.9	Deviations from average value in PRODHEL calculations of the integral weight fractions of chemical elements after 1, 3 or 5 years of cooling. . . .	107
3.10	Radial profile of burnup calculated with ALCYONE compared to the estimates deduced from Nd concentration measurements by Walker et al.	108
3.11	PRODHEL calculations of the integral weight fractions of chemical elements compared to ICP-MS measurements from Walker et al. and to CESAR calculations. . . . .	108
3.12	Deviations from the experimental measurements of average weight fractions of FPs calculated by PRODHEL and CESAR. . . . .	109
3.13	PRODHEL calculations of the local atom fractions of chemical elements compared to EPMA measurements from Walker et al. and to CESAR calculations at $r/R_{\text{pellet}}=0.1$ . . . . .	110
3.14	PRODHEL calculations of the local atom fractions of chemical elements compared to EPMA measurements from Walker et al. and to CESAR calculations at $r/R_{\text{pellet}}=0.5$ . . . . .	110
3.15	PRODHEL calculations of the local atom fractions of chemical elements compared to EPMA measurements from Walker et al. and to CESAR calculations at $r/R_{\text{pellet}}=0.8$ . . . . .	110

3.16	PRODHHEL calculations of the local atom fractions of chemical elements compared to EPMA measurements from Walker et al. and to CESAR calculations at $r/R_{\text{pellet}}=0.975$ . . . . .	111
3.17	Calculated radial profile of Cs weight fraction compared to the EPMA measurements from Walker et al. . . . .	111
3.18	Calculated radial profiles of weight fractions of Nd (left figure) and Pu (right figure) compared to the EPMA measurements. . . . .	112
3.19	The original $\text{UO}_{2\pm x}$ model proposed by Lindemer and Besmann compared to the experimental data gathered by Guéneau et al. (symbols). . . . .	121
3.20	Experimental data gathered by Guéneau et al. for $\text{UO}_{2\pm x}$ (symbols) compared to ANGE calculations (lines). . . . .	122
3.21	Calculated oxygen partial pressure in $\text{U}_{1-y}\text{Pu}_y\text{O}_{2\pm x}$ (lines) as a function of O/M, temperature and Pu mole fraction compared to measured values (symbols). . . . .	124
3.22	Calculated oxygen partial pressure in $\text{U}_{1-y}\text{Gd}_y\text{O}_{2\pm x}$ (lines) as a function of O/M, temperature and Gd mole fraction compared to measured values (symbols). . . . .	125
3.23	Calculated oxygen partial pressure in $\text{U}_{1-y}\text{La}_y\text{O}_{2\pm x}$ (lines) as a function of O/M, temperature and La mole fraction compared to measured values (symbols). . . . .	125
3.24	Calculated oxygen partial pressure in $\text{U}_{1-y}\text{Ce}_y\text{O}_{2\pm x}$ (lines) as a function of O/M, temperature and Ce mole fraction compared to measured values (symbols). . . . .	126
3.25	Calculated oxygen partial pressure in $\text{U}_{1-y}\text{Eu}_y\text{O}_{2\pm x}$ (lines) as a function of O/M, temperature and Eu mole fraction compared to measured values (symbols). . . . .	127
3.26	Calculated oxygen partial pressure in $\text{U}_{1-y-z}\text{Zr}_y\text{Ln}_z\text{O}_{2\pm x}$ (lines) as a function of O/M and mole fractions of Zr and Ln (Ln=La, Ce) compared to measured values (symbols). Both experiments and calculations performed at 1250 K. . . . .	128
3.27	Phase stability diagram of chromium in $\text{UO}_2$ . The dashed curves are the chromium iso-solubility curves. The labels in italics are the iso-solubility expressed in %wt Cr. The blue and purple points refer to the power ramps studied by Riglet-Martial. . . . .	129
3.28	Calculated mole fraction of Cr in solid solution (lines) as a function of oxygen partial pressure at different temperatures compared to experimental measurements (symbols). . . . .	130
3.29	Oxygen potential of SIMFUELS at burnups of 5 at% (left figure) and 10 at% (right figure) measured by Une and Oguma (symbols) compared to ANGE calculations (lines). . . . .	132
3.30	Schematic representation of $\text{UO}_2$ lattice when a trivalent FP replaces a U atom after fission. Left figure: perfect $\text{UO}_2$ lattice. Right figure: irradiated fuel. . . . .	133
3.31	Oxygen potential at different burnups temperatures. . . . .	134
3.32	The oxygen potential at 1500 °C at different burnups as a function of the total oxygen concentration. . . . .	135
3.33	Concentrations of volatile species important in SCC as a function of oxygen potential at 2000 °C. Fuels irradiated to 20, 40 and 60 GWd/tHM. Elemental compositions used in the calculations are given in Table 3.17. . . . .	137

3.34	Oxygen potential calculated with ANGE compared to values measured by Une et al. at different radial positions at 750 °C. Standard UO <sub>2</sub> fuel. . . . .	139
3.35	Oxygen potential calculated with ANGE compared to values measured by Une et al. at different radial positions at 750 °C. 2wt%Gd <sub>2</sub> O <sub>3</sub> -doped fuel. . . . .	139
3.36	Calculated oxygen potential compared to experimental measurements from Matzke. Burnup 28.9 GWd/tHM. O/U refers to the initial composition. . . . .	142
3.37	Calculated oxygen potential compared to experimental measurements from Matzke. Burnup 34.5 GWd/tHM. O/U refers to the initial composition. . . . .	142
3.38	Calculated oxygen potential compared to experimental measurements from Matzke. Burnup 58 GWd/tHM. O/U refers to the initial composition. . . . .	143
3.39	Calculated oxygen potential compared to experimental measurements from Matzke. Burnup 75 GWd/tHM. O/U refers to the initial composition. . . . .	143
3.40	Calculated oxygen potential compared to experimental measurements from Matzke. Burnup 200 GWd/tHM. O/U refers to the initial composition. . . . .	144
3.41	Calculated oxygen potential compared to experimental measurements from the high burnup samples studied by Matzke. . . . .	145
3.42	All the experimental data from Figures 3.36-3.40. . . . .	146
3.43	Calculated oxygen potential at different radial positions as a function of temperature compared to the values measured by Walker et al. . . . .	147
3.44	Calculated oxygen potential at different radial positions compared to the oxygen potential corresponding to three redox buffers. . . . .	148
3.45	Calculated radial profiles of oxygen potential at 750 °C and 1000 °C compared to the experimental measurements. The green line shows the oxygen potential at maximum LHR during the last irradiation cycle. . . . .	149
3.46	The O/M ratio at maximum LHR during the last irradiation cycle (line) compared to the values estimated by Walker et al. . . . .	150
4.1	Visualization of the 1D discretization used in the OXIREN model. . . . .	154
4.2	Example of the 1D discretization used in the OXIREN model. . . . .	155
4.3	O/M profiles radial calculated with OXIREN for different heats of transport. The red curve is the temperature profile. . . . .	156
4.4	Example of OXIREN calculations with a nonlinear heat of transport. . . . .	157
4.5	O/M radial profiles calculated with OXIREN (thick black curve) and OXITRAN at different times. . . . .	161
4.6	$\tilde{D}_O dt/dr^2$ for different time steps. . . . .	162
4.7	O/M radial profiles calculated with OXIREN (thick black curve) and OXITRAN at different times with a nonlinear heat of transport. . . . .	163
4.8	Examples of 2D and 3D meshes used in Cast3M. . . . .	167
4.9	Temperatures in 2D and 3D calculated with Cast3M. . . . .	167
4.10	O/M in 2D and 3D calculated with Cast3M. . . . .	168
4.11	1D, 2D and 3D O/M radial profiles at different times. . . . .	169
4.12	FE mesh of the fuel rod fragment simulated by Ramirez et al. . . . .	171
4.13	Results of the COMSOL Multiphysics simulation. Adapted from Ramirez. . . . .	172
4.14	Diffusion coefficient proposed by Ramirez et al. . . . .	173
4.15	Lewis number as a function of the stoichiometry deviation at different temperatures. Adapted from Ramirez et al. . . . .	174
4.16	2D FE mesh of the fuel rod fragment calculation performed with Cast3M. . . . .	174

4.17	Schematic representation of iterative loops called in the Cast3M script. . . . .	175
4.18	Simulated time and time step evolutions as a function of the iteration number. . . . .	176
4.19	COMSOL results from Figure 4.13 (in black) compared to the results computed with Cast3M (in red). . . . .	177
4.20	Temperature radial profiles at different times calculated with Cast3M. . . . .	177
4.21	Stoichiometry deviation radial profiles at different times calculated with Cast3M. . . . .	178
4.22	3D FE mesh of the fuel rod fragment calculation performed with Cast3M. . . . .	178
4.23	Schematic representation of the power ramp tests. The part until "t0 HP" is common for all the ramps. The solid line starting at "t0 HP" is for PR2, PR3 and PR4 and the dashed one is for PR1. Three power transients are marked as T1, T2 and T3. . . . .	180
4.24	EPMA measurements of the weight fraction of Cr in solid solution after PR1. . . . .	181
4.25	EPMA measurements of Cr weight fraction in solid solution after PR2. The red curve is the calculated temperature profile. Blue circles show the average local Cr concentration. . . . .	182
4.26	EPMA measurements of Cr weight fraction in solid solution after PR3. The red curve is the calculated temperature profile. Blue circles show the average local Cr concentration. . . . .	182
4.27	EPMA measurements of Cr weight fraction in solid solution after PR4. The red curve is the calculated temperature profile. Blue circles show the average local Cr concentration. . . . .	183
4.28	X-ray maps of Mo, Cr and O at the pellet center after power ramp PR2. . . . .	183
4.29	Oxygen potential radial profiles deduced from the Cr solubility model. . . . .	186
4.30	Burnup radial profiles of PR2, PR3 and PR4 calculated with ALCYONE. . . . .	187
4.31	O/M radial profiles from ANGE calculations. . . . .	188
4.32	Initial O/M (dashed lines), steady-state O/M calculated with OXIREN (solid lines) compared to the O/M calculated with ANGE (points). PR2 is in black and PR3 in blue. . . . .	190
4.33	Heat of transport in UO <sub>2</sub> fuels irradiated up to different burnups as a function of the O/M ratio compared to the model proposed by Janek, based on a reassessment of Sari's measures. . . . .	192
4.34	Frenkel defects concentration UO <sub>2±x</sub> calculated from Gibbs energy of formation of Frenkel defects. Adapted from Berthier et al. . . . .	194
4.35	As Figure 4.34 but based on the CALPHAD method. . . . .	194
4.36	Self-diffusion coefficient based on the work of Berthier. . . . .	196
4.37	Self-diffusion coefficient based on the work of Berthier compared to experimental data. Hyperstoichiometric domain. . . . .	196
4.38	Self-diffusion coefficient based on the work of Berthier compared to experimental data. Hypostoichiometric domain. . . . .	197
4.39	Oxygen partial pressure at 630 K as a function of the O/M ratio. Calculated with THERMOCALC. . . . .	198
4.40	Oxygen partial pressure as a function of stoichiometry deviation. Dashed lines–THERMOCALC, solid lines–fitted values. . . . .	198
4.41	Oxygen partial pressure as a function of stoichiometry deviation. Dashed lines–THERMOCALC, solid lines–fitted values. . . . .	200

4.42	Corrected diffusion coefficient based on the work of Berthinier and the diffusion coefficient proposed by Lassmann. . . . .	201
4.43	Corrected diffusion coefficient based on the work of Berthinier validated against experimental data and the model proposed by Breitung. . . . .	202
4.44	Oxygen redistribution calculated with different chemical oxygen diffusion coefficients compared to the steady state redistribution calculated with OXIREL. . . . .	203
5.1	Schematic representation of iterative loops and models called during a simulation carried out with the fuel performance code ALCYONE. . . . .	207
5.2	Schematic representation of thermochemical calculations with (bottom part) and without (top part) imposing the O/M ratio. Colors of boxes are consistent with Figure 5.1. . . . .	209
5.3	Oxygen concentration as a function of the O/M ratio at different temperatures. Left figure—fresh fuel, right figure—fuel irradiated to 35 GWd/tHM. Calculations done with ANGE. . . . .	211
5.4	Atom fraction of the representative elements as a function of burnup. Calculated with PRODHEL. . . . .	212
5.5	Proportionality factor as a function of burnup. Points are the values calculated with ANGE and the line is a linear approximation. . . . .	213
5.6	Oxygen concentrations (left figure) and O/M ratios (right figure) before and after oxygen redistribution calculated for PR2 and PR3. . . . .	214
5.7	The proportionality factor $\alpha$ of PR2 and PR3 at the pellet center. The lines are the average values for $r/R_{\text{pellet}} < 0.2$ . . . . .	215
5.8	Radial profile of total oxygen content calculated at the end of the holding period of PR2 (solid curve) and of the initial oxygen concentration (dashed curve). . . . .	216
5.9	O/M ratios obtained in the calculations with (black curve) and without (red curve) imposing the O/M ratio. . . . .	217
5.10	Oxygen potential radial profiles obtained in the calculations with (black curve) and without (red curve) imposing the O/M ratio. . . . .	217
5.11	Schematic representation of the power ramp test performed by Adamson et al. The part until "t0 ramp" is the conditioning period. The holding period starts at "t0 HP" and lasts to "t0 HP+12h". Power transients are marked as T1, T2 and T3. . . . .	220
5.12	Calculated profiles of temperature and burnup. The red dashed line corresponds to the average burnup. . . . .	221
5.13	Oxygen potentials calculated with (solid curves) and without (dashed curves) oxygen redistribution for different initial O/U ratios. Black triangles correspond to the experimental measurements from Adamson et al. . . . .	222
5.14	O/M ratios with and without oxygen transport calculated at the end of the holding period. . . . .	223
5.15	Calculated temperatures [°C] in the fuel fragment at different times during the power ramp PR2. . . . .	224
5.16	Calculated O/M ratios [-] in the fuel fragment at different times during the power ramp PR2. . . . .	225
5.17	Calculated O/M radial profiles along the mid-pellet plane of the pellet fragment at different times during PR2. . . . .	225

5.18	Calculated oxygen potentials [kJ/mol O <sub>2</sub> ] in the fuel fragment at different times during power ramp PR2. . . . .	226
5.19	Calculated radial profiles of oxygen potential $\Delta G_{O_2}$ along the mid-pellet radius at different times during power ramp PR2. The red dashed line shows the oxygen potential given by the Mo <sub>(s)</sub> /MoO <sub>2(s)</sub> redox system. The dotted lines give the oxygen potential associated with the Cr <sub>2</sub> O <sub>3(ss)</sub> /Cr <sub>(s)</sub> redox system: top line for a Cr-dopant completely dissolved in UO <sub>2</sub> (0.14 wt%, see Figure 5.20, Cr <sub>2</sub> O <sub>3(ss)</sub> t0 HP), bottom line corresponding to a residual Cr-solubility of 0.01% (see Figure 5.20, Cr <sub>2</sub> O <sub>3(ss)</sub> t0 HP+12). . . . .	227
5.20	Calculated Cr weight fraction evolution during the holding period compared to EPMA measurements after PR1 and PR2. . . . .	228
5.21	Calculated Cr <sub>2</sub> O <sub>3(ss)</sub> (upper plots) and Cr <sub>(s)</sub> (lower plots) concentrations [mol/mol UO <sub>2</sub> ] at different times during power ramp PR2. . . . .	229
5.22	Calculated concentrations of MoO <sub>2(s)</sub> (top figures), Mo <sub>(s)</sub> (middle figures) and Cs <sub>2</sub> MoO <sub>4(s,l)</sub> (bottom figures) at different times during power ramp PR2. . . . .	230
5.23	Calculated molybdenum oxides MoO <sub>x(s,l)</sub> and metallic molybdenum Mo <sub>(s)</sub> weight fraction evolution during the HP of power ramp PR1 compared to EPMA measurements after power ramps PR1 and PR2. PR1 rodlet has a lower burnup than PR2 rodlet so the Mo weight fraction is lower on average. . . . .	231
5.24	Calculated ZrO <sub>2(ss)</sub> and BaZrO <sub>3(s)</sub> concentrations compared to the EPMA measurement of Zr weight fraction after power ramp PR2. . . . .	231
5.25	Calculated release of Xe (top), Cs (middle) and I (bottom) at different times during the power ramp PR2. Units-% of initial inventory. . . . .	232
5.26	Calculated total (dissolved within grains, in intra- and inter-granular bubbles and in inter-granular pores) Xe weight fraction at the beginning and the end of the holding period of power ramp PR2 compared to EPMA and SIMS measurements. . . . .	233
5.27	Calculated CsI <sub>(g)</sub> , I <sub>(g)</sub> +2I <sub>2(g)</sub> and TeI <sub>2(g)</sub> concentrations in the fuel fragment at different times during power ramp PR2. . . . .	234
5.28	Calculated 2Cs <sub>2</sub> MoO <sub>4(s,l)</sub> and Cs <sub>(g)</sub> +2Cs <sub>2(g)</sub> concentrations in the fuel fragment at different times during power ramp PR2. . . . .	236
5.29	Calculated weight fractions of cesium at the beginning and at the end of the HP of power ramp PR2 compared to EPMA measurements after power ramps PR1 and PR2. . . . .	237
5.30	Calculated release of Cs, I and Xe during power ramp PR2. Solid lines refer to the simulation with oxygen transport, dashed lines refer to the simulation without oxygen transport (t=0 corresponds the beginning of the holding period, "t0"). . . . .	238
5.31	Schematic representation of PR5. . . . .	240
5.32	Temperature [°C] calculated at different times during PR5. . . . .	241
5.33	Hydrostatic pressure [bar] calculated at different times during PR5. . . . .	241
5.34	O/M ratio calculated at different times during PR5. . . . .	242
5.35	Oxygen potential calculated at different moments of PR5. . . . .	243
5.36	Release of Xe at different times of PR5. Units-% of initial inventory. . . . .	244
5.37	Release of Cs (top), I (middle) and Te (bottom) at different times of PR5. Units-% of initial inventory. . . . .	245

5.38	Calculated burnup radial profile along the mid-pellet plane compared to the experimental measurements. . . . .	246
5.39	Calculated concentrations of Xe, Cs, I and Te (left axis) compared to SIMS measurements of the relative concentrations (right axis). The measurement uncertainty is around 10%. Both measurements and calculations done along the mid-pellet plane. . . . .	247
5.40	Comparison of the calculated radial profiles of Xe, Cs, I and Te to the SIMS measurements along the mid-pellet plane at the end of PR5. The experimental error is estimated to be 10%. MP-Mid Pellet, IP-Inter Pellet.	248
5.41	Comparison of the calculated axial profiles of Cs, I and Te to the SIMS measurements at $r/R=0.1$ at the end of PR5. The experimental error is estimated to be 10%. . . . .	250
5.42	Concentration [mol/mol $UO_2$ ] of $I_{(g)}+2I_{2(g)}$ (upper figures) and $TeI_{2(g)}$ (lower figures) at different moments of PR5. . . . .	251
5.43	Speciation of iodine at "t0 HP" (left figure) and at "t0 HP End" (right figure) of PR5. Calculated along the mid-pellet plane. . . . .	252
5.44	Concentrations [mol/mol $UO_2$ ] of $Cs_2MoO_{4(s,l)}$ (top), $CsI_{(s,l)}$ (middle) and $CsI_{(g)}$ at different moments of PR5. . . . .	253
5.45	Concentration [mol/mol $UO_2$ ] of $Cs_{(g)}+2Cs_{2(g)}$ at different times during PR5. Note the different scales. . . . .	254
5.46	Speciation of cesium at "t0 HP" (left figure) and at "t0 HP End" (right figure) of PR5. Calculated along the mid-pellet plane. . . . .	255
5.47	Concentrations [mol/mol $UO_2$ ] $Te_{x(g)}$ (top), $BaTe_{(s)}$ (middle) and $Cs_2Te_{(s,l)}$ (bottom) at different mtimes during PR5. $Te_x$ stands for different forms of gaseous Te ( $1 \leq x \leq 5$ ) . . . . .	256
5.48	Speciation of tellurium at "t0 HP" (left figure) and at "t0 HP End" (right figure) of PR5. Calculated along the mid-pellet plane. . . . .	257
5.49	Remaining over creation ratio of Te calculated with and without oxygen transport compared to the SIMS measurements along the mid-pellet plane at the end of PR5. The experimental error is estimated to be 10%. . . . .	258
5.50	Calculated pellet radial crack opening at different times during PR5. Upper graphs give the mid-pellet plane. Lower graphs the inter-pellet plane. Isovalues give the distribution of crack opening on the fracture surface. . . . .	260
5.51	Time evolution of the maximum hoop stress at IP level (MPa), of dish filling (%), of the cladding surface concentration of 'reactive' iodine (mg/cm <sup>2</sup> ) and of the 'reactive iodine' partial pressure (Pa) during PR5. 'Reactive' iodine takes into account the iodine species $TeI_{2(g)}$ , $I_{(g)}$ and $I_{2(g)}$ . Hoop stress at IP level (Mpa), LHR (W/cm), dish filling (%) and 'Reactive' iodine partial pressure (Pa) refer to the left vertical axis. 'Reactive' iodine clad surface concentration refers to the right vertical axis. . . . .	261
5.52	Cladding strain at the triple point (black line) and the zirconia layer crack threshold (red line) of PR5. . . . .	263
5.53	Cladding temperature at the triple point during PR5. . . . .	264
5.54	Cladding crack depth calculated at the triple point during PR5. . . . .	264
5.55	Cladding crack depth calculated at the triple point during PR5 with different initial crack depths. . . . .	265
5.56	Cladding crack depth calculated at the triple point during PR5. Different curves correspond to different activation times for the I-SCC model. . . . .	266

---

5.57	Solid lines correspond to the iodine partial pressure taking into account interactions of the "reactive" iodine with the free cesium and radiolysis of CsI. Dotted lines correspond to the iodine partial pressure of the 'reactive' iodine and radiolysis of CsI. Different colors correspond to different fractions of CsI that undergo decomposition by radiolysis. . . . .	267
5.58	Cladding crack depth calculated at the triple point during PR5. . . . .	268
5.59	As Figure 5.54 but with the vertical, dashed line marking the pellet radial crack closure at "t0 HP"-24 s. . . . .	269



# List of Tables

1.1	Cumulative fission product yield of chosen isotopes for thermal fission of $^{235}\text{U}$ and $^{239}\text{Pu}$ . . . . .	7
1.2	Examples of decay chains for $^{99}\text{Y}$ and $^{135}\text{I}$ . . . . .	8
1.3	Elements considered in CESAR, representative elements and their affiliations to families. Correlations valid up to 10 at% except for Pu (valid up to 5.4 at%). . . . .	10
2.1	Oxides that may be found in the solid solution phase of irradiated $\text{UO}_2$ . . . . .	31
2.2	Thermodynamic data of selected fission products. Adapted from Lewis et al. . . . .	32
2.3	Coefficients of Equation 2.6, necessary to prepare curves from Figure 2.9. . . . .	38
2.4	Parameters for oxygen diffusion in $\text{UO}_{2\pm x}$ . . . . .	61
3.1	Elements considered in PRODHEL, representative elements and their affiliations to families. . . . .	98
3.2	Isotopes of iodine considered in PRODHEL and their half-lives. . . . .	99
3.3	Parameters used in the PRODHEL stand-alone simulation for the iodine isotopic composition. . . . .	100
3.4	Base irradiation history of the rodlet PR1. . . . .	103
3.5	Main characteristics of the simulated power ramp PR1. . . . .	103
3.6	Main characteristics of the fuel rod studied by Walker et al. Adapted from Walker et al. . . . .	105
3.7	Irradiation history of the fuel rod studied by Walker et al. Adapted from Walker et al. . . . .	106
3.8	Species and parameters of the Gibbs energy of formation used in the original $\text{UO}_{2\pm x}$ model proposed by Lindemer and Besmann. . . . .	120
3.9	Species and parameters of the Gibbs energy of formation used in this work to describe the U-O system. . . . .	121
3.10	Species and parameters of the Gibbs energy of formation used to describe the Pu-O system. . . . .	122
3.11	Species and parameters of the Gibbs energy of formation used to describe the U-Re-O systems ( $Re = Gd, La$ ). . . . .	124
3.12	Species and parameters of the Gibbs energy of formation used to describe the U-Ce-O system. . . . .	126
3.13	Species and parameters used to describe the U-Eu-O system. . . . .	127
3.14	Species and parameters for the Gibbs energy of formation used to describe the U-Zr-O system. . . . .	128
3.15	Species and parameters for the Gibbs energy of formation used to describe the U-Cr-O system. . . . .	130

3.16	Compositions of the SIMFUEL samples. Adapted from Une and Oguma.	131
3.17	Elemental compositions of irradiated fuels used in ANGE calculations.	134
3.18	Elemental compositions used in ANGE calculations for modeling Une's experiment.	138
3.19	Details of the fuel samples studied by Matzke.	140
3.20	Elemental compositions (in mol/mol UO <sub>2</sub> ) used in ANGE calculations for modeling Matzke's experiments.	141
3.21	Elemental compositions used in ANGE calculations for modeling Matzke's experiments.	145
4.1	Summary of the material properties used by Ramirez et al.	170
4.2	Main characteristics of the power ramp tests on Cr-doped fuels.	180
4.3	Main characteristics of the base irradiations preceding tests PR2, PR3 and PR4.	185
4.4	Elemental compositions used in ANGE calculations for modeling of PR2, PR3 and PR4.	188
4.5	Values of enthalpy and entropy of formation of Frenkel defects proposed by Berthinier et al.	193
4.6	Parameters of the self-diffusion coefficient of oxygen proposed by Berthinier et al.	195
4.7	Coefficients of the functions describing oxygen partial pressure.	199
5.1	Parameters used in the PRODHEL stand-alone simulation for the proportionality factor.	212
5.2	Main characteristics of the power ramped fuel reported by Adamson et al.	219
5.3	Additionally assumed characteristics needed to carry out the simulation of Adamson's experiment.	220
5.4	Main characteristics of the fuel power ramped in PR5.	239
5.5	Main characteristics of PR5.	240

# Acronyms

**ANGE** AdvaNced Gibbs Energy minimizer

**BWR** Boiling Water Reactor

**CALPHAD** CALculation of PHAse Diagrams

**CANDU** CANadian Deuterium Uranium

**CANLUB** CANdu LUBricant

**CEA** Commissariat à l'Énergie Atomique et aux énergies alternatives

**CFL** Courant-Friedrichs-Lewy condition

**CPU** Central Processing Unit

**EDF** Électricité De France

**EPMA** Electron Probe Micro-Analyzer

**EPR** European Pressurized Reactor

**ERPO** Extended Reduced Power Operations

**FE** Finite Element

**FEM** Finite Element Method

**FGR** Fission Gas Release

**FP** Fission Product

**FVM** Finite Volume Method

**HP** Holding Period

**HWR** Heavy Water Reactor

**ICP-MS** Inductively Coupled Plasma-Mass Spectrometry

**IP** Inter-Pellet

- I-SCC** Iodine induced Stress Corrosion Cracking
- LHR** Linear Heat Rate
- LWR** Light Water Reactor
- MFPR** Module for Fission Products Release
- MP** Mid-Pellet
- MOX** Mixed OXide fuel
- MTR** Materials Testing Reactor
- O/M** Oxygen over Metal ratio
- O/U** Oxygen over Uranium ratio
- PCI** Pellet-Cladding Interaction
- PCMI** Pellet-Cladding Mechanical Interaction
- PPN** Peak Power Node
- PWR** Pressurized Water Reactor
- RMC** Royal Military College of Canada
- RTL** Ramp Terminal Level
- SCC** Stress Corrosion Cracking
- SCIP** Studsvik Cladding Integrity Program
- SEM** Scanning Electron Microscopy
- SFR** Sodium Fast Reactor
- SIMS** Secondary Ion Mass Spectrometry
- SIMFUEL** SIMulated spent FUEL
- TAF-ID** Thermodynamics of Advanced Fuels–International Database

## Acknowledgements

Firstly, I would like to express my deep gratitude to Jérôme Sercombe and Chantal Riglet-Martial, my CEA research supervisors, for their patient guidance, enthusiastic encouragement and useful critiques of this research work. They were always ready to help me and their doors were always open. I would also like to say thank you to Fabienne Delage, the head of my laboratory, for her support and motivating words.

Secondly, I would like to acknowledge my thesis directors Marion Frégonèse and Patrice Chantrenne for their fresh point of view on my thesis. Their non-nuclear background and properly asked questions helped me to make my thesis more comprehensive for everyone.

I would like to thank my family for supporting me morally throughout writing this thesis and my life in general.

Last but not the least, I would like to thank Margot and my friends that I met during my stay in France. They provided relaxing distraction to rest my mind outside of my research.



# Chapter 1

## Introduction on nuclear fuel

### 1.1 Nuclear fuel behavior

#### 1.1.1 General aspects of nuclear fuel

Currently, there are worldwide 450 nuclear reactors producing almost 11% of the world's electricity. Next 60 reactors are under construction [1], which means that the nuclear industry plays and will play an important role in the electric energy generation sector. Contrary to the electricity produced from fossil fuels, the nuclear industry is characterized by low greenhouse emission and high availability of the fuel. Despite that, it still has many opponents. Lack of understanding of processes occurring inside the reactor, general fear of radiation and nuclear accidents are problems that the nuclear industry needs to face every day. To avoid further accidents, a lot of efforts have been put to improve safety standards and to fully understand and explain phenomena accompanying operation of nuclear reactors.

Source of energy in nuclear reactors is nuclear fission. This reaction occurs when a neutron splits a nucleus of a heavy atom and produces fission fragments (usually 2, rarely more) and new neutrons. One thermal fission of  $^{235}\text{U}$  liberates  $\sim 190$  MeV of energy, most in the form of kinetic energy of Fission Products (FPs).

A continuous and self-sustaining fission reaction is called a chain reaction. To obtain this reaction, certain conditions have to be met. One of them is a sufficient number of neutrons in the system. For this reason, Light Water Reactors (LWR) use fuel enriched in fissile isotopes that are more likely to be fissioned. These isotopes are usually  $^{235}\text{U}$  and  $^{239}\text{Pu}$ .

Products of nuclear reactions are radioactive and dangerous for the environment. During the whole operation of a nuclear reactor they should stay inside the fuel rod. Fuel rods are elements of fuel assemblies. For example, the European Pressurized Reactor (EPR)

will have 241 assemblies. Each one will contain 265 fuel rods. The active length of the assembly is 4.2 m whereas the total length is 4.8 m [2]. A fuel assembly spends between 2 to 6 fuel cycles inside the reactor. Duration of a cycle is 12-24 months. It depends on the initial enrichment in fissile isotopes, doped burnable poisons and the localization of the assembly in the core [3]. A schematic representation of the fuel pellet–fuel rod–fuel assembly is shown in Figure 1.1.

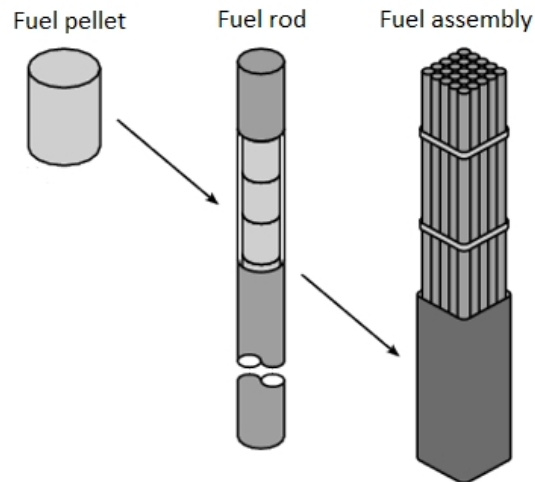


Figure 1.1: Schematic representation of a fuel pellet, a fuel rod and an assembly [4].

In a fuel rod, one may distinguish 3 main sections (Figure 1.2):

- the fuel
- the gap
- the cladding

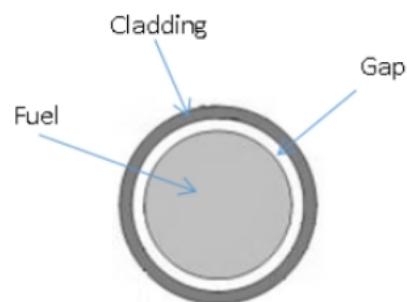


Figure 1.2: A cross section of a fuel rod of a light water reactor.

Fuel of LWRs has a shape of cylindrical pellets. Diameter of these pellets is around 8 mm whereas the height is around 10-14 mm. Chamfers and dishes (central voids at

the pellet ends) are usual to ease the introduction in the cladding and to provide extra volume. Pellets can be made of uranium dioxide ( $\text{UO}_2$ ) or Mixed OXides of uranium and plutonium (MOX). It is possible to incorporate dopants like oxides of gadolinium or chromium. Addition of these species has an impact on reactivity and grain growth respectively.

Gap separates fuel from the cladding at the beginning of the first fuel cycle. The role of the gap is to facilitate fuel fabrication and to make space for swelling fuel. During irradiation, nuclear fuel swells and changes its shape. This leads to the closure of the gap. It generally occurs after 2 years of irradiation [5]. In most cases, the initial gap is filled with helium (pressure around 30 bars) because of its chemical neutrality and good thermal conductivity. The thickness of a gap is commonly below 0.1 mm. Too thick gap would work as a thermal insulator.

Cladding is the barrier separating radioactive fuel from the primary circuit of the power plant. Currently, most of the alloys used as cladding are based on zirconium. These materials have good chemical and mechanical properties that allow standing even harsh conditions (high thermal gradients, mechanical stresses and corrosion). Moreover, zirconium is almost transparent to neutrons. The thickness of the cladding in French Pressurized Water Reactors (PWR) is  $\sim 0.57$  mm [2].

Heat generated in nuclear fuel is used to heat up the coolant, which is water in PWRs. In consequence, very high temperature gradients can be found within a fuel pellet, see Figure 1.3. The temperature difference between the center and the periphery of a fuel pellet is around 700 K and can exceed 1500 K in case of power transients.

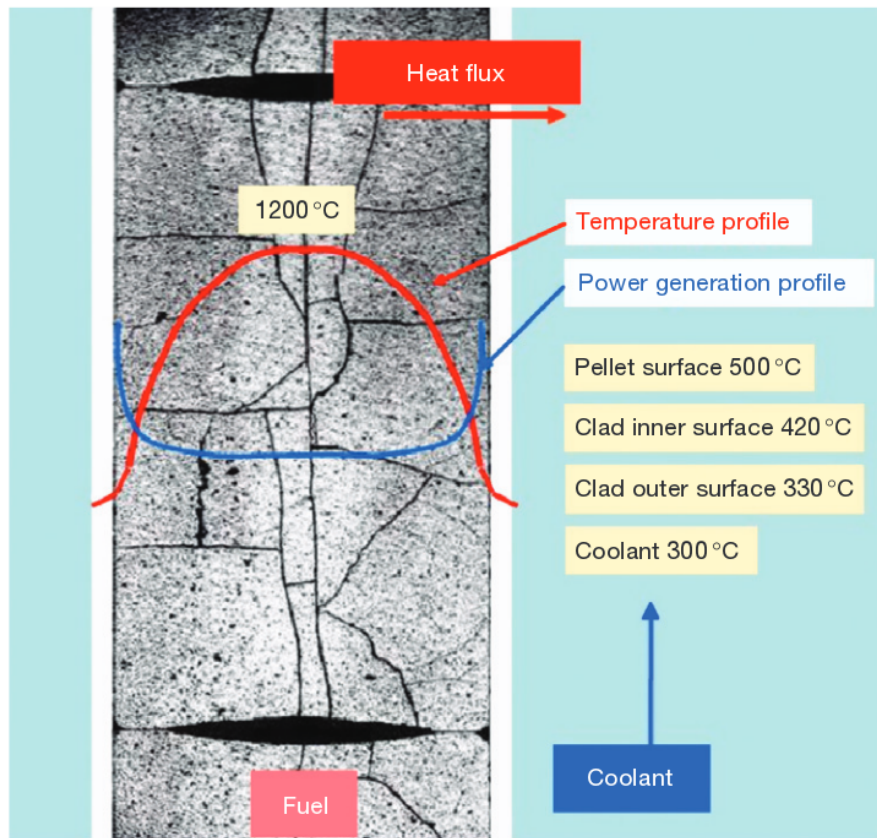


Figure 1.3: "Temperature profile in light water reactor fuel during base irradiation." Adapted from Baron and Hallstadius [3].

Hot water leaves the reactor core and is cooled down in the steam generator, which is a heat exchanger. Cold water is pumped back to the reactor core, which closes the circuit called the primary loop. The secondary loop starts in the steam generator where the heat transferred from the primary loop is used to generate steam that drives the turbine, cools down, condensates in the condenser and it is pumped back to the steam generator. The turbine is connected to the electric generator that produces electricity. A schematic representation of a PWR power plant is shown in Figure 1.4.

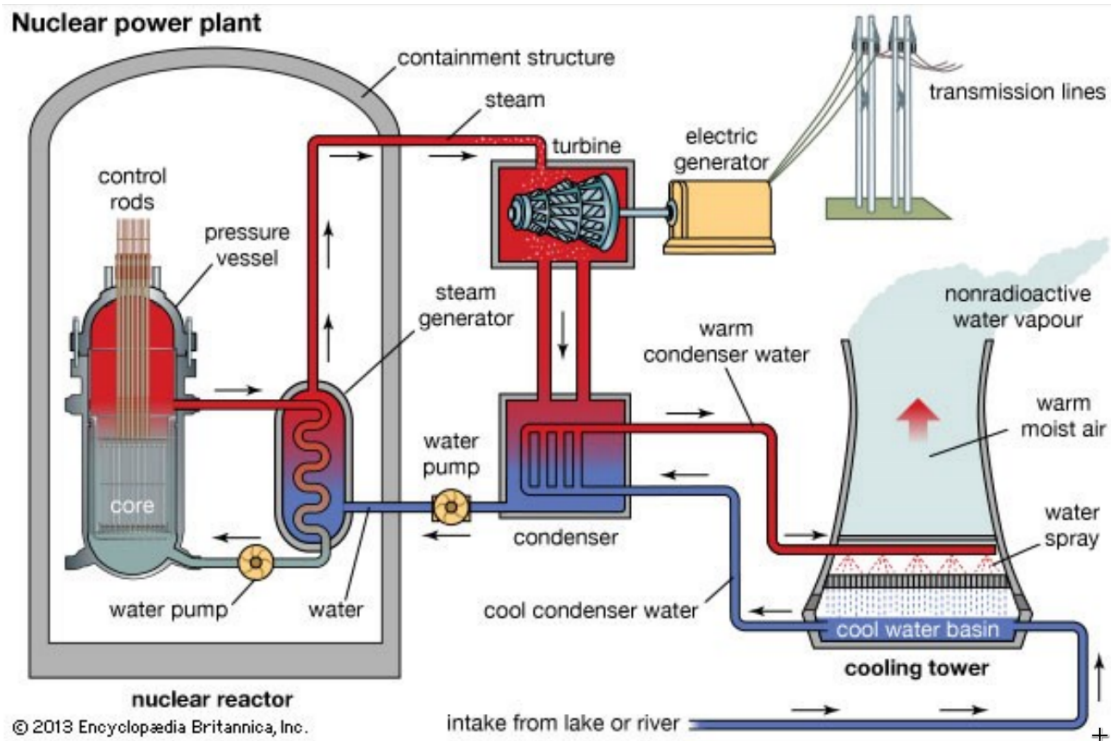


Figure 1.4: Schematic representation of a PWR nuclear power plant. Adapted from [6].

### 1.1.2 Fission Products

The elemental composition of nuclear fuel changes with irradiation. The reaction of nuclear fission splits a heavy nucleus into light ones and releases energy. The parameter describing the amount of energy released from nuclear fuel is called burnup. There are 2 main units in which burnup can be expressed:

- %FIMA (at%) – Fission per Initial Metal Atom
- GWd/tHM – GigaWatt-Days per Ton of Heavy Metal

The relation between the two units is approximately:  $1 \text{ GWd/tHM} = 0.10884 \text{ at\%}$  [3]. Modern nuclear reactors are designed to reach over 60 GWd/tHM of average discharged assembly. Values of burnup available in literature refer usually to average values of burnup of fuel pellets, rods or even fuel assemblies. At the reactor scale, the average burnup of the fuel element increases the most rapidly at the center of the core (the highest flux of neutrons). At the fuel pellet scale, burnup is strongly dependent on the radial position. Burnup estimations are based on the neodymium concentration, one of the fission products, because neodymium is immobile in  $\text{UO}_2$ . Figure 1.5 presents the measured values of neodymium and the corresponding values of burnup in a sample of

average burnup 102 GWd/tHM. As can be seen, the burnup rapidly increases near the periphery of the pellet. Increment comes from the high concentration of fissile plutonium in that region. Source of plutonium is the reaction of resonance neutron capture by the main component of the fuel which is  $^{238}\text{U}$  [7].

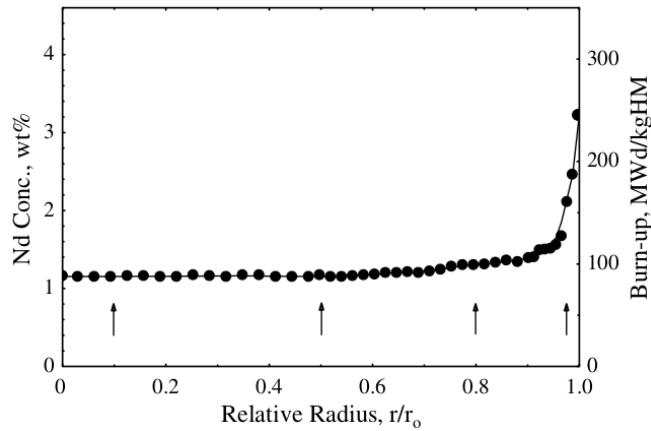


Figure 1.5: Weight fraction of neodymium (left axis) and burnup (right axis) as a function of the relative radius. Measurements come from a  $\text{UO}_2$  sample with a very high average burnup of 102 GWd/tHM. Adapted from Walker et al. [7].

Nuclear fission produces a large number of isotopes. It is important to know the exact FP yields. Some fission products release delayed neutrons that allow controlling the reactor. Few fission products are poisons [8]. To determine the maximum duration of the fuel cycle, one needs to take into account buildup of poisons [3]. Next important factor associated with fission products is decay heat generation. Most of the FPs are unstable isotopes that undergo series of decays. Short-lived FPs along with actinides are responsible for very high residual heat after shutdown of the reactor. Spent fuel has to be cooled for a few years in pools near reactors before moving to reprocessing plants for spent  $\text{UO}_2$  fuels in case of the French fuel cycle strategy.

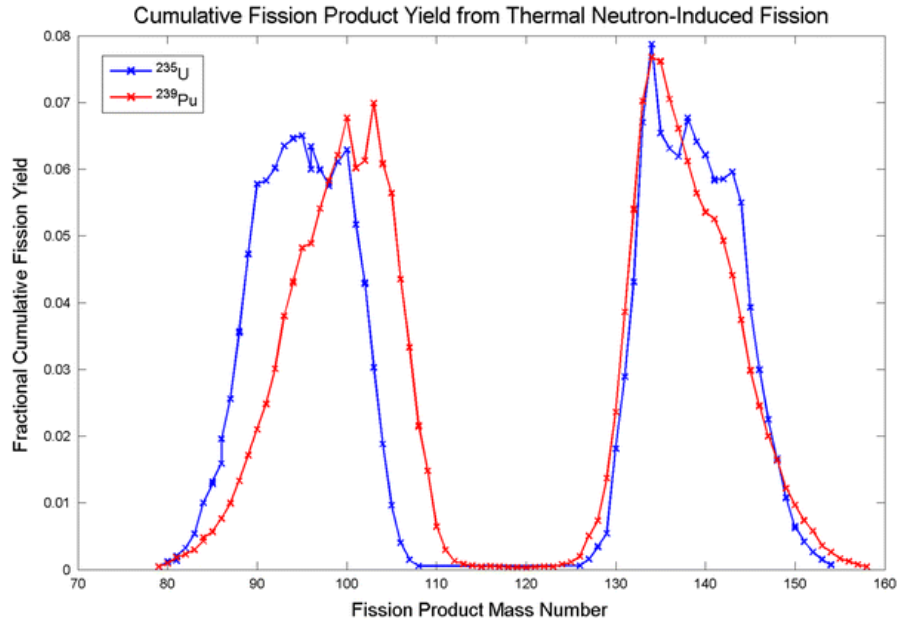


Figure 1.6: Fission product yields of  $^{235}\text{U}$  and  $^{239}\text{Pu}$  for thermal neutrons. Horizontal axis expresses the mass number and the vertical one presents the fractional cumulative fission yield. Adapted from Dayman et al. [9]

Fission product yields depend on the isotope and neutron energy. They form two picks visible in Figure 1.6. In case of  $^{235}\text{U}$ , the picks correspond to  $^{95}\text{Zr}$  (left pick) and  $^{135}\text{Xe}$  (right pick). Comparison of FP yields of  $^{235}\text{U}$  and  $^{239}\text{Pu}$  is shown in Table 1.1.

Table 1.1: Cumulative fission product yield of chosen isotopes for thermal fission of  $^{235}\text{U}$  and  $^{239}\text{Pu}$  [10].

$^{235}\text{U}$		$^{239}\text{Pu}$	
Yield (%)	Isotope	Yield (%)	Isotope
6.502	$^{95}\text{Zr}$	4.949	$^{95}\text{Zr}$
6.498	$^{95}\text{Nb}$	4.946	$^{95}\text{Nb}$
6.132	$^{99}\text{Mo}$	6.185	$^{99}\text{Mo}$
6.59	$^{133}\text{I}$	6.97	$^{133}\text{I}$
6.39	$^{135}\text{I}$	6.33	$^{135}\text{I}$
6.6	$^{133}\text{Xe}$	6.99	$^{133}\text{Xe}$
6.61	$^{135}\text{Xe}$	7.36	$^{135}\text{Xe}$
6.6221	$^{137}\text{Cs}$	6.588	$^{137}\text{Cs}$
6.315	$^{140}\text{La}$	5.333	$^{140}\text{La}$
6.314	$^{140}\text{Ba}$	5.322	$^{140}\text{Ba}$

Heavy nuclei like uranium or plutonium have greater ratio of neutrons to protons than lighter, stable isotopes. Due to this fact, FPs often have excess of neutrons. In order to reach stability, they decay by  $\beta^-$  emission (electron).

$$n \rightarrow p^+ + e^- + \bar{\nu}_e \quad (1.1)$$

In  $\beta^-$  decay, a neutron turns into a proton  $p^+$ , an electron  $e^-$  and an anti-neutrino  $\bar{\nu}_e$ . FPs undergo these decays until they turn into a stable isotope. Table 1.2 presents examples of  $\beta^-$  decay chains and half-life times (loss of half of the initial quantity).

Table 1.2: Examples of decay chains for  $^{99}\text{Y}$  and  $^{135}\text{I}$

$^{99}\text{Y} \rightarrow ^{99}\text{Mo}$

Nuclide	Half-life
$^{99}\text{Y}$	1.47 s
$^{99}\text{Zr}$	2.1 s
$^{99m}\text{Nb}$	2.6 min
$^{99}\text{Nb}$	15 s
$^{99m2}\text{Mo}$	0.76 $\mu\text{s}$
$^{99m1}\text{Mo}$	15.5 $\mu\text{s}$
$^{99}\text{Mo}$	2.75 d

$^{135}\text{I} \rightarrow ^{135}\text{Ba}$

Nuclide	Half-life
$^{135}\text{I}$	6.57 h
$^{135}\text{Xe}$	9.14 h
$^{135}\text{Cs}$	2.3E+6 y
$^{135}\text{Ba}$	stable

Isotopes present in irradiated fuel have various half-life times. It can vary from seconds to millions of years. Due to nuclear reactions, the chemical composition of irradiated fuel varies with time even outside the reactor. Fraction of short-lived isotopes decreases at the expense of long-lived and stable isotopes. A very detailed isotopic inventory of irradiated fuel can be calculated with neutron transport codes. Figure 1.7 presents an example of the evolution of fission and activation (neutron capture) products in the fuel pellet as a function of burnup calculated with the code ORIGEN-S [11].

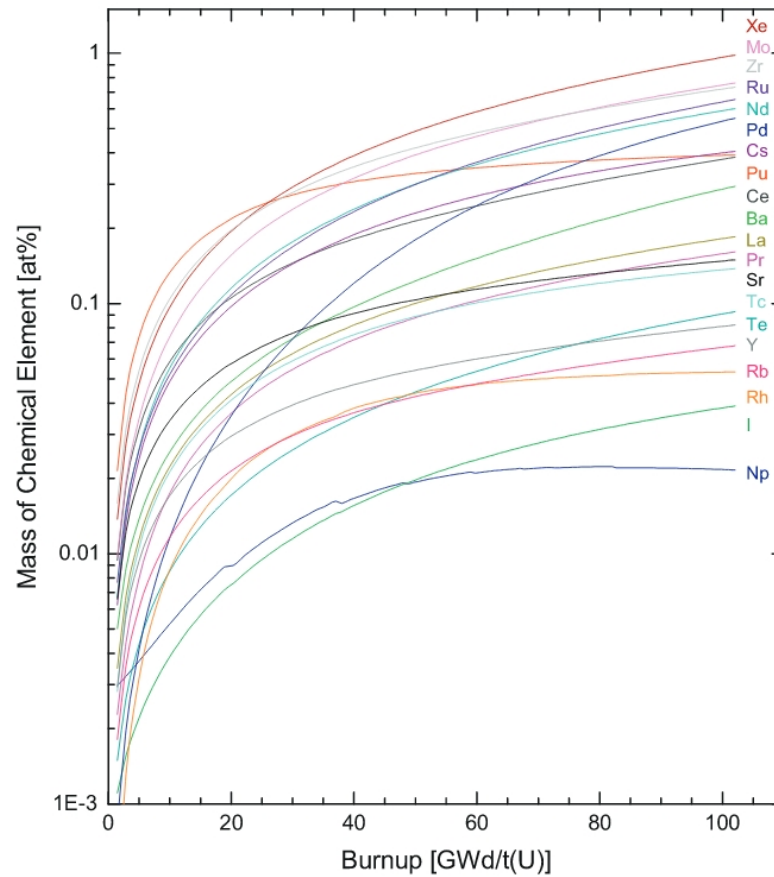


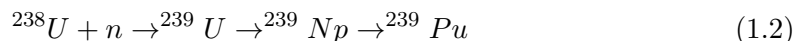
Figure 1.7: The predicted evolution of fission and activation products integrated across the pellet. Adapted from [12].

However, a very precise description of the fuel composition is not always necessary. Most of FPs estimations used in fuel performance modeling are based on empirical linear functions of the burnup which provide very close approximations of FP quantities. Table 1.3 shows estimated quantities of FPs 3 months after the end of reactor operations. One may assume that all the short-lived isotopes have disappeared. The linear correlation coefficients in Table 1.3 are based on simulations of fuel irradiation history with the neutronics code CESAR [13]. These correlation coefficients are valid for burnups up to 10 at% [14].

Table 1.3: Elements considered in CESAR, representative elements and their affiliations to families. Correlations valid up to 10 at% except for Pu (valid up to 5.4 at%).

Elements	Representative element	Creation (mol/mol UO <sub>2</sub> /at.%)	Family
Xe+Kr	Xe	$3.06 \times 10^{-3}$	Inert fission
Cs+Rb	Cs	$1.70 \times 10^{-3}$	gas and
I+Br	I	$1.31 \times 10^{-4}$	volatile fission
Te+Se	Te	$3.02 \times 10^{-4}$	products
Ba+Sr	Ba	$1.38 \times 10^{-3}$	Stable oxides
Zr+Nb	Zr	$2.62 \times 10^{-3}$	
Mo	Mo	$2.33 \times 10^{-3}$	
Ru+Tc+Rh	Ru	$2.44 \times 10^{-3}$	Metallic fission
Pd	Pd	$1.02 \times 10^{-3}$	products
Ce	Ce	$1.24 \times 10^{-3}$	Fission
Eu+Sm	Eu	$3.81 \times 10^{-4}$	products and
La+Y	La	$9.31 \times 10^{-4}$	actinides in
Gd+Nd+Pm	Gd	$1.92 \times 10^{-3}$	solid solution
Pu+Pr	Pu	$5.35 \times 10^{-3}$	in UO <sub>2</sub>
U	U	-0.0127	

One exception to a strictly linear evolution with burnup is Pu which is part of the chain:



${}^{239}\text{Pu}$  is the most abundant isotope of plutonium in irradiated fuel. It comes from activation of  ${}^{238}\text{U}$  and two beta decays of  ${}^{239}\text{U}$  and  ${}^{239}\text{Np}$ . One may see from Figure 1.7 a fast increase of Pu content at first caused by activation of  ${}^{238}\text{U}$  (see Eq. 1.2). Concentration of Pu is on the contrary nearly constant for burnups higher than 50 GWd/tHM (5.4 at%). It means that the production rate of Pu is equal to the fission rate and capture rates of Pu.

Baron and Hallstadius have presented the affiliations of FPs to families by marking them with different colors in the periodic table in Figure 1.8. It is a simple visualization showing distribution of FPs in the Mendeleev table. In reality, FPs can interact with each other to form chemical compounds belonging to different families depending on parameters like temperature or pressure.

1 H	2a																3b					4b	5b			6b		7b		2 He					
3 Li	4 Be																		5 B	6 C	7 N	8 O	9 F	10 Ne											
11 Na	12 Mg		3a			4a		5a		6a		7a		8				1b		2b		13 Al	14 Si	15 P	16 S	17 Cl	18 Ar								
19 K	20 Ca		21 Sc	22 Ti	23 V	24 Cr	25 Mn	26 Fe	27 Co	28 Ni	29 Cu	30 Zn	31 Ga	32 Ge	33 As	34 Se	35 Br	36 Kr																	
37 Rb	38 Sr	39 Y	40 Zr	41 Nb	42 Mo	43 Tc	44 Ru	45 Rh	46 Pd	47 Ag	48 Cd	49 In	50 Sn	51 Sb	52 Te	53 I	54 Xe																		
55 Cs	56 Ba	57 La	72 Hf	73 Ta	74 W	75 Re	76 Os	77 Ir	78 Pt	79 Au	80 Hg	81 Tl	82 Pb	83 Bi	84 Po	85 At	86 Rn																		
87 Fr	88 Ra	89 Ac	104 ?	105 ?	106 Sg	107 Nh	108 Hs	109 Mt																											
																		58 Ce	59 Pr	60 Nd	61 Pm	62 Sm	63 Eu	64 Gd	65 Tb	66 Dy	67 Ho	68 Er	69 Tm	70 Yb	71 Lu				
																		90 Th	91 Pa	92 U	93 Np	94 Pu	95 Am	96 Cm	97 Bk	98 Cf	99 Es	100 Fm	101 Md	102 No	103 Lr				

Oxides dissolve in fuel

Métallique precipitate (alloys)

Gaseous or volatile fission products

Céramic precipitates (oxides)

Figure 1.8: "Chemical state of the fission products in the light water reactor fuel." Adapted from Baron and Hallstadius [3].

### 1.1.3 Fuel thermomechanics

The French energy production is based on nuclear power plants, and thus the fleet of French reactors works in the load-follow mode. It means that the power of reactors is adjusted to the current electricity demand. When the demand from the power grid is high, the reactors increase their power, which is associated with power transients. Those power transients lead to changes in the fuel structure. Cracking and swelling result in deformation of the pellet. At some point, the separating gap disappears and the pellet touches the cladding. This contact is known as a Pellet-Cladding Mechanical Interaction (PCMI).

Increasing power leads to higher fuel temperature and hence to fuel swelling with maximum diameter in front of pellet ends. Thermal deformation of fuel leads to thermal stresses at the origin of fuel fragmentation, as illustrated in Figure 1.9 by cross sections of irradiated fuel. A fuel pellet submitted to a high power change resembles an hourglass, its deformation is therefore usually referred as "hourglassing". Consequence of this shape is an unbalanced gap closure. Gap closes earlier near pellet ends.

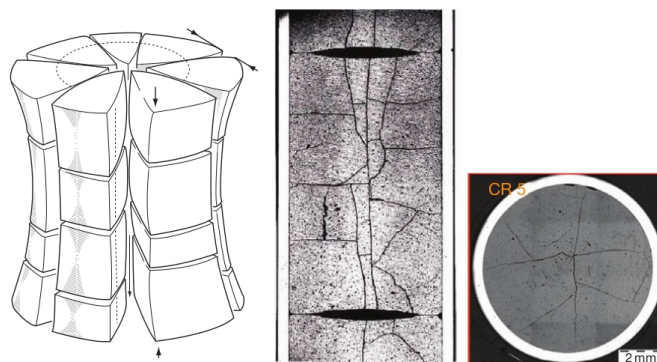


Figure 1.9: Hour-glassing of a fuel pellet [3].

Consequence of the pellet deformation and pellet-clad contact is a printing of the pellet shape in the cladding, resulting in a bamboo-like cladding. Regular ridges can thus be found in the cladding in front of pellet ends, as schematically illustrated in Figure 1.10. The difference between maximum and minimum rod diameters is dependent on the thermal gradient, the pellet length and the presence of dishes in fresh fuel [3].

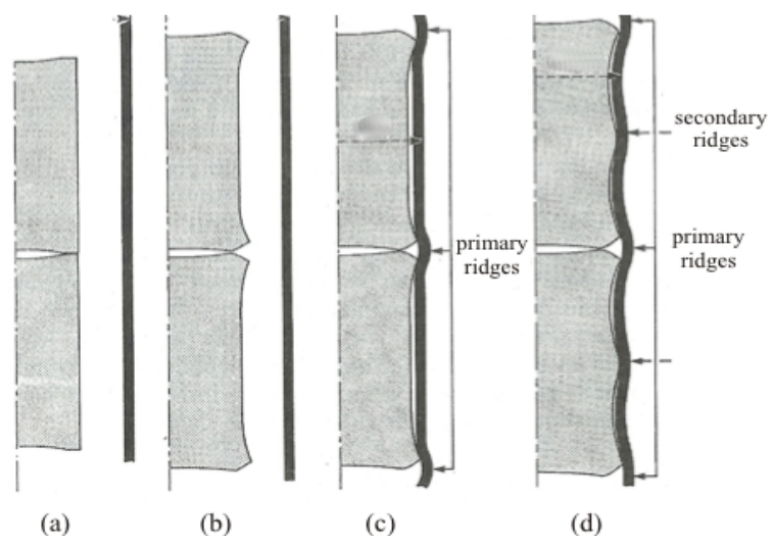


Figure 1.10: "Evolution of the gap between the cladding and the fuel during irradiation. a) fresh fuel, b) first cycle and start of second irradiation cycle, c) second half of second cycle: first cladding-pellet contact and appearance of primary ridges, d) in the case of power ramp: appearance of secondary ridges." Adapted from [15].

#### 1.1.4 Fission Gas Release

There are two noble gases among FPs. Krypton and xenon appear directly as FPs or indirectly from decays of other elements. Isotopes of xenon account for 15% of all fission

products whereas for krypton it is only  $\sim 1.5\%$  [16]. Nuclear fuel has a grain structure. Gases created by nuclear fission gather in nano-bubbles that combine at some point to form intra-granular gas bubbles. If the temperature is high enough, the bubbles migrate toward grain boundaries and form there inter-granular bubbles of micrometer size. When these bubbles connect, a tunnel on grain edges appear. Movement of the bubbles towards grain edges is faster at high temperatures. Some tunnels may collapse during cooling down. However, some of the tunnels can be observed at room temperature. Noble gases can escape the fuel microstructure by these tunnels and reach the free volume of the rod and the cladding. A schematic illustration of nuclear fuel grain structure is shown in Figure 1.11.

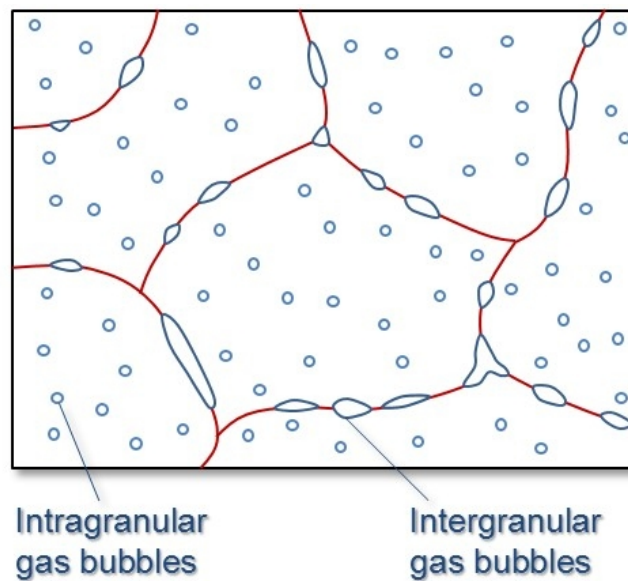


Figure 1.11: Schematic illustration of the grain structure of nuclear fuel with distinction of intra-granular and inter-granular bubbles [17].

In Figure 1.12, one may see from optical microscopy the grain boundary tunnels that form at the fuel grain faces.

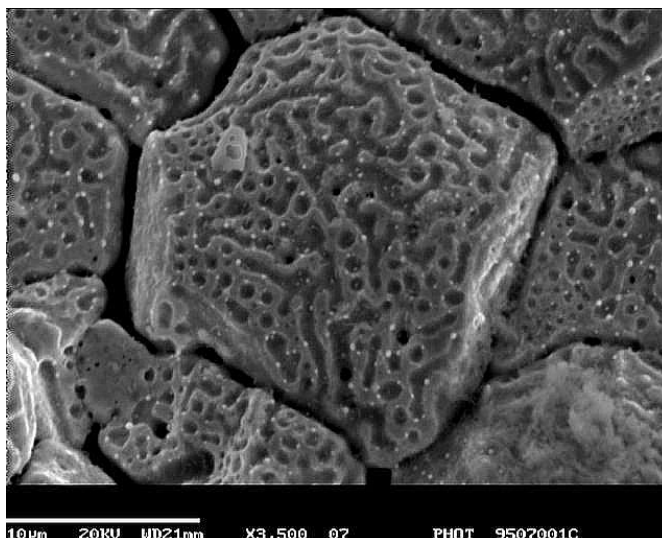


Figure 1.12: Micrograph showing tunnels on the grain face of fuel irradiated up to 22 GWd/tHM [18]. Sample power ramped in the Halden Reactor. Maximum temperature 1800 °C, holding time 1800 s.

Small quantities of fission gases can also be released at the pellet external surface by recoil or knock-out processes [19]. Fission Gas Release (FGR) is also dependent on the fuel grain size [20], larger grains leading to lower FGRs. Another consequence of the formation of intra- and inter-granular bubbles is a fission gas-induced swelling of the fuel that results from the process. The so-called fission gas swelling depends on the stress state in the fuel that can be considered as the boundary condition of the fission gas bubbles. Large compressions can hinder gas bubble growth, FGR and fuel swelling.

Besides noble gases, there are other volatile FPs. The most important are iodine, bromine, tellurium and cesium (above 1600 K). Mechanisms of release from the  $\text{UO}_2$  matrix are similar to the ones of noble gases. However, there are publications saying that the diffusion coefficient of halogens (I and Br) during irradiation is two orders of magnitude higher than that of xenon [21]. FGR is usually very limited during normal operation in reactor and increases with the fuel average burnup reaching a few % of the rare gas inventory in the most irradiated samples. In case of high power transients, the FGR kinetics and magnitude can be notably increased in consequence of the high temperatures reached at the pellet center, as illustrated in Figure 1.13. Differences in FGR seen in the graph between standard  $\text{UO}_2$  and Cr-doped  $\text{UO}_2$  are related to the much greater grain size of the latter ( $\sim 60 \mu\text{m}$  compared to  $\sim 10 \mu\text{m}$  for standard  $\text{UO}_2$ ).

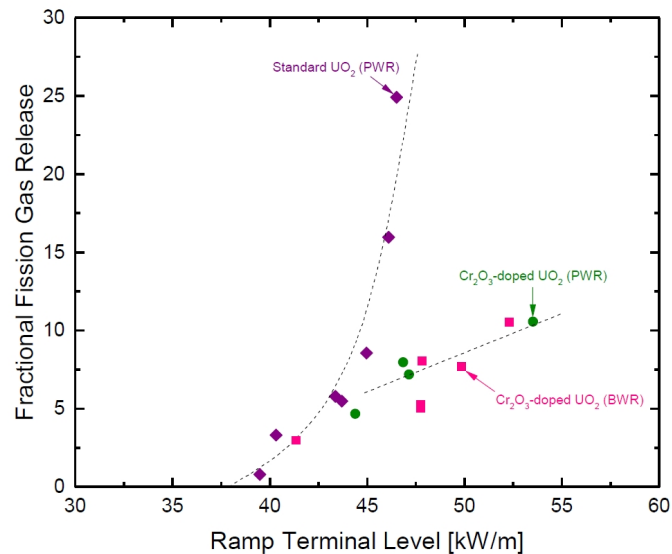


Figure 1.13: Comparison of fractional fission gas release as a function of power for different types of fuel irradiated in different reactors. The average burnup of samples is 20-40 GWd/tHM. Figure from [22].

### 1.1.5 Pellet-Cladding Interaction Failure

Swelling fuel puts pressure on the cladding and changes its shape causing tensions. Especially high tensile stresses occur in front of fuel pellets ends and in front of pellet radial cracks during high power variations [23]. Figure 1.14 presents the triple point, which is the place of the maximum stress at the fuel-clad interface. In case the power variation is too important, cladding rupture can occur, generally in front of triple points. This type of failure is referred in the nuclear community as a Pellet-Clad Interaction failure or PCI failure.

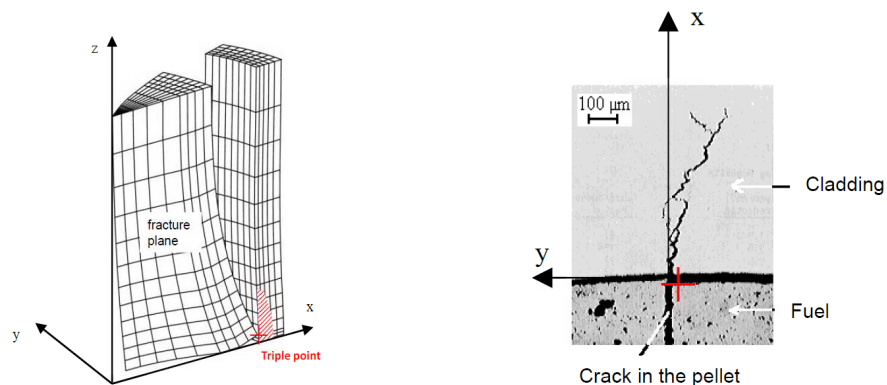


Figure 1.14: Left figure: 3D model showing the pellet cladding interaction. Right figure: Image of the crack propagation in the cladding and of its localization in front of a fuel pellet radial crack [24].

However, PCI does not stem only from mechanical interaction. Even in case of high power transients, the stresses and strains in the cladding are generally far below their expected mechanical limits. PCI failures are in fact associated with the numerous chemical species formed from FPs and released from the fuel pellet in case high temperatures are reached at the fuel pellet core. Once released from the fuel, they migrate in the radial cracks of the fuel and start interacting with the cladding, as illustrated in Figure 1.15.

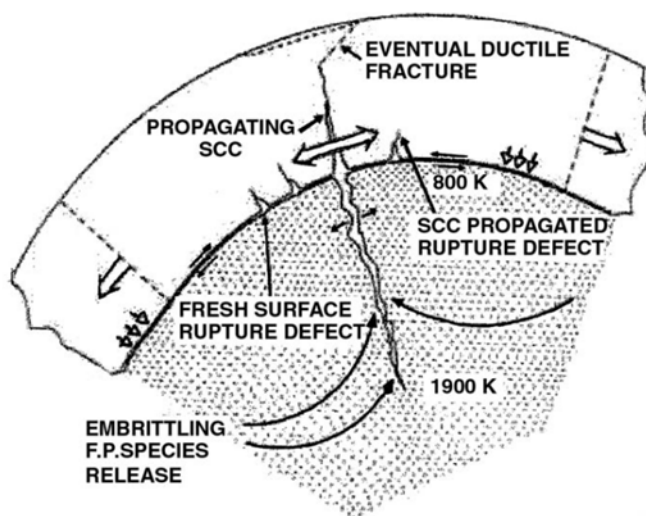


Figure 1.15: Schematic representation of of PCI in 2D. Adapted from [25].

Some of the interactions are protective for the fuel rod and some may cause failures. The first known failure by PCI was reported on June 17th, 1963. It happened in G. E. Test reactor at Vallecitos. A fuel rod failed during the start-up of the third cycle of irradiation. Researchers identified iodine as an element responsible for failures [26, 27] and started working on the so-called Iodine induced Stress Corrosion Cracking (I-SCC).

The fleet of PWRs in France has to adjust to varying power demand. It is associated with frequent power changes that cause PCI stresses. French reactors have to stand operation in nominal conditions, load follow and Extended Reduced Power Operations (ERPO). They also have to be resistant to the failure during upset conditions (Class 2 Event) [28]. Experiments simulating Class 2 Event led to the definition of a “PCI technological limit”. This criterion, not dependent on burnup, refers to the minimum hoop stress that is needed for a cladding to fail by PCI. Definition of the PCI technological limit is illustrated in Figure 1.16.

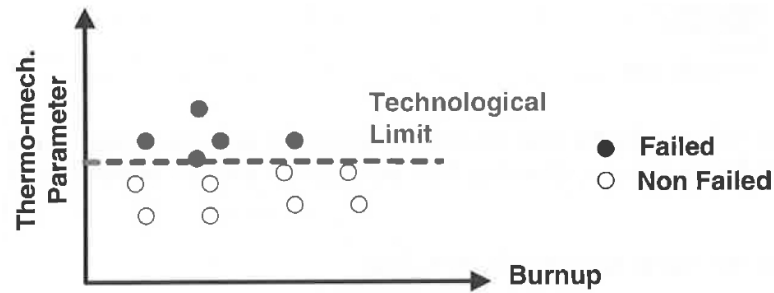


Figure 1.16: PCI technological limit [28].

To define the PCI technological limit of a nuclear fuel, the common approach is to carry out power transients on a single fuel rod in a dedicated experimental reactor with well controlled conditions. This type of experiment is called a power ramp. Before the power ramp experiment, the studied fuel is irradiated in a commercial reactor. This sequence is called the base irradiation. Once the burnup of interest is reached, part of the irradiated fuel rod is extracted (by a so-called re-fabrication process) and power ramped in a research reactor. Power ramping means submitting the rodlet to specified power transients leading higher than expected temperatures in the fuel to exacerbate the fission gas release from the fuel and the mechanical loading of the cladding, potentially till the clad failure. Figure 1.17 shows a schematic representation of a power ramp experiment.

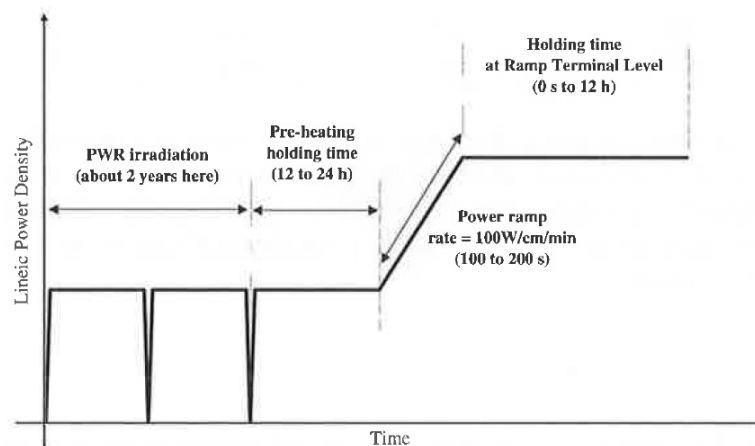


Figure 1.17: Schematic illustration of a power ramp test [24].

In the nuclear industry, power transients are usually specified from the time evolution of the Linear Power Density also called Linear Heat Rate (LHR) which has units of Watts per unit length of fuel rod. First step of a power ramp test is to reproduce the conditions that prevailed in the tested sample during the last irradiation cycle in the commercial reactor. Then, the rodlet is submitted to a power transient at a constant

rate of 100 W/cm/min till the maximum prescribed power is reached (called Ramp Terminal Level RTL). The duration of the transient is generally around 2-3 minutes. If failure of the cladding does not occur during the transient, the sample is hold at the maximum power during several hours [24]. The schematic representation shown in Figure 1.17 is only an example illustrating a power ramp experiment. Power histories can vary depending on the needs. The French Alternative Energies and Atomic Energy Commission (CEA) has an extensive database of power ramp experiments dedicated to PCI investigations [24]. An interesting conclusion coming from this database is that if PCI failure occurs, it takes place within the first minutes at the maximum power. The post-irradiation analysis of the cladding crack lengths shows that the rods with 2 cycles of irradiation (burnup within 25-45 GWd/tHM) are the most susceptible to I-SCC failure [24].

## 1.2 Modeling nuclear fuel behavior

Describing all the aspects of fuel behavior modeling is out of the scope of the present work and is available in a recent chapter of the Comprehensive Nuclear Materials [29]. In this section, the main components of a fuel performance code relevant for this thesis will be briefly recalled with a focus on the code ALCYONE, co-developed by CEA, EDF and FRAMATOME within the PLEIADES software environment. Most of fuel performance codes worldwide consider an axial discretization of the fuel rod in slices of variable height related to each other only by the flow of the coolant (no mechanical interaction) and solve independently for each slice the heat balance equation and the mechanical equilibrium equation on the 1D radial system (fuel pellet, gap, cladding, coolant) inherent to the cylindrical fuel rod geometry. This description is often referred as 1.5D. A schematic representation of the discretized fuel rod in the 1.5D scheme of ALCYONE is presented in Figure 1.18.

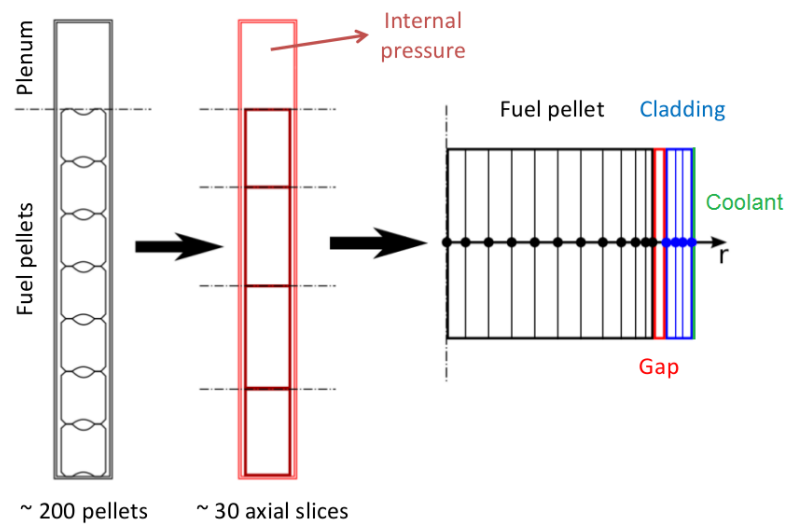


Figure 1.18: Typical fuel rod and fuel pellet discretization in the 1.5D scheme of ALCYONE.

A schematic representation of the different phenomena that need to be considered in order to simulate fuel behavior under irradiation is shown in Figure 1.19. They are briefly detailed in the next subsections.

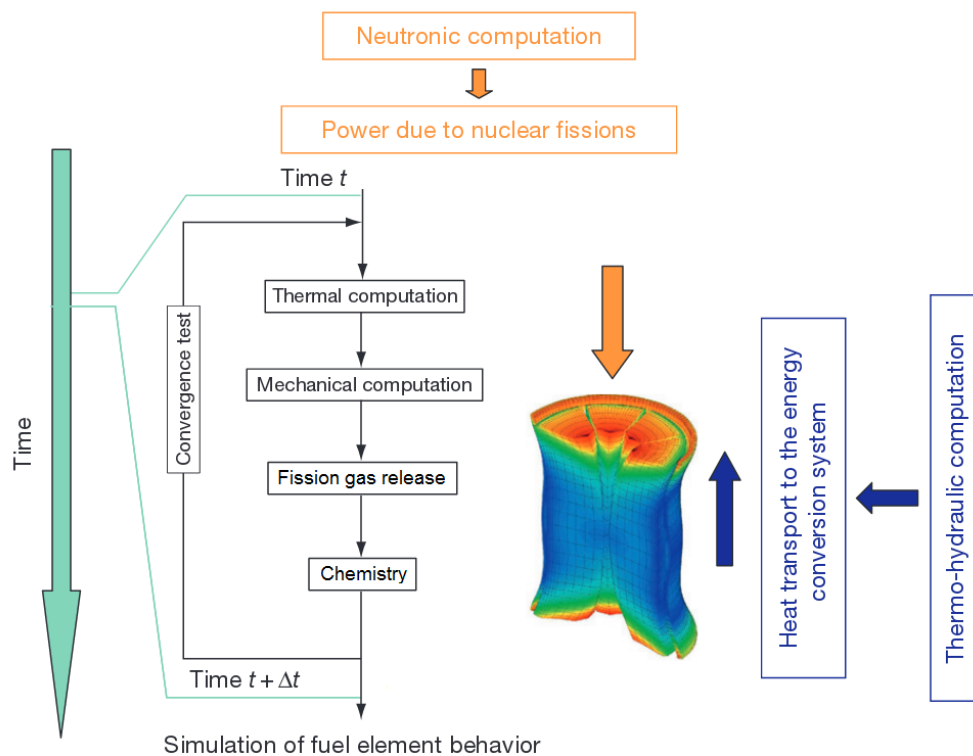


Figure 1.19: Main phenomena that need to be taken into account in fuel behavior modeling [30].

The difficulty in fuel performance modeling stems from the inter-dependence of the phenomena which result in a strongly coupled problem.

## 1.2.1 Main phenomena

### 1.2.1.1 Neutronics

The first step in fuel performance modeling is to perform neutronics calculations. Neutron fluxes and their spectrum have some impact on the generated heat and the fission products inventory in the fuel. To calculate the later, one may use sophisticated neutron transport codes like MCNP [31], Serpent [32] or APOLLO [33], that were designed to model complete reactor cores. However, in practice, simplified neutronics models adapted to specific applications are generally used in fuel performance codes, leading to much shorter calculation times. In the fuel performance code ALCYONE, the "simplified" neutronics model PRODHEL has been specifically developed for PWR fuel simulations [34]. It gives access to a very large inventory of FPs isotopes and of actinides. It also provides the heat generation rates in the fuel pellet originating from nuclear reactions. Heat generation is a very local value and varies considerably close to the pellet periphery due to fission of Pu isotopes. Example of a worldwide used model for computing the heat generation is RADAR [35].

### 1.2.1.2 Thermal calculations

The heat balance equation with the heat generated by nuclear fissions is then solved. The heat is transferred to the coolant flowing outside the fuel rod. Heat transfer must thus be considered in the cladding wall that surrounds the fuel pellets but also in the pellet-clad gap. Heat transfer depends on the fuel and clad materials thermal properties (thermal conductivity, density and heat capacity). The pellet-clad gap that closes progressively during irradiation is another important aspect of fuel performance modeling, making the thermal analysis strongly coupled with fuel and clad mechanics. In fact, the change in the gap size modifies considerably heat exchange between the fuel rod and the coolant. Sophisticated models have been developed for the heat transfer in the gap, such as URGAP which is used in ALCYONE [36]. In this model, heat transfer includes contribution from heat conduction in the gap, radiation between the pellet and clad walls and pellet-clad contact. In simulations of in-reactor nominal irradiation and power ramps, steady-state is generally considered in thermal calculations.

### 1.2.1.3 Mechanics

The fuel structure and shape changes during irradiation. The pellet swells with temperature increase and cracks in consequence of thermal stresses. The fuel pellet fragments tend to deform as a banana (or hourglass) in consequence of the radial temperature gradient. After some time, the pellet-cladding gap disappears. The fuel interacts with the cladding and deforms it. It causes stresses and strains that might lead furthermore to a loss of cladding integrity. The modeling of fuel rods mechanics forms the core of most of fuel performance codes with varying degree of complexity. The static mechanical equilibrium equation is solved in the fuel pellet and in the cladding. Upon pellet-clad gap closure, radial and tangential forces between the two structural elements are taken into account in the mechanical problem, leading to a much more complex resolution. The main source of non linearity in fuel performance codes is however associated to material behavior which are usually far from elasticity. Accurate calculation of stresses in the fuel is also important for predicting of fission gas release, the last phenomenon considered in fuel performance codes.

### 1.2.1.4 Fission gas release

Modeling of FGR is important in fuel performance simulations since it contributes to increase the fuel rod internal pressure (filled with 26 bars of He at room temperature in standard non irradiated PWR rods) that might exceed at hot state the coolant external pressure (155 bars) with deleterious consequences (gap re-opening, depleted heat transfer in the gap, temperature increase in the fuel pellet...). Modeling of fission gas release is usually limited to the noble gases xenon and krypton which constitute the bulk of fission gases in irradiated fuel. Fission gases cause furthermore swelling of the fuel pellet. In ALCYONE, the mechanistic code MARGARET has been implemented. MARGARET describes most of the fission gas transport phenomena observed in irradiated fuels, whether the gas diffusion occurs at the atomic scale or within bubbles (coalescence, thermal diffusion). Different bubble populations are considered within the fuel microstructure (nanobubbles within the grains, microbubbles at the grain boundaries, microbubbles within the grains when formation of the High Burnup Structure is likely). Fuel swelling induced by fission gas retention within the grains and at the grain boundaries are also simulated [37]. Fission gas swelling (gas bubble growth or shrinkage) is dependent on the stress state within the material, illustrating another coupling in fuel performance simulations.

## 1.2.2 Advanced thermo-mechanical modeling of PCI

ALCYONE is able to perform simulations of the fuel rod behavior in nominal conditions, power ramps and accidental conditions. It is possible to simulate different configurations

(complete fuel rod, pellet fragment with overlying cladding). The 3D scheme has been developed specifically for PCI analyses since it allows a precise description of stress-strain localization at the so-called triple point [38] (in front of a pellet radial crack and pellet end, at the clad inner wall) where PCI failures in PWRs typically occur during class 2 power transients [24]. The mesh, mechanical boundary conditions and the location of the triple point are shown in Figure 1.20. The top plane of the shown pellet fragment is called the Mid-Pellet (MP) plane while the bottom plane is called the Inter-Pellet (IP) plane. In the 3D scheme, owing to the symmetries at hand, only one fourth of a fuel pellet fragment is considered (half of the fragment height, half of the fragment angle). The fragmentation of the cylindrical fuel pellet in 8 identical pieces on average is a direct consequence of the first power excursion seen by the fuel in reactor and is therefore taken into account at the beginning of any simulation. The thermo-mechanical calculations in ALCYONE rely on the finite element code Cast3M from which nodal quantities are calculated at each time step (temperature, fuel and cladding displacements, stresses), completed by nodal estimations of fission gas swelling and release. The thermo-mechanical calculation accounts for many non-linearities, related either to material behavior (e.g., fuel and clad creep, clad plasticity, fuel cracking) or structural behavior (e.g., pellet-clad unilateral contact with friction, axial locking of the pellet and the cladding).

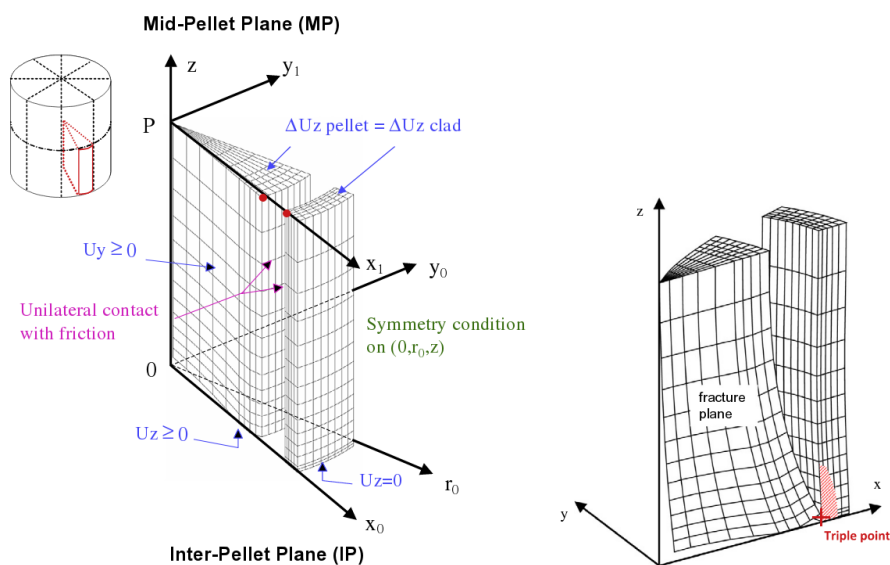


Figure 1.20: Mesh and mechanical boundary conditions used in the 3D scheme of ALCYONE (left figure) and the calculated pellet deformation (right figure) with the triple point marked in red. Figure from [14].

In this respect, the 3D scheme provides very detailed simulations of PCI accounting for most of the phenomena, as illustrated in Figure 1.21.

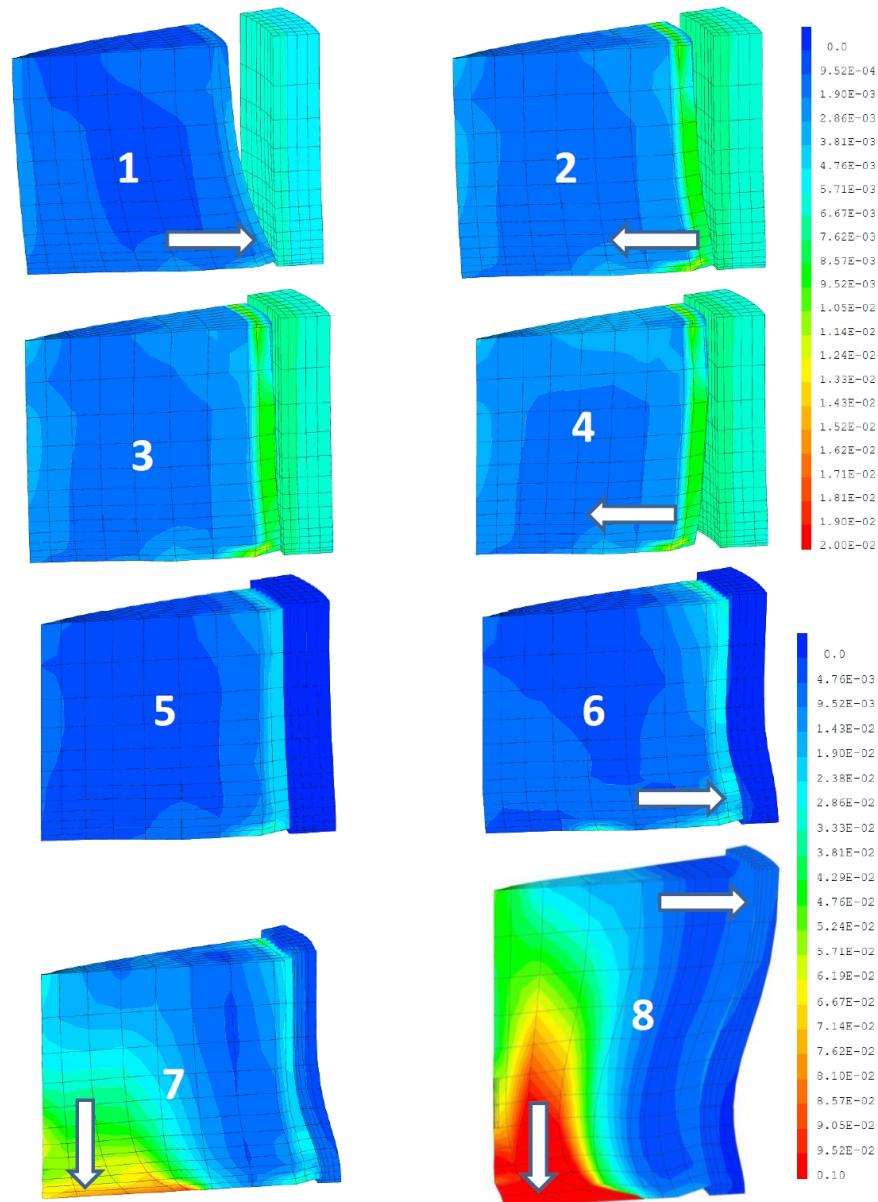


Figure 1.21: Images of 3D simulation performed in ALCYONE [39]. Colors correspond to inelastic strains in the fuel pellet. 1. 1<sup>st</sup> cycle, full power, 2. 2<sup>nd</sup> cycle, full power, 3. End of the 2<sup>nd</sup> cycle, pellet-cladding gap is closed, 4. End of the base irradiation, 5. Beginning of the power ramp, 6. Maximum linear heat rate of the power ramp, 7. Holding period of the power ramp, filling of the dishes by fuel creep, 8. Holding period of the power ramp, development of the cladding ridges.

### 1.3 Conclusions

Fuel geometry is by essence relatively simple, consisting of cylindrical fuel pellets encased in a zircaloy tube. Fuel behavior simulations are however characterized by the coupling

of several phenomena occurring at different scales (nuclear deposition at the atomic scale, fission gas release mechanisms at the scale of the fuel microstructure, thermo-mechanics at the macroscopic scale) that explains the difficulties in actually predicting with great accuracy fuel behavior. All fuel performance codes worldwide are primarily focused on thermo-mechanics as it is of primary importance to assess the mechanical resistance of the cladding during power transients, in particular for PCI studies. Less fuel performance codes deal with FGR and fission gas-induced fuel swelling owing to the complex system of equations that stems from a mechanistic description of gas diffusion, bubble formation and coalescence, channels formation at the grain boundaries, and so on. Most fission gas release models are furthermore limited to noble gas release that form the bulk of the gas phase but are of limited interest for PCI analyses.

PCI failure/non failure assessment by fuel performance calculations relies on a PCI technological limit derived from power ramps performed in Material Testing Reactors (MTR), usually based on a maximum stress or strain energy density criterion. The mechanism at the origin of PCI failures is however Iodine-Stress Corrosion Cracking, related to iodine, one of the FPs, released from the fuel during a power transient. Treating in more details PCI requires therefore a description of iodine release from the fuel which is the goal of this thesis. Several aspects have to be considered to obtain a realistic estimation of iodine release during a power transient. First, iodine is not volatile at all temperatures and can combine with other FPs to form gaseous compounds. Thermo-chemistry of FPs in the fuel should therefore be considered in fuel performance simulations. Second, there are many quantities that can influence thermochemical equilibria in nuclear fuel such as temperature, mechanical stresses and oxygen content. Their spatial and temporal evolutions during a power transient should be assessed as best as possible. While temperature and stresses are already part of fuel performance codes simulations, oxygen content is generally assumed fixed and unchanged during a power transient in PWRs.

In the next chapter, a review of existing data and models on thermochemistry of irradiated fuel will first be given to explain the importance of oxygen in the system. Literature review on oxygen transport in the fuel pellet will follow to discuss the potential evolution of oxygen related parameters during power transients. PCI failure mechanisms will then be detailed and analyzed with a focus on the chemical aspects and the potential importance of oxygen.

## Chapter 2

# Literature Review

This chapter provides a literature review concerning the phenomena important in this study. In the first section, thermochemistry of nuclear fuels is discussed. Section 2.2 presents publications concerning oxygen transport and its parameters. The data available in the open literature on the chemical aspects of PCI are discussed in Section 2.3. Fuel modeling approaches including or discussing thermochemistry and/or oxygen transport are presented in Section 2.4. Finally, in the last section, the literature review chapter is summarized and the objectives of this thesis are justified.

### 2.1 Thermochemistry of irradiated nuclear fuel

#### 2.1.1 Introduction

In irradiated oxide fuels, oxygen, FPs and actinides may interact with each other and form various chemical compounds. The mobility of these elements in the fuel microstructure and their potential interactions depend on various parameters related mainly to temperature, pressure, burnup and fission pikes density. The chemical state of FPs can be classified into the following main groups, slightly adapted from the classification proposed by Lewis [19]:

- fission gases and other volatile fission products: Kr, Xe, Br, I, Cs and Te.
- fission products forming metallic precipitates: Mo, Tc, Ru, Rh, Pd, Ag, Cd, In, Sn, Sb and Te.
- fission products forming oxide precipitates: Rb, Cs, Ba, Zr, Nb, Mo and Te.
- fission products dissolved in the fuel matrix: Sr, Zr, Nb, and the rare earths Y, La, Ce, Pr, Nd, Pm, and Sm.

As can be seen, some FPs can be found in several groups. It is for example the case of Cs which can form gaseous compounds such as cesium iodide CsI, simple oxide precipitates such as cesium oxide Cs<sub>2</sub>O or complex oxide precipitates such as cesium molybdate Cs<sub>2</sub>MoO<sub>4</sub>. The transition from one group to another depends on the local values of the temperature, pressure and burnup in the fuel. As may be expected from the radial burnup and temperature profiles at hand during irradiation, the chemical speciation of FPs is strongly dependent on the radial position along the fuel pellet radius. Speciation of FPs is also likely to change significantly between nominal irradiation and power ramps.

Another usual way of classifying the FPs compounds is to group them in different phases. Three main phases can be considered in irradiated oxide fuels:

- the gas phase (noble gases and chemically-reactive gases formed from volatile fission products),
- the fluorite solid solution (the uranium dioxide matrix with dissolved rare earths and plutonium oxides),
- the noble metal phase (Mo, Rh, Pd, Ru and Tc), which corresponds to metallic amalgams,

to which must be added all the solid or liquid stoichiometric compounds which form each a specific phase (metallic precipitates, oxide precipitates). A specificity of irradiated oxide fuels is their ability to incorporate in the UO<sub>2</sub> matrix (fluorite solid solution) a great number of FPs oxides. A schematic representation of irradiated fuel with the main phases is given in Figure 2.1.

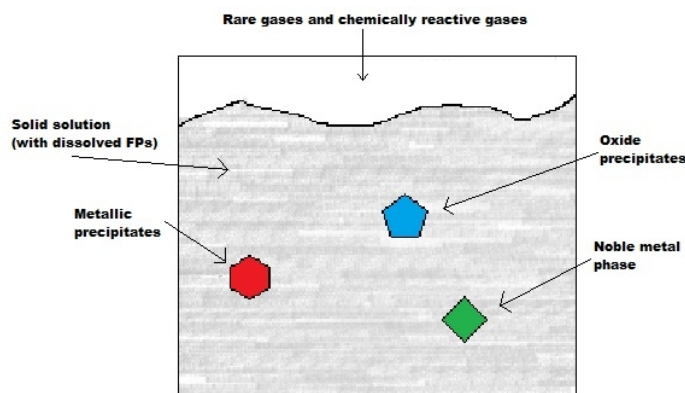
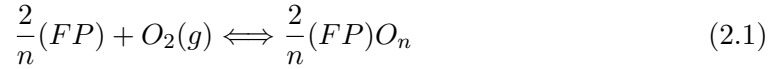


Figure 2.1: Schematic of irradiated fuel.

### 2.1.2 Oxygen potential

Fission reactions in the fuel lead to the liberation of oxygen atoms that can associate with FPs. The potential formation of FPs oxides is mostly dependent on temperature and the partial pressure of oxygen. The equilibrium oxygen pressure for the reaction involving a typical FP may be written as [19]:



where (FP) and (FP) $O_n$  denote the fission product and its oxide, respectively. Equation 2.1 yields the oxygen partial pressure as follows:

$$p_{O_2} = \exp\left(\frac{\Delta G_p}{RT}\right) \quad (2.2)$$

where  $\Delta G_p$  is the standard Gibbs energy of formation of the fission product oxide per mole of oxygen at 1 atm pressure and temperature  $T$ . Another way of expressing the oxygen partial pressure is to define the so-called "oxygen potential"  $\Delta G_{O_2}$  (which should be referred as the relative partial molar Gibbs energy of oxygen of the fission product oxide) as follows:

$$\Delta G_{O_2} = RT \ln p_{O_2} \quad (2.3)$$

The "oxygen potential" is equal to the relative partial molar Gibbs energy of oxygen of the fission product oxide. The potential formation of oxides from the fission products is summarized by the Ellingham diagram of Figure 2.2 where the "oxygen potential" of several fission products/fission products oxides reactions are plotted as a function of temperature.

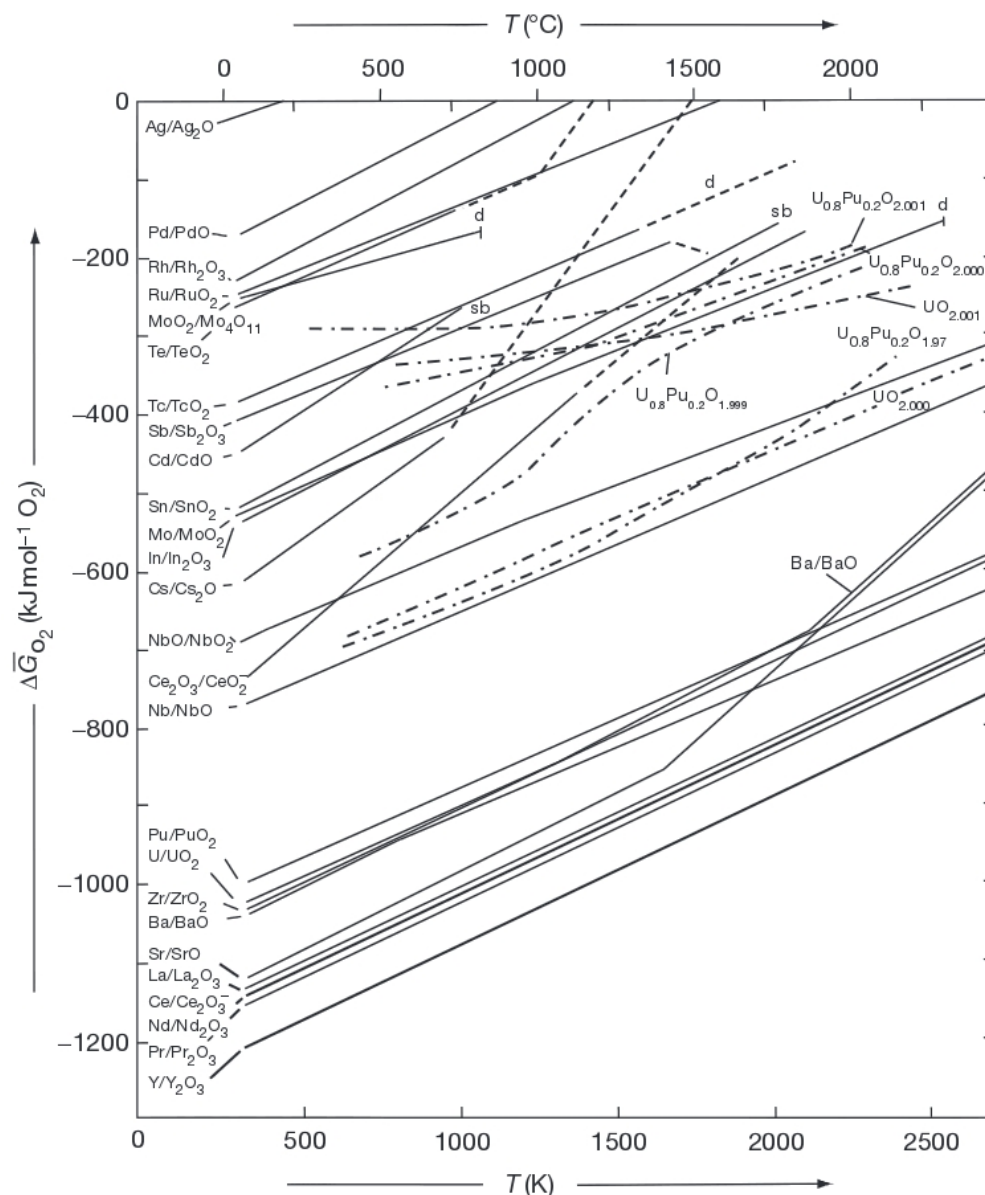


Figure 2.2: Relative partial molar Gibbs free energies of oxygen of the fission product oxides and of  $\text{UO}_{2+x}$  [19].

In Ellingham's diagram are also given the oxygen potentials of several non irradiated uranium oxides, i.e., the oxygen partial pressure in equilibrium with the fuel at a given temperature and 1 atm pressure. One may see important differences in oxygen potential in spite of small changes in stoichiometry deviations (compare the lines relative to  $\text{UO}_{2.000}$  and  $\text{UO}_{2.001}$  in the graph). The stoichiometry deviation  $x$  in uranium dioxide  $\text{UO}_{2\pm x}$  is defined by:

$$x = |2 - O/U| \quad (2.4)$$

with  $O/U$  the oxygen over uranium ratio. One of the difficulty with uranium oxides is their accommodation to important stoichiometry changes without phase changes, as

illustrated by the U-O binary phase diagram from reference [19].

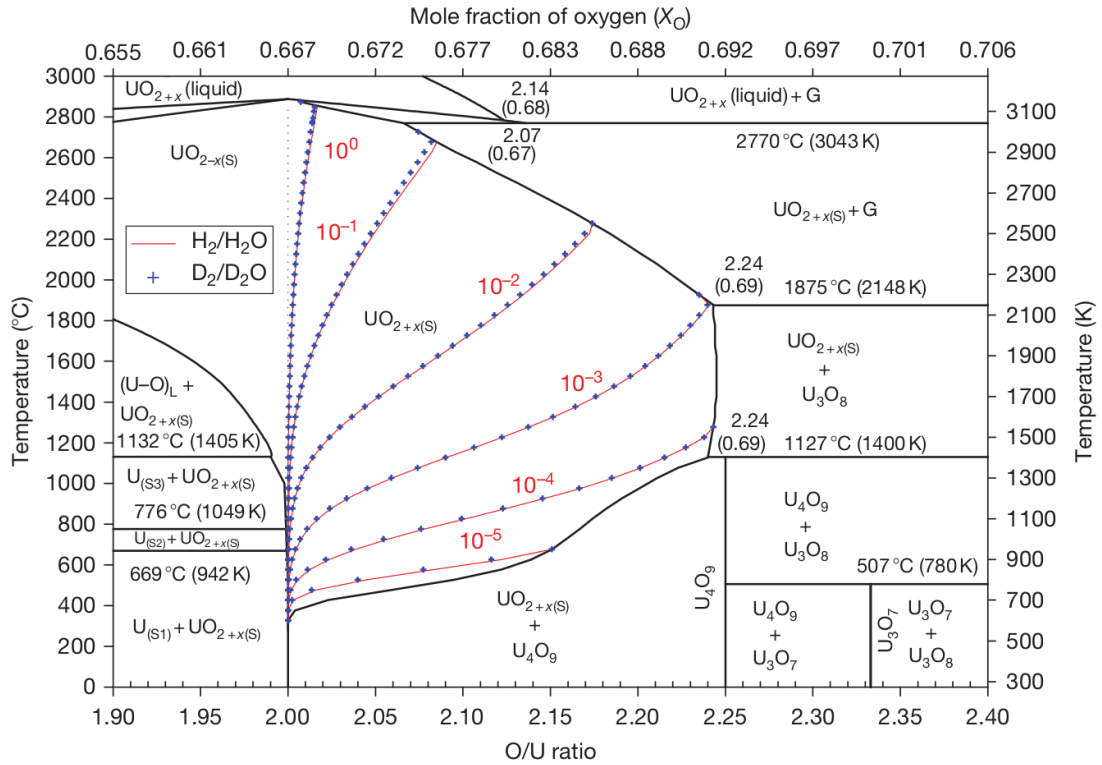


Figure 2.3: Phase diagram of the binary system U-O. The lines of constant  $H_2/H_2O$  and point of constant  $D_2/D_2O$  ratios are calculated from Equations 4 and 5 in reference [19].

The diagram in Figure 2.3, calculated with the Royal Military College of Canada (RMC) thermodynamics database, shows that  $UO_{2\pm x}$  is stable in the expected range of temperatures encountered in fuels during normal reactor operations (400 to 2500 °C). For instance, the formation of uranium oxides of higher oxidation degree ( $U_4O_9$ ) occurs at stoichiometry deviations close to 0.25. Another important point, is the marked evolution of the equilibrium oxygen partial pressures of uranium dioxide with stoichiometry deviation (marked by the O/U ratio) and temperature, as shown in Figure 2.4 from reference [40].

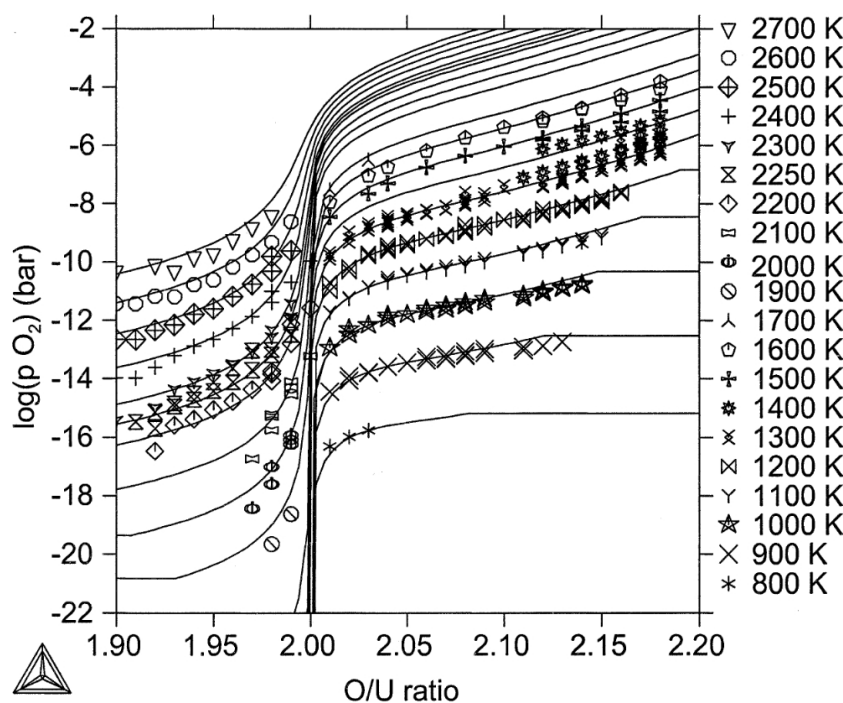


Figure 2.4: Oxygen partial pressure as a function of O/U. Symbols correspond to selected experimental data and curves present calculated values [40].

Figure 2.4 shows that the equilibrium oxygen partial pressure depends greatly on the O/U ratio of the fuel, as will be the case of the oxygen potential. In general, non irradiated uranium dioxide fuel is fabricated such as to yield an O/U ratio very close to 2, generally slightly over 2 (maximum 2.005). The oxygen potentials associated with fission products oxides of Figure 2.2 must therefore be compared with those of the non irradiated  $\text{UO}_{2.000}$  and  $\text{UO}_{2.001}$ . One may see that rare earths (La, Ce, Nd, Pr, Y), Zr, Ba and Pu oxides have oxygen potentials far lower than fresh uranium dioxides. It is therefore very likely that they will form oxides in the matrix. Some fission products oxides have oxygen potentials close or intersecting those of fresh uranium dioxide. It is in particular the case of Mo which may co-exist in metallic or oxide form in the fuel depending on temperature. Other FPs with greater oxygen potential are less likely to form oxides in the fuel.

By analogy with the O/U ratio of non irradiated oxide fuel, one usually defines the ratio of oxygen atoms to metal atoms of irradiated fuel as follows:

$$O/M_{tot} = O/(U + FPs) \quad (2.5)$$

According to Lewis, the  $O/M_{tot}$  ratio slowly increases with burnup.

### 2.1.3 Chemical state of fission products in irradiated fuel

Standard experimental techniques applied to irradiated fuel samples in PWRs to characterize the FPs include optical observations on fuel cross-sections, either from axial cuts or transverse cuts, Scanning Electron Microscopy (SEM), Electron Probe MicroAnalyzer (EPMA) and Secondary Ion Mass Spectrometry (SIMS). A very common procedure is to use transverse fuel cross-sections and perform measures at regular positions along a radius or diameter of the pellet. All techniques have limits that will be discussed in the next sections.

#### 2.1.3.1 Fission products dissolved in the fluorite solid solution

A non negligible number of FPs oxides can be dissolved in the  $\text{UO}_2$  matrix by replacing the uranium cation on the normal lattice site. Most of them are listed in Table 2.1. These oxides have different solubilities in the  $\text{UO}_2$  matrix. The experimental data concerning the solubility of these oxides in the  $\text{UO}_2$  matrix were reviewed by Kleykamp [41]. The author studied the solubility of 12 oxides that may be formed in irradiated fuel.

Table 2.1: Oxides that may be found in the solid solution phase of irradiated  $\text{UO}_2$ . Adapted from Lewis[19].

$\text{M}_2\text{O}$	$\text{MO}$	$\text{M}_2\text{O}_3$	$\text{MO}_2$
$\text{Cs}_2\text{O}$	$\text{SrO}$	$\text{Ce}_2\text{O}_3$	$\text{CeO}_2$
$\text{Rb}_2\text{O}$	$\text{BaO}$	$\text{Dy}_2\text{O}_3$	$\text{MoO}_2$
		$\text{Ho}_2\text{O}_3$	$\text{NbO}_2$
		$\text{La}_2\text{O}_3$	$\text{NpO}_2$
		$\text{Nd}_2\text{O}_3$	$\text{PuO}_2$
		$\text{Pr}_2\text{O}_3$	$\text{TeO}_2$
		$\text{Sm}_2\text{O}_3$	$\text{ZrO}_2$
		$\text{Y}_2\text{O}_3$	

According to Kleykamp, a high solubility of rare earth (Y, La, Ce, Pr, Nd) oxides is observed for a wide range of temperatures. The rare earth (RE) elements are expected to be found as  $\text{REO}_2$  and  $\text{RE}_2\text{O}_3$  oxides in the fuel matrix [41]. Actinides (Pu mainly) are also important ingredients of the solid solution. They do not show tendency to segregate and they are dissolved in the fuel matrix as oxides [19]. Gadolinium can be used as a burnable poison in oxide fuels. It belongs to lanthanides and has similar chemical behavior as lanthanum. Solubility of these elements are very similar. Europium is another lanthanide that can be applied as a burnable poison. It has high solubility exceeding 60 mol% at high temperature [42, 43].

Zirconium oxides are easily soluble in  $\text{PuO}_2$  but their solubility in  $\text{UO}_2$  is strongly dependent on temperature [41]. During normal operation of the nuclear reactor (maximum temperature  $<1200\text{ }^\circ\text{C}$ ), the maximum solubility of  $\text{ZrO}_2$  in  $\text{UO}_2$  is around 0.4 mol%. However, higher temperatures that may occur during power ramps are associated with high solubility of zirconia (15 mol% at  $1500\text{ }^\circ\text{C}$  and 51 mol% at  $1700\text{ }^\circ\text{C}$ ) [44, 45]. According to Romberger [46], zirconium has a high solubility thanks to the presence of lanthanides. Schleifer et al. [47] performed experiments in which he studied solubility of the Ln-Zr-U-O system (Ln stands for lanthanides).

Barium has a very low solubility in  $\text{UO}_2$  due to the large crystal radius of  $\text{Ba}^{2+}$ . However, its solubility can be enhanced by presence of an element with a much smaller crystal radius, as shown by Fujino [43] who carried out experiments on the system U-Ba-Y-O.

Oxides of molybdenum, tellurium and cesium are characterized by a very small solubility. These elements tend to gather in separate phases [48, 49]. Solubility of elements like Ru, Rh and Pd is below the detection limit even at very high temperatures (2100-2400 K) [48].

Available data on fission products solubility are summarized in Table 2.2.

Table 2.2: Thermodynamic data of selected fission products. Adapted from Lewis et al. [19].

Oxide	Solubility in $\text{UO}_2$ (mol%)	Temperature (K)	Excess Gibbs energy (w.r.t. solid) ( $\text{J mol}^{-1}$ )	Cations per formula mass
$\text{Cs}_2\text{O}$		2173	230	2
$\text{La}_2\text{O}_3$	69	523	$-2686 + 8.505T$	2
$\text{La}_2\text{O}_3$	50	1523		2
$\text{Pr}_2\text{O}_3$	55	1523	$-4268 + 8.505T$	2
$\text{Nd}_2\text{O}_3$	68	1523	$-7714 + 8.505T$	2
$\text{PuO}_2$	Miscible		0	1
$\text{NpO}_2$	Miscible		0	1

Dissolved FPs contents in the fuel can usually be assessed from EPMA measurements performed at regular intervals along the fuel radius. An example of EPMA profile for Nd is given in Figure 2.5, compared to that of Cs. The signal does not present significant peaks meaning that Nd is homogeneously distributed within the  $\text{UO}_2$  matrix, as would be expected from a FP oxide completely dissolved in the fuel.

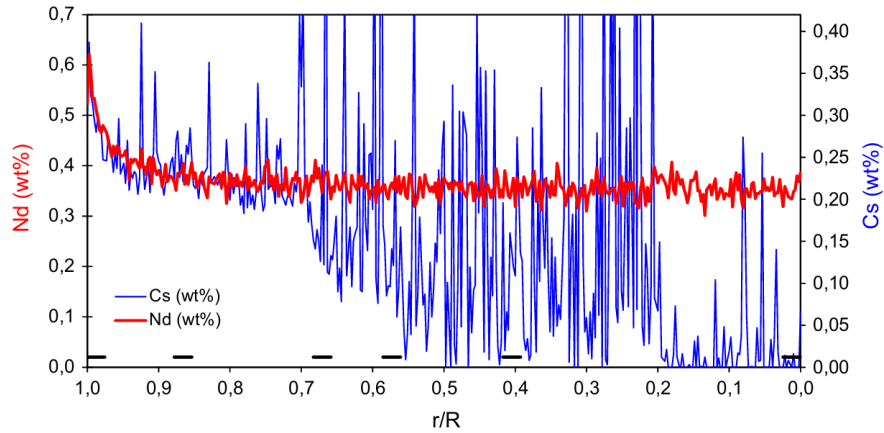


Figure 2.5: Radial EPMA profiles of Cs and Nd measured in the fuel sample irradiated to 32 GWd/tHM and power ramped at the linear heat rate of 463 W/cm during 12 h [50].

To quantify the amount of FPs oxides dissolved in the fuel, the ratio of oxygen atoms to dissolved metal atoms  $O/M$  may be used instead of the oxygen over metal ratio  $O/M_{tot}$  of Equation 2.5, which includes all the fission products, whether or not incorporated in the fluorite solid solution.

### 2.1.3.2 Fission products and dopants precipitates at the pellet center

In LWR fuel rods irradiated in normal conditions, very few observations of metallic and oxide precipitates have been reported owing to the low temperatures at hand (600-1000 °C). Most observations concern fuel rods irradiated during power ramps or high power sequences. The high temperatures reached at the pellet center (generally exceeding 1500 °C) are in favor of the existence of a local thermodynamic equilibrium.

Early observations from an LWR  $UO_2$ -Zircaloy-4 fuel rod irradiated till a burnup of 41 GWd/tHM at a high local rod power of 430 W/cm were reported by Kleykamp [51]. The maximum temperature of the central core of the pellet was estimated to be around 1800 °C. Evidence of biphasic metallic precipitates composed of Mo and Ru were found in the central part of the pellet till mid-pellet radius. The author related these observations to the existence of a noble metal phase composed of Mo, Tc, Ru, Rh and Pd, as previously identified in Sodium Fast Reactor (SFR) irradiated MOX fuels [48]. They indicate that the oxygen potential of the fuel reached low values during the high power period. From the percentage of Mo measured in the precipitates, Kleykamp estimated the local oxygen potential in the range [-420;-380] kJ/mol  $O_2$ . In the same study, Zr was found in the fuel mainly in dissolved form, as shown by the flat EPMA diametral profiles of Figure 2.6, contrary to Mo which shows a significant decrease of the

signal at the pellet center. The author could not identify any specific phase including Cs.

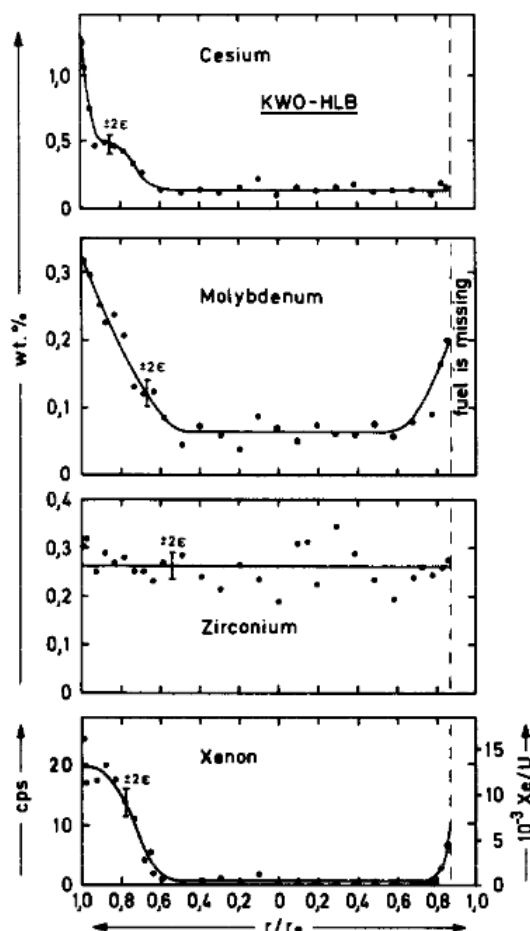


Figure 2.6: Diametrical weight fractions of Cs, Mo and Zr and of Xe bonded in the fuel rod studied by Kleykamp [51].

Observations on PWR Cr-doped  $\text{UO}_2$ -Zircaloy-4 fuel rods irradiated till a burnup of 30 GWd/tHM and power ramped at RTLs of 470 and 530 W/cm during 12 h were published by Riglet-Martial et al. [52]. The maximum temperatures at the central core of the pellet were estimated to be around 2000 and 2200 °C, respectively. Evidence of co-localized Mo, Ru and Cr metallic precipitates were found in the central part of the pellets till approximately mid-radius, as shown by the X-ray maps of Figure 2.7.

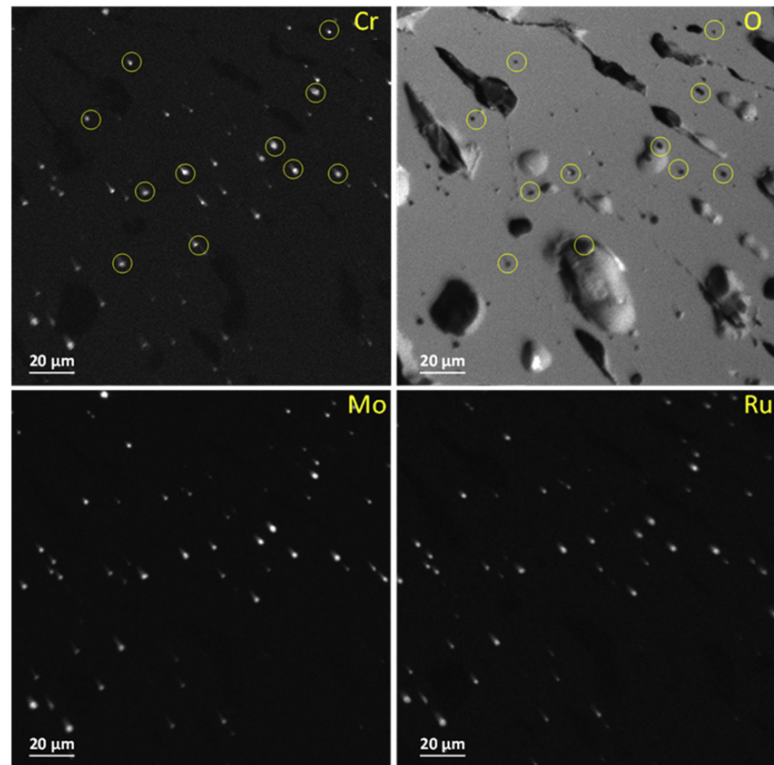


Figure 2.7: X-ray maps of Cr, O, Mo and Ru in the fuel studied by Riglet-Martial et al. [52]. Brighter color corresponds to a higher concentration.

EPMA radial profiles of Cr and Mo furthermore indicated drastic changes in the measured signals along the fuel pellet radius. While a high content was recorded from the periphery till mid-pellet radius, consistent with the initial dopant content and fission products content expected at this burnup, a sharp decrease of the content was measured in the fuel pellet core, see Figure 2.8.

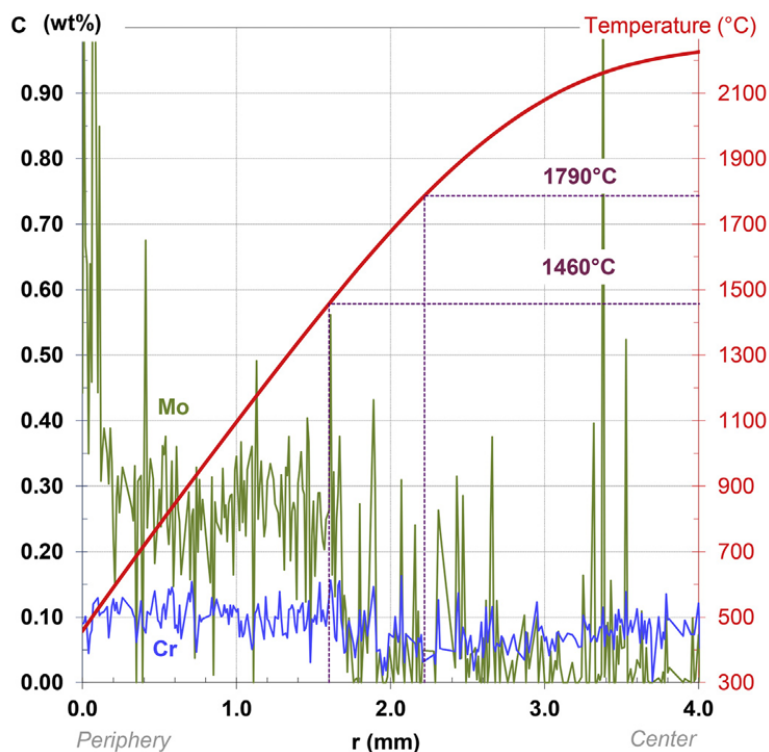


Figure 2.8: Radial profiles of the EPMA measures of Cr and Mo (left axis) and of the temperature (right axis) in the fuel studied by Riglet-Martial et al. [52].

The change in the signal between the cold and hot sections of the pellet was interpreted as a change in the chemical form of Mo and Cr in the fuel. The peaks observed in the EPMA signals are characteristics of large or small precipitates. While Mo is usually considered having a low solubility in uranium oxides, Cr is known to have a measurable solubility (around 0.1 wt% after fabrication) which depends mostly on the oxygen partial pressure and temperature [53].

The relation between the oxygen potential and chromium solubility in fresh  $\text{UO}_2$  has been described by Riglet-Martial et al. [53]. They have proposed a chromium solubility model based on experimental results and thermodynamic calculations. Figure 2.9 shows the evolution of the Cr solubility with oxygen partial pressure and temperature.

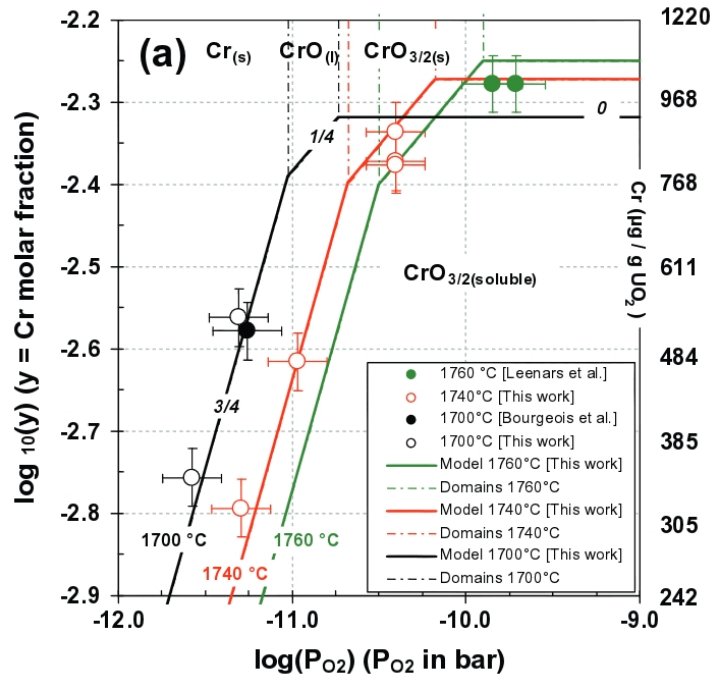


Figure 2.9: Relation between chromium mole fraction in  $\text{UO}_2$  (i.e., chromium solubility) and oxygen partial pressure for various temperatures. One may notice the stability areas for  $\text{Cr}_{(s)}$ ,  $\text{CrO}_{(l)}$  and  $\text{CrO}_{3/2(s)}$ . Figure adapted from [53]. Experimental data from [53–55].

The curves describing chromium solubility are calculated with the following equation:

$$\log_{10} y_{Cr} = q \log_{10} p_{O_2} + V + \frac{U}{T} \quad (2.6)$$

where

$q$ ,  $V$  and  $U$  - coefficients from Table 2.3

$y_{Cr}$  - chromium mole fraction

$p_{O_2}$  - oxygen partial pressure [bar]

$T$  - temperature [K]

Table 2.3: Coefficients of Equation 2.6, necessary to prepare curves from Figure 2.9. Table adapted from [53].

Chromium phase	Slope q	V, v(J/K Mol)	U ( $\times 10^{-4}$ ), u * $10^{-4}$ (J/Mol)
Cr <sub>2</sub> O <sub>3</sub>	0.00	0.1385	-0.4827
		-2.651	9.242
CrO	0.25	-4.872	1.034
		93.28	-19.80
Cr ( $T > 1651$ °C)	0.75	-8.391	2.816
Cr ( $T < 1651$ °C)	0.75	160.63	-53.91
		-6.076	2.370
		116.32	-45.38

The measured Cr content at the pellet center after the power ramp being above the detection limit of the EPMA device (0.005 wt%), Equation 2.6 was used to assess the oxygen potential (or partial oxygen pressure) of the fuel pellet core. The authors estimated the oxygen potential to be within [-450;-350] kJ/mol O<sub>2</sub> for the temperature range [1550;2000] °C, consistent with the earlier estimations of Kleykamp [51] and the presence of metallic Mo and Ru.

In a recent paper [56], Desgranges et al. analyzed the FPs distribution in a fission gas bubble located within a fuel grain situated near the pellet center of a PWR Cr-doped UO<sub>2</sub>-M5 fuel rod of average burnup 36 GWd/tHM that had been ramped till an RTL of 470 W/cm during 12 h. The analyzed fission gas bubble of radius close to 1  $\mu$ m was formed in consequence of the power transient, according to the authors. SIMS images after sputtering and EPMA mapping showed the presence of Xe, Cs, Te, I, Ba, Ru, Tc, Mo, Pd and Cr in the bubble. The noble metal phase composed of Mo, Ru, Tc and Pd was found in two metallic precipitates close to the bubble boundaries. Cs, Te and I were also found co-located in the bubble but in two "precipitates" distinct from the ones including noble metals. The round shape of the precipitates led the authors to suggest the formation of a possible Cs-Te-I liquid phase at hot state. Another striking observation was the lack of specific phase formation outside of the fission gas bubbles.

### 2.1.3.3 Volatile fission products at the pellet-clad interface

It is impossible to directly observe the chemical speciation of volatile FPs in the fuel during in-reactor irradiation. Only the volatile FPs that have been released from the fuel and are found in the pellet-clad gap or at the clad inner surface can be assessed after irradiation. If some co-localization of FPs is found, it does not imply that the chemical form existed in the fuel prior to its release. It is possible that interaction of FPs and formation of the compounds occurred in the fuel pellet clad gap. In high burnup fuel rods, the analysis is further complicated by the formation of a U-Zr-O layer between the fuel and the cladding with a high concentration in FPs [57]. Most observations refer

to power ramped fuel samples since the high temperatures reached at the pellet center lead to significant loss of volatile FPs.

Kleykamp analyzed the pellet-clad interface of the previously discussed LWR  $\text{UO}_2\text{-Zr}_4$  fuel rod irradiated till a burnup of 41 GWd/tHM at a high local rod power of 430 W/cm. He found evidence of U, Zr and Cs in the gap region but without complete spatial coincidence. He considered there could be formation of some Cs-Zr oxide that could however not be identified.  $\alpha\text{-Zr}$  and  $\text{ZrO}_2$  layers of maximum 20  $\mu\text{m}$  thick were identified on the cladding inner side from which the local oxygen potential at the fuel external surface was estimated to reach a very low value of -800 kJ/mol  $\text{O}_2$ . According to the author, the excess oxygen of the analyzed fuel, slightly hyperstoichiometric upon fabrication ( $\text{O}/\text{U} = 2.003$ ), was likely gettered by the zircaloy cladding during irradiation. This conclusion appears questionable because, as shown by systematic recording of maximum zirconia layer thickness from SEM images of irradiated fuel [58, 59], the formation of a homogeneous zirconia layer at the pellet clad interface is a process that can take several years in reactor. The zirconia layer is generally strongly discontinuous both in the axial and circumferential directions even in fuel rods with average burnups of 40 GWd/tHM. An example of a zirconia layer is shown in Figure 2.10.

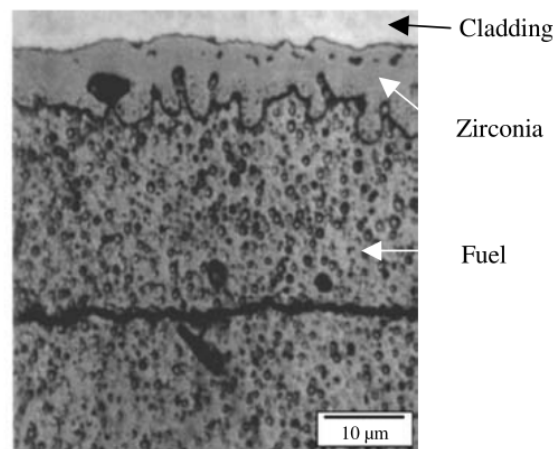


Figure 2.10: Zirconia layer on the cladding inner wall observed in a  $\text{UO}_2$  fuel rod after 5 cycles [60].

A very different conclusion was drawn by Desgranges et al. in their analyses of the chamfer region of a  $\text{UO}_2\text{-Zr}_4$  fuel pellet irradiated till a burnup of 32 GWd/tHM and subsequently power ramped at an RTL of 470 W/cm during 12 h [50]. The lack of pellet clad contact in this specific region allowed the authors to give estimations of phase formation without any impact from the cladding. Based on quantitative estimations by EPMA of the Cs-I-Te-Mo-Ba-U-O concentrations in this region and thermochemical calculations, the authors concluded that a  $\gamma\text{U}_4\text{O}_9$  phase rich in Cs and other FPs was likely to have formed at the grain boundaries of the  $\text{UO}_2$  sample. The corresponding

oxygen potential was estimated to be greater than  $-350 \text{ kJ/mol O}_2$  at  $400 \text{ }^\circ\text{C}$ , therefore far above that of the expected Mo-MoO<sub>2</sub> buffer.

Desgranges et al. analyzed the release of Xe, Cs, Te and I from UO<sub>2</sub>-ZrO<sub>2</sub> irradiated samples [61] (average burnups of 26 and 35 GWd/tHM). The first rodlet (26 GWd/tHM) was subsequently ramped till a RTL of 450 W/cm followed by an immediate unloading (no holding period at RTL). The second rodlet (35 GWd/tHM) was ramped till an RTL of 520 W/cm maintained during 90 s. Figure 2.11 shows SIMS measurements of the radial profiles of these FPs along the fuel pellet radius after the power transients. Note that SIMS measurements are not quantitative (except for Xe) but relative to a stable isotope in the fuel (<sup>238</sup>U for cations, <sup>18</sup>O for anions). The measurements are compared in each case to estimations of the quantity of FPs resulting from the fission reactions (curve "creation" in the graphs).

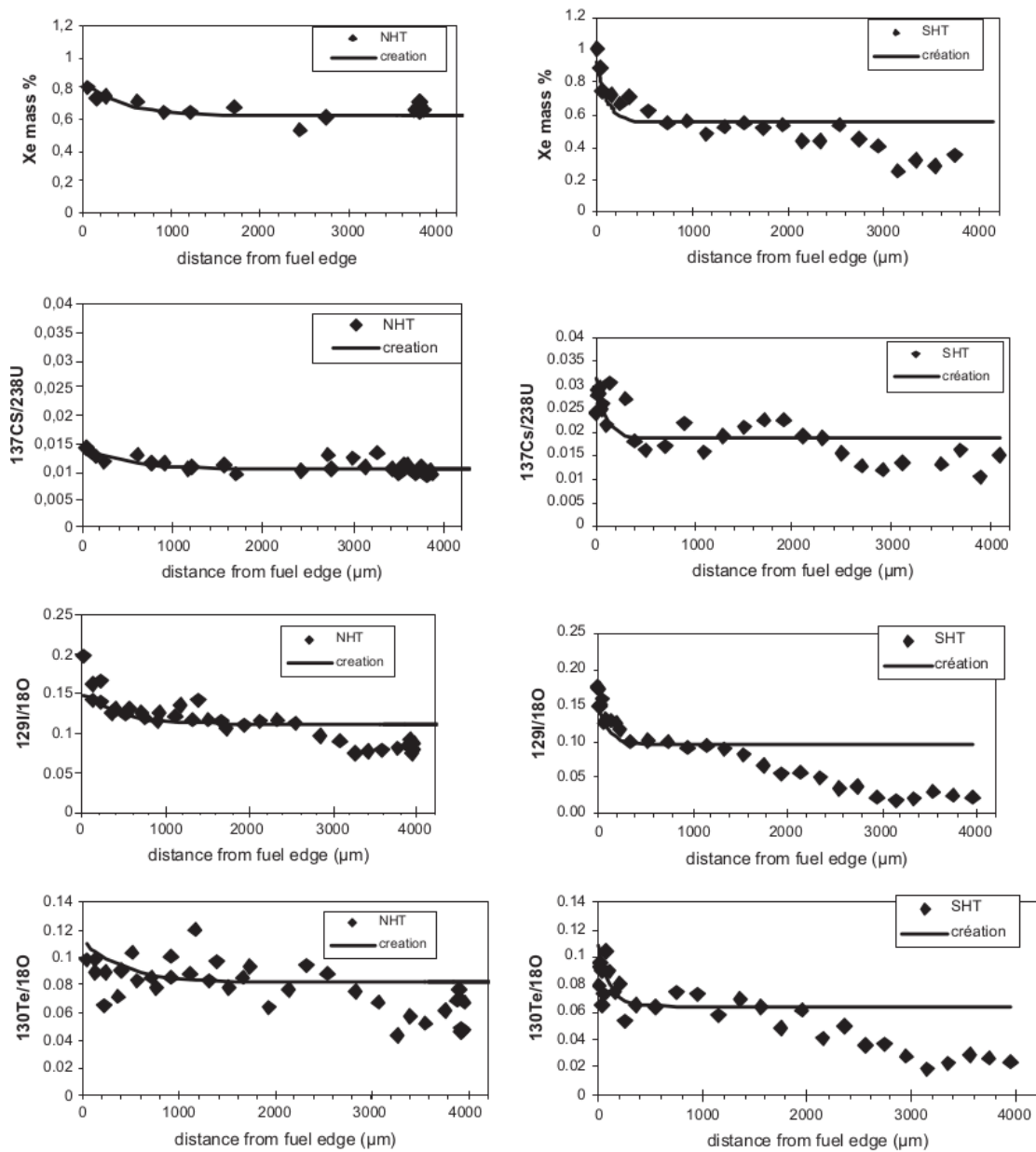


Figure 2.11: SIMS measurements presenting radial distribution of Xe, Cs, I and Te along the mid-pellet plane. NHT–no holding time, SHT–short holding time. Adapted from [61].

As can be observed, the greatest differences between the creation line and the measurements points took place at the pellet center where the higher temperatures were reached. Three main observations were reported by Desgranges et al. from the SIMS profiles. First, the Xe and Cs profiles were found to be very close, meaning that the release of these two volatile FPs is driven by similar mechanisms, as reported by other authors from out-of-pile annealing experiments [62]. Second, the Te and I profiles were found well correlated to each other and significantly different from those of Xe and Cs, indicating a more important and faster release of these FPs during the power transients.

In particular, the first ramp test with no holding time at RTL showed a non negligible loss of Te and I but no release of Cs and Xe. Desgranges et al. confirmed these results by performing SIMS ionic images of the pellet clad interface on the same sample. SIMS images revealed the presence of high concentrations of  $^{129}\text{I}$  and  $^{130}\text{Te}$  in most case co-localized at the clad inner surface, see Figure 2.12.

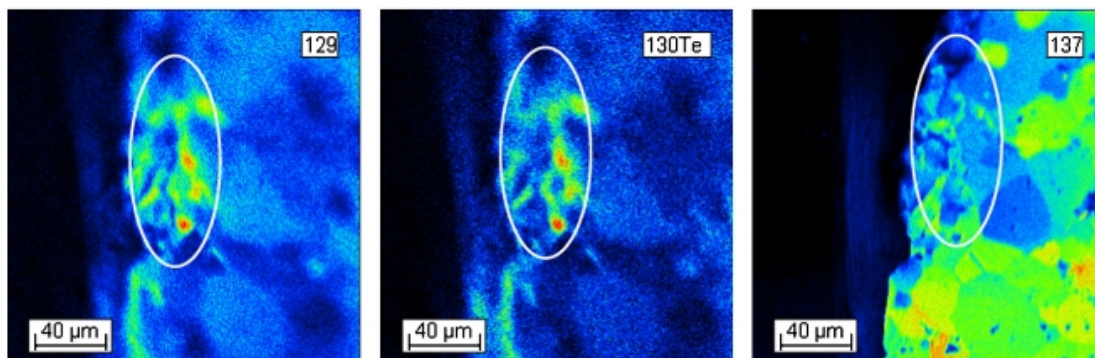


Figure 2.12: SIMS images presenting  $^{129}\text{I}$ ,  $^{130}\text{Te}$  and  $^{137}\text{Cs}$  near the pellet periphery. Dark blue corresponds to the lowest concentration and red to the highest concentration [61].

High concentrations of  $^{137}\text{Cs}$  were also observed but could not be correlated with  $^{129}\text{I}$  and  $^{130}\text{Te}$ . A rather surprising observation since the presence of CsI compounds in the fuel pellet clad gap is well supported by experimental characterization [14, 63] and highly expected since its formation is thermodynamically favored [5]. What is not clear is whether CsI compounds are formed before reaching the gap (i.e., in the fuel) or in the gap [19]. To discuss this point, Desgranges et al. proposed a thermodynamic study of the quaternary chemical system Cs-O-I-Te in the thermal conditions of the fuel pellet periphery (600 °C), summarized in Figure 2.13. Assuming that the oxygen partial pressure in this region is controlled by the irradiated fuel (see the black point in the left figure), they concluded that the most likely gas compounds in the gap would be  $\text{TeI}_{2(g)}$  and  $\text{Cs}_2\text{I}_{2(g)}$ , in consistency with the SIMS images.

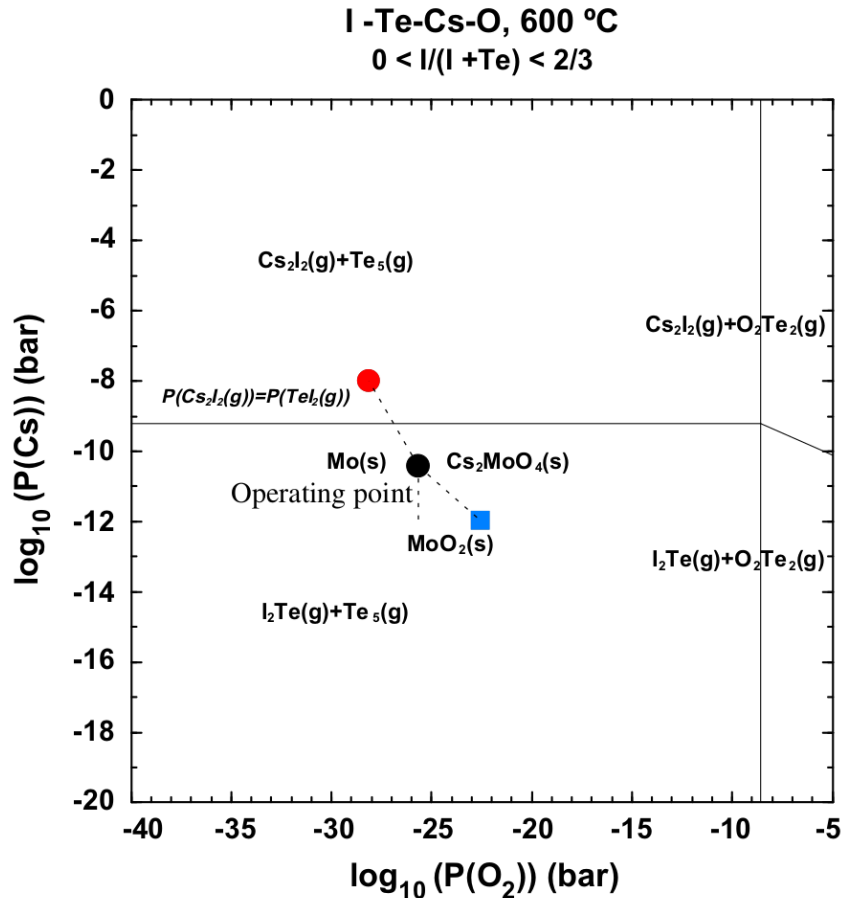


Figure 2.13: Cs-I-O-Te gas phase diagram at 600 °C with the assumption that  $0 < \frac{I}{I+Te} < \frac{2}{3}$ . The red and blue points refer to the experiments studied by Desgranges et al. Figure adapted from [61].

#### 2.1.4 Oxygen potential measurements in irradiated fuel

Because of its importance with regards to FPs speciation, great efforts have been put over the years to measure the oxygen potential of irradiated fuel. Some experiments on irradiated and SIMulated irradiated FUELS (called SIMFUEL) have been performed [7, 64–67]. All the authors used the solid state galvanic cell method to measure the oxygen potential. Most of the measurements were made at temperatures between 750 and 1000 °C and are therefore representative of irradiated fuel in normal operating conditions. They are presented in Sections 2.1.4.1 and 2.1.4.2. A few measures were performed on irradiated fuels after power ramps. They show the impact of the power transient on the oxygen potential and are detailed in Section 2.1.4.3.

The galvanic cell consists of a reference electrode, a working electrode and a solid oxide electrolyte. The electromotive force between the reference and working electrodes is

related to the oxygen potential. The oxygen potential of the reference electrode is known and the oxygen potential of the studied sample can be determined.

#### 2.1.4.1 SIMulated irradiated FUEL (SIMFUEL)

Une and Oguma prepared SIMFUEL samples by mixing oxides powders of Zr, Nd, Y, Ce and Pr with an initially stoichiometric  $\text{UO}_2$  powder [64]. The authors used fission products that are expected to form soluble oxides in the fuel matrix. Three samples were prepared that simulated irradiated fuel of average burnups 2, 5 and 10 at% (which corresponds to 18, 46 and 92 GWd/tHM respectively according to the relation given in Section 1.1.2).

The authors measured the oxygen potential of the SIMFUEL samples at 1000 and 1300 °C. The impact of fission products addition on the oxygen potential was clearly seen at 1300 °C. Oxygen potentials measured in the 10 at% burnup sample were the highest. It was concluded that oxygen potential increases linearly with burnup. Second conclusion drawn was that oxygen potential increases with increasing O/M ratio. Experimental measurements are shown in Figure 2.14.

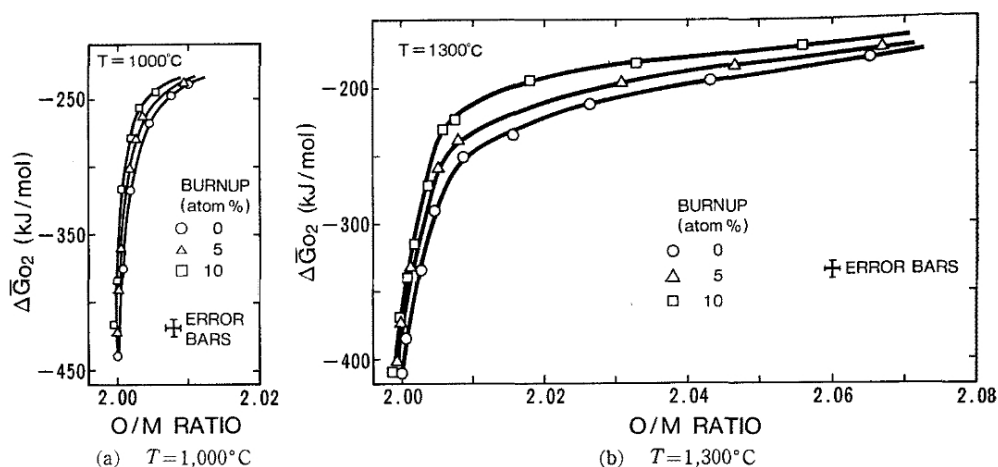


Figure 2.14: Oxygen potential of SIMFUELS of increasing burnups (2, 5 and 10 at%) as a function of the O/M ratio at 1000 and 1300 °C. Adapted from [64].

#### 2.1.4.2 Irradiated fuel in normal operating conditions

Une et al. carried out one more experiment a few years later [65]. The authors measured the oxygen potential in irradiated  $\text{UO}_2$  and  $\text{UO}_2\text{-Gd}_2\text{O}_3$  samples (weight fraction of  $\text{Gd}_2\text{O}_3$  – 2%). The samples were irradiated in commercial BWRs. The range of burnups was 13-30 GWd/tHM. Oxygen potential was measured at 750 °C which corresponds to the external temperature of a fuel pellet. Experimental measurements are shown in

Figure 2.15. It can be noticed that samples with higher burnup have higher oxygen potential. Oxygen potential seems to decrease from the rim region to the fuel pellet center. The experiments showed that the gadolinium-doped samples had slightly lower oxygen potentials than the  $\text{UO}_2$  samples in spite of close burnups.

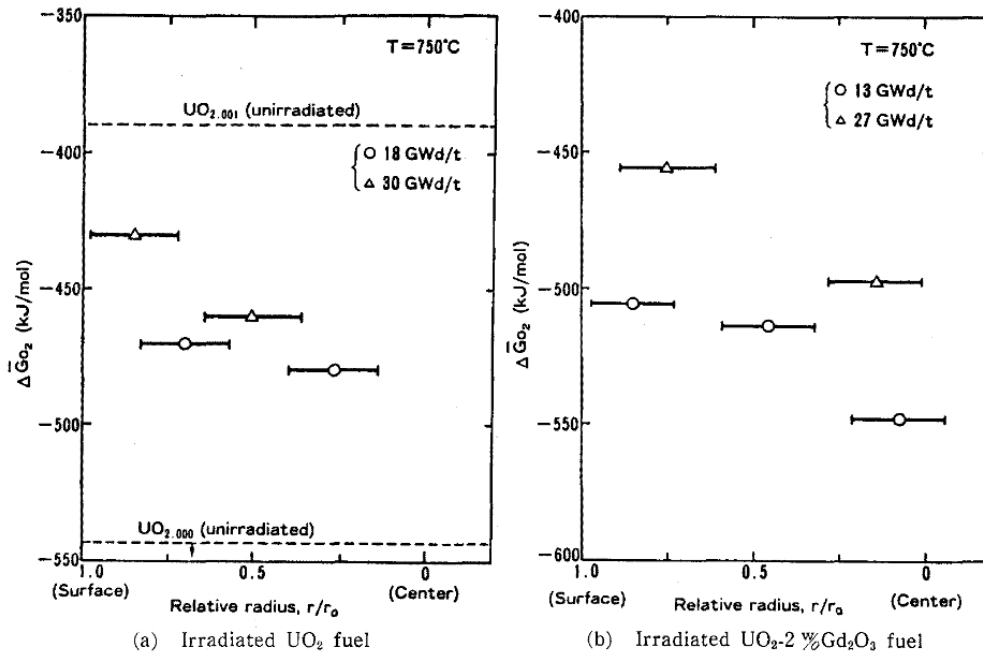


Figure 2.15: Oxygen potential measured in irradiated  $\text{UO}_2$  (a) and gadolinium-doped fuel (b). Adapted from [65].

All measurements are upper bounded by the  $\text{Mo}/\text{MoO}_2$  redox buffer, as shown by Ellingham diagram. The oxygen potential corresponding to this redox system at  $750^\circ\text{C}$  is around  $-404$  kJ/mol  $\text{O}_2$ .

Matzke also carried out experiments on irradiated fuel [67]. The author measured the oxygen potential in uranium dioxide fuels irradiated in a commercial LWR. The measurements obtained on four samples with three different burnups are shown in Figure 2.16. The measurements were repeated three times on every sample (1<sup>st</sup>, 2<sup>nd</sup> and 3<sup>rd</sup> run in the figure). One can notice a small scatter between runs. The author explained that it could be a result of rearrangement, precipitation or compound formation of fission products during the first run. An alternative explanation is a surface oxidation of samples varying between runs.

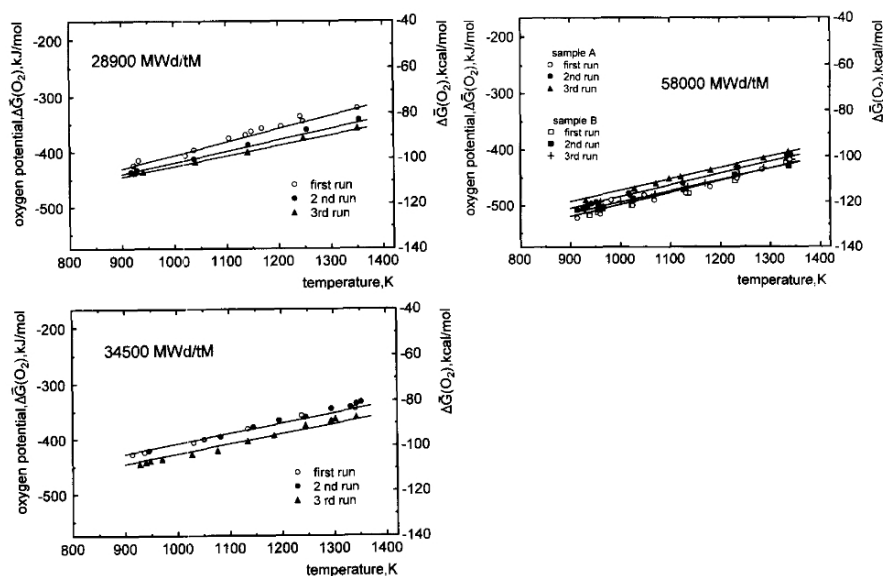


Figure 2.16: Oxygen potential measurements of samples with burnups of 28.9 GWd/tHM (top left), 34.5 GWd/tHM (bottom left) and 58 GWd/tHM (top right). Adapted from [67].

While the samples with 28.9 and 34.5 GWd/tHM average burnups have very close oxygen potentials, a significant decrease of the oxygen potential was observed on the measurements relative to the high burnup sample (58 GWd/tHM average burnup). Matzke has reported that this decrease may be caused by an unusual irradiation history with high power during the first cycle, lower during the second one and high again in the last cycle. The author concluded that the measured values indicated a probable buffering of the oxygen potential by Mo/MoO<sub>2</sub> (28.9 and 34.5 GWd/tHM) or by the Zr/ZrO<sub>2</sub> (58 GWd/tHM) from the cladding. As explained before, the Zr/ZrO<sub>2</sub> buffering is likely to occur in consequence of the pellet-clad gap closing during irradiation. Oxygen from the fuel pellet rim leads to the formation of an internal layer of zirconia approximately 10  $\mu\text{m}$  thick that certainly influences the oxygen potential of the fuel. The high average burnup of one of the fuel is consistent with the presence of a continuous layer of zirconia at the pellet-clad interface [68].

Matzke measured the oxygen potential in the rim region of a highly irradiated fuel [66]. Fuel was irradiated in a PWR reactor up to an average burnup of 75 GWd/tHM. According to numerical calculations and measurements of the concentration in Nd, the rim region had a very high burnup, exceeding 200 GWd/tHM [69, 70]. The author measured the oxygen potential in samples from the rim region and from the central part of the pellet. The rim zone being very narrow (<0.5 mm) and the variation of burnup being very important, the three studied samples from this small region had different burnups. The authors indicated that the burnups of the sample fell in the range 75-200 GWd/tHM without more precision. Comparison of the measured oxygen potentials in this region with those from the center of the fuel is shown in Figure 2.17.

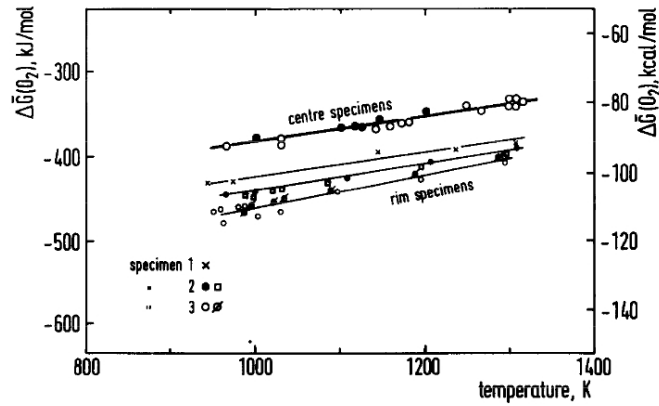


Figure 2.17: Oxygen potential at the center compared to oxygen potential from the rim region [66]. Specimens 1, 2 and 3 were sampled from the rim of the fuel pellet.

Oxygen potentials measured in the rim region were very low despite the very high burnups of the samples. All measured values were surprisingly in the range of those relative to fresh, stoichiometric  $\text{UO}_2$  fuel. Due to the high burnup and the location of the samples (pellet periphery), nearly all fissions can be attributed to Pu (low initial  $^{235}\text{U}$  enrichment). The authors concluded that the low oxygen potentials measured in the rim region could be explained by the possible buffering by  $\text{Zr}/\text{ZrO}_2$ .

The most recent measurements of oxygen potentials in irradiated fuel were published by Walker et al. [7]. The authors investigated a fuel pellet with an average burnup of 102 GWd/tHM irradiated in a commercial PWR (9 cycles). Initially, the pellet had a standard enrichment of 3.5% and was slightly hyperstoichiometric. Oxygen potentials were measured at 4 radial positions. The authors pointed out that there were big uncertainties concerning the oxygen potentials measured at the center of the pellets. The measurements at four radial positions at two different temperature increase with radius, which is shown in Figure 2.18.

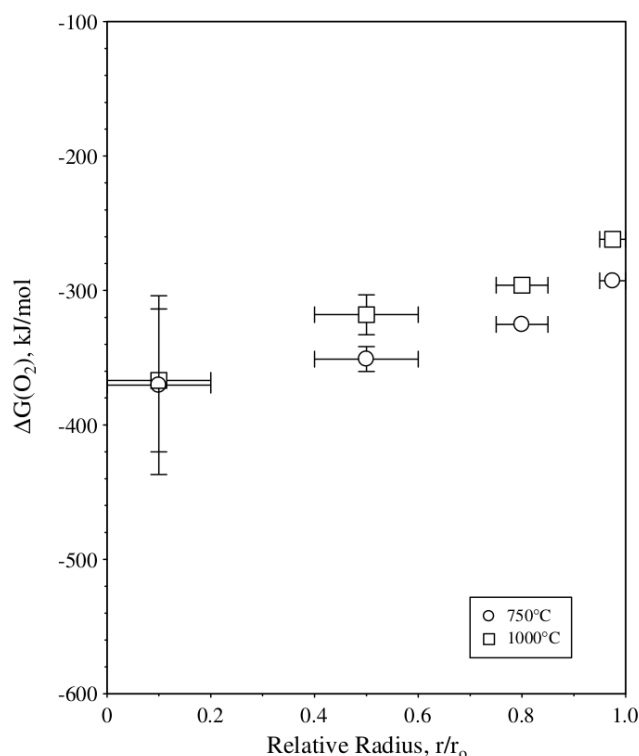


Figure 2.18: Comparison of oxygen potentials at different temperatures [7].

The measured oxygen potentials were found to increase with temperature and burnup, but not linearly as found by Une and Oguma for burnup. The highest oxygen potential was measured in the sample coming from the pellet periphery ( $r/R=0.98$ ), reaching  $-275$  kJ/mol  $O_2$  at  $1000$  °C. In disagreement with the measurements of Matzke (see Figure 2.17), the authors concluded that oxygen potential increases even at very high burnups and that the measured values cannot be attributed anymore to Mo/MoO<sub>2</sub> buffering. The measured oxygen potential in the rim region of the fuel was attributed by the author to an increasing quantity of oxide phases non dissolved in the fuel matrix (BaO, MoO<sub>2</sub> and Cs<sub>2</sub>O), in consequence of the likely reach of the solubility limit for a number of FPs. Based on the measurements of Corcoran [71] and from thermodynamic calculations of this high burnup fuel, Loukusa et al. attributed the high oxygen potential of the pellet periphery to the formation of the UMoO<sub>6</sub> oxide [72], only possible at burnups exceeding 50 GWd/tHM.

Together with direct measurements of the oxygen potential, Walker provided estimates of the O/M ratio of the fuel. Based on ICP-MS (Inductively Coupled Plasma Mass Spectrometry) measurements of the FPs contents at four radial positions and on assumptions on the quantity of oxide phases not dissolved in the fuel, he found that the O/M ratio had decreased during the nominal irradiation (initial O/M ratio of 2.005) reaching 1.982 at the pellet center and 1.955 at the pellet periphery, see white squares in Figure 2.19.

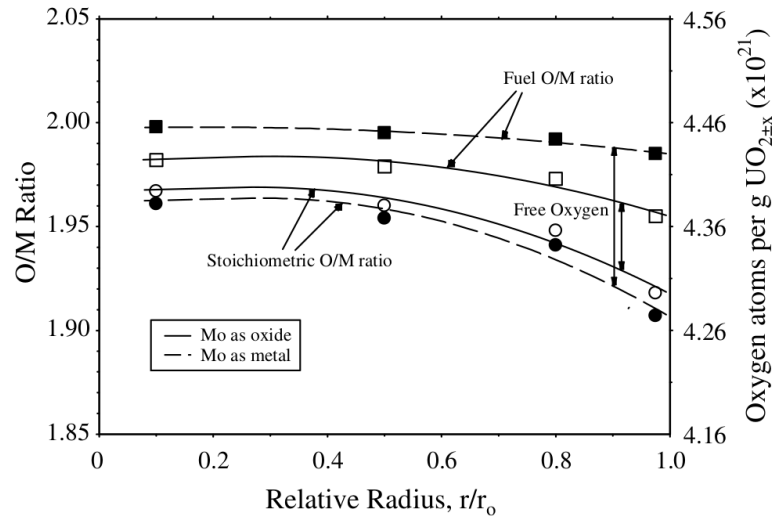


Figure 2.19: "Fuel and stoichiometric O/M ratios and the quantity of free oxygen as a function of radial position in the high burnup fuel." Fuel O/M ratio—the ratio of oxygen to FPs and actinides in solid solution and FPs forming secondary phases, stoichiometric O/M ratio—the average O/M ratio of all the FPs and actinides combined with oxygen to form stoichiometric oxides. Adapted from Walker et al. [7].

As for the oxygen potential, the O/M values are in contradiction with former estimates of the evolution of the O/M ratio of the fuel where it is stated that an initially slightly hyperstoichiometric fuel should yield an O/M close to 2 after irradiation, owing to the oxygen gathered by the cladding [51].

### 2.1.4.3 Irradiated fuel in power ramps

There are very few measurements of the oxygen potential of irradiated fuel after a power ramp. Adamson et al. measured the oxygen potential in various radial positions along the fuel pellet diameter of a BWR  $\text{UO}_2\text{-ZrO}_2$  fuel rodlet of average burnup 11.4 GWd/tHM which was irradiated at an average power of 365 W/cm [73]. The initial O/U ratio of the fuel was  $2.0015 \pm 0.0015$ . The samples were drawn off power within one minute which was considered quite effective to freeze the oxygen gradients within the fuel<sup>1</sup>. The fuel maximum temperature during the irradiation sequence was estimated over 1600 °C owing to the large diameter of the pellets (> 12 mm). Oxygen potential measurements were performed at 750 °C and are summarized in Figure 2.20 as LIT2/3.

<sup>1</sup>Note that the quenching of fuel rods used for oxygen potential measurements is rarely mentioned in the open literature and makes any interpretation of the results delicate

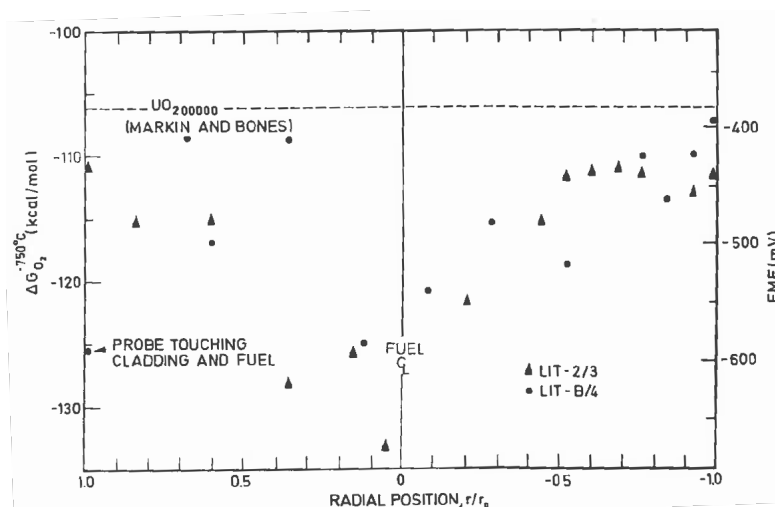


Figure 2.20: Oxygen potential measured in the fuel rods LIT-2/3 and LIT-B/4 studied by Adamson et al. [73].

The oxygen potential was found to increase with the radial position from a minimum value at the pellet center of  $-540$  kJ/mol  $O_2$  till  $-460$  kJ/mol  $O_2$  at the pellet periphery. According to Ellingham diagram and assuming that the Mo/MoO<sub>2</sub> oxide buffer controls the oxygen partial pressure, the oxygen potential should be around  $-264$  kJ/mol  $O_2$  at  $1600$  °C. The authors attributed the very low oxygen potential at the pellet center to a migration of oxygen from hot to cold regions of the fuel. Connected to these measurements, they estimated that the O/M ratio decreased at the pellet center during the power sequence till  $\sim 1.997$  while it increased at the pellet outer surface till  $\sim 1.999$ .

Adamson et al. measurements are in line with the estimations from Riglet-Martial et al. based on chromium solubility in Cr-doped UO<sub>2</sub> fuel rodlets after power ramps, as detailed in Section 2.1.3.2. According to the latter authors, these results are evidence of a significant reductive perturbation in the high temperature section of the pellets during the power transients. The evolution of the fuel may be summarized by Figure 2.21, based on thermodynamic calculations of an irradiated UO<sub>2</sub> fuel of average burnup 30 GWd/tHM.

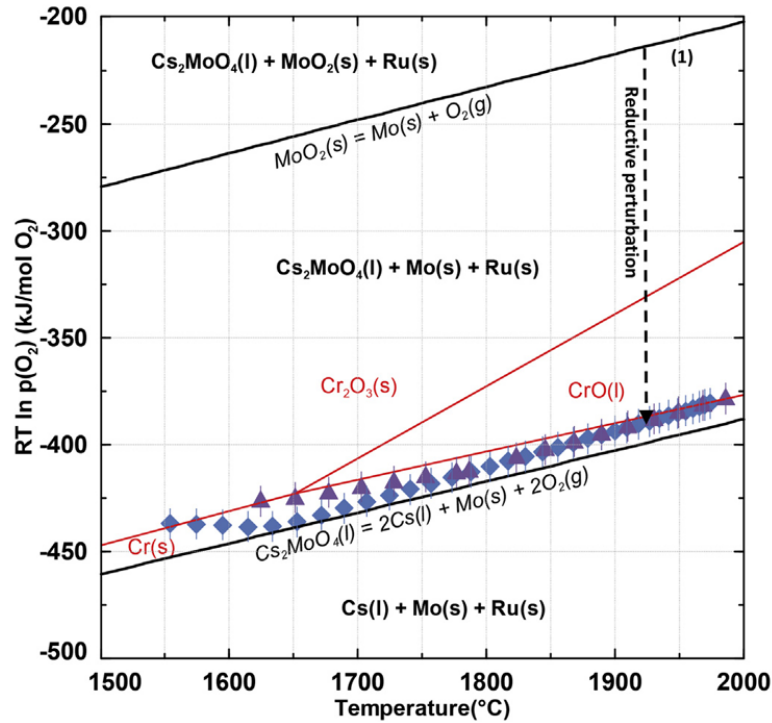


Figure 2.21: Evidence of the strong reduction of oxygen potential during the power ramp. Calculations performed with the Factsage software [74, 75]. The blue and purple points show the equilibrium state after two power ramps studied by Riglet-Martial et al. [52].

Curve (1) in the figure represents the oxygen potential of the fuel if it was controlled, as expected, by the Mo/MoO<sub>2</sub> oxide buffer. Experimental points give the calculated oxygen potentials in the two studied fuel pellets after power transients at 470 and 530 W/cm<sup>2</sup>, as deduced from chromium weight fraction measurements by EPMA. From the thermodynamic calculations, it appears that the post-ramp state is in the vicinity of the Cs<sub>2</sub>MoO<sub>4</sub>/Cs + Mo redox system. This was found consistent with the stabilization of intermetallic phases of Mo, Ru and Cr as observed experimentally (see Figure 2.7). The reductive perturbation during the power transient is indicated by the dotted line. As Adamson et al., the authors attributed this perturbation to oxygen redistribution from the hot center to the cold periphery induced by the thermal gradient. A non discussed point in the work of Riglet-Martial et al. is the possible oxygen back redistribution in the fuel during the cooling down period at the end of the power ramps. It is therefore not excluded that the estimated oxygen potentials are upper bounds of the levels reached during the power transient. Note that cesium molybdate, Cs<sub>2</sub>MoO<sub>4</sub>, a complex oxide, has never been observed in irradiated PWR fuels but is known to be formed at the pellet-clad interface of SFR fuels [76].

Besmann et al. performed thermodynamic calculations of most of the aforementioned fuels with oxygen potential measurements (Une et al., Adamson et al., Matzke, Walker

et al.) [77]. Only the measures relative to the fuel mid-pellet radius and performed at 750 °C were considered. They plotted the selected oxygen potential measurements in function of burnup and showed that a bi-linear trend appeared, see Figure 2.22.

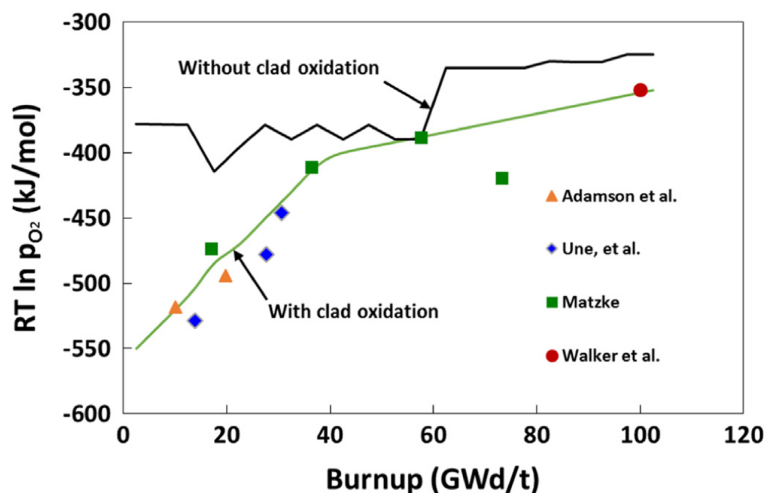


Figure 2.22: Oxygen potential calculated at 750 °C without and with oxygen loss due to cladding oxidation. Adapted from Besmann [77].

One interesting point is that the authors had to remove oxygen from the system to obtain meaningful estimates of the oxygen potential. They attributed however the oxygen deficiency to the development with burnup of the zirconia layer at the pellet clad interface. Seducing as it is, this hypothesis does not explain how oxygen from mid-pellet radius reached the pellet periphery during irradiation, whether released in a gaseous compound or by diffusion in the fuel. It was furthermore shown by Minne that oxygen liberated at the pellet periphery by fission reactions is largely sufficient to explain the formation of a  $\sim 10 \mu\text{m}$  layer of zirconia [59].

### 2.1.5 Conclusions

Evidence of a reductive perturbation in the fuel pellet core during power ramps was pointed out by a few authors based on direct measurements of the oxygen potential, indirect estimations of oxygen potential from dopants solubility or thermodynamic calculations. This apparent decrease of the oxygen potential is consistent with the stabilization of intermetallic phases as observed experimentally. Authors attribute these changes to oxygen transport in the fuel in relation to the high thermal gradient at hand, a phenomenon referred as oxygen thermal diffusion [78].

## 2.2 Oxygen transport in the fuel

In this section, the literature on oxygen transport in nuclear fuels by thermal diffusion is reviewed. The main parameters governing oxygen transport are then discussed.

### 2.2.1 Theory

#### 2.2.1.1 Introduction

Matter transport (actinides, fission products and oxygen) in nuclear fuels has first been studied in (SFR) fuels due to the high temperature gradients encountered, which lead to composition gradients (uranium, plutonium, oxygen and fission products). Matter transport has been attributed to thermal diffusion in the solid, by analogy with the phenomenon first studied by Soret in certain aqueous solutions. The application of the thermal diffusion theory to nuclear fuels was published in the 70's by Bober and Schumacher [78]. In PWR fuels, the temperatures are usually too low to lead to observable thermal diffusion of uranium, plutonium and FPs. For this reason, the presentation of thermal diffusion mechanisms in this section will be restricted to the most mobile element, oxygen. At moderate temperatures, solid state mass transport is considered the dominant process at the origin of oxygen redistribution. A review of matter transport phenomena in SFR fuels was recently proposed by Welland [79]. The general description of thermal diffusion in solids is obtained from the thermodynamics of irreversible processes. The basic idea is that for numerous irreversible processes, there exist linear relations between the thermodynamic forces and the fluxes. In the case of simultaneous heat and mass transport, the matter and heat fluxes ( $\underline{J}_k$  and  $\underline{J}_q$  respectively), are related as follows to their respective thermodynamic forces  $\underline{X}_k$  and  $\underline{X}_q$ :

$$\underline{J}_k = \sum_{j=1}^n a_{kj} \underline{X}_j + a_{kq} \underline{X}_q, \quad k = 1, \dots, n$$

$$\underline{J}_q = \sum_{j=1}^n a_{qj} \underline{X}_j + a_{qq} \underline{X}_q \quad (2.7)$$

where the  $a_{kj}$ ,  $a_{kq}$ ,  $a_{qj}$  and  $a_{qq}$  are the phenomenological coefficients. In general, the following thermodynamic forces are used:

$$\underline{X}_k = -\text{grad}(\mu_k) \quad (2.8)$$

$$\underline{X}_q = -\frac{1}{T} \text{grad}(T) \quad (2.9)$$

with  $T$  the absolute temperature and  $\mu_k$  the chemical potential per mole of component  $k$  given by:

$$\mu_k = \mu_k^\circ + RT \ln \gamma_k x_k \quad (2.10)$$

where  $\mu_k^\circ$  is the standard chemical potential,  $R$  the gas constant,  $\gamma_k$  the activity coefficient and  $x_k$  the mole fraction of component  $k$ . The set of equations 2.7 can be applied to diffusion processes in which the interactions with vacancies in the solid lattice are or not involved. With mathematical manipulations, the mass and heat fluxes can be expressed as a function of the mole fraction gradients instead of the chemical potential gradients resulting in the standard equations for thermal diffusion as described in the next sections. Complete derivation of the thermal diffusion equations starting from the theory of irreversible processes is detailed in Appendix A.

### 2.2.1.2 Thermal diffusion in hypostoichiometric fuels

Thermal diffusion in non irradiated hypostoichiometric mixed oxide fuels has been formulated by Bober and Schumacher [78]. Hypostoichiometric mixed oxide fuel consists of a  $U_{1-q}Pu_qO_{2-x}$  matrix where  $x = 2 - O/(U + Pu) > 0$  is the stoichiometry deviation and  $q$  the mole fraction of Pu. These fuel materials are used in SFRs. Stoichiometry deviations can reach high values (0.2-0.4). According to Bober and Schumacher, the thermal diffusion process can be adequately represented by a binary system including oxygen atoms and oxygen vacancies. The evolution of the system is governed by the flux of oxygen vacancies  $\underline{J}_v$  in the lattice defined by:

$$\underline{J}_v = -N\tilde{D}_v \left[ \underline{\text{grad}}(x_v) + \frac{(1-x_v)x_v}{1 + (\partial \ln \gamma_v / \partial \ln x_v)} \frac{Q_v^*}{RT^2} \underline{\text{grad}}(T) \right] \quad (2.11)$$

with

$N$ -total number of oxygen atoms per unit volume

$\tilde{D}_v$ -chemical diffusion coefficient of oxygen vacancies

$x_v$ -atomic fraction of oxygen vacancies

$1 + (\partial \ln \gamma_v / \partial \ln x_v)$ -thermodynamic factor

$\gamma_v$ -activity coefficient of oxygen vacancies

$Q_v^*$ -molar heat of transport of oxygen vacancies

$R$ -gas constant

$T$ -absolute temperature

The specificity of thermal diffusion is the oxygen vacancies flux that results from the application of a thermal gradient ( $\underline{\text{grad}}(T) \neq 0$ ), even if there is no concentration gradient ( $\underline{\text{grad}}(x_v) = 0$ ). A number of interesting properties are derived from the theory of irreversible processes at the origin of the thermal diffusion formulation. In the binary system at hand, there is equivalence between the oxygen vacancies and oxygen atoms fluxes ( $\underline{J}_O = -\underline{J}_v$ ), diffusion coefficients of oxygen vacancies and atoms ( $\tilde{D}_{O_v} = \tilde{D}_v$ ), heats of oxygen vacancies and atoms transport ( $Q_{O_v}^* = Q_v^*$ ) and thermodynamic factors ( $1 + \partial \ln \gamma_v / \partial \ln x_v = 1 + \partial \ln \gamma_o / \partial \ln x_o$  with  $x_o = 1 - x_v$  the atomic fraction of oxygen

atoms). This implies that a unique equation needs to be solved to describe the evolution of the oxygen in the material. Furthermore, in non irradiated mixed oxide fuels, Bober and Schumacher show that the oxygen vacancy concentration and the stoichiometry deviation are related as follows:

$$x = 2x_v \quad (2.12)$$

The thermal diffusion equation can therefore be equivalently formulated as a function of the stoichiometry deviation. To further simplify the system, Bober and Schumacher consider a dilute solution of oxygen vacancies. In this case, the  $\partial \ln \gamma_v / \partial \ln x_v$  term disappears and  $1 - x_v$  equals approximately 1.

The transient thermal diffusion equation in hypostoichiometric mixed oxide reads as follows:

$$N \frac{\partial x_v}{\partial t} = -\text{div.} (\underline{J}_v) \quad (2.13)$$

Lassmann proposed the first transient solution for thermal diffusion at the end of the 80's, a model that was implemented in the fuel performance code TRANSURANUS and applied to SFR fuels [36]. Considering the axial symmetry of the fuel rod and the lack of axial gradients, reformulating the problem in terms of the stoichiometry deviation, the following equation was solved by the author:

$$\frac{\partial x}{\partial t} = \frac{1}{r} \frac{\partial}{\partial r} \left\{ r \tilde{D}_{Ov} \left( \frac{\partial x}{\partial r} + x \frac{Q_{Ov}^*}{RT^2} \frac{\partial T}{\partial r} \right) \right\} \quad (2.14)$$

where  $r$  is the fuel pellet radius. Equation 2.14 depends on two parameters: the so-called chemical diffusion coefficient of oxygen  $\tilde{D}_{Ov}$  and the heat of transport of oxygen  $Q_{Ov}^*$  in hypostoichiometric fuel.

### 2.2.1.3 Thermal diffusion in hyperstoichiometric fuels

In a hyperstoichiometric oxide or mixed oxide fuel  $U_{1-q}Pu_qO_{2+x}$  (with  $x = O/(U + Pu) - 2 > 0$ ), another diffusion mechanism needs to be considered: the movement of interstitial oxygen atoms to neighboring interstitial sites without permanently displacing lattice atoms. According to Bober and Schumacher, the flux of interstitial oxygen atoms has negligible effect on the overall oxygen atoms. Thus, it is possible to describe the evolution of the material by only considering the flux of oxygen interstitial atoms which can be expressed as follows:

$$\underline{J}_i = -N \tilde{D}_{O_i} \left[ \underline{\text{grad}}(x_i) + \frac{x_i}{1 + (\partial \ln \gamma_i / \partial \ln x_i)} \frac{Q_{O_i}^*}{RT^2} \underline{\text{grad}}(T) \right] \quad (2.15)$$

where

$N$ —total number of oxygen atoms per unit volume  
 $\tilde{D}_{O_i}$ —chemical diffusion coefficient of oxygen interstitials  
 $x_i$ —atomic fraction of oxygen interstitials  
 $1 + (\partial \ln \gamma_i / \partial \ln x_i)$ —thermodynamic factor  
 $\gamma_i$ —activity coefficient of oxygen interstitials  
 $Q_{O_i}^*$ —molar heat of transport of oxygen interstitials  
 $R$ —gas constant  
 $T$ —absolute temperature

Considering a dilute solution of oxygen interstitial, the equation can be further simplified since the  $\partial \ln \gamma_i / \partial \ln x_i$  term disappears. The transient thermal diffusion equation in hyperstoichiometric fuel reads as follows:

$$N \frac{\partial x_i}{\partial t} = \text{div.} (\underline{J}_i) \quad (2.16)$$

As for hypostoichiometric fuel, the stoichiometry deviation is related to the oxygen interstitial atomic fraction as follows:

$$x = x_i \quad (2.17)$$

The thermal diffusion equation can therefore be equivalently formulated as a function of the stoichiometry deviation. Noting that Equation 2.14 equally applies to (hypo-) or hyperstoichiometric fuel and provided the assumption of a dilute solution of (vacancies) interstitials is considered, Lassmann applied the thermal diffusion equation 2.14 to PWR hyperstoichiometric fuels [36] with a specific heat of transport of oxygen interstitials  $Q_{O_i}$ . The diffusion coefficient of oxygen interstitials was considered equal to that of oxygen vacancies  $\tilde{D}_{O_v} = \tilde{D}_{O_i} = \tilde{D}_O$ .

One dimensional simulations of oxygen radial redistribution in hyperstoichiometric uranium oxide have been detailed by Ozrin et al. [80]. The authors used the formulation with the thermodynamic factor and coupled their macroscopic thermal diffusion calculations with FPs diffusion at the grain scale.

Two- and three-dimensional thermal diffusion simulations were performed by Ramirez et al. [81] and Mihaila et al. [82, 83] based also on the formulation with the thermodynamic factor (without the hypothesis of a dilute solution of interstitial atoms). The COMSOL commercial software was used to solve the thermal diffusion equation for hyperstoichiometric uranium oxide fuel in the following form:

$$\frac{\partial x}{\partial t} = \text{div.} \left\{ \tilde{D}_{O_i} \left( \underline{\text{grad}}(x) + \frac{x}{F(x, T)} \frac{Q_{O_i}^*}{RT^2} \underline{\text{grad}}(T) \right) \right\} \quad (2.18)$$

Equation 2.18 depends on three parameters: the chemical diffusion coefficient of oxygen interstitials  $\tilde{D}_{O_i}$ , the heat of transport of oxygen interstitials  $Q_{O_i}^*$  and the thermodynamic factor  $F(x, T) = 1 + \partial \ln \gamma_i / \partial \ln x_i$  in hyperstoichiometric fuel. In these works, the oxygen thermal diffusion equation was coupled with the heat transport equation, most of the parameters being dependent on temperature and stoichiometry deviation. The impact of oxygen redistribution on the maximum fuel temperature was studied.

Higgs et al. included thermal diffusion of oxygen in numerical simulations of defective fuels in CANDU reactors to model the pronounced oxidation of the fuel resulting from the ingress of water vapor [84]. Welland extended the work to couple oxygen thermal diffusion and heat transport in CANDU fuels with consideration of non congruent fuel melting [85]. Oxygen thermal diffusion was implemented in solid and liquid uranium oxide.

## 2.2.2 Chemical diffusion coefficient of oxygen

Discussion on chemical diffusion coefficient of oxygen will be limited to uranium oxides ( $\text{UO}_{2\pm x}$ ) since this work will only concern PWR standard oxide fuels. In his first implementation of transient thermal diffusion [86], Lassmann used the following expression for the chemical diffusion coefficient of oxygen, based on the review of experimental data of Matzke [87]:

$$\tilde{D}_O = 1.39 \times 10^{-6} \exp(-75900/RT) \quad (2.19)$$

with  $\tilde{D}_O$  in  $\text{m}^2/\text{s}$  and  $T$  the temperature in K. Due to the scattering of data, the known dependency of the chemical diffusion coefficient on the hypo- or hyperstoichiometry of the fuel was neglected by the author.

Since then, a few authors have proposed more precise estimations of the chemical diffusion coefficient of oxygen with a clear separation between the hypo- and hyperstoichiometric domains. They are usually based on measurements of the self-diffusion coefficient of oxygen, obtained from the evolution of a radioactive oxygen tracer ( $^{18}\text{O}$ ) in the fuel. In these tracer experiments, no oxygen chemical potential gradient is considered. During self-diffusion, vacancies and interstitials execute a random walk among sites in the crystal structure. The trajectories they follow involve a series of discrete jumps and each jump is uncorrelated with the previous one. There are many publications concerning the self-diffusion coefficient of oxygen in uranium dioxide. They present values of the self-diffusion coefficient for a wide range of temperatures and stoichiometry deviations. The first attempt to gather them was made by Breitung in 1978 [88]. He collected all the available data and compared to his model. To determine the self-diffusion coefficient, Breitung used the dynamical theory of self-diffusion. This theory is first described in the next section. A second way to estimate the self-diffusion coefficient is to define

the mobilities of point defects, as proposed by Moore et al. [89]. The mobility based approach is also described in the next section.

From the estimation of self-diffusion coefficients, and by considering the relation between the chemical potential and the mole fraction of oxygen, it is possible to determine the chemical diffusion coefficient which relates the molar flux to the mole fraction gradient. The last part of this section will detail the derivation of the chemical diffusion coefficient.

### 2.2.2.1 Self-diffusion coefficient (or tracer diffusion coefficient)

#### The dynamical theory of self-diffusion

To describe the self-diffusion coefficient, Breitung used the dynamical theory of self-diffusion. This theory proposed by Rice [90] assumes that Frenkel defect pairs formation has the biggest impact on the self-diffusion coefficient.

In the dynamical theory, concentration of oxygen vacancies  $[V_O]$  and oxygen interstitials  $[O_i]$  may be expressed as:

$$[V_O] = \frac{-x - K_{FO} + [(x + K_{FO})^2 + 4K_{FO}]^{1/2}}{2} \quad (2.20)$$

$$[O_i] = \frac{x - K_{FO} + [(x + K_{FO})^2 + 4K_{FO}]^{1/2}}{2} \quad (2.21)$$

where  $x$  is the stoichiometry deviation of the fuel. Establishment of Equations 2.20 and 2.21 are explained in details in Appendix B.  $K_{FO}$  from Equations 2.20 and 2.21 is the Frenkel pair formation constant dependent on enthalpy  $\Delta H_{FO}$  and entropy  $\Delta S_{FO}$  of formation of Frenkel defects:

$$K_{FO} = \exp\left(\frac{-\Delta H_{FO}}{R_g T} + \frac{\Delta S_{FO}}{R_g}\right) \quad (2.22)$$

Equations 2.20, 2.21 and 2.22 may be used to write a single equation for the oxygen self-diffusion coefficient in hypo- and hyperstoichiometric fuels. The self-diffusion coefficient of oxygen in non-stoichiometric  $UO_2$  reads as follows:

$$D_O^* = D_{V_O}^0 [V_O] \exp\left(\frac{-\Delta H_{V_O}^m}{R_g T}\right) + 2D_{O_i}^0 [O_i] \exp\left(\frac{-\Delta H_{O_i}^m}{R_g T}\right) \quad (2.23)$$

$\Delta H_{V_O}^m$  and  $\Delta H_{O_i}^m$  are migration enthalpies of oxygen vacancies and interstitials respectively.  $\Delta H_{V_O}^m$  describes the energy which an atom needs to cross the potential barrier between its position and a nearby vacancy site.  $\Delta H_{O_i}^m$  is the amount of energy needed by an atom to jump from its position to a non-lattice site.  $D_{V_O}^0$  and  $D_{O_i}^0$  are constant parameters for oxygen vacancies and interstitials, respectively [88].

Breitung's approach was re-evaluated by Berthinier et al. [91]. The author used new experimental results to improve the model. By optimizing the parameters of the Frenkel pair defects model, better agreement with the experimental data has been achieved. However, there are still values that differ from the calculations significantly. The highest inconsistency is near the exact stoichiometry. These differences are up to few orders of magnitude. The author explains that by the existence of unknown phenomena controlling the self-diffusion. Comparison between the model with the parameters proposed by Berthinier and the experiments can be found in Figure 2.23 (hyperstoichiometric fuel) and Figure 2.24 (hypostoichiometric fuel).

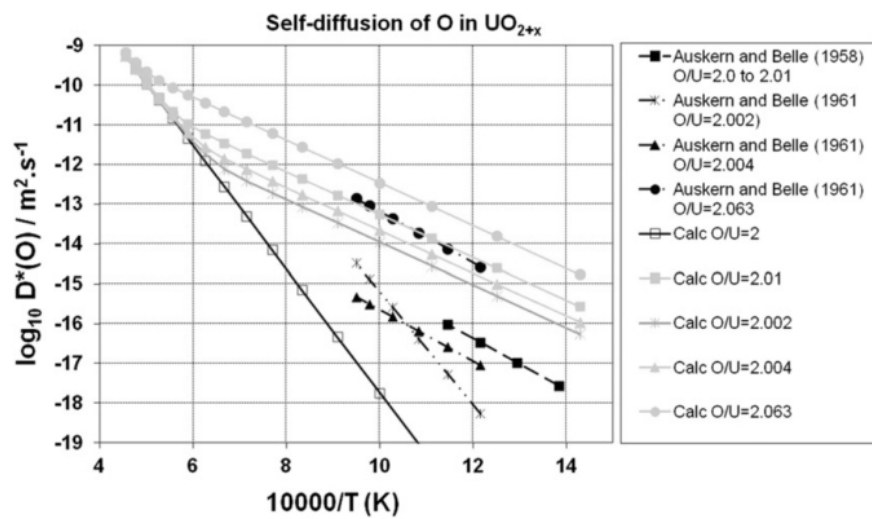


Figure 2.23: Figure from Berthinier et al. [91]. Comparison of the self-diffusion coefficient of oxygen proposed by the author with the experimental data [92,93]. Values for the hyperstoichiometric domain.

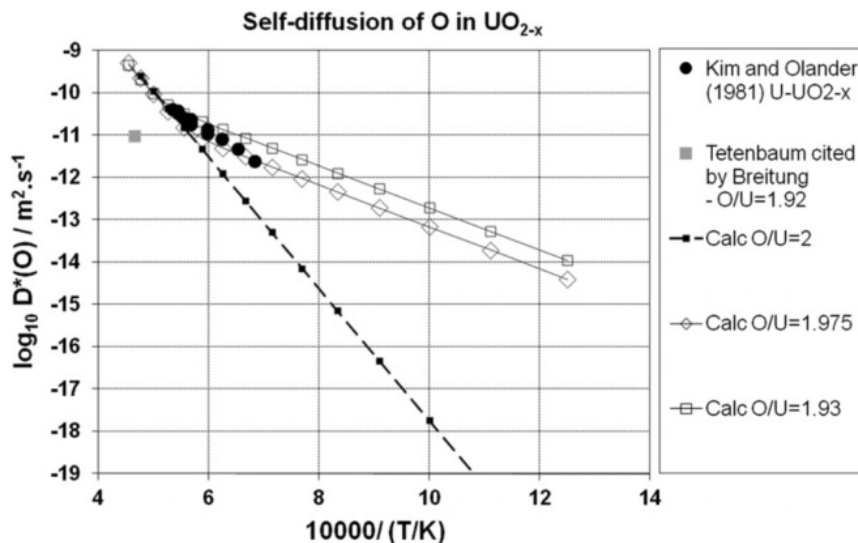


Figure 2.24: Figure from Berthier et al. [91]. Comparison of the self-diffusion coefficient of oxygen proposed by the author with the experimental data [88,94]. Values for the hypostoichiometric domain.

#### Mobility based self-diffusion model

Moore et al. have done an assessment of a mobility based oxygen diffusion model [89]. The authors model atomic transport using point defect diffusion with a CALPHAD-type description of the defect structure. The thermodynamic model used in the assessment is based on the work of Guéneau et al. [40]. The authors use 3 sub-lattices:

$$(U^{3+}, U^{4+}, U^{5+})_1 (O^{2-}, V_O)_2 (O^{2-}, V_O)_1 \quad (2.24)$$

The first lattice concerns metal atoms, the second one describes oxygen atoms on the tetrahedral site of the fluorite structure and the third one includes additional oxygen atoms incorporated in the interstitial positions. Oxygen vacancies may be present on the second and third sub-lattices.

Contrary to the dynamical theory of diffusion, Moore et al. use mobilities of point defects. This approach has been proposed by Andersson and Agren [95]. The Nernst-Einstein equation gives the following relation between the mobility and the self-diffusion coefficient of oxygen:

$$D_O^* = M_O^* RT \quad (2.25)$$

where

$D_O^*$  - self-diffusion of oxygen [ $m^2/s$ ]

$M_O^*$  - mobility of oxygen in  $UO_2$  [ $m^2 mol/s/J$ ]

$T$  - temperature [K]

$R$  - gas constant [J/mol/K]

Since the authors treat oxygen sub-lattices separately, the mobility of oxygen can be expressed as:

$$M_O^* = M_{V_o} + M_{I_o} \quad (2.26)$$

with

$M_{V_o}$  - mobility of oxygen vacancies

$M_{I_o}$  - mobility of oxygen interstitials

These individual mobility terms are expanded as follows:

$$M_{V_o} = y_{V_o} (1 - y_{V_o}) M_{V_o}^0 \exp\left(\frac{-Q_{V_o} + y_{V_o} (1 - y_{V_o}) (A - BT)}{RT}\right) \quad (2.27)$$

$$M_{I_o} = y_{I_o} (1 - y_{I_o}) M_{I_o}^0 \exp\left(\frac{-Q_{I_o} + y_{I_o} (1 - y_{I_o}) A}{RT}\right) \quad (2.28)$$

$M_{V_o}^0$  and  $M_{I_o}^0$  are pre-factors that give information on the atomic vibrational frequency and jump distances.  $Q_{V_o}$  and  $Q_{I_o}$  are activation energies.  $A$  and  $B$  are parameters of the Redlich Kister polynomials describing interaction between species on each sub-lattice.  $y_{V_o}$  and  $y_{I_o}$  are the site fractions of point defects. Parameters  $Q_i$ ,  $M_i^0$ ,  $A$  and  $B$  were adjusted in order to fit experimental measurements. Results are in Table 2.4.

Table 2.4: Parameters for oxygen diffusion in  $UO_{2\pm x}$  [89].

Assessed Oxygen Mobility Parameters			
Regular Oxygen Sublattice ( $M_{V_o}$ )		Regular Oxygen Sublattice ( $M_{I_o}$ )	
$Q_{V_o}$	53498 [J/mol]	$Q_{I_o}$	95411 [J/mol]
$M_{V_o}^0$	$4.38 \times 10^{-12}$ [ $m^2/s$ ]	$M_{I_o}^0$	$2.76 \times 10^{-12}$ [ $m^2/s$ ]
A-BT	2234 [J/mol]-19.91T	A	-90548 [J/mol]

Calculated oxygen self-diffusion coefficients are in good agreement with experimental data on hypo- and hyperstoichiometric oxide fuel, as shown in Figure 2.25.

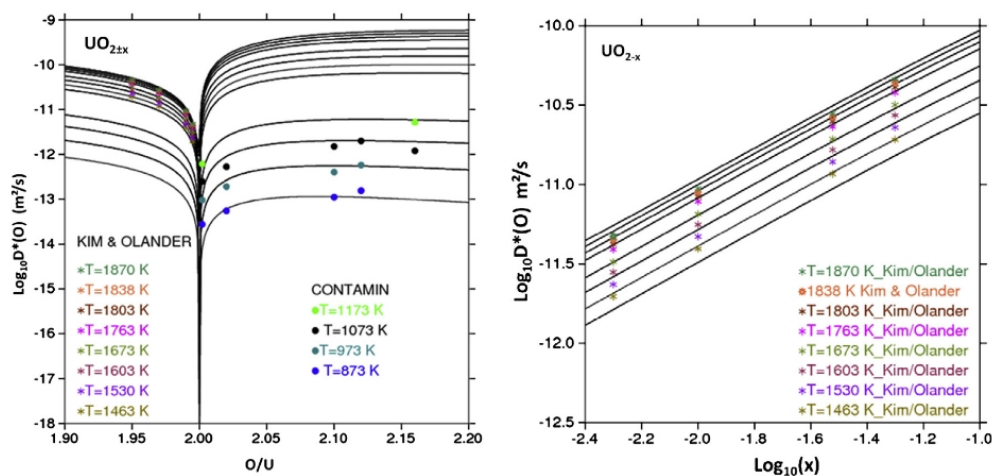


Figure 2.25: Calculated values of oxygen self-diffusion compared to experimental data from [94, 96].

### 2.2.2.2 Chemical diffusion coefficient of oxygen

The chemical diffusion coefficient is usually defined from the self-diffusion coefficient by consideration of a thermodynamic factor such that:

$$\tilde{D}_O = D_O^* \frac{\partial \ln a_O}{\partial \ln x_O} \quad (2.29)$$

where:

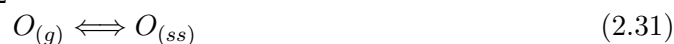
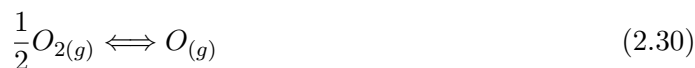
$x_O$ -atom fraction of oxygen [-]

$D_O^*$ -self-diffusion coefficient of oxygen [ $m^2/s$ ]

$a_O$ -activity of oxygen [-]

Note that the term  $(\partial \ln a_O / \partial \ln x_O)$  is the thermodynamic factor previously defined in thermal diffusion Equations 2.11 and 2.15 since  $a_O = \gamma_O x_O$  with  $\gamma_O$  the activity coefficient.

To relate oxygen activity in the solid solution  $a_O$  to the more practical oxygen partial pressure in equilibrium with the solid, the following equilibrium conditions between gaseous dioxygen  $O_{2(g)}$  and oxygen in the fluorite solid solution  $O_{(ss)}$  has to be written:



From these equilibria, the chemical potentials of oxygen in the solid and in the gas phase may be related as follows:

$$\mu_{O(ss)} = \mu_O = \frac{1}{2}\mu_{O_2(g)} = \frac{1}{2}\mu_{O_2(g)}^p + \frac{1}{2}RT \ln p_{O_2} \quad (2.32)$$

with  $\mu_{O_2(g)}^p$  the standard chemical potential of gaseous dioxygen and  $p_{O_2}$  the oxygen partial pressure.

The relation between oxygen activity and oxygen partial pressure follows from equation 2.32:

$$\ln a_O = \frac{1}{2} \ln p_{O_2} \quad (2.33)$$

Derivation of the logarithm of oxygen activity with respect to the logarithm of oxygen atom fraction ( $x_O = (2+x)/(3+x)$ ) in a  $UO_{2+x}$  leads the expression of the thermodynamic factor in the following form:

$$\frac{\partial \ln a_O}{\partial \ln x_O} = \frac{1}{2}(3+x)(2+x) \frac{\partial \ln p_{O_2}}{\partial x} \quad (2.34)$$

The complete derivation of Equation 2.34 is detailed in Appendix A. Considering that uranium dioxide is a multi-component system (U and O), most authors refer to the inter-diffusion coefficient of oxygen instead of the chemical diffusion coefficient. Darken's relation is then used to calculate the inter-diffusion coefficient of oxygen in uranium dioxide from the self-diffusion coefficients of the individual components and their atom fractions [97]. As the self-diffusion coefficient of uranium is several order of magnitude smaller than that of oxygen, a general assumption is to consider uranium atoms immobile, leading to the approximate expression of equation 2.35:

$$\tilde{D}_O = x_U D_O^* \frac{\partial \ln a_O}{\partial \ln x_O} \quad (2.35)$$

where

$x_U = 1/(3+x)$  is the uranium atom fraction.

Combined with the expression (2.34) of the thermodynamic factor, the so-called chemical diffusion coefficient of oxygen (in reality the inter-diffusion coefficient) takes the well-known following form:

$$\tilde{D}_O = D_O^* \frac{2+x}{2} \frac{\partial \ln p_{O_2}}{\partial x} \quad (2.36)$$

Note that this equation applies equally to hyper- and hypostoichiometric fuel. In the latter case,  $x < 0$ . The difficulty in the estimation of the chemical diffusion coefficient lies in the derivation of the oxygen partial pressure with the stoichiometry deviation, as can be expected from the general shape of the curves given in Figure 2.4.

Equation 2.36 has been used by Breitung [88] to calculate the chemical diffusion coefficient of oxygen. Measurements on hypostoichiometric uranium dioxide being not available at the time, the author prepared calculations for the hyperstoichiometric domain only. The  $\partial \ln p_{O_2} / \partial x$  function was derived from the Blackburn model [98, 99].

Breitung's approach to the chemical diffusion of oxygen was improved by Berthinier [91] by the use of the uranium oxide model available in the Thermodynamics of Advanced Fuels-International Database (TAF-ID) [40], illustrated in Figure 2.4, probably the most complete model available today on uranium dioxide [100]. From thermodynamic calculations performed with the THERMOCALC software of the equilibrium oxygen partial pressures as a function of the stoichiometry deviation and temperature, the author proposed mathematical functions to approximate the relation between the partial pressure  $p_{O_2}$ , the temperature  $T$  and the stoichiometry deviation  $x$ . The equation describing the equilibrium oxygen partial pressure in stoichiometric uranium dioxide depends only on temperature:

$$p_{O_2}(T) = 10^{\frac{-276.39}{RT} + 7.0024} \quad (2.37)$$

In the hypostoichiometric domain, the following relation was defined:

$$p_{O_2}(x, T) = 10^{\frac{-610}{RT} - 4.2 \times \log_{10} |x| + 11.9} \quad (2.38)$$

In the hyperstoichiometric domain, the relation reads:

$$p_{O_2}(x, T) = 10^{\frac{-116}{RT} - 1.95 \times \log_{10} |x| + 4.59} \quad (2.39)$$

The calculated oxygen partial pressures from these functions are shown in Figure 2.26.

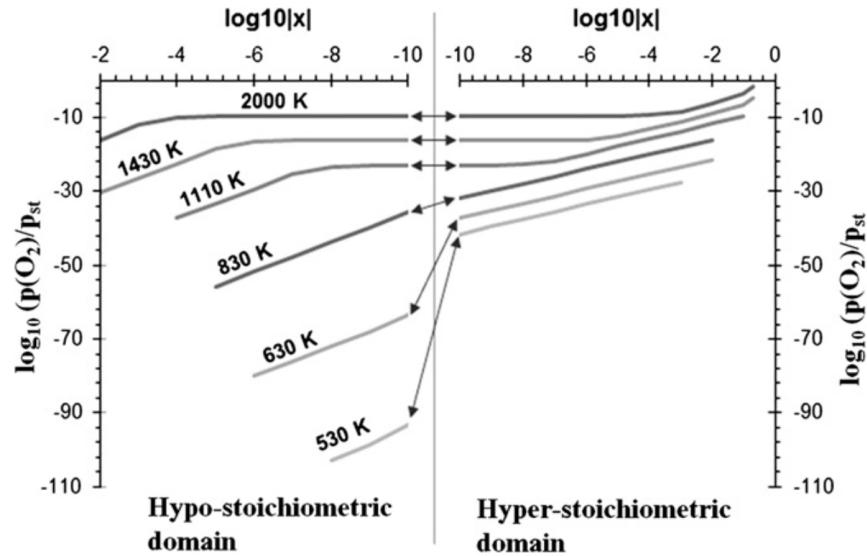


Figure 2.26: Oxygen partial pressure as a function of the logarithm of the stoichiometry deviation. Different curves correspond to different temperatures. Calculations done by Berthnier et al. [91].

Derivation of these functions with respect to stoichiometry deviation led to estimations of the thermodynamic factor and of the chemical diffusion coefficient of oxygen that was compared to available experimental data. As can be expected, the resulting chemical diffusion coefficients depend on temperature and stoichiometry deviation.

Moore et al. [89] also prepared an assessment of the chemical diffusion coefficient of oxygen from their model of oxygen mobility and from thermodynamic calculations performed with the uranium dioxide TAF-ID model [40] to get the thermodynamic factor.

The comparison to available experimental measures in hyperstoichiometric fuel is shown in Figure 2.27.

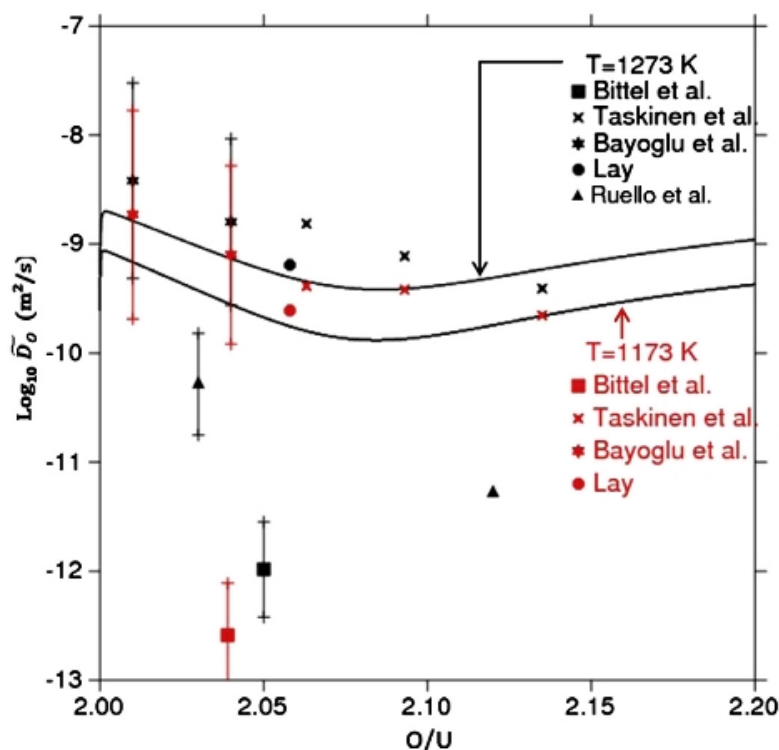


Figure 2.27: Oxygen chemical diffusion coefficient as a function of O/U. Comparison of calculations with experiments [101–105]. Figure adapted from [89].

As can be seen, the scatter of experimental data is very important. Very few data are furthermore available in the hypostoichiometric domain.

### 2.2.3 Heat of oxygen transport

There are very few measurements of the heat of oxygen transport in oxide fuels. The most comprehensive work published on the topic is that of Sari and Schumacher from 1976 [106]. In the experiments carried out by the authors, samples of hypo- and hyperstoichiometric mixed oxide fuels with various plutonium content ( $U_{1-q}Pu_qO_{2+x}$  with  $x = O/(U + Pu) - 2$  and  $q$  the Pu content) have been submitted to a temperature gradient in the axial or radial direction. After the tests, the O/M ratios were measured at the center and at the periphery of the samples (or at the extremities in case of an axial temperature gradient) by determination of the weight change after equilibration of the samples in a CO/CO<sub>2</sub> environment. The heat of oxygen (vacancy or interstitial) transport  $Q_O^*$  was estimated as follows from the steady-state solution of the thermal diffusion Equations 2.11 and 2.15 considering a dilute solution of vacancies and interstitials oxygen atoms:

$$\ln \frac{x_2}{x_1} = \frac{Q_O^*}{R} \left( \frac{1}{T_2} - \frac{1}{T_1} \right) \quad (2.40)$$

where

$x_1$  and  $x_2$  are the stoichiometry deviations at the center and periphery (i.e. extremities) of the fuel pellet

$T_1$  and  $T_2$  are the temperatures at the center and periphery (i.e. extremities) of the fuel pellet

The most important result obtained by the authors is the opposite evolution of oxygen flux in hypo- and hyperstoichiometric mixed oxide fuels. In hypostoichiometric fuel, oxygen vacancies were found to increase in the hot part of the sample, leading smaller than initial O/M ratios while the O/M ratios in the cold part increased during the experiments. In hyperstoichiometric fuel, the hot part of the sample saw an increase of oxygen interstitials (i.e. the O/M ratios increased) while the O/M ratios in the cold part decreased with respect to the initial value.

The calculated heat of oxygen transport are represented in Figure 2.28 as a function of the O/M ratios of the fuels.

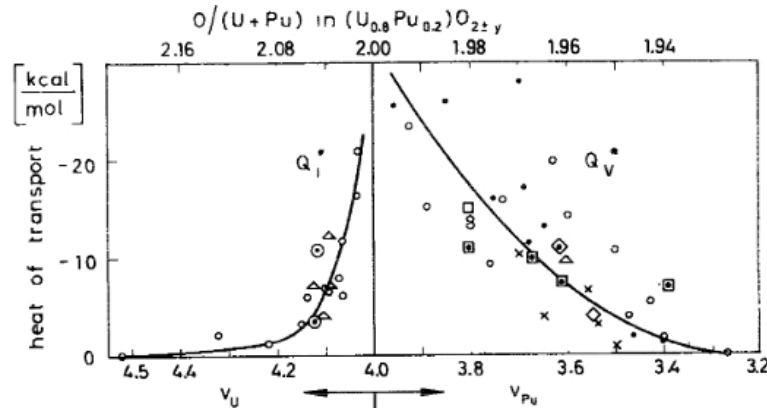


Figure 2.28: Figure from [106]. Data comes from Sari and other authors [73,107]. Different symbols correspond to different concentration of plutonium in samples.

Negative heats of transport were identified by Sari and Schumacher in hypo- and hyperstoichiometric fuels with decreasing values when closer to the strict stoichiometry (oxygen thermal diffusion more difficult when less oxygen vacancies and interstitials) and increasing values as stoichiometry deviation becomes important. The authors derived mathematical expressions to express the heat of transport as a function of Pu or U valence. For hypostoichiometric fuel:

$$Q_{O_v}^* = -3.96 \times 10^6 + 2.37 \times 10^6 V_{Pu} - 3.6 \times 10^5 V_{Pu}^2 \quad (2.41)$$

where  $V_{Pu}$  is the valence of plutonium and  $Q_{O_v}^*$  is given in J/mol. The idea behind the use of plutonium valence is to relate the stoichiometry deviation to the conversion of  $Pu^{4+}$  atoms into  $Pu^{3+}$  atoms assuming  $U_{1-q}Pu_qO_{2-x}$  can be considered as an ideal solution of  $1 - q$  mole fraction of  $UO_2$  and  $q$  mole fraction of  $PuO_{2-m}$  where  $m = x/q$ .

In  $\text{PuO}_{2-x}$ , the fraction of plutonium in the 3+ valence state is  $2x$ , and the average valency of plutonium ions is:

$$V_{Pu} = 4 - \frac{2x}{q} \quad (2.42)$$

For hyperstoichiometric fuel, the heat of transport of oxygen interstitials is expressed by:

$$Q_{O_i}^* = -3.5 \times 10^{34} \exp(-17V_U) \quad (2.43)$$

where  $V_U$  is the valence of uranium and  $Q_{O_i}^*$  is given in J/mol. Assuming again that  $\text{U}_{1-q}\text{Pu}_q\text{O}_{2+x}$  can be considered as an ideal solution of  $1-q$  mole fraction of  $\text{UO}_{2+m}$  and  $q$  mole fraction of  $\text{PuO}_2$ , the stoichiometry deviation is now related to the conversion of two  $\text{U}^{4+}$  atoms into  $\text{U}^{5+}$  atoms for each additional  $\text{O}^{2-}$  ion. Thus, the fraction of uranium in the 5+ valence state is  $2x$ . The valence of uranium in the hyperstoichiometric material is given by:

$$V_U = 4 + \frac{2x}{1-q} \quad (2.44)$$

The authors also concluded that heat of transport is quasi-independent of the plutonium concentration in the fuel. For this reason, most of the thermal diffusion simulations performed on hyperstoichiometric  $\text{UO}_{2+x}$  fuels have been based on Sari and Schumacher experimental results, usually with a reevaluation of the heat of transport expressions in function of the stoichiometry deviation [81–83, 86].

Finally, it must be mentioned that most of Sari and Schumacher's experiments have been performed on samples closed in metal covers to avoid matter exchange with the surroundings. This encapsulation led to the creation of an electronic short-circuit. Beside the oxygen point defects flux, there is a non-zero electron flux as well. Presence of this flux might have affected the measured values of the heat of transport of oxygen. Janek and Timm estimated the electron flux and proposed estimations of the heat of transport due to thermal diffusion only [108]. The obtained evolution of the heat of transport is summarized in Figure 2.29 and compared to Sari and Schumacher's measures.

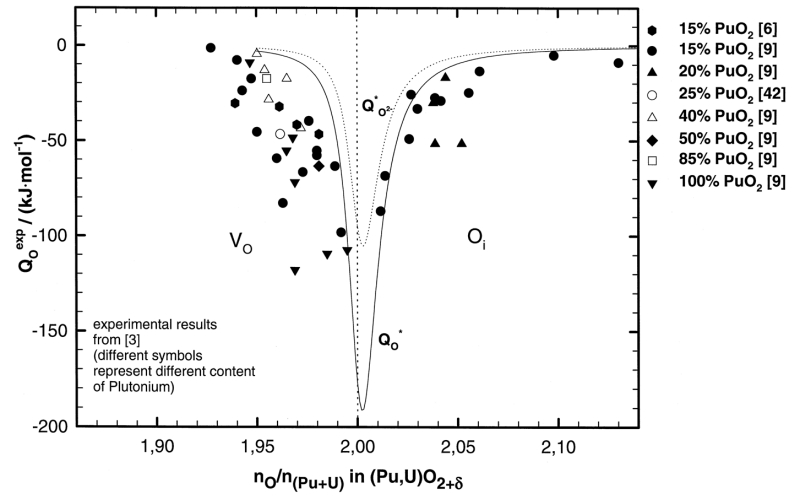


Figure 2.29: Heat of transport calculated by Timm and Janek (solid line) compared to the experimental data from Sari [106], Evans [109] and Adamson [73].

The authors showed that the evolution of the heat of transport close to stoichiometry might be much more pronounced than expected from the measurements.

## 2.2.4 Conclusions

Oxygen redistribution in nuclear fuels has been mostly studied in SFR mixed oxide fuels. Thermal diffusion induced by the thermal gradient at hand during reactor operation is considered as the dominant process behind any change in oxygen content along the fuel pellet radius. Laboratory experiments have shown that thermal diffusion leads to an increase of the oxygen vacancies in the hot part of a hypostoichiometric fuel pellet. This phenomenon might be related to the reductive perturbation evidenced in the fuel pellet core during power ramps, as discussed in the previous section. Since the chemical speciation of the fission gases released from the fuel depends greatly on the oxygen potential of the fuel, the reductive perturbation might have implications on I-SCC, a phenomenon related to iodide gases. For this reason, the chemical aspects of I-SCC are reviewed in the next section.

## 2.3 PCI failure by I-SCC

In this section, the data available in the open literature on the chemical aspects of PCI failure by I-SCC are recalled. Some models developed to describe crack propagation by I-SCC in irradiated zircaloy claddings are described in a second time.

### 2.3.1 I-SCC mechanisms

#### 2.3.1.1 Introduction

Iodine is generally accepted to be the main cause of stress corrosion cracking of zircaloy claddings. Normal operation of the nuclear reactor does not cause significant iodine release [110]. According to [111], release of iodine starts when the linear power rate is greater than 300 W/cm. The clad inner wall temperature exceeds 340 °C, temperature at which iodine is expected to be very reactive with zirconium [5]. Ruptured fuel pins show transgranular and intergranular crack propagation. The development and propagation of cracks related to I-SCC has been studied extensively in out-of-pile experiments. A review of the test conditions and results can be found in references [5, 23] and [112]. The propagation of cracks induced by I-SCC in the thickness of a zircaloy cladding is generally believed to be governed by different processes and parameters [113]:

- a pre-requisite to I-SCC is the breaking of the internal zirconia layer that form on the clad inner surface, leading to a radial crack that reach bare zircaloy. Le Boulch et al. [114] and Sidky [5] reported that a minimum strain of less than 0.5% can crack the oxide layer. Lewis et al. suggested a minimum strain of 0.4-0.5% based on the simulation of an extensive database of power ramps on CANDU fuel rods [115].
- the subsequent propagation of the radial crack within the bare zircaloy requires the establishment of adequate chemical conditions at the crack tip, often associated to a Van Arkel process with iodine transport in the crack. This mechanism requires time and is usually referred as the incubation period (slow crack propagation).
- once a proper chemical environment holds at the crack tip, and a critical crack depth  $a_{SCC}$  is reached (related to a threshold stress intensity factor  $K_I^{I-SCC}$ ), the propagation rate of cracks by I-SCC changes. It is first intergranular, as shown by many SEM observations.
- when the progression within the clad thickness reaches several tens of  $\mu\text{m}$ , the intergranular propagation shifts to fast intragranular propagation.
- the last mechanism involves the ductile shear failure of the remaining clad ligament when the crack reaches a few hundreds of  $\mu\text{m}$ .

#### 2.3.1.2 Zirconium iodides

Iodine chemically interacts with zirconium, impurities and alloy components. Reaction rates are dependent on temperature and iodine partial pressure. Various zirconium iodides can be formed. Cubicciotti et al. [116] give the chemical thermodynamics of

the Zr-I system. Figure 2.30 gives the equilibrium phases present as a function of the iodine partial pressure and temperature. Possible iodides are:  $ZrI_{1.1}$ - $ZrI_{1.3}$  (non-stoichiometric monoiodide),  $ZrI_{1.9}$ - $ZrI_{2.1}$  (diiodide),  $ZrI_{2.8}$ - $ZrI_{3.4}$  (triiodide) and volatile tetraiodide  $ZrI_4$ . Cubicciotti et al. indicate that iodine can be chemisorbed on bare Zr surface.

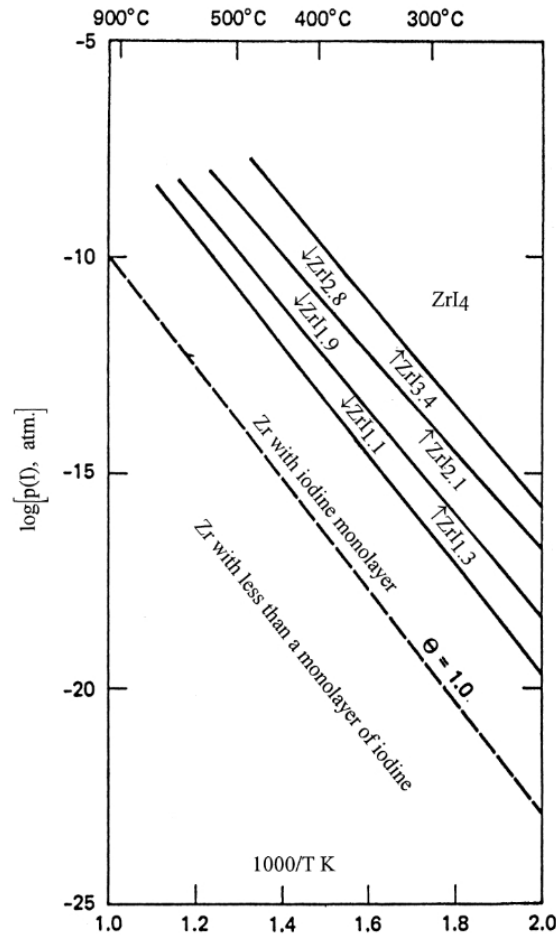
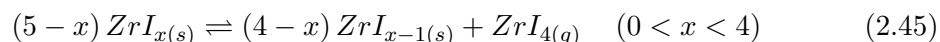


Figure 2.30: Pressure of iodine and species that it forms with zirconium as a function of temperature.  $\Theta$  is the amount of iodine needed to form a monolayer [116].

Peehs et al. studied the kinetics of  $I_2/Zr$  reactions at 400 °C in laboratory experiments and analyzed the  $ZrI_x$  layers [117]. They found that the iodine to zirconium ratio has to be higher than 2 to cause I-SCC. The authors suggested that only  $ZrI_4$  is volatile at the cladding temperature and that it plays a crucial role in I-SCC. Peehs et al. proposed a mechanism that explain the formation process of  $ZrI_{4(g)}$ . When iodine reaches a freshly exposed Zr site,  $ZrI_{(s)}$  must be the first compound formed, because  $Zr + I = ZrI$  has an equilibrium constant  $K_p$  which fixes the partial iodine pressure. This pressure is less than the one fixed by the higher iodide which forms next in the sequence  $ZrI_{(s)} + I = ZrI_{2(s)}$ . This means that  $ZrI_{2(s)}$  cannot form on Zr without  $ZrI_{(s)}$  intervening. In the same

way, two more successive reactions will give  $ZrI_{4(s)}$ . Four layers of different zirconium iodides will therefore form successively, if sufficient iodine pressure is available. At each reaction step, the  $ZrI_{4(g)}$  partial pressure is determined by the equilibrium between the two successive zirconium iodides:



### 2.3.1.3 Van Arkel reaction

Once the internal zirconia layer (a few  $\mu\text{m}$  thick) that forms during reactor operation is cracked (a minimum strain of less than 0.5% is necessary to break the layer, see Section 2.3.1.1), gaseous iodine can reach bare Zr and the first stage of SCC takes place, usually referred as the incubation period. Existence of initial flaws in the cladding inner surface is therefore not necessary for I-SCC to occur. The formation of  $ZrI_{4(g)}$  is essential to deepen the crack in the zirconia layer by removing Zr but is not essential to cause cracking since iodine will cause cracking by lowering the Zr bond energy [5]. The presence of a temperature gradient between the crack mouth and the crack tip drives a cyclic mechanism that is thought to be responsible for the crack propagation and explains the low quantities of iodine needed in I-SCC failures. This self-sustaining process is called the Van Arkel reaction [115, 118]. This mechanism is illustrated in Figure 2.31, reproduced from [23].

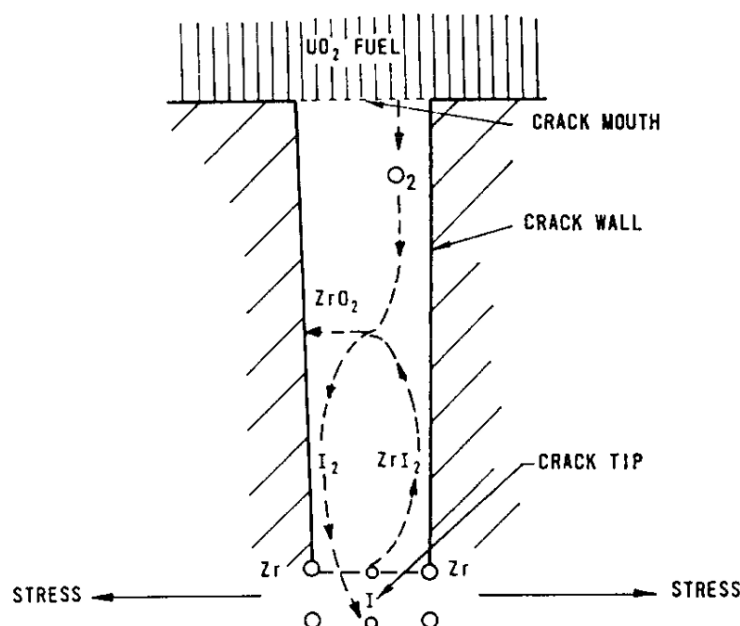


Figure 2.31: Mechanism of SCC assuming presence of gaseous iodine [23].

In this mechanism, iodine reacts with zirconium at the crack tip and forms  $ZrI_{4(g)}$  after the successive iodides. Gaseous  $ZrI_4$  decomposes increasingly to Zr and iodine at increasing temperatures (van Arkel process) and so it can ferry Zr from the crack tip (cooler, near water) where it forms  $ZrI_4$  to the crack mouth (hotter, near fuel) where it thermally decomposes, dumping Zr and forming iodine gas which goes down the crack tip again to form  $ZrI_4$  cyclically [5]. As implied by the Van Arkel reaction, only a small initial quantity of gaseous iodine is necessary to initiate the process which is then self-sustained. Regeneration of gaseous iodine depends on the gaseous oxygen available from the fuel.

In relation to the van Arkel process, it is usually believed that much of the incubation period may be due to the formation of a critical  $ZrI_4$  concentration. In this respect, failure times in laboratory I-SCC experiments performed with  $ZrI_{4(g)}$  are much less than with gaseous iodine [5]. The detrimental role of oxygen has furthermore been confirmed by Yang and Tsai [119] which showed that the failure times in laboratory I-SCC tests performed with  $ZrI_{4(g)}$  decreased at high oxygen partial pressure (82 Pa). They attributed this result to the dissociation of  $ZrI_4$  in the oxygen containing environment according to:  $ZrI_{4(g)} + O_{2(g)} \rightleftharpoons ZrO_{2(s)} + 4I_{(g)}$ , which led to the generation of gaseous iodine. Comparing tests performed in gaseous iodine and gaseous zirconium tetraiodide (with 82 Pa and  $10^{-45}$  Pa partial oxygen pressures), they showed that the failure times of the different batch could all be ordered as a function of the monoatomic iodine partial pressure in equilibrium with  $ZrI_{4(g)}/Zr_{(s)}$ .

### 2.3.2 Iodine thresholds for I-SCC

A critical threshold in iodine is required for I-SCC to occur. Several authors published experimental results with varying iodine content and expressed the iodine threshold in grams of iodine per unit surface of inner cladding wall [120–124]. Obtained thresholds vary significantly. Tasooji et al. [125] calculated concentration of  $10^{-4}$  g/cm<sup>2</sup> whereas Busby et al. [126] say that even  $5 \times 10^{-6}$  g/cm<sup>2</sup> of iodine on the Zircaloy surface has an impact on failure time. The dispersion of these experimental thresholds is due to the large variability of the experimental conditions explored, mostly as regard temperature and oxygen partial pressure. According to Sidky, if gaseous iodine is postulated as the main cause for I-SCC, thresholds should not be expressed in g/cm<sup>2</sup> of clad surface which is relevant for solid iodides, but in g/cm<sup>3</sup> of free volume in contact with the cladding [5]. An alternative threshold which seems more consistent with I-SCC mechanisms is the iodine partial pressure of the atmosphere in contact with the clad inner wall.

A series of very comprehensive I-SCC experiments have been performed in the frame of the Studsvik Cladding Integrity Program (SCIP). A sophisticated experimental technique has been developed where a cladding tube is loaded by a pre-notched alumina

hollow specimen in which a conical mandrel is forced axially. The experimental assembly used in the test is shown in Figure 2.32. The tests can be performed under controlled atmosphere of iodine and oxygen (continuous flow in an argon carrier).

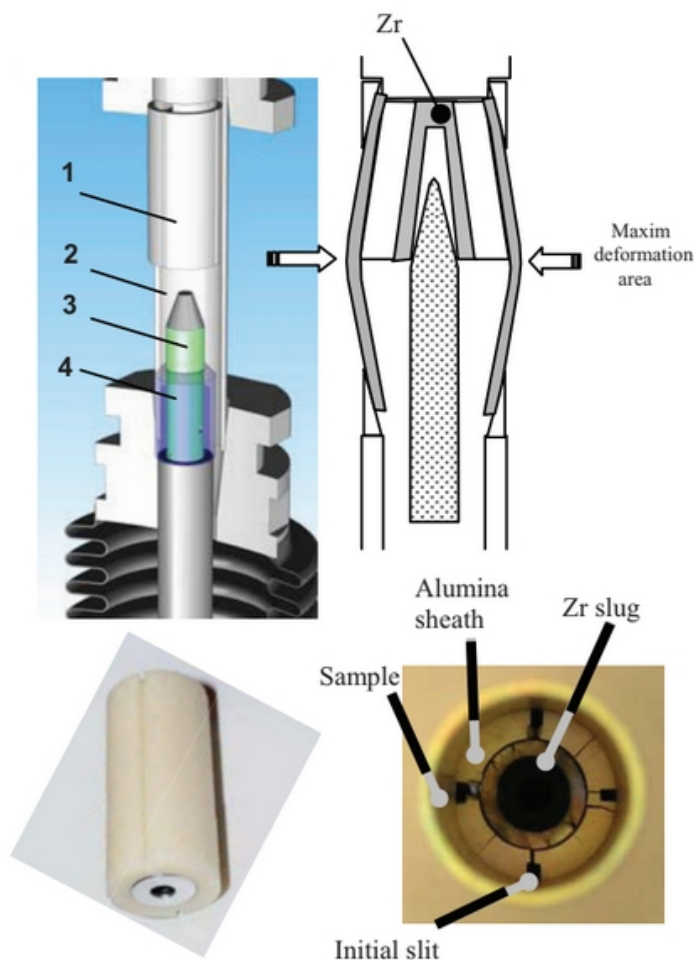


Figure 2.32: “Expanding mandrel sample configuration for I-SCC investigations of irradiated fuel cladding materials, the alumina insert with 4 longitudinal slits and the pure Zr mandrel in the central part and a cross section of a cladding sample after mandrel testing [127]; 1–alumina sheath; 2–Zircaloy cladding (sample); 3–plunger; 4–channel from pure Zr” [128].

The device reproduces the localized loading conditions taking place in reactor during PCI (stress concentration in front of opening radial pellet cracks). The fuel pellet is simulated by the alumina sheath with 4 notches representing the cracked fuel pellet. The notches are also used to transport iodine to the cladding inner wall. The Zr mandrel inside the alumina sheath expands radially when compressed axially. It causes cracking of the cladding sample. When it fails, oxygen goes through the crack. The failure is detected by the oxygen content increase. The experimental setup was designed and installed in a hot cell in order to perform experiments on irradiated cladding. Anghel et al. investigated the impact of iodine partial pressure on the strain to failure and failure

times of irradiated Zy2 samples [128] with an average burnup of 49 GWd/tHM. The experiments were performed at 320 °C with diiodine partial pressures ranging from 0 to 200 Pa. The oxygen partial pressure was assumed very low due to the incorporation of an oxygen getter (Zr tube) at the flow inlet. Three constant strain rate stages were applied to the sample: the first stage with a fast strain rate simulating the fast expansion of the fuel and the cladding during a power ramp, the second one with a slow strain rate simulating the slow expansion at RTL related to fission gas swelling of the pellet. Results are shown in Figure 2.33.

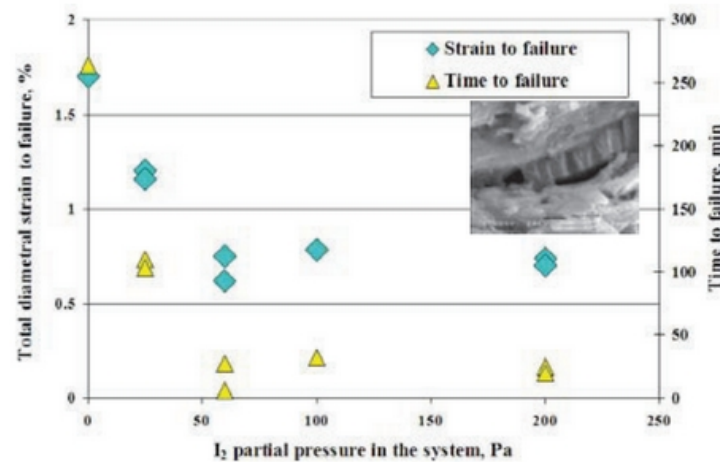


Figure 2.33: Total diametral strain to failure (blue points) and time to failure (yellow points) as a function of  $I_2$  partial pressure. Figure from [128].

Anghel et al. concluded that only the experiments with a partial diiodine pressure exceeding 60 Pa led to failure by I-SCC (small time to failure of less than 15 minutes and limited plastic strains). The results were confirmed by SEM observations of the failed cladding samples which showed typical signs of I-SCC (fracture surface usually exhibit cleavage-like planes with some fluting [5], i.e., plastic failure of grains). No real impact of the diiodine partial pressure was observed in the limited range studied 60-200 Pa. Other tests performed at 60 Pa diiodine partial pressure but with different temperatures and strain rates also resulted in systematic failure of the samples. The tests have been simulated with the finite element code CAST3M to estimate the local stress state in front of the notches. Hoop stresses of 400-500 MPa are reached depending on the friction coefficient at the alumina sheath - cladding interface, in the range of expected stresses at the fuel clad interface during power ramps [14]. In their I-SCC tests in carefully controlled oxygen and iodine environment (internal pressurized tubes), Yang and Tsai showed that failure of the samples could take place at iodine concentrations as low as  $0.012 \text{ mg/cm}^3$  (temperature 360 °C), corresponding to partial diiodine pressures of  $P_{I_2} = 245 \text{ Pa}$  and that the failure time decreases with increasing iodine concentrations [119]. Peehs et al. reports that the time to failure is inversely proportional to iodine concentration [5, 129].

The work of Anghel et al. concerns laboratory experiments on irradiated claddings. The experiments reproduce PCI as well as possible. Stress concentration in front of pellet cracks are represented by notches in the alumina ring. The cladding samples are irradiated to the burnup at which PCI failures are likely to occur. Gaseous iodine is provided. Oxygen content is low. The temperatures used in the experiments are close to those expected on the cladding inner wall during in-reactor operation. This is the reason why the critical diiodine partial pressure of 60 Pa will be used in this work to assess I-SCC initiation.

### 2.3.3 Origin of iodine in reactor

There is no consensus on the origin of the iodine involved in I-SCC in reactor. This stems from the fact that cesium as a fission product is 10 times more abundant than iodine and that the formation of cesium iodide CsI is thermodynamically favored at all temperatures. A reasonable conclusion is that most of iodine released from the fuel pellet should be found bound with cesium. Deposits of cesium iodide have been observed near pellet cracks and cladding cracks by many authors [5]. In theory, gaseous CsI<sub>(g)</sub> is not expected to react with Zr, implying that another mechanism needs to be taken into account to free iodine. Laboratory experiments show that CsI does not cause I-SCC in the absence of radiation [5,130]. Dissociation of CsI by fission fragments (radiolysis) has been studied by several authors, mostly by calculations. Burns et al. estimated that radiolysis of CsI can cause enough iodine pressure for Zr-I reactions and I-SCC to take place, but that iodine pressure from chemical thermodynamics alone would not [130]. Later calculations by Ball et al. lead to similar conclusions [131]. Konashi et al. studied the iodine partial pressure evolution in an LWR fuel rod induced by radiolysis of CsI<sub>(s)</sub> by fission fragments and concluded that this mechanism could generate enough iodine to cause SCC of zircaloy cladding [132]. Frégonèse et al. have used the CsI<sub>(s)</sub> decomposition rate versus distance from the fuel pellet surface later published by Konashi et al. [133] in their estimation of thermally released iodine in the fuel rodlet free volume during a power ramp. They considered CsI<sub>(s)</sub> radiolysis in the inter-pellet zone and in the fuel pellet radial cracks. Assuming that CsI<sub>(s)</sub> decomposition would take place in a 5 μm thick layer from the fuel pellet surface, they calculated a potential for dissociation of 20%.

A counter-argument to the predominance of CsI is suggested by the faster transport of iodine compared to cesium within the fuel which could lead to a surplus of iodine over cesium in the fuel-clad gap during a power transient [5]. In this case, free iodine would be available to initiate I-SCC. The differences in cesium and iodine release could be associated to the formation of non volatile cesium compounds in the fuel (cesium molybdate, cesium oxides) that would limit the actual release of cesium. Radial SIMS

profiles of cesium and iodine performed after a power ramp seem to accredit this hypothesis [61], cesium release being much less than iodine. From their SIMS observations of the pellet-clad gap, Desgranges et al. have associated I-SCC with the presence of gaseous tellurium iodides  $\text{TeI}_{x(g)}$ , probably released from the fuel pellet center during the power ramp. According to the classification by Cox of gaseous iodide compounds as a function of the time to failure in out-of-pile I-SCC tests, tellurium tetraiodide is one of the most efficient. Baurens et al. performed 3D thermo-chemical-mechanical simulations of PCI with ALCYONE where they showed that the contribution of  $\text{I}_g$ ,  $\text{I}_{2(g)}$  and  $\text{TeI}_{2(g)}$  released from the fuel to the iodine partial pressure in the neighborhood of the clad inner wall is sufficient to exceed the low 60 Pa identified in the mandrel tests of the SCIP project [14]. This result was obtained in spite of the fact that 90% of released iodine was found associated with cesium. The same authors investigated the impact of the reductive perturbation described in the previous sections on the speciation of gaseous iodides in the fuel [134]. The calculation results are presented in Figure 2.34.

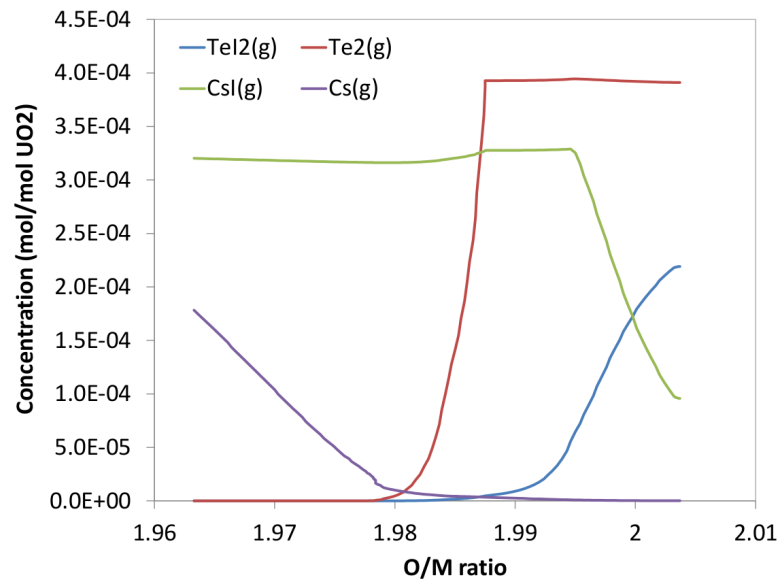


Figure 2.34: Concentration of some chemically reactive species as a function of the O/M ratio calculated at 2000 °C. Adapted from Sercombe et al. [134].

Thermochemical simulations showed that the reductive perturbation (decrease of O/M ratio from an initial value of 2) would lead to the disappearance of  $\text{TeI}_{2(g)}$  from the fuel hot part and to an increase of the concentration in gaseous cesium. Obviously, as stated by the authors, it could have a major impact on I-SCC propensity.

## 2.3.4 Modelling of I-SCC

### 2.3.4.1 Crack propagation in the cladding

I-SCC has been studied by Le Boulch et al. [114]. The authors have carried out a series of internal pressurization tests to investigate and model the different stages of I-SCC: 1) the crack initiation phase, 2) the incubation phase, 3) the crack propagation phase.

The authors have studied both irradiated and non irradiated stress-relieved Zircaloy-4 cladding samples to investigate the impact of irradiation on I-SCC susceptibility. The pressurization tests have been performed in inert and iodine environments. The iodine concentration in the tests was around  $1.5 \text{ mg/cm}^2$  of clad internal surface, far above the thresholds discussed in Section 2.3.2. The temperatures in the experiments were  $350 \text{ }^\circ\text{C}$ ,  $420 \text{ }^\circ\text{C}$  and  $488 \text{ }^\circ\text{C}$ . The samples were initially smooth, which allowed to study the crack initiation and incubation phases. The results of the pressurization test on non irradiated samples are shown in Figure 2.35. It can be seen that the time to failure decreases with increasing temperature and stress. Also, the presence of iodine visibly reduces the time to failure.

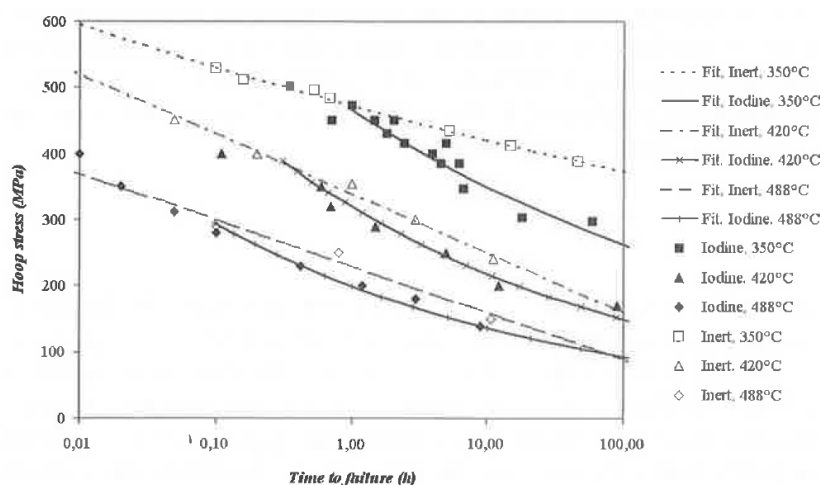


Figure 2.35: Impact of temperature on the evolution of the time to failure as a function of the hoop stress during internal pressurization tests on smooth, non irradiated specimens. Results obtained under inert and iodine environments. Figure adapted from Le Boulch et al. [114].

Figure 2.36 presents the time to failure measured in irradiated and non irradiated samples at  $350 \text{ }^\circ\text{C}$ .

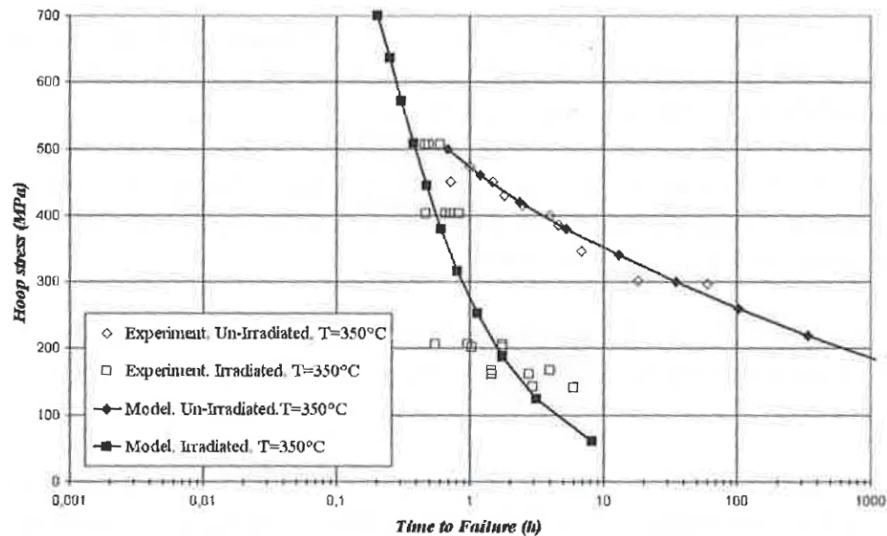


Figure 2.36: Comparison between experimental data and the model proposed by Le Boulch et al. [114]. Irradiated and non irradiated samples are compared at 350 °C.

The impact of irradiation is tremendous, leading to a marked dependency on the stress level. Times to failure at 400-500 MPa drop down to around 30 minutes on irradiated samples.

Internal pressurization tests have also been performed on non-irradiated, pre-cracked samples. Crack propagation rates have been estimated from these experiments. The obtained results, shown in Figure 2.37, suggest that a stress intensity factor threshold for I-SCC propagation may exist. The authors estimated its value at  $K_I^{I-SCC} = 4.2 \text{ MPa}\sqrt{m}$ . According to these experiments, when the stress intensity factor  $K$  exceeds around  $6 \text{ MPa}\sqrt{m}$ , the crack propagation rate is independent of temperature.

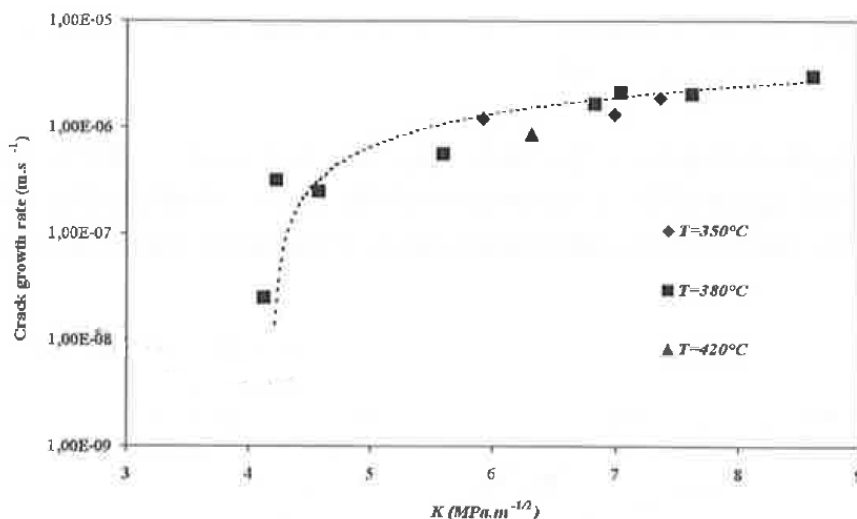


Figure 2.37: Stress corrosion crack growth rate as a function of the applied stress intensity factor during internal pressurization tests on pre-cracked, non irradiated specimens. Figure adapted from Le Boulch et al. [114].

These experimental data have been used by Le Boulch et al. to model the three phases of I-SCC. The authors assumed that iodine was always in sufficient quantity to induce I-SCC. For this reason, no dependency on the iodine concentration was considered.

### 1) Crack initiation phase

According to the authors, there are two conditions necessary for crack initiation: 1) the existence of incipient cracks in the protective zirconia layer and 2) a positive tensile hoop stress. The first condition is usually met when the cladding hoop strain is high enough to brake the zirconia layer. To find the critical strain value, Le Boulch et al. have simulated the internal pressurization tests with the finite element code Cast3M [135]. The authors concluded that for irradiated samples, the critical hoop strain is below 0.5%.

### 3) Crack propagation phase

As concluded from Figure 2.37, the crack propagation rate is independent of temperature and it needs a threshold stress intensity factor  $K_I^{I-SCC}$  to start. According to Le Boulch et al., the crack propagation rate can be expressed as follows:

$$\dot{a} = C \left( 1 + D \left( K - K_I^{I-SCC} \right) \right) \quad (2.46)$$

where  $a$  is the crack depth,  $K$  is the stress intensity factor and  $C$  and  $D$  are constant parameters that need to be identified. The  $K$  factor is given by the relation:

$$K = \alpha \sigma \sqrt{\pi a} \quad (2.47)$$

where  $\alpha$  is the crack shape coefficient and  $\sigma$  is the applied hoop stress. The experimental data from Figure 2.37 have been used to fit the coefficients  $C$  and  $D$  ( $C = 10^{-10}$  m/s and  $D = 5500 \frac{1}{\text{MPa}\sqrt{\text{m}}}$ ). These parameters are valid for non irradiated Zircaloy-4. Crack propagation experiments have not been done on irradiated samples. The same parameters are used to model I-SCC propagation in irradiated cladding.

## 2) Incubation phase

The incubation phase takes place between the crack initiation and crack propagation phases. It is considered as the most important phase in I-SCC, even if the crack depth due to this phase does not exceed 10-20  $\mu\text{m}$ . It is a slow process that gives its overall kinetics to I-SCC failure. This phase ends when the threshold stress intensity factor  $K_I^{I-SCC}$  is reached. The duration of this incubation phase  $t_{sub}$  is estimated as follows:

$$t_{sub} = t_R - t_Z - t_{propa} \quad (2.48)$$

where  $t_R$  is the time to failure measured in the pressurization tests on smooth samples,  $t_Z$  is the time needed to brake the zirconia layer (assumed to be equal to zero in irradiated materials) and  $t_{propa}$  is the duration of the crack propagation phase.

Based on the tests performed on non irradiated samples, the incubation phase appears to be dependent on temperature and has been treated with an exponential term such that:

$$t_{sub} = A e^{\frac{Q}{T}} \sigma^B \quad (2.49)$$

where  $A$ ,  $B$  and  $Q$  are three constant coefficients. Also, the threshold stress intensity factor  $K_I^{I-SCC}$  defines the critical crack depth  $a_{SCC}$  where the incubation phase ends:

$$a_{SCC} = \frac{1}{\pi} \left( \frac{K_I^{I-SCC}}{\alpha \sigma} \right)^2 \quad (2.50)$$

By assuming that the crack propagation rate during the incubation phase is equal to the mean crack growth rate, the following relation can be written:

$$\dot{a} = \frac{a_{SCC}}{t_{sub}} \quad (2.51)$$

The experimental data from Figure 2.36 have been used to fit the parameters for non irradiated and irradiated materials:

$$\alpha = 1, Q = 20240K, A = 6.44 \times 10^{49}, B = -7 \quad \text{for non irradiated Zircaloy-4} \quad (2.52)$$

$$\alpha = 1, Q = 20240K, A = 97.562, B = -1.5 \quad \text{for irradiated Zircaloy-4} \quad (2.53)$$

Validation of the model against the experimental measurements on the non irradiated and irradiated samples is shown in Figure 2.36. The comparison shows that the model

predicts the times to failure properly.

### 2.3.4.2 Iodine chemistry and transport model

Crack propagation models usually do not consider iodine chemistry and transport in the process. One of the most complete model for I-SCC on this topic has been proposed by Lewis et al. [115] and applied to CANDU fuel rods. The diffusion equations used in the model were solved in the COMSOL Multiphysics [136]. In order to develop their model, Lewis et al. have considered the following phenomena:

- iodine isotopes diffusion in the fuel matrix and release to the gap
- CsI decomposition by radiolysis in the gap for the production of  $I_{2(g)}$
- $I_{2(g)}$  diffusion in the gap towards the crack site
- Formation of gaseous  $ZrI_{4(g)}$  at the crack tip by the Van Arkel reaction

The simulated phenomena are schematically represented in Figure 2.38.

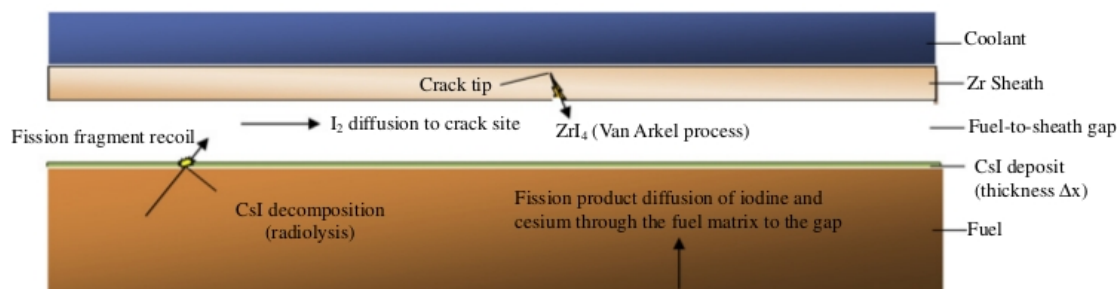


Figure 2.38: Schematic representation of the I-SCC process. Adapted from [115].

First step in the modeling of I-SCC consisted in the description of iodine release from the fuel matrix. The authors used the well-known Booth model to account for solid-state lattice diffusion of iodine isotopes (stable isotopes  $^{127}\text{I}$ ,  $^{129}\text{I}$ , and radioactive isotopes  $^{131}\text{I}$ - $^{135}\text{I}$ ) in the fuel matrix till the fuel-clad gap [137, 138]. In the Booth model, diffusion is considered to occur in idealized fuel grain spheres of radius  $a$ . Fission product release to the fuel-clad gap occurs when isotopes reach the idealized grain boundaries. The Booth diffusion model for a time-dependent diffusion coefficient  $D(t)$  and fission products generation rate at time  $t$  is expressed as follows:

$$\frac{\partial C(r, t)}{\partial t} = \frac{D(t)}{r^2} \frac{\partial}{\partial r} \left( r^2 \frac{\partial C(r, t)}{\partial r} \right) - \lambda C(r, t) + \frac{F_f(t)y}{V} \quad (2.54)$$

where

$C(r, t)$  is the fission product concentration in the idealized fuel grain of radius  $a$ ,

$V$  is the volume of this grain,

$\lambda$  - the decay constant

$F_f$  - the fission rate

$y$  - the fission product yield

Booth proposed an approximate analytical solution to this equation which takes the following simplified form [139]:

$$\left(\frac{R}{B}\right)_{diff} \approx 3\sqrt{\frac{D'}{\lambda}} \quad (2.55)$$

where

$(R/B)_{diff}$  is the release over birth ratio (released quantity of isotope divided by the production),

$D' = D/a^2$  is the solid-state empirical diffusion coefficient (or apparent diffusion coefficient) which accounts for such effects as radiation damage, atomic diffusion, gas-bubble nucleation, bubble migration and bubble coalescence.

The empirical diffusion coefficient  $D'$  is fitted to sweep gas experiments performed on operating CANDU fuels. This technique relies on the forced flow of an inert carrier gas through the fuel sample in order to retrieve the fission products released from the fuel. The concentrations of fission products isotopes is then measured in a gamma-ray spectrometer leading on-line measurements of the isotopes release rates. In the sweep experiments, no iodine release was measured which led to the assumption that all iodine released from the fuel reacted with cesium in the fuel-clad gap and led to the formation of a  $\text{CsI}_{(s)}$  layer at the surface of the fuel pellet fragments. The diffusion coefficient is identified from the release of Xe isotopes, daughter of iodine isotopes.

The deposited concentration of a given iodine isotope  $C_{fs,i}$  (and associated cesium) atoms on the fuel surface is obtained from the mass balance equation as follows:

$$\frac{dC_{fs,i}}{dt} = \frac{R_{diff,i}}{S_T} - \lambda_i C_{fs,i} \quad (2.56)$$

where

$R_{diff,i}$  is the release rate from the fuel,

$S_T$  is the total fuel surface.

Radioactive decay of the short lived isotopes is considered. The thickness of the CsI layer can be estimated from the sum of the deposited concentration of the seven iodine isotopes.

The free iodine necessary for I-SCC is then associated with the radiolysis of CsI. Decomposition of CsI is due to the fission fragment bombardment that reach the fuel surface. The release rate of a recoil fission fragment from the fuel surface  $R^{rec}$  is given by:

$$R^{rec} = \frac{1}{4} \mu (S/V)_f F_f y_{ff} \zeta_{skin} \quad (2.57)$$

where

$\mu$  - average range of fission fragments in  $UO_2$  ( $\sim 7.7 \mu m$ )

$(S/V)_f$  - geometric surface to volume ratio of the fuel body

$y_{ff}$  - fission fragment yield [(2 recoil particles)/fission]

$\zeta_{skin}$  - fission rate enhancement factor (due to plutonium buildup on the outer edge of the fuel pellet)

The release rate of iodine  $R_J$  from the radiolysis of CsI is then expressed as a function of the recoil fission fragment rate  $R^{rec}$  by:

$$R_J = R^{rec} Y_I (dE/dx) \Delta x \zeta_{free} \zeta_{Canlub} \quad (2.58)$$

where

$\Delta x$  is the thickness of the CsI deposit

$\zeta_{Canlub}$  is a factor accounting for the impurities of the internal layer of CANDU claddings (called CANLUB) that can bind iodine

$dE/dx$  is the energy loss per path length in the surface deposit ( $\sim 460$  eV/Angström)

$Y_I$  is the number of iodine atoms liberated per unit energy deposited (0.23 atom/eV)

The term  $\zeta_{free}$  equals 1 when the appropriate stress/strain conditions are met to initiate I-SCC. Loading parameters (maximum power, maximum power increase during the ramp, holding time at maximum power) are used to define the critical mechanical conditions leading to I-SCC. Although the CsI can recombine after dissociation, that effect is ignored in the model, leading to a conservative estimation of iodine release from CsI radiolysis.

Next step is to model diffusion of free iodine towards the crack site. The authors consider axial diffusion in the gap of a binary mixture of iodine and helium according to a standard diffusion equation given by:

$$\frac{\partial C_{g,i}}{\partial t} = D_{AB} \frac{\partial^2 C_{g,i}}{\partial x^2} - \lambda_i C_{g,i} + R_{g,i} \quad (2.59)$$

where  $D_{AB}$  is the binary diffusion coefficient from the Chapman-Enskog kinetic theory [140]. The diffusion of iodine in the clad crack is neglected since its dimension is small compared to the rod length.

To model the crack propagation, Lewis et al. consider that iodine reacts instantaneously with zirconium to form gaseous  $ZrI_4$ . The release rate of  $ZrI_4$  from the crack is as follows:

$$R_{Zr} = \frac{1}{2} R_{crack,T} \quad (2.60)$$

and depends only on the amount of iodine that reaches the crack site per unit time,  $R_{crack,T}$ , evaluated from the diffusion equation. The crack is simplistically modeled as a right cylindrical cone with a typical crack base width of 5  $\mu\text{m}$ . Breaking of the cladding is assumed when the crack length reaches the clad thickness.

The I-SCC model has been benchmarked using 172 power ramp cases from commercial reactors and 163 from experimental irradiations [115]. As in other models dealing with iodine release from the fuel [141], no chemical association with other fission products is considered to occur within the fuel. A strong argument in favor of this assumption is the very low burnup of the fuels used in CANDUs which greatly limits the fission product inventory and hence the possible chemical association of fission products. As can be foreseen from the system of equations at hand, the kinetics of I-SCC propagation in the clad wall depend mostly on the iodine release kinetics from the fuel, the CsI radiolysis rate and the transport of free iodine to the crack site.

In later work, Oussoren used the FAST fuel performance code [142, 143] to simulate the CANDU database in order to estimate the temperature and the stress/strains at the pellet-clad interface during the power transients [144]. From these estimations and the definition of related I-SCC thresholds, he post-processed crack propagation in the cladding thickness with the consideration of iodine release, CsI decomposition, iodine diffusion in the gap from Lewis model. And also included the kinetics related to the incubation and crack propagation phases, as proposed by Le Boulch [114]. So far, this approach is the most complete on PCI failure of cladding related to I-SCC.

### 2.3.5 Conclusions

I-SCC models describe the propagation of a crack in the zircaloy cladding. They are either based on the mechanical stresses calculated at the crack tip assuming iodine is available or based on iodine transport and cesium iodide radiolysis assuming the mechanical stresses/strains necessary to initiate I-SCC are met. None of these approach

consider fuel thermochemistry in the process. Iodine release from the fuel is based on solid-state diffusion of the isotopes with no consideration of the potential association with other fission products prior to its release in the fuel-clad gap. No consideration of the possible change of the oxygen potential in the fuel and of its impact on iodine chemistry is neither part of I-SCC models.

## 2.4 Thermochemistry and oxygen transport in nuclear fuel simulations

Fuel modeling approaches where fuel thermochemistry and/or oxygen thermal diffusion are included or discussed are presented in the last section of this chapter.

### 2.4.1 Thermochemical database

To predict irradiated fuel thermochemistry, the standard procedure is to perform calculations of thermodynamic equilibria on the fission products inventory in the  $\text{UO}_2$  matrix. Thermodynamic equilibrium calculations are difficult and time-consuming since they concern a very large number of fission products and of potential reactions between them. Generally, to reduce the computational cost, the fission products are grouped in families with similar chemical behavior. The second difficulty comes from the non homogeneous distribution of fission products, temperature and mechanical pressure within the fuel during reactor operation, meaning that a single thermodynamic equilibrium calculation has no chance to be representative of the overall fuel behavior. Fuel performance simulations require therefore a non negligible number of thermodynamic equilibrium calculations at each time step with a very large range of temperatures, typically 400–2500 °C. The quality of the simulations rely on the thermodynamic database used to define all the potential compounds likely to form in nuclear fuel. Generally, several hundreds of them are considered in nuclear fuel thermochemistry. The standard way to achieve thermodynamic equilibrium is to determine the combination of chemical species and phases that minimize the total Gibbs energy of the system subjected to mass balance constraints and at prescribed temperature and pressure conditions. The theoretical and numerical background behind thermodynamic equilibrium calculations has been established in the seventies and has led to the development of several Gibbs energy minimizers such as SOLGASMIX [145] and THERMOCALC [146]. In recent years, efforts have been made to develop Gibbs energy minimizers that can be readily implemented in fuel performance codes. This includes THERMOCHIMICA developed by Piro [147] and NUTS developed by Loukusa [148]. CEA has coupled its fuel performance code ALCYONE with the Gibbs energy minimizer SOLGASMIX, renamed AdvaNced Gibbs Energy minimizer (ANGE) at this occasion.

There are several thermodynamic databases developed by different organizations for different types of reactors and fuels. These databases define the thermodynamic properties (such as the free enthalpy of formation) of expected chemical compounds as a function of temperature and pressure and their belonging to the different phases likely to form in nuclear fuel. One of the most complete database has been developed by the RMC. It has been prepared for CANDU reactors [19, 149]. In the last years, the international project TAF-ID has been launched with a collaboration of many countries in order to define a unified and as complete as possible thermodynamic database for nuclear fuel [100]. Currently, TAF-ID takes into account 40 fission products. The database includes at present 204 binary and 63 ternary compounds. Although CEA is involved in the development of the TAF-ID, an older database will be used in this work. It was developed in the 90's by Garcia et al. [150] and Dumas [151] mostly for application to SFR fuels and extended by Baurens [62]. The Gibbs energy minimizer ANGE is used to calculate the thermodynamic equilibrium with this database. Recent work by Introini has made possible fuel performance simulations with the TAF-ID [152] but this functionality was not available in 2016 when this thesis started.

#### 2.4.2 MFPR

MFPR (Module for Fission Products Release) is a mechanistic code developed within a collaboration between IBREA (Russia) and IRSN (France). It gives a detailed description of the evolution of the fuel micro-structure and of fission gas transport in nominal to accidental conditions. Thermochemical equilibrium calculations are included in MFPR to determine the compounds that form in the wide range of temperatures encountered (500-3000 K). The code takes furthermore into account the solid state diffusion of fission products towards grain boundaries where they can form gas bubbles and solid phase precipitates. Mobility of fission products depends on the fuel oxidation state [153]. Currently, MFPR is a sub-module of the fuel performance code SFPR (Single Fuel Rod ↔ Performance) [154].

Ozrin implemented in MFPR a model for radial redistribution of oxygen by thermal diffusion [80]. He treated the problem at two different scales. The first scale is defined by the grain size. The author described the fuel as a multiphase system composed of the fluorite solid solution, solid precipitates and the gas phase. He calculated local thermodynamic equilibria which give values of the oxygen potential and O/M ratio at different radial positions in the fuel. The second scale is defined by the pellet radius where oxygen redistribution is driven by the temperature gradient and the oxygen concentration gradient (hyperstoichiometric fuel is considered). Ozrin compared his simulation results to the experimental measurements of oxygen potential from Walker et al. [7] on a  $\text{UO}_2$

PWR fuel irradiated up to a very high average burnup (102 GWd/tHM). Oxygen potentials obtained by Ozrin were far from experimental data, except near the pellet center, as shown in Figure 2.39.

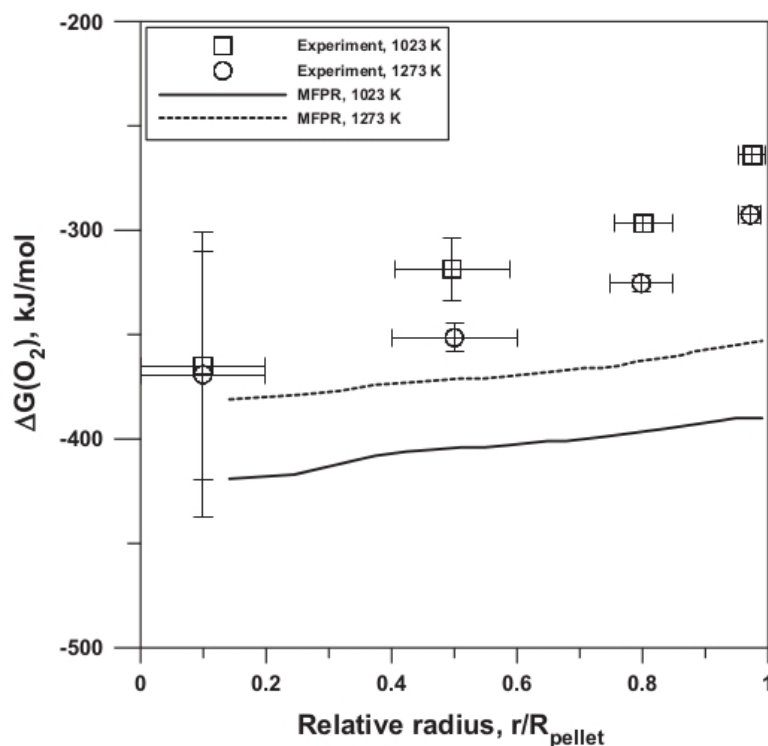


Figure 2.39: Comparison of results obtained by Ozrin with experimental work done by Walker et al. [7].

Ozrin underlined that Walker's oxygen potential measurements were much greater than those reported by other authors (see section 2.1.4.2) on irradiated fuels but with lower average burnups. The author did not explain why he included oxygen thermal diffusion in MFPR but it may be due to the high oxygen potential measured by Walker at the pellet periphery that could stem from oxygen redistribution. The irradiation conditions of the PWR fuel studied by Walker were in fact characterized by two irradiation cycles at high power (340 and 290 W/cm) which could have led to high temperatures in the fuel and hence to oxygen thermal diffusion.

### 2.4.3 THERMOCHIMICA

Piro et al. included the Gibbs energy minimizer THERMOCHIMICA (that Piro developed [147]) in the Advanced Multi-Physics (AMP) platform, where coupling between a wide-variety of external software packages can be achieved. As Ozrin, the authors performed simulations of the high burnup fuel studied by Walker et al. [7]. The detailed isotopic composition of the fuel was estimated from the ORIGEN-S code [11] while the

thermal analysis of the fuel during reactor operation was based on the models available in the FRAPCON fuel performance code [155]. The fuel burnup was calculated from the TUBRNP model from the TRANSURANUS fuel performance code.

Piro et al. reported a very good agreement between measured and calculated fission products inventory, O/M ratios and oxygen potentials at various positions along the fuel pellet radius. Comparison of the calculated/measured oxygen potentials is presented in Figure 2.40 (same data as in Figure 2.39).

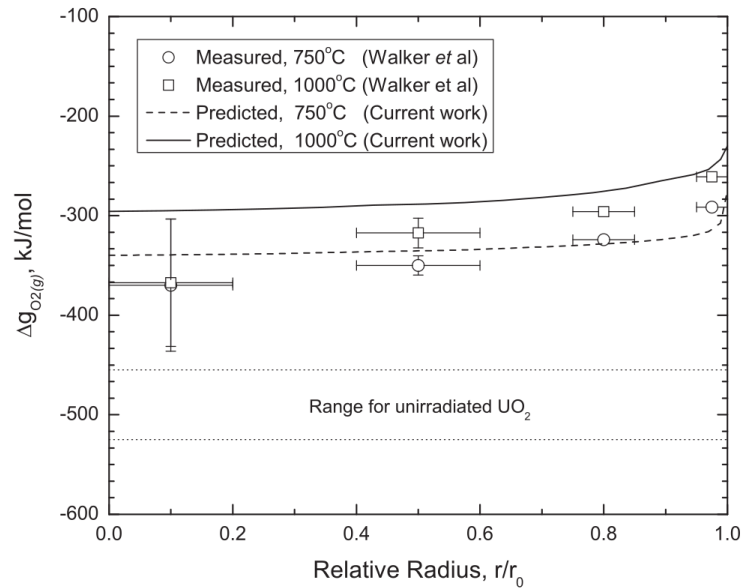


Figure 2.40: Comparison of the oxygen potential calculated by Piro et al. [12] with experimental data from Walker et al. [7].

Comparison of calculated/measured O/M ratios in the fluorite solid solution is shown in Figure 2.41.

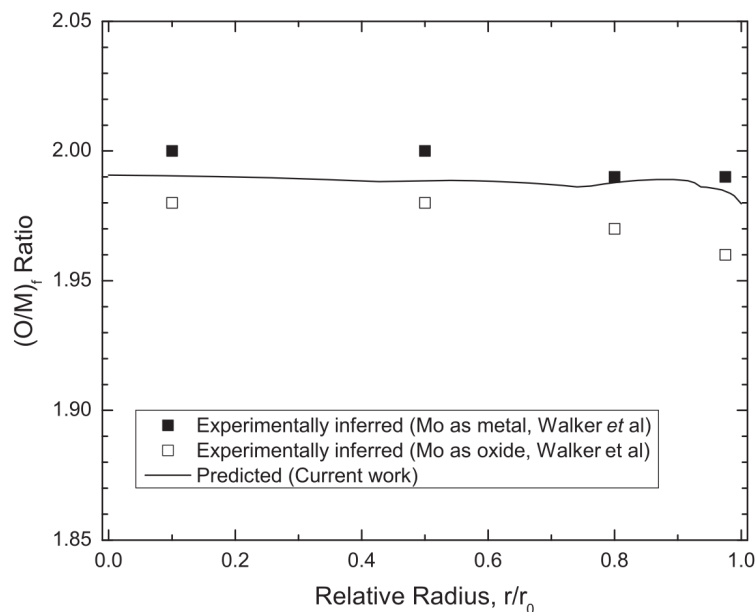


Figure 2.41: O/M ratio predicted by Piro et al. [12] (line) compared to the values estimated by Walker et al. [7] (points).

The authors attribute the good results to the sophisticated description of the fuel thermochemistry available in the RMC database that includes the contribution of multiple phases. In calculations of the same fuel with the RMC database but with the NUTS Gibbs energy minimizer [72], Loukusa et al. attributed the high oxygen potential values at the pellet periphery to the formation of  $\text{UMoO}_6$  from  $\text{MoO}_2$  and  $\text{UO}_2$ . He showed that the reaction was likely to take place when the local burnup exceeds 50 GWd/tHM. Note that the O/M of the fuel estimated by Piro et al. appears to be slightly less than 2 showing that it decreased with respect to the initial value (2.005).

Piro et al. report calculations of the radial profile of oxygen potential in the fuel during in-reactor operation, as shown in Figure 2.42.

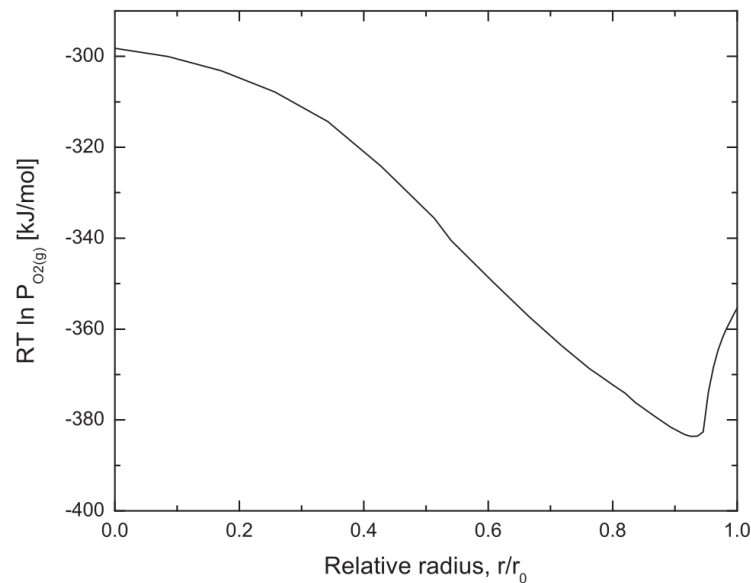


Figure 2.42: Oxygen potential during in-reactor operation. Calculated by Piro et al. [12].

The obtained spatial variation along the radius is convex, which is due to competing effects from temperature and local burnup variations (higher at the pellet periphery due to Pu fissions), according to the authors. They discuss the potential consequences of this convex profile in case oxygen thermal diffusion is included in the simulations. Instead of a one direction oxygen redistribution (from the hot part of the fuel to the cold part or reverse) as expected from the equations derived in Section 2.2, they inferred that most of oxygen interstitials would be driven from the bulk of the material to the pellet center but also to the pellet surface near the pellet rim due to the change in curvature of the oxygen potential. This complex thermal diffusion cannot be captured by a model based on the stoichiometry deviation gradient.

A preliminary inclusion of fuel thermodynamic calculations with THERMOCHIMICA in the multi-dimensional BISON fuel performance code has been presented by Besmann et al. [156]. In particular, the authors tried to couple the oxygen thermal diffusion model in hyperstoichiometric fuel proposed by Ramirez et al. [81] with THERMOCHIMICA. The authors concluded that the oxygen thermal diffusion problem was difficult to couple with fuel thermodynamic equilibrium since both calculations were related by the O/M ratio of the fluorite solid solution, an output in both cases. Recently, Simunovic et al. proposed a novel formulation of the thermal diffusion problem based on the Planck potential gradient [157] ( $\mu/T$  with  $\mu$  the chemical potential) instead of the standard stoichiometry deviation gradient. A first coupling of thermodynamic equilibrium calculations of irradiated fuel with thermal diffusion was achieved, based on the TAF-ID database and the oxygen mobilities identified by Moore and al. [89, 158]. Contrary to

the O/M ratio, the oxygen potential can be used as an input in the thermodynamic equilibrium calculation, which facilitates the coupling.

#### 2.4.4 ALCYONE and ANGE

Implementation of the Gibbs energy minimizer ANGE in the fuel performance code ALCYONE was recently achieved by Baurens [14, 62]. The fission products inventory was estimated from independent calculations performed with the depletion code CESAR [13]. Thermo-mechanical simulations of PCI with ALCYONE provided estimates of the temperature and pressure at each node of the finite element mesh. These parameters together with the fission products inventory were used to initiate the thermodynamic equilibrium calculations with ANGE. In return, ANGE provided the mole fractions of the chemical species formed in the fuel as well as the O/M ratio and the oxygen potential at all finite element nodes of the mesh and at every time step.

As in MFPR, ALCYONE simulations include a fission gas model called MARGARET to estimate the fraction of noble gases released from the fuel. Solid-state diffusion, bubble formation and migration in the fuel grains, bubble coalescence and gathering at the grain boundaries, interconnection of bubbles and release to the free volume are mechanisms that are explicitly described in MARGARET. A preliminary coupling with thermodynamic equilibrium calculations has been defined to determine the release of the minor gases formed in the fuel since they can be of importance for I-SCC. The release of minor gases was defined from their concentration in the fuel and from the flux of noble gases in intergranular bubbles to the free volume given by MARGARET. The coupling has been used to estimate the release of gaseous iodine compounds ( $I_g$ ,  $I_{2(g)}$ ,  $TeI_{2(g)}$  and  $CsI_{(g)}$ ) in the fuel-clad gap during a power ramp and the resulting iodine partial pressure. The coupling is schematically described in Figure 2.43.

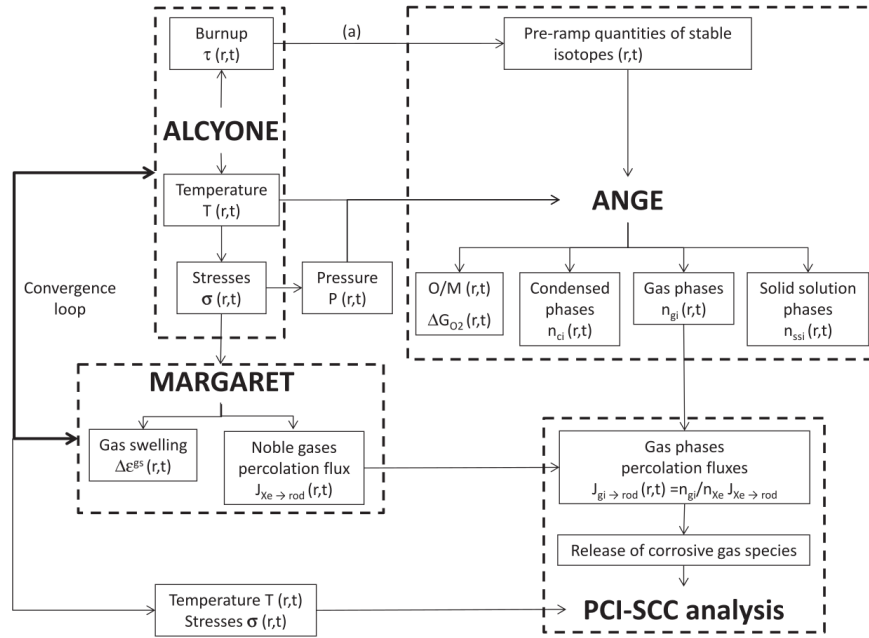


Figure 2.43: Schematic representation of the thermochemical solver ANGE implementation into the fuel performance code ALCYONE. Adapted from Baurens et al. [14].

The calculated evolution of  $\text{TeI}_{2(g)}$  in the 3D simulations of Baurens, one of the possible iodides involved in I-SCC during a power ramp, is illustrated in Figure 2.44.

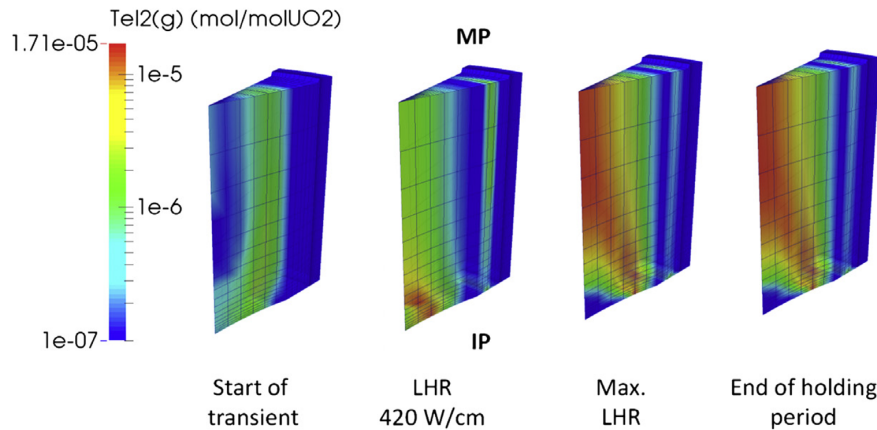


Figure 2.44:  $\text{TeI}_{2(g)}$  at different times during the power ramp simulated by Baurens et al. [14].

The release of tellurium diiodide was found particularly important near pellet ends where I-SCC failure are known to occur.

A first coupling between thermodynamic equilibrium calculations with ANGE and the oxygen thermal diffusion model of Lassmann [86] was proposed by Baurens [62, 134].

The author used the redistribution model to find the radial profile of O/M in the fuel at each time step and then changed the oxygen content at each node along the radius to obtain a similar distribution of O/M in the fuel with ANGE. The method required several thermodynamic equilibrium calculations at each time step and at each node, making it unsuitable in 3D simulations of PCI. Another limitation came from the non conservation of the oxygen content in the fuel pellet. Baurens showed however that some typical observations could be reproduced with oxygen thermal diffusion, such as the precipitation of metallic fission products during a power ramp. The chemical composition of the gas phase in the fuel was also shown to change significantly with oxygen redistribution [134], as the iodides released from the fuel. Consequences on I-SCC were foreseen by the authors.

### 2.4.5 Conclusions

A review of the few nuclear fuel performance simulations including thermodynamic equilibrium calculations and/or oxygen thermal diffusion calculations has been presented in this section. Due to the high computer cost required by thermodynamic equilibrium calculations, only one dimensional simulations have been performed so far. Only Baurens [14] has proposed simulations of PCI including irradiated fuel thermochemistry and oxygen thermal diffusion. Preliminary conclusions from this work demonstrate that oxygen redistribution can have a major impact on the fission gases released from the fuel during a power ramp and might modify the chemical conditions at the clad inner wall leading to I-SCC.

## 2.5 Goal of the work

Irradiated nuclear fuel is a very complex chemical system. Chemistry has huge impact on material properties. Swelling, creep and cracking lead to deformation of the fuel pellet and interaction with the cladding. By pellet-cladding interaction one may understand not only mechanical processes but also chemical. There are iodide gas species formed in the fuel that can reduce the cladding resistance to stress and induce a cracking process. When submitted to high power changes, these gas species, released from the fuel, can reach the cladding inner wall and initiate a stress corrosion cracking process leading to clad failure.

A lot of work has been done in the past years on pellet-cladding interaction and stress corrosion cracking. Numerous experiments and observations have provided an understanding of the main phenomena occurring during irradiation. It has led to the development of multidimensional and multiphysics codes simulating in-reactor behavior of nuclear fuel. CEA, FRAMATOME and EDF jointly develop the fuel performance code

ALCYONE. This code is able to simulate most of the thermo-mechanical phenomena taking place during irradiation (creep, plasticity, friction...) but also the fission gas behavior in the fuel pellet. In recent years, ALCYONE has been upgraded to include a description of thermodynamic equilibria in the fuel during irradiation, with a strong focus on the minor fission gases related to iodine, cesium and tellurium. Three dimensional simulations of PCI including fuel thermochemistry are now performed on a routine basis.

However, there are important phenomena influencing fuel behavior that have not been fully implemented in ALCYONE yet. One of them is oxygen thermal diffusion which is thought to be at the origin of a number of observations after power transients such as the precipitation of metallic fission products. Oxygen redistribution in the fuel pellet when submitted to a power transient seems to be a potentially important factor with respect to PCI failures by I-SCC. This oxygen redistribution can possibly change the oxygen potential along the radius. It can therefore strongly affect the chemical state of fission products in the fuel and the concentration of minor fission gases including those which might react with the cladding when released from the fuel.

The main objective of this thesis is to implement a robust oxygen thermal diffusion model into the fuel performance code ALCYONE that can be used in 3D simulations of PCI. Expected outcome is the prediction of potential risks of PCI failure by I-SCC during operation of nuclear reactors in normal and off-normal conditions and the development of PCI remedies based on the optimization of fuel pellet composition. The main parameters of the oxygen thermal diffusion (the oxygen diffusion coefficient and the heat of transport of oxygen) are known for fresh  $\text{UO}_2$  and  $(\text{U}, \text{Pu})\text{O}_2$  but experimental data concerning irradiated fuel are not available. Derivation of these parameters valid for irradiated fuel is in the scope of this thesis. Lack of experimental measurements must be compensated by thermochemical computations and analysis of observations made after power ramp tests which allow some estimation of the parameters.

In chapter 3 of this thesis, the modeling of irradiated fuel thermochemistry available in ALCYONE is detailed. Applications to the available experimental measurements of oxygen potential in irradiated fuels are presented to check the capability of the thermodynamic models to catch the spatial and temporal variation of oxygen potential due to irradiation.

In chapter 4, robust numerical solutions for oxygen thermal diffusion are proposed and assessed by comparison to models from the open literature. A finite element based solution is derived that can be implemented in the 3D scheme of ALCYONE fuel performance code. The parameters for oxygen thermal diffusion in irradiated fuels are then discussed and assessed from available observations on oxygen potential tracers.

In the last chapter, the oxygen thermal diffusion problem is coupled to fuel thermochemistry in ALCYONE fuel performance code and applied to 3D simulations of PCI.

Conclusions are drawn on the impact of oxygen redistribution on PCI failure propensity by I-SCC.

## Chapter 3

# Thermochemical modeling of nuclear fuel

This chapter presents the models used in this thesis to estimate the FPs inventory and the chemical species that are formed in the fuel during typical irradiation sequences in commercial and experimental reactors. In the first section, the neutronics model PRODHEL is presented and assessed by comparison to available measures of FPs in irradiated fuels. In the second section, the Gibbs energy minimization technique behind the thermochemical solver ANGE is explained and calculations performed on binary or ternary U-O-FPs systems are presented to show the capacity of the thermodynamic database at catching the pronounced evolution of the oxygen potential with stoichiometry deviation and soluble FPs content. In the last section, thermodynamic calculations of irradiated fuels are presented and compared to experimental measures of oxygen potentials when available.

### 3.1 Neutronics model PRODHEL

#### 3.1.1 Fission Products isotopes in irradiated fuel

The first step in modeling nuclear fuel thermochemistry is to compute the FP inventory. In previous works performed with ALCYONE [14,62], the FPs content of irradiated fuel was based on a set of linear correlation coefficients derived from CESAR calculations and given in Table 1.3. These simple, empirical, linear evolutions with burnup gave the FPs content with a sufficient precision at least for the application to power ramps. However, they were not applicable to normal operating conditions in reactor since they gave concentrations of long-lived and stable isotopes only. To open new opportunities for ALCYONE fuel performance simulations, the neutronics model PRODHEL has been developed. It can compute the isotopic composition of irradiated fuel during different

scenarii including base irradiation and power transients. The model can be used as a stand-alone program or within ALCYONE fuel performance code.

Initially, only the chains of actinides (U, Pu, Am, Cm, Np) were taken into account in PRODHEL in order to calculate the radial power density profile in the fuel pellet and the local helium production due to  $\alpha$  decay. Recently, PRODHEL has been extended to the following FPs: Xe, Kr, Cs, Rb, I, Br, Te, Se, Mo, Tc, Ru, Rh, Pd, Sr, Ba, Y, La, Nd, Pm, Eu, Gd, Ce, Pr, Nb and Zr. The model uses the neutronics database JEFF 3.1.1 of JANIS [159]. Overall, PRODHEL includes 194 isotopes of FPs and 23 isotopes of actinides. To simplify the neutronics calculations, only highly abundant FPs in irradiated fuel and their isotopes having a significant impact on the isotopic inventory are considered, i.e., isotopes with neutronics cross-sections above 0.1 barn.

Implementation of the extended version of PRODHEL has been done for the needs of this work. Considered elements as well as the representative elements used in further thermochemical computations (see Section 3.2) are shown in Table 3.1. PRODHEL has been successfully validated by comparison to the evolution code CESAR [13] and to the core-wide neutronics code APOLLO [160]. The advantage of PRODHEL over CESAR is its integration in the fuel performance code ALCYONE. The advantage over APOLLO is its simplicity, which is sufficient for the needs of fuel performance analysis. PRODHEL can be used to simulate standard UO<sub>2</sub>, MOX and Gd-doped fuels.

Table 3.1: Elements considered in PRODHEL, representative elements and their affiliations to families.

<b>Element</b>	<b>Representative element</b>	<b>Family</b>
He+Xe+Kr	He	Inert fission
Cs+Rb	Cs	gas and
I+Br	I	volatile fission
Te+Se+Ge+As	Te	products
Ba+Sr	Ba	Stable oxides
Zr+Nb	Zr	
Mo	Mo	
Ru+Tc+Rh	Ru	Metallic fission
Pd+Sn+Sb	Pd	products
Ce+Pr	Ce	Fission
Eu+Sm	Eu	products and
La+Y	La	actinides in
Gd+Nd+Pm	Gd	solid solution
Pu+Np+Am+Cm	Pu	in UO <sub>2</sub>

Table 3.1 differs from Table 1.3 mentioned in Section 1.1.2 since more elements are available from PRODHEL calculations. It has been decided to represent Ce and Pr with the same representative element since both are lanthanides. Before, Pr was represented by Pu. In the current division into groups, Pu is together with other actinides Np, Am and Cm.

### 3.1.2 Evolution of iodine isotopes

PRODHEL is able to calculate a detailed isotopic composition at any moment. It allows to study the evolution of elements such as iodine, which is important from the point of view of PCI. A common hypothesis used in previous simulations of PCI was to consider only the stable iodine isotopes [14]. PRODHEL has been used to follow the evolution of iodine isotopes during typical reactor sequences. Half-lives of calculated isotopes are presented in Table 3.2. There are two stable or quasi-stable isotopes,  $^{127}\text{I}$  and  $^{129}\text{I}$ .

Table 3.2: Isotopes of iodine considered in PRODHEL and their half-lives.

Isotope	Half-life
$^{127}\text{I}$	stable
$^{128}\text{I}$	24.99 min
$^{129}\text{I}$	$1.57 \times 10^7$ y
$^{130}\text{I}$	12.36 h
$^{131}\text{I}$	8.02 d
$^{132}\text{I}$	2.29 h
$^{133}\text{I}$	20.8 h
$^{135}\text{I}$	6.57 h

The schematic of the power sequence used in the simulation is shown in Figure 3.1. The parameters used in PRODHEL are in Table 3.3. The fuel is assumed to be irradiated at LHR of 200 W/cm till a high average burnup of 60 GWd/tHM (4-5 years in reactor). Figure 3.2 shows the calculated time evolution of the iodine isotopes considered in PRODHEL after reactor shutdown. It can be noticed that the most abundant isotopes of iodine are found as stable  $^{127}\text{I}$  and  $^{129}\text{I}$ . Other isotopes are present in lower quantities and their concentrations are negligible after the first 2 months.

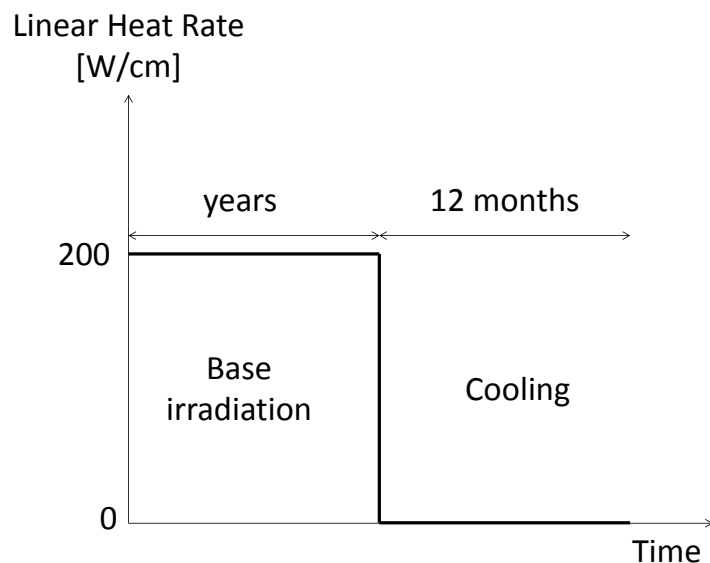


Figure 3.1: Schematic representation of the power sequence used in the simulation of iodine isotopic evolution.

Table 3.3: Parameters used in the PRODHEL stand-alone simulation for the iodine isotopic composition.

LHR [W/cm]	Enrichment [% $^{235}\text{U}$ ]	Burnup [GWd/tHM]	Radius [mm]
200	3.5	60	4.1

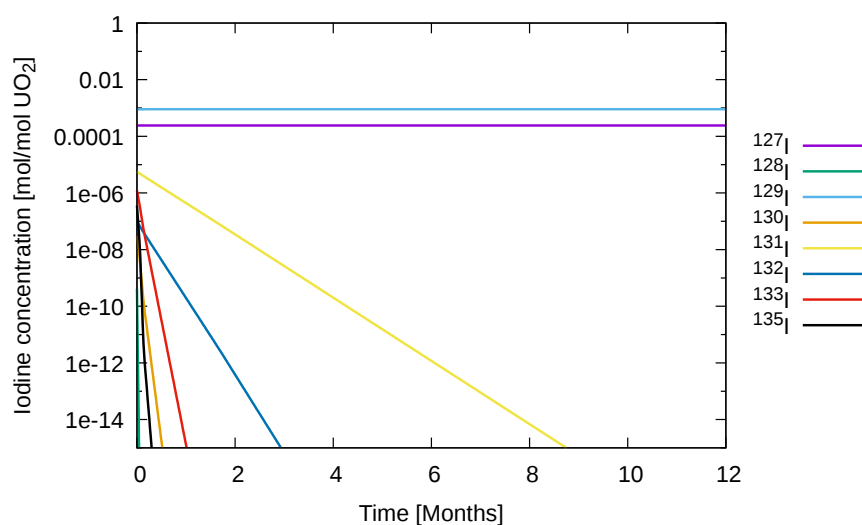


Figure 3.2: Concentrations of iodine isotopes calculated in PRODHEL plotted as a function of time at zero power. The plot starts at the end of base irradiation. Simulation parameters are given in Table 3.3.

Power ramp tests usually include a conditioning period before the power transient, aiming at retrieving the thermo-mechanical conditions that the fuel had at the end of reactor operation. The iodine isotopic evolution during the conditioning period has been studied with PRODHEL. The simulation started with the isotopic composition calculated previously in the fuel that reached 60 GWd/tHM. Then, the fuel spent 3 months at zero power. The cooling period was followed by the conditioning period. The schematic representation of the power sequence used in the simulation is shown in Figure 3.3.

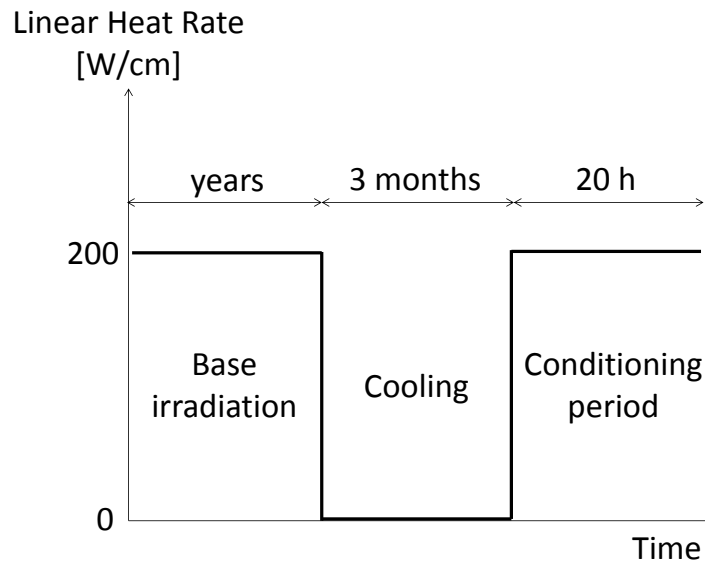


Figure 3.3: Schematic representation of the power sequence used in the iodine isotopic evolution during the conditioning period.

Figure 3.4 shows evolution of iodine isotopes during a 20 hour-long conditioning period at the linear heat rate of 200 W/cm. One may see that except for  $^{127}\text{I}$  and  $^{129}\text{I}$ , concentrations of iodine isotopes increase to nearly constant values within the first hour.

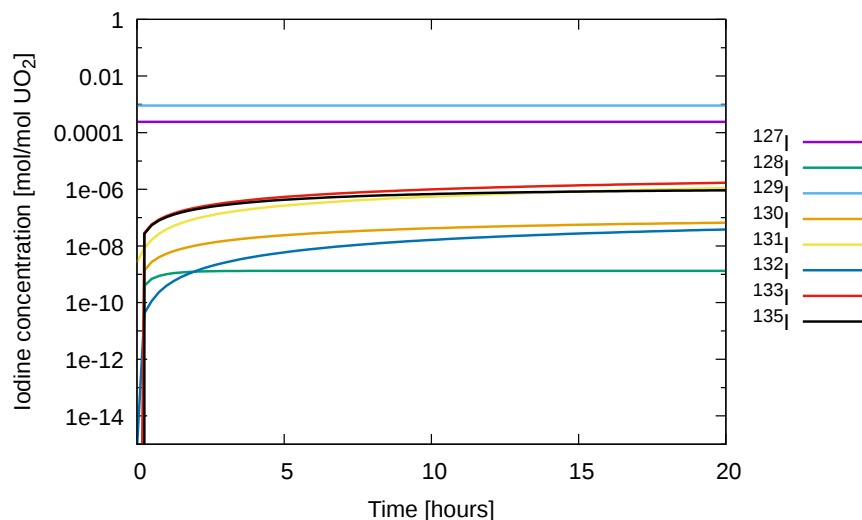


Figure 3.4: Concentrations of iodine isotopes considered in PRODHEL plotted as a function of time during a pre-ramp conditioning period. The plot starts after 3 months at zero power. Simulation parameters are given in Table 3.3.

Only the stable isotopes  $^{127}\text{I}$  and  $^{129}\text{I}$  are found in significant quantities. The other isotopes are furthermore found in negligible quantities, i.e.  $^{128}\text{I}$ ,  $^{130}\text{I}$  -  $^{135}\text{I}$  since they have much shorter half-lives. The half-lives also explain the quasi-constant concentrations of the short-lived isotopes in Figure 3.4. The production rate of these isotopes is balanced by their decay rate. These simulations justify the consideration of only the stable iodine isotopes in PCI analyses of power ramps.

Examples of complete isotopic compositions calculated with PRODHEL at different burnups at the end of base irradiation and after 3 months of cooling are shown in Appendix C.

### 3.1.3 Validation on a low burnup fuel

In the present work, PRODHEL estimations have been compared to very detailed weight fraction measurements of FPs by EPMA after one of the power ramp experiments performed by CEA and named PR1 in this work. The studied fuel rod underwent two irradiation cycles in a commercial PWR in France and then was used to fabricate a rodlet for the ramp test. Details of the base irradiation and the ramp test are shown in Tables 3.4 and 3.5.

Table 3.4: Base irradiation history of the rodlet PR1.

Reactor cycle	Average linear power [W/cm]	Cumulative average burnup [GWd/tHM]
1	137	17
2	188	32

There were 2.7 years between the base irradiation and the ramp test and this period has been taken into account in the simulation. The schematic representation of PR1 is shown in Figure 3.5. The duration of PR1 is around 18 h, which means that the burnup increase during this short period can be neglected when compared to the base irradiation duration (more than 2 years). However, it has been simulated in order to properly reproduce the entire experimental procedure.

Table 3.5: Main characteristics of the simulated power ramp PR1.

Test name	% $^{235}\text{U}$	Average burnup [GWd/tHM]	Max. LHR [W/cm]	Holding Period [h]	Cond. Period Power [W/cm]	Cond. Period [h]
PR1	4.9	32	470	0	169	18

The power transients shown in Figure 3.5 last a few minutes and have no impact on the elemental composition.

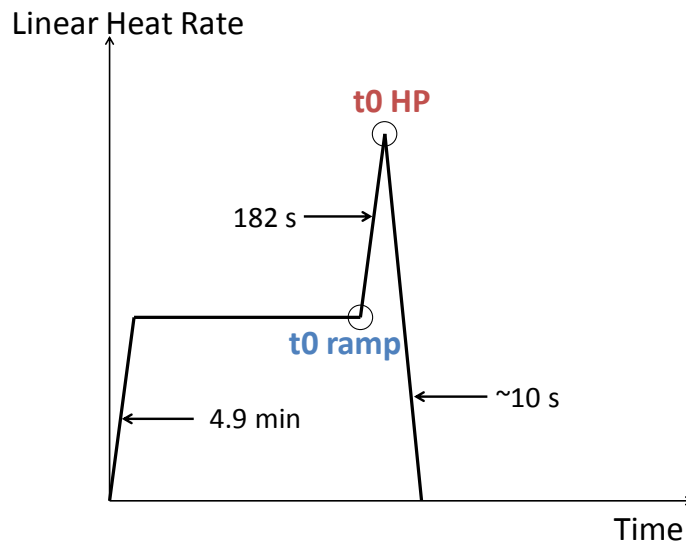


Figure 3.5: Schematic representation of PR1. The conditioning period lasts until "t0 ramp". The maximum LHR is reached at "t0 HP". Durations of power transients are marked.

The radial profiles of FPs have been calculated with PRODHEL implemented within the fuel performance code ALCYONE. Figure 3.6 shows the calculated versus measured FP inventory along the fuel pellet radius. The agreement is good except for FPs in very low quantities such as Te. The highest deviation is for this element and it reaches about 35%. Other deviations range from  $< 1\%$  for Pu to around 7% for Mo. However, the Pu profile is not very well predicted along the entire radius. PRODHEL calculations at the pellet periphery ( $r/R_{\text{pellet}} > 0.8$ ) underestimate the Pu content by around 20%. The Pu content measured at the periphery is not as steep as the Pu profiles of samples irradiated in LWRs reported by Lassmann et al [161]. Thus the EPMA measurement of Pu at the pellet periphery is questionable. The mentioned deviations are calculated as follows:

$$\text{Deviation} = \frac{|w_{\text{exp}} - w_{\text{calc}}|}{w_{\text{exp}}} \times 100\% \quad (3.1)$$

with  $w_{\text{exp}}$ —measured weight fraction and  $w_{\text{calc}}$ —calculated weight fraction. Dashed lines in Figure 3.6 are calculated with the correlation coefficients based on CESAR calculations (see Table 1.3) and the burnup profile of Figure 3.7. Weight fractions predicted with these coefficients are in a comparably good agreement with PRODHEL except for Pu, which is much better predicted by PRODHEL.

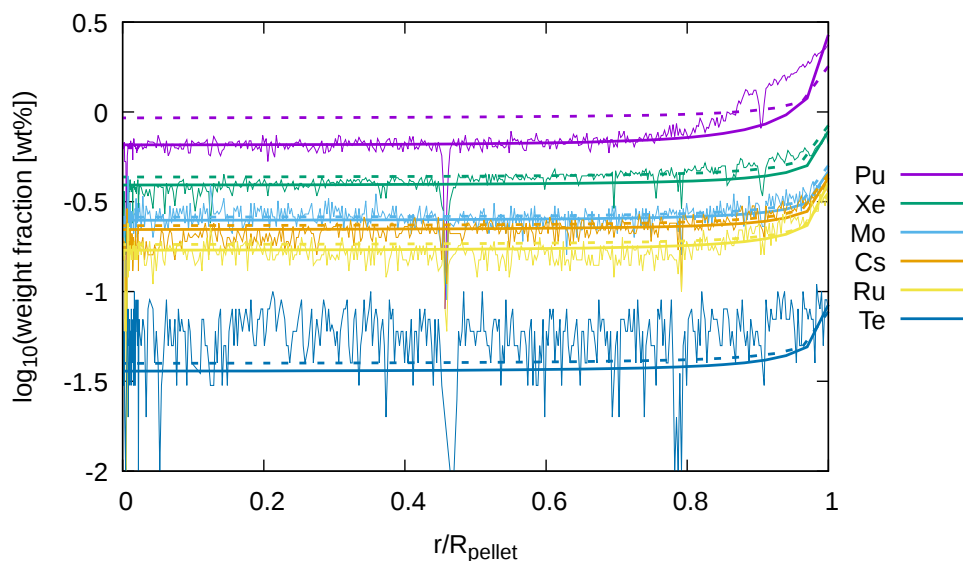


Figure 3.6: Weight fractions of some FPs calculated with PRODHEL (thick lines) and with CESAR (dashed lines) compared to EPMA measurements (thin lines) after the PR1 test.

The above comparison concerns a fuel with a burnup (32 GWd/tHM) that falls in the critical burnup range for PCI failure in PWRs [30-45 GWd/tHM]. It shows that PRODHEL calculations are able to very closely estimate the FPs inventory in the fuel.

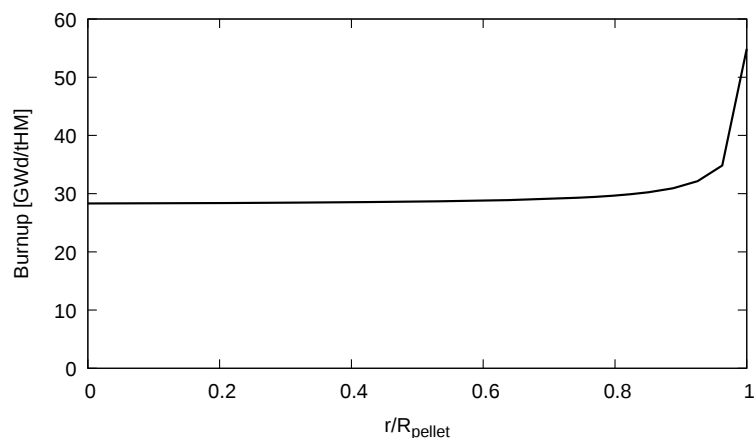


Figure 3.7: Calculated burnup radial profile of PR1.

### 3.1.4 Validation on a high burnup fuel

To validate PRODHEL on a high burnup fuel, the work of Walker et al. [7] has been analyzed. The authors have studied a fuel that has reached a very high burnup (102 GWd/tHM on average). The characteristics of the studied sample and the power history are shown in Tables 3.6 and 3.7.

Table 3.6: Main characteristics of the fuel rod studied by Walker et al. Adapted from Walker et al. [7].

Pellet diameter [mm]	9.3
Initial enrichment [%]	3.5
Fuel density [%TD]	95
2D grain size [ $\mu\text{m}$ ]	9-12
O/M	2.005
Diametrical gap [ $\mu\text{m}$ ]	160-190
He fill gas pressure [bar]	22.5
Cladding material	Zr-based alloy

Table 3.7: Irradiation history of the fuel rod studied by Walker et al. Adapted from Walker et al. [7].

Reactor cycle	Max. average linear power [W/cm]	Cumulative average burnup [GWd/tHM]
1	340	19
2	290	37
3	230	48
4	200	59
5	180	67
6	170	72
7	160	82
8	140	90
9	140	98

ALCYONE with PRODHEL has been used to simulate the experiment according to the fuel pellet characteristics and the power history reported by Walker et al. [7]. The authors did not specify the cooling time between the end of irradiation and the measurements. To take into account the composition change due to radioactive decays, the concentrations of the representative elements after different cooling times have been studied. The calculated elemental compositions of Walker's fuel after 1, 3 and 5 years of cooling are shown in Figure 3.8. Differences between different cooling times are not visible in this figure.

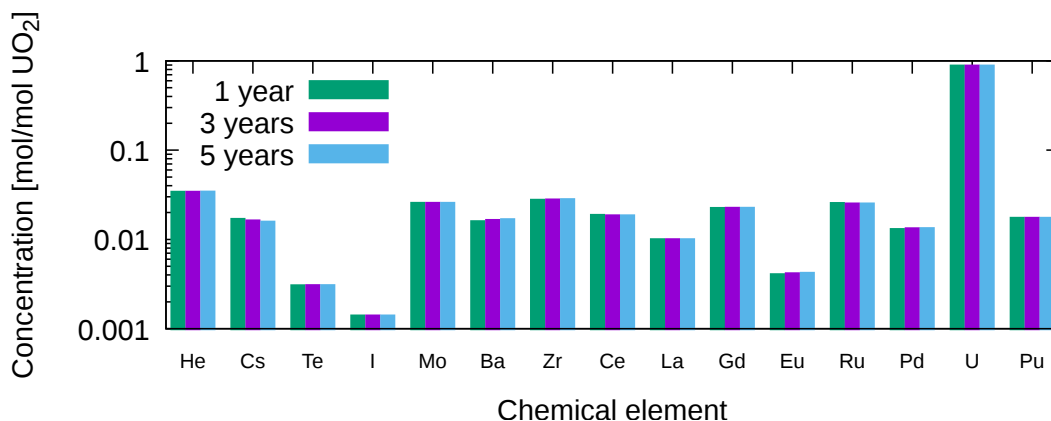


Figure 3.8: PRODHEL calculations of the integral weight fractions of chemical elements after 1, 3 or 5 years of cooling.

To show the difference in concentrations between the cooling times, the deviation from the average value for each element has been calculated using the following expression:

$$\text{Deviation from average} = \frac{|C_{\text{average}} - C_i|}{C_{\text{average}}} \times 100\% \quad (3.2)$$

where  $C_{average}$  is the average value of the element from three simulations with different cooling times and  $C_i$  is the value calculated in the simulation with the cooling time  $i$  ( $i=1, 3, 5$ ). The deviations are shown in Figure 3.9.

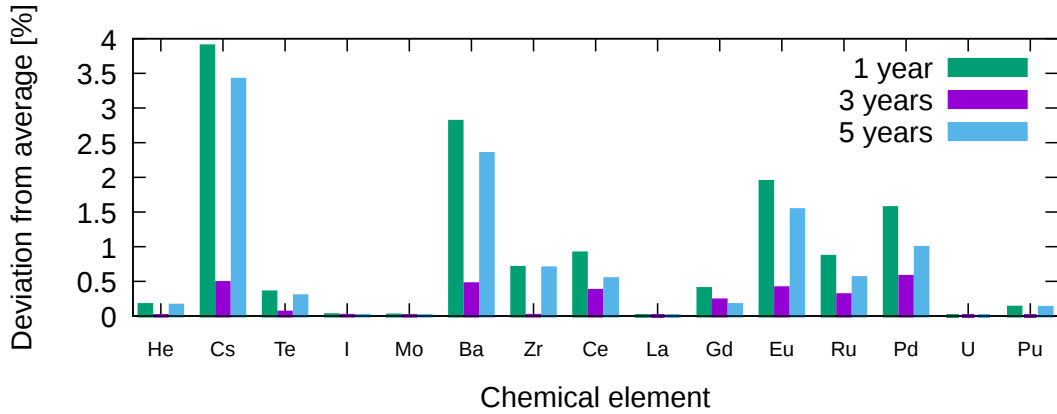


Figure 3.9: Deviations from average value in PRODHEL calculations of the integral weight fractions of chemical elements after 1, 3 or 5 years of cooling.

The highest deviation, reaching 4 % is calculated for Cs. Other noticeable deviations exceeding 1% are for Ba, Eu and Pd. It can be concluded from this analysis that the cooling time varying from one year to five years does not have a significant impact on the concentration of representative elements. In the comparisons with experimental measurements, a cooling time of 3 years is considered since this duration is in the range of usual cooling times at CEA between power ramps and experimental measurements.

The burnup radial profile calculated with ALCYONE is very close to the one reported by Walker et al. as shown in Figure 3.10. The deviation at the pellet center is around 4% while the maximum deviation is around 8% at  $r/R_{pellet} = 0.8$ .

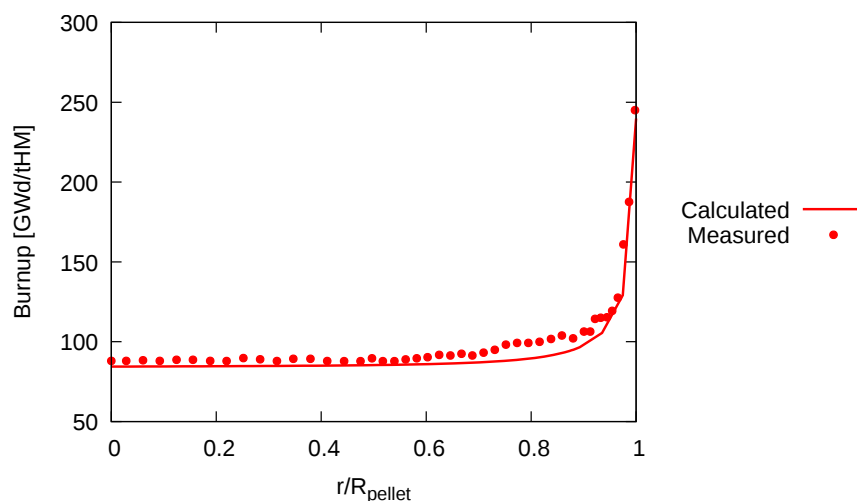


Figure 3.10: Radial profile of burnup calculated with ALCYONE compared to the estimates deduced from Nd concentration measurements by Walker et al. [7].

Walker et al. have measured the average FP inventory in the fuel pellet. The authors used the ICP-MS method for the average value. The predicted radial average FP inventory in the fuel pellet is shown in Figure 3.11 and compared to Walker's measurements. This figure also includes the values calculated with the coefficients of Table 1.3 and the burnup profile of Figure 3.10.

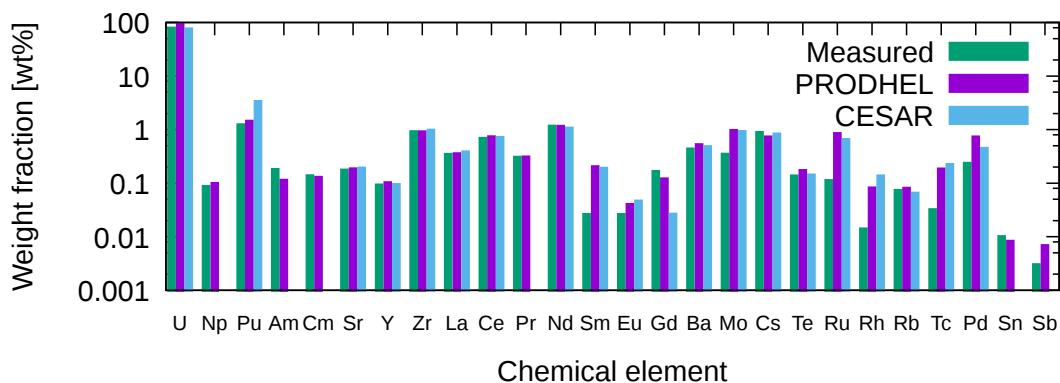


Figure 3.11: PRODHEL calculations of the integral weight fractions of chemical elements compared to ICP-MS measurements from Walker et al. [7] and to CESAR calculations.

PRODHEL and CESAR results compared to ICP-MS measurements show that PRODHEL is in a better agreement with the measures for most of the considered elements. All the deviations between the neutronics calculations and the experimental values calculated with Equation 3.1 are shown in Figure 3.12.

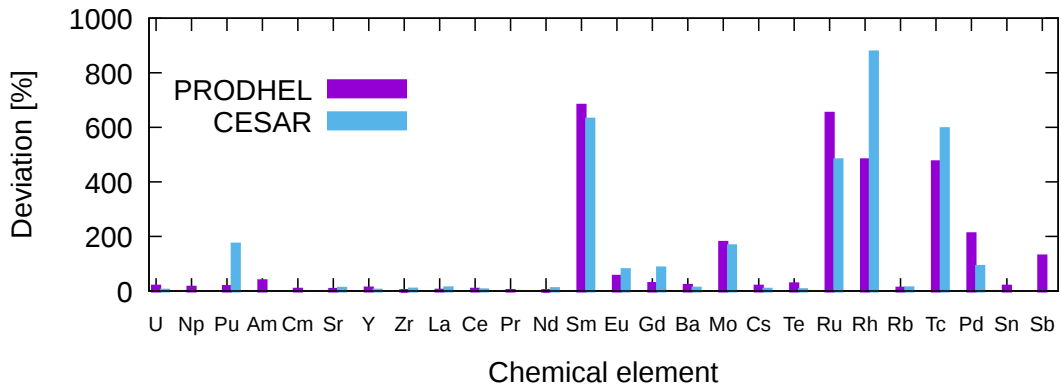


Figure 3.12: Deviations from the experimental measurements of average weight fractions of FPs calculated by PRODHEL and CESAR.

Very large deviations are observed for Pd, Mo, Rh, Ru and Tc. However, as reported by Walker et al., all these metals are insoluble in  $\text{HNO}_3$ , the solvent used in the ICP-MS analysis. They were part of the residue remaining from the fuel dissolution. The authors mentioned that for this reason concentrations of these elements measured by ICP-MS were underestimated. The calculated Sm weight fractions also show a very high deviation. Walker et al. have reported that the Sm weight fraction is exactly the same as the Eu weight fraction, which was unexpected by the authors. According to PRODHEL and CESAR calculations, the Sm content should be around 10 times higher than that of Eu. The deviation of Sb is not satisfying either. According to the work of May et al. [162], those discrepancies might be caused by polyatomic interferences during ICP-MS analysis, such as  $^{135}\text{Ba}^{16}\text{O}^+$  on  $^{151}\text{Eu}^+$ ,  $^{130}\text{Ba}^{16}\text{OH}^+$  and  $^{99}\text{Ru}^{16}\text{O}_3^+$  on  $^{147}\text{Sm}^+$ ,  $^{105}\text{Pd}^{16}\text{O}^+$  on  $^{121}\text{Sb}$ . Neutronics calculations of Walker's experiment have also been performed by Piro et al. [12]. The authors used the ORIGEN-S [11] code and obtained results very similar to those from PRODHEL (overestimation of Pd, Mo, Rh, Ru and Tc).

Walker et al. also measured by EPMA the local FPs inventories at 4 radial positions  $r/R_{\text{pellet}}=0.1, 0.5, 0.8, 0.975$  where  $r/R_{\text{pellet}}$  is the relative radius of the pellet. Calculated local inventories are compared to measurements in Figures 3.13–3.16. In addition, these figures include inventories calculated with CESAR's correlation coefficients, given in Table 1.3, and the burnup profile of Figure 3.7.

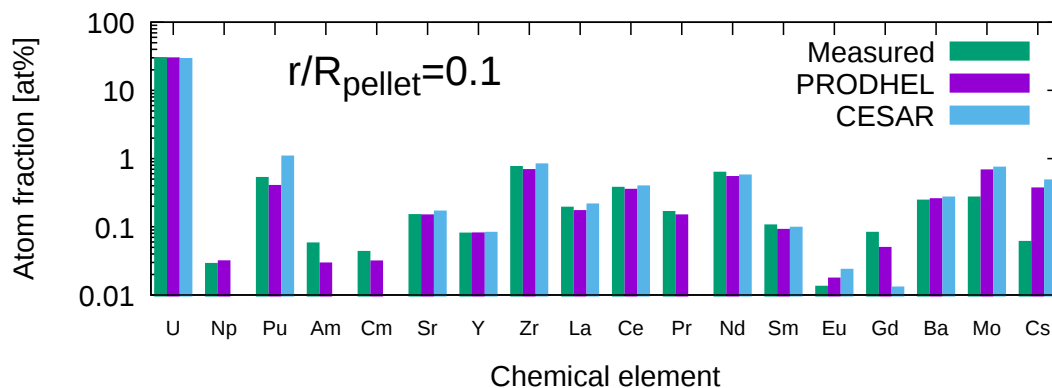


Figure 3.13: PRODHEL calculations of the local atom fractions of chemical elements compared to EPMA measurements from Walker et al. [7] and to CESAR calculations at  $r/R_{\text{pellet}}=0.1$ .

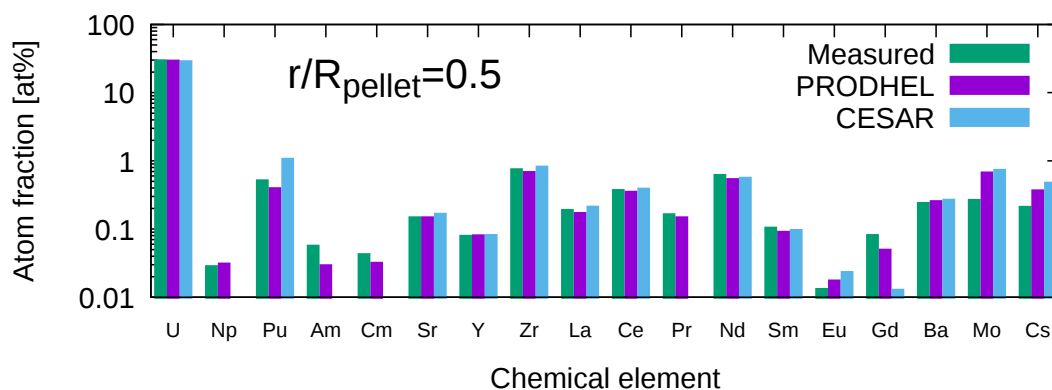


Figure 3.14: PRODHEL calculations of the local atom fractions of chemical elements compared to EPMA measurements from Walker et al. [7] and to CESAR calculations at  $r/R_{\text{pellet}}=0.5$ .

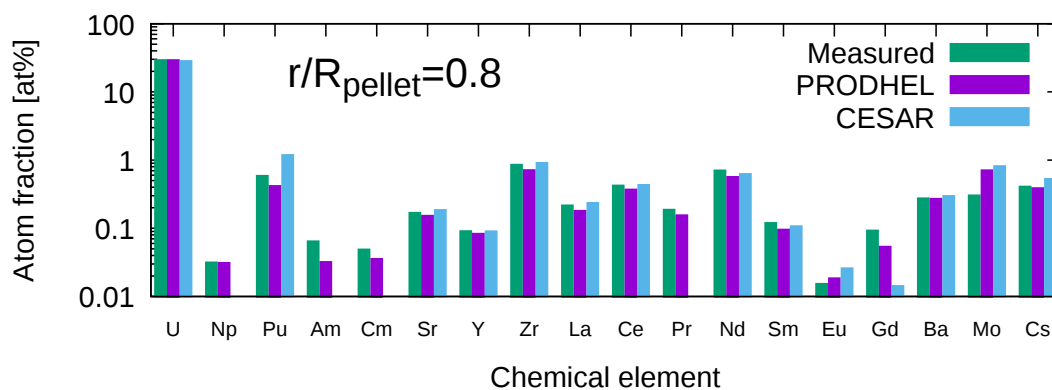


Figure 3.15: PRODHEL calculations of the local atom fractions of chemical elements compared to EPMA measurements from Walker et al. [7] and to CESAR calculations at  $r/R_{\text{pellet}}=0.8$ .

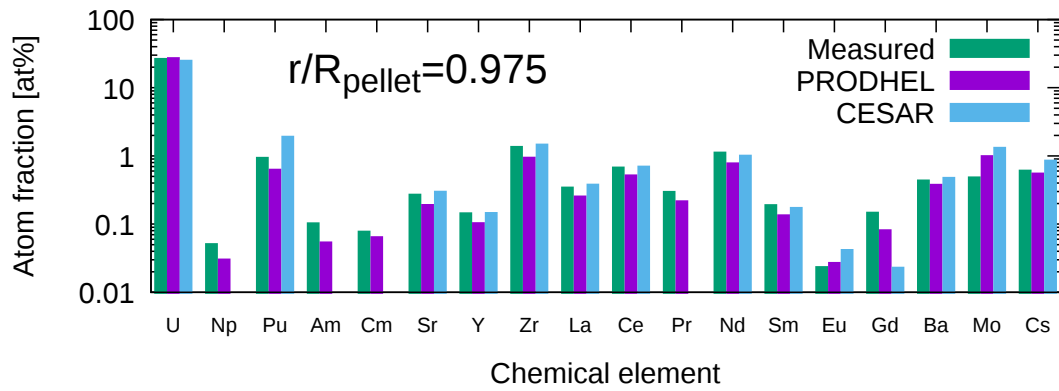


Figure 3.16: PRODHEL calculations of the local atom fractions of chemical elements compared to EPMA measurements from Walker et al. [7] and to CESAR calculations at  $r/R_{\text{pellet}}=0.975$ .

In general, PRODHEL predictions of FPs and actinides concentrations are more precise than those from CESAR. Deviation of the PRODHEL prediction of U (around 3%) is also lower than that of CESAR (around 5%). One may notice that the concentration of Cs calculated by PRODHEL in the central part of the pellet ( $r/R_{\text{pellet}}=0.1$  and  $0.5$ ) is overestimated (Figures 3.13 and 3.14) while it is close to measurements at the other radial positions (Figures 3.15 and 3.16). This result can be explained by high cesium release from the central part of the pellet as measured by Walker et al. and shown in Figure 3.17.

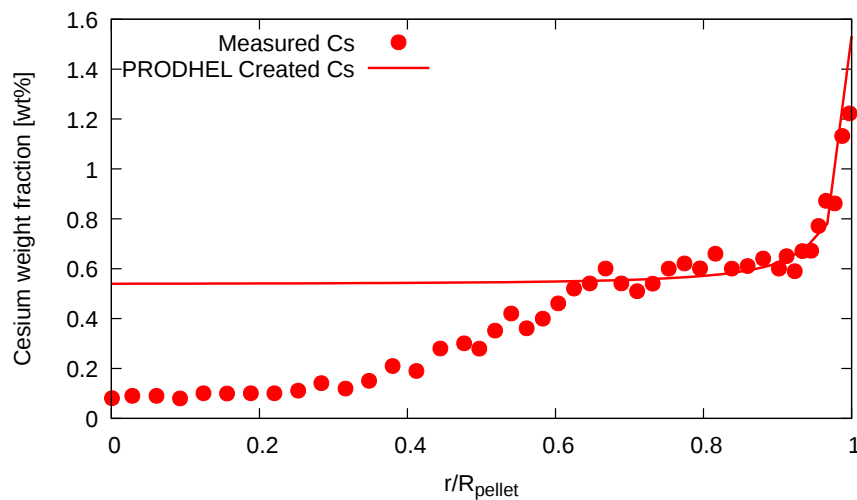


Figure 3.17: Calculated radial profile of Cs weight fraction compared to the EPMA measurements from Walker et al. [7].

Concentrations of nearly all elements (except Eu and Mo) at the pellet periphery are slightly underestimated by PRODHEL, as shown in Figure 3.16. It may be caused by some uncertainty on the radial position of the EPMA measurements. Near the rim

region, burnup increases rapidly with radius (see Figure 3.10) and even a small variation in radius may lead to a significant difference in elemental composition.

Walker et al. have also given the complete radial profiles of Pu and Nd from EPMA measurements. However, as pointed by Piro et al. [12], integration of EPMA profiles leads to average contents that significantly differ from the average values obtained by ICP-MS. Using the trapezoidal rule, Piro and al. integrated the EPMA radial profile of Pu and found an average value 29% lower than the one reported by Walker et al from ICP-MS measurements. This difference was attributed to a larger uncertainty in EPMA measurements. This calculation has been repeated in this work. Integration of EPMA profiles using the same method gives average concentrations of Pu and Nd in the fuel pellet lower by 31% and 12% as compared to ICP-MS measurements. Piro et al. proposed to normalize the EPMA profile in order to be consistent with average concentrations from ICP-MS which present less uncertainties. As shown in Figure 3.18, the normalized EPMA profiles are in better agreement with the calculated profiles, in particular for Pu.

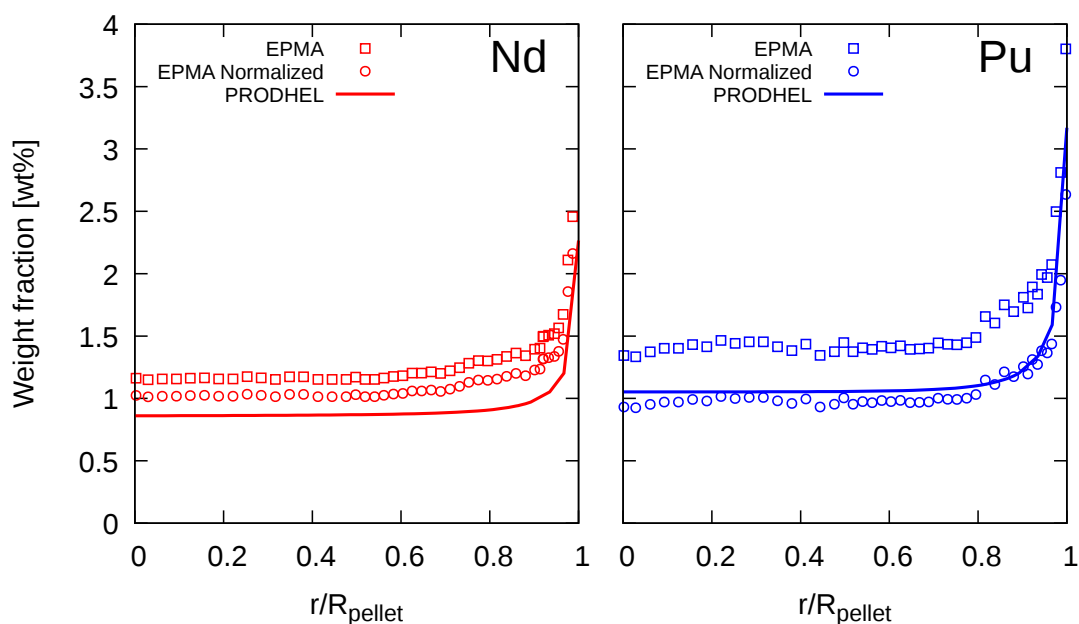


Figure 3.18: Calculated radial profiles of weight fractions of Nd (left figure) and Pu (right figure) compared to the EPMA measurements from [7].

To summarize, PRODHEL gives consistent estimations of the FPs and actinides inventory in fuel irradiated up to high burnups. The radial profiles are also well reproduced with a marked increase near the pellet periphery. The comparison to local measurements at the pellet periphery is more imprecise since a very strong variation of burnup is encountered in the rim region of the fuel which might have led to some leveling of the concentrations.

## 3.2 Thermochemical solver ANGE

All thermodynamics calculations are carried out using the code ANGE [150] (for Advanced Gibbs Energy), based on SOLGASMIX [145]. ANGE uses the Gibbs energy minimization method to find the thermodynamic equilibrium of a multicomponent and multiphase system at given temperature and pressure. A brief presentation of the minimization method will be given in the first part of this section since modifications have been introduced to couple oxygen thermal diffusion and thermochemistry, as discussed in Section 5.1.2.

The calculations require an extensive thermodynamic database including the possible chemical compounds that can form from the FPs, uranium, oxygen and actinides. In ANGE database, the following phases are considered :

- a gas phase
- a solid solution phase for the FPs and actinides dissolved in uranium dioxide
- a noble metal phase
- pure condensed phases

The main compounds of each phase are described in the second and third part of this section. The validity of the solid solution phase model is checked in the last part of this section by comparing the calculated oxygen potentials at various temperatures with data from the open literature on binary or ternary systems.

### 3.2.1 Gibbs energy minimization method

The minimum of the Gibbs energy of a system corresponds to its energy at thermodynamic equilibrium. By minimizing the Gibbs energy, one can predict the composition of the chemical system at equilibrium. In this part, the Gibbs energy minimization method is briefly presented. It is based on the work of Eriksson [163], and thus the nomenclature and symbols proposed by the author are used in this section.

The method can be explained by considering a system composed of  $s$  pure condensed phases and one gas phase consisting of  $m$  compounds. The Gibbs energy of the system is given by:

$$G = \sum_{k=1}^m n_k^g g_k^g + \sum_{k=1}^s n_k^c g_k^c \quad (3.3)$$

where  $n_k^g$  is the number of moles of each gaseous compound and  $n_k^c$  is the number of moles of each condensed phase.  $g_k^g(T, P)$  and  $g_k^c(T)$  are the partial molar Gibbs energies of the compound  $k$  of the gas mixture and of the  $k$ -th pure condensed phase, also equal

to the chemical potentials of the compounds and phases. Assuming that the gas mixture is ideal, the Gibbs energy of the system  $G$  divided by  $RT$  for convenience, is given by:

$$G/RT = \sum_{k=1}^m n_k^g \left[ \frac{g_k^{\circ g}}{RT} + \ln P + \ln x_k^g \right] + \sum_{k=1}^s n_k^c \frac{g_k^{\circ c}}{RT} \quad (3.4)$$

where  $x_k^g = \left( n_k^g / \sum_{k=1}^m n_k^g \right)$  is the mole fraction of the gaseous compound  $k$  in the mixture.  $g_k^{\circ g}(T)$  and  $g_k^{\circ c}(T)$  are, respectively, the partial molar Gibbs energies of the compound  $k$  of the gas mixture and of the  $k$ -th condensed phase at the total pressure 1 bar and at the temperature  $T$ .  $P$  is the pressure of the gas mixture. The goal of the minimization method is to find the numbers of moles of each compound ( $n_k^g$  and  $n_k^c$ ) that minimize the total Gibbs energy of the system under mass balance constraints for the chemical elements from which the compounds are formed. These constraint conditions are introduced to ensure that the number of moles of each chemical element is conserved. They take the following form:

$$\sum_{k=1}^m a_{kj}^g n_k^g + \sum_{k=1}^s a_{kj}^c n_k^c = b_j \quad j = 1, \dots, NE \quad (3.5)$$

where  $a_{kj}^{g,c}$  is the number of atoms of  $j$ -th element in the  $k$ -th compound of the system.  $b_j$  is the quantity of the  $j$ -th chemical element in the system.  $NE$  is the number of chemical elements.

As can be seen, Equation 3.4 is non-linear and it needs an iterative treatment. The algorithm used in ANGE is based on the work of Eriksson [163]. The conservation conditions given by Equation 3.5 are treated by the Lagrange method of undetermined multipliers. Practically, the function that needs to be minimized takes the following form:

$$L(n_k^g, n_k^c, \lambda_j) = \frac{G}{RT} - \sum_{j=1}^{NE} \left[ \lambda_j \left( \sum_{k=1}^m a_{kj}^g n_k^g + \sum_{k=1}^s a_{kj}^c n_k^c - b_j \right) \right] \quad (3.6)$$

with

$$\frac{G}{RT} = \left( \sum_{k=1}^m n_k^g \frac{g_k^{\circ g}}{RT} + \ln P \sum_{k=1}^m n_k^g + \sum_{k=1}^m n_k^g \ln \frac{n_k^g}{\sum_{k=1}^m n_k^g} \right) + \sum_{k=1}^s n_k^c \frac{g_k^{\circ c}}{RT} \quad (3.7)$$

where the mole fraction  $x_k^g$  of the gas  $k$  was replaced by  $n_k^g / \sum_{k=1}^m n_k^g$ . The constants  $\lambda_j$  from Equation 3.6 are the Lagrange multipliers, additional unknowns of the system (with the  $n_k^g, k = 1, \dots, m$  and  $n_k^c, k = 1, \dots, s$ ). The minimum of the function  $L$  is reached when the partial derivatives with respect to the  $n_k^g, n_k^c$  and  $\lambda_j$  are null, leading the following

system of equations:

$$\begin{aligned}
 (1) \quad & \frac{g_k^{\circ g}}{RT} + \ln P + \ln \frac{n_k^g}{N^g} - \sum_{j=1}^{NE} a_{kj}^g \lambda_j = 0, \quad k = 1, \dots, m \\
 (2) \quad & \frac{g_k^{\circ c}}{RT} - \sum_{j=1}^{NE} a_{kj}^c \lambda_j = 0, \quad k = 1, \dots, s \\
 (3) \quad & \sum_{k=1}^m a_{kj}^g n_k^g + \sum_{k=1}^s a_{kj}^c n_k^c - b_j = 0, \quad j = 1, \dots, NE
 \end{aligned} \tag{3.8}$$

The first line is given by the derivative  $\partial L / \partial n_k^g$  (gaseous compounds), the second one by  $\partial L / \partial n_k^c$  (condensed phases) and the third one by  $\partial L / \partial \lambda_j$  (Lagrange multipliers). The total number of moles in the gas phase  $\sum_{k=1}^m n_k^g$  has been replaced by  $N^g$ . The total number of equations and of unknowns is  $m + s + NE$ .

In case no gaseous compounds are formed, the system described by Equation 3.8 is linear as a function of the number of moles of condensed phases and of the Lagrange multipliers. To solve the system in the presence of gaseous compounds, Eriksson chose to linearize the  $\ln n_k^g / N^g$  term in the  $m$  equations 3.8.(1) using the Taylor function ( $\ln x \approx \ln y + (x - y/y)$ ):

$$\ln \frac{n_k^g}{N^g} \approx \ln \frac{y_k^g}{Y^g} + \frac{n_k^g}{y_k^g} - \frac{N^g}{Y^g} \tag{3.9}$$

with  $y_k^g$  an initial estimate of the number of moles of the  $k$ th gaseous compound  $n_k^g$ ,  $Y^g = \sum_{k=1}^m y_k^g$  an initial estimate of the total number of moles in the gas phase. By introducing Equation 3.9 into Equation 3.8.(1), each number of moles  $n_k^g$  can be expressed as a function of the initial estimations ( $y_k^g$  and  $Y^g$ ) and of the total number of moles of the gas phase  $N^g$ :

$$n_k^g = y_k^g \left[ -\frac{g_k^{\circ g}}{RT} - \ln P - \ln \frac{y_k^g}{Y^g} + \frac{N^g}{Y^g} + \sum_{j=1}^{NE} a_{kj}^g \lambda_j \right] \quad k = 1, \dots, m \tag{3.10}$$

Eriksson separated the known and unknown parts of Equation 3.10 by defining the quantity  $f_k^g$  given by:

$$f_k^g = y_k^g \left[ \frac{g_k^{\circ g}}{RT} + \ln P + \ln \frac{y_k^g}{Y^g} \right] \quad k = 1, \dots, m \tag{3.11}$$

which allows to rewrite Equation 3.10 in the following form:

$$n_k^g = y_k^g \left[ \frac{N^g}{Y^g} + \sum_{j=1}^{NE} a_{kj}^g \lambda_j \right] - f_k^g \quad k = 1, \dots, m \tag{3.12}$$

where the only unknown is  $N^g / Y^g$ , which is the ratio of the total numbers of moles in the gas phase obtained in two successive iterations. This parameter is also the convergence criterion of the iterative scheme. Its value tends to one. Summing all equations 3.12 for

all the gaseous compounds leads to a single equation of the form:

$$\sum_{j=1}^{NE} \lambda_j \sum_{k=1}^m a_{kj}^g y_k^g = \sum_{k=1}^m f_k^g \quad (3.13)$$

Introducing the number of moles  $n_k^g$  from Equation 3.12 into Equations 3.8.(3) leads to the following linear system:

$$\begin{aligned} (1) \quad & \frac{g_k^{\circ c}}{RT} - \sum_{j=1}^{NE} a_{kj}^c \lambda_j = 0, & k = 1, \dots, s \\ (2) \quad & \sum_{j=1}^{NE} \lambda_j \sum_{k=1}^m a_{kj}^g y_k^g = \sum_{k=1}^m f_k^g, & k = 1, \dots, m \\ (3) \quad & \sum_{i=1}^{NE} \lambda_i \sum_{k=1}^m a_{kj}^g a_{ki}^g y_k^g + \left[ \frac{N^g}{Y^g} - 1 \right] \sum_{k=1}^m a_{kj}^g y_k^g + \sum_{k=1}^s a_{ij}^c n_k^c = \\ & = \sum_{k=1}^m a_{kj}^g (f_k^g - y_k^g) + b_j, & j = 1, \dots, NE \end{aligned} \quad (3.14)$$

The Gaussian elimination method is used to solve this system. One obtains the  $s$  numbers of moles of condensed phases  $n_k^c$ , the  $NE$  Lagrange multipliers and the ratio  $N^g/Y^g$ . The  $y^g$  and  $Y^g$  estimates are updated and the system of Equation 3.14 is iteratively solved till convergence is reached. The  $m$  numbers of moles of gaseous compounds are then calculated from Equation 3.12. The system size is related to the number of chemical elements  $NE$  and to the number of pure phases  $s$ . The number of considered chemical compounds in each phase is quasi-unlimited.

Taking into account the solubility of certain compounds in  $UO_2$  requires the consideration of an additional phase into the multiphase system described previously. The Gibbs energy of the system with  $d$  compounds in the solid solution phase  $s$  can be expressed as:

$$\begin{aligned} \frac{G}{RT} = & \left( \sum_{k=1}^m n_k^g \frac{g_k^{\circ g}}{RT} + \ln P \sum_{k=1}^m n_k^g + \sum_{k=1}^m n_k^g \ln \frac{n_k^g}{\sum_{k=1}^m n_k^g} \right) + \\ & + \left( \sum_{k=1}^d n_k^s \frac{g_k^{\circ s}}{RT} + \sum_{k=1}^d n_k^s \ln \frac{n_k^s}{N^s} \right) + \sum_{k=1}^s n_k^c \frac{g_k^{\circ c}}{RT} \end{aligned} \quad (3.15)$$

where the solid solution phase is assumed to be ideal to simplify the equation. The solid solution phase consists of  $d$  species with mole numbers  $n_k^s$ . The number of moles of all the species present in the solid solution is given by:

$$N^s = \sum_{k=1}^d n_k^s \quad (3.16)$$

The  $NE$  equations of conservation for each of the chemical elements in the system described in Equation 3.5 has to be rewritten to include the compounds in the solid

solution phase:

$$\sum_{k=1}^m a_{kj}^g n_k^g + \sum_{k=1}^d a_{kj}^s n_k^s + \sum_{k=1}^s a_{kj}^c n_k^c = b_j \quad j = 1, \dots, NE \quad (3.17)$$

It leads to  $d$  new equations in the system 3.8. These new equations come from the partial derivatives of the function  $L$  with respect to the mole numbers  $n_k^s$  ( $\partial L / \partial n_k^s$  with  $k = 1, \dots, d$ ):

$$\frac{g_k^{os}}{RT} + \ln \frac{n_k^s}{N^s} - \sum_{j=1}^{NE} a_{kj}^s \lambda_j = 0 \quad k = 1, \dots, d \quad (3.18)$$

By linearizing the natural logarithms of Equations 3.18 using the Taylor function, this will yield to an additional equation in the system 3.14 and to an additional unknown ( $N^s / Y^s$  with  $Y^s = \sum_{k=1}^d y_k^s$ ), similar to the one defined for the gas phase:

$$\begin{aligned} (1) \quad & \frac{g_k^{oc}}{RT} - \sum_{j=1}^{NE} a_{kj}^c \lambda_j = 0, \quad k = 1, \dots, s \\ (2) \quad & \sum_{j=1}^{NE} \lambda_j \sum_{k=1}^m a_{kj}^g y_k^g = \sum_{k=1}^m f_k^g, \\ (3) \quad & \sum_{j=1}^{NE} \lambda_j \sum_{k=1}^d a_{kj}^s y_k^s = \sum_{k=1}^d f_k^s, \\ (4) \quad & \sum_{i=1}^{NE} \lambda_i \sum_{k=1}^m a_{kj}^g y_{ki}^g y_k^g + \left[ \frac{N^g}{Y^g} - 1 \right] \sum_{k=1}^m a_{kj}^g y_k^g + \\ & + \sum_{i=1}^{NE} \lambda_i \sum_{k=1}^d a_{kj}^s a_{ki}^s y_k^s + \left[ \frac{N^s}{Y^s} - 1 \right] \sum_{k=1}^d a_{kj}^s y_k^s + \\ & + \sum_{k=1}^s a_{kj}^c n_k^c = \\ & = \sum_{k=1}^m a_{kj}^g (f_k^g - y_k^g) + \sum_{k=1}^d a_{kj}^s (f_k^s - y_k^s) + b_j, \end{aligned} \quad j = 1, \dots, NE \quad (3.19)$$

where the  $m$  and  $d$  terms  $f_k^g$  and  $f_k^s$  can be expressed as a function of the  $y_k^g$  and  $y_k^s$  estimates according to:

$$\begin{aligned} f_k^g &= y_k^g \left[ \frac{g_k^{og}}{RT} + \ln P + \ln \frac{y_k^g}{Y^g} \right] \quad k = 1, \dots, m \\ f_k^s &= y_k^s \left[ \frac{g_k^{os}}{RT} + \ln \frac{y_k^s}{Y^s} \right] \quad k = 1, \dots, d \end{aligned} \quad (3.20)$$

The system given of Equations 3.19 contains  $s + NE + 2$  equations with an identical number of unknowns: the  $s$  numbers of moles  $n_k^c$ , the  $NE$  Lagrange multipliers  $\lambda_j$ , the ratios  $N^g / Y^g$  and  $N^s / Y^s$ . The system is linear as a function of each of these unknowns and it can be solved with the Gaussian elimination method. The last phase considered in ANGE database is the noble metal phase which can be introduced in the system in a similar manner.

### 3.2.2 Thermodynamic database

In order to run Gibbs energy minimization calculations, it is necessary to define the thermodynamic quantities  $g^\circ/RT$  for each compound of each phase or each pure condensed phase. According to Eriksson, there are two alternative methods to calculate the  $g^\circ/RT$ . First, by the expression:

$$\frac{g^\circ}{RT} = \frac{\Delta_f G^\circ}{RT} \quad (3.21)$$

where  $\Delta_f G^\circ$  denotes the Gibbs energy of formation from the elements in their chosen reference state.  $\Delta_f G^\circ$  can be expressed by a function of temperature in the following form:  $\Delta_f G^\circ = a/T + b + cT + dT^2 + eT^3 + fT \ln T$ . Alternatively,  $g^\circ/RT$  can be calculated by:

$$\frac{g^\circ}{RT} = \frac{1}{R} \left[ \frac{G^\circ - H_{298}^\circ}{T} \right] + \frac{\Delta_f H_{298}^\circ}{RT} \quad (3.22)$$

where  $\frac{G^\circ - H_{298}^\circ}{T}$  is the free energy function and  $\Delta_f H_{298}^\circ$  is the heat of formation at 298 K. Each of these two conventions gives the same result for the equilibrium calculation, provided consistency is maintained. The thermodynamic database of ANGE has been built using the first method. The  $\Delta_f G^\circ$  functions are expressed as simple linear functions of temperature:

$$\Delta_f G^\circ = b + cT \quad (3.23)$$

For a given compound in a phase or a condensed phase, several linear  $\Delta_f G^\circ$  functions can be defined depending on the temperature range.

The actinides and fission products considered in ANGE database are summarized in Table 3.1. In order to simplify the system, elements with expected close chemical behavior are grouped together leading to 14 representative elements. They have been classified in five different families: 1) inert fission gases and volatile fission products, 2) stable oxides, 3) molybdenum, 4) metallic FPs and 5) FPs and actinides in solid solution in  $\text{UO}_2$ . All chemical elements to which must be added oxygen (O), uranium (U) and chromium in case the fuel is doped (Cr), lead to a total of 17 representatives elements (He, Cs, I, Te, Ba, Zr, Mo, Ru, Pd, Ce, Eu, La, Gd, Pu, U, O, Cr). The compounds and stoichiometric phases considered in ANGE thermodynamic database that can form from these elements are briefly discussed below:

- The gas phase includes 61 species with as main components,  $\text{Xe}_{(g)}$ ,  $\text{Cs}_{(g)}$ ,  $\text{Cs}_{2(g)}$ ,  $\text{CsI}_{(g)}$ ,  $\text{Cs}_2\text{I}_{2(g)}$ ,  $\text{I}_{(g)}$ ,  $\text{I}_{2(g)}$ ,  $\text{Te}_{(g)}$ ,  $\text{Te}_{2(g)}$ ,  $\text{Te}_{3(g)}$ ,  $\text{Te}_{5(g)}$ ,  $\text{TeI}_{2(g)}$ ,  $\text{Cs}_2\text{MoO}_{4(g)}$ . Special attention was given to tellurium, for which major experimental results were obtained recently at CEA [61], evincing the occurrence of gaseous tellurium–iodine compounds in power-ramped  $\text{UO}_2$  fuel rods. As mixed tellurium–iodine compounds were not taken into account initially, the thermodynamical functions of

the gas  $\text{TeI}_{2(g)}$  given in the SGPS database of the FactSage software [74, 75] were introduced into ANGE. Then, in consistency with experimental observations, the dominant gaseous iodine species formed in an irradiated fuel at high temperatures ( $>1200$  K) are  $\text{TeI}_{2(g)}$  and  $\text{CsI}_{(g)}$  with relative fractions in the gas phase depending on the cesium and oxygen partial pressures.

- The pure condensed phases include solid and liquid uranates, molybdates and zirconates, such as  $\text{Cs}_2\text{UO}_{4(s)}$ ,  $\text{Cs}_2\text{MoO}_{4(s,l)}$ ,  $\text{Cs}_2\text{ZrO}_{3(s)}$ ,  $\text{BaZrO}_{3(s)}$ , and other important compounds such as  $\text{MoO}_{2(s)}$ ,  $\text{MoO}_{3(s,l)}$ ,  $\text{CsI}_{(s,l)}$ ,  $\text{Te}_{(s,l)}$ ,  $\text{Cs}_{(s,l)}$ ,  $\text{Cs}_2\text{Te}_{(s,l)}$ ,  $\text{BaTe}_{(s)}$ . A total of 82 stoichiometric separate phases is considered in the database. Recent re-evaluations at CEA of the Gibbs energy functions of  $\text{Cs}_2\text{Te}_{(s,l)}$  were added to the database [164]. Most other thermodynamic data come from the SGPS database of the FactSage software.
- The noble metal phase includes 3 representative species [151] that are often observed simultaneously in irradiated fuels in amalgam form:  $\text{Mo}_{(s)}$ ,  $\text{Ru}_{(s)}$  (for Ru + Tc + Rh) and  $\text{Pd}_{(s)}$ . They are treated on the basis of results obtained by Yamawaki et al. [165].
- The fluorite oxide solid solution contains 17 dissolved species that will be detailed in the next section. Prior to calculations, the  $\Delta_f G^\circ$  data for all relevant compounds were checked and updated to enlarge their validity up to 2300 K.

To check the thermodynamic database, cross-comparison of basic thermodynamic equilibrium calculations performed with ANGE and the FactSage software (without the fluorite solid solution) on typical irradiated fuel compositions and at various temperatures were performed.

### 3.2.3 The Fluorite solid solution phase

The fluorite solid solution phase includes binary and ternary compounds of U, Pu, rare earths, Eu, Zr and Cr. Overall, this phase contains 17 species that will be detailed in the next subsections. The validity of the fluorite solid solution model of the thermodynamic database of ANGE will be showed by comparing experimental and calculated oxygen potentials for a number of binary and ternary chemical systems relevant for nuclear fuels.

#### 3.2.3.1 U-O system

The U-O system, representative of non irradiated uranium dioxide fuel, has been carefully examined over the years and its thermodynamic behavior is well characterized. The thermochemical parameters, temperature ( $T$ ) and oxygen partial pressure ( $p_{O_2}$ ),

are known to affect the stoichiometry deviation, expressed as  $x$  in  $\text{UO}_{2\pm x}$ . In the thermodynamic database of ANGE, the thermodynamic model proposed by Lindemer and Besmann [166] is used. It includes fictitious species to describe non-stoichiometric  $\text{UO}_2$ , namely  $\text{U}_{1/3(ss)}$  to model hypostoichiometry and, both  $\text{U}_4\text{O}_9(ss)$  and  $\text{U}_3\text{O}_7(ss)$  to model the hyperstoichiometric domain.

The thermodynamic parameters used for the Gibbs energies of formation (Equation 3.23) are given in Table 3.8.

Table 3.8: Species and parameters used in the original  $\text{UO}_{2\pm x}$  model of Lindemer and Besmann [166].

<b>Compound</b>	<b>Limit temperature [K]</b>	<b><math>b</math> [J/mol]</b>	<b><math>c</math> [J/mol/K]</b>
$\text{UO}_{2(ss)}$	3000	-1080000	169.0
$\text{U}_4\text{O}_9(ss)$	3000	-2250000	391.4
$\text{U}_3\text{O}_7(ss)$	3000	-3396400	569.9
$\text{U}_{1/3(ss)}$	3000	73433	-18.4

The thermodynamic model proposed by Lindemer and Besmann has been established on an extensive set of experimental measurements of oxygen partial pressures in equilibrium with non stoichiometric and stoichiometric uranium dioxides. Since then, the CALPHAD based model of Guéneau et al. [40], the most detailed description of non stoichiometric  $\text{UO}_2$ , has been established on a selection of these experimental measurements. In Figure 3.19, the evolution of the oxygen partial pressure of non irradiated  $\text{UO}_{2\pm x}$  fuel with temperature and O/U ratio as calculated with ANGE database is compared to the most recent set of data gathered by Guéneau et al. [40].

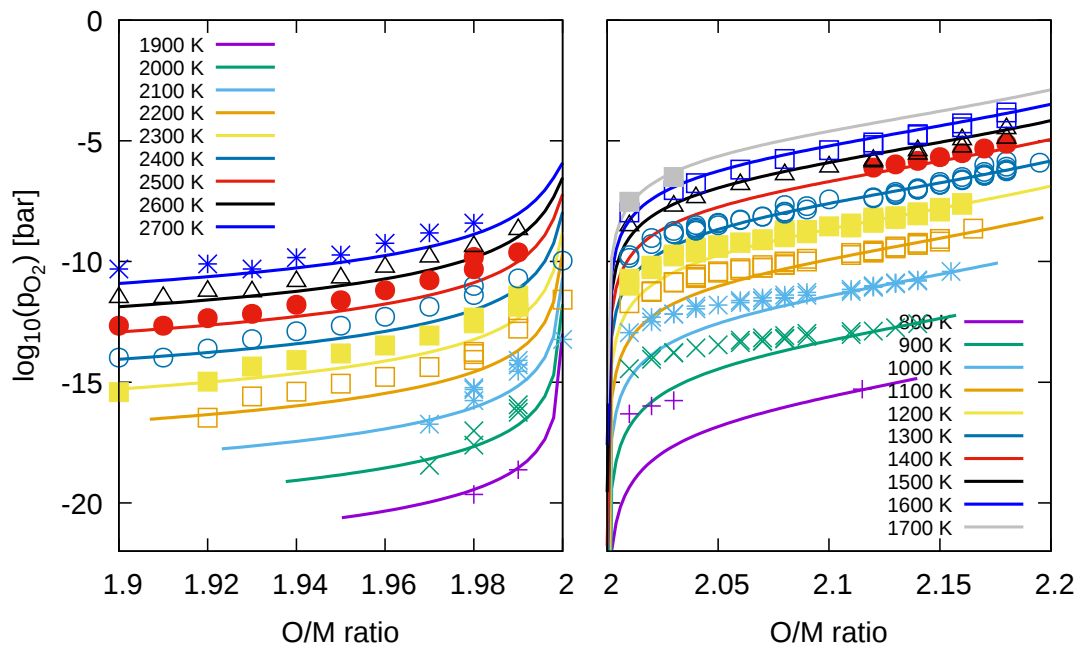


Figure 3.19: The original  $UO_{2\pm x}$  model proposed by Lindemer and Besmann [166] (lines) compared to the experimental data gathered by Guéneau et al. [40] (symbols).

The experimental measurements are satisfactorily reproduced with the thermodynamic model proposed by Lindemer and Besmann [166], except in the low temperature region of the hyperstoichiometric domain. These experimental data have been used to reevaluate the model of Lindemer et Besmann [166]. It turned out that the data can be represented more precisely without considering  $U_4O_9(ss)$  as shown in Figure 3.20 and with a slight modification of the Gibbs energy of formation of  $U_3O_7(ss)$  and  $U_{1/3}(ss)$ . Optimized parameters are given in Table 3.9.

Table 3.9: Species and parameters of the Gibbs energy of formation used in this work to describe the U-O system.

Compound	Limit temperature [K]	$b$ [J/mol]	$c$ [J/mol/K]
$UO_{2(ss)}$	3000	-1080000	169.0
$U_3O_7(ss)$	3000	-3382979	558.7
$U_{1/3}(ss)$	3000	73333	-18.9

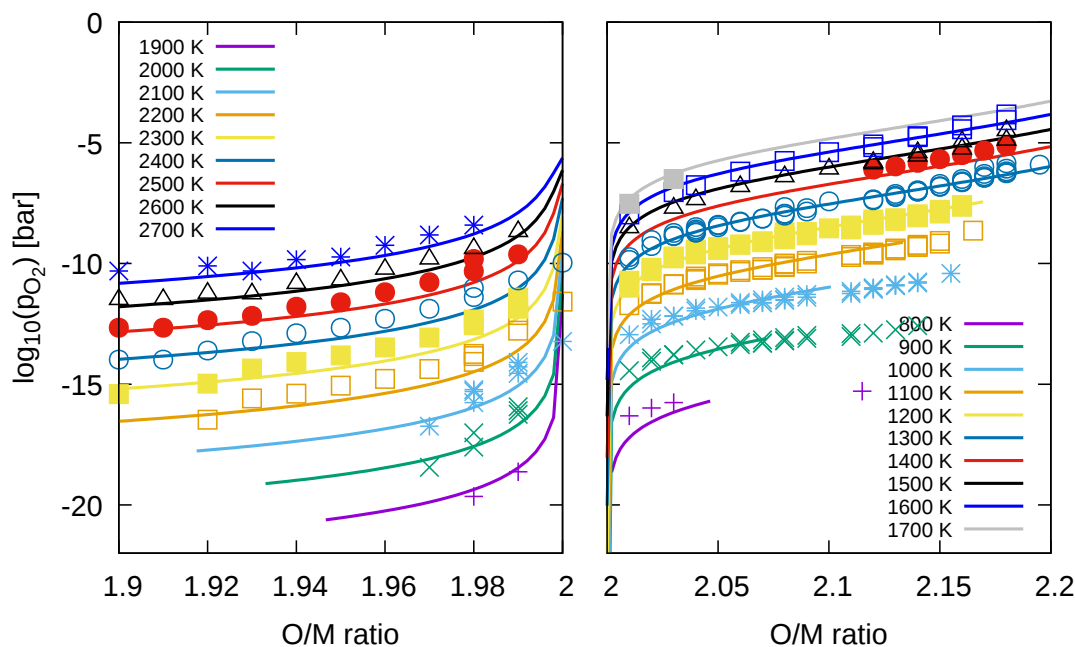


Figure 3.20: Experimental data gathered by Guéneau et al. [40] for  $\text{UO}_{2\pm x}$  (symbols) compared to ANGE calculations (lines) using the optimized Lindemer and Besmann model.

### 3.2.3.2 U-Pu-O system

The U-Pu-O system has been well studied since it is important for the MOX fuels that have been used in SFRs. Numerous experimental measurements are available. The thermodynamic description is based on the work of Besmann and Lindemer [167]. The fictitious species considered ( $\text{Pu}_{4/3}\text{O}_{2(ss)}$  and  $\text{PuO}_{2(ss)}$ ) and their Gibbs energies of formation are presented in Table 3.10.

Table 3.10: Species and parameters of the Gibbs energy of formation used to describe the Pu-O system.

Compound	Limit temperature [K]	$b$ [J/mol]	$c$ [J/mol/K]
$\text{U}_{1/3}\text{Pu}_{4/3}\text{O}_{2(ss)}$	3000	73433	-18.4
$\text{Pu}_{4/3}\text{O}_{2(ss)}$	3000	-1091900	169.7
$\text{PuO}_{2(ss)}$	2663	-1047800	187.7

Contrary to the U-O system, a good fit of experimental oxygen partial pressures could not be obtained by Besmann and Lindemer on the assumption of an ideal mixture of

$\text{Pu}_{4/3}\text{O}_{2(ss)}$  and  $\text{PuO}_{2(ss)}$ . Interaction terms had to be introduced based on the Redlich-Kister polynomial formulation. The partial molar Gibbs energies read as follows:

$$\begin{aligned} g_{\text{PuO}_{2(ss)}} &= \Delta_f G_{\text{PuO}_{2(ss)}}^\circ + RT \ln(x_{\text{PuO}_{2(ss)}}) \\ &+ (-41510 + 30.2T)x_{\text{Pu}_{4/3}\text{O}_{2(ss)}} [-2x_{\text{PuO}_{2(ss)}} + x_{\text{Pu}_{4/3}\text{O}_{2(ss)}} \\ &\quad + 2x_{\text{PuO}_{2(ss)}}(x_{\text{PuO}_{2(ss)}} - x_{\text{Pu}_{4/3}\text{O}_{2(ss)}})] \end{aligned} \quad (3.24)$$

$$\begin{aligned} g_{\text{Pu}_{4/3}\text{O}_{2(ss)}} &= \Delta_f G_{\text{Pu}_{4/3}\text{O}_{2(ss)}}^\circ + RT \ln(x_{\text{Pu}_{4/3}\text{O}_{2(ss)}}) \\ &+ (-41510 + 30.2T)x_{\text{PuO}_{2(ss)}} [2x_{\text{Pu}_{4/3}\text{O}_{2(ss)}} \\ &\quad - x_{\text{PuO}_{2(ss)}} - 2x_{\text{Pu}_{4/3}\text{O}_{2(ss)}}(x_{\text{Pu}_{4/3}\text{O}_{2(ss)}} - x_{\text{PuO}_{2(ss)}})] \end{aligned} \quad (3.25)$$

where  $x_{\text{PuO}_{2(ss)}}$  and  $x_{\text{Pu}_{4/3}\text{O}_{2(ss)}}$  are mole fractions of  $\text{PuO}_{2(ss)}$  and  $\text{Pu}_{4/3}\text{O}_{2(ss)}$  in the solid solution.

A third fictitious species,, not present in the original publication of Lindemer and Besmann, was added in ANGE database to describe very hyperstoichiometric MOX fuels:  $\text{U}_{1/3}\text{Pu}_{4/3}\text{O}_{2(ss)}$ . Its Gibbs energy of formation is equal to that of  $\text{U}_{1/3(ss)}$  given in Table 3.9. It must be mentioned that this species is of little interest in this work but it has been kept for consistency with former thermodynamic calculations performed at CEA.

Figure 3.21 shows ANGE calculations of the U-Pu-O system compared to selected experimental data [168–170]. Only the experiments performed on UPuO fuels with the lowest Pu contents have been considered here since Pu is only present in small quantities in the  $\text{UO}_2$  fuels of interest in this work (fission product).

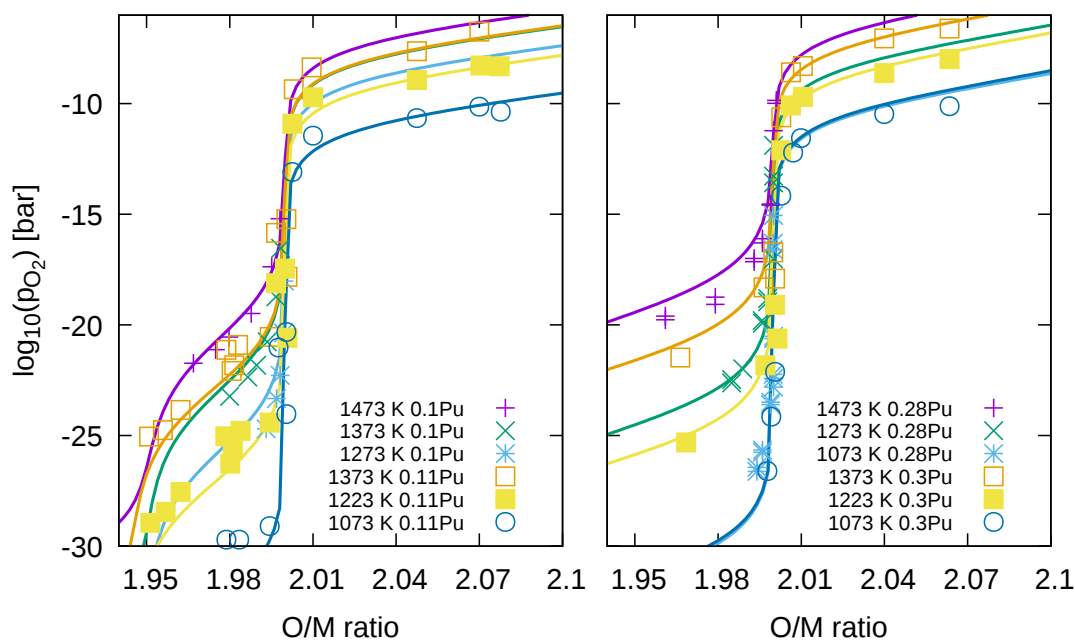


Figure 3.21: Calculated oxygen partial pressure in  $U_{1-y}Pu_yO_{2\pm x}$  (lines) as a function of O/M, temperature and Pu mole fraction compared to measured values (symbols). Experimental data from [168–170].

### 3.2.3.3 U-Gd-O and U-La-O systems

The thermodynamic representation of rare earths solubility in ANGE database is the one proposed by Lindemer and Brynstad [167]. The authors investigated the following rare earth: Y, La, Nd and Gd. In the thermodynamic database, Y is represented by La and Nd by Gd which reduces the thermodynamic data to La and Gd. The fictitious species considered by Lindemer and Brynstad are  $URE_2O_{6(ss)}$  and  $Re_{4/3}O_{2(ss)}$  with  $Re = La, Gd$ . The functions describing the Gibbs energies of formation of these species in the solid solution are exactly the same. They can be found in Table 3.11.

Table 3.11: Species and parameters of the Gibbs energy of formation used to describe the U-Re-O systems ( $Re = Gd, La$ ).

Compound	Limit temperature [K]	$b$ [J/mol]	$c$ [J/mol/K]
$URE_2O_{6(ss)}$	3000	-3234500	522.5
$Re_{4/3}O_{2(ss)}$	3000	-1203700	187.5

ANGE calculations of Gd and La solubility compared to experimental data are shown in Figures 3.22 and 3.23 respectively. As for Pu, the La and Gd contents in published experiments are higher than what can be expected in irradiated  $UO_2$  fuels.

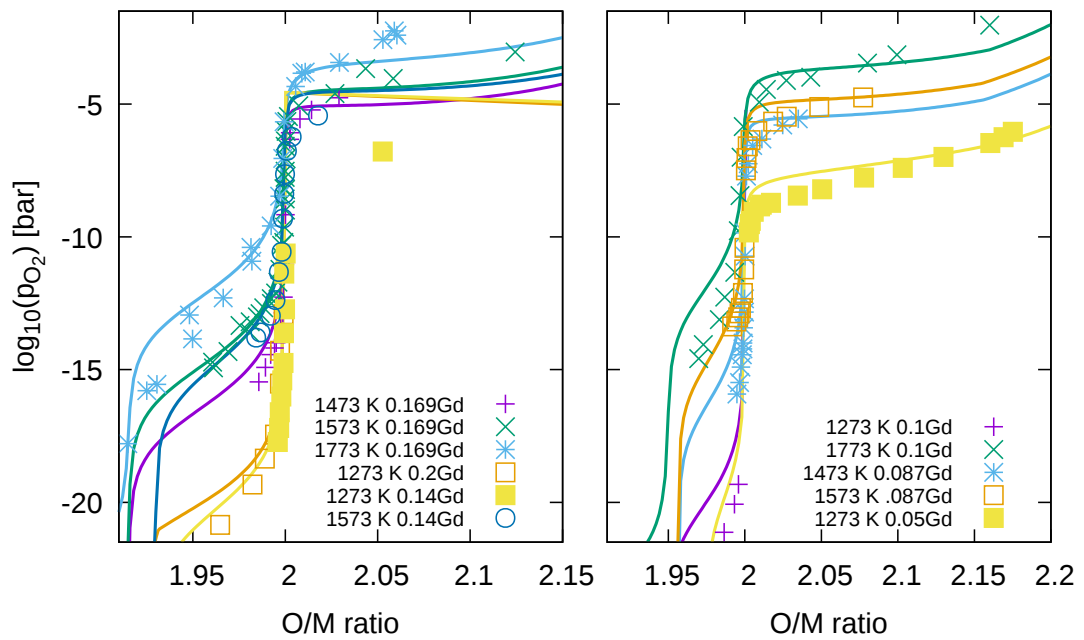


Figure 3.22: Calculated oxygen partial pressure in  $U_{1-y}Gd_yO_{2\pm x}$  (lines) as a function of O/M, temperature and Gd mole fraction compared to measured values (symbols). Experimental data from [171–173].

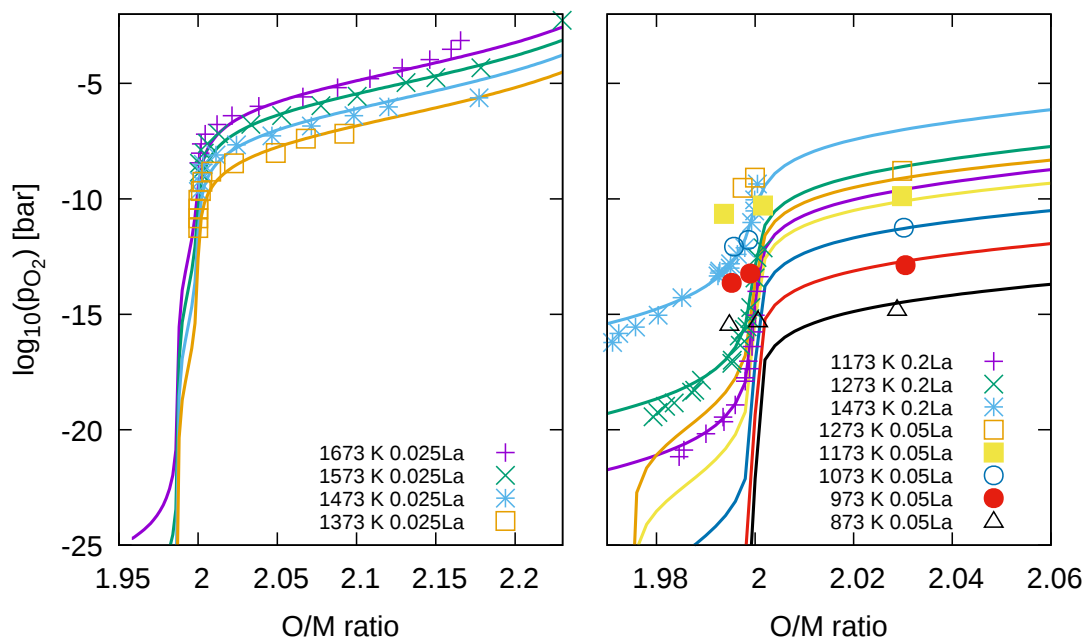


Figure 3.23: Calculated oxygen partial pressure in  $U_{1-y}La_yO_{2\pm x}$  (lines) as a function of O/M, temperature and La mole fraction compared to measured values (symbols). Experimental data from [174–176].

### 3.2.3.4 U-Ce-O system

In spite of being also part of the rare earth family, Ce has a different behavior than Gd and La and it cannot be represented by the same model. The thermodynamic description of the U-Ce-O system is based on the work of Lindemer and Brynstad [167]. The authors expressed the Gibbs energy of formation of the fictitious species  $\text{Ce}_{4/3}\text{O}_{2(ss)}$  in function of the cerium content since a marked dependency of the parameters  $b$  and  $c$  was observed. The parameters relative to the lowest Ce contents are of interest in this work and are given in Table 3.12.

Table 3.12: Species and parameters of the Gibbs energy of formation used to describe the U-Ce-O system.

Compound	Limit temperature [K]	$b$ [J/mol]	$c$ [J/mol/K]
$\text{CeO}_{2(ss)}$	3000	-1021670	164.2
$\text{Ce}_{4/3}\text{O}_{2(ss)}$	3000	-1120367	157.5

The validation against experimental data is shown in Figure 3.24. Again, only the tests performed on the UCeO fuels with the lowest Ce contents ( $< 0.3$ ) have been considered.

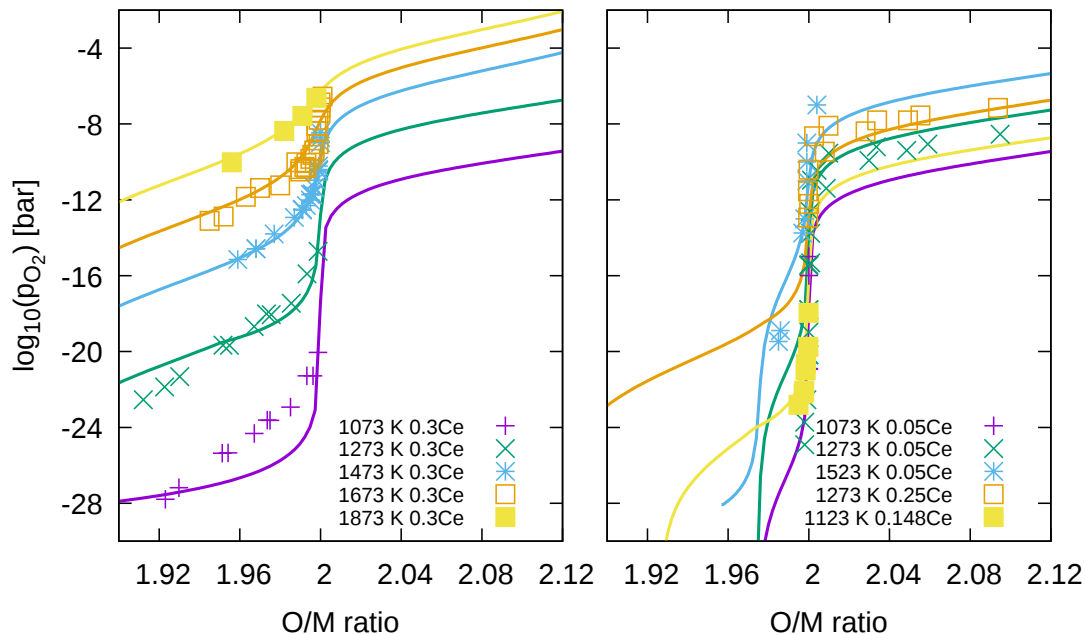


Figure 3.24: Calculated oxygen partial pressure in  $\text{U}_{1-y}\text{Ce}_y\text{O}_{2\pm x}$  (lines) as a function of O/M, temperature and Ce mole fraction compared to measured values (symbols). Experimental data from [177–179].

### 3.2.3.5 U-Eu-O system

There is not much experimental work done on the U-Eu-O system. The available experiments have been analyzed by Dumas [151]. The author based his model on the experimental work of Fujino [43]. Dumas introduced three fictitious species to describe Eu solubility in  $\text{UO}_2$ ,  $\text{EuO}_{(ss)}$ ,  $\text{Eu}_{4/3}\text{O}_{2(ss)}$ ,  $\text{UEuO}_{3.83(ss)}$  and proceeded similarly as Lindemer and Besmann to fit the Gibbs energy of formation of these species. The parameters describing the system are given in Table 3.13.

Table 3.13: Species and parameters used to describe the U-Eu-O system.

Compound	Limit temperature [K]	$b$ [J/mol]	$c$ [J/mol/K]
$\text{EuO}_{(ss)}$	2000	-569592	102.3
$\text{Eu}_{4/3}\text{O}_{2(ss)}$	1300	-1102485	206.0
	3000	-1095228	201.5
$\text{UEuO}_{3.83(ss)}$	3000	-2000020	325.0

Validation of the model against the experiments of Fujino [43] is shown in Figure 3.25.

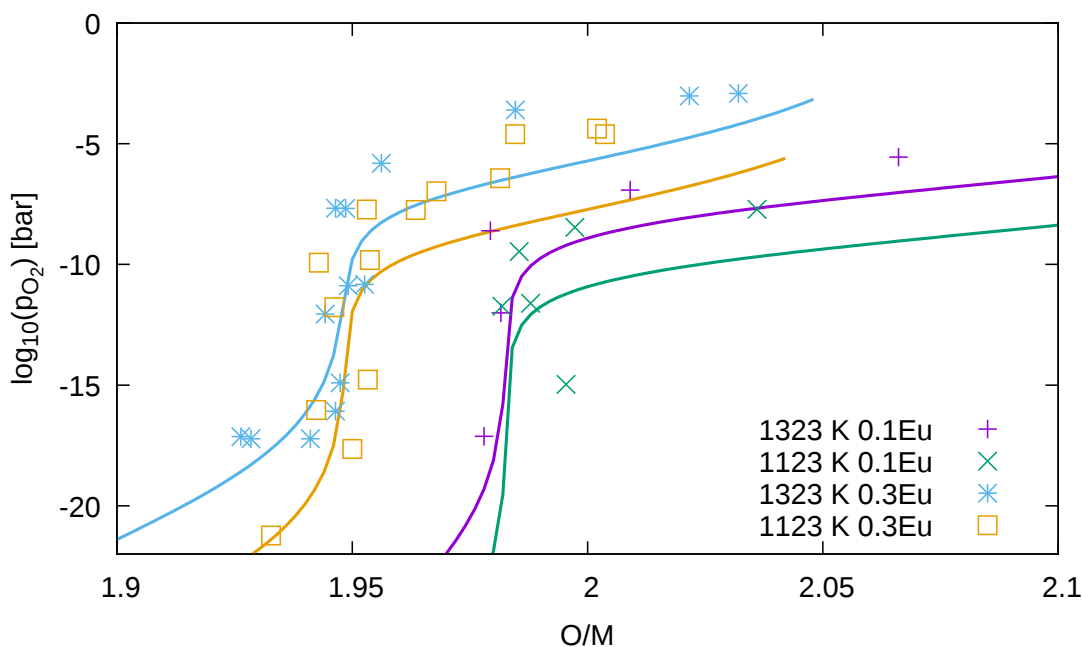


Figure 3.25: Calculated oxygen partial pressure in  $\text{U}_{1-y}\text{Eu}_y\text{O}_{2\pm x}$  (lines) as a function of O/M, temperature and Eu mole fraction compared to measured values (symbols). Experimental data from [43].

### 3.2.3.6 U-Zr-O system

The solubility of Zr in irradiated  $\text{UO}_2$  fuel is not fully understood and experimental data are limited. Dumas [151] has tried to find a thermodynamic description of zirconium behavior based on experimental data from Schleifer et al. [47] relative to complex quaternary systems U-Zr-Re-O (with Re=La, Nd or Ce). The parameters for the Gibbs energies of formations identified by Dumas are summarized in Table 3.14.

Table 3.14: Species and parameters used to describe the U-Zr-O system [151].

Compound	Limit temperature [K]	$b$ [J/mol]	$c$ [J/mol/K]
$\text{ZrO}_2(ss)$	1407.98	-1096709	186.5
	2550	-1079458	174.2

Validation of the model proposed by Dumas against the experimental data from Schleifer et al. [47] is shown in Figure 3.26. The calculated values are far from the experimental measurements.

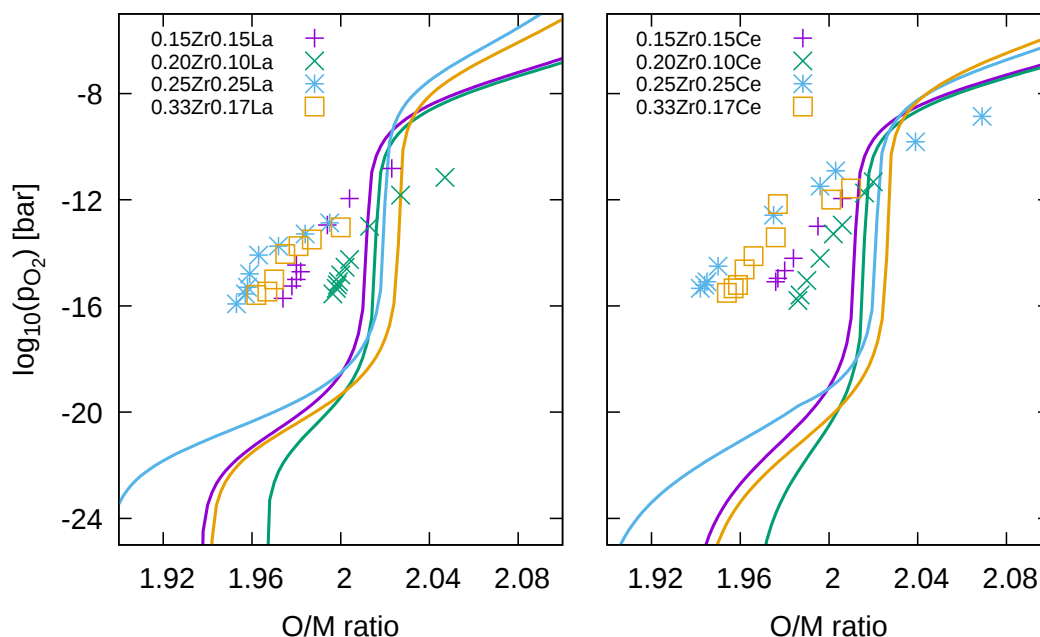


Figure 3.26: Calculated oxygen partial pressure in  $\text{U}_{1-y-z}\text{Zr}_y\text{Ln}_z\text{O}_{2\pm x}$  (lines) as a function of O/M and mole fractions of Zr and Ln (Ln=La, Ce) compared to measured values (symbols). Both experiments and calculations performed at 1250 K. Experimental data from [47].

Unsuccessful tries have been made to find a better representation based on the experimental work of Schleifer et al. and considering the three quaternary systems U-Zr-La-O,

U-Zr-Nd-O, U-Zr-Ce-O [47]. It has not been possible to find a model which led to a good agreement with both the ternary systems U-La-O, U-Gd-O and U-Ce-O and the quaternary systems of Schleifer et al. In spite of its shortcomings, the model proposed by Dumas has been kept in this work.

### 3.2.3.7 Chromium solubility model

Chromium is introduced during sintering to enhance grain growth of  $\text{UO}_2$  fuel. Cr presents a limited solubility which depends on temperature and oxygen partial pressure. A solubility model has been proposed by Riglet-Martial et al. [53] where the soluble compound is  $\text{CrO}_{3/2(ss)}$ . A complete description of the phase diagram of Cr in  $\text{UO}_2$  requires the consideration of the following pure condensed phases:  $\text{Cr}_{(s)}$ ,  $\text{Cr}_{(l)}$ ,  $\text{Cr}_2\text{O}_{3(s)}$  and  $\text{CrO}_{(l)}$ , that can appear depending on the conditions, as illustrated in Figure 3.27.

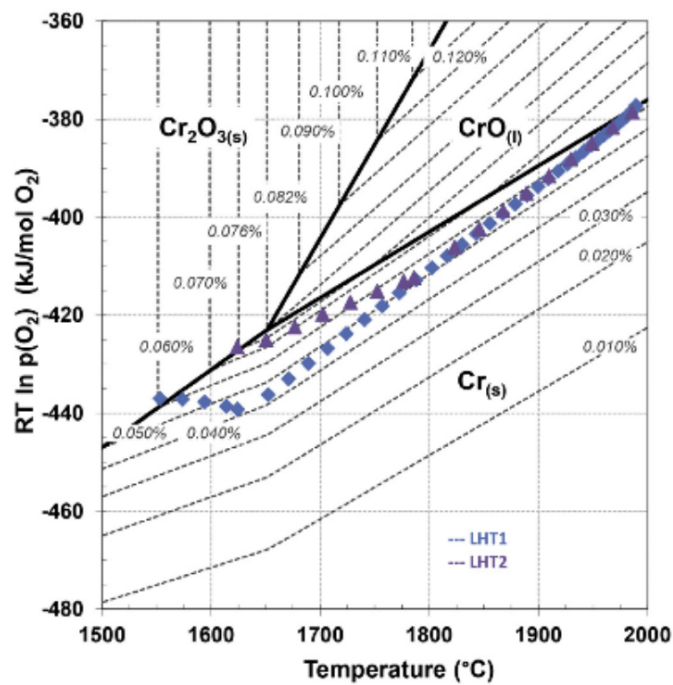


Figure 3.27: Phase stability diagram of chromium in  $\text{UO}_2$ . The dashed curves are the chromium iso-solubility curves. The labels in italics are the iso-solubility expressed in %wt Cr. The blue and purple points refer to the power ramps studied by Riglet-Martial [52].

The parameters for the Gibbs energies of formations of the U-Cr-O system identified by Riglet-Martial are given in Table 3.15. These are corrected values obtained after re-assessment of the experimental solubility data from reference [53]. Some values are thus slightly different than those from the original publication (see Table 2.3).

Table 3.15: Species and parameters for the Gibbs energy of formation used to describe the U-Cr-O system. Corrected parameters obtained after re-assessment of the data from [53].

Compound	Limit temperature [K]	$b$ [J/mol]	$c$ [J/mol/K]
$\text{CrO}_{3/2(ss)}$	3000	-469918	125.09
$\text{Cr}_{(s)}$	2130	0	0
$\text{Cr}_{(l)}$	2130	24340	-11.42
	3000	18410	-8.56
$\text{Cr}_2\text{O}_{3(s)}$	2000	-1092420	237.94
$\text{CrO}_{(l)}$	3000	-239925	15.76

Validation of ANGE calculations (lines) against experimental measurements (symbols) of Cr solubility is shown in Figure 3.28. The lines represent the maximum mole fraction of Cr in the fluorite solid solution under the given temperature and oxygen partial pressure conditions. The weight fraction of Cr used in the simulations is consistent with the introduction of 0.2 wt% of  $\text{Cr}_2\text{O}_{3(s)}$  during fabrication of the fuel.

The chromium solubility model has been validated only up to 1800 °C.

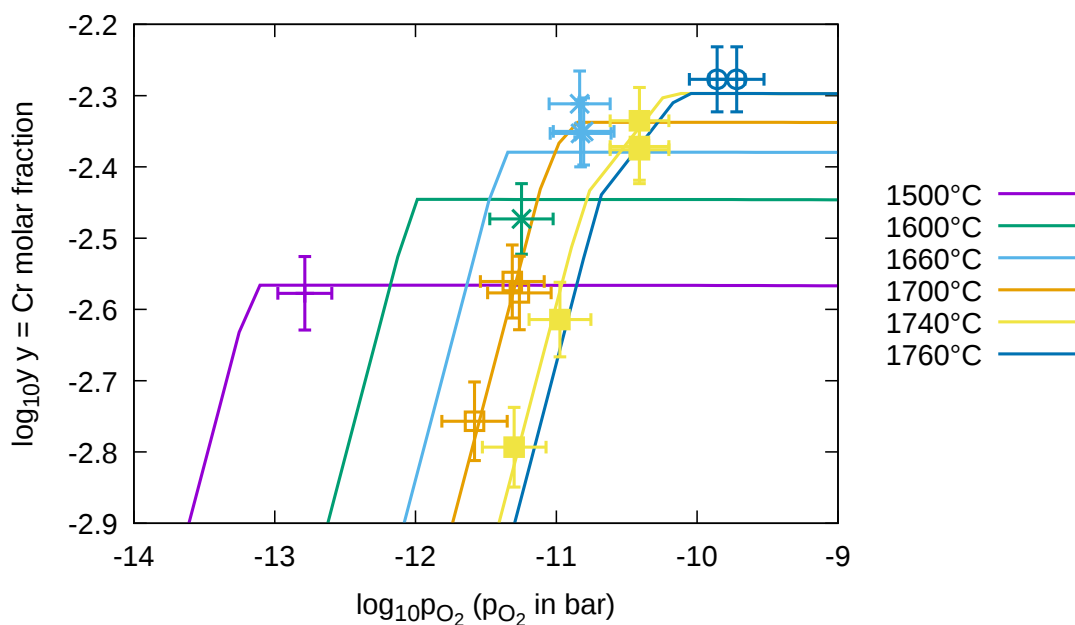


Figure 3.28: Calculated mole fraction of Cr in solid solution (lines) as a function of oxygen partial pressure at different temperatures compared to experimental measurements (symbols) from [53, 55, 180].

### 3.2.3.8 Validation on SIMFUELS

The overall validity of the solid solution model used in ANGE was checked by numerical modeling of laboratory experiments performed on simulated irradiated fuels (SIMFUEL). Une and Oguma [64] have prepared samples simulating irradiated fuel by adding oxides of Zr, Nd, Y, Ce and Pr to  $\text{UO}_2$ . Three samples were prepared to simulate irradiated fuels with burnups of 2, 5 and 10 at%. Compositions of the samples are shown in Table 3.16. Une and Oguma measured the oxygen potential at 1000 °C and 1300 °C by thermogravimetry. The consequences of FPs addition were clearly observed at 1300 °C leading to a significant increase of the oxygen potential in the hyperstoichiometric domain. Experimental measurements of Une and Oguma compared to ANGE calculations are shown in Figure 3.29. Pr, Nd and Y used by the authors are not explicitly considered in the database of ANGE. These elements are represented by Ce, Gd and La respectively.

Table 3.16: Compositions of the SIMFUEL samples. Adapted from Une and Oguma [64].

<b>Metal</b>	<b>2% at.</b>	<b>5% at.</b>	<b>10% at.</b>
U	98.21	95.52	91.01
Zr	0.74	1.86	3.73
Ce	0.25	0.62	1.24
Pr	0.12	0.30	0.60
Nd	0.58	1.46	2.93
Y	0.10	0.24	0.49

The comparison confirms that the solid solution model used in ANGE is able to reproduce the increase in oxygen potential with the burnup. The evolution of the oxygen potential in the hyperstoichiometric domain is well reproduced with ANGE. The predicted values near the exact stoichiometry are also close to the measurements at 1000 °C. Small differences in simulated/measured oxygen potentials are observed at 1300 °C (see the blue and orange curves) with a slightly faster decrease of the O/M ratio in the simulations.

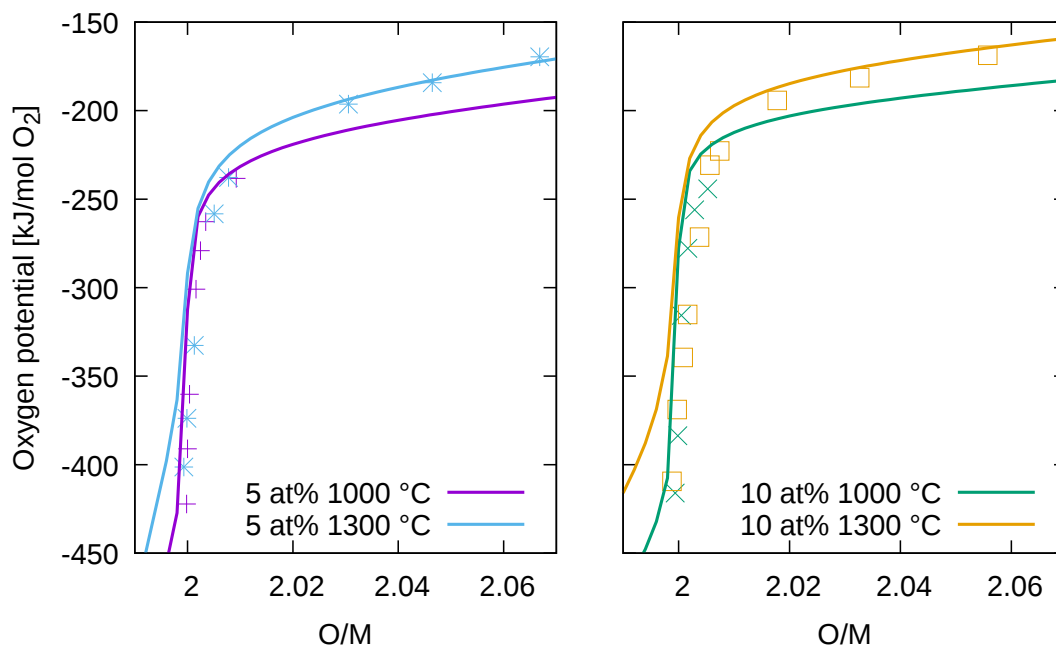


Figure 3.29: Oxygen potential of SIMFUELS at burnups of 5 at% (left figure) and 10 at% (right figure) measured by Une and Oguma [64] (symbols) compared to ANGE calculations (lines).

### 3.3 Thermochemical modeling of irradiated fuels

#### 3.3.1 General aspects

##### 3.3.1.1 Oxygen potential and stoichiometry deviation

Incorporation of FPs with various valencies into the initial  $\text{UO}_2$  matrix changes the O/M ratio (defined as  $\text{O}/[\text{U}+\text{FP}_{(ss)}]$ ) of the material. As described in the last section, trivalent rare earths, highly abundant FPs in irradiated fuel, can be incorporated in the lattice. Figure 3.30, adapted from Olander [181], illustrates the consequences of FPs incorporation in the uranium dioxide solid solution. The left figure shows the state before irradiation, the system contains only oxygen anions and uranium cations. The right figure shows the system with 2 trivalent FPs cations that replaced 2 uranium cations after fission. Electrical neutrality implies the creation of an anion vacancy in the fluorite structure. In consequence, the O/M ratio of the system decreases compared to its initial value.

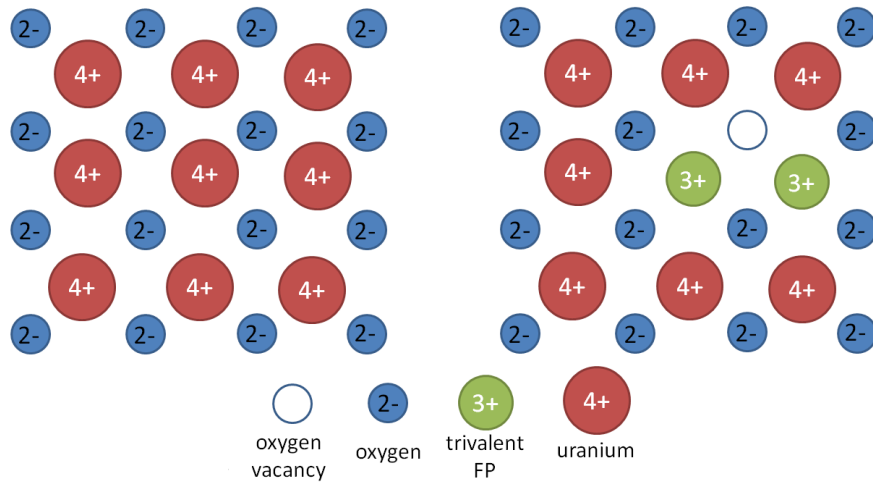


Figure 3.30: Schematic representation of  $\text{UO}_2$  lattice when a trivalent FP replaces a U atom after fission (adapted from Olander [181], chapter 12, Figure 12.8). Left figure: perfect  $\text{UO}_2$  lattice. Right figure: irradiated fuel.

Thermochemical calculations of irradiated fuels performed by several authors have shown that the oxygen potential versus O/M ratio curves significantly differ from that of non-irradiated fuels because of the numerous FPs in the material [72, 112]. In Figure 3.31, the oxygen potentials calculated at different temperatures with ANGE are plotted in function of the O/M ratio of the fluorite solid solution for non irradiated and irradiated  $\text{UO}_2$  fuels up to different burnups (20, 40, 60 GWd/tHM), typical of PWR irradiation sequences. The elemental compositions, shown in Table 3.17, were calculated with PRODHEL, considering a  $\text{UO}_2$  fuel pellet of radius 4.1 mm and an initial enrichment of 3.5%. The linear heat rate was assumed to be constant and equal to 200 W/cm.

Table 3.17: Elemental compositions of irradiated fuels used in ANGE calculations.

Element	Concentration (mol/mol UO <sub>2</sub> ) at burnup of		
	20 GWd/tHM	40 GWd/tHM	60 GWd/tHM
He	$6.56 \times 10^{-3}$	$1.15 \times 10^{-2}$	$1.97 \times 10^{-2}$
Cs	$3.75 \times 10^{-3}$	$6.56 \times 10^{-3}$	$1.12 \times 10^{-2}$
I	$2.80 \times 10^{-4}$	$4.68 \times 10^{-4}$	$8.02 \times 10^{-4}$
Te	$6.89 \times 10^{-4}$	$1.20 \times 10^{-3}$	$2.06 \times 10^{-3}$
Ba	$3.31 \times 10^{-3}$	$5.80 \times 10^{-3}$	$9.93 \times 10^{-3}$
Zr	$6.18 \times 10^{-3}$	$1.08 \times 10^{-2}$	$1.85 \times 10^{-2}$
Mo	$5.30 \times 10^{-3}$	$9.27 \times 10^{-3}$	$1.60 \times 10^{-2}$
Ru	$5.01 \times 10^{-3}$	$8.76 \times 10^{-3}$	$1.50 \times 10^{-2}$
Pd	$1.44 \times 10^{-3}$	$2.52 \times 10^{-3}$	$4.32 \times 10^{-3}$
Ce	$2.64 \times 10^{-3}$	$4.61 \times 10^{-3}$	$7.91 \times 10^{-3}$
Eu	$8.69 \times 10^{-4}$	$1.52 \times 10^{-3}$	$2.61 \times 10^{-3}$
La	$2.21 \times 10^{-3}$	$3.87 \times 10^{-3}$	$6.63 \times 10^{-3}$
Gd	$4.50 \times 10^{-3}$	$7.88 \times 10^{-3}$	$1.35 \times 10^{-2}$
Pu	$6.52 \times 10^{-3}$	$1.14 \times 10^{-2}$	$1.96 \times 10^{-2}$
U	$9.73 \times 10^{-1}$	$9.53 \times 10^{-1}$	$9.18 \times 10^{-1}$

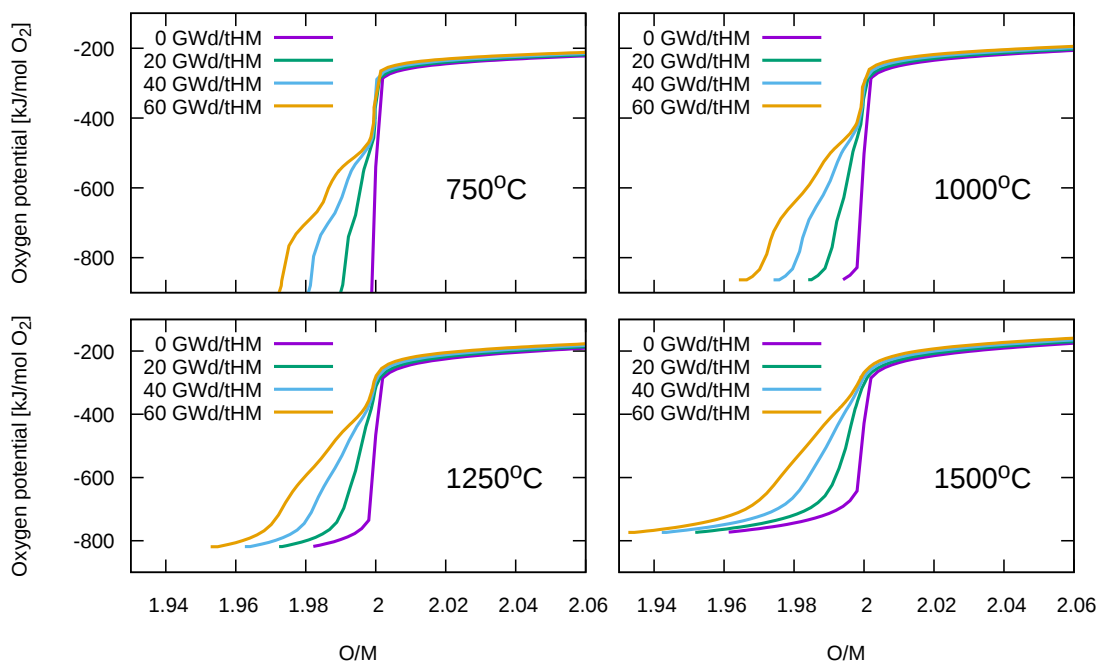


Figure 3.31: Oxygen potential at different burnups and temperatures. Elemental compositions used in calculations are given in Table 3.17.

One may observe that the curve for non irradiated fuel shown in Figure 3.31 presents

a strong increase of the oxygen potential in the vicinity of the exact stoichiometry. In irradiated fuel, the oxygen potential increase is not as marked and the transition seems to be shifted towards lower values of the O/M ratio when the fuel burnup increases. With increasing burnup, the oxygen potential of the fuel increases while its O/M ratio decreases. This is due to i) the increase in solid solution of fission products of valence  $< +4$  (trivalent rare earth mainly) which contributes to decrease the O/M ratio, ii) the consecutive liberation of oxygen in excess which contributes to enhance the  $O_2$  partial pressure (i.e. the oxygen potential). Temperature is a factor having a strong impact on the oxygen potential - O/M ratio curves. In Figure 3.31, one may see that the oxygen potential transition between hypo and hyperstoichiometry is shifted towards lower values of the O/M ratio with increasing temperature. It is a consequence of the solubility of FPs which increases with temperature.

The complexity of irradiated fuel is also associated with the presence of numerous redox systems likely to affect the oxygen potential. Redox pairs work as oxido-reduction buffers. At a constant temperature, the oxidizing or reducing components of a redox pair may keep a constant oxygen potential in spite of adding or removing oxygen from the system. The effect of redox systems on the oxygen potential can be seen in Figure 3.32 as "steps" where the oxygen potential increases softly. Calculated oxygen potentials are this time expressed as a function of the total oxygen content of the fuel.

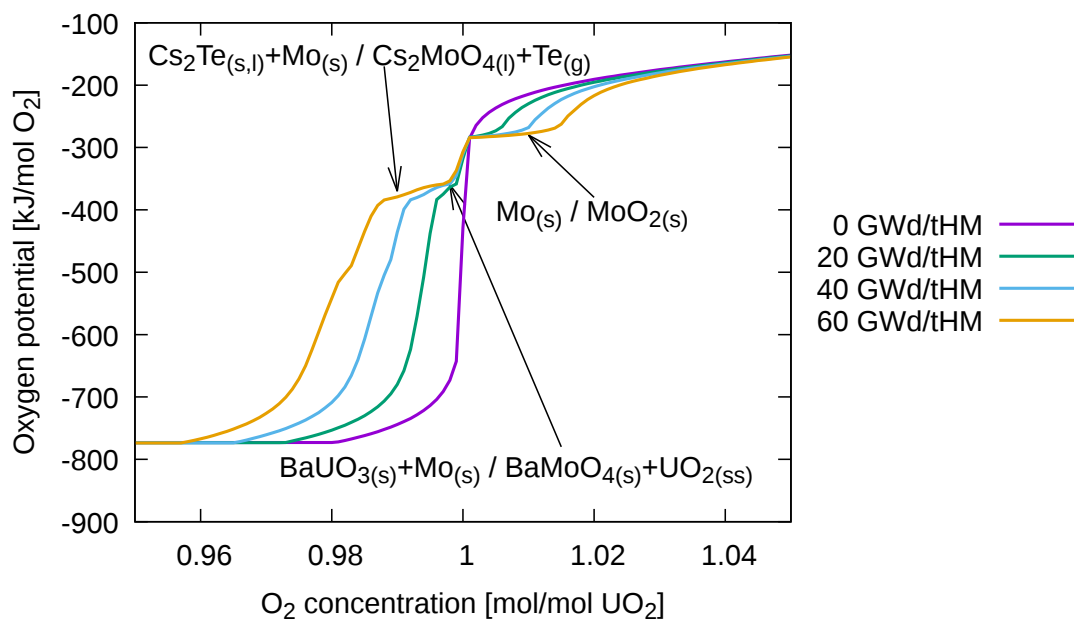
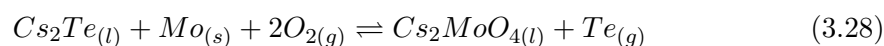


Figure 3.32: The oxygen potential at 1500 °C at different burnups as a function of the total oxygen concentration. Elemental compositions used in calculations are given in Table 3.17.

A redox pair that is of great importance in  $\text{UO}_2$  fuels at oxygen content  $> 1$  mol  $\text{O}_2$ /mol  $\text{UO}_2$ , is that of molybdenum defined by the following reaction:



As long as the reductant  $\text{Mo}_{(s)}$  and the oxidant  $\text{MoO}_{2(s)}$  are simultaneously present in the system, the  $\text{O}_2$  partial pressure (or oxygen potential) at a given temperature remains stabilized, even though the total amount of oxygen varies, see Figure 3.32. Two other significant redox systems are shown in Figure 3.32. They are described by the reactions 3.27–3.28 below.



### 3.3.1.2 Gas phase

As shown in the last subsection, a variation of the oxygen potential of the fuel can be expected with burnup. The oxygen potential of the fuel has a strong impact on the speciation of all phases, and the gas phase in particular. Figure 3.33 shows the calculated concentrations of the gaseous compounds of importance for I-SCC that are likely to form in an initially stoichiometric  $\text{UO}_2$  fuel irradiated up to burnups of 20, 40 and 60 GWd/tHM and heated at 2000 °C, a typical temperature occurring at the pellet center during power ramps. At high oxygen potentials, the gas phase contains a significant quantity of  $\text{CsI}_{(g)}$ ,  $\text{I}_{(g)}$  and  $\text{Te}_{2(g)}$ . As the oxygen potential is lowered,  $\text{I}_{(g)}$  disappears from the gas phase while  $\text{Cs}_{(g)}$  is formed in great quantity. The curves at different burnups show a similar behavior, the main difference is the range of values that increases with burnup.

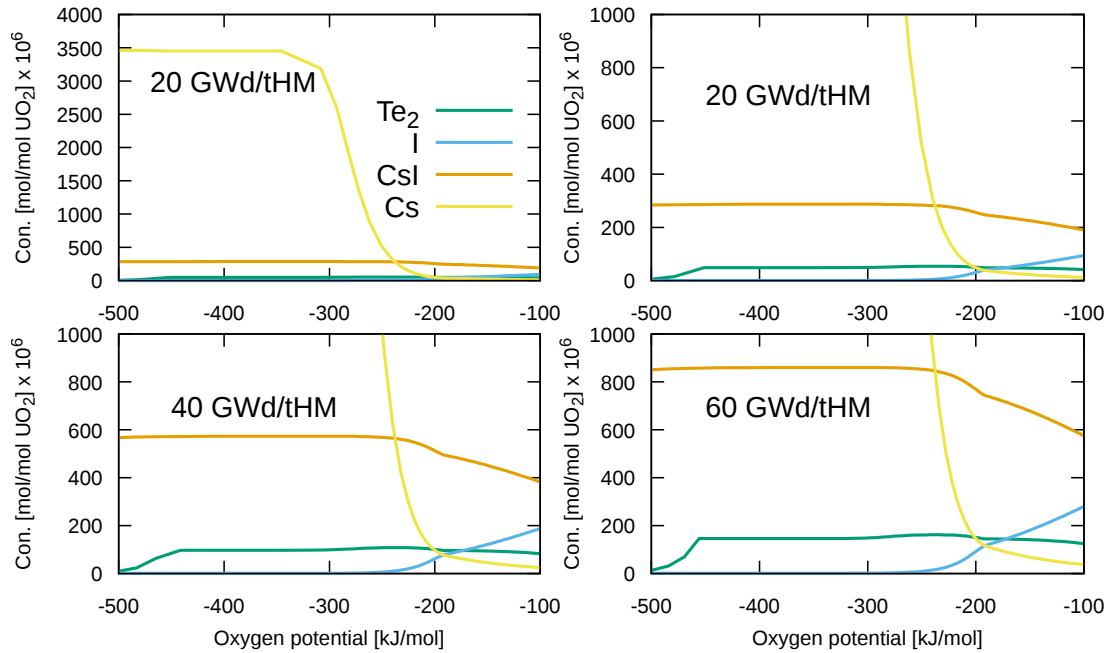


Figure 3.33: Concentrations of volatile species important in SCC as a function of oxygen potential at 2000 °C. Fuels irradiated to 20, 40 and 60 GWd/tHM. Elemental compositions used in the calculations are given in Table 3.17.

### 3.3.2 Oxygen potential measurements in irradiated fuel

In this section, several experiments on irradiated fuels have been simulated with ANGE to assess the capacity of the thermodynamic database to catch the evolution of the oxygen potential with irradiation.

#### 3.3.2.1 Irradiated BWR fuels

Une et al. have measured the oxygen potential in two types of irradiated BWR fuel [65]: a standard  $\text{UO}_2$  irradiated up to burnups of 18 and 30 GWd/tHM, a 2wt%  $\text{Gd}_2\text{O}_3$ -doped  $\text{UO}_2$  fuel irradiated up to burnups of 13 and 27 GWd/tHM. The authors have made measurements at different positions along the fuel pellet radii. It has not been possible to simulate this experiment properly using ALCYONE and PRODHHEL since they are not designed to model BWR fuels behavior. Therefore it has been assumed that the samples at different radial positions have the same burnup and thus the same elemental composition. Two of the samples may come from the rim region but their radial positions have high uncertainties and for the needs of this work it is assumed that they have the same burnup as the other samples. Since the authors did not give any irradiation history details, it has been assumed that the studied fuels have been irradiated at a constant LHR of 200 W/cm and that the initial enrichment is close to

3.5%. The elemental compositions calculated with PRODHEL under these assumptions and used to study Une's experiments are given in Table 3.18.

Table 3.18: Elemental compositions used in ANGE calculations for modeling Une's experiment.

Element	Concentration (mol/mol UO <sub>2</sub> ) at burnup of			
	18 GWd/tHM	30 GWd/tHM	13 GWd/tHM +2wt%Gd <sub>2</sub> O <sub>3</sub>	27 GWd/tHM +2wt%Gd <sub>2</sub> O <sub>3</sub>
He	$6.27 \times 10^{-3}$	$1.14 \times 10^{-2}$	$4.41 \times 10^{-3}$	$1.006 \times 10^{-2}$
Cs	$3.51 \times 10^{-3}$	$6.17 \times 10^{-3}$	$2.48 \times 10^{-3}$	$5.47 \times 10^{-3}$
Te	$5.10 \times 10^{-4}$	$9.84 \times 10^{-4}$	$3.47 \times 10^{-4}$	$8.53 \times 10^{-4}$
I	$2.53 \times 10^{-4}$	$4.90 \times 10^{-4}$	$1.71 \times 10^{-4}$	$4.25 \times 10^{-4}$
Mo	$4.86 \times 10^{-3}$	$8.69 \times 10^{-3}$	$3.43 \times 10^{-2}$	$7.68 \times 10^{-3}$
Ba	$2.93 \times 10^{-3}$	$5.11 \times 10^{-3}$	$2.10 \times 10^{-3}$	$4.53 \times 10^{-3}$
Zr	$5.62 \times 10^{-3}$	$9.59 \times 10^{-3}$	$4.06 \times 10^{-2}$	$8.57 \times 10^{-3}$
Ce	$3.78 \times 10^{-3}$	$6.58 \times 10^{-3}$	$2.71 \times 10^{-3}$	$5.85 \times 10^{-3}$
La	$2.04 \times 10^{-3}$	$3.52 \times 10^{-3}$	$1.46 \times 10^{-3}$	$3.13 \times 10^{-3}$
Gd	$4.01 \times 10^{-3}$	$7.23 \times 10^{-3}$	$3.29 \times 10^{-2}$	$3.61 \times 10^{-2}$
Eu	$7.13 \times 10^{-4}$	$1.44 \times 10^{-3}$	$4.69 \times 10^{-4}$	$1.24 \times 10^{-3}$
Ru	$4.83 \times 10^{-3}$	$8.99 \times 10^{-3}$	$3.34 \times 10^{-3}$	$7.87 \times 10^{-3}$
Pd	$1.23 \times 10^{-3}$	$3.27 \times 10^{-2}$	$7.02 \times 10^{-4}$	$2.64 \times 10^{-3}$
Pu	$6.95 \times 10^{-3}$	$9.63 \times 10^{-3}$	$5.53 \times 10^{-3}$	$9.03 \times 10^{-3}$
U	$9.73 \times 10^{-1}$	$9.53 \times 10^{-1}$	$9.80 \times 10^{-1}$	$9.58 \times 10^{-1}$

Une et al. reported that the initial O/M ratios of the samples have not been precisely measured but their values were close to 2.000. To analyze the impact of the uncertainty on the initial O/U ratio of the fuel, the UO<sub>2</sub> samples have been simulated with  $\pm 0.0025$  mol O<sub>2</sub>/mol UO<sub>2</sub>, to which corresponds initial O/U ratios ranging from 1.995 to 2.005. In the case of Gd-doped fuel, the 2 wt% addition of Gd<sub>2</sub>O<sub>3</sub> lowers the initial O/M ratio to around 1.985. Then, a variation of  $\pm 0.0025$  mol O<sub>2</sub>/mol UO<sub>2</sub> was used to estimate the uncertainty of the initial O/M ratio (between 1.98 and 1.99).

Simulated oxygen potentials at different radial positions are compared to experimental measurements and shown in Figures 3.34 and 3.35. Upper and lower values of calculated oxygen potentials correspond to higher/lower oxygen contents and are shown with error bars. Additionally, both figures include for comparison a horizontal dashed line which corresponds to the redox system Mo<sub>(s)</sub>/MoO<sub>2(s)</sub>.

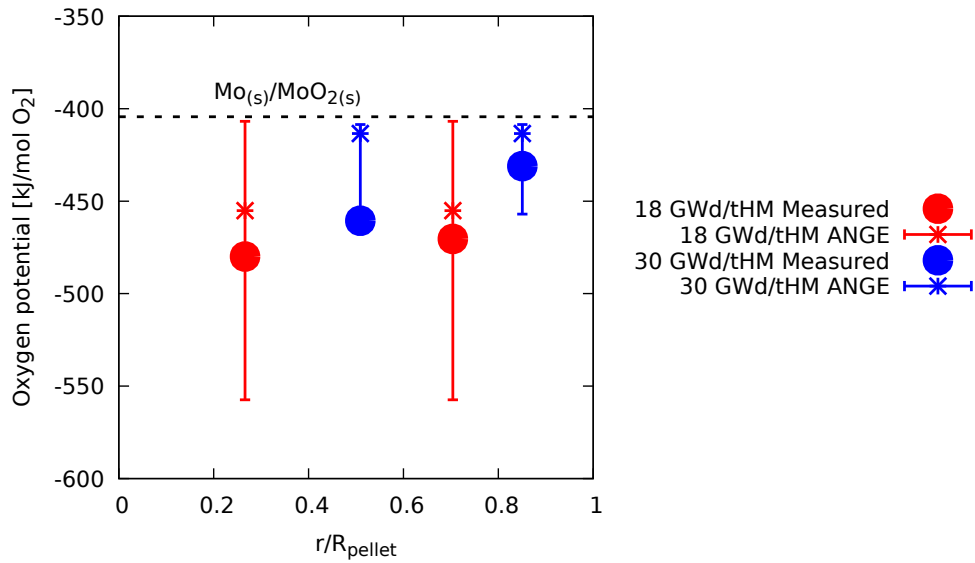


Figure 3.34: Oxygen potential calculated with ANGE compared to values measured by Une et al. [65] at different radial positions at 750 °C. Standard  $\text{UO}_2$  fuel. The horizontal dashed line corresponds to the  $\text{Mo}/\text{MoO}_2$  redox system.

Comparison of ANGE calculations to experimental measurements performed on irradiated  $\text{UO}_2$  fuels leads to a good agreement. All the calculated values are within 50 kJ/mol  $\text{O}_2$  from experimental measurements, the later are within the error bars.

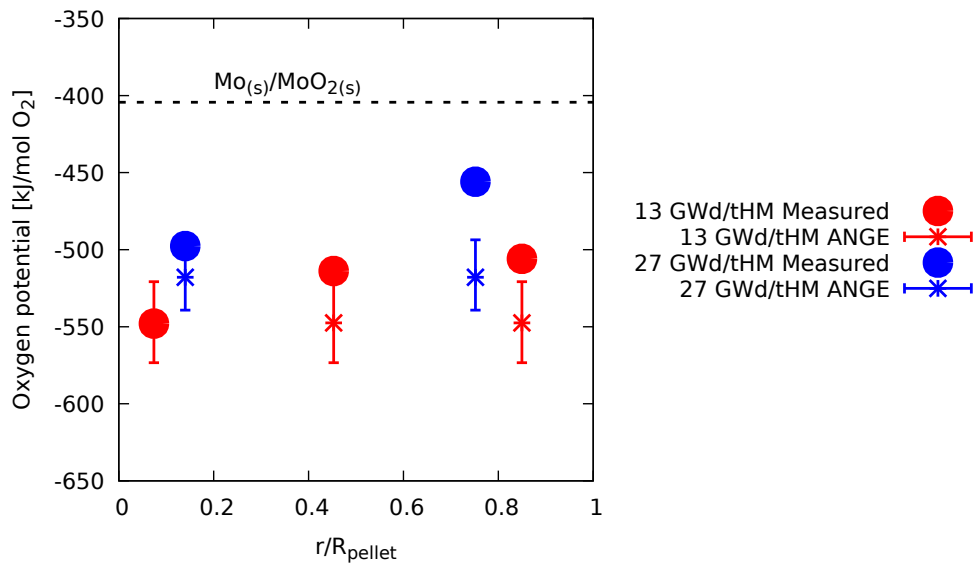


Figure 3.35: Oxygen potential calculated with ANGE compared to values measured by Une et al. [65] at different radial positions at 750 °C. 2wt% $\text{Gd}_2\text{O}_3$ -doped fuel. The horizontal dashed line corresponds to the  $\text{Mo}/\text{MoO}_2$  redox system.

Simulation of the  $\text{Gd}_2\text{O}_3$ -doped fuel shows that ANGE calculations underestimate oxygen potential for every sample, as shown in Figure 3.35. The oxygen potentials calculated for the three samples at the pellet center ( $r/R_{\text{pellet}} < 0.5$ ) are quite close to the experimental measurements with a difference of less than 50 kJ/mol  $\text{O}_2$ . The predicted oxygen potential of the 27 GWd/tHM sample at  $r/R_{\text{pellet}} = 0.8$  is however underestimated by around 50 kJ/mol  $\text{O}_2$  while the 13 GWd/tHM sample, which is the closest to the periphery, is underestimated by around 10 kJ/mol  $\text{O}_2$ .

One may notice that the measured oxygen potential increases with radius despite very similar burnup. Une et al. suggest that such radial profiles of oxygen potential could be caused by thermal diffusion of oxygen from the pellet center towards the periphery. It is also visible that oxygen potential increases with burnup. This behavior is correctly predicted by ANGE calculations.

### 3.3.2.2 Irradiated PWR fuels

Next simulations concern two experiments carried out by Matzke. In the first one, the author has measured the oxygen potential of LWR samples irradiated up to different burnups [67]. In the second one, Matzke has studied samples irradiated in the Danish Heavy Water Reactor (HWR) in Risø up to a very high burnup. As in the case of Une's experiments, Matzke does not give the data necessary to model the entire irradiation history of the studied fuels. The author gives only the initial enrichment and the average burnup of the investigated samples. These values are shown in Table 3.19. Samples 1, 2 and 3 were irradiated in the LWR and samples 4a and 4b in the Risø reactor.

Table 3.19: Details of the fuel samples studied by Matzke. Adapted from [67].

Sample	Initial enrichment [%]	Burnup [GWd/tHM]	Radius [mm]
LWR			
1	6.85	28.9	not reported
2	5.0	34.5	not reported
3	8.25	58	not reported
Risø			
4a	1.46	75	6.35
4b	1.46	up to 200	6.35
RIM zone of 4a			

The fuels 1-3 were fabricated with a high  $^{235}\text{U}$  enrichment and their final burnup is mostly related to the fission of this isotope. The fuel 4 had a lower enrichment but it reached a much higher burnup. Such high burnup is a consequence of  $^{239}\text{Pu}$  thermal fissions. Burnups reached by fission of different isotopes result in different elemental

compositions. Initial enrichment of the samples has been taken into account in PRODHEL calculations. Matzke has not detailed the fuel characteristics nor the irradiation histories. It has been assumed in PRODHEL calculations that the radius of the samples 1-3 is 4 mm and the LHR is 200 W/cm. These values are standard for LWRs. For the samples irradiated in the Risø reactor, the same LHR has been used but with a pellet radius of 6.35 mm, as reported by Matzke. The elemental compositions obtained from PRODHEL and used for the thermochemical analyses are those corresponding to the average burnups of samples. They are summarized in Table 3.20.

Table 3.20: Elemental compositions (in mol/mol  $\text{UO}_2$ ) used in ANGE calculations for modeling Matzke's experiments [66, 67].

Element	Number of the sample				
	1	2	3	4a	4b
He	$1.12 \times 10^{-2}$	$1.42 \times 10^{-2}$	$3.22 \times 10^{-2}$	$2.71 \times 10^{-2}$	$8.14 \times 10^{-2}$
Cs	$6.86 \times 10^{-3}$	$8.09 \times 10^{-3}$	$1.72 \times 10^{-2}$	$1.21 \times 10^{-2}$	$2.82 \times 10^{-2}$
Te	$8.98 \times 10^{-4}$	$1.21 \times 10^{-3}$	$2.86 \times 10^{-3}$	$2.69 \times 10^{-3}$	$8.29 \times 10^{-3}$
I	$4.37 \times 10^{-4}$	$5.94 \times 10^{-4}$	$1.33 \times 10^{-3}$	$1.28 \times 10^{-3}$	$2.81 \times 10^{-3}$
Mo	$9.07 \times 10^{-3}$	$1.11 \times 10^{-2}$	$2.54 \times 10^{-2}$	$1.89 \times 10^{-2}$	$5.41 \times 10^{-2}$
Ba	$5.72 \times 10^{-3}$	$6.80 \times 10^{-3}$	$1.68 \times 10^{-2}$	$1.02 \times 10^{-2}$	$3.45 \times 10^{-2}$
Zr	$1.09 \times 10^{-2}$	$1.27 \times 10^{-2}$	$2.89 \times 10^{-2}$	$1.73 \times 10^{-2}$	$4.77 \times 10^{-2}$
Ce	$6.88 \times 10^{-3}$	$8.33 \times 10^{-3}$	$1.85 \times 10^{-2}$	$1.40 \times 10^{-2}$	$3.92 \times 10^{-2}$
La	$3.89 \times 10^{-3}$	$4.60 \times 10^{-3}$	$1.02 \times 10^{-2}$	$6.71 \times 10^{-3}$	$1.74 \times 10^{-2}$
Gd	$7.66 \times 10^{-3}$	$9.40 \times 10^{-3}$	$2.21 \times 10^{-2}$	$1.65 \times 10^{-2}$	$5.23 \times 10^{-2}$
Eu	$1.35 \times 10^{-3}$	$1.83 \times 10^{-3}$	$4.17 \times 10^{-3}$	$3.27 \times 10^{-3}$	$6.75 \times 10^{-3}$
Ru	$8.33 \times 10^{-3}$	$1.09 \times 10^{-2}$	$2.38 \times 10^{-2}$	$2.22 \times 10^{-2}$	$6.12 \times 10^{-2}$
Pd	$1.88 \times 10^{-3}$	$3.76 \times 10^{-3}$	$1.14 \times 10^{-2}$	$1.54 \times 10^{-2}$	$5.22 \times 10^{-2}$
Pu	$7.48 \times 10^{-3}$	$9.92 \times 10^{-3}$	$1.53 \times 10^{-2}$	$1.47 \times 10^{-2}$	$1.46 \times 10^{-2}$
U	$9.55 \times 10^{-1}$	$9.43 \times 10^{-1}$	$8.76 \times 10^{-1}$	$8.99 \times 10^{-1}$	$7.23 \times 10^{-1}$

To account for the possible uncertainty on the initial O/U ratio of the samples, the oxygen concentration used in the simulations has been assumed to vary from 0.9975 to 1.0025 mol  $\text{O}_2$ /mol  $\text{UO}_2$ . To this range corresponds an initial stoichiometry range of 1.995-2.005. The calculations have been performed at temperatures ranging from 800 to 1400 K. The simulation results are compared to experimental data in Figures 3.36-3.40. The results corresponding to the samples with initial O/U ratios of 1.995, 2.000 and 2.005 are represented by dotted, solid and dashed lines, respectively. Additionally, each figure includes for comparison a red curve which gives the oxygen potential prescribed by the  $\text{Mo}_{(s)}/\text{MoO}_{2(s)}$  redox buffer.

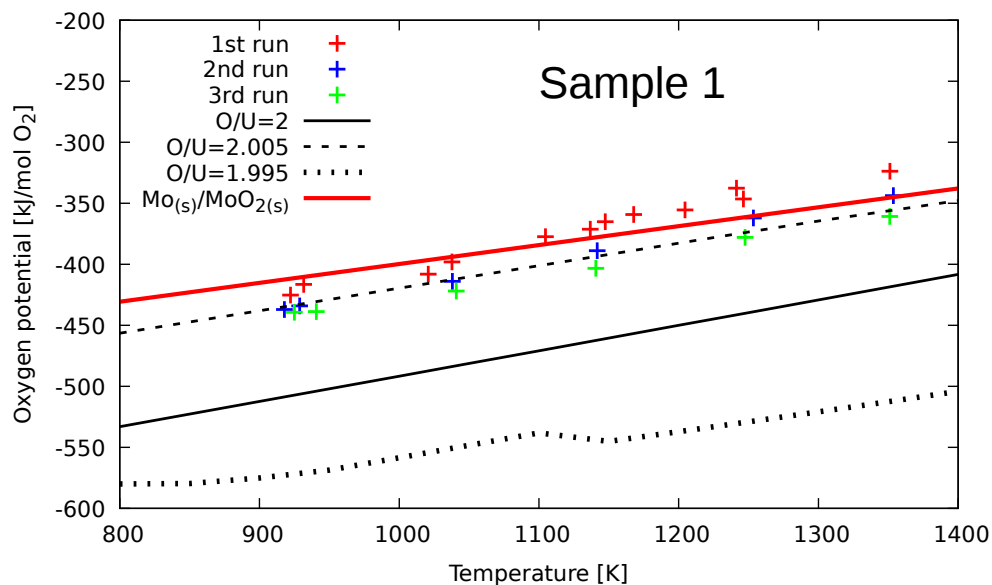


Figure 3.36: Calculated oxygen potential compared to experimental measurements from Matzke [67]. Burnup 28.9 GWd/tHM. O/U refers to the initial composition.

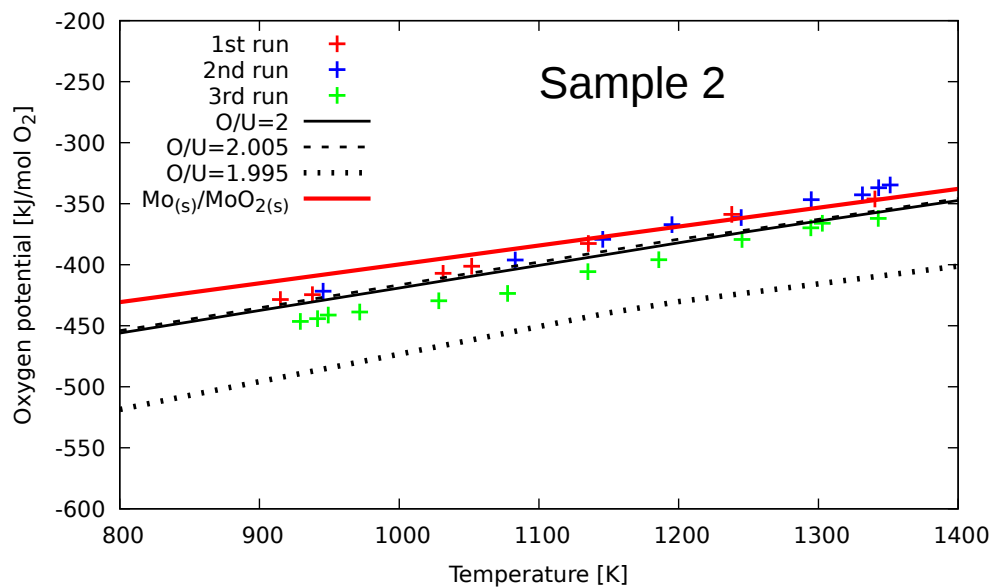


Figure 3.37: Calculated oxygen potential compared to experimental measurements from Matzke [67]. Burnup 34.5 GWd/tHM. O/U refers to the initial composition.

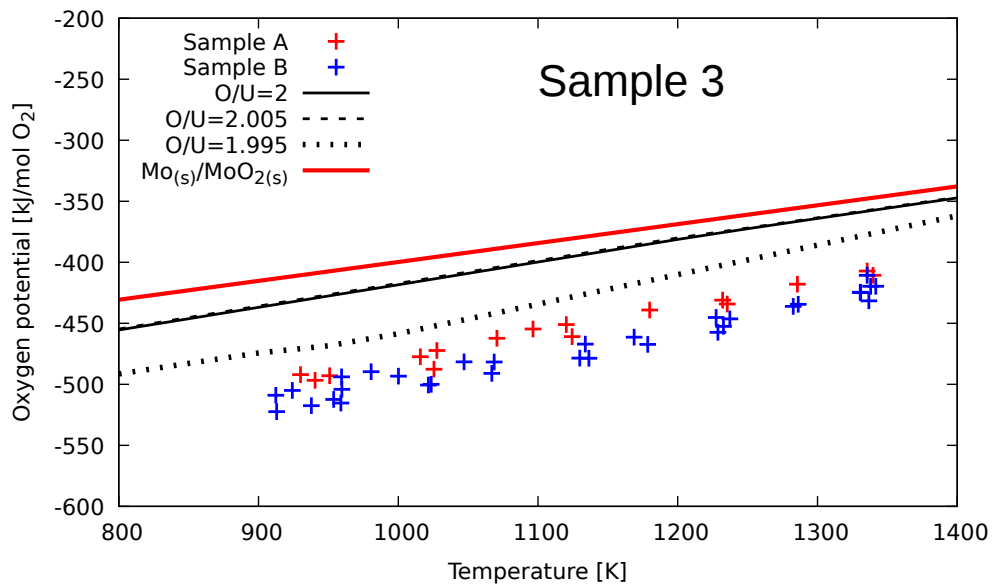


Figure 3.38: Calculated oxygen potential compared to experimental measurements from Matzke [67]. Burnup 58 GWd/tHM. O/U refers to the initial composition.

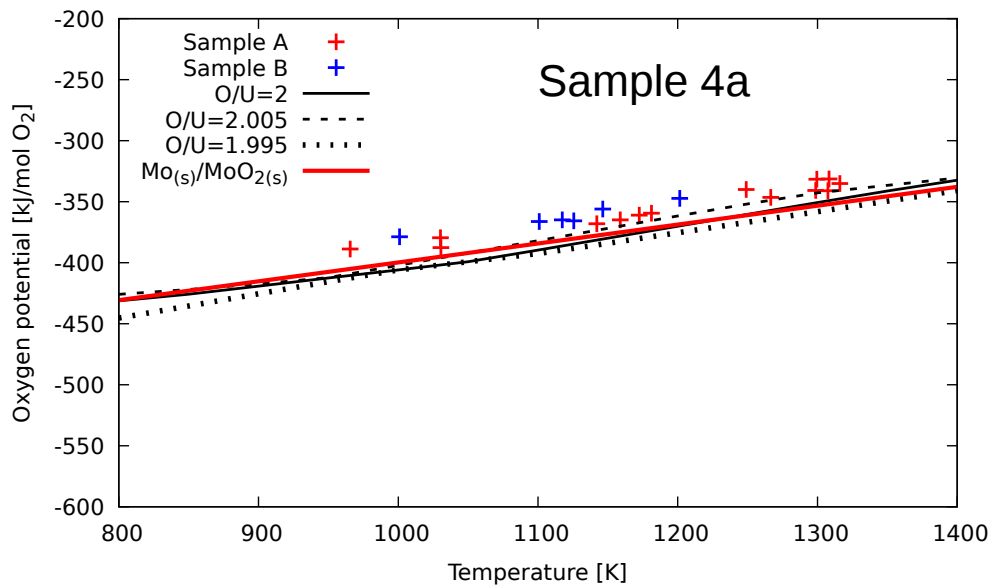


Figure 3.39: Calculated oxygen potential compared to experimental measurements from Matzke [66]. Burnup 75 GWd/tHM. O/U refers to the initial composition.

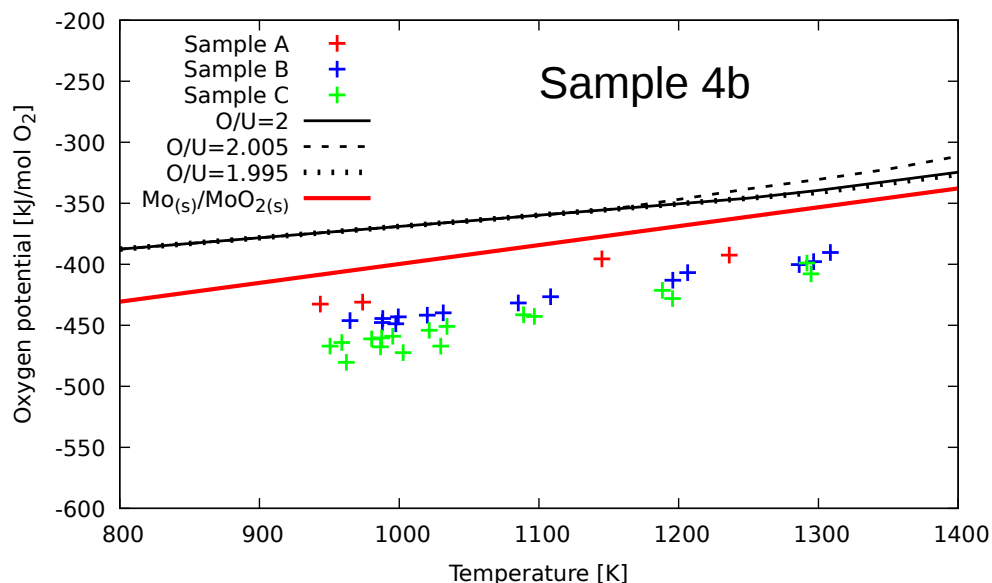


Figure 3.40: Calculated oxygen potential compared to experimental measurements from Matzke [66]. Burnup 200 GWd/tHM. O/U refers to the initial composition.

Experimental measurements of the oxygen potential in the samples of burnups 28.9, 34.5 and 75 GWd/tHM are close to ANGE simulation results and generally consistent with the oxygen potential given by the Mo redox buffer. The oxygen potentials measured in the samples of burnup 58 GWd/tHM are visibly overestimated by ANGE but within acceptable error (50 kJ/mol O<sub>2</sub>) when the fuel is assumed to have an initial O/U ratio of 1.995. This shows that the uncertainty on the initial oxygen content can lead to significant differences on the oxygen potential of the irradiated fuel. The largest difference between calculated and measured oxygen potentials is obtained on the high burnup samples (4b), see Figure 3.40. Matzke reported that a burnup gradient was likely to exist in the samples taken from the rim of the fuel pellet and that the specified burnup of 200 GWd/tHM might not be realistic. To investigate the impact of burnup on the calculated oxygen potential, an additional set of calculations with PRODHEL and ANGE were performed. The elemental compositions used are in Table 3.21 and the calculated oxygen potentials of the high burnup samples (75-100-125-150-175-200 GWd/tHM) are plotted in Figure 3.41. The initial O/U ratio was assumed equal to 2.

Table 3.21: Elemental compositions used in ANGE calculations for modeling Matzke's experiments [66].

Element	Concentration (mol/mol UO <sub>2</sub> ) at burnup of			
	100 GWd/tHM	125 GWd/tHM	150 GWd/tHM	175 GWd/tHM
He	$3.61 \times 10^{-2}$	$4.61 \times 10^{-2}$	$5.69 \times 10^{-2}$	$6.84 \times 10^{-2}$
Cs	$1.54 \times 10^{-2}$	$1.82 \times 10^{-2}$	$2.09 \times 10^{-2}$	$2.33 \times 10^{-2}$
Te	$3.69 \times 10^{-3}$	$4.72 \times 10^{-3}$	$5.82 \times 10^{-3}$	$7.00 \times 10^{-3}$
I	$1.65 \times 10^{-3}$	$1.99 \times 10^{-3}$	$2.30 \times 10^{-3}$	$2.58 \times 10^{-3}$
Mo	$2.53 \times 10^{-2}$	$3.18 \times 10^{-2}$	$3.87 \times 10^{-2}$	$4.60 \times 10^{-2}$
Ba	$1.52 \times 10^{-2}$	$2.00 \times 10^{-2}$	$2.55 \times 10^{-2}$	$3.17 \times 10^{-2}$
Zr	$2.29 \times 10^{-2}$	$2.86 \times 10^{-2}$	$3.47 \times 10^{-2}$	$4.12 \times 10^{-2}$
Ce	$1.83 \times 10^{-2}$	$2.29 \times 10^{-2}$	$2.79 \times 10^{-2}$	$3.32 \times 10^{-2}$
La	$8.75 \times 10^{-3}$	$1.08 \times 10^{-2}$	$1.29 \times 10^{-2}$	$1.51 \times 10^{-2}$
Gd	$2.27 \times 10^{-2}$	$2.91 \times 10^{-2}$	$3.61 \times 10^{-2}$	$4.36 \times 10^{-2}$
Eu	$4.21 \times 10^{-3}$	$5.00 \times 10^{-3}$	$5.74 \times 10^{-3}$	$6.46 \times 10^{-3}$
Ru	$2.88 \times 10^{-2}$	$3.60 \times 10^{-2}$	$4.37 \times 10^{-2}$	$5.17 \times 10^{-2}$
Pd	$2.25 \times 10^{-2}$	$2.95 \times 10^{-2}$	$3.67 \times 10^{-2}$	$4.43 \times 10^{-2}$
Pu	$1.58 \times 10^{-2}$	$1.61 \times 10^{-2}$	$1.59 \times 10^{-2}$	$1.53 \times 10^{-2}$
U	$8.68 \times 10^{-1}$	$8.36 \times 10^{-1}$	$8.01 \times 10^{-1}$	$7.65 \times 10^{-1}$

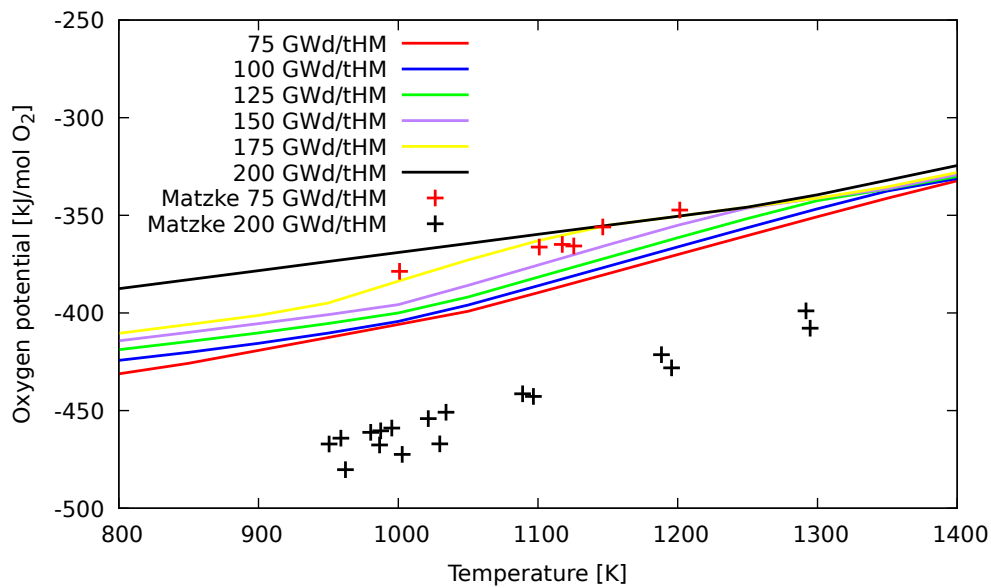


Figure 3.41: Calculated oxygen potential compared to experimental measurements from the high burnup samples studied by Matzke. [66].

As can be seen, the oxygen potentials calculated for the 75 GWd/tHM fuel are the closest to the experimental measures of Matzke. However, the simulations still underestimate

the oxygen potential by more than 50 kJ/mol O<sub>2</sub>. Figure 3.42 shows all the experimental measures of Matzke together [66, 67].

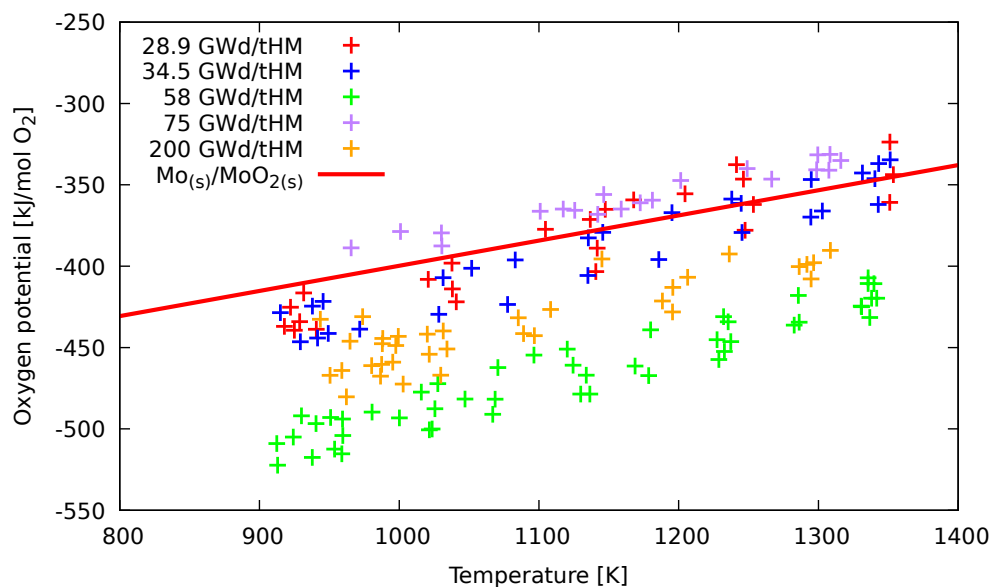


Figure 3.42: All the experimental data from Figures 3.36-3.40 [66, 67].

One may notice that no clear trend with burnup increase can be derived from the presented data. Considering the LWR samples with a burnup between 28.9 and 58 GWd/tHM and the HWR high burnup samples separately, Matzke concluded that the oxygen potential decreases when the fuel burnup increases. An opposite conclusion was proposed by Ue et al. [65] from his measurements on BWR fuels. As shown by Figure 3.41, ANGE calculations lead to an increasing oxygen potential with the fuel burnup, particularly at temperatures below 1200 K.

### 3.3.2.3 High burnup irradiated PWR fuel

The last simulated experiment is the one carried out by Walker et al. [7] and already used to assess PRODHHEL calculations in Section 3.1.4. The authors have measured the oxygen potential in a very high burnup fuel sample at four radial positions. The data necessary to perform a detailed simulation of the experiment, i.e., the pellet characteristics and the irradiation history, are given in Tables 3.6 and 3.7.

ALCYONE simulations of Walker's fuel were performed in two parts. In the first one, the nominal (base) irradiation in the commercial reactor has been simulated. The FPs inventory obtained at the end of this sequence from PRODHHEL is detailed in Section 3.1.1. In the second part, thermodynamic equilibrium calculations with ANGE at different temperatures were carried out to obtain estimates of the oxygen potential along

the fuel radius that have then been compared to the measurements of Walker et al. The authors did not give the cooling time between the end of the base irradiation and the oxygen potential measurements. In this work, this time is assumed to be 3 years.

Walker et al. have reported an initial O/U ratio for the fuel of 2.005. Walker et al. have measured the oxygen potential at four radial positions and at temperatures ranging from 700 °C to 1100 °C. The calculated oxygen potentials at the four positions and at the different temperatures with ANGE are compared to Walker's measures in Figure 3.43.

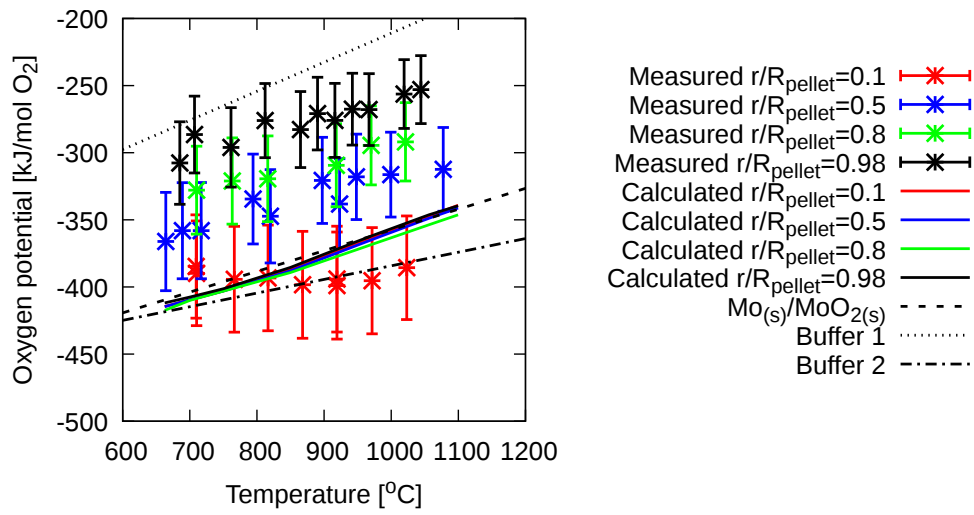


Figure 3.43: Calculated oxygen potential at different radial positions as a function of temperature compared to the values measured by Walker et al. [7].

As may be noticed, the thermodynamic equilibrium calculations are far from the measures, except at the pellet center ( $r/R_{pellet} = 0.1$ ) where an almost constant oxygen potential of -400 kJ/mol  $O_2$  was reported. However, the authors mentioned that they were not able to correctly measure the oxygen potential at the pellet center, and thus these values cannot be used as a reliable reference. At all positions, the calculated oxygen potentials increase with temperature, which is the expected behavior. No radial evolution of the oxygen potential was however obtained with ANGE, the four calculated values being in the vicinity of the oxygen potential given by the redox system  $Mo_{(s)}/MoO_{2(s)}$ , as shown in Figure 3.44.

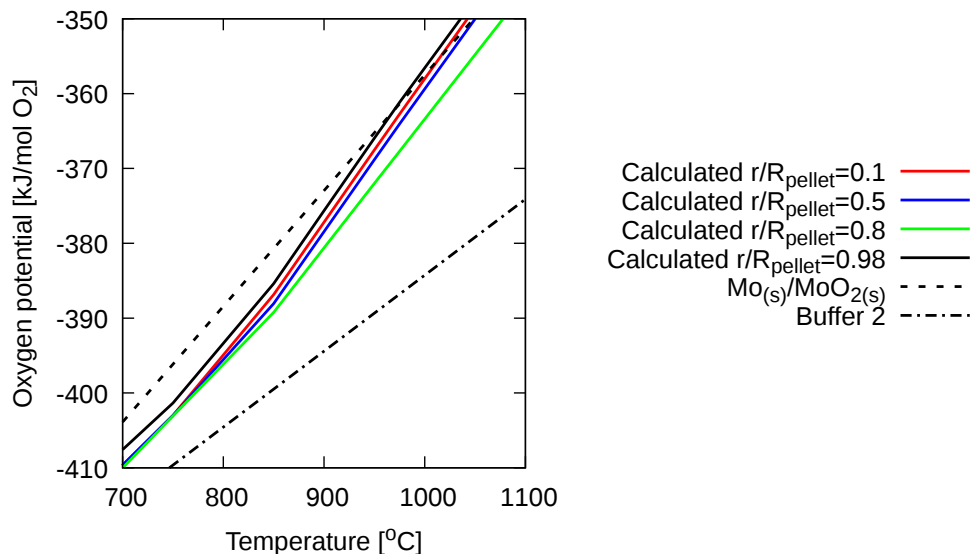
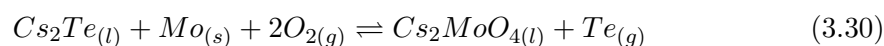
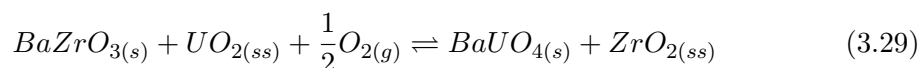


Figure 3.44: Calculated oxygen potential at different radial positions compared to the oxygen potential corresponding to two redox buffers.

Investigations lead to identify two other redox systems that could possibly control the oxygen potential of the samples at the center and at the periphery. These two redox systems are given in Equations 3.29 and 3.30 and plotted in Figures 3.43 and 3.44. 'Buffer 1' and 'Buffer 2' refer respectively to Equations 3.29 and 3.30.



Walker et al. have also plotted the oxygen potential at 750 °C and 1000 °C as a function of  $r/R_{\text{pellet}}$ . Their measurements show an increase of the oxygen potential with the radius. According to ANGE computations, the oxygen potential is nearly constant along the pellet radius except at the periphery where it slightly increases. Comparison is shown in Figure 3.45. Compared to the measures of Matzke on the high burnup fuel (decreasing oxygen potential with increasing burnup) [66], one may notice that the evolution of the oxygen potential with burnup reported by Walker shows the opposite trend.

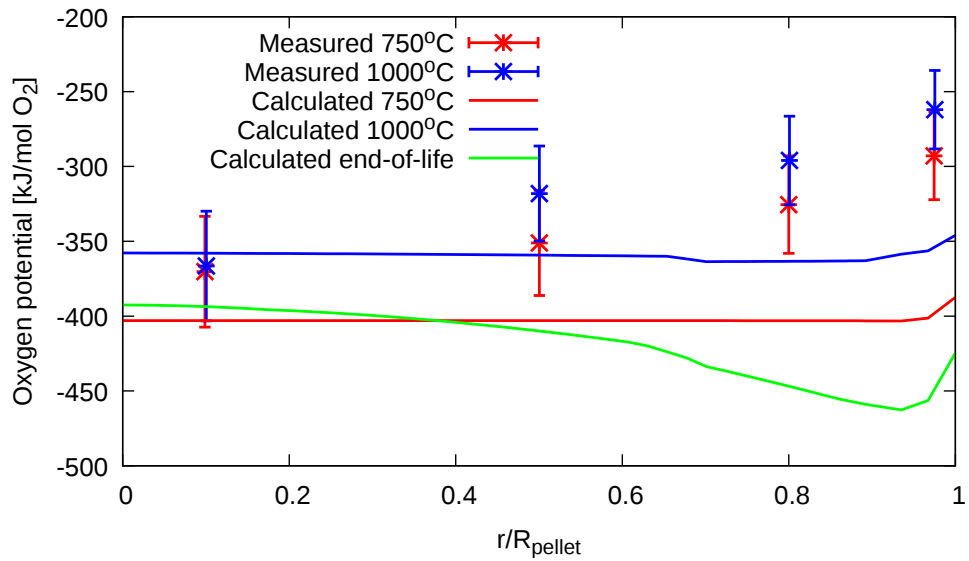


Figure 3.45: Calculated radial profiles of oxygen potential at 750 °C and 1000 °C compared to the experimental measurements from [7]. The green line shows the oxygen potential at maximum LHR during the last irradiation cycle.

The green curve shows the calculated oxygen potential profile at the hottest moment of the last irradiation cycle. The profile is non-convex. The change of curvature near the pellet periphery is caused by two competing effects on oxygen potential: i) the temperature decrease near the periphery and ii) the burnup increase in the rim of the pellet. Similarly shaped end-of-life oxygen potential profiles have been obtained by Piro et al. [12] and Loukusa et al. [72].

The oxygen potentials at 750 and 1000 °C obtained with ANGE are not consistent with the thermochemical simulations of the same fuel performed by Piro et al. [12] and Loukusa et al. [72]. Both authors found an increase of the oxygen potential of the fuel with the fuel pellet radius and burnup. Results from Piro and Loukusa are similar because they have used the same thermochemical database from RMC [19,149]. According to Loukusa, the high oxygen potential obtained in the simulations is due to the formation of  $UMoO_{6(s)}$  when the burnup exceeds 50 GWd/tHM. The oxygen potential of the fuel is buffered by the following reaction:



To improve the simulations with ANGE,  $UMoO_{6(s)}$  has been added to the thermodynamic database and new calculations performed. The Gibbs energy of formation of this compound, used in this work, is the one proposed by Dharwadkar [182]. The formation of  $UMoO_{6(s)}$  has not been obtained in the simulations, even with consideration of the uncertainty on the initial O/U ratio of the fuel (from 2 to 2.01).  $UMoO_{6(c)}$  was found

in the calculation only when the initial O/U reached 2.03. Such high oxygen concentration at the pellet periphery could be a result of oxygen thermal diffusion, a possible mechanism during nominal irradiation in consequence of the first two irradiation cycles performed at LHR around 300 W/cm.

Figure 3.46 compares the O/M profile calculated at the hottest moment of the last irradiation cycle to the values estimated by Walker. The predicted radial profile is consistent with the blue dots, i.e. with Walker's values assuming that Mo is metallic and not dissolved in oxide form in the solid solution. The same assumption is made in the database of ANGE where Mo does not contribute to the O/M ratio.

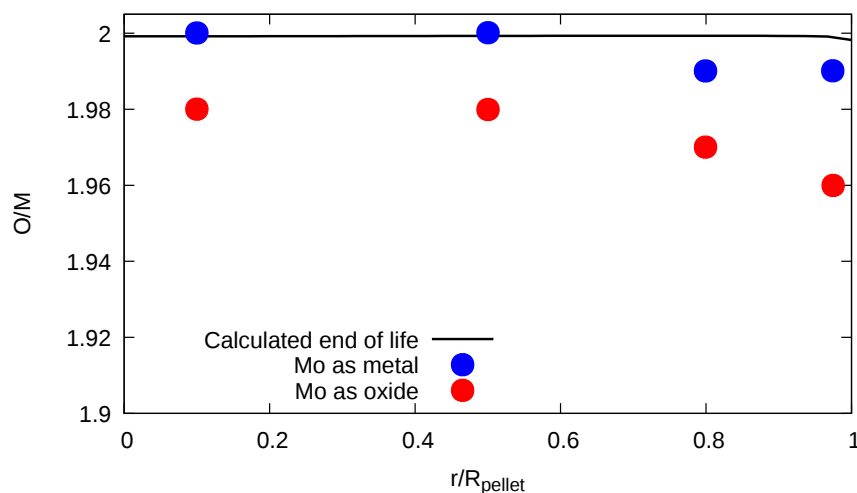


Figure 3.46: The O/M ratio at maximum LHR during the last irradiation cycle (line) compared to the values estimated by Walker et al. [7].

### 3.4 Summary

Thermochemical modeling of nuclear fuels has been presented in this chapter. In the first part, the neutronics model PRODHEL has been introduced. Successful validation by comparison to FPs and actinides inventory in medium and high burnup fuels has been presented. PRODHEL is able to return a detailed isotopic composition at any time of the fuel irradiation cycles, which has been demonstrated by the analysis of iodine isotopes evolution during nominal irradiation and a power ramp.

In the second part, the thermochemical solver ANGE and its thermodynamic database have been presented. The solid solution phase has been detailed and validated against experiments on solubility of fission products. The validation shows a good agreement for all the considered elements except for Zr. Solubility of zirconium is still unclear and more work is required to correctly describe the U-Zr-O system. The complete solid solution

model has been compared to oxygen potential measurements on SIMFUEL samples, showing consistent estimations.

Finally, available experiments on irradiated nuclear fuels have been simulated using PRODHEL and ANGE. Oxygen potential calculated in fuels irradiated up to around 60 GWd/tHM are in satisfactory agreement with experimental measurements. Modeling of high burnup fuels shows that the calculated oxygen potential are inconsistent with the reported experimental values. More efforts are therefore required to model high burnup fuels correctly. It must however be emphasized that the oxygen potential evolution with burnup increase is not clear among researchers and that opposite trends are reported, making any conclusion highly speculative.

In high burnup fuels, differences between calculated and measured oxygen potentials could possibly be explained by oxygen thermal diffusion leading to an enrichment in oxygen of the fuel periphery. Thus, oxygen transport should be taken into account in simulations of irradiated fuel thermochemistry.

The impact of the oxygen potential of the fuel on the speciation in the gas phase has also been studied with ANGE. The concentration of gas species potentially detrimental to the cladding (iodine particularly) varies significantly with the oxygen potential. Any oxygen thermal diffusion process in the fuel should therefore have a major impact on the speciation of the gas phase.

## Chapter 4

# Oxygen thermal diffusion

The goal of this work is to study the impact of oxygen transport on speciation of fission products during power ramps, which will help to predict PCI failures. In order to do that, it is necessary to implement an oxygen transport model in the fuel performance code ALCYONE. ALCYONE is able to perform calculations in different geometries. For this reason, two solutions for the oxygen transport problem have been developed. The Finite Volume Method (FVM) has been applied to the 1.5D scheme and the Finite Element Method (FEM) to the 2D and 3D geometries. Both solutions have been validated against each other and against the steady-state solution given by the OXIREM model from Lassmann [86]. The first part of this chapter presents the solutions developed for oxygen transport. The second part of this chapter presents the application of the FEM to the 2D and 3D solution of a coupled heat and oxygen transport problem from the open literature in order to check the robustness of the proposed algorithms. The two main parameters governing oxygen transport are studied in the third part of this chapter: the heat of transport of oxygen and the oxygen chemical diffusion coefficient.

### 4.1 Numerical solutions in 1D radial

#### 4.1.1 Steady-state temperature profile

For the presentation of the numerical methods used to solve the oxygen thermal diffusion problem, it is not necessary to fully couple heat and oxygen transport. Oxygen transport under a fixed, parabolic radial temperature profile might be considered. The temperature profile can be calculated from the steady-state solution of the heat balance equation in cylindrical coordinates written as follows:

$$\frac{1}{r} \frac{d}{dr} \left[ \lambda r \frac{dT}{dr} \right] + \dot{Q} = 0 \quad (4.1)$$

where

$r$ –radius [m]

$T$ –temperature [K]

$\lambda$ –thermal conductivity [W/m/K]

$\dot{Q}$ –heat generation rate [W/m<sup>3</sup>]

The heat generation rate can be estimated from the linear heat rate  $P_l$  [W/m] and from the fuel pellet surface  $S = \pi R_{pellet}^2$  with  $R_{pellet}$  the fuel pellet radius [m]. Considering a constant thermal conductivity  $\lambda$  together with a boundary condition consisting of a constant temperature  $T_0$  at the fuel pellet external radius, the solution of Equation 4.1 reads as follows:

$$T(r) = T_0 + \frac{P_l}{4\pi R_{pellet}^2 \lambda} (R_{pellet}^2 - r^2) \quad (4.2)$$

Equation 4.2 gives the temperature at each point of the fuel pellet radius  $r$ .

In the following applications presented in this chapter, the parameters of Equation 4.2 will take the following numerical values:  $R_{pellet} = 4.1$  mm (the standard pellet size in French PWR fuel rods),  $T_0 = 750$  K, thermal conductivity of the fuel  $\lambda = 2$  W/m/K and  $P_l = 40000$  W/m. These parameters give a temperature radial profile representative of the one occurring during power ramps. This profile is shown by the red curve in Figure 4.3. The maximum temperature reaches 2250 K at the pellet center. This temperature profile will be used in all the oxygen transport models shown in this chapter.

#### 4.1.2 Steady-state solution (OXIRED)

The OXIRED solution proposed by Lassmann [86] is first recalled since it will serve as a reference for the other solutions developed in this work. OXIRED gives the steady-state solution of oxygen thermal diffusion in a cylindrical fuel pellet. It consists in solving the following general thermal diffusion equation (see Section 2.2.1.2) which can be applied to hypostoichiometric or hyperstoichiometric fuel:

$$N \frac{\partial x}{\partial t} = -\frac{1}{r} \frac{\partial}{\partial r} (rJ) \quad (4.3)$$

with  $J$  as the oxygen interstitial or vacancy flux given by:

$$J = -N \tilde{D}_O \left( \frac{\partial x}{\partial r} + \frac{xQ_O^*}{RT^2} \frac{\partial T}{\partial r} \right) \quad (4.4)$$

where:

$N$ -total number of oxygen atoms per unit volume

$x$ -the stoichiometry deviation [-]

$\tilde{D}_O$ -the chemical diffusion coefficient [ $\text{m}^2/\text{s}$ ]

$Q_O^*$ -the heat of transport of oxygen [ $\text{J}/\text{mol}$ ]

Lassmann has applied Neumann boundary conditions on both boundaries  $r = 0$  and  $r = R_{\text{pellet}}$ . The author has assumed that the flux  $J$  is null:

$$J(r = 0) = 0 \quad (4.5)$$

$$J(r = R_{\text{pellet}}) = 0 \quad (4.6)$$

These conditions ensure conservation of oxygen vacancies or interstitials in the fuel pellet. The steady-state solution of Equation 4.3 ( $\frac{\partial x}{\partial t} = 0$ ) is equivalent to the following condition:

$$\frac{dx}{dr} + x \frac{Q_O^*}{RT^2} \frac{dT}{dr} = 0 \quad (4.7)$$

In OXIREED, the fuel is divided in  $N$  concentric rings with  $N + 1$  nodes. An example of discretization is shown in Figure 4.1.

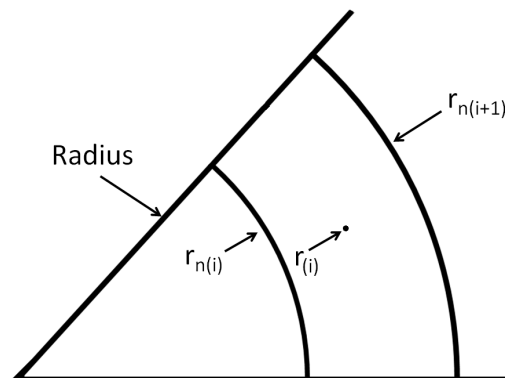


Figure 4.1: Visualization of the 1D discretization used in the OXIREED model.

The simulated fuel pellet is here divided in  $N=40$  rings. The mesh is shown in Figure 4.2. The width of rings decreases with radius, which results in a denser mesh at the periphery. This particular mesh comes from the fuel performance code ALCYONE. Such discretization is common in fuel performance modeling. Dots correspond to ring boundaries  $r_{n(i)}$ .

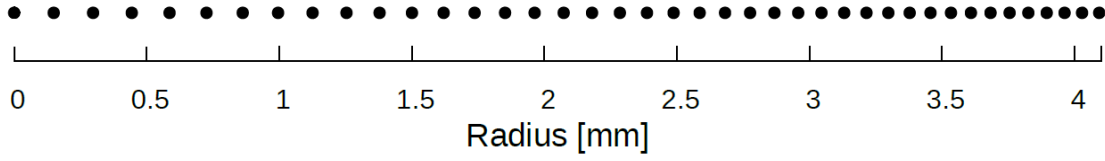


Figure 4.2: Example of the 1D discretization used in the OXIRE model.

The relation between the stoichiometry deviations  $x$  in two neighboring ring centers  $r_{(i+1)}$  and  $r_{(i)}$  can be expressed as:

$$\int_{x_{(i)}}^{x_{(i+1)}} \frac{dx}{x} = - \int_{T_{(i)}}^{T_{(i+1)}} \frac{Q_O^*}{R} \frac{dT}{T^2} \quad (4.8)$$

$$x_{(i+1)} = x_{(i)} \exp \left[ \frac{Q_{On(i+1)}^*}{R} \left( \frac{1}{T_{(i+1)}} - \frac{1}{T_{(i)}} \right) \right] = x_{(i)} a_{(i)} \quad (4.9)$$

where  $x_{(i)}$  is the stoichiometry at the center of the  $i$ -th ring.  $Q_{On(i+1)}^*$  is the heat of transport of oxygen at the interface between rings  $i$  and  $i+1$ . It can be approximated in the following way:

$$Q_{On(i+1)}^* = \frac{Q_{O(i)}^* + Q_{O(i+1)}^*}{2} \quad (4.10)$$

One can see that  $x_{(i+1)}$  depends on  $x_{(i)}$ . Equation 4.9 can be extended to express the result in each ring  $i$  as a function of the stoichiometry deviation in the first ring  $x_{(1)}$ :

$$\begin{aligned} x_{(2)} &= x_{(1)} a_{(1)} \\ x_{(3)} &= x_{(2)} a_{(2)} = x_{(1)} a_{(1)} a_{(2)} \\ &\vdots \\ x_{(N)} &= x_{(N-1)} a_{(N-1)} = x_{(1)} a_{(1)} \dots a_{(N-1)} \end{aligned} \quad (4.11)$$

As a result of the boundary conditions used by Lassmann in the OXIRE model, the average stoichiometry deviation  $\bar{x}$  in the fuel pellet before and after redistribution is conserved, which leads to the following equation:

$$\bar{x} R_{pellet}^2 = \sum_{i=1}^N \left[ \left( r_{n(i+1)}^2 - r_{n(i)}^2 \right) x_{(i)} \right] \quad (4.12)$$

By combining Equations 4.9 and 4.12, one gets the stoichiometry deviation in the first ring as follows:

$$x_{(1)} = \frac{\bar{x} R_{pellet}^2}{\sum_{i=1}^N \left( r_{n(i+1)}^2 - r_{n(i)}^2 \right) \prod_{j=1}^{i-1} a_{(j)}} \quad (4.13)$$

Once  $x_{(1)}$  is found, the values in other nodes can be calculated using Equation 4.9. The average stoichiometry deviation of the oxygen steady-state redistribution  $\bar{x}_{final}$ , which

is calculated as follows:

$$\bar{x}_{final} = \frac{\sum_{i=1}^N \left[ x^{(i)} \left( r_{n(i+1)}^2 - r_{n(i)}^2 \right) \right]}{R_{pellet}^2} \quad (4.14)$$

should be the same as the initial stoichiometry deviation  $\bar{x}$ .

Examples of oxygen redistribution calculated with the OXIREC solution are shown in Figure 4.3. All the calculations have been performed with an initial stoichiometry deviation  $\bar{x} = 0.005$ . The heat of transport  $Q_O^*$  is here negative which would correspond to an initially hypostoichiometric fuel ( $O/M < 2$ ). The plots are expressed in function of the O/M ratio instead of the stoichiometry deviation  $x$ , recalling that the relation between these two quantities is as follows:

$$O/M = 2 - x \quad (4.15)$$

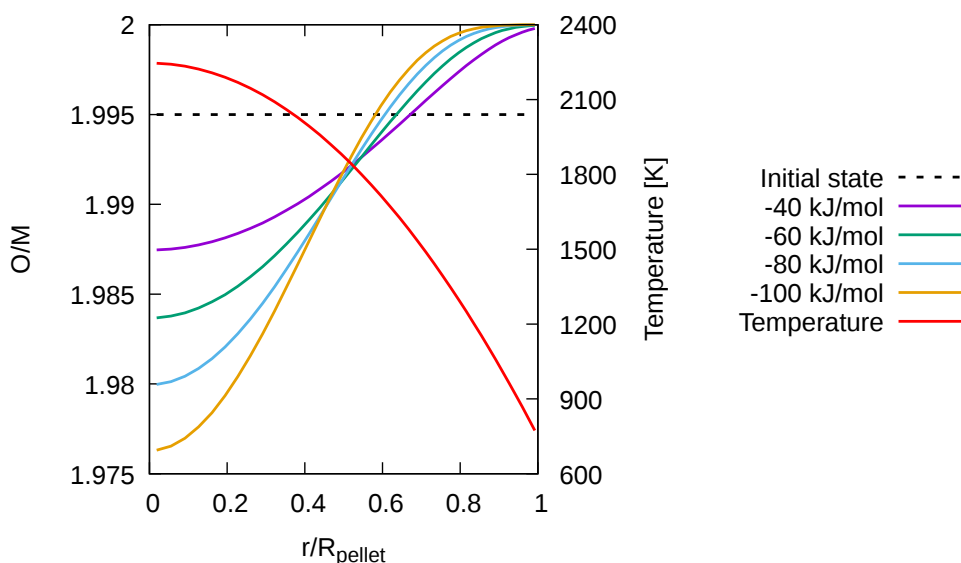


Figure 4.3: O/M profiles calculated by OXIREC for different heats of transport. The red curve is the temperature radial profile.

It can be noticed that the difference between O/M ratios at the pellet center and at the periphery increases with decreasing  $Q_O^*$ . Lower values of  $Q_O^*$  lead to steeper O/M radial profiles. Another important observation is that the cylindrical geometry can lead to a very low O/M ratio at the pellet center even if the initial stoichiometry deviation is small (0.005 in the present calculation). The O/M ratios at the pellet center can even be lower with non-constant values of the heat of transport. To illustrate this point, the

nonlinear heat of transport given by Equation 4.16 has been used in OXIREd.

$$Q_O^* = 5 \times 10^4 \ln(x), \text{ minimum value: } Q_O^* = -10^7 \text{ J/mol} \quad (4.16)$$

The stoichiometry deviation dependence and strong non-linearity of Equation 4.16 requires iterations to ensure numerical convergence. In practice, one needs to repeat the OXIREd calculations until the convergence condition given in Equation 4.17 is fulfilled.

$$\sum_{i=1}^N \left| x_{(i)}^{k+1} - x_{(i)}^k \right| < 10^{-7} \quad (4.17)$$

where  $x_{(i)}^{k+1}$  and  $x_{(i)}^k$  are the stoichiometry deviations at the center of the  $i$ -th ring and at the iteration  $k+1$  and  $k$ , respectively. The iteration  $k+1$  uses the heat of transport expressed as a function of the stoichiometry deviation from the  $k$ -th iteration. The convergence is ensured when the difference between iterations is sufficiently small.

OXIREd calculations with a nonlinear heat of transport have been carried out and are shown in Figure 4.4. The discretization, initial stoichiometry deviation and temperature profile are unchanged. Ten iterations on average are needed for convergence. The oxygen redistribution calculated with a constant heat of transport shown in Figure 4.3 did not require iterations to converge.

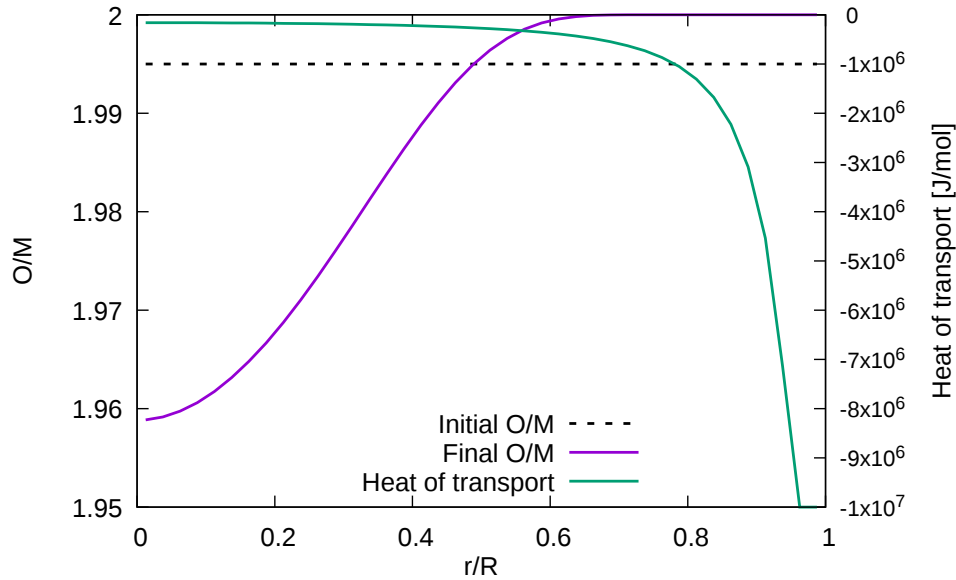


Figure 4.4: Example of OXIREd calculations with a nonlinear heat of transport.

The OXIREd calculations with a non-constant heat of transport give lower O/M ratios at the pellet center when compared to the O/M radial profiles of Figure 4.3. Also, it can be noticed that in spite of a very steep O/M profile, the calculated values do not exceed 2 ( $x=0$ ). Only the size of the O/M=2 zone increases.

### 4.1.3 Transient solution (OXITRAN)

The most basic geometry included in ALCYONE fuel performance code is the 1.5D scheme where the fuel rod is divided into axial slices, each slice into concentric rings. The 1.5D scheme is illustrated in Figure 1.18. The axial coupling is only for thermo-hydraulics. The oxygen transport problem is therefore 1D radial.

The FVM has been chosen to solve the oxygen transport equation because it is very fast and simple. Also, it implicitly ensures the conservation of matter (oxygen vacancies or interstitial atoms). Both explicit and implicit schemes have been tested in this work. The latter ensures numerical stability when it comes to deal with very steep O/M profiles related to a nonlinear heat of transport  $Q_O^*$ . The implicit scheme requires more mathematical operations to find the solution but the CPU time required for thermal diffusion is negligible when compared to the time needed for thermomechanical or thermochemical calculations in ALCYONE. In this work, the oxygen transport transient solution is called 'OXITRAN'.

The 1D oxygen transport equation in radial coordinates is given by Equation 4.4. The discretization of the fuel pellet considered in the FVM is shown in Figure 4.2. Integration of Equation 4.4 in each concentric ring ( $i$ ) is at the root of the FVM:

$$\int_{r_{n(i)}}^{r_{n(i+1)}} r \frac{\partial x}{\partial t} dr = \int_{r_{n(i)}}^{r_{n(i+1)}} \left[ \frac{\partial}{\partial r} \left\{ r \tilde{D}_O \left( \frac{\partial x}{\partial r} + \frac{x Q_O^*}{RT^2} \frac{\partial T}{\partial r} \right) \right\} \right] dr \quad (4.18)$$

The left side of Equation 4.18 can be approximated as follows:

$$\int_{r_{n(i)}}^{r_{n(i+1)}} r \frac{\partial x}{\partial t} dr \approx r_{(i)} (r_{n(i+1)} - r_{n(i)}) \frac{\partial x}{\partial t} \quad (4.19)$$

The time evolution of  $x$  can be expressed by the first order approximation such that:

$$\frac{\partial x}{\partial t} \approx \frac{x_{(i)}^{t+dt} - x_{(i)}^t}{dt} \quad (4.20)$$

where  $x_{(i)}^{t+dt}$  and  $x_{(i)}^t$  are stoichiometry deviations at times  $t + dt$  and  $t$  respectively. The first order is sufficient because the time steps used in the OXITRAN solution can be very small. Combining Equations 4.18, 4.19 and 4.20 gives:

$$r_{(i)} (r_{n(i+1)} - r_{n(i)}) \frac{x_{(i)}^{t+dt} - x_{(i)}^t}{dt} = \int_{r_{n(i)}}^{r_{n(i+1)}} \left[ \frac{\partial}{\partial r} \left\{ r \tilde{D}_O \left( \frac{\partial x}{\partial r} + \frac{x Q_O^*}{RT^2} \frac{\partial T}{\partial r} \right) \right\} \right] dr \quad (4.21)$$

$$r_{(i)} (r_{n(i+1)} - r_{n(i)}) \frac{x_{(i)}^{t+dt} - x_{(i)}^t}{dt} = \left[ r \tilde{D}_O \left( \frac{\partial x}{\partial r} + \frac{x Q_O^*}{RT^2} \frac{\partial T}{\partial r} \right) \right]_{r_{n(i)}}^{r_{n(i+1)}} \quad (4.22)$$

The right side of Equation 4.22 can be expressed at each ring boundary by:

$$\begin{aligned}
& \left[ r \tilde{D}_O \left( \frac{\partial x}{\partial r} + \frac{x Q_O^*}{RT^2} \frac{\partial T}{\partial r} \right) \right]_{r_{n(i+1)}} = \\
& = r_{n(i+1)} \tilde{D}_{On(i+1)} \frac{\partial x}{\partial r} \Big|_{n(i+1)} + r_{n(i+1)} \left( \frac{x \tilde{D}_O Q_O^*}{RT^2} \right)_{n(i+1)} \frac{\partial T}{\partial r} \Big|_{n(i+1)} \\
& - r_{n(i)} \tilde{D}_{On(i)} \frac{\partial x}{\partial r} \Big|_{n(i)} - r_{n(i)} \left( \frac{x \tilde{D}_O Q_O^*}{RT^2} \right)_{n(i)} \frac{\partial T}{\partial r} \Big|_{n(i)}
\end{aligned} \tag{4.23}$$

The gradients of stoichiometry deviation and temperature at the ring boundaries  $r_{n(i+1)}$  and  $r_{n(i)}$  can be expressed in the following way as a function of the same quantities at the center of the rings:

$$\begin{aligned}
\frac{\partial x}{\partial r} \Big|_{n(i+1)} &= \frac{x_{(i+1)}^{t+dt} - x_{(i)}^{t+dt}}{r_{(i+1)} - r_{(i)}} \\
\frac{\partial x}{\partial r} \Big|_{n(i)} &= \frac{x_{(i)}^{t+dt} - x_{(i-1)}^{t+dt}}{r_{(i)} - r_{(i-1)}} \\
\frac{\partial T}{\partial r} \Big|_{n(i+1)} &= \frac{T_{(i+1)}^{t+dt} - T_{(i)}^{t+dt}}{r_{(i+1)} - r_{(i)}} \\
\frac{\partial T}{\partial r} \Big|_{n(i)} &= \frac{T_{(i)}^{t+dt} - T_{(i-1)}^{t+dt}}{r_{(i)} - r_{(i-1)}}
\end{aligned} \tag{4.24}$$

Equations 4.24 are the first order approximations. The small ring sizes  $dr$  used in ALCYONE (see Figure 4.2) allows one to make this approximation.

In order to simplify further notations, one may define the following quantities:

$$A_{pi} = \frac{r_{n(i+1)}}{r_{(i)}} \frac{dt}{(r_{n(i+1)} - r_{n(i)}) (r_{(i+1)} - r_{(i)})} \tag{4.25}$$

$$A_{mi} = \frac{r_{n(i)}}{r_{(i)}} \frac{dt}{(r_{n(i+1)} - r_{n(i)}) (r_{(i)} - r_{(i-1)})} \tag{4.26}$$

The discretization of the pellet in  $N$  rings leads to the following system written in a matrix from:

$$\underbrace{\begin{bmatrix} a_{1,1} & a_{1,2} & 0 & 0 \\ a_{2,1} & a_{2,2} & \ddots & 0 \\ 0 & \ddots & \ddots & a_{N-1,N} \\ 0 & 0 & a_{N,N-1} & a_{N,N} \end{bmatrix}}_A \underbrace{\begin{bmatrix} x_{(1)}^{t+dt} \\ x_{(2)}^{t+dt} \\ \vdots \\ x_{(N)}^{t+dt} \end{bmatrix}}_X = \underbrace{\begin{bmatrix} b_1 \\ b_2 \\ \vdots \\ b_N \end{bmatrix}}_B \tag{4.27}$$

where for  $2 \leq i \leq N - 1$

$$\begin{aligned}
a_{i,i-1} &= -A_{mi} \tilde{D}_{On(i)} \\
a_{i,i} &= 1 + A_{mi} \tilde{D}_{On(i)} + A_{pi} \tilde{D}_{On(i+1)} \\
a_{i,i+1} &= -A_{pi} \tilde{D}_{On(i+1)}
\end{aligned} \tag{4.28}$$

$$\begin{aligned}
b_i = c_{(i)}^t + A_{pi} \left( \frac{x \tilde{D}_O Q_O^*}{RT^2} \right)_{n(i+1)} \left( T_{(i+1)}^{t+dt} - T_{(i)}^{t+dt} \right) \\
- A_{mi} \left( \frac{x \tilde{D}_O Q_O^*}{RT^2} \right)_{n(i)} \left( T_{(i)}^{t+dt} - T_{(i-1)}^{t+dt} \right)
\end{aligned} \quad (4.29)$$

In order to ensure matter conservation (oxygen vacancies or interstitials), it is assumed that the flux of oxygen at the pellet center and at the periphery is null. These are the Neumann boundary conditions given by Equations 4.5 and 4.6. This assumption imposes that  $A_{mi} = 0$  in the first ring ( $i = 1$ ), which leads to:

$$\begin{aligned}
a_{1,1} &= 1 + A_{p1} \tilde{D}_{On(2)} \\
a_{1,2} &= -A_{p1} \tilde{D}_{On(2)} \\
b_1 &= c_{(1)}^t + A_{p1} \left( \frac{x \tilde{D}_O Q_O^*}{RT^2} \right)_{n(2)} \left( T_{(2)}^{t+dt} - T_{(1)}^{t+dt} \right)
\end{aligned} \quad (4.30)$$

and  $A_{pi} = 0$  in the last ring ( $i = N$ ), leading to:

$$\begin{aligned}
a_{N,N-1} &= -A_{m(N)} \tilde{D}_{On(N)} \\
a_{N,N} &= 1 + A_{m(N)} \tilde{D}_{On(N)} \\
b_N &= c_{(N)}^t - A_{mn} \left( \frac{x \tilde{D}_O Q_O^*}{RT^2} \right)_{n(N)} \left( T_{(N)}^{t+dt} - T_{(N-1)}^{t+dt} \right)
\end{aligned} \quad (4.31)$$

The diffusion coefficient  $\tilde{D}_O$  and the term  $\frac{x \tilde{D}_O Q_O^*}{RT^2}$  need to be calculated at the rings boundaries  $r_{n(i+1)}$  and  $r_{n(i)}$ . They are estimated as follows from the same quantities at the ring centers:

$$\begin{aligned}
\tilde{D}_{On(i)} &= \frac{r_{(i)} - r_{(i-1)}}{\frac{r_{(i)} - r_{n(i)}}{\tilde{D}_O(T_{(i)})} + \frac{r_{n(i)} - r_{(i-1)}}{\tilde{D}_O(T_{(i-1)})}} \\
\tilde{D}_{On(i+1)} &= \frac{r_{(i+1)} - r_{(i)}}{\frac{r_{(i+1)} - r_{n(i+1)}}{\tilde{D}_O(T_{(i+1)})} + \frac{r_{n(i+1)} - r_{(i)}}{\tilde{D}_O(T_{(i)})}} \\
\left( \frac{x \tilde{D}_O Q_O^*}{RT^2} \right)_{n(i)} &= \frac{r_{(i)} - r_{(i-1)}}{\frac{(r_{(i)} - r_{n(i)}) RT_{(i)}^2}{x_{(i)} \tilde{D}_O(T_{(i)}) Q_O^*(x_{(i)})} + \frac{(r_{n(i)} - r_{(i-1)}) RT_{(i-1)}^2}{x_{(i-1)} \tilde{D}_O(T_{(i-1)}) Q_O^*(x_{(i-1)})}} \\
\left( \frac{x \tilde{D}_O Q_O^*}{RT^2} \right)_{n(i+1)} &= \frac{r_{(i+1)} - r_{(i)}}{\frac{(r_{(i+1)} - r_{n(i+1)}) RT_{(i+1)}^2}{x_{(i+1)} \tilde{D}_O(T_{(i+1)}) Q_O^*(x_{(i+1)})} + \frac{(r_{n(i+1)} - r_{(i)}) RT_{(i)}^2}{x_{(i)} \tilde{D}_O(T_{(i)}) Q_O^*(x_{(i)})}}
\end{aligned} \quad (4.32)$$

$$\begin{aligned}
&= \frac{r_{(i)} - r_{(i-1)}}{\frac{(r_{(i)} - r_{n(i)}) RT_{(i)}^2}{x_{(i)} \tilde{D}_O(T_{(i)}) Q_O^*(x_{(i)})} + \frac{(r_{n(i)} - r_{(i-1)}) RT_{(i-1)}^2}{x_{(i-1)} \tilde{D}_O(T_{(i-1)}) Q_O^*(x_{(i-1)})}} \\
&= \frac{r_{(i+1)} - r_{(i)}}{\frac{(r_{(i+1)} - r_{n(i+1)}) RT_{(i+1)}^2}{x_{(i+1)} \tilde{D}_O(T_{(i+1)}) Q_O^*(x_{(i+1)})} + \frac{(r_{n(i+1)} - r_{(i)}) RT_{(i)}^2}{x_{(i)} \tilde{D}_O(T_{(i)}) Q_O^*(x_{(i)})}}
\end{aligned} \quad (4.33)$$

There are other options to calculate the parameters at the rings boundaries such as the arithmetic mean but numerical tests have shown that utilizing the harmonic mean leads to less restrictions on the time step.

In order to calculate  $x^{t+dt}$ , the system of  $N$  Equations 4.27 needs to be solved. The tridiagonal matrix algorithm (also known as Thomas Algorithm) has been used to solve the system. It is a simplified version of the Gaussian elimination method, adjusted to tridiagonal matrices. It is explained in details in Appendix D.

The OXITRAN solution has been validated by comparison to the OXIREDD steady state solution. The diffusion coefficient used in the OXITRAN solution is the one proposed by Lassmann [86] which depends only on temperature:

$$\tilde{D}_O = 1.39 \times 10^{-6} \exp(-75900/RT) [m^2/s] \quad (4.34)$$

Results of OXITRAN calculations at different times are shown in Figure 4.5. The initial stoichiometry deviation is 0.005 (O/M=1.995) and the heat of transport is -100 kJ/mol. The time step is 0.5 s. The oxygen redistribution after 500 s is already significant and it is close to the steady state. After 1000 s, the OXITRAN results are nearly the same as OXIREDD. After 10000 s, OXITRAN gives exactly the same results as OXIREDD meaning that the steady state is reached. Such time periods of several hours at high temperatures are typical of power ramps.

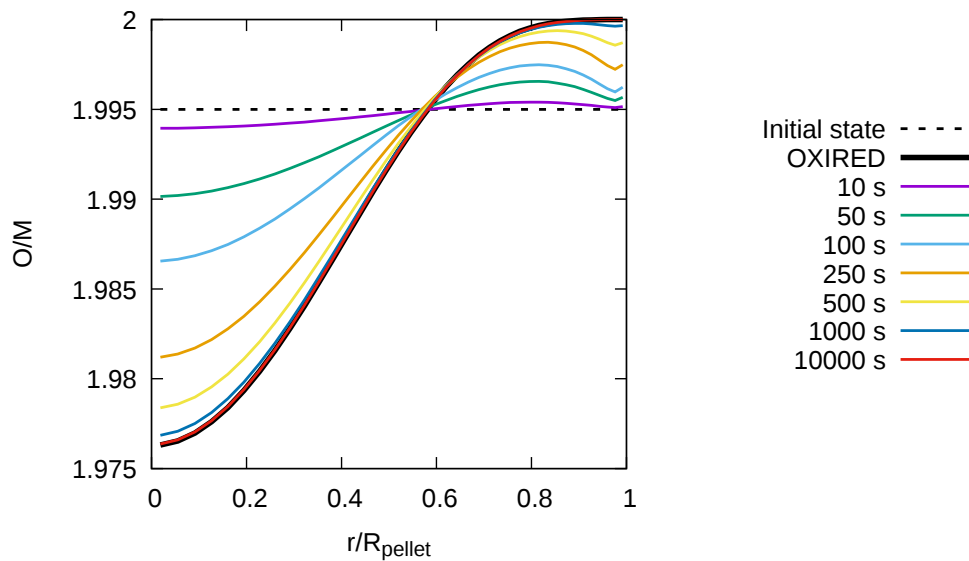


Figure 4.5: O/M radial profiles calculated with OXIREDD (thick black curve) and OXITRAN at different times.

In case of a nonlinear heat of transport, the O/M profiles can be very steep. It may lead to difficulties in numerical convergence. In order to solve this issue, a convergence condition has been introduced. Practically, the matrix  $X$  in Equation 4.27 is recalculated in an iterative process until the sum of absolute values of differences of  $x$  at two successive iterations is lower than  $10^{-6}$ .

$$\sum_{i=1}^N \left| x_{(i)}^{t+dt(k+1)} - x_{(i)}^{t+dt(k)} \right| < 10^{-6} \quad (4.35)$$

where  $x_{(i)}^{t+dt(k)}$  is the stoichiometry deviation at the center of the  $i$ -th ring, at iteration  $k$  and time  $t + dt$ . Numerical stability increases for shorter time steps and wider rings.

The traditional Courant-Friedrichs-Lewy (CFL) condition [183], given in Equation 4.36, has been used to define an optimal time step:

$$\frac{\tilde{D}_O dt}{dr^2} < C_{max} \quad (4.36)$$

For explicit schemes,  $C_{max}$  is typically of the order of 0.5. Implicit schemes are more stable, and thus the value of  $C_{max}$  may be larger. A set of OXITRAN simulations with a non-constant heat of transport function (given in Equation 4.16) has been carried out to study the CFL condition as a function of the time step (the mesh is given in Figure 4.2). Time steps of 0.1, 0.5, 1, 2 and 3 s have been used in the simulations. The results are shown in Figure 4.6.

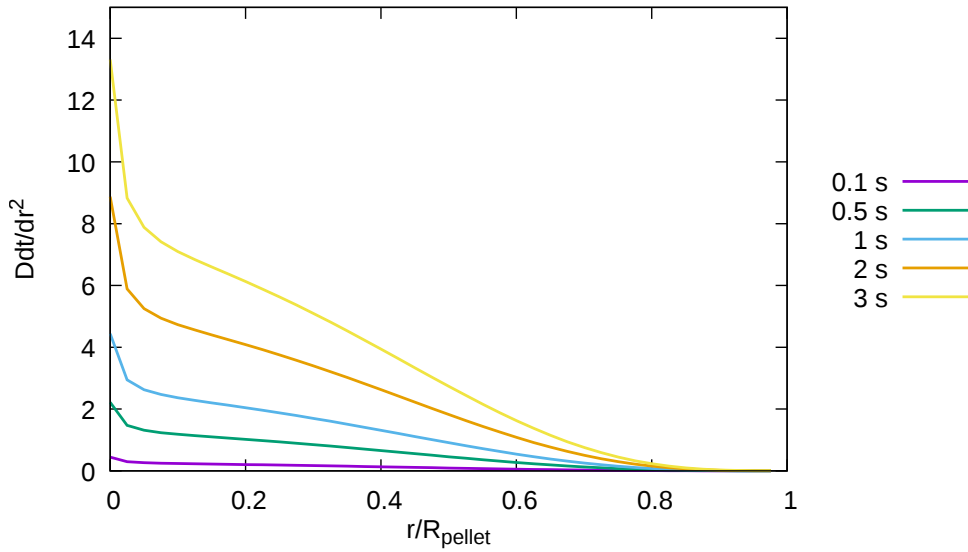


Figure 4.6:  $\tilde{D}_O dt/dr^2$  for different time steps.

With the mesh used in ALCYONE simulations, the CFL number is larger at the pellet center and it decreases rapidly with the pellet radius. It is a consequence of the higher temperature (faster diffusion) and larger mesh size  $dr$  at the pellet center. Thus convergence issues could occur preferentially at the pellet center. The calculations with a time step greater than 3 s did not converge. It can be concluded from the convergence analysis that  $C_{max}$  is around 15 for the thermal conditions, diffusion coefficient and heat of transport considered in the present calculation. Since other transport parameters might lead to greater diffusion coefficients and heat of transport, a maximum time step of 0.5 s has been prescribed in all further calculations to ensure convergence even in case of strong non-linearities. Figure 4.7 shows the evolution of the O/M profiles calculated with OXITRAN using the nonlinear heat of transport given in Equation 4.16.

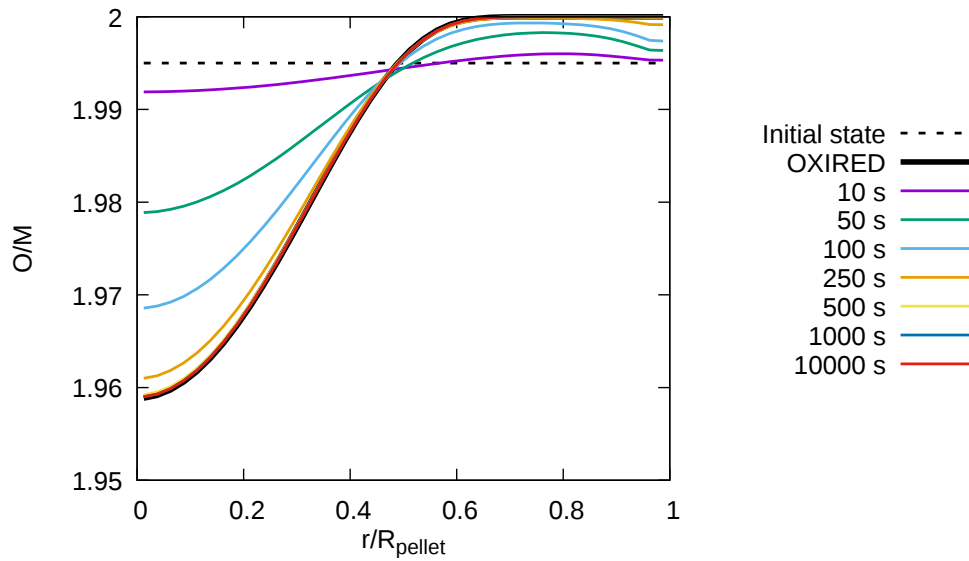


Figure 4.7: O/M radial profiles calculated with OXIREDD (thick black curve) and OXITRAN at different times with a nonlinear heat of transport.

OXITRAN results with a nonlinear heat of transport show that the oxygen redistribution is very close to reach the steady state after 250 s (OXIREDD solution), half the time required in the calculations with the constant heat of transport, as shown in Figure 4.5.

## 4.2 Numerical solution in 2D and 3D

### 4.2.1 Transient solution

The oxygen transport problem has been solved in 2D and 3D with the FE code Cast3M developed by CEA [135]. Cast3M is widely used in CEA projects for thermal diffusion problems, in particular in the fuel performance code ALCYONE. Thus the choice of using Cast3M also for solving the oxygen transport problem. The Cast3M code includes a "SORET" matrix operator that can be used to calculate the thermal gradient term  $\frac{xQ_O^*}{RT^2} \text{grad}(T)$  of the oxygen diffusion transport equation. Unfortunately, the SORET operator cannot be used in Cast3M pre-defined transient algorithms. For this reason, the solution of the oxygen transport problem has been completely rebuilt in this work from the standard solution of the thermal heat transport problem by the  $\theta$ -method [184], detailed in Appendix E.

In 2D and 3D, the transport equation taking into account thermal diffusion can be expressed as follows:

$$\frac{\partial x}{\partial t} = \text{div.} \left[ \tilde{D}_O \left( \underline{\text{grad}}(x) + \frac{xQ_O^*}{RT^2} \underline{\text{grad}}(T) \right) \right] \quad (4.37)$$

where  $\underline{\text{grad}}$  and  $\text{div.}$  are the gradient and divergence operators. The same equation can be expressed in a more general way by:

$$\frac{\partial x}{\partial t} + \text{div.}(\underline{J}) = 0 \quad (4.38)$$

with  $\underline{J}$  the oxygen flux vector:

$$\underline{J} = -\tilde{D}_O \left( \underline{\text{grad}}(x) + \frac{xQ_O^*}{RT^2} \underline{\text{grad}}(T) \right) \quad (4.39)$$

In Cast3M, the heat transport equation is solved using the Galerkin method. To apply this method to the oxygen transport Equation 4.38, one needs to multiply it by an arbitrary function  $\Theta^*$  (smooth on the domain  $\Omega$ ) and integrate the system over the entire domain  $\Omega$ .

$$\int_{\Omega} \frac{\partial x}{\partial t} \Theta^* dV + \int_{\Omega} \text{div.}(\underline{J}) \Theta^* dV = 0. \quad (4.40)$$

By integrating the second term by parts one gets two integrals defined over the domain  $\Omega$  and the external surface  $\partial\Omega$  respectively.

$$\int_{\Omega} \frac{\partial x}{\partial t} \Theta^* dV - \int_{\Omega} \underline{J} \cdot \underline{\text{grad}}(\Theta^*) dV + \int_{\partial\Omega} \underline{J} \cdot \underline{n} \Theta^* dS = 0 \quad (4.41)$$

where  $\underline{n}$  is the vector normal to the surface  $\partial\Omega$ . The third term can be split in two depending on the type of boundary conditions, i.e., imposed stoichiometry deviation  $x$  or imposed flux  $\underline{J}_0$ .

$$\int_{\partial\Omega} \underline{J} \cdot \underline{n} \Theta^* dS = \underbrace{\int_{\partial\Omega_x} -\tilde{D}_O \left[ \underline{\text{grad}}(x) + \frac{xQ_O^*}{RT^2} \underline{\text{grad}}(T) \right] \cdot \underline{n} \Theta^* dS}_{\text{imposed stoichiometry deviation}} + \underbrace{\int_{\partial\Omega_J} \underline{J}_0 \Theta^* dS}_{\text{imposed flux}} \quad (4.42)$$

where  $\partial\Omega_x$  and  $\partial\Omega_J$  are surfaces of  $\partial\Omega$  that correspond to the boundary conditions with prescribed stoichiometry deviation  $x$  and flux  $\underline{J}$ , respectively. By choosing a  $\Theta^*$  function that is null on  $\partial\Omega_x$  and noting that in the current application to oxygen redistribution in fuel pellets, the oxygen flux at the fuel boundaries is generally null ( $\underline{J}_0 = 0$  on  $\partial\Omega_J$ ), Equation 4.41 becomes:

$$\int_{\Omega} \frac{\partial x}{\partial t} \Theta^* dV + \int_{\Omega} \tilde{D}_O \left[ \underline{\text{grad}}(x) + \frac{xQ_O^*}{RT^2} \underline{\text{grad}}(T) \right] \cdot \underline{\text{grad}}(\Theta^*) dV = 0 \quad (4.43)$$

The FEM allows one to approximate the unknown  $x$  and the test function  $\Theta^*$  in each element by interpolation of the nodal values  $x_i$  and  $\Theta_i^*$  such that:

$$x(\underline{u}) = \sum_{i=1}^{N_e} x_i(t) N_i(\underline{u}) = x_i(t) N_i(\underline{u}) \quad (4.44)$$

and

$$\Theta^*(\underline{u}) = \sum_{j=1}^{N_e} \Theta_j^*(t) N_j(\underline{u}) = \Theta_j^* N_j(\underline{u}) \quad (4.45)$$

where  $N_e$  is the number of nodes of a typical element.  $N_i(\underline{u})$  is the shape function associated to the node  $i$  with position vector  $\underline{u}$ . By substituting Equations 4.44 and 4.45 in Equation 4.43 one obtains:

$$\Theta_j^* \left( \left[ \int_{\Omega^e} N_i N_j dV \right] \frac{\partial x_i}{\partial t} + \left[ \int_{\Omega^e} \tilde{D}_O \left( \underline{\text{grad}}(N_i) + N_i \underline{\text{grad}}(T) \frac{Q_O^*}{RT^2} \right) \cdot \underline{\text{grad}}(N_j) dV \right] x_i \right) = 0 \quad (4.46)$$

This equation, which is solved for each element  $\Omega^e$ , must be fulfilled for all values of  $\Theta_j^*$ . By analogy with the thermal problem, the system of equations can be written as follows:

$$\underline{\underline{C}} \cdot \dot{\underline{X}} + \underline{\underline{K}}^* \cdot \underline{X} + \underline{\underline{S}}^* \cdot \underline{X} = 0 \quad (4.47)$$

where

$\underline{X}$ —vector of stoichiometry deviations at nodes

$\dot{\underline{X}}$ —vector of time derivatives of stoichiometry deviation at nodes

$\underline{\underline{C}}$ —capacity matrix:

$$\underline{\underline{C}} = \int_{\Omega^e} N_i N_j dV \quad (4.48)$$

$\underline{\underline{K}}^*$ —conductivity matrix:

$$\underline{\underline{K}}^* = \int_{\Omega^e} \tilde{D}_O \underline{\text{grad}}(N_i) \cdot \underline{\text{grad}}(N_j) dV \quad (4.49)$$

$\underline{\underline{S}}^*$ —Soret matrix:

$$\underline{\underline{S}}^* = \int_{\Omega^e} \tilde{D}_O \frac{Q_O^*}{RT^2} \underline{\text{grad}}(N_k) \cdot \underline{\text{grad}}(N_j) T_k N_i dV \quad (4.50)$$

The theta method used in Cast3M thermal solver has been applied to Equation 4.47 resulting in the following matrix system:

$$\underline{\underline{C}} \frac{\underline{X}^{t+dt(k)} - \underline{X}^t}{\Delta t} + \underline{\underline{K}}^* \left[ \theta \underline{X}^{t+dt(k)} + (1 - \theta) \underline{X}^{t(k)} \right] + \underline{\underline{S}}^* \left[ \theta \underline{X}^{t+dt(k)} + (1 - \theta) \underline{X}^t \right] = 0 \quad (4.51)$$

leading to:

$$\underline{X}^{t+dt} = \left[ \frac{1}{\Delta t} \underline{C} + \theta \underline{K}^* + \theta \underline{S}^* \right]^{-1} \underline{X}^t \left[ \frac{1}{\Delta t} \underline{C} + (\theta - 1) \underline{K}^* + (\theta - 1) \underline{S}^* \right] \quad (4.52)$$

with

- $\Delta t$ -time step
- $X^{t+dt}$ -stoichiometry deviation at time  $t + dt$
- $X^t$ -stoichiometry deviation at time  $t$

$0 \leq \theta \leq 1$  is the relaxation coefficient. For  $\theta = 0$  the scheme is purely explicit, for  $\theta = 1$ , purely implicit.  $\underline{C}$  does not depend on temperature nor stoichiometry deviation.  $\underline{K}^*$  depends on temperature and  $\underline{S}^*$  depends on stoichiometry deviation, which means that Equation 4.47 requires an iterative process to ensure convergence. As for the FVM, the solution is recalculated from Equation 4.47 (using the previous iteration solution to estimate the  $\underline{K}^*$  and  $\underline{S}^*$  matrices) until the maximum difference in stoichiometry deviation between two successive iterations becomes less than  $10^{-6}$ . The impact of different values of  $\theta$  has been studied. A series of simulations with the nonlinear heat of transport given in 4.16 has shown that the solution is obtained in less iterations when  $\theta$  increases. Thus,  $\theta = 1$  has been chosen and will be used in this work.

Oxygen transport calculations in Cast3M require more CPU time than the finite volume solution of OXITRAN, and thus using very small time steps as in the latter takes too much time. To reduce CPU time, a simple time adaptive algorithm has been introduced. It uses the following equation:

$$\max \left( \underline{X}^{t+dt(k+1)} - \underline{X}^{t+dt(k)} \right) < 10^{-6} \quad (4.53)$$

to check the numerical convergence. If the condition is not fulfilled after  $k = 10$  iterations, the time step is divided by 2 and the calculation repeated. If there is no convergence after 10 divisions, further calculation is abandoned. In the application to the non linear heat of transport of Equation 4.16, the initial time step of 10 s was divided only once and the subsequent 5 s time step was sufficient to reach convergence.

2D and 3D geometries in ALCYONE describe one-eighth of a fuel pellet fragment with the overlaying gap and cladding. Examples of meshes are shown in Figure 4.8.

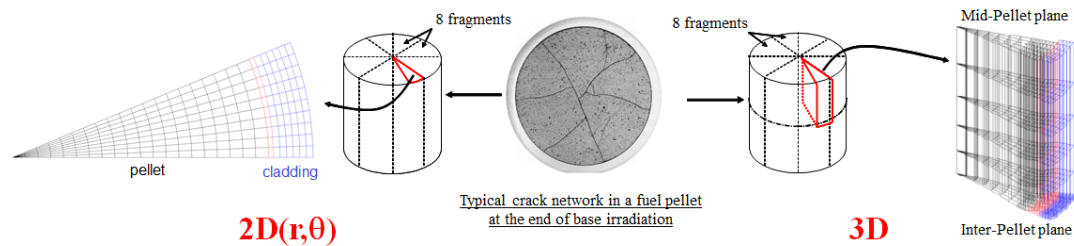


Figure 4.8: Examples of 2D and 3D meshes used in Cast3M.

The oxygen transport model has been written as a stand-alone Cast3M script. Simulations of oxygen redistribution in a fuel pellet fragment have been performed with 2D and 3D FE meshes close to those used in ALCYONE fuel performance code. The steady-state temperature distribution used in the simulations depends only on the radial coordinate and is given by Equation 4.2. The shape of the fuel fragment has been simplified because no dish or chamfer has been introduced. The simplified geometry and the lack of thermal gradient other than radial allows to compare the results from the 2D and 3D FE simulations to the 1D results from the FVM. The temperature distributions in the 2D and 3D models are plotted in Figure 4.9.

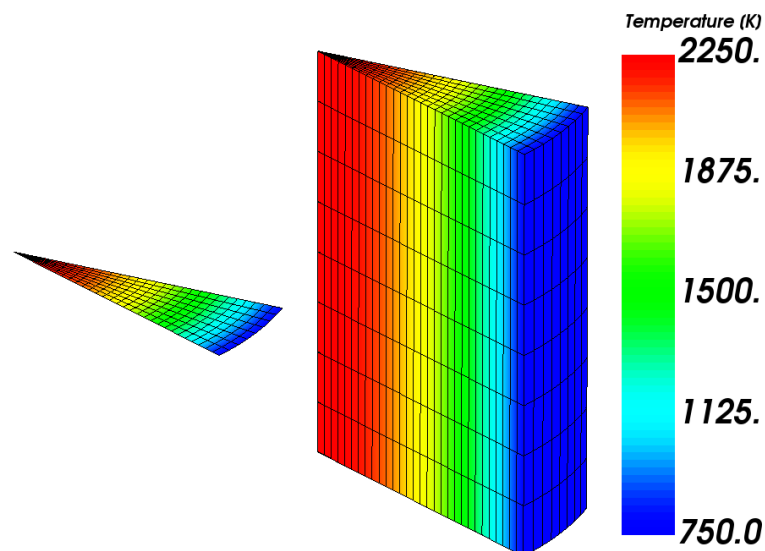


Figure 4.9: Temperatures in 2D and 3D calculated with Cast3M.

The initial stoichiometry deviation in the pellet is 0.005 ( $O/M=1.995$ ). It is assumed that the flux of oxygen on all external surfaces is null, which leads to oxygen conservation in the pellet fragment. The heat of transport of oxygen is  $-100$  kJ/mol and the diffusion coefficient is the one given in Equation 4.34. The distribution of the  $O/M$  ratio resulting

from oxygen redistribution calculated in 2D and 3D after 10000 s (steady-state) are shown in Figure 4.10.

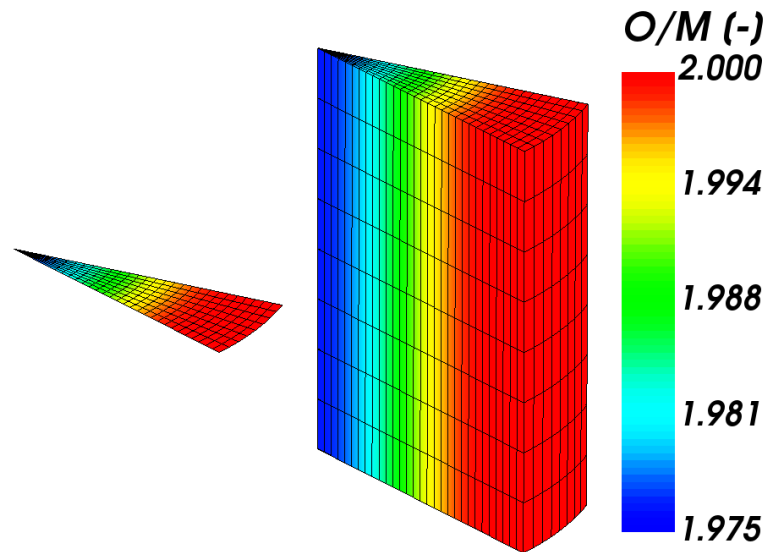


Figure 4.10: O/M in 2D and 3D calculated with Cast3M.

#### 4.2.2 Cross-comparison of 1D and 2D/3D solutions

A detailed comparison of the solutions in the different geometries has been done to check the consistency between the FEM and FVM. The radial profiles of temperature in the 1D, 2D and 3D simulations are identical. The initial stoichiometry deviation is 0.005. The simulations have been carried out with a constant heat of transport of -100 kJ/mol and with the diffusion coefficient mentioned previously (Equation 4.34). The comparison of the radial profiles of O/M ratio calculated at different times is shown in Figure 4.11.

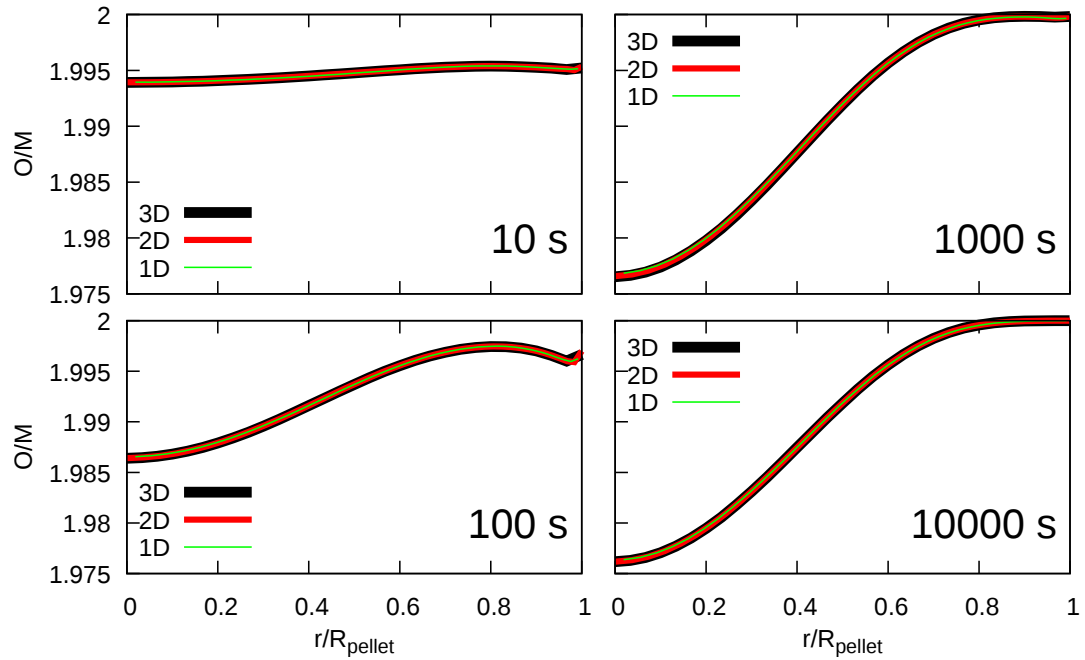


Figure 4.11: 1D, 2D and 3D O/M radial profiles at different times.

It can be seen that radial profiles of O/M ratio calculated at different times during the oxygen redistribution process are exactly the same meaning that the results from the finite element method used in 2D and 3D are consistent with the results from the finite volume method used in 1D.

### 4.2.3 Coupled heat and oxygen transport in 2D/3D

#### 4.2.3.1 COMSOL based solution

To check more thoroughly the 2D and 3D FE solutions developed in this work, a challenging simulation, based on Ramirez et al. [81], has been carried out. The authors used the COMSOL Multiphysics<sup>TM</sup> code to perform coupled heat and oxygen transport simulations of a reactor start-up in 2D. Ramirez et al. simulated a 22.5° angular section of a cylindrical fuel rod including heat transport in the helium gap and the cladding. The fuel pellet radius is 4.3 mm, the radial gap width is 0.03 mm and the cladding thickness is 0.5 mm. The heat and oxygen transport equations used by the authors are given by:

$$\rho C_p \frac{\partial T}{\partial t} = \text{div.} [k \underline{\text{grad}}(T)] + \dot{Q} \quad (4.54)$$

with

- $\rho$ —density [kg/m<sup>3</sup>]

- $C_p$ –heat capacity [J/kg/K]
- $k$ –thermal conductivity [W/m/K]
- $\dot{Q}$ –heat generation rate [W/m<sup>3</sup>]

$$\frac{\partial x}{\partial t} = \text{div.} \left[ \tilde{D}_O \left( \underline{\text{grad}}(x) + \frac{xQ_O^*}{F_{TD}RT^2} \underline{\text{grad}}(T) \right) \right] \quad (4.55)$$

where  $F_{TD}$  is the thermodynamic factor. Values and functions describing the parameters of Equations 4.54 and 4.55 are summarized in Table 4.1. One needs to remark that the heat and oxygen transport equations are fully coupled since the thermal conductivity coefficient  $k(\text{UO}_2)$  and the oxygen diffusion coefficient  $\tilde{D}_O(\text{UO}_2)$  depend on both temperature and stoichiometry deviation.

Table 4.1: Summary of the material properties used by Ramirez et al. [81].

Property	Dependence on temperature $T$ (K) and stoichiometry deviation $x$	Units	Reference
$C_p(\text{UO}_2)$	$264256 + 47T$	J kg <sup>-1</sup> K <sup>-1</sup>	[81]
$\rho(\text{UO}_2)$	$10960(a + bT + cT^2 + dT^3)^{-3}$ $a = 0.997, b = 9.082 \times 10^{-6}$ $c = -2.705 \times 10^{-10}, d = 4.391 \times 10^{-13}$ } $T < 923K$ $a = 0.997, b = 1.179 \times 10^{-5}$ $c = -2.429 \times 10^{-9}, d = 1.219 \times 10^{-12}$ } $T > 923K$	kg m <sup>-3</sup>	[185]
$k(\text{UO}_2)$	$k(T, x) = \lambda_0(T) \frac{\arctan[\theta(T, x)]}{\theta(T, x)} + 5.95 \times 10^{-11}T^3$ $\lambda_0(T) = [3.24 \times 10^{-2} + 2.51 \times 10^{-4}T]^{-1}$ $\theta(T, x) = 3.67 \exp(-4.73 \times 10^{-4}T) \sqrt{2x\lambda_0(T)}$	W m <sup>-1</sup> K <sup>-1</sup>	[186]
$Q_O^*(\text{UO}_2)$	$Q_O^*(x) = -1380.8 - 134435.5 \exp(-x/0.0261)$	J mol <sup>-1</sup>	[106]
$\tilde{D}_O(\text{UO}_2)$	$\log[\tilde{D}_O(T, x)] = -9.386 - \frac{4.26 \times 10^3}{T} + 1.2 \times 10^{-3}Tx + 7.5 \times 10^{-4}T \log\left(\frac{2+x}{x}\right)$	m <sup>2</sup> s <sup>-1</sup>	[86]
$F_{TD}(\text{UO}_2)$	$F_{TD}(T, x) = \frac{2+x}{2(1-3x)(1-2x)}$		[166]
$\rho(\text{He})$	$0.0818 - 8.275 \times 10^{-5}(T - 600)$	kg m <sup>-3</sup>	[187]
$C_p(\text{He})$	5190	J kg <sup>-1</sup> K <sup>-1</sup>	
$k(\text{He})$	$0.0468 + 3.81 \times 10^{-4}T - 6.79 \times 10^{-8}T^2$	W m <sup>-1</sup> K <sup>-1</sup>	
$\rho(\text{clad})$	7817	kg m <sup>-3</sup>	
$C_p(\text{clad})$	420	J kg <sup>-1</sup> K <sup>-1</sup>	
$k(\text{He})$	$10.98 + 0.014T - 7.44T^2$	W m <sup>-1</sup> K <sup>-1</sup>	

It must be emphasized that the parameters for oxygen transport refer only to hyperstoichiometric fuel. Ramirez et al. have studied the evolution of temperature and stoichiometry deviation during a reactor start-up. The power increase used in the simulation is given in Equation 4.56. As stated by the authors, this equation is rather a simple model

of quickly varying power source than an attempt to precisely model reactor behavior.

$$\dot{Q}(t) = \dot{Q}_0 + \frac{\dot{Q}_{max} - \dot{Q}_0}{1 + 10 \exp(10 - t/45)} \quad (4.56)$$

The initial heat generation rate is  $\dot{Q}_0=0 \text{ W m}^{-3}$  and it increases rapidly to reach its maximum value of  $2.8 \times 10^8 \text{ W m}^{-3}$ . The authors have prescribed a constant temperature on the outer surface of the cladding  $T_B = 750 \text{ K}$ . Heat transport is considered in the fuel pellet, in the gap and in the cladding. It is assumed that the stoichiometry deviation on the outer fuel surface ( $x_B$ ) is also prescribed. Three values of  $x_B$  were considered in the simulations of Ramirez et al. : 0.1, 0.01 and 0.001. The authors have studied the impact of this parameter on temperature evolution in the fuel pellet. Ramirez et al. have assumed that the flux of oxygen on the other surfaces is null. The oxygen transport problem is solved only in the fuel pellet. The finite element mesh and the boundary conditions used by the authors are shown in Figure 4.12.

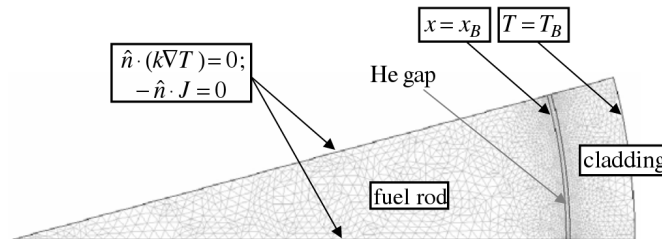


Figure 4.12: FE mesh of the fuel rod fragment simulated by Ramirez et al. Adapted from Ramirez et al. [81].

Initially, the temperature and stoichiometry deviations fields are uniform, and thus  $T_0=750 \text{ K}$  and  $x_0$  has values of 0.1, 0.01 and 0.001. The results calculated by Ramirez et al. are shown in Figure 4.13.

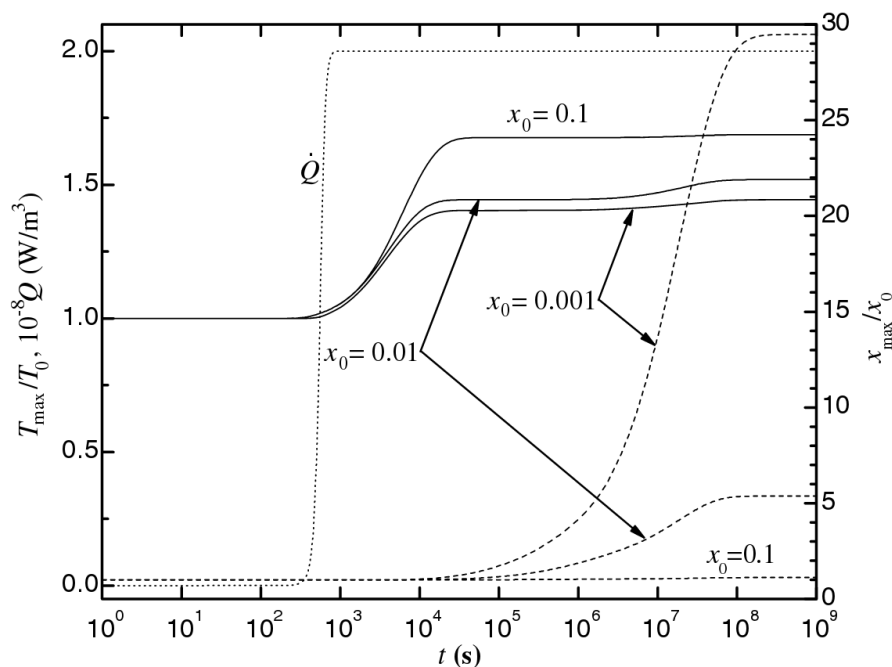


Figure 4.13: Results of the COMSOL Multiphysics simulation. Solid lines:  $T_{max}/T_0$ , dashed lines:  $x_{max}/x_0$ , dotted line:  $\dot{Q}$ . Adapted from Ramirez [81].

Figure 4.13 presents relative temperatures  $T_{max}/T_0$  (solid lines), relative stoichiometry deviations  $x_{max}/x_0$  (dashed lines) and the heat generation rate  $\dot{Q}$  (dotted line).  $T_{max}$  and  $x_{max}$  are the temperature and the stoichiometry deviation at the pellet center and  $T_0$  and  $x_0$  are initial values. The temperature profiles reach a quasi-steady state after around  $5 \times 10^4$  s. Significant oxygen transport occurs after this time because the radial temperature gradient is then sufficiently high. The highest relative stoichiometry variation  $x_{max}/x_0$  is for the lowest initial stoichiometry deviation and it reaches nearly 30. On the contrary, in the case of the highest initial stoichiometry deviation ( $x_0=0.1$ ), the  $x_{max}/x_0$  is nearly constant during the simulation. The change in stoichiometry deviation modifies the thermal properties of the fuel and hence the temperatures at the pellet center. The most visible change is for the initial stoichiometry  $x_0 = 0.01$ .  $T_{max}$  for this sample increases by 60 K at  $t = 10^6$  s. The oxygen redistribution is more significant for lower stoichiometry deviations because the heat of transport used by Ramirez et al. is very nonlinear near the exact stoichiometry. The late oxygen diffusion can be explained by the function used by Ramirez et al. for the chemical diffusion coefficient. One can see in Figure 4.14 that oxygen diffusion is much faster at high temperatures and low stoichiometry deviations.

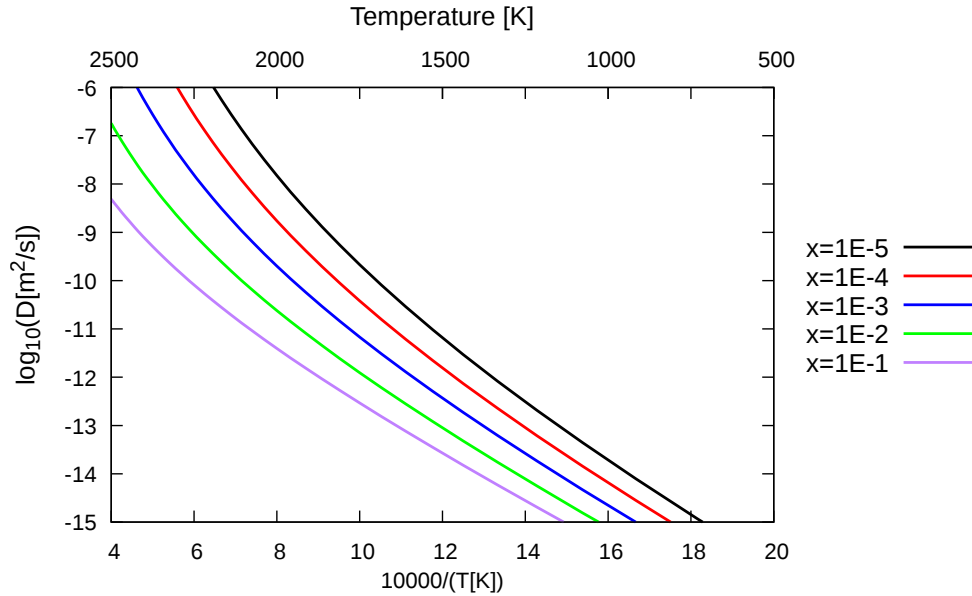


Figure 4.14: Diffusion coefficient proposed by Ramirez et al. [81].

To compare the heat and oxygen diffusion rates, Ramirez et al. have calculated the Lewis number  $Le$ , given by:

$$Le = \frac{k}{\rho C_p} / \tilde{D}_O \quad (4.57)$$

The Lewis number can be understood as the ratio of the times required to reach steady-states in heat and oxygen transport. Ramirez et al. plotted the Lewis number as a function of the stoichiometry deviation at different temperatures, reproduced in Figure 4.15. One can see that at 800 K the Lewis number reaches values around  $10^4$ . It means that the heat transport is four orders of magnitude faster than oxygen diffusion. The diffusion rates are similar at 1400 K when the Lewis number is close to 1. According to the curves, oxygen diffusion can even be faster than the heat diffusion ( $Le < 1$ ) at high temperatures and low stoichiometry deviations.

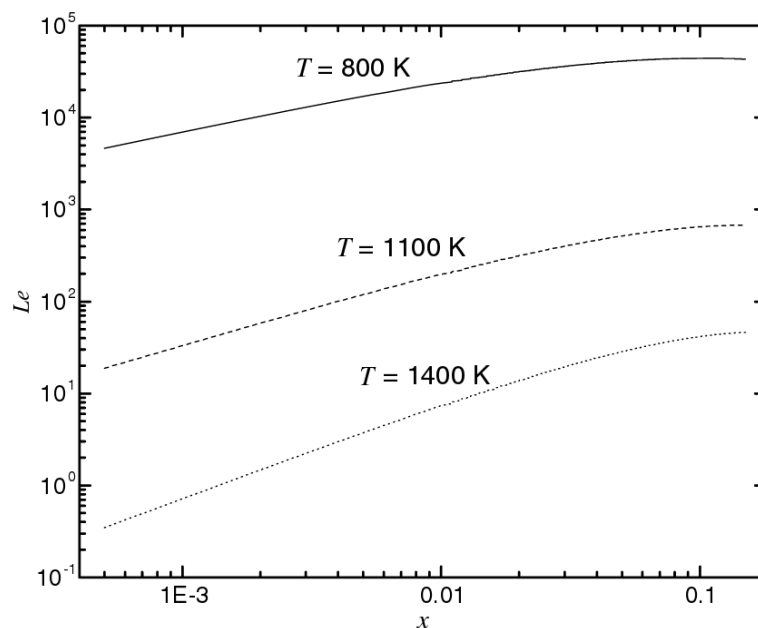


Figure 4.15: Lewis number as a function of the stoichiometry deviation at different temperatures. Adapted from Ramirez et al. [81].

#### 4.2.3.2 Cast3M solution

The simulation of Ramirez et al. has been repeated. All the equations and parameters proposed by the authors have been used in a Cast3M script in order to perform exactly the same simulation. The 2D finite element mesh generated in Cast3M, used in the simulation is shown in Figure 4.16. It is much more refined than the standard mesh used in ALCYONE. All the boundary conditions shown in Figure 4.12 have been applied.

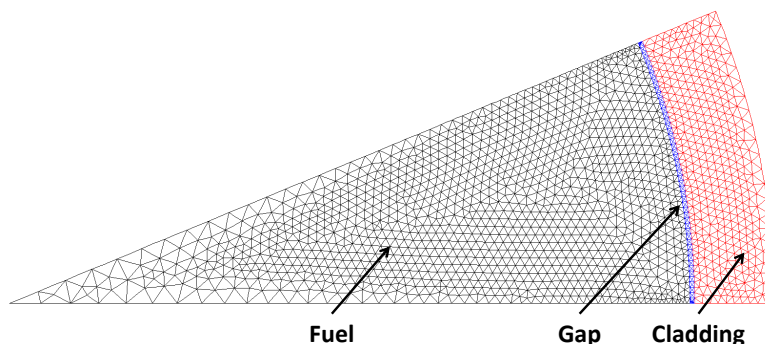


Figure 4.16: 2D FE mesh of the fuel rod fragment calculation performed with Cast3M.

In order to perform coupled heat–oxygen diffusion simulations, an algorithm containing two iterative loops has been developed, as shown in Figure 4.17. At the beginning of each time step, the thermal calculation is performed. Upon convergence, the oxygen transport calculation is launched. These two successive calculations are included in a global loop that is repeated until convergence of the coupled problem. This global loop is often referred as the Picard iterative process. It can be employed to solve coupled systems of differential equations [188], as in the case of the coupled heat and oxygen transport problem considered in this work. As explained before, the evolution of the stoichiometry deviation depends on temperature, and vice-versa. Convergence of the heat and oxygen transport equations is assumed when the following condition is fulfilled at all nodes:

$$\max(T^p - T^{p-1}) < 10^{-5} \text{ and } \max(x^p - x^{p-1}) < 10^{-5} \quad (4.58)$$

where  $p$  and  $p - 1$  refer to the current and the previous Picard iterations, respectively. This condition takes place in Figure 4.17 as the "Picard convergence test" box.

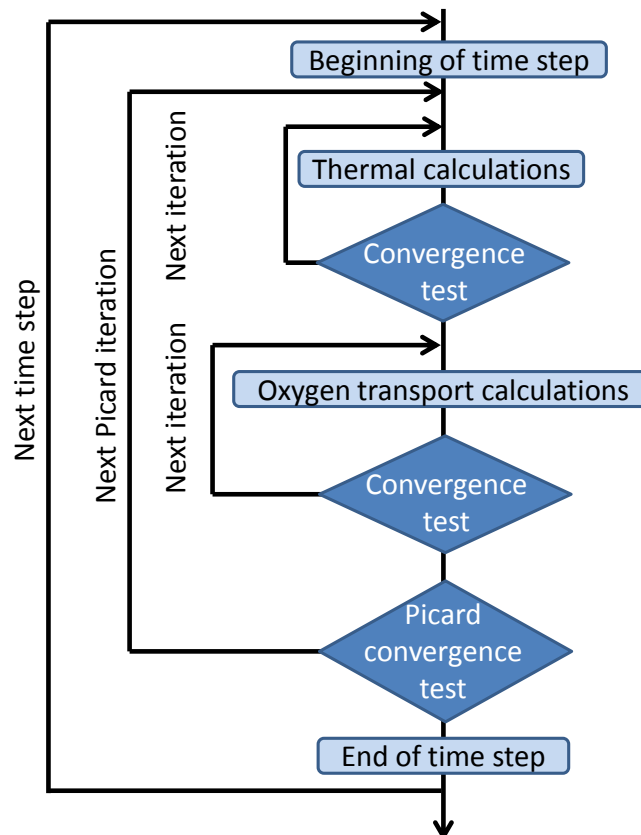


Figure 4.17: Schematic representation of iterative loops called in the Cast3M script.

The time step division method, described in the previous section, has not been applied in this simulation. The time step is expressed as a function of the Picard iteration

number  $i$  by:

$$dt = \exp\left(i^{1/2}\right) - \exp\left((i-1)^{1/2}\right) \quad (4.59)$$

The time step size and the total time are plotted as a function of the iteration number  $i$  in Figure 4.18. The time step increases exponentially to the maximum value  $dt = 2.5 \times 10^7$  s at  $i = 430$ . At this iteration the total simulated time is  $10^9$  s (around 31.7 years).

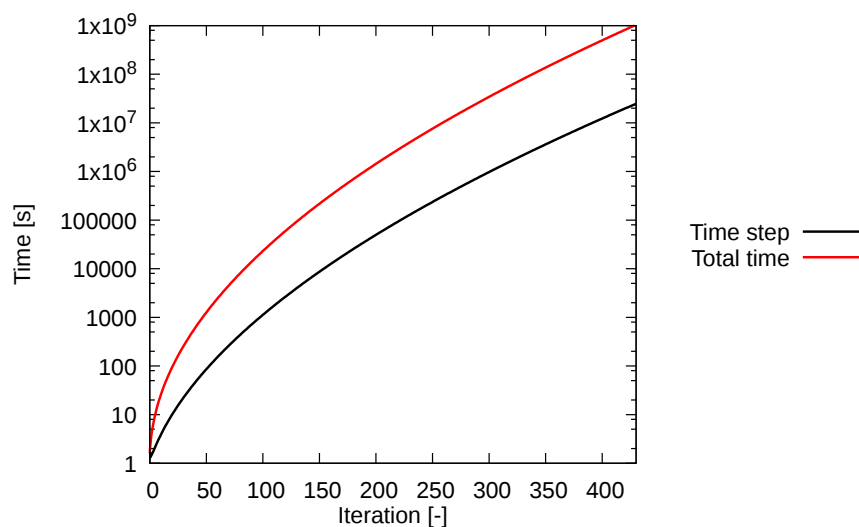


Figure 4.18: Simulated time and time step evolutions as a function of the iteration number.

Results of the Cast3M simulation (in red) are compared in Figure 4.19 to those obtained by Ramirez et al. (in black). The temperatures and stoichiometry deviations calculated with Cast3M are very close to the ones calculated by Ramirez et al. It confirms that the oxygen transport equation is correctly solved in the Finite Element code Cast3M and can be used in fuel performance simulations of power transients.

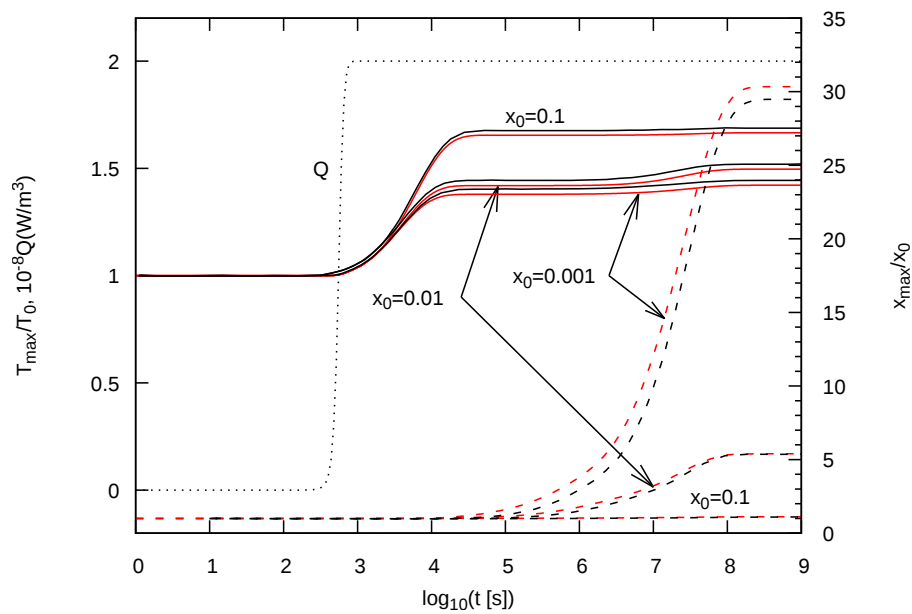


Figure 4.19: COMSOL results from Figure 4.13 (in black) compared to the results computed with Cast3M (in red).

Figure 4.20 shows the temperature radial profiles calculated at different times during the simulation with the initial stoichiometry deviation  $x = 0.001$ . One can clearly see that the most significant temperature increase occurs between  $10^3$  and  $10^4$  s, which is around 3 hours. After this time the temperature at the pellet center increases by only 50 K.

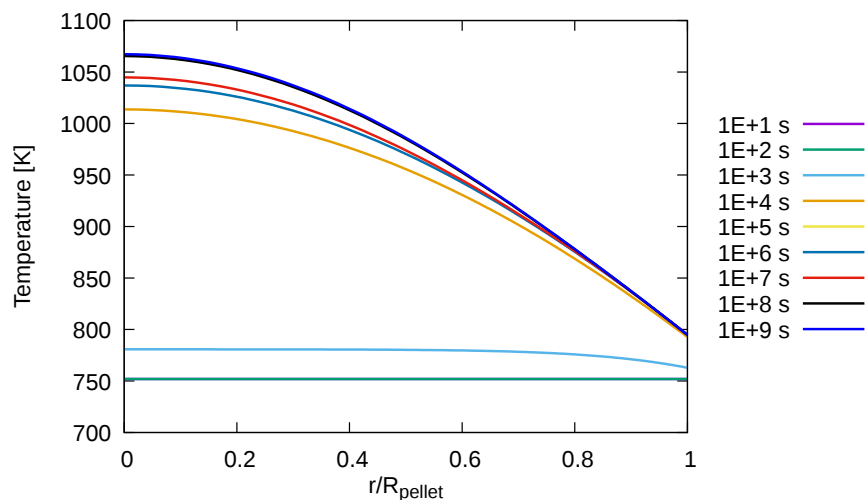


Figure 4.20: Temperature radial profiles at different times calculated with Cast3M.

The stoichiometry deviation radial profiles at different times are presented in Figure 4.21. The redistribution starts being noticeable after  $10^5$  s (around one day) when the temperature is quasi-constant. More than three years ( $10^8$  s) are needed to reach the steady-state, where the stoichiometry radial profile is close to the final profile calculated after  $10^9$  s.

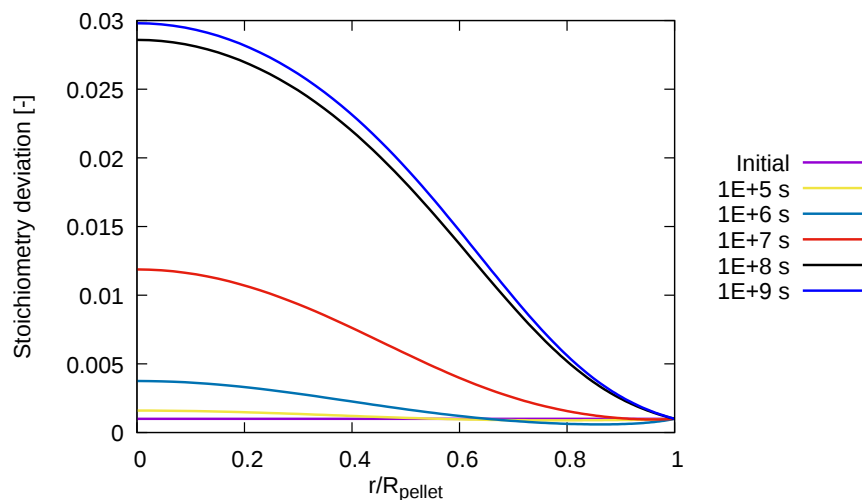


Figure 4.21: Stoichiometry deviation radial profiles at different times calculated with Cast3M.

The 2D simulation of Ramirez et al. has been repeated in 3D with Cast3M. Figure 4.22 presents the 3D mesh used in the simulation. The shown pellet fragment is 0.03 mm thick. All the parameters are the same as in the 2D simulation. The 2D boundary conditions shown in 4.12 are extended in 3D, i.e., the 2D boundary conditions on the contours of Figure 4.12 are the same at each axial position in the 3D simulation.

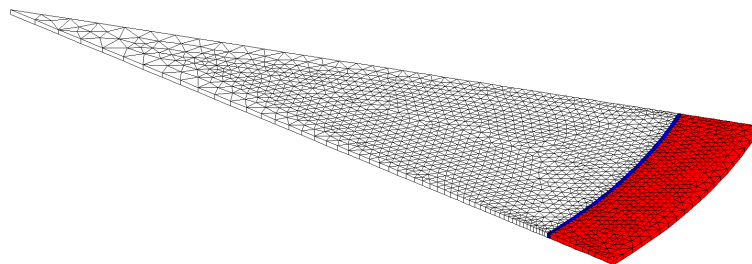


Figure 4.22: 3D FE mesh of the fuel rod fragment calculation performed with Cast3M.

Zero heat and oxygen flux are furthermore prescribed on the lower and upper surfaces of the fuel pellet fragment such that there is no axial temperature or stoichiometry gradients in the simulated fuel pellet. Thus, the radial temperature and stoichiometry

deviation profiles at each of axial positions are exactly the same. Obtained curves are the same as those calculated in 2D and shown in Figure 4.20. The stoichiometry deviation radial profiles calculated at different times are exactly the same as those obtained in the 2D simulation and presented in Figure 4.21.

### 4.3 Parameters of oxygen transport in irradiated fuel

This section presents the determination of the two main parameters governing oxygen transport in nuclear fuels: the heat of oxygen transport  $Q_O^*$  and the chemical diffusion coefficient of oxygen  $\tilde{D}_O$ .

#### 4.3.1 Heat of transport

Concerning the heat of transport, most of the simulations presented in the open literature are concerned with hyperstoichiometric fuel and use the experimental heat of transport measured by Sari and Schumacher [106] on non-irradiated fuels. In Section 3.3.1, it was shown from the simulations of irradiated fuel thermochemistry with ANGE that the material becomes slightly hypostoichiometric with irradiation ( $O/M < 2$ ). The experimental data of Sari and Schumacher obtained on hypostoichiometric materials refer to mixed oxide fuels and can hardly be applied to  $UO_2$  fuels since the evolution of the measured heat of transport was related to the Pu valence. It must furthermore be mentioned that Sari and Schumacher's heats of oxygen transport were possibly overestimated due to thermoelectric interference with the external cover [108].

In this work, to overcome these difficulties, the heat of transport has been identified by inverse analysis using the weight fractions of chromium measured by EPMA along the pellet radius after several power ramps [52]. The advantage of this approach, originally proposed by Baurens [62], is to use experimental data on irradiated fuels to derive the heat of transport. The entire fitting procedure is detailed in this section.

##### 4.3.1.1 Experimental observations

Four power ramps with post-irradiation measurements of Cr by EPMA are available at CEA to identify the heat of oxygen transport in irradiated  $UO_2$ . They were all performed on Cr-doped  $UO_2$  fuel rods with dopant contents of 1600 or 2000 ppm and in the same Materials Testing Reactor OSIRIS [24]. Details of these experiments (referred as PR1 to PR4) are shown in Table 4.2.

Table 4.2: Main characteristics of the power ramp tests on Cr-doped fuels.

Test name	% $^{235}\text{U}$	Dopant $\text{Cr}_2\text{O}_{3(s)}$ [ppm]	Initial O/U	Average burnup [GWd/tHM]	Max. LHR [W/cm]	Cond. Period [h]	Cond. Power [W/cm]	Period [h]	Holding Period [h]	T2 [s]	T3 [s]
PR1	4.9	1600	2.00±0.01	32	470	18	169	0	182	~10	
PR2	4.9	1600	2.00±0.01	38.8	468	18	196	12	161	~10	
PR3	3.7	2000	2.00±0.01	29.9	467	16	203	12	152	~10	
PR4	3.7	2000	2.00±0.01	26.7	535	20	198	12	198	~10	

A schematic representation of the ramp test sequence is given in Figure 4.23.

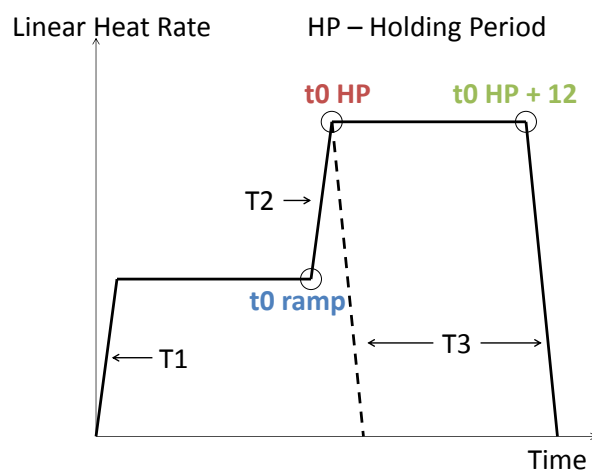


Figure 4.23: Schematic representation of the power ramp tests. The part until "t0 HP" is common for all the ramps. The solid line starting at "t0 HP" is for PR2, PR3 and PR4 and the dashed one is for PR1. Three power transients are marked as T1, T2 and T3.

All power ramps start with a conditioning period of 16 to 20 hours at a power level (169-203 W/cm) close to the one seen by the fuel rod during the last irradiation cycle in the commercial PWR that preceded the power ramp. At the end of the conditioning period ("t0 ramp"), the power starts to increase (transient of duration T2) until it reaches its maximum at "t0 HP" (468-535 W/cm). The power increase rate is close to 100 W/cm/min. Duration of the transient is less than 3 minutes. In PR2, PR3 and PR4 the Holding Period (HP) at the maximum LHR lasted 12 h, ending at "t0 HP+12h" as represented in Figure 4.23. In PR1, the power was immediately decreased after reaching the maximum LHR (no holding period, dashed line in Figure 4.23). In all power ramps, the return to zero power takes around 50 minutes (transient of duration T3). All the fuel rodlets survived the transient undamaged in spite of the very high LHR reached.

The Cr radial profile after PR1 as measured by EPMA is presented in Figure 4.24 and has been obtained for the sake of this PhD.

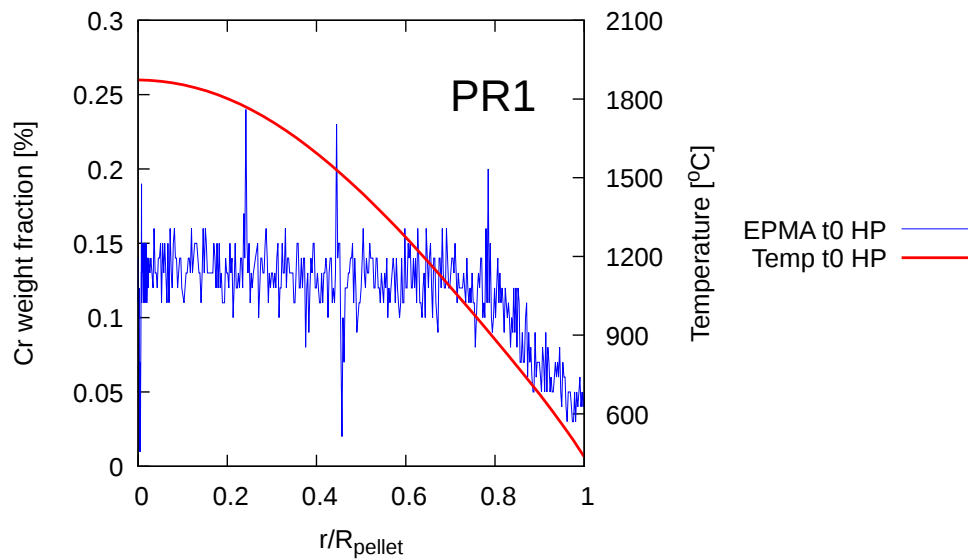


Figure 4.24: EPMA measurements of the weight fraction of Cr in solid solution after PR1.

As reported by Riglet-Martial [53], the solubility of Cr in fresh uranium dioxide as  $\text{Cr}_2\text{O}_3(ss)$  is close to 0.1 wt% (sintering temperature 1700-1760 °C). As can be seen from Figure 4.24, the Cr content measured after PR1 is consistent with the solubility of Cr in fresh  $\text{UO}_2$  meaning that the high temperatures (around 2200 K) reached at the pellet center during the power ramp had no impact on the chromium oxide  $\text{Cr}_2\text{O}_3(ss)$  dissolved in the fuel. It must be emphasized that the Cr content decrease observed at the periphery of PR1 is due to the evaporation of part of the Cr during the fabrication process and is not induced by the power ramp.

The Cr radial profiles after PR2, PR3 and PR4 as measured by EPMA are presented in Figure 4.25-4.27.

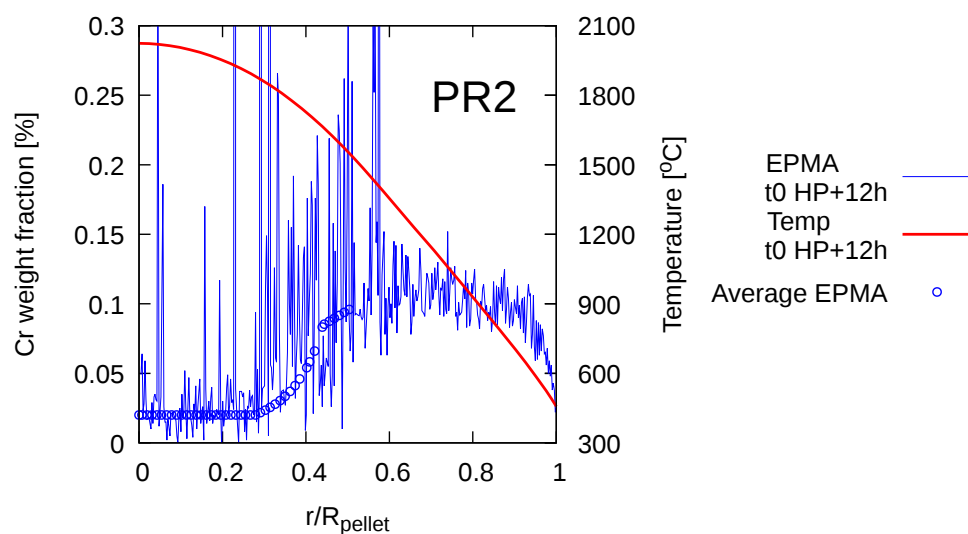


Figure 4.25: EPMA measurements of Cr weight fraction in solid solution after PR2. The red curve is the calculated temperature profile. Blue circles show the average local Cr concentration.

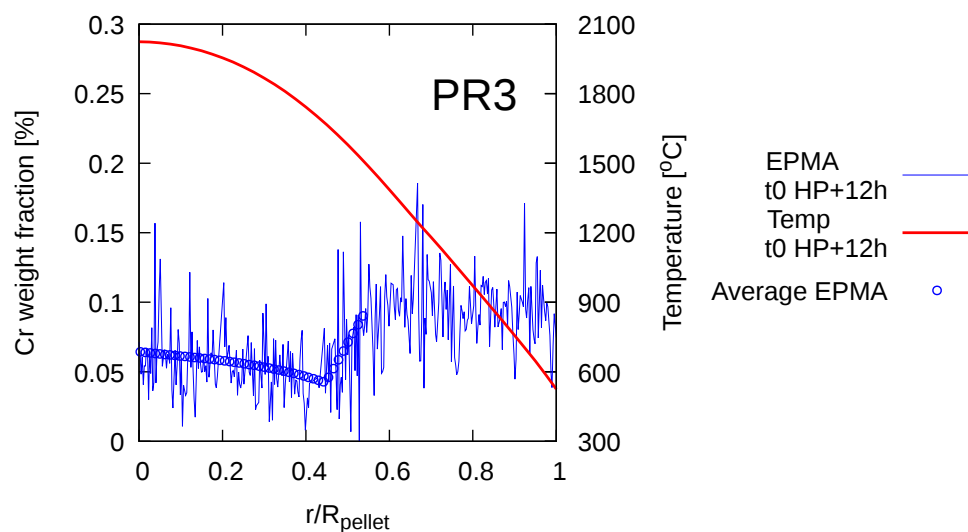


Figure 4.26: EPMA measurements of Cr weight fraction in solid solution after PR3. The red curve is the calculated temperature profile. Blue circles show the average local Cr concentration.

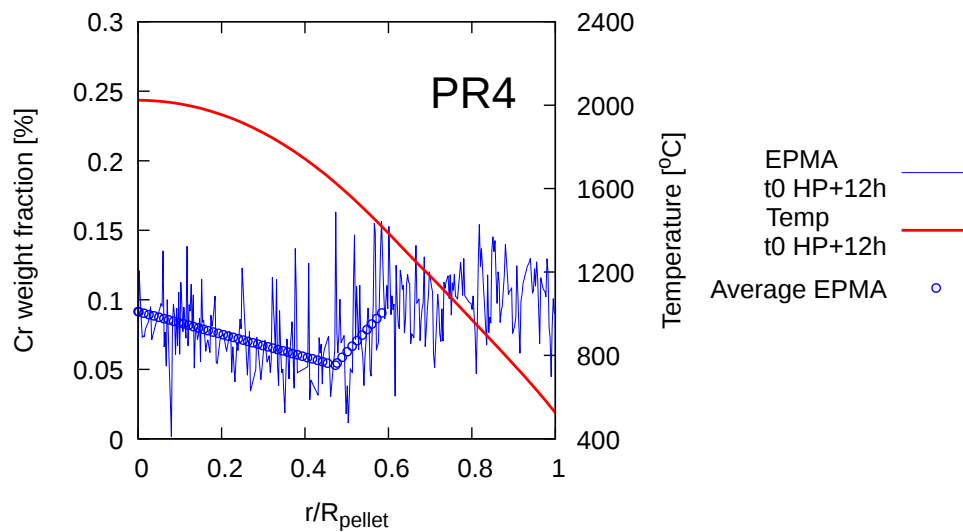


Figure 4.27: EPMA measurements of Cr weight fraction in solid solution after PR4. The red curve is the calculated temperature profile. Blue circles show the average local Cr concentration.

As reported by Riglet-Martial [52] and mentioned in Section 2.1.3.2, the EPMA Cr radial profiles measured after power ramps where a long HP of 12 h at maximum LHR has taken place, show a noticeable decrease of Cr content in the central part of the fuel pellet. This decrease has been attributed to the reduction of the chromium oxide  $\text{Cr}_2\text{O}_3(ss)$  initially dissolved in the fuel into metallic chromium precipitates. In fact, X-ray images of the pellet center of PR2 have indicated that the spots where Cr and Mo are visible, show a deficit in oxygen, as illustrated in Figure 4.28. X-ray images of PR3 and PR4 have shown similar results.

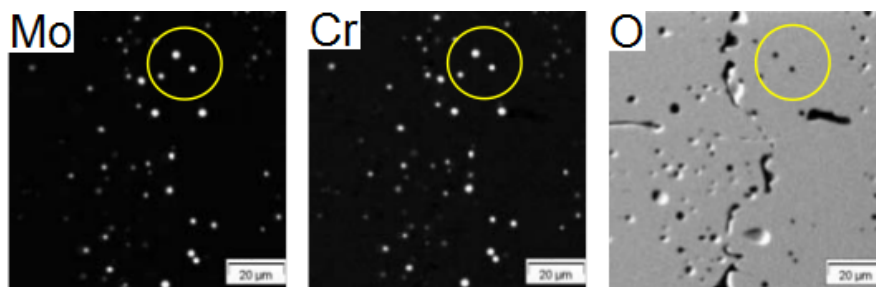


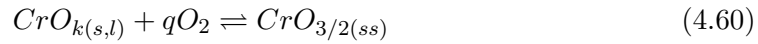
Figure 4.28: X-ray maps of Mo, Cr and O at the pellet center after power ramp PR2 [52].

The Cr reduction at the pellet center has therefore been attributed to a reductive perturbation that could be explained by oxygen redistribution during the long holding period

at maximum LHR (and high temperature gradient). It must be emphasized that similar observations were made on samples with different initial Cr content and different irradiation conditions (different burnups). Also, not mentioned in Table 4.2, PR1 and PR2 were cladded with M5 while PR3 and PR4 were cladded with Stress-Relieved Zy4. Another important observation is that the residual Cr content measured by EPMA at the pellet center is non zero and can therefore be used to assess the oxygen potential reached by the fuel during the holding period of the power ramp, assuming the 10 seconds long return to zero power did not impact the Cr profile. Finally, one may notice that the EPMA profiles of PR2, PR3 and PR4 give Cr content close to the solubility of Cr in fresh  $\text{UO}_2$  ( $\sim 0.1\%$ ) from mid-radius till the pellet periphery. The temperatures in this part are usually not exceeding 1800 K, therefore below the sintering temperature of  $\sim 2000$  K. It is therefore very likely that the high Cr content measured by EPMA in this region shows the lack of evolution of the material during the power ramps in spite of the temperature increase.

#### 4.3.1.2 Oxygen potential reached at the pellet center

The EPMA profiles of Cr can be used to estimate the oxygen potential reached at the pellet center during the power ramps. The chromium solubility model proposed by Riglet-Martial et al. [53] describes the solubilization in the fuel of the chemical species  $\text{CrO}_{k(s,l)}$  (with  $k = 0, 1$  or  $3/2$ ) according to the following equation:



where the possible  $\text{CrO}_{k(s,l)}$  compounds are given in Table 3.15 and  $q = (3/2 - k)/2$ . The equilibrium constant of the reaction can be expressed as follows:

$$K_s(T) = \frac{y_{Cr}}{P_{O_2}^q} \quad (4.61)$$

where the activity of  $\text{CrO}_{3/2(ss)}$  has been replaced by the Cr mole fraction  $y_{Cr}$ . Riglet-Martial et al. expressed the Gibbs energy of the reaction  $\Delta G_r^\circ(T) = -RT \log(K_s(T))$  as a linear function of temperature leading to the following relation between the Cr mole fraction  $y_{Cr}$  dissolved in the fuel and the oxygen partial pressure  $p_{O_2}$  and the temperature:

$$\log_{10} y_{Cr} = q \log_{10} p_{O_2} + V + \frac{U}{T} \quad (4.62)$$

where  $q$ ,  $V$  and  $U$  are coefficients from Table 2.3. EPMA profiles are usually given in Cr weight fraction  $w$ , which can be simply expressed as follows as a function of the Cr mole fraction:

$$w(\text{Cr}) = \frac{y_{Cr} M_{Cr}}{(1 - y_{Cr}) M_U + y_{Cr} M_{Cr} + 2M_O} \quad (4.63)$$

with  $M_{Cr}$ ,  $M_U$  and  $M_O$  the molar densities of Cr, U and O, respectively. Note that the FPs are neglected since they only represent a small percentage of the fuel mass. As shown by the phase diagram of Figure 3.27,  $CrO_{3/2(ss)}$  might be formed from  $CrO_{3/2(s)}$ ,  $CrO_{(l)}$  or  $Cr_{(s)}$  depending on temperature and oxygen potential. Below 1650 °C, only the chemical compounds  $CrO_{3/2(s)}$  and  $Cr_{(s)}$  are stable. Above this temperature, the three compounds might be stable in the fuel. According to Equation 4.62, in the predominance domain of  $CrO_{3/2(s)}$ , the Cr mole fraction does not depend any more on the oxygen partial pressure ( $q = 0$ ). The determination of the oxygen partial pressure from the EPMA Cr profiles can therefore only be achieved in the region where  $CrO_{(l)}$  or  $Cr_{(s)}$  precipitates are found, i.e., in the central part of the fuel pellet till approximately mid-radius.

To find the oxygen potential ( $RT \ln p_{O_2}$ ) at various locations along the fuel pellet radius, it is necessary to estimate the chromium weight fractions and the temperatures along the radius. To do so, an averaging of the EPMA measurements every 5  $\mu\text{m}$  resulting in around 80 points, as shown in Figures 4.25-4.27, has been made. The temperatures  $T$  have been estimated from 1D simulations of the base irradiation and of the power ramps carried out in ALCYONE. The base irradiation conditions are given in Table 4.3. 'Cooling time' is the time between the base irradiations and the power ramps. 'Average LHR' gives the LHR of the fuel pellet where the Cr content was measured.

Table 4.3: Main characteristics of the base irradiations preceding tests PR2, PR3 and PR4.

Test name	Radius [mm]	% $^{235}\text{U}$	Dopant $Cr_2O_{3(ss)}$ [wt%]	Initial O/U	Average burnup [GWd/tHM]	Average LHR [W/cm]	Cooling Time [y]
PR2	4.096	4.9	0.16	2.00±0.01	38.8	192	4.8
PR3	4.0945	3.7	0.20	2.00±0.01	29.9	248	1.3
PR4	4.0945	3.7	0.20	2.00±0.01	26.7	231	1.7

The power ramp experiments are simulated with the data given in Table 4.2. The calculated radial temperature profiles at "t0 HP+12h" are plotted as red curves in Figures 4.25-4.27. The averaged weight fractions of Cr and the simulated temperature profiles have been used to estimate the oxygen potential at the pellet center according to Equation 4.62. The radial profiles of oxygen potential till mid-radius of the pellets are shown in Figure 4.29.

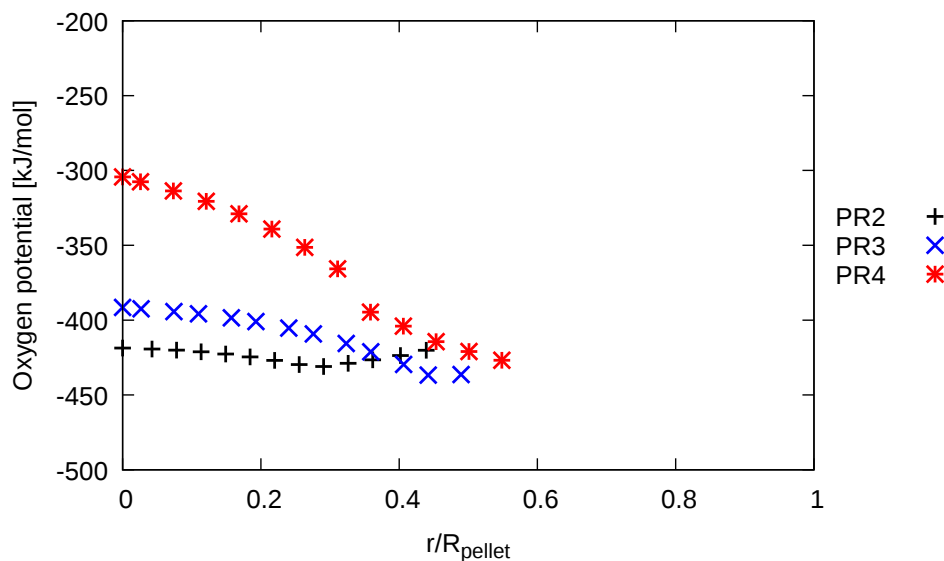


Figure 4.29: Oxygen potential radial profiles deduced from the Cr solubility model.

Only the central part (until around  $r/R_{pellet}=0.5$ ) of the pellets has been considered for the reason mentioned above. It may also not be granted that the entire fuel pellet is in thermodynamic equilibrium. It is assumed that only the high temperatures encountered at the pellet center ensure thermodynamic equilibrium during the 12h long HP (2000-2500 K). The remaining part of the pellet and in particular the pellet periphery is not hot enough (700-800 K). It can be noticed that the oxygen potentials reached at the pellet center in PR2 and PR3 till mid-radius are nearly constant and close to each other ( $\sim -400$  kJ/mol  $O_2$  and  $\sim -420$  kJ/mol  $O_2$ ) as could be expected from the similarities of the power ramps (max. temperature around 2200 K). On the contrary, PR4 in which the temperature reached the highest value (2500 K) gives a somewhat higher oxygen potential (-300 to -400 kJ/mol  $O_2$ ) which seems furthermore to follow the temperature radial profile. It must be emphasized that the chromium solubility model is valid till temperatures  $\sim 2100$  K and that any extrapolation at higher temperatures is questionable. It is also possible that the high temperature reached during PR4 have led to some partial reversibility of oxygen redistribution during the return to zero power phase. The measured EPMA profile could therefore not be representative of the holding period at maximum LHR.

#### 4.3.1.3 O/M ratios reached at the pellet center

The oxygen potentials deduced from the Cr solubility model are not sufficient to estimate the heat of oxygen transport. The oxygen thermal diffusion model used in this work is expressed as a function of the stoichiometry deviation  $x$  or equally as a function

of the oxygen over metal ratio O/M in the fluorite solid solution. The O/M ratios corresponding to the oxygen potentials of Figure 4.29 can be calculated with ANGE by performing a set of thermochemical equilibrium calculations at prescribed temperature, pressure and oxygen potentials. The temperatures and pressures are extracted from ALCYONE simulations of the power ramps. The elemental compositions needed to run ANGE have been calculated with PRODHEL, also included in ALCYONE fuel performance code. The concentrations of representative elements are shown in Table 4.4. Calculated values are average values returned by PRODHEL at the pellet center. This simplification is possible because the burnup radial profiles in the central part of the pellets are nearly flat, as shown in Figure 4.30.

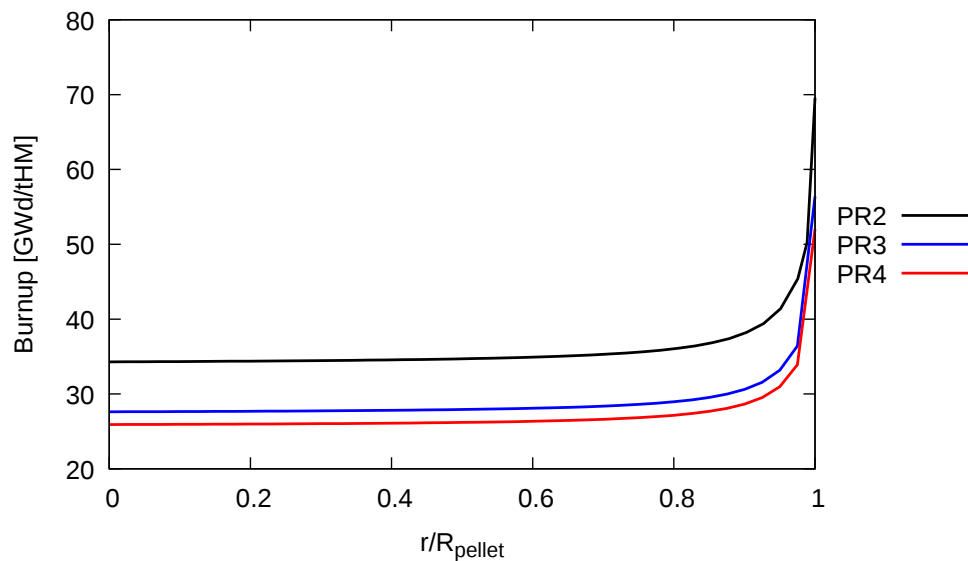


Figure 4.30: Burnup radial profiles of PR2, PR3 and PR4 calculated with ALCYONE.

Table 4.4: Elemental compositions used in ANGE calculations for modeling of PR2, PR3 and PR4.

Representative element	Concentration [mol/mol UO <sub>2</sub> ]		
	PR2	PR3	PR4
He	$1.12 \times 10^{-2}$	$9.23 \times 10^{-3}$	$8.67 \times 10^{-3}$
Cs	$6.02 \times 10^{-3}$	$5.00 \times 10^{-3}$	$4.70 \times 10^{-3}$
Te	$1.11 \times 10^{-3}$	$8.96 \times 10^{-4}$	$8.40 \times 10^{-4}$
I	$4.56 \times 10^{-4}$	$3.76 \times 10^{-4}$	$3.52 \times 10^{-4}$
Mo	$8.88 \times 10^{-3}$	$7.14 \times 10^{-3}$	$6.72 \times 10^{-3}$
Ba	$5.69 \times 10^{-3}$	$4.35 \times 10^{-3}$	$4.12 \times 10^{-3}$
Zr	$1.06 \times 10^{-2}$	$8.23 \times 10^{-3}$	$7.80 \times 10^{-3}$
Ce	$6.46 \times 10^{-3}$	$5.42 \times 10^{-3}$	$5.05 \times 10^{-3}$
La	$3.72 \times 10^{-3}$	$2.97 \times 10^{-3}$	$2.81 \times 10^{-3}$
Gd	$7.53 \times 10^{-3}$	$5.98 \times 10^{-3}$	$5.67 \times 10^{-3}$
Eu	$1.58 \times 10^{-3}$	$1.10 \times 10^{-3}$	$1.05 \times 10^{-3}$
Ru	$8.38 \times 10^{-3}$	$6.99 \times 10^{-3}$	$6.52 \times 10^{-3}$
Pd	$2.53 \times 10^{-3}$	$2.02 \times 10^{-3}$	$1.85 \times 10^{-3}$
Pu	$9.02 \times 10^{-3}$	$7.85 \times 10^{-3}$	$7.53 \times 10^{-3}$
U	$9.54 \times 10^{-1}$	$9.63 \times 10^{-1}$	$9.65 \times 10^{-1}$
Cr	$5.00 \times 10^{-3}$	$7.03 \times 10^{-3}$	$7.03 \times 10^{-3}$

O/M values returned by ANGE are shown in Figure 4.31.

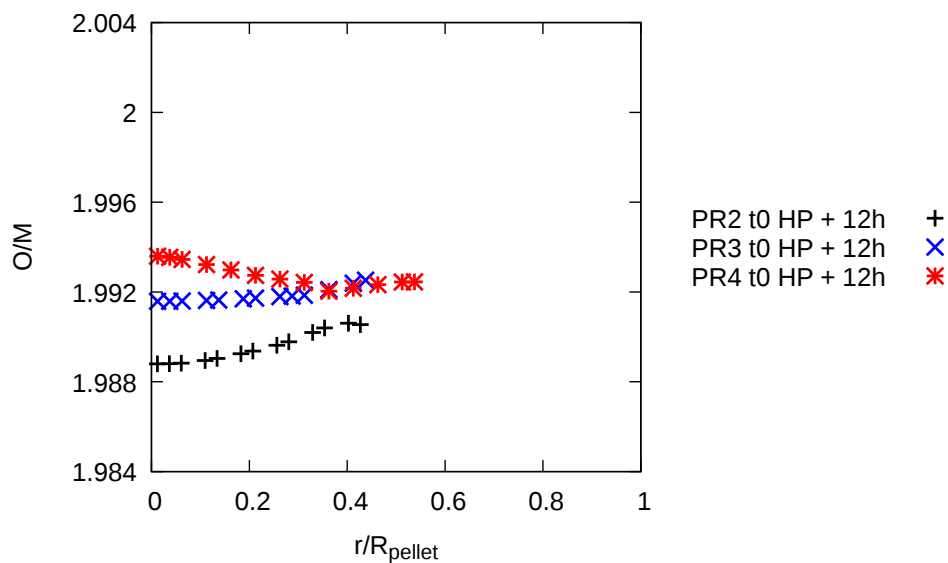


Figure 4.31: O/M radial profiles from ANGE calculations.

One may notice that the values are still very close to 2 and within experimental error  $2 \pm 0.01$  which might explain why oxygen redistribution is generally not considered in PWR fuels simulations. The relative position of the O/M profiles is similar to the one obtained from the oxygen potential profiles. Comparing PR2 and PR3, it appears that PR2 has the lowest post-ramp O/M ratios ( $\sim 1.989$  compared to  $\sim 1.992$ ) owing to its higher burnup (38.8 for 29.9 GWd/tHM). As discussed in Section 3.3.1, an increasing burnup leads to a decreasing O/M ratio at a given oxygen potential. One may see that the O/M ratio at the pellet center of PR4 is higher in spite of the higher temperatures reached during this transient. This result is unexpected since solubility of fission products in solid solution increases with temperature and should therefore lead to a lower O/M ratio. As explained before, the validity of the chromium solubility model and a possible reversibility during the return to zero power could be at the origin of the discrepancies. For these reasons, the O/M ratios estimated from PR4 have not been taken into account in the derivation of the heat of oxygen transport.

#### 4.3.1.4 Heat of oxygen transport fitting

The post-ramp O/M profiles of Figure 4.31 characterize the state of the fuel when steady-state oxygen thermal diffusion is reached at the end of the HP of the ramp. To estimate the magnitude of oxygen redistribution during the power ramps, it is now necessary to estimate the O/M radial profiles at the start of the HP of the ramp, i.e., when oxygen thermal diffusion started. It is important to recall that the temperature radial profile does not evolve during the HP of the ramp. To estimate the O/M radial profiles at the start of the HP, a second series of thermochemical equilibrium calculations with ANGE are performed, this time at prescribed temperature, pressure and oxygen content (post-ramp calculations are performed at prescribed oxygen potential), the latter being equal to the initial oxygen content of the fuel after fabrication. The calculated O/M radial profiles are plotted as dashed lines in Figure 4.32. The post-ramp radial profiles deduced from the EPMA Cr profiles are recalled in the same Figure (points).

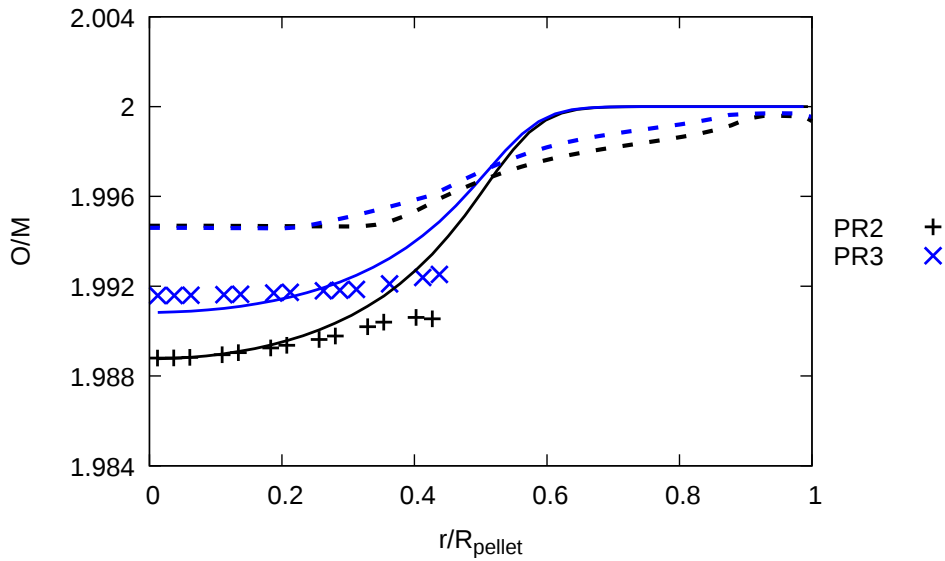


Figure 4.32: Initial O/M (dashed lines), steady-state O/M calculated with OXIREM (solid lines) compared to the O/M calculated with ANGE (points). PR2 is in black and PR3 in blue.

The O/M profiles at the start of the HP of PR2 and PR3 are very close to each other with a value of  $\sim 1.994$  at the pellet center. Again, the stoichiometry deviation is very small, within the measurements error. While the O/M ratio decreased from 1.994 to 1.989 during the HP of PR2, a smaller decrease took place in PR3 (1.994 to 1.992). It is these changes in O/M ratios that will be used to fit the heat of oxygen transport assuming that steady-state oxygen thermal diffusion is reached during the 12 h long HPs and considering that the radial temperature profiles are constant (the LHRs are constant during the HPs). In these specific conditions, the O/M change at the pellet center depends only on the heat of oxygen transport  $Q_O^*$  and on the average O/M ratio along the fuel pellet radius.

Since steady-state is reached, the OXIREM model described in Section 4.1.2 has been used to fit the heat of oxygen transport to the change in O/M ratio during the power ramp. A non linear relation for the heat of transport of oxygen has been chosen, based on the following mathematical form:

$$Q_O^* = A \exp \left[ B \left( 4 + \frac{2(O/M - 2)}{0.0127\tau_c} \right) \right] \text{ [J/mol]} \quad (4.64)$$

where  $A$  and  $B$  are the coefficients to be fitted. Equation 4.64 is similar in its form to the one proposed by Lassmann for hypostoichiometric mixed oxide fuel [86]. Lassmann's expression was dependent on the valence of Pu ( $V_{Pu} = 4 + \frac{2(O/M - 2)}{q}$  with  $q$  the Pu mole fraction) because the deficit in oxygen was associated with plutonia assuming that the hypostoichiometric fuel may be considered as a solid solution of  $UO_2$  and  $PuO_{2-x}$ .

An extension of this approach to a solid solution containing several fission products leading to a hypostoichiometric irradiated fuel has been proposed by Baurens [62]. It basically consists in relating the heat of transport to the mole fraction of fissioned uranium atoms ( $0.0127\tau_c$  with  $\tau_c$  the burnup in at%), the latter being an indicator of the FPs inventory in the fuel.

In the first step of the fitting, the O/M radial profile in the fuel pellet at the start of the HP has been used to estimate the average O/M ( $\overline{O/M} = 2 - \bar{x}$  with  $\bar{x}$  the average stoichiometry deviation) in the fuel. OXIREd is then used to calculate the O/M radial profile at steady-state from the average O/M ratio and from the radial temperature and burnup profiles of Figure 4.30. The fitting of parameters  $A$  and  $B$  for the heat of oxygen transport (Equation 4.64) has been done with the Solver package available in Excel [189]. The solver optimizes the parameters by minimizing the error  $E$ . The optimization is done using the Generalized Reduced Gradient (GRG) method and it requires imposing the starting values  $A$  and  $B$ . As reported by the Solver developers, in nonlinear problems, the program returns only a locally optimal solution, and thus it is suggested to repeat the fitting procedure with different starting values. This suggestion has been followed. The author has chosen starting values that lead to a good fit in particular at the pellet center ( $r/R_{\text{pellet}} < 0.3$ ). Fission gas release during the first few minutes of a power ramp is the highest at the very center and for this reason it is important to correctly estimate the impact of oxygen transport on thermochemistry in this region. Convergence of the solver was based on a minimization of the difference between the steady-state O/M ratios of OXIREd and the O/M ratios calculated from the Cr content by EPMA, according to:

$$E_{PR_i} = \sum_{j=1}^N \left| \frac{O}{M}_{Cr(j)} - \frac{O}{M}_{OXIREd(j)} \right| \quad (4.65)$$

where  $N$  is the number of points used to calculate the error. The sum of errors from PR2 and PR3 has been used for the fitting. The heat of oxygen transport with the fitted parameters is given by:

$$Q_O^* = -8.87 \times 10^{-4} \exp \left[ 4.94 \left( 4 + \frac{2(O/M - 2)}{0.0127\tau_c} \right) \right] [\text{J/mol}] \quad (4.66)$$

The O/M radial profiles in the fuel pellet calculated with the fitted heat of transport are represented with solid lines in Figure 4.32 and compared to the O/M profiles at the start of the HP (represented with dashed lines) and to the O/M ratios deduced from EPMA measurements of the Cr content.

The fitted heat of oxygen transport leads to O/M radial profiles in good agreement with the O/M ratios deduced from the Cr content. As expected, the difference is the lowest at the pellet center ( $r/R_{\text{pellet}} < 0.3$ ).

The plot of Equation 4.66 shown in Figure 4.33 indicates a pronounced evolution of the heat of transport at a transition O/M ratio that decreases with burnup. The corrected heat of transport estimated by Janek [108] from Sari and Schumacher's measures on uranium plutonium mixed oxide fuels [106] is close to the function used in this work.

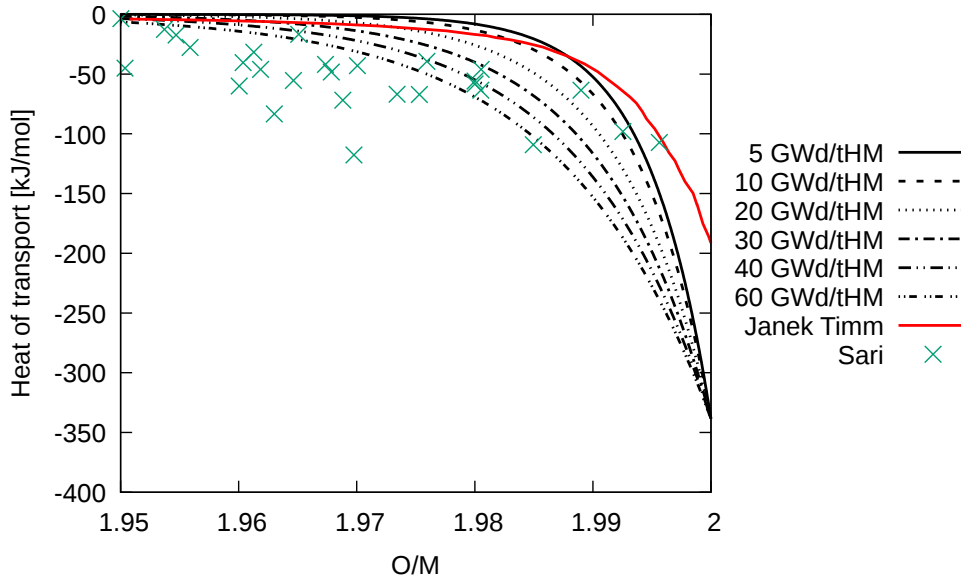


Figure 4.33: Heat of transport in  $\text{UO}_2$  fuels irradiated up to different burnups as a function of the O/M ratio compared to the model proposed by Janek [108], based on a reassessment of Sari's measures [106].

### 4.3.2 Chemical diffusion coefficient of oxygen

The second parameter of importance is the chemical diffusion coefficient of oxygen. As discussed in Section 2.2.1.2, most of the available measures concerning oxygen diffusion refer to self-diffusion experiments and have usually been performed on hyperstoichiometric non irradiated uranium dioxide. No measurement is available in irradiated fuels. There are furthermore very few measurements of the chemical diffusion coefficient of oxygen in non irradiated fuels. For this reason, the most recent work on oxygen diffusion in uranium dioxide have tried to assess the chemical diffusion coefficient of oxygen from the self-diffusion coefficient and from the thermodynamic factor, according to the following Equation:

$$\tilde{D}_O = D_O^* \frac{2 \pm x}{2} \frac{\partial \ln p_{O_2}}{\partial x} \quad (4.67)$$

where  $D_O^*$  and  $\tilde{D}_O$  are the self- and chemical diffusion coefficients, respectively. The self-diffusion coefficient can be related to the concentration of point defects (oxygen vacancies, interstitials or stoichiometry deviation) and to the temperature. The thermodynamic factor is also a function of these parameters. The chemical diffusion coefficient of oxygen should therefore depend on temperature and stoichiometry deviation. The

temperature dependency has been considered by Lassmann in his oxygen thermal diffusion model (see Equation 4.34) but not stoichiometry deviation. To assess the impact of the latter parameter, this section presents the different steps leading to the derivation of the chemical diffusion coefficient in non irradiated uranium dioxides from the self-diffusion coefficient, as proposed by Berthnier et al. [91].

#### 4.3.2.1 Concentration of point defects

Concentration of point defects is the root of the models proposed by both Berthnier et al. [91] and Moore et al. [89] to calculate the self-diffusion coefficient of oxygen. Moore used the CALPHAD-based  $\text{UO}_{2\pm x}$  model of Guéneau et al. [40] to calculate the concentrations of point defects, direct outputs of the thermochemical equilibrium calculations. As the thermochemical solver ANGE implemented in the fuel performance code ALCYONE is not able to deal with such sublattice representations of  $\text{UO}_2$ , the approach proposed by Breitung assuming that the main defect is a Frenkel pair, subsequently reassessed by Berthnier, was adopted. According to these authors, the concentrations of vacancies  $[V_O]$  and interstitial atoms  $[O_i]$  can be expressed as a function of the stoichiometry deviation of the fuel  $x$  (in  $\text{UO}_{2+x}$ ) according to Equations 4.68 and 4.69, respectively.

$$[V_O] = \frac{-x - K_{FO} + [(x + K_{FO})^2 + 4K_{FO}]^{1/2}}{2} \quad (4.68)$$

$$[O_i] = \frac{x - K_{FO} + [(x + K_{FO})^2 + 4K_{FO}]^{1/2}}{2} \quad (4.69)$$

where  $K_{FO}$  is the Frenkel pair formation constant dependent on the enthalpy  $\Delta_f H_{FO}^\circ$  and entropy  $\Delta_f S_{FO}^\circ$  of formation of Frenkel defects:

$$K_{FO} = \exp\left(\frac{-\Delta_f H_{FO}^\circ}{RT} + \frac{\Delta_f S_{FO}^\circ}{R}\right) \quad (4.70)$$

Derivation of Equations 4.68 and 4.69 is shown in Appendix B. In this work, the enthalpy and entropy from Equation 4.70 are those reassessed by Berthnier et al. They are given in Table 4.5.

Table 4.5: Values of enthalpy and entropy of formation of Frenkel defects proposed by Berthnier et al. [91].

Variable	Value
$\Delta_f H_{FO}^\circ$	395000 J/mol
$\Delta_f S_{FO}^\circ$	140 J/mol/K

Examples of point defect concentrations evolution with stoichiometry deviation and temperature are shown in Figure 4.34. Oxygen vacancies/interstitials are predominant in hypostoichiometric/hyperstoichiometric fuel, respectively. The concentration of defects

increases with temperature, becoming insensitive to stoichiometry deviation at 2500 K. An apparent symmetry stems from the model since the concentration of the oxygen sites is assumed constant, implying that  $[V_O] + [O_i] = 1$ . These curves can be compared to the evolution of the point defect concentrations obtained from the CALPHAD-based  $UO_2$  model shown in Figure 4.35 (courtesy of C. Guéneau). They have been calculated with the commercial THERMOCALC software [190].

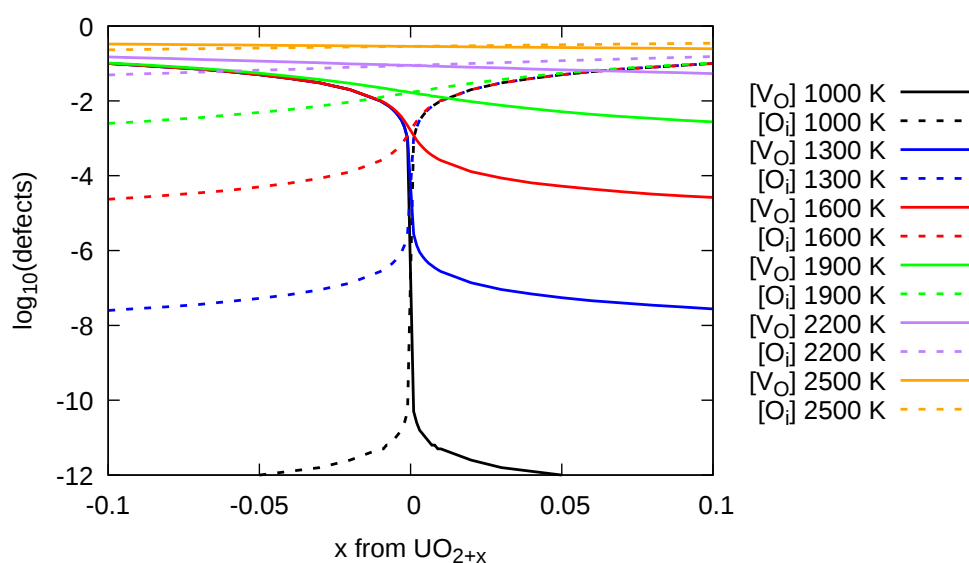


Figure 4.34: Frenkel defects concentration  $UO_{2\pm x}$  calculated from Gibbs energy of formation of Frenkel defects. Adapted from Berthiner et al. [91]. Solid lines correspond to vacancies and dashed lines to interstitial atoms.

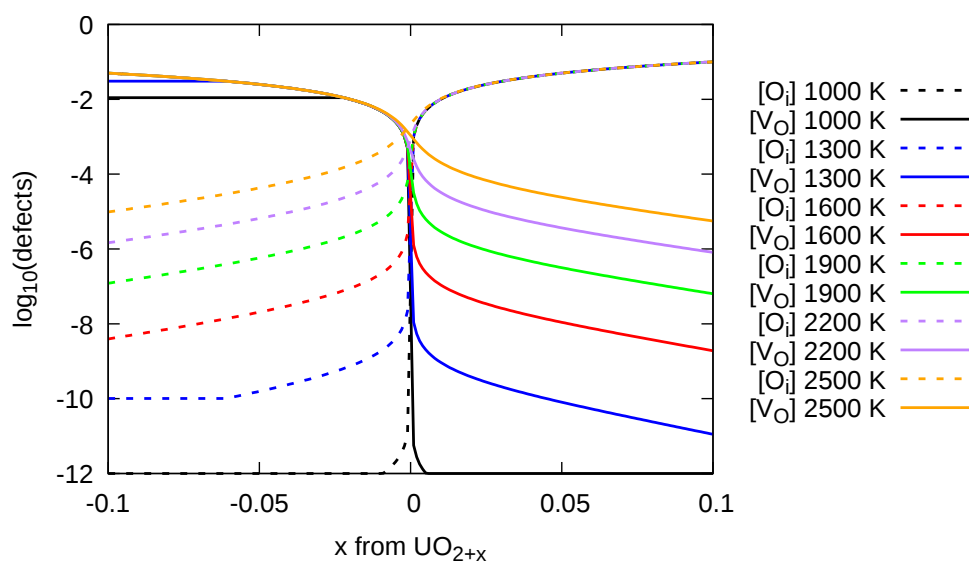


Figure 4.35: As Figure 4.34 but based on the CALPHAD method [191].

Important differences in concentrations of point defects can be observed when comparing Figures 4.34 and 4.35. The differences can reach several orders of magnitude even at high temperatures. It is therefore not possible to use the Frenkel pair model to derive the oxygen self-diffusion coefficient from Moore's model [89].

#### 4.3.2.2 Self-diffusion coefficient of oxygen

Berthnier et al. [91] have applied the approach of Breitung [88] to reevaluate the self-diffusion coefficient of oxygen from available experimental data. The expression of the self-diffusion coefficient used by the authors, valid in both hypo and hyperstoichiometric domains, is as follows:

$$D_O^* = D_{V_O}^0 [V_O] \exp\left(\frac{-\Delta H_{V_O}^m}{RT}\right) + 2D_{O_i}^0 [O_i] \exp\left(\frac{-\Delta H_{O_i}^m}{RT}\right) \quad (4.71)$$

where  $\Delta H_{V_O}^m$  and  $\Delta H_{O_i}^m$  are the migration enthalpies of oxygen vacancies and interstitial atoms, respectively.  $D_{V_O}^0$  and  $D_{O_i}^0$  are the pre-exponential coefficients for oxygen vacancies and interstitial atoms. Berthnier et al. have adjusted these parameters to fit experimental data on oxygen self-diffusion coefficients. The parameters are given in Table 4.6.

Table 4.6: Parameters of the self-diffusion coefficient of oxygen proposed by Berthnier et al. [91].

Variable	Value
$\Delta H_{V_O}^m$	95000 J/mol
$D_{V_O}^0$	$2.5 \times 10^{-7} \text{ m}^2/\text{s}$
$\Delta H_{O_i}^m$	99585 J/mol
$D_{O_i}^0$	$1.33/2 \times 10^{-6} \text{ m}^2/\text{s}$

The evolution of the self-diffusion coefficient of oxygen with stoichiometry deviation and temperature, according to Equation 4.71, is plotted in Figure 4.36.

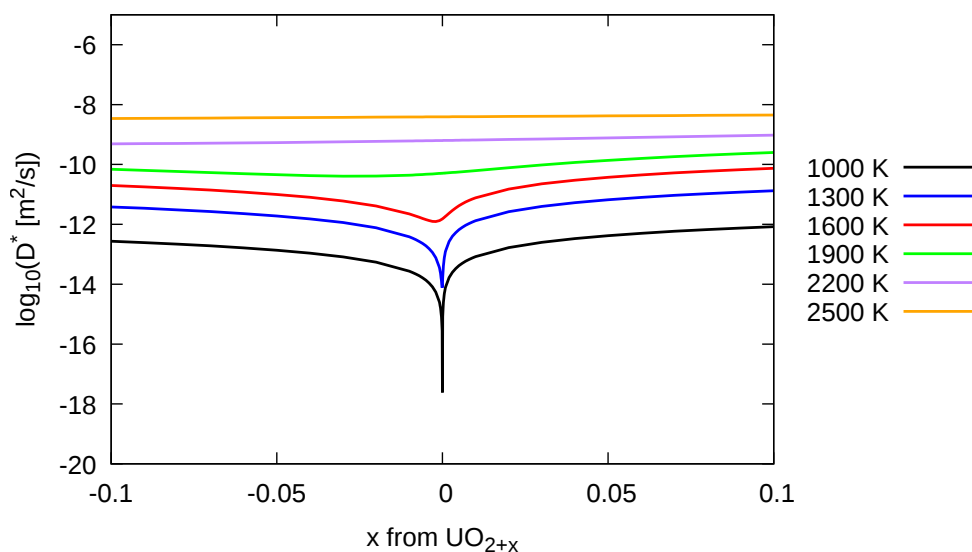


Figure 4.36: Self-diffusion coefficient based on the work of Berthinier [91].

A discontinuity at the exact stoichiometry can be seen at low temperatures. It is a consequence of the low point defect concentration (vacancies and interstitials) near the strict stoichiometry as shown in Figure 4.34. One may also notice that, according to the model, the oxygen self-diffusion coefficient in hypostoichiometric fuel is slightly lower than in hyperstoichiometric fuel. The self-diffusion coefficient calculated from Equation 4.71 can also be compared to the experimental measures available on hyper and hypostoichiometric fuels, as shown in Figures 4.37 and 4.38, respectively.

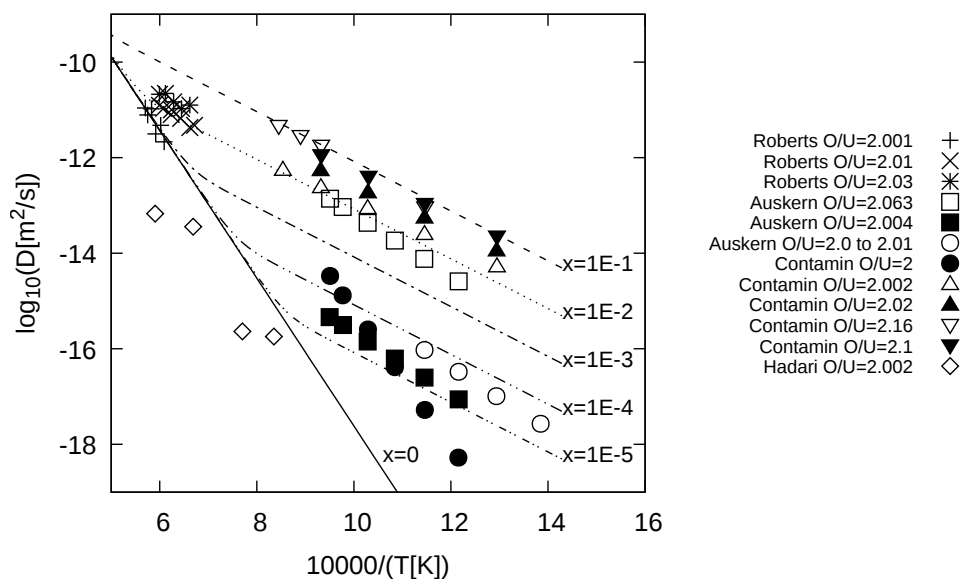


Figure 4.37: Self-diffusion coefficient based on the work of Berthinier [91] compared to experimental data [92, 93, 96, 192, 193]. Hyperstoichiometric domain.

Calculated values of the oxygen self-diffusion coefficient in the hyperstoichiometric domain are in an acceptable agreement with experimental data from [92, 93, 96, 192, 193].

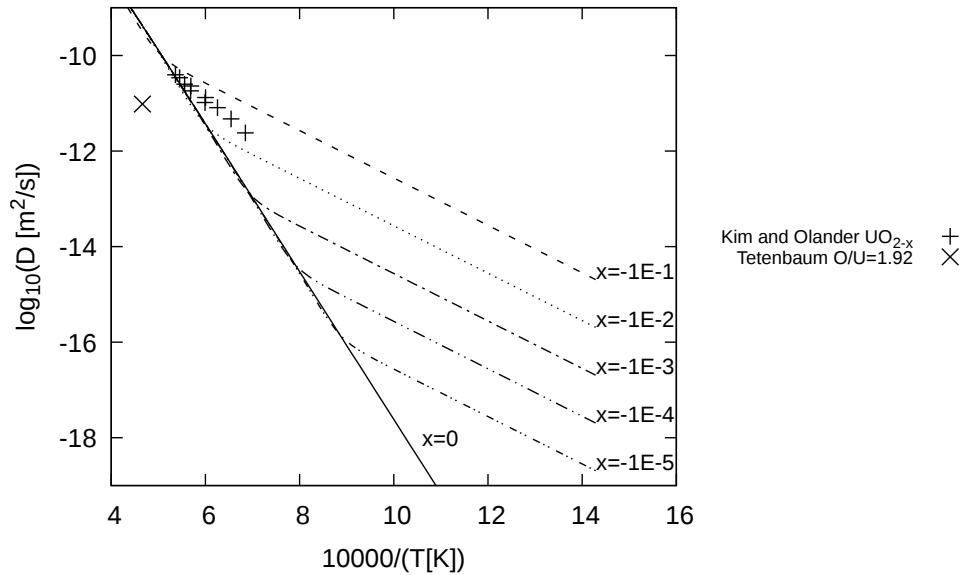


Figure 4.38: Self-diffusion coefficient based on the work of Berthinier [91] compared to experimental data [88, 94]. Hypostoichiometric domain.

As can be seen, the fit proposed by Berthinier et al. in the hypostoichiometric domain cannot be fully validated since the experimental data are scarce.

#### 4.3.2.3 Thermodynamic factor

In order to calculate the chemical diffusion coefficient, the  $\frac{\partial \ln p_{O_2}}{\partial x}$  derivative from Equation 4.67 needs to be determined. To do that, Berthinier et al. have plotted the oxygen partial pressure as a function of the stoichiometry deviation (in a log-log scale) at different temperatures and then described it using mathematical functions (see Figure 2.26). The authors used the THERMOCALC software [190] with the CALPHAD-based  $UO_{2\pm x}$  model of Guéneau et al. [40]. Berthinier's procedure has been repeated for this work with the same software and model for  $UO_2$ . It was found that the discontinuity between hypo- and hyperstoichiometry at low temperature that can be seen in Figure 2.26 of Berthinier is due to the use of the default precision in THERMOCALC ( $10^{-12}$ ), not sufficient to catch the evolution of the oxygen partial pressure near exact stoichiometry. The discontinuity disappears when the precision is set to a much lower value ( $10^{-60}$ ). The stoichiometry deviation -  $\log_{10}(p_{O_2})$  curves calculated for hypo- and hyperstoichiometric  $UO_2$  join then nicely, as can be seen in Figure 4.39. This problem only concerns the low temperature range since the gap between the pressure curves becomes smaller at high temperatures.

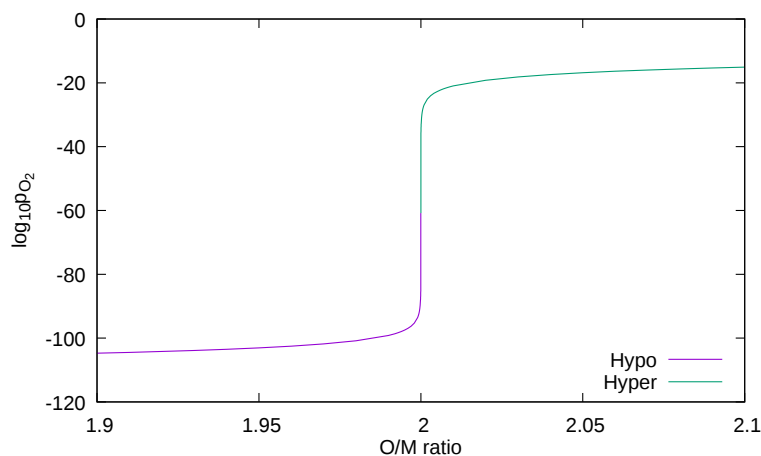


Figure 4.39: Oxygen partial pressure at 630 K as a function of the O/M ratio. Calculated with THERMOCALC.

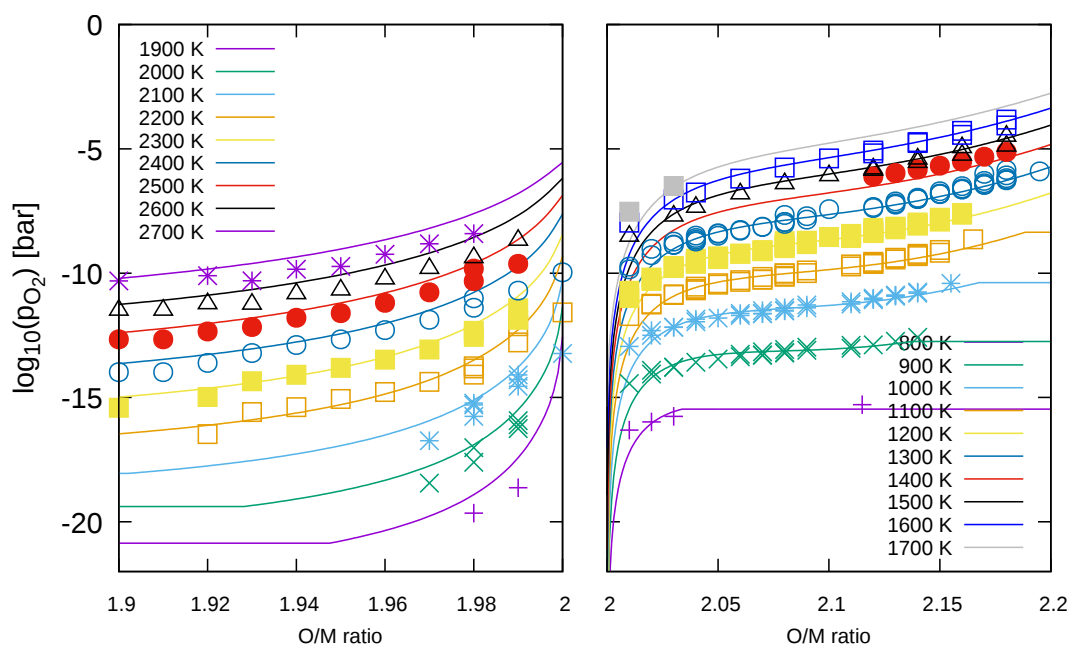


Figure 4.40: Oxygen partial pressure as a function of stoichiometry deviation. Dashed lines–THERMOCALC, solid lines–fitted values.

In consequence, the fitting of the oxygen partial pressure curves had to be reassessed entirely. The oxygen partial pressure - stoichiometry deviation curves recalculated for this work are compared to the experimental data gathered by Guéneau et al. in Figure 4.40. The calculations are consistent with the original  $\text{UO}_2$  model of Guéneau et al. and might be compared to those obtained with the Lindermer & Besmann model used in ANGE, see Figure 3.20. It can be concluded that both models lead to very close agreement with the oxygen partial pressure measurements in the limited range of

stoichiometry deviation of interest in PWR fuels. Following the methodology proposed by Berthinier, the oxygen partial pressure curves calculated with THERMOCALC are plotted as a function of the stoichiometry deviation (log-log scale) in Figure 4.41. They are marked as thick dashed lines. These curves can be described by five linear functions each. The function connecting the hypo- and hyperstoichiometric domains depends only on temperature and is expressed by:

$$f_{con}(T) = p_{O_2} = 10^{\frac{-378147}{RT} + 11.3639} \quad (4.72)$$

The four functions pointed in Figure 4.41 are described by the following expressions:

$$f_i(x, T) = p_{O_2} = 10^{\frac{A_i}{RT} + B_i + C_i \log_{10} |x|} \quad (4.73)$$

The coefficients  $A$ ,  $B$  and  $C$  are given in Table 4.7. These coefficients come from the fitting performed in Microsoft Excel with the Solver package [189].

Table 4.7: Coefficients of the functions describing oxygen partial pressure.

Function number	Coefficient A	Coefficient B	Coefficient C
1	-640109	11.905	-5.563
2	-498316	11.376	-2.062
3	-255897	11.517	2.122
4	-101454	10.203	5.897

In order to obtain continuous functions in the hypo- and hyperstoichiometric domains, the following expressions can be used:

$$f_{hypo} = \frac{1}{f_1^{-1} + f_2^{-1} + f_{con}^{-1}} \quad (4.74)$$

$$f_{hyper} = f_3 + f_4 + f_{con} \quad (4.75)$$

The oxygen partial pressures curves from Equations 4.74 and 4.75 are shown in Figure 4.41 as thin, solid lines. As can be seen, the fit is very good even at very high stoichiometry deviations.

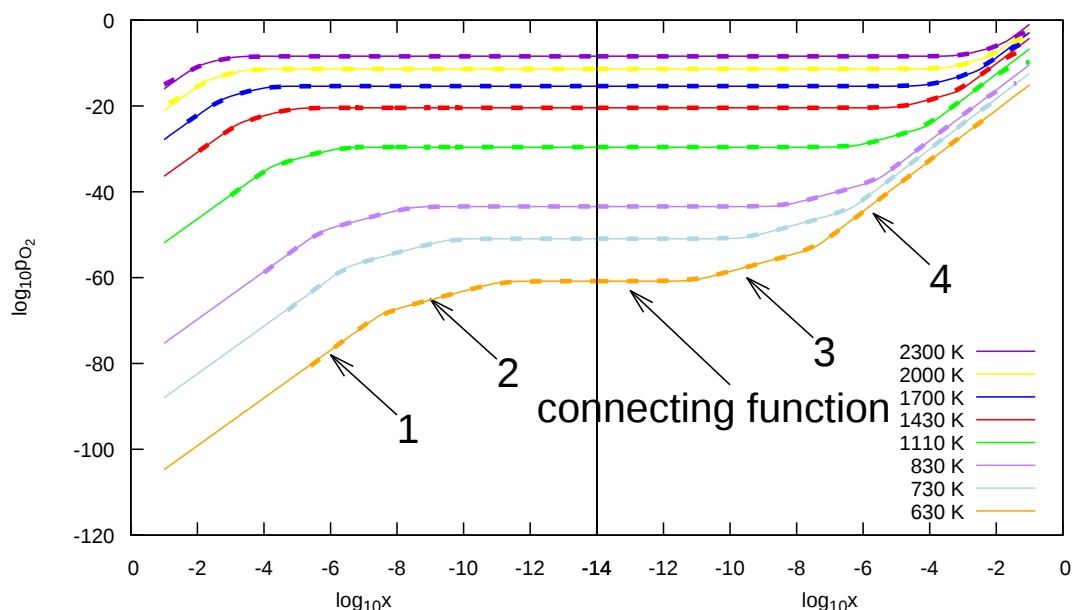


Figure 4.41: Oxygen partial pressure as a function of stoichiometry deviation. Dashed lines—THERMOCALC, solid lines—fitted values.

Berthnier used a single function per domain to describe the oxygen pressure curves. Derivation of the functions with respect to stoichiometry deviation led direct estimations of the derivative of the partial oxygen pressure  $\frac{\partial \ln p_{O_2}}{\partial x}$  in each domain. In this work, two functions are used to describe each domain, meaning that some transition has to be considered. The  $\frac{\partial \ln p_{O_2}}{\partial x}$  derivative for the hypostoichiometric domain is given by:

$$\frac{\partial \ln f_{\text{hypo}}}{\partial x} = \frac{1}{[\max(\frac{c_1}{x}; \frac{c_2}{x})]^{-1} + [f_{\text{low}}]^{-1}} \quad (4.76)$$

The  $\frac{\partial \ln p_{O_2}}{\partial x}$  derivative in the hyperstoichiometric domain can be expressed by:

$$\frac{\partial \ln f_{\text{hyper}}}{\partial x} = \frac{1}{[\max(\frac{c_3}{x}; \frac{c_4}{x})]^{-1} + [f_{\text{low}}]^{-1}} \quad (4.77)$$

where  $f_{\text{low}}$  is the function representing the  $\frac{\partial \ln p_{O_2}}{\partial x}$  derivative at very low stoichiometry deviations. It is given by:

$$f_{\text{low}} = \frac{\partial \ln p_{O_2}}{\partial x} = 10^{\frac{A}{RT} - B} \quad (4.78)$$

The coefficients  $A$  and  $B$  have been fitted using the method proposed by Berthnier. The oxygen partial pressures calculated at  $x = \pm 10^{-10}$  in both domains have been used in the following equation to find the derivative at the temperatures considered in the

plots of Figure 4.41:

$$f_{low}(T) = \frac{\ln p_{O_2}^{hyper}(T) - \ln p_{O_2}^{hypo}(T)}{2 \times 10^{-10}} \quad (4.79)$$

The plot of the logarithm of the function  $f_{low}$  as a function of the inverse of temperature shows that a straight line with  $A = 59828$  and  $B = -0.233$  gives a correlation coefficient very close to 1.

#### 4.3.2.4 Chemical diffusion coefficient of oxygen

The derivatives given in Equations 4.76 and 4.77 can be used in Equation 4.67 to calculate the chemical diffusion coefficient of oxygen. Values of this coefficient for different stoichiometry deviations are plotted in Figure 4.42. Also, they are compared to the diffusion coefficient proposed by Lassmann (Equation 4.34)[86].

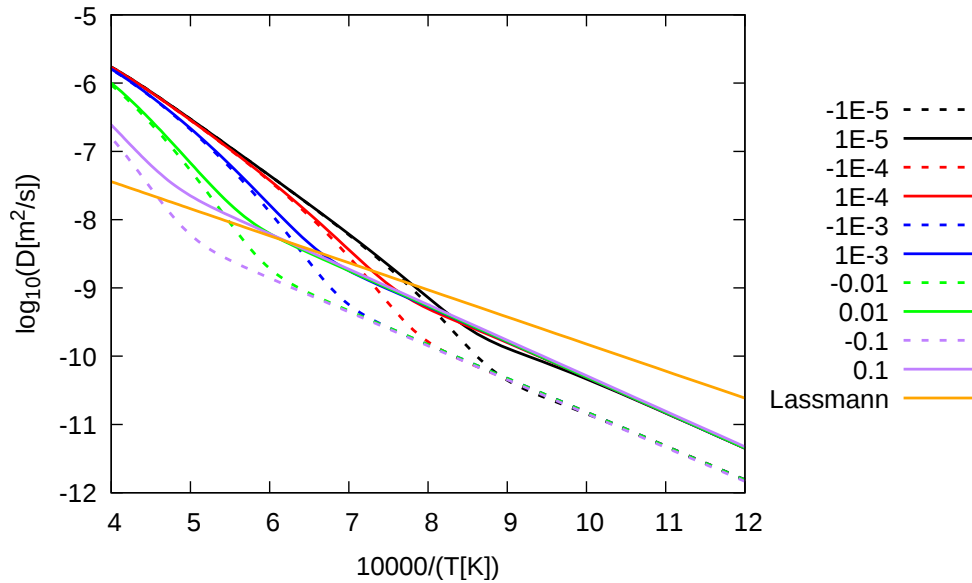


Figure 4.42: Corrected diffusion coefficient based on the work of Berthinier [91] and the diffusion coefficient proposed by Lassmann [86].

As can be seen, the impact of stoichiometry deviation might not be negligible. At high temperatures, a  $10^{-2}$  change in stoichiometry deviation can lead to a factor 10 change in the chemical diffusion coefficient. At low temperatures, stoichiometry deviation does not seem to have some impact on the diffusion coefficient. The oxygen chemical diffusion coefficient found in this work is greater than Lassmann's coefficient at high temperatures but is lower at low temperatures.

Figure 4.43 shows calculated chemical oxygen diffusion coefficient compared to selected experimental data in the hyperstoichiometric domain. The calculated coefficients are in acceptable agreement with some of the experimental points from Bayoglu [101] and

Ruello et al. [102]. The model is close to the experiments of Lay [105] and slightly underestimates the data from Taskinen [104]. Overall, one may however notice that there is no consistency between experimental measurements, in particular as a function of the stoichiometry deviation.

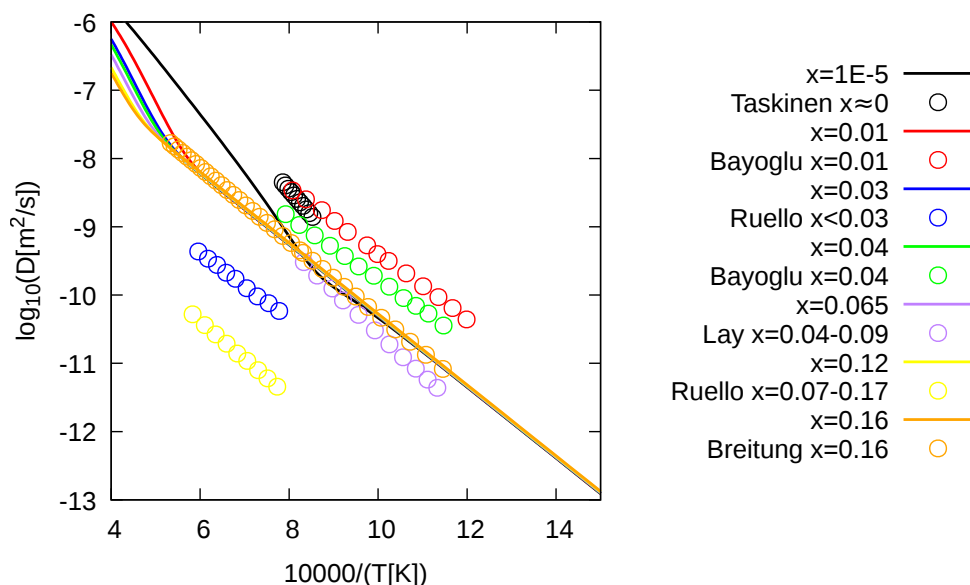


Figure 4.43: Corrected diffusion coefficient based on the work of Berthinier [91] validated against experimental data [102,104,105,194] and the model proposed by Breitung [88].

The oxygen chemical diffusion coefficient for the hypostoichiometric domain is more important in this work because according to thermochemical calculations carried out with ANGE, nuclear fuel becomes hypostoichiometric with irradiation. Unfortunately there is absolutely no experimental measurement to validate the model.

#### 4.3.2.5 Impact of stoichiometry deviation on thermal diffusion kinetics

The OXITRAN solution has been applied to investigate the impact of the stoichiometry deviation dependency of the chemical diffusion coefficient of oxygen on the oxygen redistribution kinetics. The simulated fuel pellet has a radius of 4 mm and an initial O/M ratio equal to 1.995. It is discretized in 40 cylindrical rings. The temperature profile is calculated with Equation 4.2 and shown by the red curve in Figure 4.3. The heat of transport is -100 kJ/mol. The time step size used in the simulation is 1 s. Results of OXITRAN calculations are shown in Figure 4.44. The O/M radial profiles calculated with Lassmann's chemical diffusion coefficient (dependent on temperature only) and the reassessed chemical diffusion coefficient from Berthinier (dependent on stoichiometry deviation and temperature) are plotted at different times (10, 100, 1000 and 10000 s) and compared to the steady state redistribution calculated with OXIREED.

According to the curves shown in Figure 4.44, oxygen transport is the fastest at the pellet center where temperatures are the highest. The difference in kinetics related to the diffusion coefficient models is particularly important in this region. After 10 seconds, Lassmann's model gives an O/M radial profile which is still very close to the initial O/M ratio while Berthinier's model gives a visibly lower O/M ratio at the pellet center. This result is consistent with the plots of Figure 4.42 where a higher diffusion coefficient is expected at high temperature with Berthinier's model. After 100 seconds, the differences in oxygen redistribution kinetics are however reduced, Lassmann's and Berthinier's models give similar O/M ratios at the pellet center. After 1000 seconds, steady-state is reached with Lassmann's coefficient while Berthinier's models leads to a slower increase of the O/M ratio at the pellet periphery. Again, this result is consistent with the relative positions of the models in the low temperature region of Figure 4.42. After 10000 seconds, steady-state is nearly reached with both models.

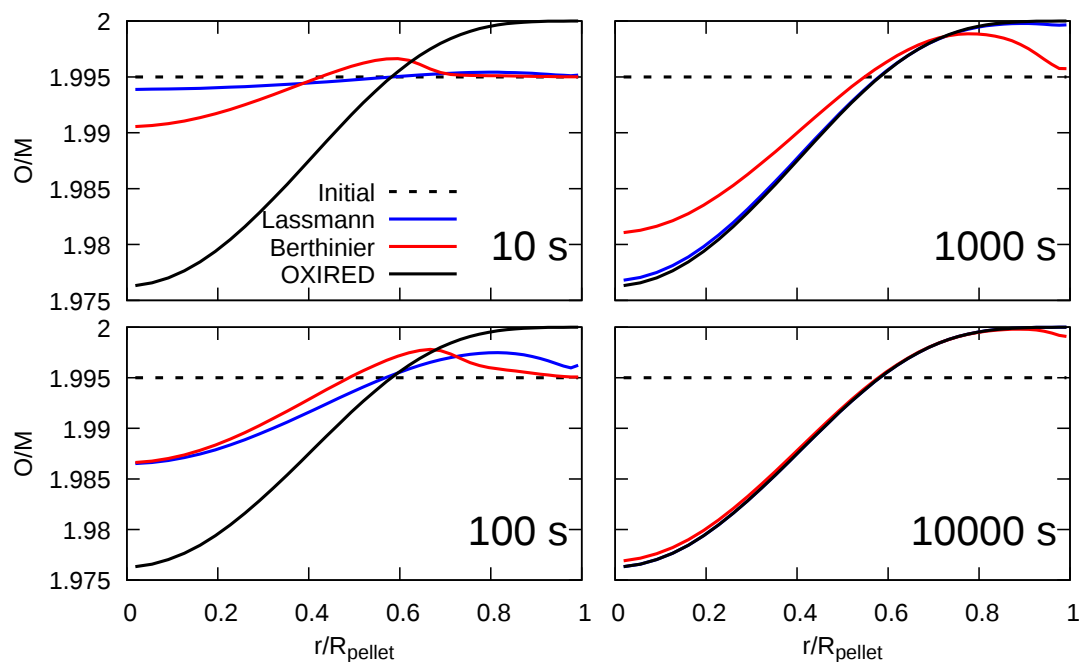


Figure 4.44: Oxygen redistribution calculated with different chemical oxygen diffusion coefficients compared to the steady state redistribution calculated with OXIRE.

These calculations show that the stoichiometry deviation dependency of the oxygen chemical diffusion coefficient might be important in the simulation of fuel behavior during power ramps since failure of the cladding by I-SCC usually occurs within the first minutes at RTL. Any change of the O/M ratio in the fuel might lead to some changes in the chemical speciation of fission gases released from the fuel during this period [134].

### 4.3.3 Summary

Numerical solutions for oxygen thermal diffusion in the fuel pellet have been detailed in this chapter. They have been derived to be usable in ALCYONE fuel performance code. First, the steady state solution (OXIRED) proposed by Lassmann has been described. It has been used as a reference solution to test the other numerical methods described in this chapter. A solution for the 1D radial transient thermal diffusion equation (named OXITRAN), based on the Finite Volume Method, has been implemented and tested with nonlinear parameters to check its robustness.

ALCYONE 2D and 3D simulations being based on the Finite Element code Cast3M, solutions for the transient thermal diffusion equation in 2D and 3D based on the Finite Element Method have then been detailed. Since the treatment of thermal diffusion transients is not available as a standard procedure in Cast3M, the method used in Cast3M to solve the heat transport equation has been adapted in this work to the thermal diffusion problem. The 2D and 3D FE based solutions have been validated by comparison to the 1D transient solution given by OXITRAN. Convergence criteria have been proposed in order to ensure that the problem can be solved in a reasonable CPU time. Additionally, the 2D and 3D solutions have been verified by comparison to the coupled thermal–oxygen transport problem with heat source term and fast change of power density treated in 2D with the COMSOL software by Ramirez et al [81]. The obtained evolutions of temperature and stoichiometry deviation in the fuel pellet are very close to those reported by Ramirez et al, demonstrating that the implementation in Cast3M is correct.

The estimation of the important parameters for oxygen thermal diffusion in irradiated fuel have also been presented in this chapter. First, the heat of oxygen transport has been derived from the Cr EPMA radial profiles measured after several power ramps on Cr-doped  $\text{UO}_2$  fuels and from the solubility model of Cr in non irradiated  $\text{UO}_2$ . The method lead to an expression for the heat of oxygen transport that depends on both stoichiometry deviation and burnup. The advantage of this approach is the identification of the heat of transport from measurements performed on irradiated fuels.

The second parameter is the oxygen chemical diffusion coefficient. Since there is no experimental measure in irradiated fuels and not many experimental data on non irradiated hypostoichiometric fuels, the chemical diffusion coefficient has been estimated from the self-diffusion coefficient (for which more experimental data are available) and from the thermodynamic factor, as proposed by Berthinier et al. The thermodynamic factor had to be reassessed entirely from THERMOCALC calculations on the  $\text{UO}_{2\pm x}$  CALPHAD-based model of Guéneau et al. The derived chemical diffusion coefficient depends on temperature and stoichiometry deviation. The impact of the latter parameter on the kinetics of oxygen redistribution has been studied with OXITRAN showing

that the stoichiometry deviation dependency of the chemical diffusion coefficient might be important in the simulations of clad failure during power ramps by I-SCC.

## Chapter 5

# Thermochemistry–oxygen transport coupling in ALCYONE

This chapter details the coupling procedure between the thermochemical solver ANGE and the oxygen thermal diffusion model implemented in the fuel performance code ALCYONE. 1D and 3D simulations of power ramps are presented to illustrate the coupling and its impact on PCI and clad failure propensity by I-SCC.

### 5.1 Coupling procedure

#### 5.1.1 ALCYONE algorithm

The simulations described in this work have been performed with ALCYONE V2.0, the newest version of the code released in December 2016. Details are given in reference [195]. A schematic representation of the models called during a time step of a simulation with ALCYONE fuel performance code is given in Figure 5.1.

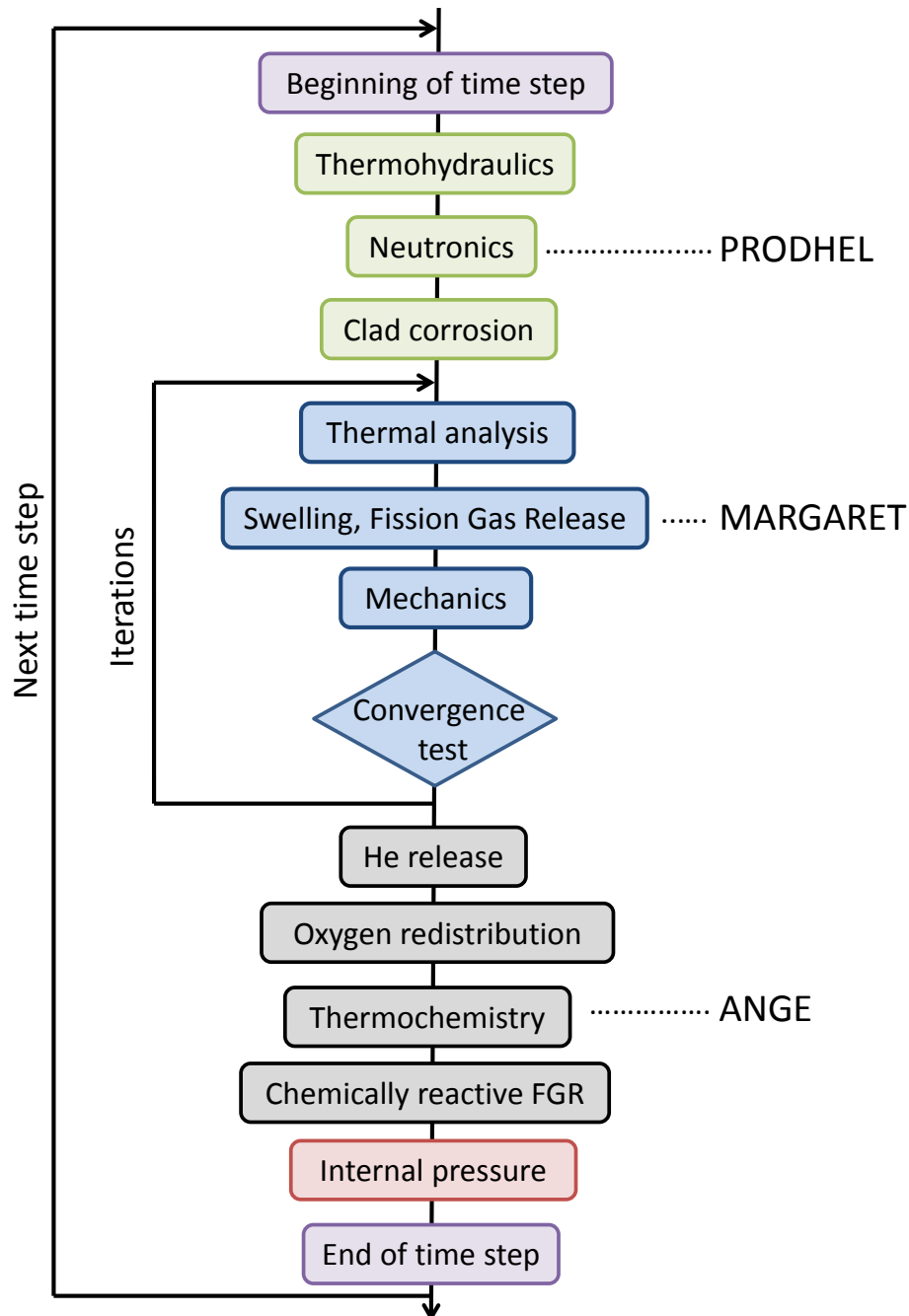


Figure 5.1: Schematic representation of iterative loops and models called during a simulation carried out with the fuel performance code ALCYONE.

In the core of the program (blue boxes), temperature, mechanical stresses, fission gas induced strains and FGR are calculated at each node (local quantities) and at each time step. Upon convergence of this main loop, an oxygen thermal diffusion calculation ("oxygen redistribution") is performed at the pellet fragment scale. In the 1D radial scheme of ALCYONE, the OXITRAN solution has been implemented to this end. In the 2D/3D schemes, a Cast3M procedure has been added. The thermal diffusion calculation gives the change in O/M at each node during the time step. From this local O/M and

the elemental composition of the fuel calculated by the neutronics model PRODHEL, the temperature and the pressure in the fuel rod calculated previously, thermochemical calculations are performed with ANGE ("Thermochemistry"). They give the chemical state of the system at each node including the concentration of chemically reactive fission gases. Release of these gases is then estimated in proportion to the release of noble gases and to the concentration of noble gases at inter-granular sites calculated by MARGARET [14].

To reduce the CPU time, the oxygen redistribution step is only performed once the thermo-mechanical problem is solved. In fact, the thermal analysis, the fission gas swelling and the mechanics are strongly coupled and may require numerous iterations to reach convergence. Oxygen redistribution is only introduced in ALCYONE to study its impact on the fuel thermochemistry. Oxygen redistribution would have to be included in the iterations loop if the thermal or mechanical parameters depended on stoichiometry deviation, as in the case treated by Ramirez et al., see Section 4.2.3. The very small deviation from stoichiometry that are expected in PWR  $\text{UO}_2$  fuels (within the uncertainty on the initial O/M ratio, i.e.,  $2 \pm 0.01$ ) have led us to neglect this dependency. This is however not the case with fuel thermochemistry since any small change in stoichiometry deviation can greatly change the concentration of chemically reactive fission gases.

A more detailed description of the coupling between oxygen redistribution and fuel thermochemistry is given in Figure 5.2. The coupled scheme is compared to the previous implementation of the sole thermochemical calculations in ALCYONE. In the latter ones, the thermochemical solver requires the elemental composition, the pressure and the temperature as inputs. It must be emphasized that the local oxygen concentrations are not a result of neutronics calculations. The oxygen content depends only on the initial fuel composition. A schematic representation of the standard thermochemical computations is shown in the top part of Figure 5.2 (above the dashed line).

In the coupled scheme, thermochemical calculations are performed with prescribed O/M ratios. They are schematically represented in the bottom part of Figure 5.2 (below the dashed line). The main difference with the standard calculations stems from the fact that the O/M ratios calculated with the oxygen redistribution model are used 1) to impose the O/M ratios in the thermochemical solver and 2) to modify the  $\text{O}_2$  contents. The procedures for imposing the O/M ratio and modifying the local oxygen concentration are detailed in Sections 5.1.2 and 5.1.3 respectively.

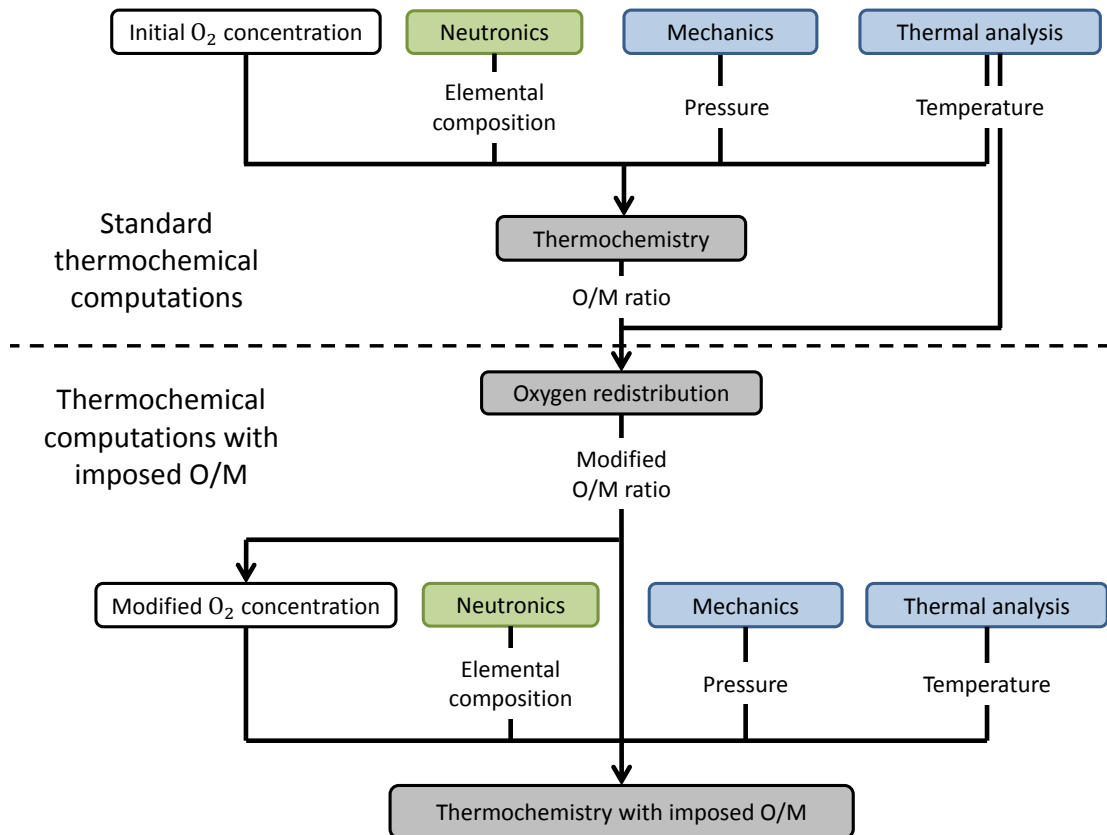


Figure 5.2: Schematic representation of thermochemical calculations with (bottom part) and without (top part) imposing the O/M ratio. Colors of boxes are consistent with Figure 5.1.

### 5.1.2 Thermochemical calculations at prescribed O/M ratio

There are several difficulties in the combination of oxygen transport and thermochemical calculations in a fuel performance code. The main one stems from the fact that the O/M ratio is an output of both calculations [156]. In former work, thermochemical calculations were repeated at each node with varying total oxygen content in the system till the O/M ratio from the thermal diffusion calculation was reached locally [134]. The CPU time associated increased so much that only 1D simulations could be performed.

In this work, to improve the coupling between the thermochemical solver ANGE and the thermal diffusion problem and render 3D simulations possible, an additional constraint in the minimization calculation performed at each node has been added in order to fix the O/M ratio. Recalling that the Lagrange multiplier method is used to enforce the conservation of elements in the system, specific conditions can be introduced by the inclusion of a virtual element of quantity zero [196].

Using the notations of Section 3.2.1, and recalling that the O/M ratio refers to the solid solution, the O/M ratio can be written as follows:

$$O/M = \frac{\sum_{k=1}^d a_{kJ}^s n_k^s}{\sum_{j=1, NE}^{j \neq J} \sum_{k=1}^d a_{kj}^s n_k^s} \quad (5.1)$$

where the  $J$ th index corresponds to oxygen. This expression can be transformed into the following equation:

$$\sum_{k=1}^d a_{kJ}^s n_k^s - O/M \sum_{j=1, NE}^{j \neq J} \sum_{k=1}^d a_{kj}^s n_k^s = 0 \quad (5.2)$$

which takes a form similar to Equation 3.17 of conservation of each element in the system. Prescribing the O/M ratio can therefore be done by adding a virtual element in the system of quantity equal to zero ( $b_{NE+1} = 0$  with  $NE$  the number of non virtual elements). The equation of conservation of the virtual element reads as follows:

$$\sum_{k=1}^m a_{k(NE+1)}^g n_k^g + \sum_{k=1}^d a_{k(NE+1)}^s n_k^s + \sum_{k=1}^s a_{k(NE+1)}^c n_k^c = 0 \quad (5.3)$$

where the coefficients  $a_{ij}$  associated to the gas phase ( $g$ ), the solid solution phase ( $s$ ) and the pure condensed phases ( $c$ ) take the following values to match Equation 5.2:

$$a_{k(NE+1)}^g = 0, \quad a_{k(NE+1)}^s = a_{kJ}^s - O/M \sum_{j=1, NE}^{j \neq J} a_{kj}^s, \quad a_{k(NE+1)}^c = 0 \quad (5.4)$$

### 5.1.3 Evolution of oxygen content with O/M ratio

Oxygen thermal diffusion leads to a local change in the O/M ratio. In parallel, the total oxygen content at each node must be changed accordingly since oxygen is assumed to migrate only in the solid solution. The change in the total oxygen concentration  $n_{O_2}^{tot}$  depends a priori on many local factors such as temperature, total pressure, fission products content (burnup) and dopant content. Considering that the variations of the O/M ratio are small within each time step  $\Delta t$ , the oxygen concentration at time  $t + \Delta t$  can be calculated as follows:

$$n_{O_2}^{tot(t+\Delta t)} = n_{O_2}^{tot(t)} + \alpha (O/M^{t+\Delta t} - O/M^t) \quad (5.5)$$

as a function of the same quantity at the beginning of the time step.  $\alpha$  is the proportionality factor that can be determined from preliminary thermochemical calculations performed on the studied irradiated fuels. Provided a constant proportionality factor

is used at each node, the simultaneous conservation of the total oxygen content and of oxygen vacancies in the fuel pellet fragment is granted.

### 5.1.3.1 Standard $\text{UO}_2$ fuel

For fresh  $\text{UO}_2$ , in the range of O/M ratios that can be expected in a nearly stoichiometric fuel pellet [1.99-2], the relation between the total oxygen concentration  $n_{\text{O}_2}^{\text{tot}}$  and the O/M ratio is the following:

$$n_{\text{O}_2}^{\text{tot}} = \frac{1}{2} \times O/M \quad (5.6)$$

and thus the proportionality factor  $\alpha = 1/2$ . This function is based on calculations performed with ANGE on the U-O system where the total oxygen content is changed stepwise. Three high temperatures that are representative of those occurring at the pellet center during power ramps have been considered. The evolution of total oxygen concentration  $n_{\text{O}_2}^{\text{tot}}$  versus the calculated O/M ratio is plotted in Figure 5.3 (left graph).

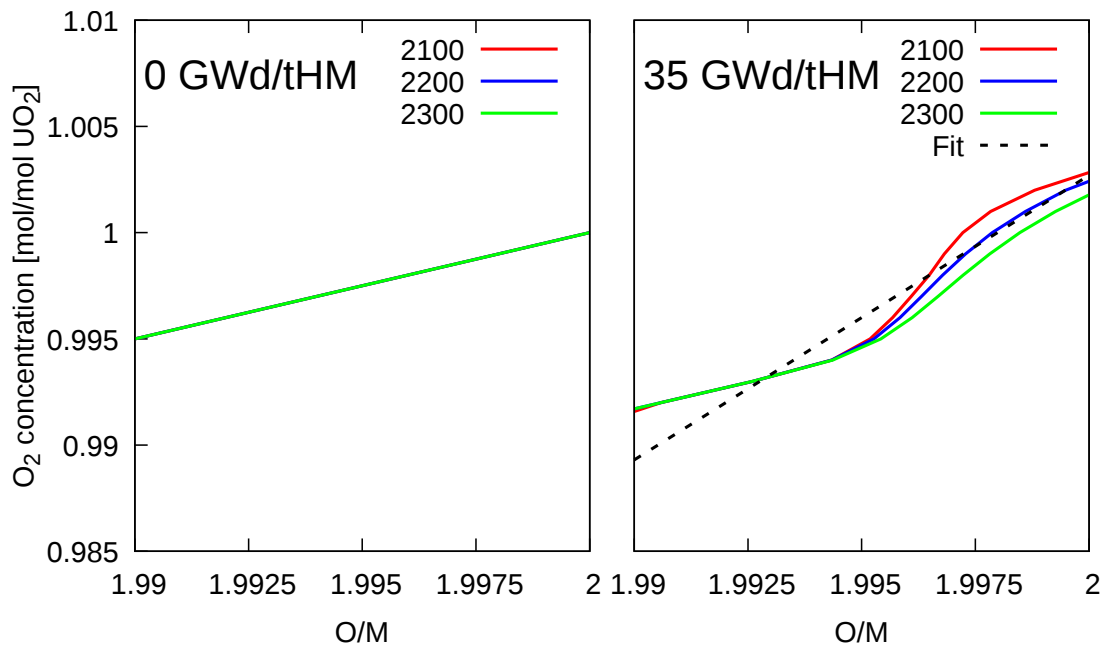


Figure 5.3: Oxygen concentration as a function of the O/M ratio at different temperatures. Left figure–fresh fuel, right figure–fuel irradiated to 35 GWd/tHM. Calculations done with ANGE.

To analyze the impact of irradiation on the proportionality factor, a series of calculations has been performed with PRODHEL used as a stand-alone model to estimate the fuel composition as a function of burnup. The fuel characteristics and irradiation LHR are given in Table 5.1. The burnup range studied is 0-50 GWd/tHM.

Table 5.1: Parameters used in the PRODHEL stand-alone simulation for the proportionality factor.

LHR	Enrichment	Burnup	Radius
[W/cm]	[% $^{235}\text{U}$ ]	[GWd/tHM]	[mm]
200	3.5	0-50	4.1

The evolution of the representative elements (see Table 3.1) from PRODHEL calculations is plotted as a function of the average burnup in Figure 5.4.

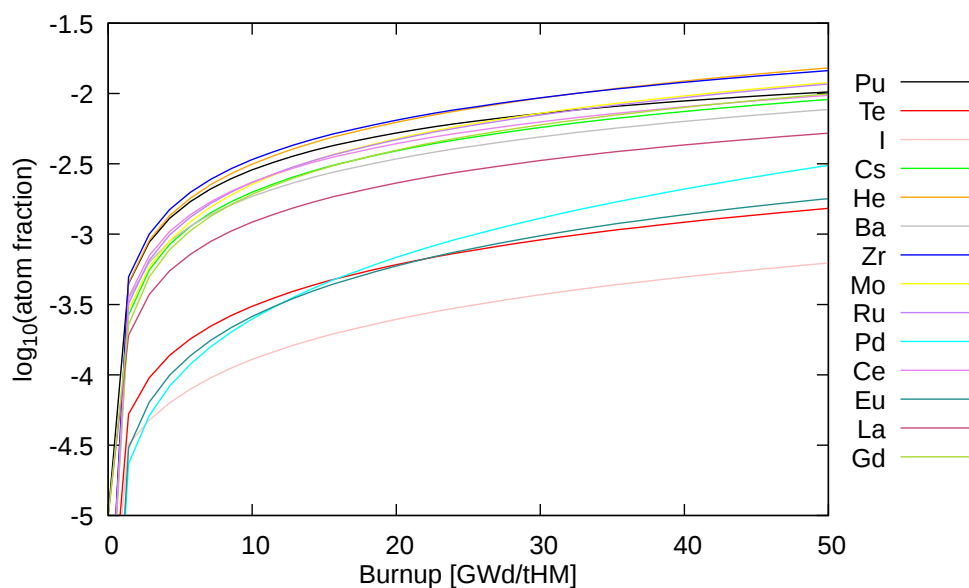


Figure 5.4: Atom fraction of the representative elements as a function of burnup. Calculated with PRODHEL.

Figure 5.3 (right graph) shows the O/M curves calculated with ANGE for the fuel composition corresponding to an average burnup of 35 GWd/tHM. The initial O/U ratio used in the computations was 2. The presence of fission products changes the evolution of the O/M ratio with the total oxygen content. As can be seen, the evolution is nonlinear but we chose to approximate it with a linear function:

$$n_{O_2}^{tot} = 1.3398 \times \frac{O}{M} - 1.6769 \quad (5.7)$$

which gives a proportionality factor equal to 1.3398 in the limited O/M range studied. PRODHEL fuel compositions of Figure 5.4 have been used to study the change in the proportionality factor  $\alpha$  with the average burnup. The proportionality factor has been calculated for  $\text{UO}_2$  fuels irradiated up to 50 GWd/tHM with constant steps of 5 GWd/tHM. The evolution with burnup is shown in Figure 5.5.

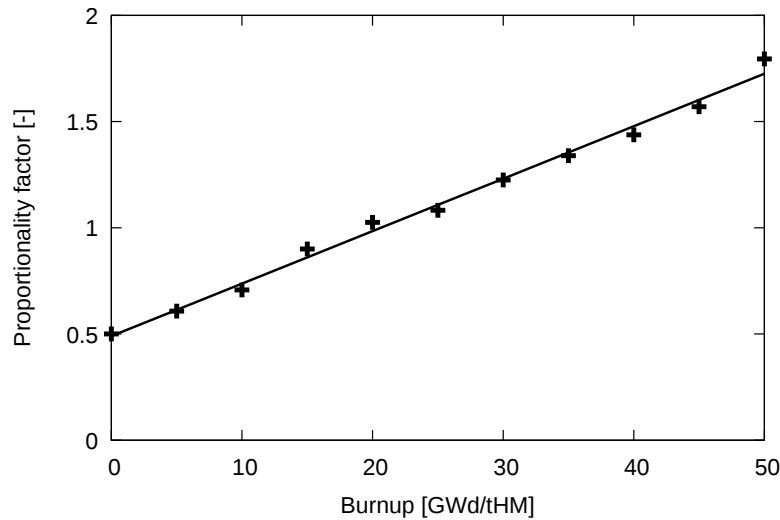


Figure 5.5: Proportionality factor as a function of burnup. Points are the values calculated with ANGE and the line is a linear approximation.

The proportionality factors calculated at different burnups are shown as points in Figure 5.5. As can be seen, the increase with burnup is nearly linear and can be approximated with the following simple expression:

$$\alpha = 0.0247 \times BU + 0.4902 \quad (5.8)$$

where  $BU$  is the average burnup of the fuel in GWd/tHM. The  $\alpha$  coefficient given by Equation 5.8 is plotted in Figure 5.5 as the black line and will be used in simulations of irradiated  $UO_2$  fuels in this work.

### 5.1.3.2 Cr-doped fuel

Tries have been made to derive a proportionality factor  $\alpha$  for Cr-doped irradiated fuels by applying the same method as for irradiated  $UO_2$ . It turned out that the  $O/M-n_{O_2}^{tot}$  curves, similar to those presented in Figure 5.3, were strongly nonlinear and could not be used to deduce  $\alpha$ . Alternatively, the proportionality factor has been estimated from the calculations done previously to derive the heat of transport of oxygen (see Section 4.3.1). ANGE calculations that were performed at prescribed oxygen potential to get the O/M ratios at the pellet centers (see Figure 4.31) also returned the total oxygen contents. These local oxygen contents characterize the state of the fuel after oxygen redistribution. The initial oxygen concentrations in the fuel can be easily calculated from the initial O/U ratio of the fuel (close to 2) and from the dopant concentration (introduced as  $Cr_2O_{3(s)}$ ). In PR2 and PR3, that have been used for the heat of oxygen transport fitting, the initial oxygen concentrations are 1.0038 mol  $O_2$ /mol  $UO_2$  and 1.0053 mol  $O_2$ /mol  $UO_2$ , respectively. The total oxygen concentrations calculated at the pellet center before and after oxygen redistribution in PR2 and PR3 are shown in

Figure 5.6 (left graph). The O/M ratios calculated at the pellet center before and after oxygen redistribution in PR2 and PR3 are recalled in the same Figure (right graph).

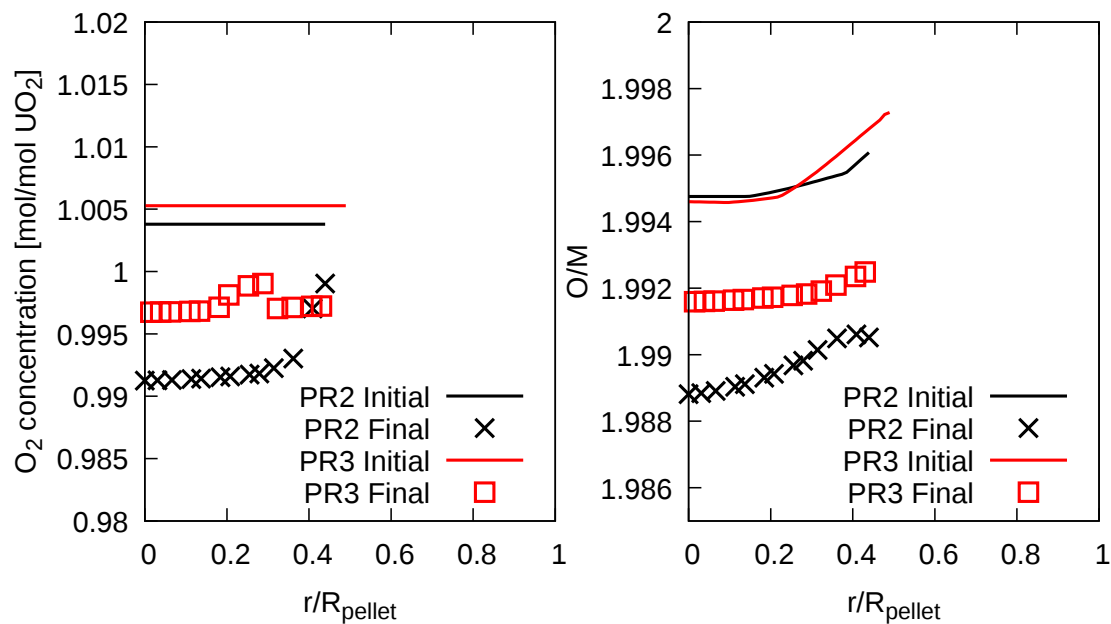


Figure 5.6: Oxygen concentrations (left figure) and O/M ratios (right figure) before and after oxygen redistribution calculated for PR2 and PR3.

These quantities can be used to estimate the proportionality factor  $\alpha$  according to the following equation:

$$\alpha = \frac{n_{O_2}^{tot(final)} - n_{O_2}^{tot(initial)}}{O/M^{(final)} - O/M^{(initial)}} \quad (5.9)$$

The proportionality factors from PR2 and PR3 are plotted in Figure 5.7 as a function of the fuel pellet radius.

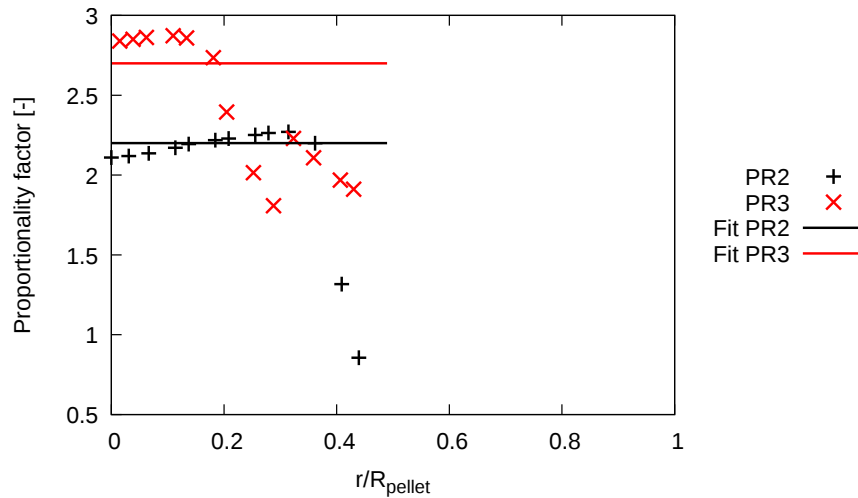


Figure 5.7: The proportionality factor  $\alpha$  of PR2 and PR3 at the pellet center. The lines are the average values for  $r/R_{\text{pellet}} < 0.2$ .

As it can be seen,  $\alpha$  is non constant radially in both PR2 and PR3. However, at the pellet center ( $r/R_{\text{pellet}} < 0.2$ ), where the fitting of the heat of transport was done, the proportionality factors are nearly constant. The average values of  $\alpha$  in this region are approximately equal to 2.2 and 2.7 in PR2 and PR3, respectively. These values will be used in the simulations of irradiated Cr-doped fuels to estimate the oxygen content evolution with the change in O/M ratio.

#### 5.1.4 Verification of the proposed coupled solution

The solutions implemented for the oxygen thermal diffusion equation guaranty that the average O/M ratio in the fuel pellet fragment remains constant, i.e., the conservation of oxygen vacancies is granted. Imposing the O/M ratios calculated by the oxygen thermal diffusion solutions in the thermodynamic equilibrium calculations is a necessary condition to fulfill the same condition. Since the total oxygen content evolves proportionally to the O/M ratio change, the conservation of the total oxygen content in the fuel pellet fragment during the calculation stems from the constant average O/M ratio. Clearly, imposing the O/M ratios might influence the chemical speciation in the fuel estimated from the thermodynamic equilibrium calculations. In this section, thermochemical calculations with and without imposing the O/M ratios are compared. To this end, the radial profile of O/M ratio calculated from the oxygen thermal diffusion equation applied to PR2 is considered, see Figure 4.32. In the first step, the radial profile of total oxygen content after oxygen redistribution  $n_{\text{O}_2}^{\text{tot}(final)}$  is calculated with Equation 5.5 and the proportionality factor equal to 2.2, as discussed in the previous section. The calculated

radial profile (final) is plotted in Figure 5.8 together with the initial oxygen content of the fuel, equal to 1.0038 mol/mol  $\text{UO}_2$ .

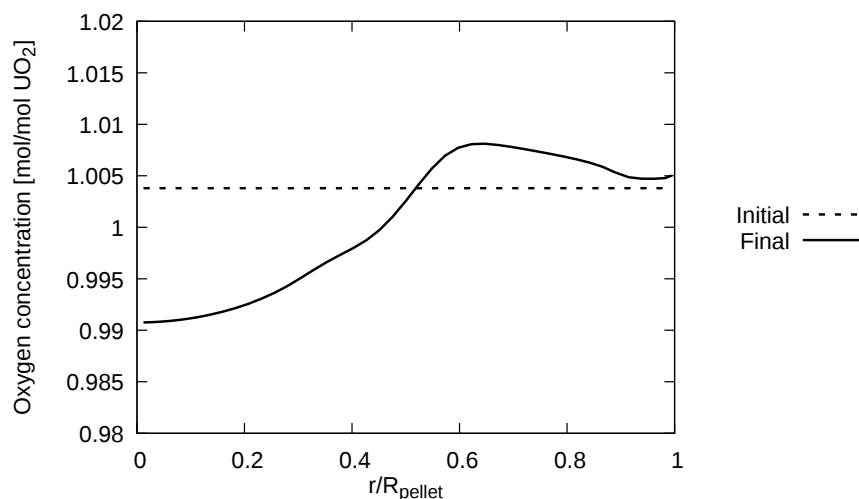


Figure 5.8: Radial profile of total oxygen content calculated at the end of the holding period of PR2 (solid curve) and the initial oxygen concentration (dashed curve).

In the second step, thermochemical calculations with the imposed O/M ratios are performed. For the sake of simplification, the elemental composition is assumed to be constant along the radius. It is given in Table 4.4. The temperature profile is the one shown in Figure 4.25. The "final" total oxygen contents of Figure 5.8 are used in these computations. The thermochemical calculations with the imposed O/M ratios return as expected a radial profile of O/M ratio that is identical to the one prescribed. The "imposed" radial profile is represented by the black curve in Figure 5.9.

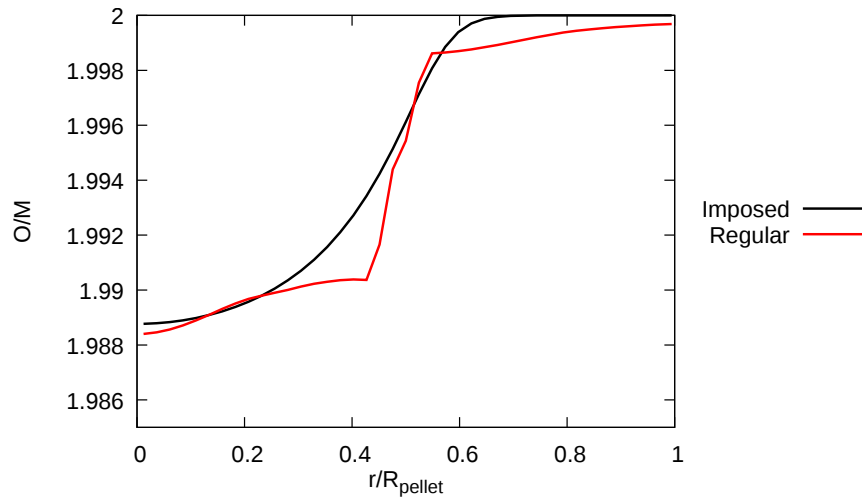


Figure 5.9: O/M ratios obtained in the calculations with (black curve) and without (red curve) imposing the O/M ratio.

In the last step, the same thermochemical calculations are repeated without imposing the O/M ratio. They results in the "regular" O/M ratios represented by the red curve in Figure 5.9. As can be seen, the black and red curves are very close to each other at the pellet center. The biggest difference occurs at mid-radius. The change in O/M ratio in the calculations without imposed O/M is much steeper there. Also, the strict stoichiometry (O/M=2) at the pellet periphery is not reached in these calculations. Figure 5.10 shows the oxygen potential radial profiles calculated with and without imposing the O/M ratio. The curves are nearly identical. Again, the most visible difference occurs at mid-radius.

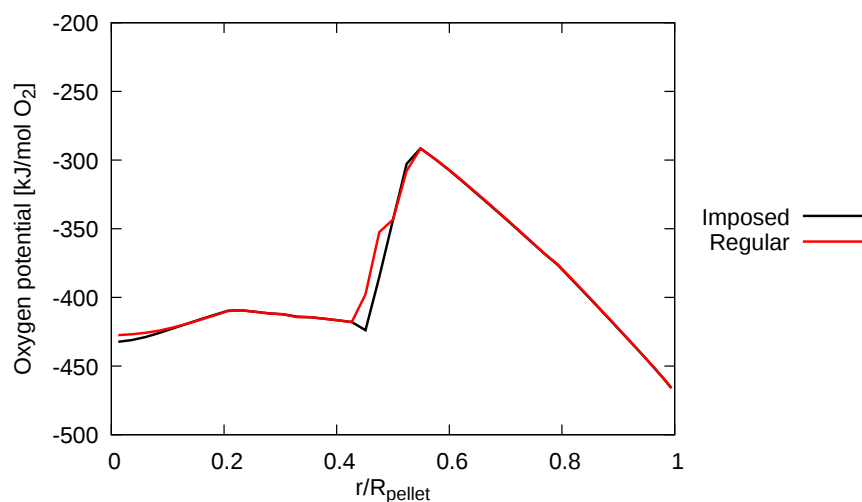


Figure 5.10: Oxygen potential radial profiles obtained in the calculations with (black curve) and without (red curve) imposing the O/M ratio.

The above comparison shows that the radial profiles of O/M ratios and oxygen potentials calculated with and without prescribing the O/M ratio do not differ much. The evolutions of the O/M ratio along the fuel pellet radius are slightly different but the oxygen potential evolutions are almost the same, which means that the major chemical compounds calculated in the gas phase and in the condensed phases should be similar in both calculations. This additional condition on the O/M ratio ensures the conservation of the average O/M ratio in the fuel pellet in the thermochemical calculations. In this respect, it significantly facilitates the thermochemistry-oxygen transport coupling by avoiding CPU-costly iterations.

### 5.1.5 Coupling strategy in power ramps

It must be stressed that thermochemical calculations are only performed during power ramps simulations with ALCYONE because the high temperatures at the pellet center guarantee that thermodynamic equilibrium is reached at least in this part of the pellet. For PCI analyses, this central hot pellet center is furthermore the location where the bulk of FGR takes place. The thermochemical–oxygen transport coupling can furthermore be uncoupled to some extent during the power transient for the following reasons:

- During the short power transient (duration a few tens of seconds) that precedes the long holding period at maximum power (duration usually around 10-20 hours), oxygen migration can be neglected, as inferred by the Cr EPMA profile of PR1 (no evolution during the transient). For this reason, only local thermochemical equilibrium calculations are performed during the power increase phase.
- During the long holding period, power variations are usually small leading a stable temperature distribution in the fuel pellet. Since the FP content and distribution in the fuel pellet is also stable (nominal irradiation that precedes the power ramp is at the origin of the bulk of FPs), thermochemical equilibria in the pellet will evolve mainly in consequence of oxygen transport by thermal diffusion in the solid solution. Thus, during the plateau at maximum power, oxygen transport in the pellet is first calculated, followed by local thermochemical calculations at prescribed O/M ratio.
- While the formation of internal zirconia during base irradiation leads to a decrease of the oxygen content in the pellet [77], there is no evidence that additional zirconia is formed during a power ramp. This result can be attributed to the slow evolution of zirconia thickness once the layer is formed [197]. In consequence, the flux of oxygen on the surface of the simulated fuel fragment during the power ramp can be assumed null at all time, meaning that the average oxygen content in the fuel pellet is constant.

This uncoupled analysis would not be possible in case of nominal irradiation since an oxygen source term that stems from the oxygen liberated by uranium fission would have to be included in the oxygen transport equation [80]. The release of oxide fission gases from the fuel pellet during the power ramp is neglected, which might prove to be wrong in the case of initially hyperstoichiometric fuels where the excess oxygen can lead to a pronounced oxidation of cracks formed by I-SCC [198].

### 5.1.6 Validation in 1D

To check the fuel performance modeling with oxygen thermal diffusion and thermochemistry and to validate the proportionality factor  $\alpha$  for standard  $\text{UO}_2$  fuel, the experiment presented by Adamson et al. [73] has been simulated. The authors carried out a power ramp on a BWR fuel rod irradiated to an average burnup of 11.4 GWd/tHM. They then measured the oxygen potential along the fuel pellet radius at 750 °C. The measurements showed low oxygen potentials in the central part (-550 kJ/mol  $\text{O}_2$ ) of the pellet and high oxygen potentials at the pellet periphery, see Figure 2.20. The authors concluded that the oxygen potential gradient can be explained by oxygen thermal diffusion from the pellet center to the periphery.

A 1D radial fuel performance simulation in ALCYONE including oxygen thermal diffusion has been carried out to model Adamson’s experiment. In the first stage, the base irradiation is simulated. Adamson et al. do not give enough information on base irradiation to perform a detailed simulation. The authors reported the initial O/M ratio of the fuel, the  $^{235}\text{U}$  enrichment, the pellet radius and the final average burnup. These parameters are given in Table 5.2. Since these data are not sufficient to properly model the base irradiation, additional assumptions have been made. A constant LHR of 200 W/cm has been assumed till the average burnup calculated in the simulation reached 11.4 GWd/tHM, the value reported by Adamson. The calculated burnup radial profile and its average value are shown in Figure 5.12. It must be emphasized that ALCYONE is not validated to simulate BWR fuels and thus burnup may not be simulated correctly.

Table 5.2: Main characteristics of the power ramped fuel reported by Adamson et al. [73].

<b>Fuel pin name</b>	<b>Radius [mm]</b>	<b>Initial enrichment % <math>^{235}\text{U}</math></b>	<b>Initial O/U</b>	<b>Average burnup [GWd/tHM]</b>	<b>Max. LHR [W/cm]</b>
LIT2/3	6.2	2.55	2.0015±0.0015	11.4	365

In the second stage, the power ramp experiment is simulated. Again, Adamson et al. have not reported all the details needed to simulate precisely the power ramp. It has been assumed that the experiment carried out by Adamson was similar to the power

ramps performed by CEA. The schematic representation of the power sequence is shown in Figure 5.11.

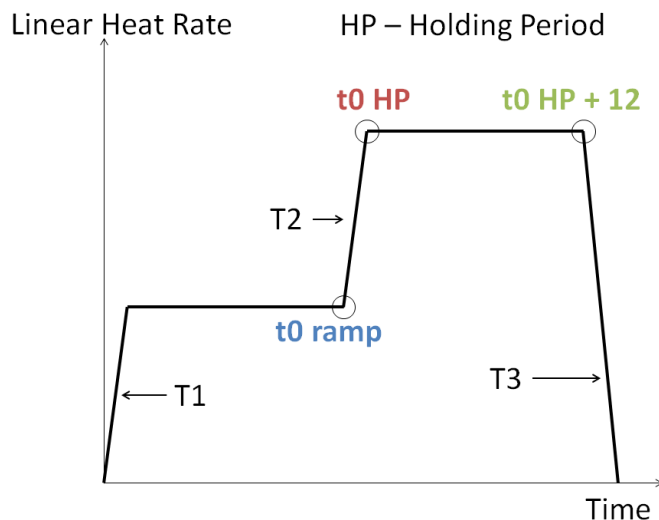


Figure 5.11: Schematic representation of the power ramp test performed by Adamson et al. [73]. The part until "t0 ramp" is the conditioning period. The holding period starts at "t0 HP" and lasts to "t0 HP+12h". Power transients are marked as T1, T2 and T3.

Additional parameters that are necessary to perform the power ramp simulation are shown in Table 5.3. The duration of the conditioning and holding periods and of the power transients T1-T3 is similar to those of the power ramps carried out at CEA (see Table 4.2).

Table 5.3: Additionally assumed characteristics needed to carry out the simulation of Adamson's experiment [73].

Cond. Period [h]	Cond. Power [W/cm]	Holding Period [h]	T1 [min]	T2 [s]	T3 [min]
18	169	12	60	120	30

The temperature calculated at the pellet center during the holding period is 1617 °C. It is close to the temperature reported by Adamson et al., which is 1605 °C. The temperature calculated at the periphery (541 °C) is only one degree higher than the temperature reported by Adamson et al. The calculated temperature profile is shown in Figure 5.12.

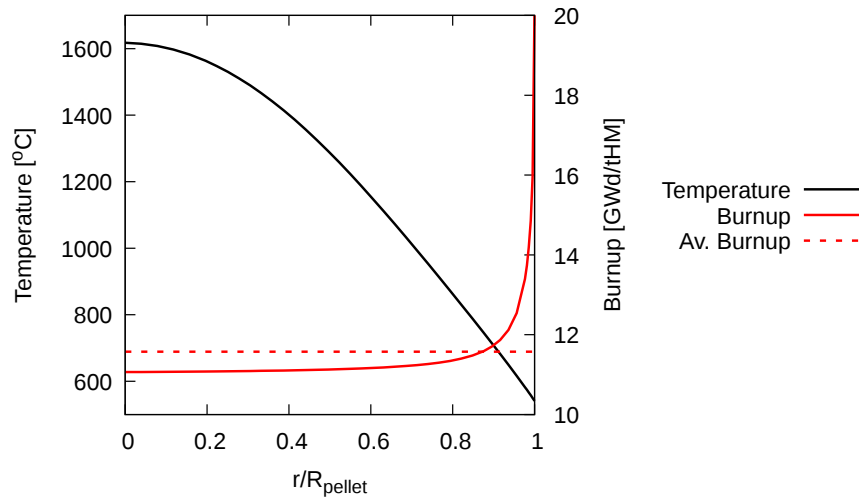


Figure 5.12: Calculated profiles of temperature and burnup. The red dashed line corresponds to the average burnup.

Oxygen thermal diffusion is considered only during the holding period leading to the highest temperature gradient in the fuel pellet. The proportionality factor  $\alpha$  is calculated with Equation 5.9. Its value at 11.4 GWd/tHM is 0.5686. The diffusion coefficient derived from Berthinier et al's approach [91] is used. Calculations show that the 12 hour-long holding period is long enough to reach the oxygen redistribution steady state. Adamson et al. reported that the initial O/U ratio of the fuel equals 2.0015 with an uncertainty of 0.0015. Thus, three simulations with three different initial O/U ratios (2.0000, 2.0015 and 2.0030) have been carried out. Also, these three simulations have been repeated without oxygen redistribution for comparison.

In the last stage of the simulation, the studied fuel is uniformly heated up to 750 °C. The oxygen potential at this temperature is calculated and compared to the experimental measurements. The results obtained for the different initial O/U ratios are shown in Figure 5.13.

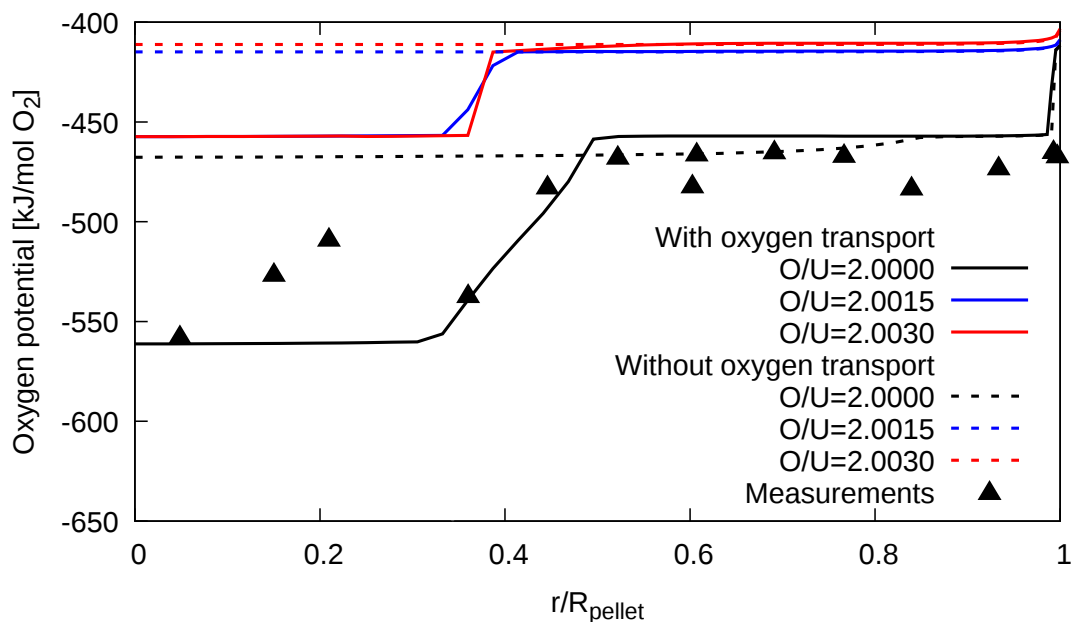


Figure 5.13: Oxygen potentials calculated with (solid curves) and without (dashed curves) oxygen redistribution for different initial O/U ratios. Black triangles correspond to the experimental measurements from Adamson et al. [73].

The solid curves in Figure 5.13 have been calculated with oxygen thermal diffusion and the dashed ones without it. It can be seen that the calculation with the initial O/U ratio of 2.0000 and including oxygen thermal diffusion gives a radial profile of oxygen potential that is close to the measures reported by Adamson et al. (black triangles), in particular at the pellet center. Simulations with higher initial O/U ratios overestimate the oxygen potential by around 100 kJ/mol O<sub>2</sub> at the pellet center and by 50 kJ/mol O<sub>2</sub> at the pellet periphery. Simulations without oxygen thermal diffusion show that the calculated oxygen potential is nearly constant along the entire radius. Oxygen transport changes the oxygen potential mainly at the pellet center ( $r/R_{\text{pellet}} < 0.5$ ). The oxygen potential close to the pellet periphery is very similar with and without oxygen transport.

The O/M ratios calculated at the end of the holding period are plotted in Figure 5.14 for the simulation with an initial O/U ratio of 2.0000 and accounting for thermal diffusion of oxygen. The O/M ratio calculated at the pellet center is close to 1.997, which is the value estimated by Adamson et al. The O/M ratio calculated at the periphery is 2 while Adamson reported O/M=1.999. Although the calculated value is higher than the one estimated by Adamson, the tendency is good because the O/M ratio increases along the fuel pellet radius. It needs to be stressed that the values reported by Adamson are estimations and not measurements.

The red curve is the O/M ratio calculated without oxygen transport. It increases slowly along the radius from 1.999 at the center to reach around 1.9998 at the periphery. The O/M ratio calculated at the pellet center is overestimated when compared to the value reported by Adamson (1.997). The value calculated at the periphery is close to the O/M ratio predicted by Adamson (1.999).

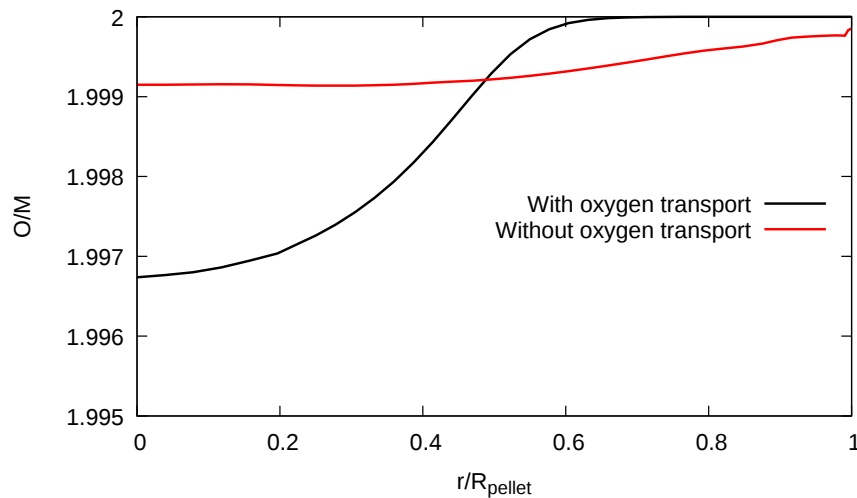


Figure 5.14: O/M ratios with and without oxygen transport calculated at the end of the holding period.

The simulation of Adamson’s experiment can be considered as a validation of the OXI-TRAN model and of the parameters governing oxygen transport. It shows that oxygen thermal diffusion included in fuel performance simulations can help to reproduce measurements of oxygen potential in power ramped irradiated fuel, especially at the pellet center where FGR takes place.

### 5.1.7 Validation in 3D

#### 5.1.7.1 Characteristics of the power ramp

To check the overall response of ALCYONE 3D scheme with the oxygen redistribution thermochemical coupling, the power ramp PR2 that was used to derive the heat of oxygen transport is simulated. Details of the experiment are given in Table 4.2. The rod was fabricated by Framatome with an initially stoichiometric Cr-doped  $\text{UO}_2$  fuel and a M5<sup>®</sup> cladding. The rod was irradiated in an EDF commercial PWR during 3 cycles and then sliced in order to fabricate a short rodlet that was ramped by CEA in the OSIRIS test reactor. The average burnup of the rodlet (38.8 GWd/tHM) is within the critical burnup range for PCI failure [112]. The power ramp sequence is detailed

in Figure 4.23. In spite of the high LHR reached during the power ramp (RTL of 470 W/cm) and the 12h long holding period, the rodlet survived the transient undamaged.

The 3D simulation presented hereafter concerns the fuel pellet located at the axial position of the maximum LHR (or PPN for Peak Power Node) in the PR2 rodlet. A standard 3D calculation of the base irradiation sequence is first performed with ALCYONE. In the next parts, the analysis of PR2 simulation results will be focused on the 12h long plateau where the thermochemical and oxygen transport calculations are both performed. Interestingly, this rodlet was extensively analyzed after the power ramp with measurements of numerous radial profiles of metallic and volatile fission products. The presentation will highlight the consequences of oxygen thermal diffusion on the fission products thermochemistry and release. In general, the results are presented at four specific times during the power ramp: when the LHR reaches 420 W/cm (two thirds of the transient), at RTL ("t0 HP"), after 2 minutes at RTL ("t0 HP+2min") and after 12 hours at RTL ("t0 HP+12h"). To better highlight the changes during the HP of PR2, experimental data from PR1 will be added in some Figures. We recall that PR1 had no HP, and thus gives the actual state of the FPs in the fuel pellet at "t0 HP".

### 5.1.7.2 Evolution of the O/M ratio and of the oxygen potential

The temperature distribution calculated in the fuel pellet fragment at different times of PR2 is illustrated in Figure 5.15.

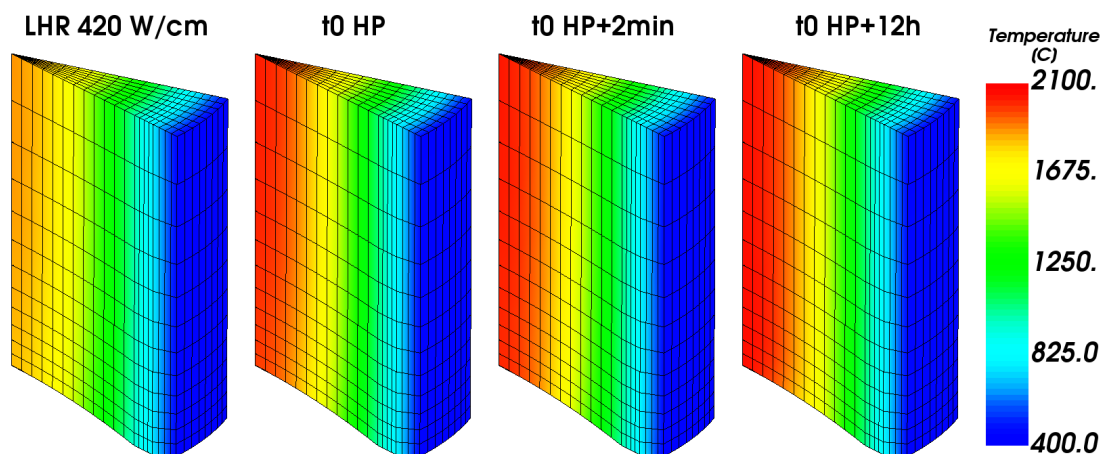


Figure 5.15: Calculated temperatures [ $^{\circ}\text{C}$ ] in the fuel fragment at different times during the power ramp PR2.

The maximum temperature is close to 2100  $^{\circ}\text{C}$  at the pellet center. As can be seen, the temperature distribution does not evolve during the HP and presents a negligible axial temperature gradient. Oxygen redistribution will therefore be mostly driven by the radial temperature gradient. Figure 5.16 shows 3D plots of the calculated O/M

ratio in the fuel fragment at different times during the HP of PR2. Radial profiles of the O/M ratio along the mid-pellet plane of the pellet fragment (top of the fragment) are furthermore plotted in Figure 5.17.

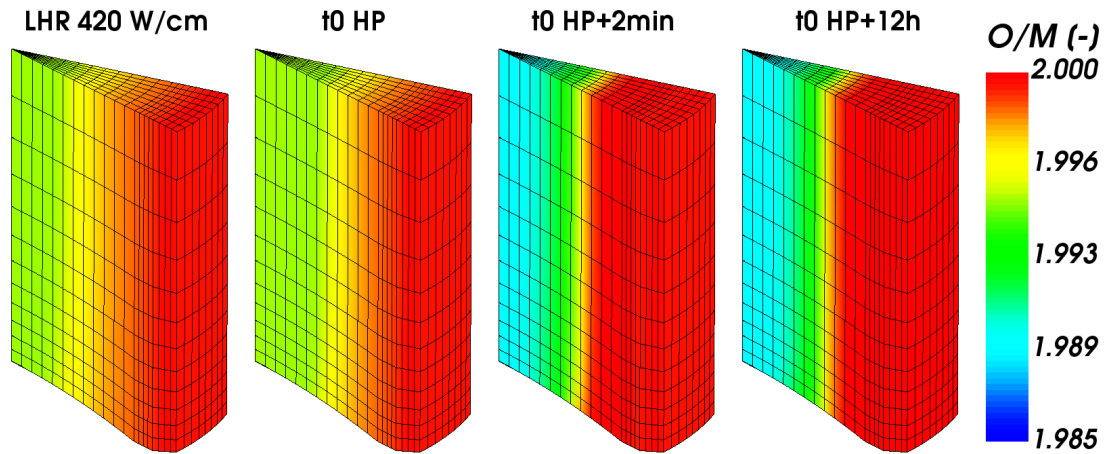


Figure 5.16: Calculated O/M ratios [-] in the fuel fragment at different times during the power ramp PR2.

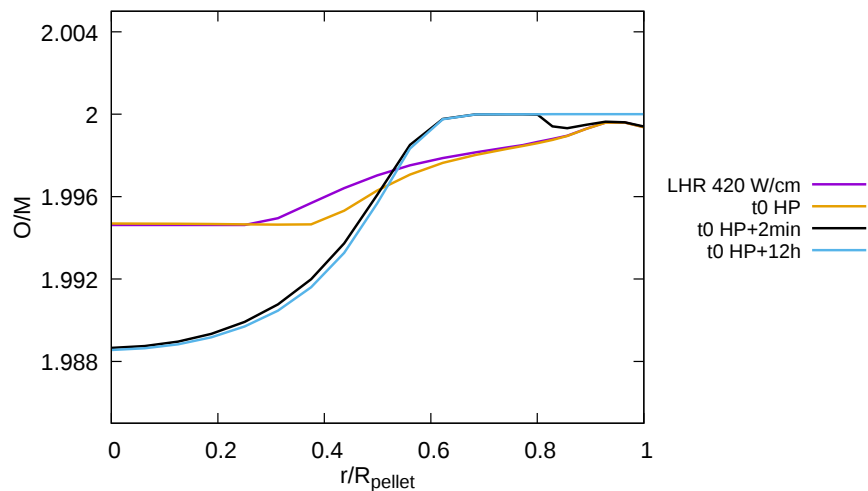


Figure 5.17: Calculated O/M radial profiles along the mid-pellet plane of the pellet fragment at different times during PR2.

According to the thermochemical calculations, the irradiated fuel is slightly hypostoichiometric (as defined in Section 3.3.1) at the beginning of the HP ("t0 HP"). The O/M ratio increases along the fuel pellet radius from 1.994 at the pellet center to nearly 2 at the pellet periphery. The formation of internal zirconia during nominal irradiation is not included which would certainly lower the O/M ratio at the pellet periphery. During the HP, oxygen thermal diffusion leads to a decrease of the O/M ratio (down to  $\sim 1.989$ )

at the center of the pellet and to an increase at the pellet periphery (up to 2). Oxygen redistribution kinetics, driven by the diffusion coefficient adapted from Berthinier et al. [91], is very fast. After 2 minutes, the radial profile of O/M ratio is already close to the steady-state profile calculated after 12 hours.

Figure 5.18 shows 3D plots of the calculated oxygen potential in the fuel fragment at different times during the HP of PR2.

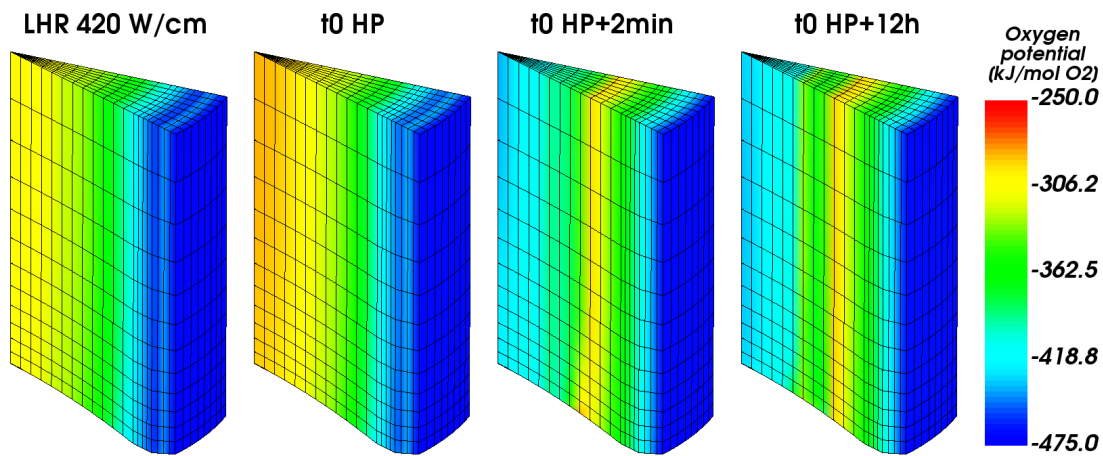


Figure 5.18: Calculated oxygen potentials [kJ/mol O<sub>2</sub>] in the fuel fragment at different times during power ramp PR2.

Radial profiles of the oxygen potential along the mid-pellet plane of the pellet fragment (top of the fragment) are furthermore plotted in Figure 5.19. As for temperature and the O/M ratio, the oxygen potential gradient in the fuel pellet fragment is mainly radial.

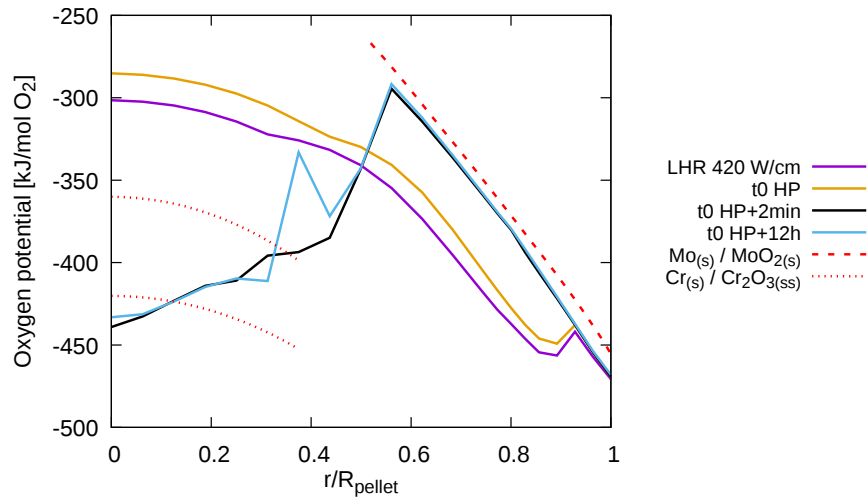


Figure 5.19: Calculated radial profiles of oxygen potential  $\Delta G_{O_2}$  along the mid-pellet radius at different times during power ramp PR2. The red dashed line shows the oxygen potential given by the  $\text{Mo}_{(s)}/\text{MoO}_{2(s)}$  redox system. The dotted lines give the oxygen potential associated with the  $\text{Cr}_2\text{O}_{3(ss)}/\text{Cr}_{(s)}$  redox system: top line for a Cr-dopant completely dissolved in  $\text{UO}_2$  (0.14 wt%, see Figure 5.20,  $\text{Cr}_2\text{O}_{3(ss)}$  t0 HP), bottom line corresponding to a residual Cr-solubility of 0.01% (see Figure 5.20,  $\text{Cr}_2\text{O}_{3(ss)}$  t0 HP+12).

It is worth recalling that the temperature distribution during the holding period of the power ramp is quasi-constant, so one may attribute oxygen potential changes to oxygen thermal diffusion only. At the beginning of the HP ("t0 HP"), the oxygen potential follows the temperature gradient, with a maximum of  $-300$  kJ/mol  $\text{O}_2$  at the pellet center and a minimum of  $-450$  kJ/mol  $\text{O}_2$  close to the pellet periphery. At the end of the HP, the oxygen potential decreases to  $-440$  kJ/mol  $\text{O}_2$  at the pellet center while it remains close to  $-450$  kJ/mol  $\text{O}_2$  at the periphery. The evolution along the radius is however strongly marked with nearly constant oxygen potential up to a relative radius of 0.4 followed by a sudden increase to  $-300$  kJ/mol  $\text{O}_2$  at a relative radius of 0.6. Oxygen potential at the center is within those associated to the  $\text{Cr}_{(s)}/\text{Cr}_2\text{O}_{3(ss)}$  equilibrium. At the pellet periphery, the oxygen potential is very close to the one given by the  $\text{Mo}_{(s)}/\text{MoO}_{2(s)}$  equilibrium. The oxygen potential of these redox systems are shown in Figure 5.19 by dotted and dashed lines respectively.

### 5.1.7.3 Impact of oxygen transport on metallic oxides

The decrease of the oxygen potential at the pellet center has important consequences on some of the metallic FPs and added dopants. As expected from the fit of the heat of oxygen transport, chromium oxides are partially reduced. Figure 5.20 shows the calculated radial profiles of Cr content in solid solution ( $\text{Cr}_2\text{O}_{3(ss)}$ ) at the beginning

(thick orange curve) and at the end (thick blue curve) of the HP of PR2 compared to EPMA measurements (thin blue curve).

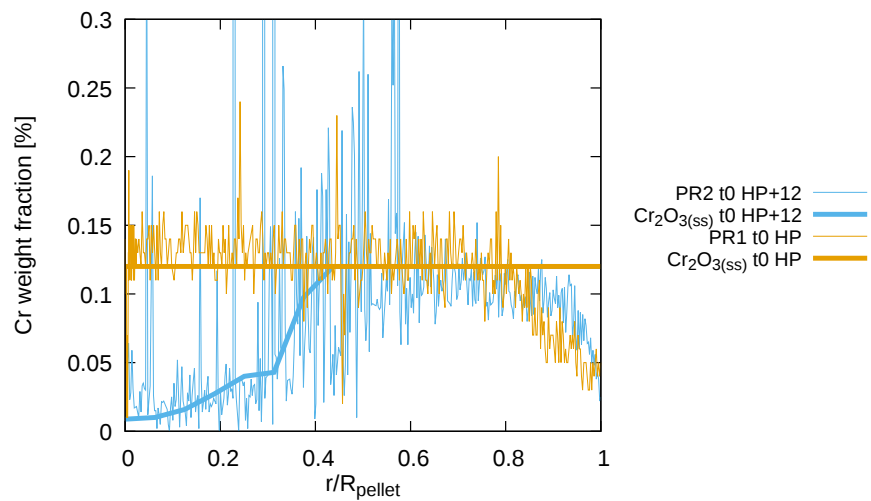


Figure 5.20: Calculated Cr weight fraction evolution during the holding period compared to EPMA measurements after PR1 and PR2.

The thin orange curve shows the measured Cr content after PR1, which is similar to the as fabricated content. The evolution of chromium speciation in the 3D simulation of PR2 is shown in Figure 5.21.

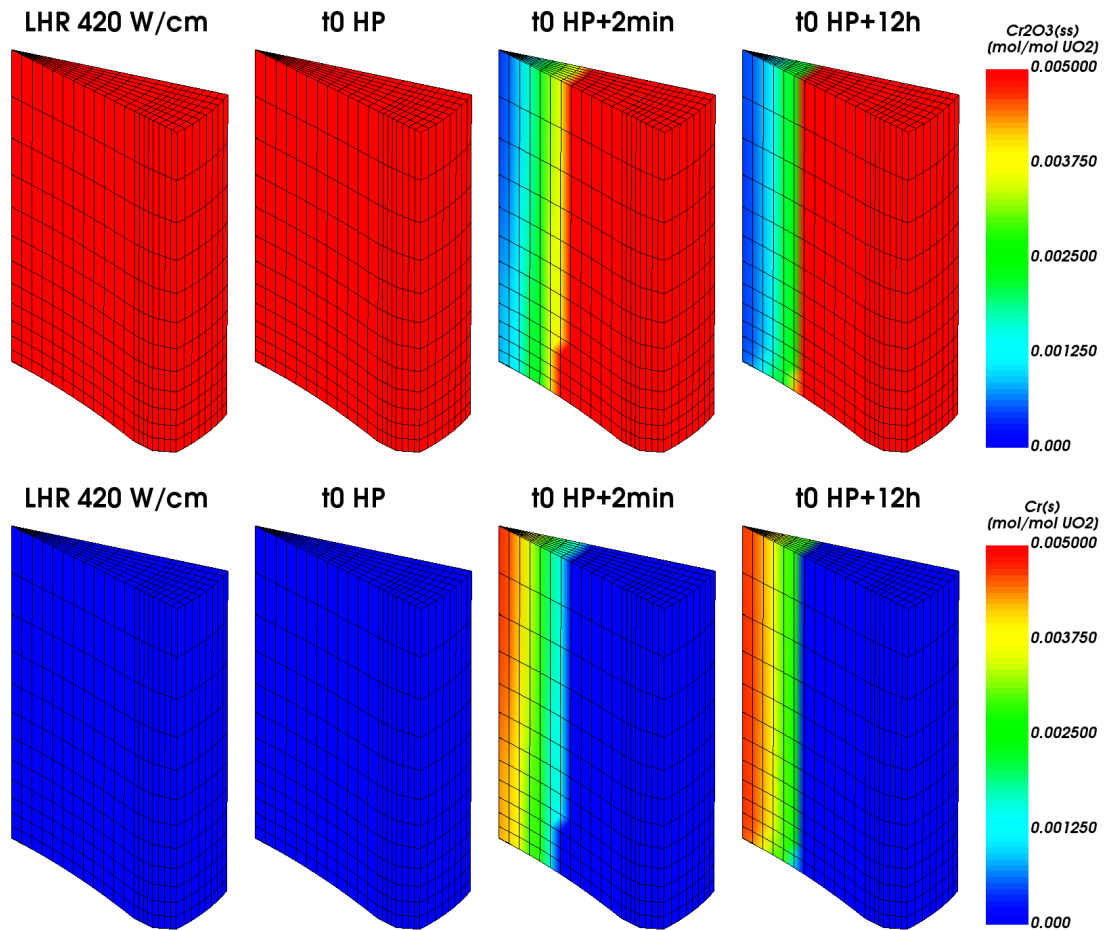


Figure 5.21: Calculated  $\text{Cr}_2\text{O}_3(ss)$  (upper plots) and  $\text{Cr}(s)$  (lower plots) concentrations [mol/mol  $\text{UO}_2$ ] at different times during power ramp PR2.

As can be inferred from these results, the sole elevation of the fuel temperature in the transient part of PR2 during a few tens of seconds did not lead to a reduction of chromium oxide ( $\text{Cr}_2\text{O}_3(ss)$ ) into metallic chromium ( $\text{Cr}(s)$ ). According to the calculations, oxygen thermal diffusion during the HP is at the origin of the lower Cr content in solid solution after PR2. The reduction of chromium soluble oxides into metallic chromium is further confirmed by X-ray images of the central part of the fuel pellet after PR2, see Figure 4.28. One can find a massive precipitation of metallic Cr (central image, white spots) which is not associated with oxygen (right image, black spots).

Similar observations are available for molybdenum, see Figure 4.28 where white spots in the Mo X-ray distribution (left image) are not associated to oxygen (right image, black spots). As stated before, in the thermochemical database of ANGE, Mo is not included in the fluorite solid solution model. One may however estimate the impact of oxygen redistribution by plotting the calculated concentrations of Mo in oxide form ( $\text{MoO}_2(s)$  and  $\text{Cs}_2\text{MoO}_4(s)$  mainly) and that of Mo in metallic form ( $\text{Mo}(s)$ ) during the HP of PR2, see Figure 5.22.

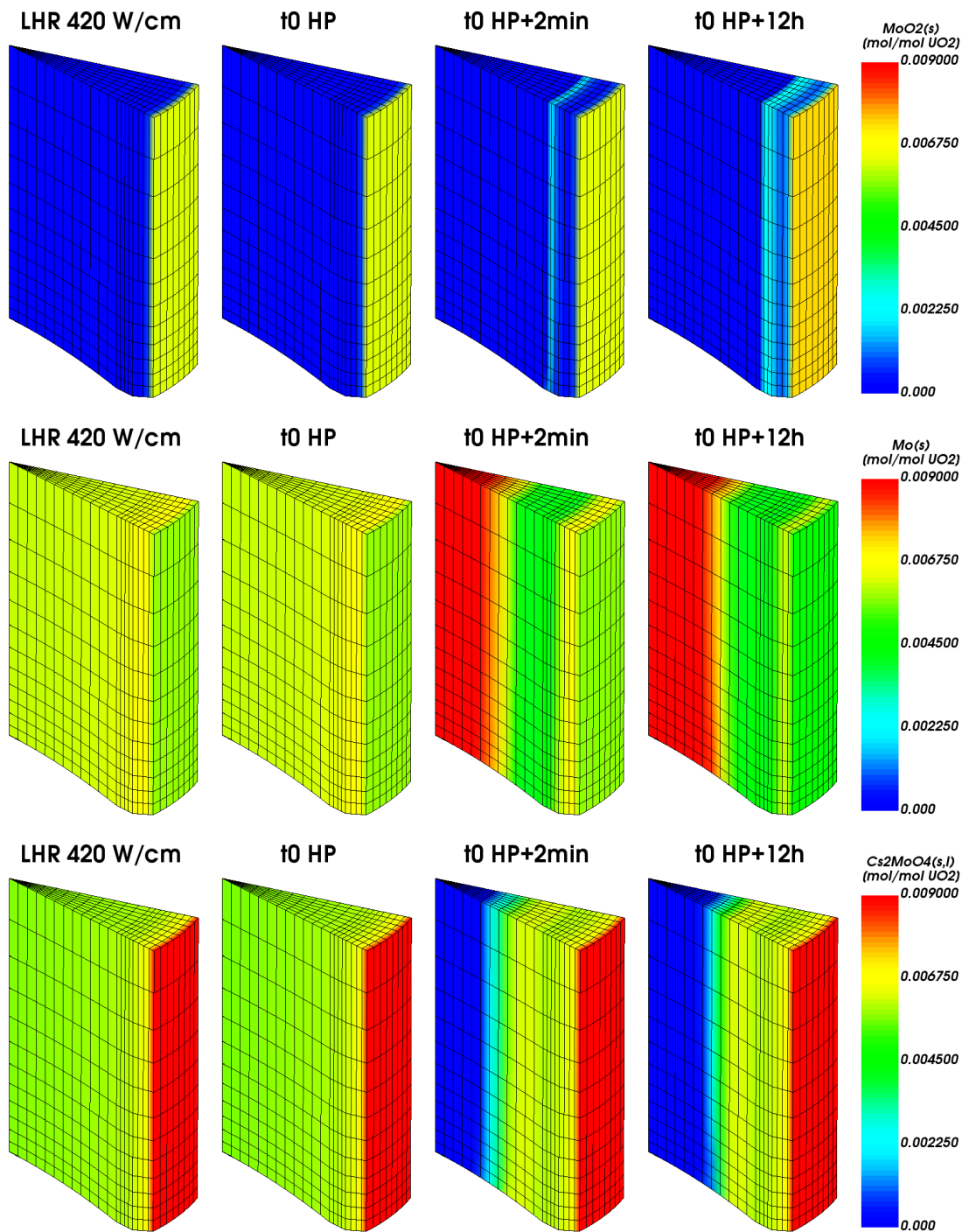


Figure 5.22: Calculated concentrations of  $\text{MoO}_2(s)$  (top figures),  $\text{Mo}(s)$  (middle figures) and  $\text{Cs}_2\text{MoO}_4(s,l)$  (bottom figures) at different times during power ramp PR2.

Oxygen transport by thermal diffusion leads to a reduction of  $\text{Cs}_2\text{MoO}_4(s,l)$  at the pellet center and to the precipitation of  $\text{Mo}(s)$ . EPMA measurements may be compared to the concentrations of these molybdenum species at the end of the HP, see Figure 5.23.

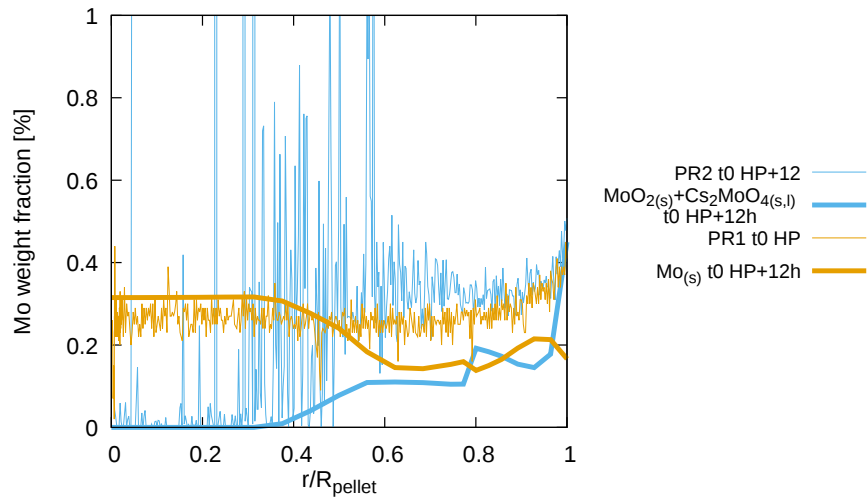


Figure 5.23: Calculated molybdenum oxides  $\text{MoO}_{x(s,l)}$  and metallic molybdenum  $\text{Mo}_{(s)}$  weight fraction evolution during the HP of power ramp PR1 compared to EPMA measurements after power ramps PR1 and PR2. PR1 rodlet has a lower burnup than PR2 rodlet so the Mo weight fraction is lower on average.

The blue and orange thin curves represent the Mo content measured by EPMA after PR2 and PR1, respectively. As for Cr, the profile after PR1 (similar to the one obtained before the power ramp) shows that the reduction of Mo oxides at the pellet center is not a consequence of the sole temperature elevation during the power transient phase. Oxygen transport by thermal diffusion explains the pronounced increase of metallic Mo during the HP.

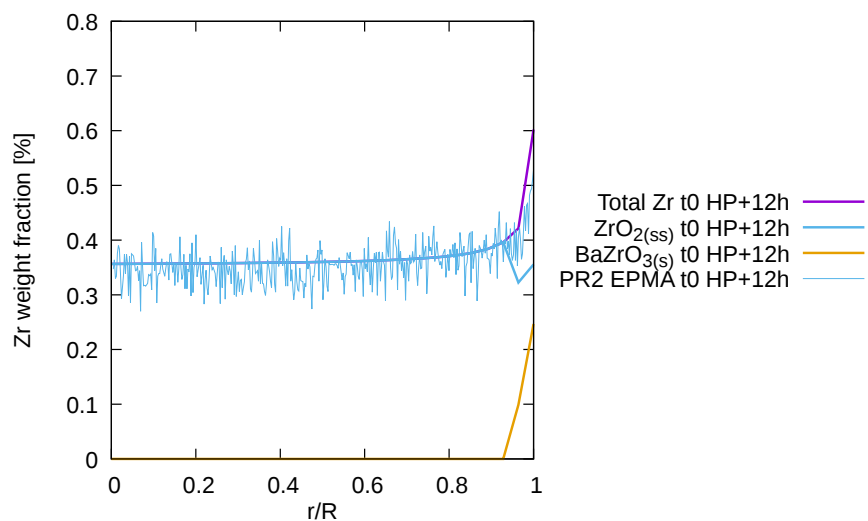


Figure 5.24: Calculated  $\text{ZrO}_{2(ss)}$  and  $\text{BaZrO}_{3(s)}$  concentrations compared to the EPMA measurement of Zr weight fraction after power ramp PR2.

Among the other metals, zirconium is a very abundant FP and is found mostly in oxide form in the irradiated fuel pellet, see Figure 5.24 where EPMA measurements after PR2 are also indicated. Zirconium is found as  $ZrO_{2(ss)}$  in the entire pellet radius except at the periphery where one can also find  $BaZrO_{3(s)}$ . Reduction of the zirconium oxide into metallic zirconium would require oxygen potentials lower than  $-650$  kJ/mol  $O_2$  at the pellet center, which are not reached here in spite of the oxygen redistribution.

#### 5.1.7.4 Noble Fission Gas Release

The evolution of noble gas release during the HP of PR2 is illustrated by the 3D plots of the xenon released fraction (in % of the initial inventory) given in Figure 5.25.

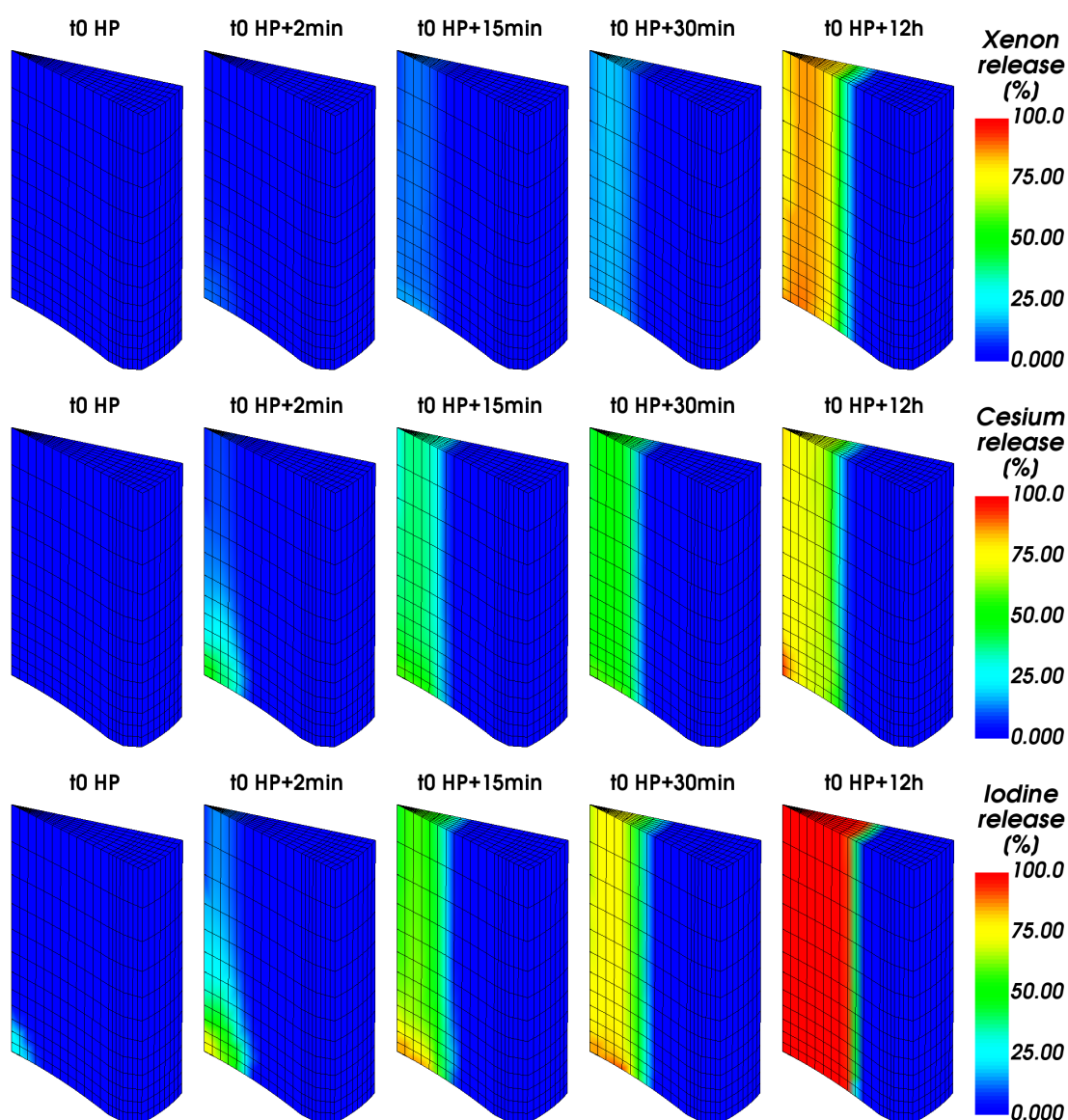


Figure 5.25: Calculated release of Xe (top), Cs (middle) and I (bottom) at different times during the power ramp PR2. Units—% of initial inventory.

As can be seen, the release of xenon is very small during the first minutes of the HP compared to the end of it. The release begins near the dish in consequence of the lower hydrostatic pressure which favors the expansion of inter-granular fission gas bubbles [14]. At the end of the 12 h long HP, xenon release from the pellet center reaches 90%. The calculated radial profiles at the beginning and at the end of the HP (along the inter-pellet plane) are compared in Figure 5.26 to xenon weight fractions from EPMA and SIMS measurements.

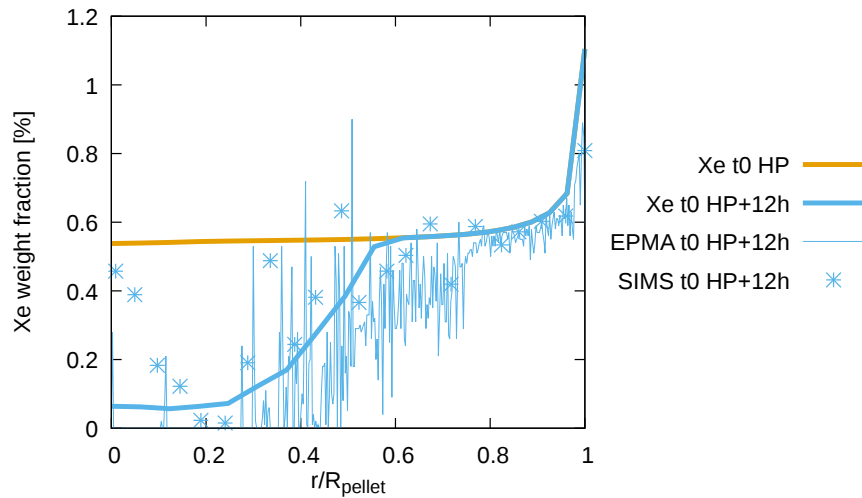


Figure 5.26: Calculated total (dissolved within grains, in intra- and inter-granular bubbles and in inter-granular pores) Xe weight fraction at the beginning and the end of the holding period of power ramp PR2 compared to EPMA and SIMS measurements.

The agreement is fair considering the dispersion of experimental measures. It must be recalled that EPMA measurements underestimate the xenon inventory since large gas bubbles are characterized by a peak in the radial profile and are therefore not included in the base line. SIMS measurements are more representative of the total xenon left in the fuel pellet after PR2. Calculations lead to a FGR of around 17% to be compared with the 8% measured in the fuel rodlet. The difference stems from the fact that the 3D simulation is local and concerns only the fuel pellet situated at PPN.

### 5.1.7.5 Iodine release and speciation

The evolution of iodine release during the HP of PR2 is illustrated by the 3D plots of the iodine released fraction (in % of the initial inventory) given in Figure 5.25. The evolution of iodine is similar to that of xenon with a beginning near pellet dishes and a final release of 100% up to mid pellet radius. The chemical speciation of gaseous iodine must be discussed since it is of importance for PCI failure analyses. Most of the iodine

in the fuel pellet fragment leads to the formation of  $\text{CsI}_{(g)}$ , as can be seen from the 3D plots of Figure 5.27.

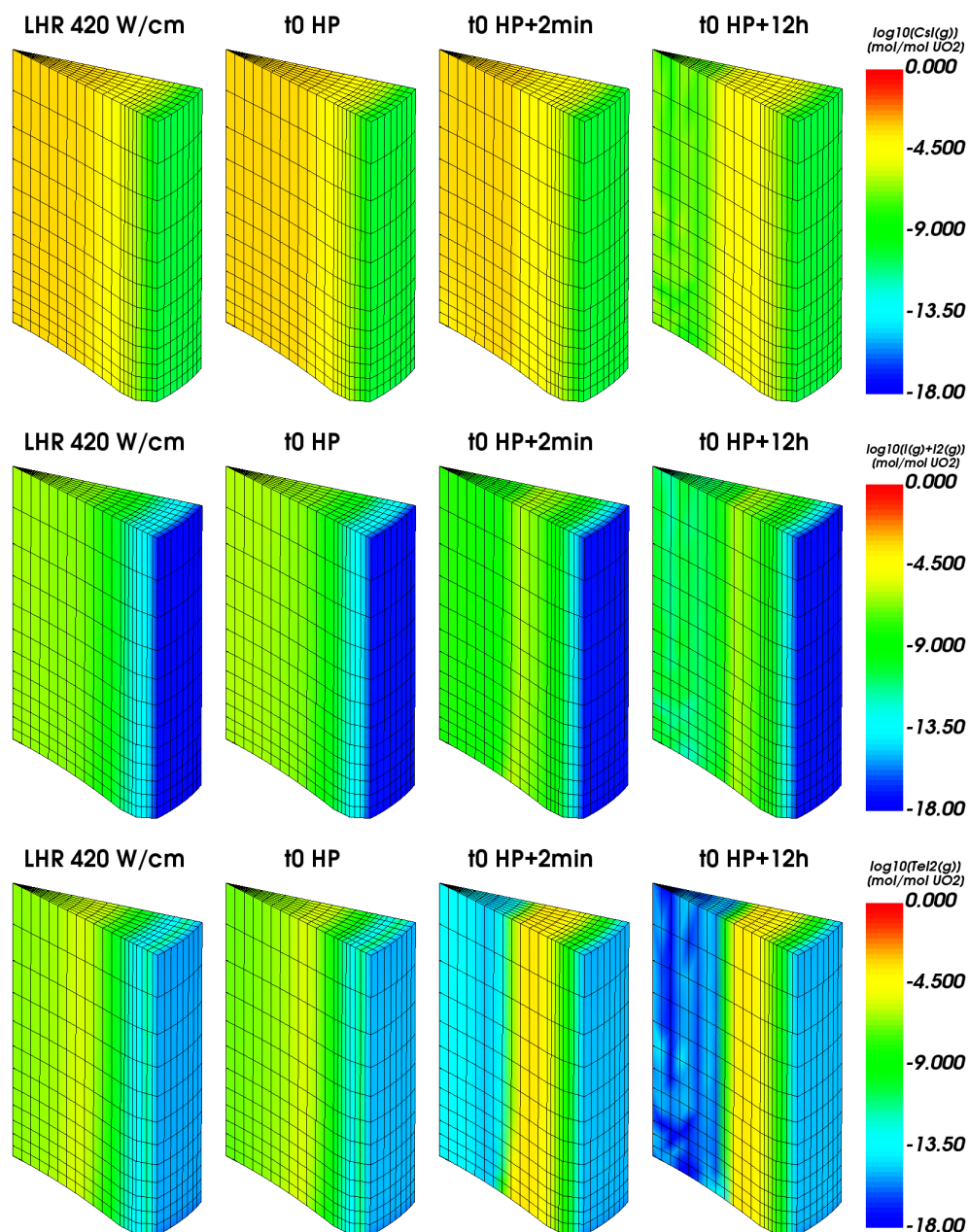


Figure 5.27: Calculated  $\text{CsI}_{(g)}$ ,  $\text{I}_{(g)}+2\text{I}_{2(g)}$  and  $\text{TeI}_{2(g)}$  concentrations in the fuel fragment at different times during power ramp PR2.

The progressive release of  $\text{CsI}_{(g)}$  during the HP explains the lower concentration in the pellet fragment at the end of the power plateau ("t0 HP + 12h"). Apart from  $\text{CsI}_{(g)}$ , a small part of iodine forms gas species in the pellet ( $\text{I}_{(g)}$ ,  $\text{I}_{2(g)}$  and  $\text{TeI}_{2(g)}$ ) that are likely to react with the Zr-cladding to form  $\text{ZrI}_{4(g)}$  and hence induce I-SCC if released from the fuel [14]. Figure 5.27 presents the evolution of their concentration in the fuel pellet

during the power ramp PR2. One may see that the concentration of these three iodine gas species is highest at the pellet center at the beginning of the HP ("t0 HP"), meaning that a small proportion of iodine released from the fuel will consist in deleterious gases for the cladding (see Figure 5.25 where nearly 30% of the total iodine left the pellet near the dish at "t0 HP"). Later, after oxygen redistribution, the concentration of these species at the pellet center is around 3 orders of magnitude lower, the maximum concentration being now found between mid-radius and the pellet periphery. Since this part of the pellet does not really contribute to the overall FGR, this means that the release of iodine after a few minutes of HP and in consequence of oxygen transport by thermal diffusion will mainly consist in  $\text{CsI}_{(g)}$ .

#### 5.1.7.6 Cesium release and speciation

The evolution of cesium release during the HP of PR2 is similar to that of iodine and xenon, as illustrated by the 3D plots of cesium released fraction (in % of the initial inventory) given in Figure 5.25. Cesium release at the beginning of the HP ("t0 HP") is lower than that of iodine but increases during the first minutes of the HP and reaches 90% near the pellet center at the end of the HP. This result is a direct consequence of oxygen redistribution.

Figure 5.28 shows the evolution of  $\text{Cs}_2\text{MoO}_4_{(s,l)}$  and of gaseous cesium ( $\text{Cs}_{(g)} + 2\text{Cs}_2_{(g)}$ ) in the 3D simulation of PR2.

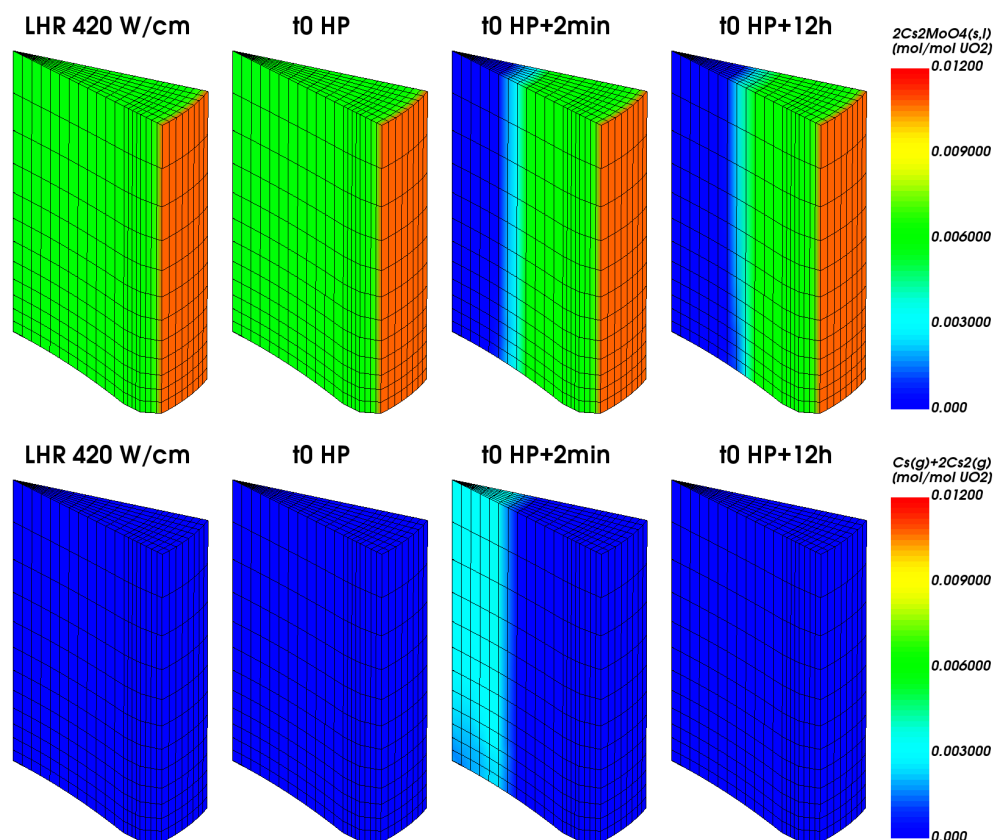


Figure 5.28: Calculated  $2\text{Cs}_2\text{MoO}_{4(s,l)}$  and  $\text{Cs}_{(g)}+2\text{Cs}_{2(g)}$  concentrations in the fuel fragment at different times during power ramp PR2.

At the beginning of the HP ("t0 HP"), high quantities of Mo and Cs are bound together as  $\text{Cs}_2\text{MoO}_{4(s,l)}$ . A small fraction of Cs is in the gas phase, mostly associated to I (around one tenth since there is around ten times more Cs than I in the fuel pellet at the end of base irradiation). Reduction of  $\text{Cs}_2\text{MoO}_{4(s,l)}$  at the pellet center in consequence of oxygen redistribution liberates most of the cesium which then forms gaseous compounds (mainly  $\text{Cs}_{(g)}$  and  $\text{Cs}_{2(g)}$ ) that can be released from the pellet. One clearly see that the reduction of cesium molybdate is associated with the formation of gaseous cesium. Concentration of gaseous cesium is lower at the end of the HP ("t0 HP + 12h") because it has been released from the fuel pellet fragment.

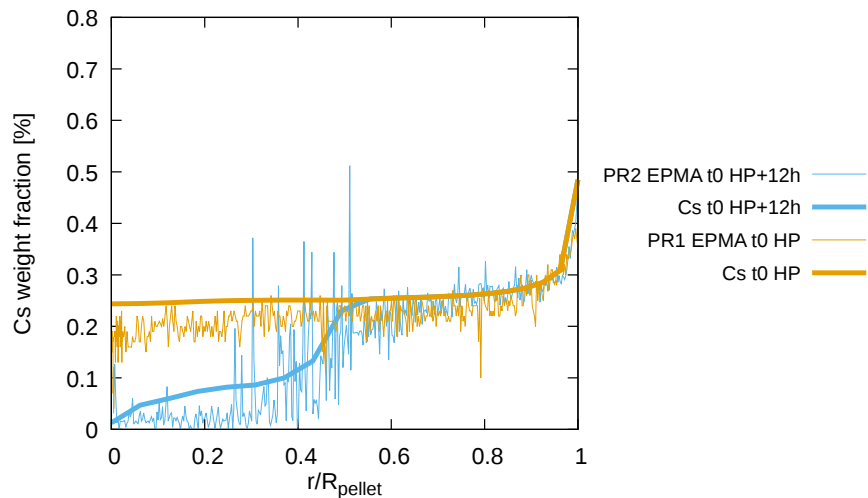


Figure 5.29: Calculated weight fractions of cesium at the beginning and at the end of the HP of power ramp PR2 compared to EPMA measurements after power ramps PR1 and PR2.

Figure 5.29 shows the calculated weight fractions of Cs at the end of the HP of PR2 compared to EPMA measurements after PR1 and PR2. Again, PR1 EPMA radial profile is representative of the state of cesium before oxygen redistribution takes place and is very close to the pre-ramp cesium distribution in the pellet. At the end of PR2, the calculated quantity of Cs in the central part of the pellet has considerably decreased which is consistent with EPMA measurements.

#### 5.1.7.7 FGR from the fuel pellet fragment

Figure 5.30 shows the evolution during the HP of PR2 of the released fractions of cesium, iodine and xenon integrated on the fuel pellet fragment (solid lines).

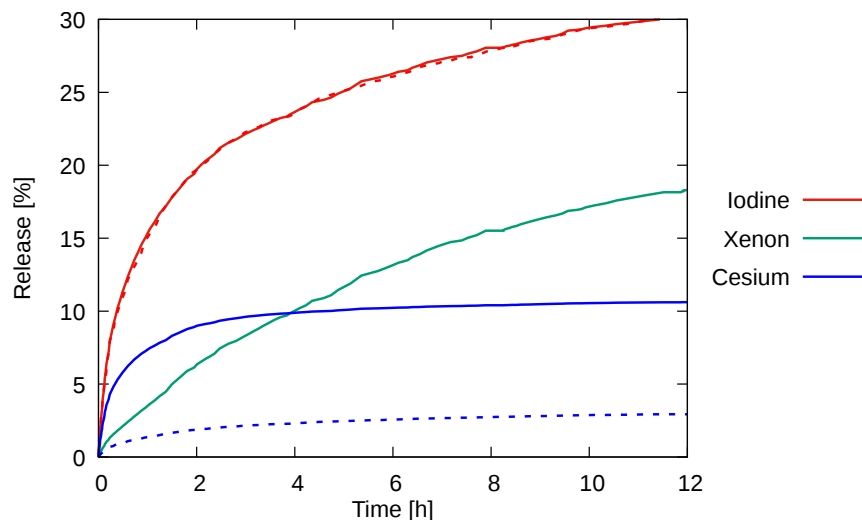


Figure 5.30: Calculated release of Cs, I and Xe during power ramp PR2. Solid lines refer to the simulation with oxygen transport, dashed lines refer to the simulation without oxygen transport ( $t=0$  corresponds the beginning of the holding period, "t0").

As was expected from the 3D plots, there is a significant difference between the FGR of Xe-Cs on the one hand and of iodine on the other hand. Iodine release reaches 30% while Xe and Cs releases reach 17% and 10% respectively. An even greater difference in the release of Xe-Cs and I-Te was reported by Baurens [14] from a 3D thermo-chemical-mechanical simulation of a short power ramp. Baurens' results are recovered here if the 3D simulation of PR2 is performed without oxygen transport. Iodine and xenon release are not changed by removing oxygen transport but cesium release is. The dashed blue line indicates that cesium release in this case does not exceed 2% at the end of the HP. This result is a consequence of the cesium speciation in the fuel pellet, where most of cesium remains in stable solid or liquid cesium molybdates and cannot be released from the fuel.

## 5.2 3D simulation of PCI-SCC

Baurens et al. have simulated a short holding period power ramp to validate the implementation of the thermochemical solver ANGE in the fuel performance code ALCYONE V1.4 [14]. The authors studied the speciation and the release of the fission products I, Cs and Te. Also, the conditions leading to PCI-SCC were investigated. The studied fuel is interesting for a PCI-SCC analysis because of a very high LHR was reached during the test (520 W/cm), which led to formation of cracks on the internal cladding surface with a maximum depth of around 100  $\mu\text{m}$ . In spite of the cracks, the fuel rod survived the transient leading to a rare case of a power ramp where I-SCC started but did not lead

to cladding failure. This result can be explained by the short duration of the holding period (90 s), which was not sufficient for the crack penetration across the entire clad thickness.

Baurens' simulation has been carried out with ALCYONE V1.4 including the fission gas release model MARGARET [37] and the thermochemical solver ANGE [150] i.e., the models used in this work. However, major modifications in the fuel performance code ALCYONE have taken place since Baurens' publication in 2014. The neutronics model PRODHEL has been implemented and it can be used instead of the empirical correlations based on the CESAR code (given in Table 1.3). Also, the database of ANGE has been updated, as described in Section 3.2.2.

Baurens' simulation has been repeated in this work to study the impact of oxygen thermal diffusion on the speciation of fission products and on the release of iodine, tellurium and cesium. Baurens' work on I-SCC initiation has been extended to the evaluation of clad crack depth calculations using the I-SCC model proposed by Le Boulch et al. [199], described in Section 2.3.4.1.

### 5.2.1 Characteristics of the power ramp

The studied fuel is an initially stoichiometric  $\text{UO}_2$  clad with stress-relieved Zircaloy-4. The 3D simulation has been performed in two stages. In the first one, the base irradiation is simulated. The studied fuel rod has undergone three irradiation cycles in a commercial PWR. The fuel characteristics used in the base irradiation simulation are shown in Table 5.4.

Table 5.4: Main characteristics of the fuel power ramped in PR5.

<b>Fuel material</b>	<b>Cladding material</b>	<b>Initial enrichment [%]</b>	<b>Irradiation cycles</b>	<b>Average cycle power [W/cm]</b>	<b>Reached burnup [GWd/tHM]</b>
$\text{UO}_2$	Zircaloy-4	4.5	3	178-260-214	35

The irradiated fuel rod was used to fabricate the rodlet, which was then power ramped in the OSIRIS reactor. The maximum linear heat rate reached in the experiment is 520 W/cm, which is higher than in the power ramps studied previously in this work (see Table 4.2). The power ramp test sequence is illustrated in Figure 5.31.

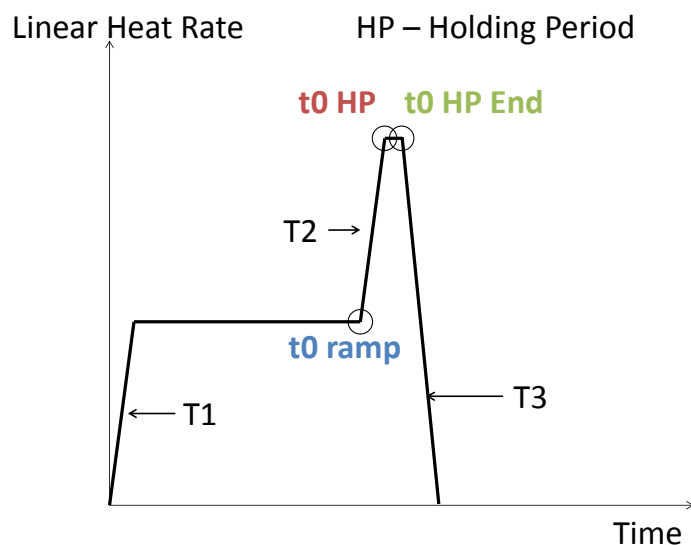


Figure 5.31: Schematic representation of PR5.

PR5 starts with a conditioning period that lasts until "t0 ramp" in Figure 5.31. Then, the power is increased until it reaches its maximum value at "t0 HP" when the holding period starts. It lasts until "t0 HP End". The duration and power of the different periods of PR5 are given in Table 5.5.

Table 5.5: Main characteristics of PR5.

Test name	Max. LHR [W/cm <sup>2</sup> ]	Cond. Period [h]	Cond. Power [W/cm <sup>2</sup> ]	Period Holding Period [s]	T1 [min]	T2 [s]	T3 [s]
PR5	520	16	180	90	4.9	192	6

## 5.2.2 Temperature and pressure

Figure 5.32 shows the calculated temperatures in the fuel fragment at different times during the power ramp. During the conditioning period, the temperature at the pellet center reaches around 900 °C and at the periphery 400 °C. Such temperature distribution occur during normal reactor operation. The temperature at "LHR 420 W/cm<sup>2</sup>" is much higher at the center and reaches around 1850 °C. This LHR occurs after two third of the transient T2. The temperature distributions at the beginning ("t0 HP") and the end ("t0 HP End") of the holding period are nearly the same because the LHR is constant during the plateau. The temperature at the pellet center is around 2200 °C. The axial temperature gradient is much less significant than the radial one. It is a consequence of the complete fuel-cladding gap closure during the power ramp.

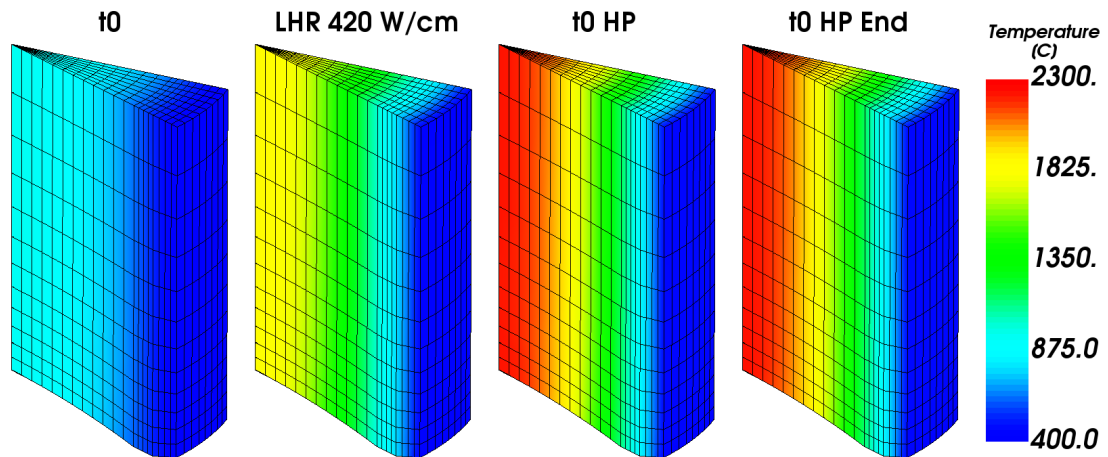


Figure 5.32: Temperature [ $^{\circ}\text{C}$ ] calculated at different times during PR5.

Figure 5.33 gives the hydrostatic pressure calculated at the same times than the temperatures. The hydrostatic pressure distribution is similar to the one reported by Baurens et al. but the values are slightly higher. During the power transient ("LHR 420 W/cm"), the hydrostatic pressure is maximum at the mid-pellet plane ( $\sim 2500$  bar) and minimum near the dish plane (80 bars) due to the axial deformation possible in this region. During the HP, fuel pellet creep leads to a relaxation of the stresses and hence to a decrease of the hydrostatic pressure leading to less axial variation along the fuel centerline. Hydrostatic pressure is very important for the model MARGARET since it controls the size of the fission gas bubbles at inter-granular sites and hence the FGR to the rod free volume [14].

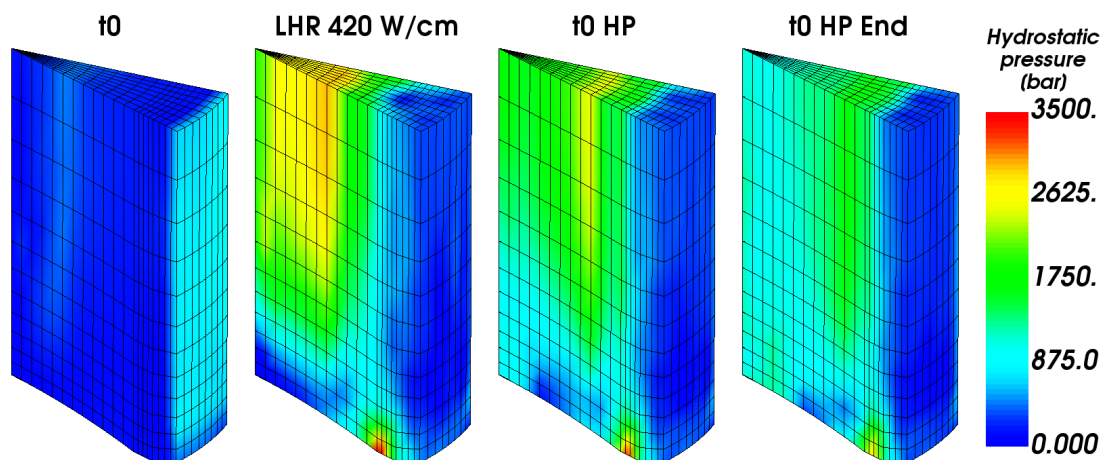


Figure 5.33: Hydrostatic pressure [bar] calculated at different times during PR5.

### 5.2.3 O/M ratio and oxygen potential

The oxygen over metal ratio calculated at different times during PR5 is shown in Figure 5.34. The O/M ratio at "t0" is above 1.999 in the entire fuel pellet fragment. It is a consequence of the low temperatures occurring during the conditioning period. At such temperatures (900 °C), the solid solution phase consists mostly of  $\text{UO}_2$  (with  $\text{O/M}=2$ ) because the solubility of trivalent fission products is limited. With temperature increase, the O/M ratio decreases in consequence of the increased solubility of FPs. This effect can be observed when the LHR reaches 420 W/cm. The O/M ratio in the hot part decreases to around 1.997. Oxygen thermal diffusion starts at "t0 HP" and lasts until "t0 HP End". The O/M ratio at "t0 HP" is similar to the one calculated at "LHR 420". The O/M ratio at the pellet center decreases to 1.992 at the end of the holding period, which is a direct consequence of oxygen redistribution. The O/M at the pellet periphery increases but it does not reach 2 everywhere meaning that the oxygen redistribution steady state has not been reached.

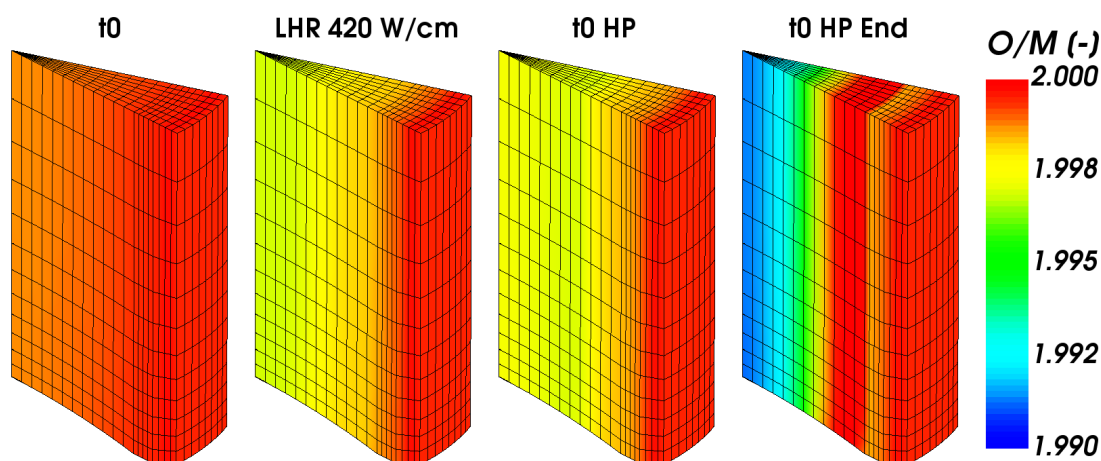


Figure 5.34: O/M ratio calculated at different times during PR5.

The oxygen potential calculated in the fuel fragment is shown in Figure 5.35. Between "t0" and "t0 HP", the oxygen potential increases at the pellet center from -450 kJ/mol  $\text{O}_2$  to -250 kJ/mol  $\text{O}_2$ . The increase at the periphery is less significant because the temperature at the pellet edge is nearly constant. The values at the pellet center at "t0 HP End" are lower than at "t0 HP", in consequence of oxygen redistribution towards the cold periphery of the pellet. The oxygen potential at the pellet center is reduced to -350 kJ/mol  $\text{O}_2$  at "t0 HP End". The highest values are found at  $r/R_{\text{pellet}} = 0.6$ . This result is due to oxygen thermal diffusion which has not reached steady-state. In consequence, the O/M ratio is not the highest at the pellet periphery but at  $r/R_{\text{pellet}} = 0.6$  (see Figure 5.34). Since the total oxygen content is related to the change in O/M ratio, the locally increased oxygen content leads to a peak in oxygen potential.

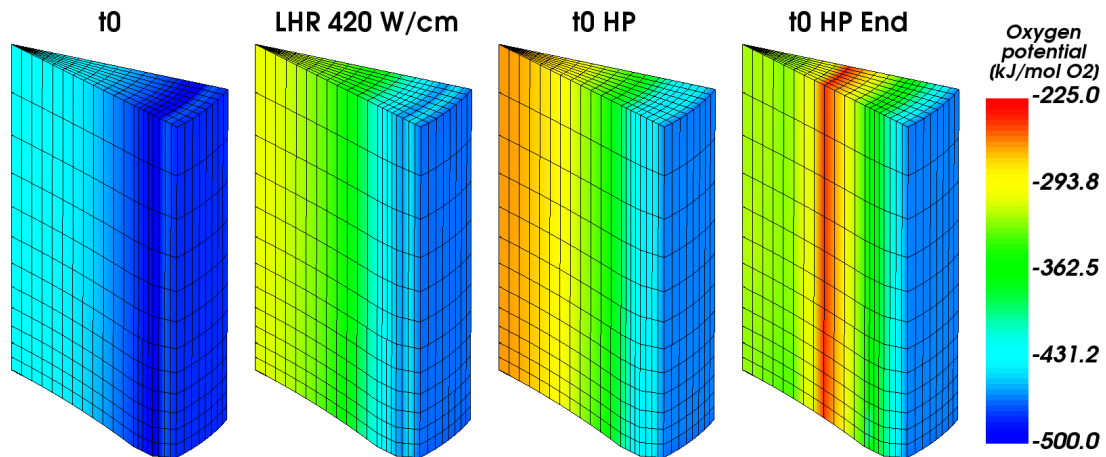


Figure 5.35: Oxygen potential calculated at different moments of PR5.

#### 5.2.4 Fission Gas Release

The calculated release of Xe at different times during PR5 is shown in Figure 5.36. Only the Xe released during the power ramp (Xe released minus Xe lost at the end of base irradiation) is here reported. It can be seen that the release before the start of the power transient (" $t_0$ ") is negligible. During the power transient ("LHR 420 W/cm"), Xe is first released near the pellet dish, in consequence of the lower hydrostatic pressure in this region which favors bubble size growth and hence bubble interconnection at grain boundaries, the prerequisite condition for release to the free volume of the rod. Xe release increases till the end of the transient (" $t_0$  HP"). During the holding period of 90s, the fraction of released Xe becomes more uniform along the fuel centerline in consequence of the smoother hydrostatic pressure distribution. Xe release reaches around 25% near the pellet dish at " $t_0$  HP End".

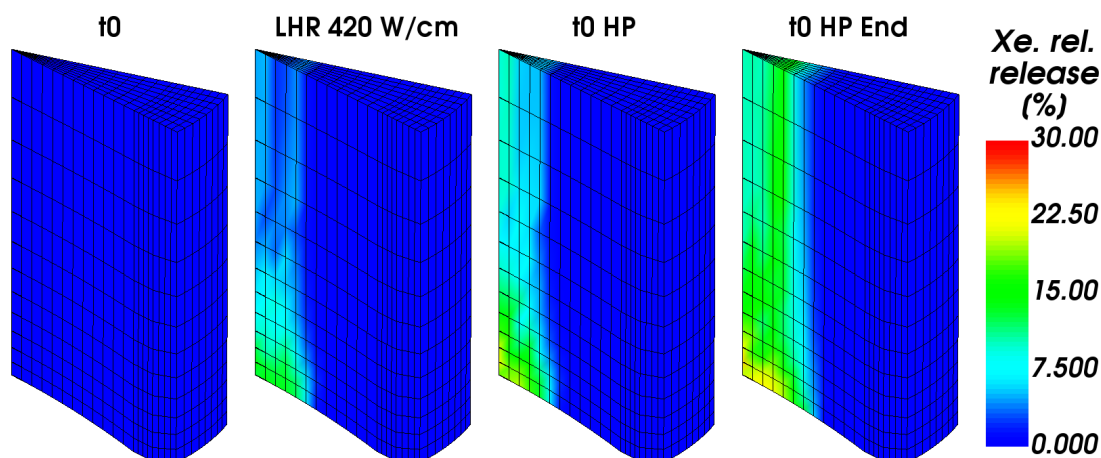


Figure 5.36: Release of Xe at different times of PR5. Units—% of initial inventory.

The calculated releases of Cs, I and Te during PR5 are shown in Figure 5.37. They are all correlated with the release of Xe from the fuel fragment but start at different times depending on the availability of the FPs in the gas phase. Cs release begins during the transient (between "LHR 420 W/cm" and " $t_0$  HP") near the dish. During the holding period Cs is released from the entire pellet central core. At " $t_0$  HP End", Cs release reaches around 15% along the pellet centerline with a maximum exceeding 20% at the IP level.

The release of iodine begins sooner during the transient than that of cesium. At "420 W/cm", it already reaches 25% along the fuel pellet centerline. At the end of the transient (" $t_0$  HP"), it reaches 75% near the dish and 50% at mid-pellet level. During the holding period, iodine release increases in the radial direction but not in magnitude.

The release of Te is close to that of I and begins also during the transient. At "LHR 420" 25% is already released near the dish. At the end of the transient, 70% of the Te has been released from this region while only 30% is lost at mid-pellet level. During the holding period, the release becomes more uniform along the centerline but it remains higher at the IP level. During the plateau, Te release spreads in the radial direction, as iodine.

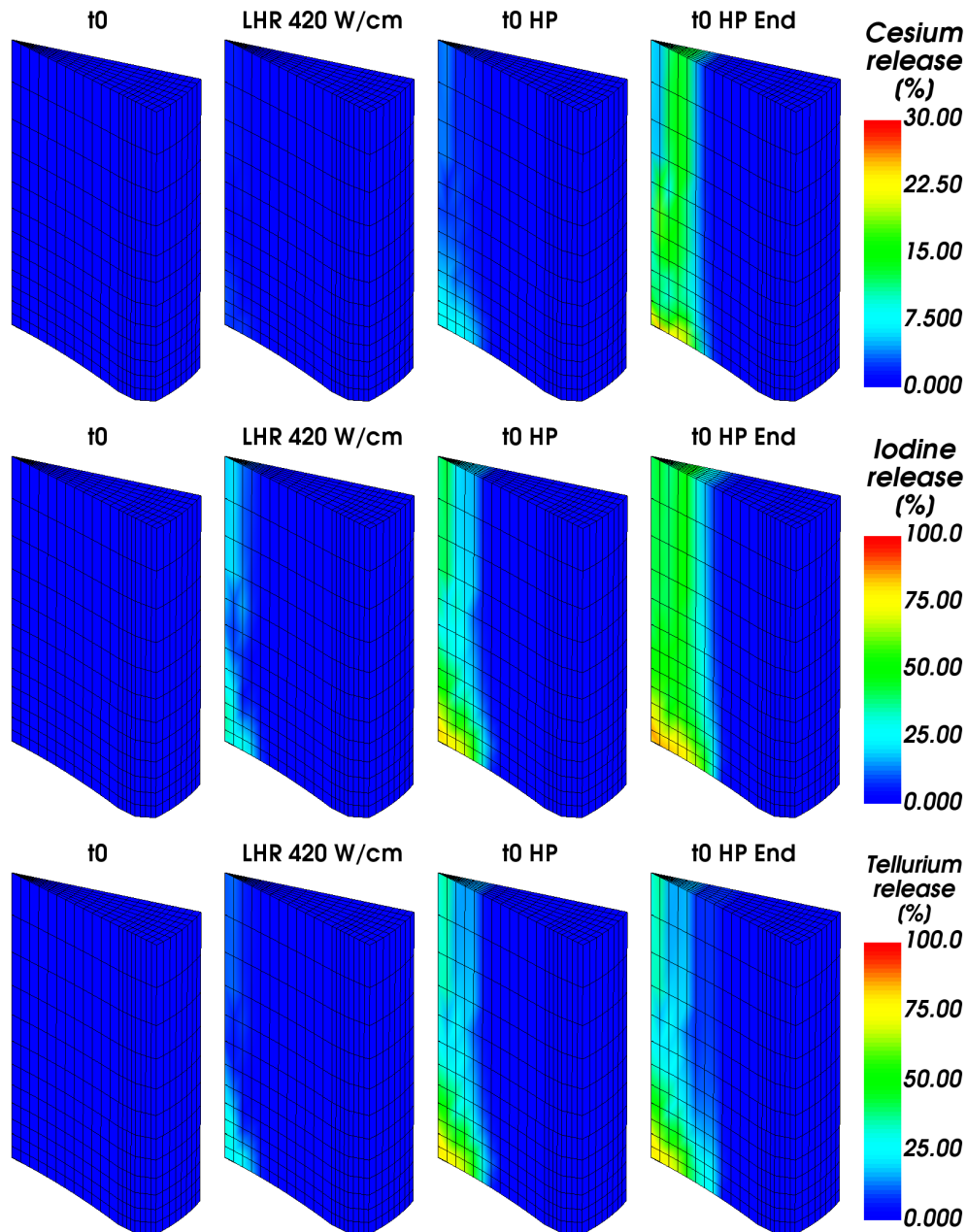


Figure 5.37: Release of Cs (top), I (middle) and Te (bottom) at different times of PR5. Units—% of initial inventory.

### 5.2.5 Burnup and pre-ramp elemental composition

The calculated radial profile of burnup is plotted in Figure 5.38 (solid line) and compared to experimental measurements. The latter are derived from measures of Nd concentration in the fuel [200]. The experimental error is around 10%, according to Desgranges et al. [61]. The calculated burnup radial profile is within the error bars for almost all the experimental points meaning that the burnup prediction is correct.

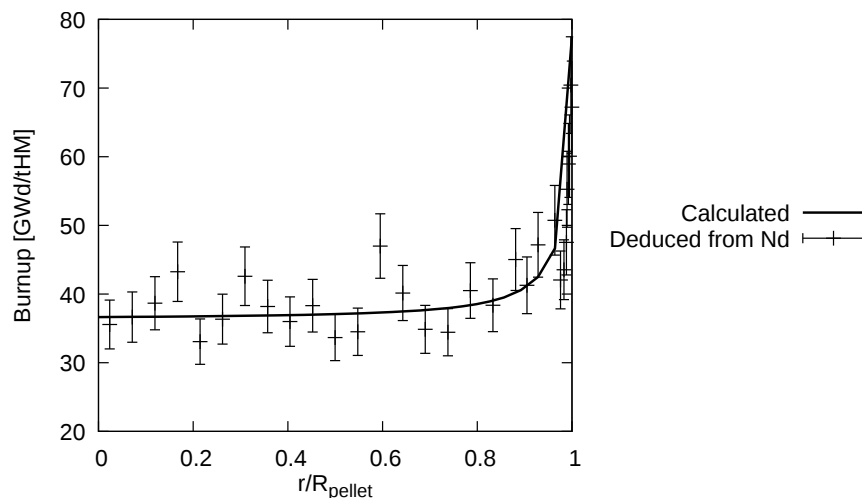


Figure 5.38: Calculated burnup radial profile along the mid-pellet plane compared to the experimental measurements.

Figure 5.39 shows the calculated radial profiles of Xe, Cs, I and Te compared to the SIMS measurements performed before the power ramp experiment. The predicted values refer to the mid-pellet plane. Only the experimental points for Xe are absolute quantities that can be compared to calculations. The SIMS measurement of Cs are given by the ratio of  $^{137}\text{Cs}/^{238}\text{U}$ . The experimental measurements of I and Te are expressed by the ratios  $^{129}\text{I}/^{18}\text{O}$  and  $^{130}\text{I}/^{18}\text{O}$ , respectively. The  $^{238}\text{U}$  and  $^{18}\text{O}$  references in SIMS measurements are chosen because they are not expected to vary significantly in the radial direction. PRODHEL does not include the isotope  $^{18}\text{O}$  in its neutronics database. Thus, the direct comparison of these ratios with the simulation results is not possible. However, in Section 3.1.1, it has been checked that PRODHEL returned correct estimations of fission product concentrations in an irradiated fuel (PR1) of close burnup (32 GWd/tHM) tested at CEA in the same MTR OSIRIS. A qualitative assessment of the calculated radial profiles, marked by lines in Figure 5.39, can however be made by adjusting the vertical axis to present the calculated profiles with a magnitude similar to that of the SIMS experimental points.

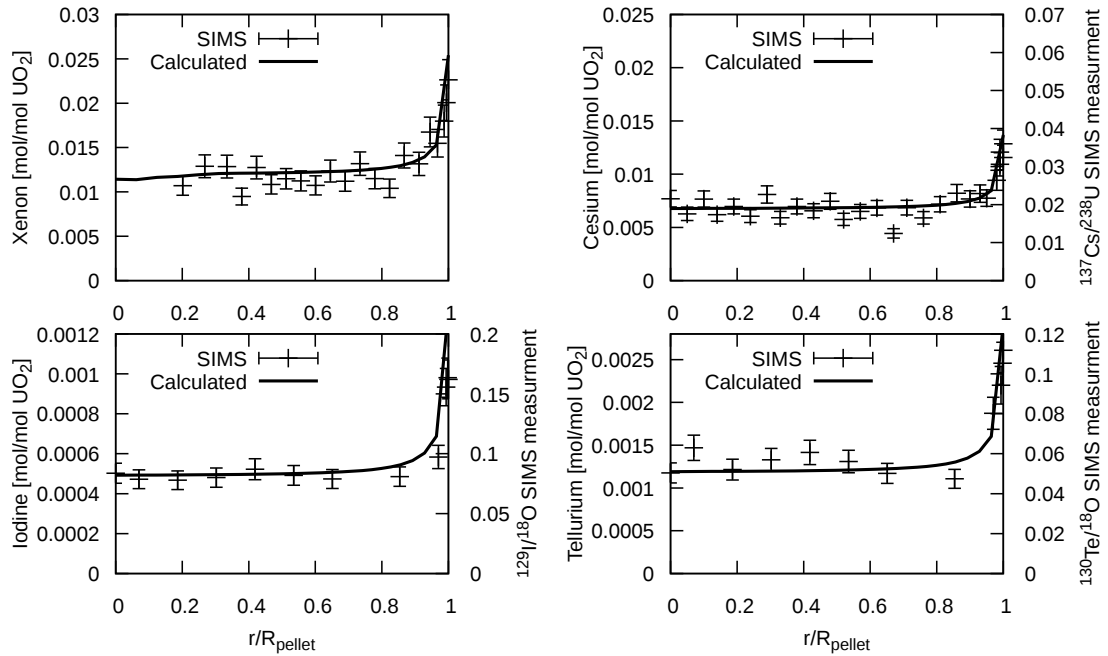


Figure 5.39: Calculated concentrations of Xe, Cs, I and Te (left axis) compared to SIMS measurements of the relative concentrations (right axis). The measurement uncertainty is around 10%. Both measurements and calculations done along the mid-pellet plane.

As can be seen, the calculated radial profiles present a consistent shape compared to the measurements. Another important observation is that the measured radial profiles of I, Te and Cs present nearly constant concentrations at the pellet center, meaning that these volatile fission products were not released during base irradiation. On the contrary, ALCYONE simulation of PR5 gives a 10% decrease of the Xe content at the pellet center up to a relative radius of 0.2. Unfortunately, measurements have not been made in this region. This local decrease of the Xe content leads to an 0.6% loss of Xe from the pellet fragment during base irradiation prior to the power ramp.

## 5.2.6 Post-ramp elemental composition

Figure 5.40 shows the radial profiles of the same fission products as in Figure 5.39, but calculated at the end of the power ramp. Two radial profiles are plotted in each graph, one corresponding to the MP plane and one to the IP plane. To compare experimental measures to the simulation profiles, the following procedure has been applied. The experimental points in Figure 5.39 have been used to estimate the radial profiles of the studied fission products before the ramp test. Then the SIMS measurements carried out after the ramp have been divided by the pre-ramp radial profiles to get the fractions of volatile fission products remaining in the fuel (relative to the pre-ramp quantity). This method is based on the assumption that the creation of stable isotopes during the power

ramp experiment is negligible and that the radial profiles of the reference isotopes  $^{18}\text{O}$  and  $^{238}\text{U}$  did not change during the power transient. In Section 3.1.2, it was checked that the quantity of iodine created during the power ramp was negligible. Some experimental points obtained with this procedure are greater than 1. It can be explained by the high uncertainty relative to SIMS measurements.

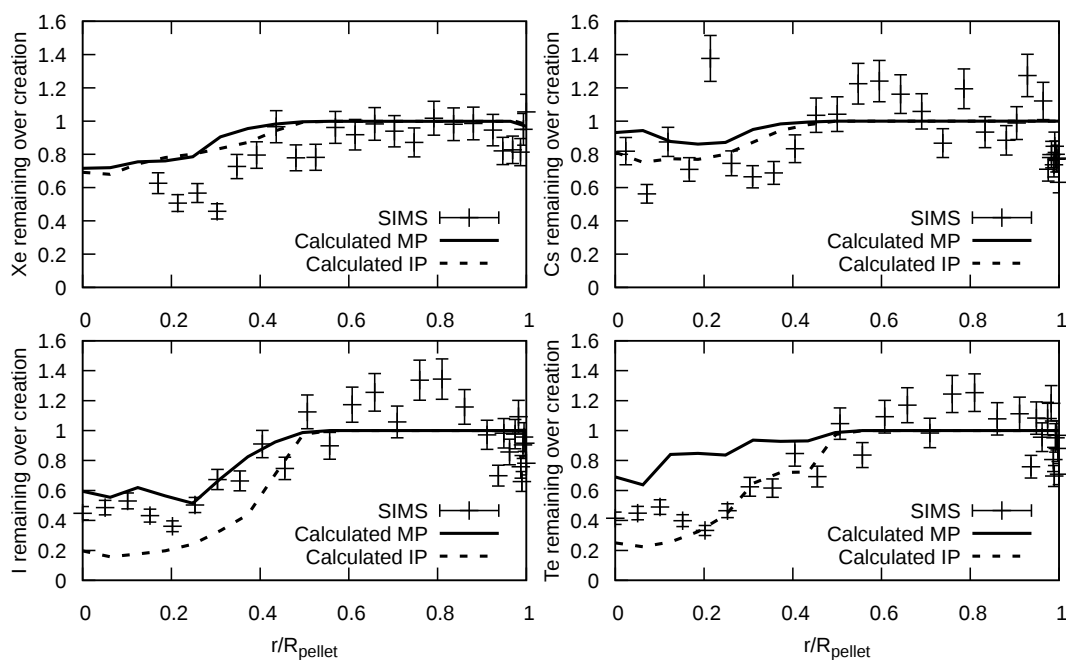


Figure 5.40: Comparison of the calculated radial profiles of Xe, Cs, I and Te to the SIMS measurements along the mid-pellet plane at the end of PR5. The experimental error is estimated to be 10%. MP-Mid Pellet, IP-Inter Pellet.

The calculated remaining fraction of Xe is in a good agreement with the experimental measures along the pellet radius. The experimental points at the very center are not available but it can be estimated that the remaining Xe fraction is around 60% (assuming a flat profile), whereas the calculated fraction is 70%. The profiles calculated along both IP and MP planes are similar.

The SIMS measurements concerning Cs are characterized by a high dispersion, which can be related to the high volatility of the FP. In spite of this fact, it can be seen that the Cs remaining fraction at the pellet center is close to 80%, meaning that Cs release occurred in this region. The profile calculated along the MP plane is partially consistent with this observation. According to the simulation, the Cs release at the MP level occurs at the pellet center and reaches 15%. The release there is associated with oxygen transport liberating high amount of gaseous cesium, as will be explained latter. The Cs remaining fraction calculated along the inter-pellet plane is slightly lower and fits the experimental points better.

The SIMS measurements of iodine and tellurium show a similar pattern. They indicate a massive release from the pellet center. The remaining fractions of iodine calculated at the IP and MP levels are 20% and 60% respectively. According to the SIMS measurements, the remaining fraction of iodine at the pellet center is around 40% which is within the calculated curves.

The tellurium release calculated at the MP level is significantly underestimated. The experimental results indicate that around 40% have remained at the pellet center whereas the value calculated at the MP plane is close to 70%. The remaining fraction calculated at the IP plane is 20% at the pellet center which means that the experimental points measured for  $r/R < 0.5$  are within the IP and MP profiles.

Compared to the results of Baurens et al., it appears that the release of Xe and I calculated in this work are similar. Baurens obtained a better prediction of the Te release but the Cs release estimated in this work is closer to experimental measures at the pellet center. The Cs release calculated by Baurens was close to zero. The origin of these differences is explained in Section 5.2.7, and is a consequence of oxygen thermal diffusion, as discussed in the next section.

Figure 5.41 presents the axial profiles of the remaining fractions of Cs, I and Te. They are calculated at  $r/R=0.1$  and compared to the SIMS measurements. The experimental points were obtained using the same method as for the radial profiles of Figure 5.40. Although the experimental points are scattered, the remaining over creation ratios suggest a rather uniform axial distributions of Cs, I and Te. The calculated remaining fractions of these elements are of the same order of magnitude as the experimental ones along the entire pellet height. However, the values calculated at the IP level are systematically lower than those calculated near the MP plane. It is a consequence of the non-uniform pressure distribution in the simulated fuel fragment as shown in Figure 5.33. FGR during the power ramp is higher near the pellet dish because the hydrostatic pressure is lower in that part.

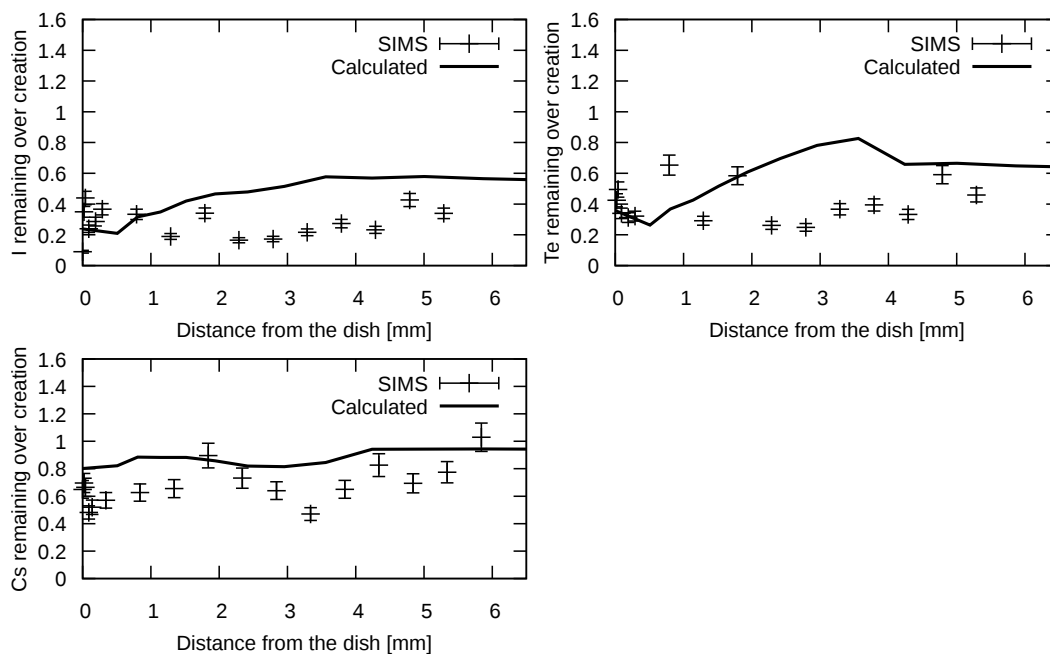


Figure 5.41: Comparison of the calculated axial profiles of Cs, I and Te to the SIMS measurements at  $r/R=0.1$  at the end of PR5. The experimental error is estimated to be 10%.

## 5.2.7 Thermochemistry of I, Cs and Te

### 5.2.7.1 Iodine

At first, the chemical speciation of iodine in the fuel during PR5 is studied. Figure 5.42 shows the evolution of  $I_{(g)} + 2I_{2(g)}$  and  $TeI_{2(g)}$  in the fuel during PR5. These gas compounds can react with Zr-based claddings to form the volatile  $ZrI_{4(g)}$  suspected to be at the origin of I-SCC. It can be seen that free iodine ( $I_{(g)} + 2I_{2(g)}$ ) is formed between "LHR 420 W/cm" and "t0 HP" (LHR 520 W/cm) when the pellet center is the hottest. Its concentration increases significantly during the holding period but only at  $r/R_{pellet} = 0.6$  and this result can be associated to the local increase of the O/M ratio (and oxygen content) at this position. The second gas compound is  $TeI_{2(g)}$ . It can be observed at the end of the holding period near mid-radius. Its formation is a consequence of oxygen transport as well.

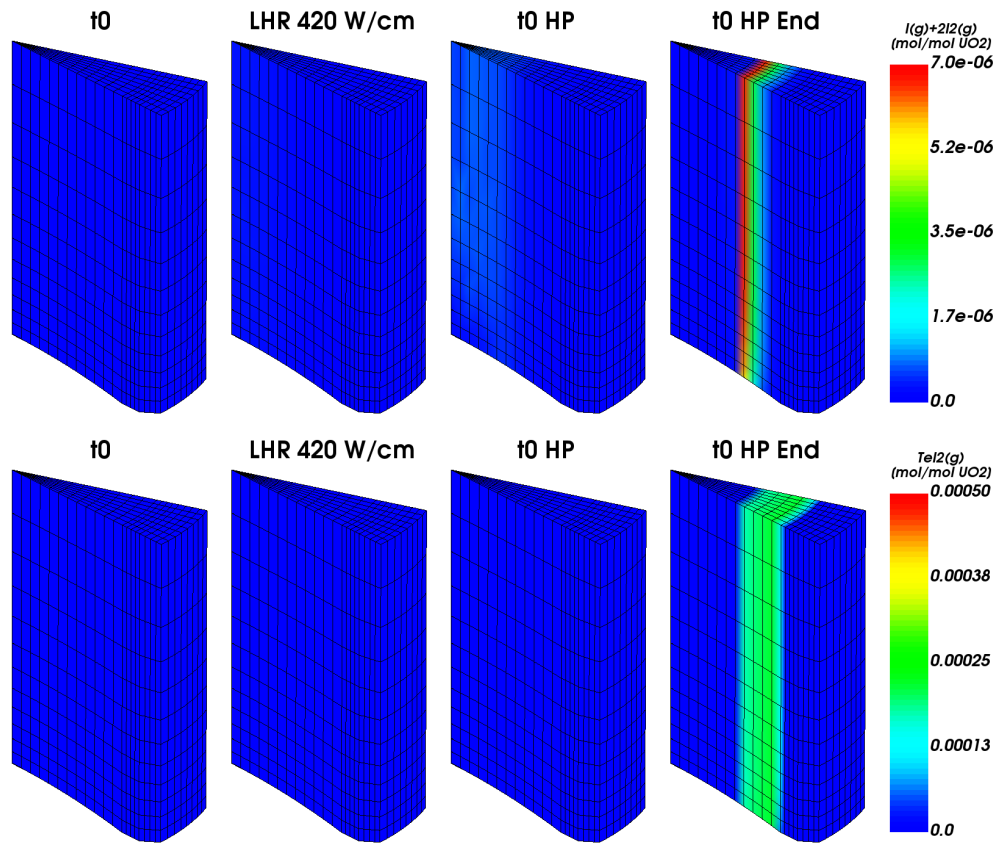


Figure 5.42: Concentration [mol/mol  $UO_2$ ] of  $I(g)+2I_2(g)$  (upper figures) and  $TeI_2(g)$  (lower figures) at different moments of PR5.

Figure 5.43 shows the speciation of iodine along the fuel pellet radius at the mid-pellet plane. Weight fractions of the most abundant species are plotted at the beginning (left graph) and at the end (right graph) of the holding period. The vast majority of iodine is bound as  $CsI$ , gaseous at the pellet center and condensed at the periphery. Also,  $Cs_2I_2(g)$  can be observed near mid-radius. Oxygen transport leads to the formation of  $TeI_2(g)$  from  $r/R_{pellet} = 0.6$  to  $r/R_{pellet} = 0.8$ , which is shown in the right graph.  $I(g)$  and  $I_2(g)$  shown in Figure 5.42 have low weight fractions and are not visible in Figure 5.43.

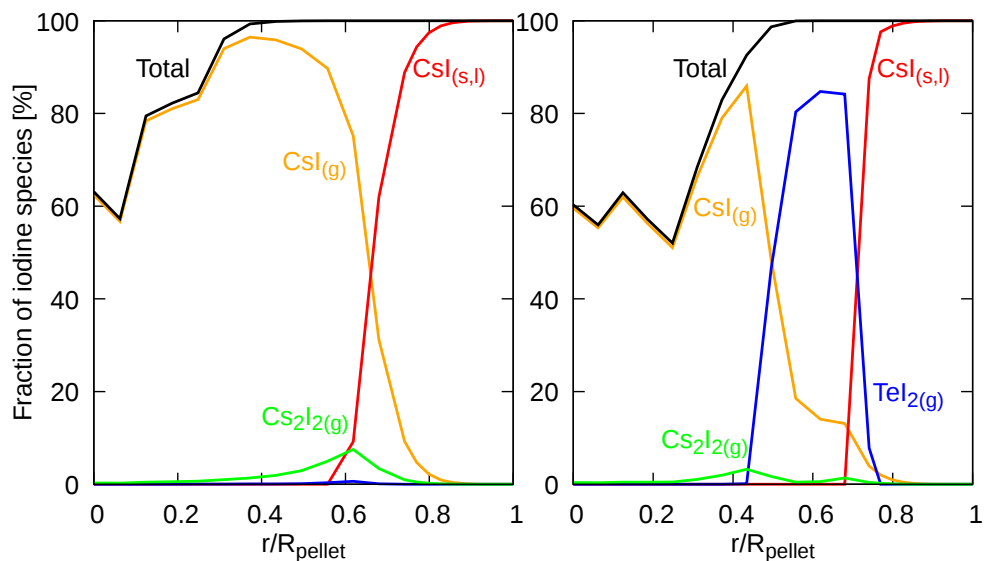


Figure 5.43: Speciation of iodine at "t0 HP" (left figure) and at "t0 HP End" (right figure) of PR5. Calculated along the mid-pellet plane.

### 5.2.7.2 Cesium

Figure 5.44 gives the 3D distribution of the most abundant cesium chemical compounds. At all time, most of the Cs is found in solid or liquid cesium molybdate  $\text{Cs}_2\text{MoO}_{4(s,l)}$ . Besides that, cesium interacts with iodine to form  $\text{CsI}_{(s,l)}$ . The condensed cesium iodide is more stable at the lower temperatures of the pellet periphery whereas gaseous  $\text{CsI}_{(g)}$  is formed at the hot pellet center during the transient and partly released during the holding period. The reduction of cesium molybdate can be observed at the pellet center at the end of the holding period. It is caused by both oxygen transport and thermal decomposition.

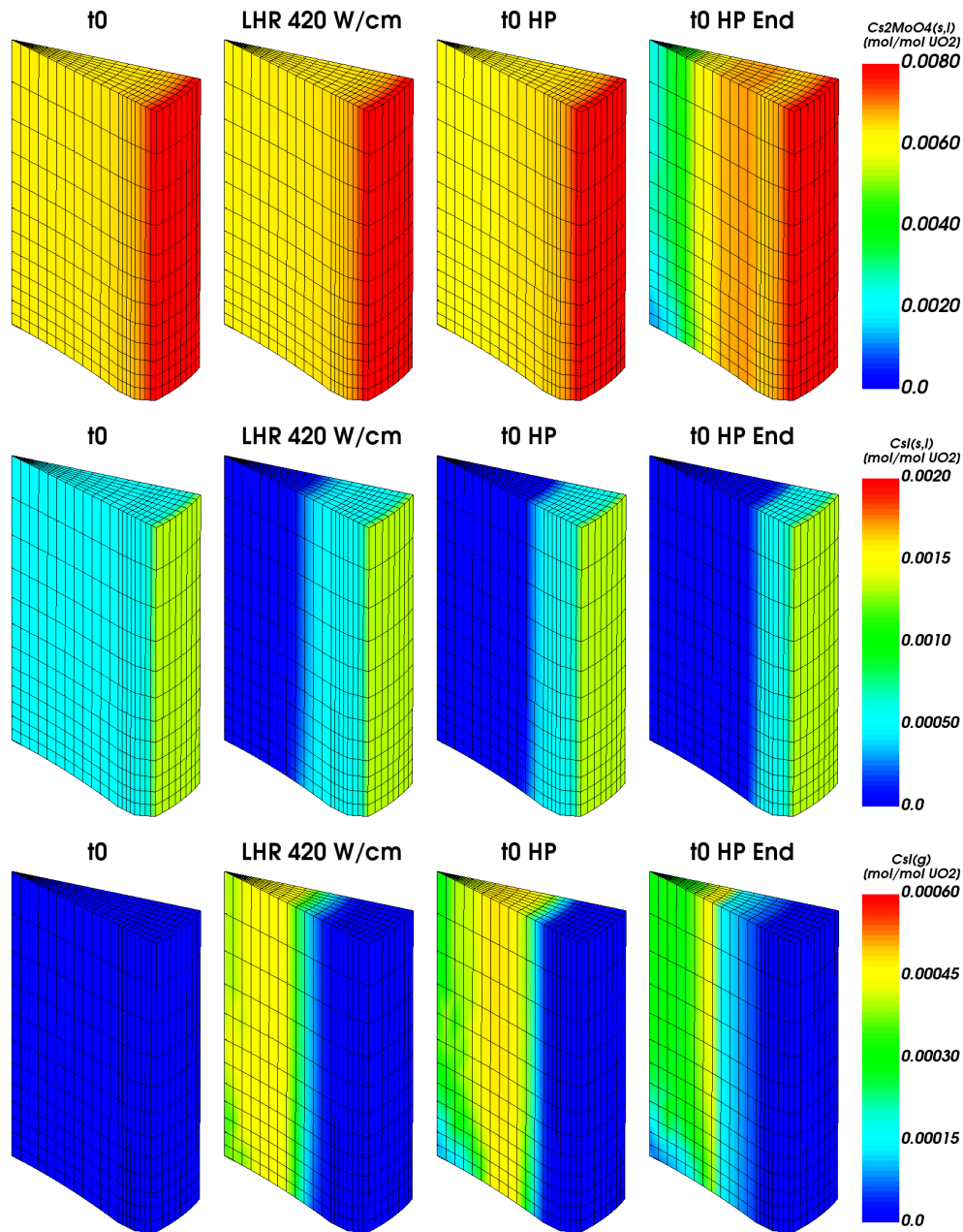


Figure 5.44: Concentrations [mol/mol  $\text{UO}_2$ ] of  $\text{Cs}_2\text{MoO}_4(s,l)$  (top),  $\text{CsI}(s,l)$  (middle) and  $\text{CsI}(g)$  at different moments of PR5.

The chemical speciation of Cs calculated at "t0 HP" in PR5 and PR2 are similar. The main difference is the presence of gaseous cesium  $\text{Cs}(g) + 2\text{Cs}_2(g)$  in much greater quantity in PR5. The temperature at the pellet center of PR5 is higher than in PR2 and it leads to the formation of gaseous Cs during the transient. It appears in small quantities at the pellet center at "t0 HP" and its concentration strongly increases during the holding period, in relation to oxygen redistribution. The calculated distribution of gaseous Cs in the pellet fragment during PR5 is shown in Figure 5.45.

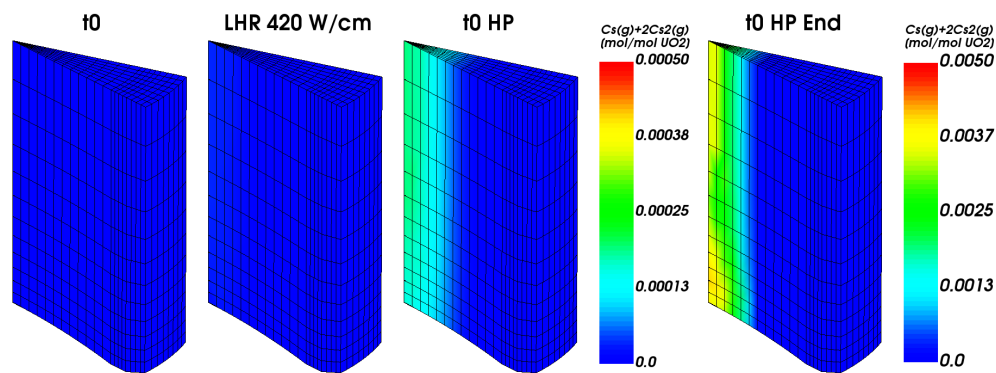


Figure 5.45: Concentration [mol/mol  $\text{UO}_2$ ] of  $\text{Cs}_{(g)}+2\text{Cs}_{2(g)}$  at different times during PR5. Note the different scales.

Figure 5.46 shows the calculated weight fractions of main cesium chemical compounds along a fuel pellet radius (mid-pellet plane) at "t0 HP" (left graph) and "t0 HP End" (right graph). In the left graph, around 90% of Cs is bounded as  $\text{Cs}_2\text{MoO}_{4(s,l)}$ . Less than 10% is found as  $\text{CsI}_{(g)}$  or  $\text{CsI}_{(s,l)}$ . Small amounts of gaseous cesium  $\text{Cs}_{(g)}+\text{Cs}_{2(g)}$  are visible at the pellet center. The fraction of  $\text{Cs}_2\text{I}_{2(g)}$  is low and it is hardly seen near  $r/R_{\text{pellet}} = 0.6$ . The right graph presents the chemical speciation affected by oxygen redistribution. Less oxygen at the pellet center leads to the decomposition of cesium molybdate and to the liberation of high amounts of gaseous Cs.  $\text{Cs}_{(g)}+\text{Cs}_{2(g)}$  account for nearly 60% of cesium at the fuel pellet center and its fraction decreases to 0% at  $r/R_{\text{pellet}} = 0.4$ . The rest of the Cs from the decomposed  $\text{Cs}_2\text{MoO}_{4(s,l)}$  interacts with tellurium to form  $\text{Cs}_2\text{Te}_{(s,l)}$ . The speciation at the pellet periphery is not strongly influenced by oxygen redistribution.

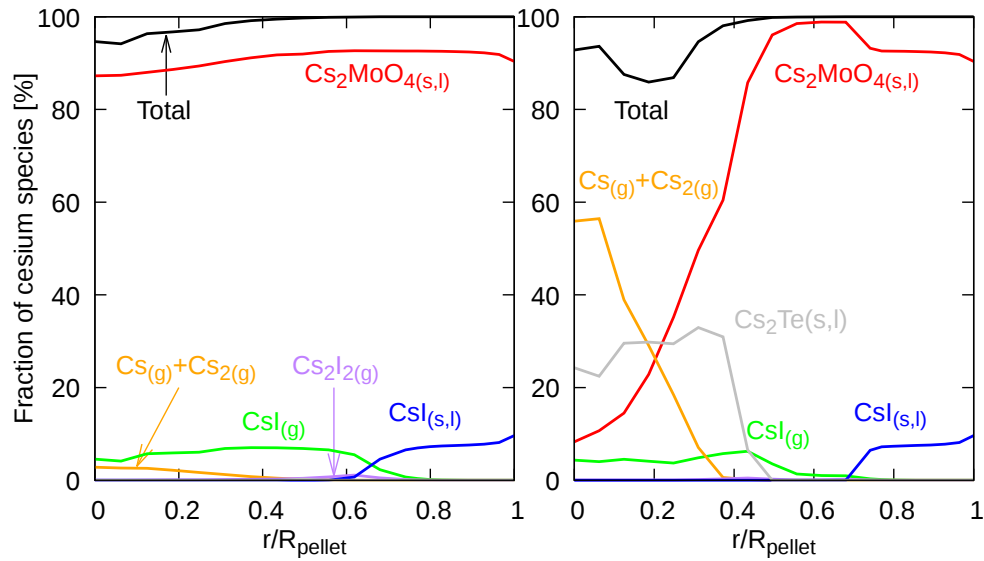


Figure 5.46: Speciation of cesium at "t0 HP" (left figure) and at "t0 HP End" (right figure) of PR5. Calculated along the mid-pellet plane.

The high concentration of gaseous Cs during the holding period, obtained thanks to oxygen thermal diffusion, results in a non negligible Cs release from the pellet center that is consistent with the measured post-ramp radial profiles, see Figure 5.40. In this respect, Cs release is much better predicted when compared to the simulation of Baurens, where over 90% of the Cs at the pellet center was in condensed form (in  $\text{CsO}_{2(ss)}$  and  $\text{Cs}_2\text{MoO}_{4(s,l)}$ ), which led to a very high retention (around 95%). The evolution of Cs chemical speciation during PR5 induced by oxygen redistribution and the lack of Cs compounds in the solid solution phase explain the differences with respect to Baurens' work.

### 5.2.7.3 Tellurium

The calculated spacial distribution of the most abundant Te chemical compounds during PR5 is shown in Figure 5.47. The fragments at the top of the Figure present the sum of the main gaseous Te compounds formed in the fuel ( $\text{Te}_{(g)}$ ,  $\text{Te}_{2(g)}$ ,  $\text{Te}_{3(g)}$  and  $\text{Te}_{5(g)}$ ). They appear at the pellet center during the power transient and come from the decomposition with temperature of  $\text{BaTe}_{(s)}$ , which evolution is shown in the fragments at the center of the Figure 5.47. Oxygen transport during the holding period leads to the liberation of gaseous Cs that interacts with the gaseous Te compounds to form  $\text{Cs}_2\text{Te}_{(s,l)}$  at the pellet center, which is shown in the fragments at the bottom of Figure 5.47.

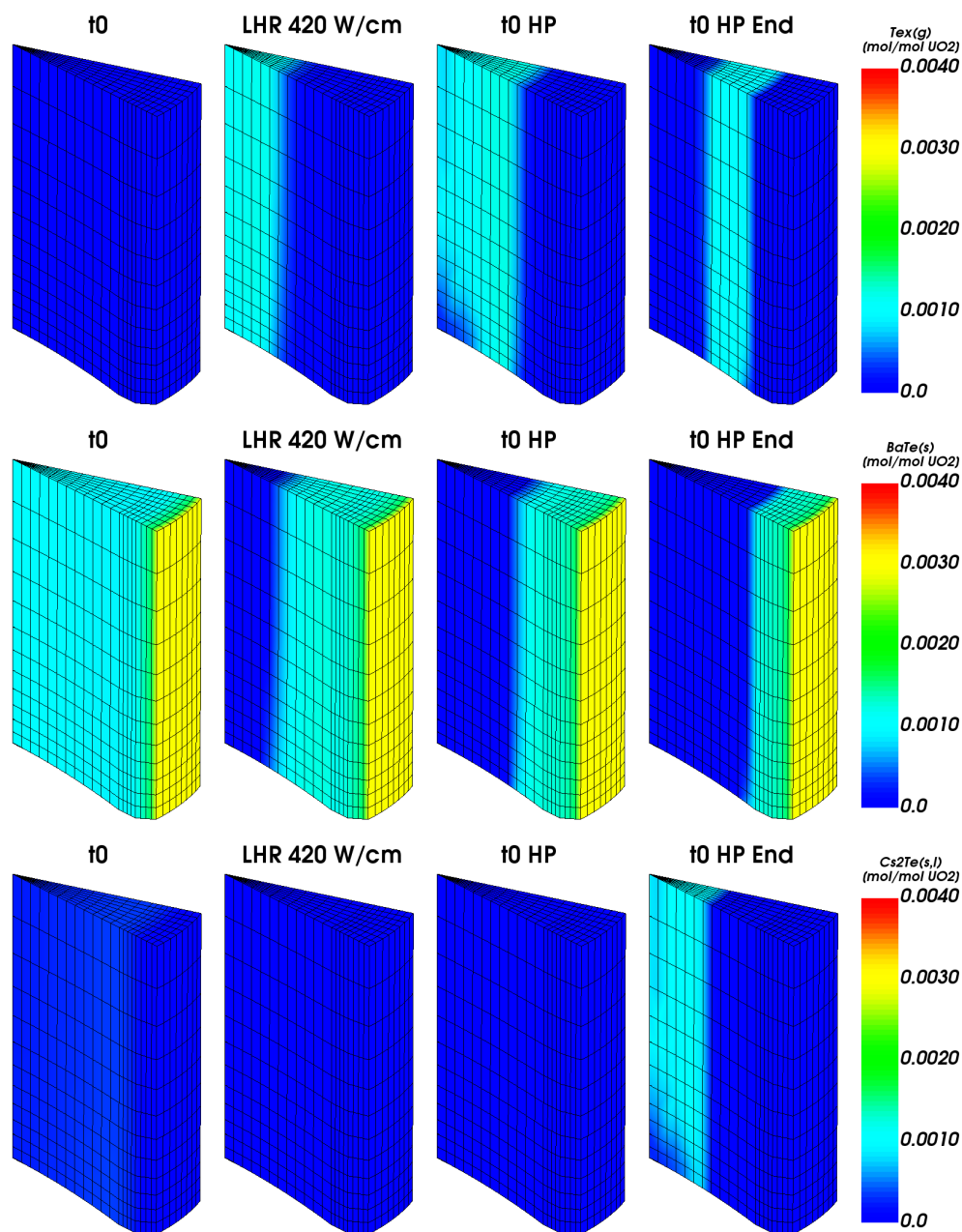


Figure 5.47: Concentrations [mol/mol  $\text{UO}_2$ ]  $\text{Te}_{x(g)}$  (top),  $\text{BaTe}_{(s)}$  (middle) and  $\text{Cs}_2\text{Te}_{(s,l)}$  (bottom) at different mtimes during PR5.  $\text{Te}_x$  stands for different forms of gaseous Te ( $1 \leq x \leq 5$ )

Figure 5.48 shows the evolution of the Te chemical compounds formed along a fuel pellet radius (mid-pellet plane). At the beginning of the holding period (left graph), nearly all Te is found in the gas phase ( $\text{Te}_{x(g)}$ ) at the pellet center and in solid  $\text{BaTe}_{(s)}$  at the periphery.  $\text{Cs}_2\text{Te}_{(s,l)}$  and  $\text{TeI}_{2(g)}$  are formed near mid-radius but they account for less than 1% of the total amount of Te. At the end of the holding period (right graph), Te at the pellet center is mostly found associated to Cs in  $\text{Cs}_2\text{Te}_{(s,l)}$ . The fraction of gaseous Te is still high after oxygen redistribution but only at mid-radius. A small fraction of

Te near  $r/R_{\text{pellet}} = 0.6$  is associated to I and forms  $\text{TeI}_{2(g)}$ . At the pellet periphery, Te is still found in solid  $\text{BaTe}_{(s)}$ .

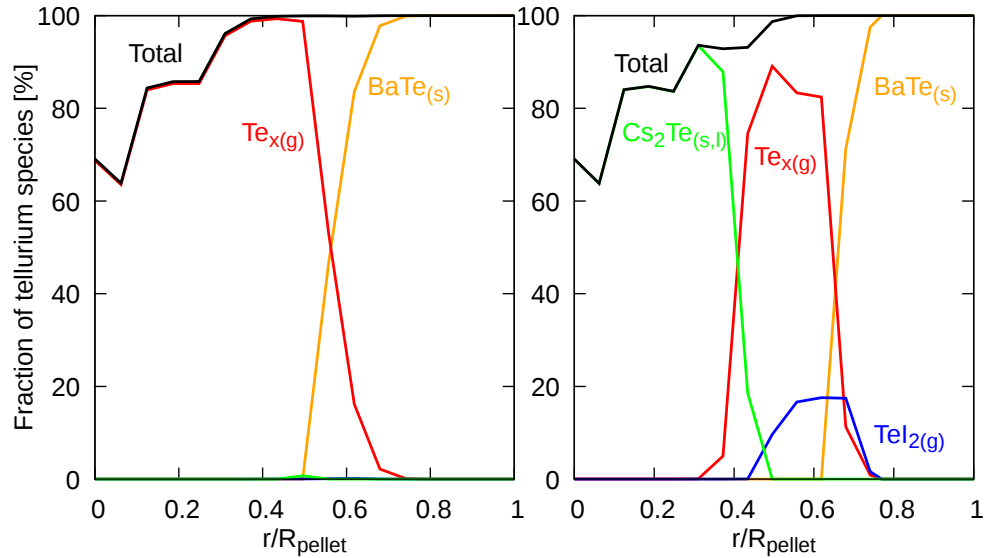


Figure 5.48: Speciation of tellurium at "t0 HP" (left figure) and at "t0 HP End" (right figure) of PR5. Calculated along the mid-pellet plane.

The formation of  $\text{Cs}_2\text{Te}_{(s,l)}$  is a direct consequence of oxygen redistribution. Compared to the calculation of Baurens without oxygen thermal diffusion, it leads to a smaller calculated release of Te (at mid-pellet level) and to an overestimation of the remaining quantity of Te in the fuel at the end of PR5, see Figure 5.40.

The remaining fraction of Te along the mid-pellet plane calculated without oxygen redistribution is shown in Figure 5.49. It is compared to the SIMS measurements and to the curve calculated with oxygen transport, same as in Figure 5.40. The solid curve referring to the calculations with oxygen thermal diffusion visibly overestimates the Te content but the dashed line, calculated without oxygen transport is close to the experimental measurements. However, the fraction remaining at the pellet center ( $r/R_{\text{pellet}} < 0.2$ ) is still over estimated by around 20%. Baurens obtained a better prediction since FGR in his simulations was higher.

This discrepancy might be related to an insufficient description of the Cs-Te system in the thermodynamic database with possibly an overestimation of the stability of the  $\text{Cs}_2\text{Te}_{(s,l)}$  compound.

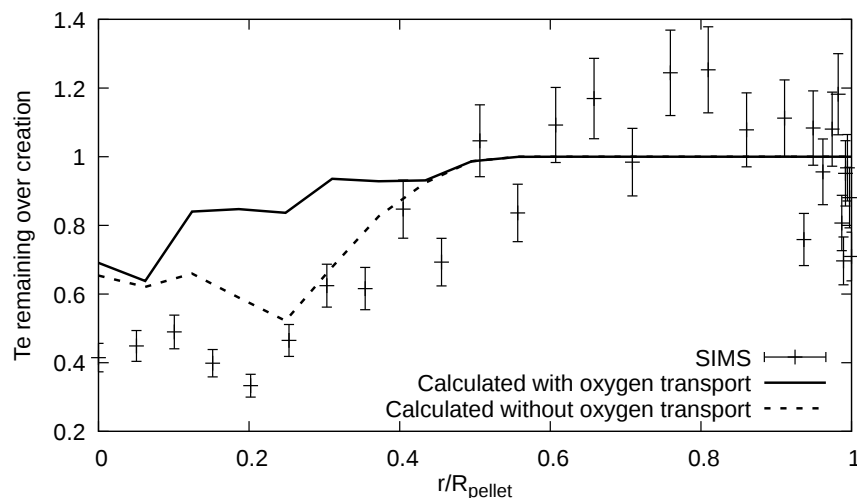


Figure 5.49: Remaining over creation ratio of Te calculated with and without oxygen transport compared to the SIMS measurements along the mid-pellet plane at the end of PR5. The experimental error is estimated to be 10%.

## 5.2.8 I-SCC modeling

### 5.2.8.1 Initiation criteria

Baurens et al. have discussed the conditions leading to I-SCC initiation by considering three criteria [14] related to the stress in the cladding, the presence of "reactive" iodine and the accessibility of the clad inner surface to gases released from the fuel pellet core. The stress considered by the authors was the average hoop stress in the clad thickness at the exact location of the triple point (see Figure 1.14 for the triple point position). It reached a maximum close to 500 MPa fifty seconds before the start of the holding period. The quantity of the so-called "reactive" iodine (i.e., iodine from  $I_{(g)}$ ,  $I_{2(g)}$  and  $TeI_{2(g)}$ ) that is expected to react with bare zirconium to form  $ZrI_{4(g)}$  released by the pellet during the power transient was used to estimate the "reactive" iodine partial pressure in the vicinity of the clad inner wall. It was calculated from both the free volume of the fuel pellet (radial cracks, dishes, chamfer) and of the fuel rod (plenum volume divided by the number of fuel pellets) and from the temperature of the clad inner wall, assuming ideal gas behavior. It was found that the minimum diiodine partial pressure (60 Pa) identified in out-of-pile mandrel tests to induce I-SCC failures in irradiated clad tubes [128], was exceeded by a factor greater than 10 during the holding period of the power ramp. The accessibility of the gases released from the fuel pellet core to the clad inner surface was evaluated by studying the temperatures at which the different iodides ( $CsI_{(g)}$ ,  $I_{(g)}$ ,  $I_{2(g)}$  and  $TeI_{2(g)}$ ) will condense along the radial crack path. It was concluded that only  $CsI_{(g)}$  was likely to condense during its transport from the pellet center to the clad inner

surface (condensation of  $\text{CsI}_{(g)}$  is expected between 680 and 1600 °C). For this reason, its contribution to the "reactive" iodine was neglected.

These quantities have been reconsidered in the present work as follows. First, the "reactive" iodine partial pressure taking into account iodine from  $\text{TeI}_{2(g)}$ ,  $\text{I}_{(g)}$  and  $\text{I}_{2(g)}$  has been calculated according to the ideal gas equation:

$$p_I = \frac{n_I RT_{clad}}{V_{dish} + V_{crack}} \quad (5.10)$$

where  $n_I$  is the number of moles of iodine released from the fuel pellet,  $T_{clad}$  is the clad inner wall temperature [K] at the triple point,  $V_{dish}$  and  $V_{crack}$  are the volumes of the pellet dish and of the pellet radial crack [ $\text{m}^3$ ]. Contrary to Baurens, the contribution of the plenum to the total volume has not been considered, which seemed more appropriate in a fuel rodlet with a closed pellet-clad gap and therefore no axial communication between the pellets.

The "reactive" iodine clad surface concentration  $c_{clad}$  [ $\text{mg}/\text{cm}^2$ ] has also been calculated with the following expression:

$$c_{clad} = \frac{m_I}{\phi_{crack} h_{pellet}/2} \quad (5.11)$$

where  $m_I$  is the mass of released "reactive" iodine [mg],  $\phi_{crack}$  is the crack tip opening [cm] and  $h_{pellet}$  is the pellet height [cm]. As can be inferred, only the clad surface that is not in contact with the pellet fragment (in front of pellet radial cracks) is considered.

Instead of the average hoop stress in the clad thickness, the hoop stress at the exact triple point has been considered since it is more representative of the local conditions leading to I-SCC initiation.

The first two quantities depend on the radial crack and dish volumes and on the crack tip opening. The spatial distributions of the crack openings calculated at different times during PR5 are shown in Figure 5.50.

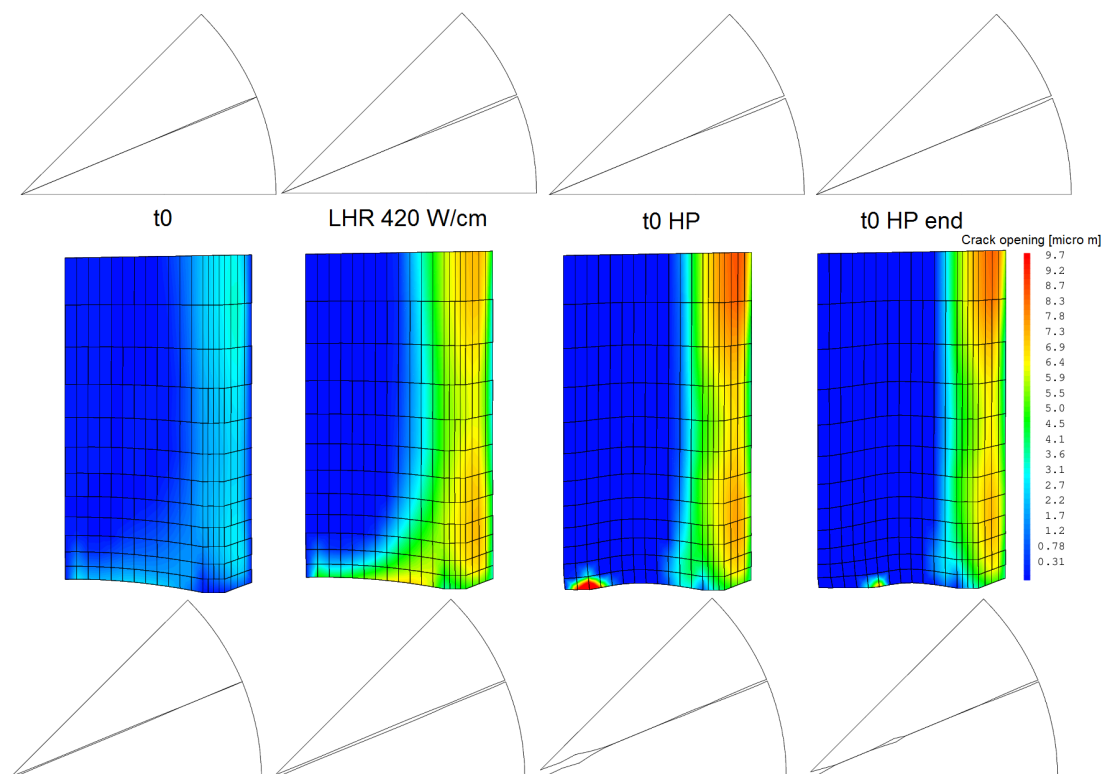


Figure 5.50: Calculated pellet radial crack opening at different times during PR5. Upper graphs give the mid-pellet plane. Lower graphs the inter-pellet plane. Isovalues give the distribution of crack opening on the fracture surface.

In consequence of the radial temperature gradient, the radial crack is already open at the beginning of the transient ("t0"). At mid-pellet level, the crack opening concerns only one third of the radius while at inter-pellet level, the crack opening occurs all along the radius, consequence of the pellet fragment axially non uniform deformation which liberates space at pellet ends. The crack tip opening is around  $3 \mu\text{m}$ . The same configuration holds during the transient except that the crack tip opening becomes wider and reaches around  $10 \mu\text{m}$  ("LHR 420 W/cm"). At the end of the transient and during the holding period, fuel creep leads to the filling of the dish and to the closure of the radial crack along the inter-pellet plane (between  $r/R=1/3$  and  $r/R=2/3$  approximately). The maximum crack tip opening remains around  $10 \mu\text{m}$ . These radial cracks are the only path where gas compounds released from the pellet center can migrate during the power transient to reach the cladding. As can be seen in Figure 5.50, the dish is not completely filled in the present simulation. Numerical integration of the crack openings given in Figure 5.50 with respect to the fracture surface is performed at each time step to estimate the evolution of the crack volume. In a similar way, the dish geometry is integrated at each time step to estimate the dish volume.

The hoop stress at the triple point and the "reactive" iodine partial pressure are plotted in Figure 5.51, together with the evolution of the dish filling ( $100 \times (V_{dish}^o - V_{dish})/V_{dish}^o$

with  $V_{dish}^{\circ}$  the as fabricated dish volume) and of the LHR.  $t = 0$  refers here to the "t0 HP". The hoop stress behaves similarly to the curve calculated by Baurens. It reaches a maximum value fifty seconds before the beginning of the holding period and then it decreases. The maximum hoop stress exceeds 600 MPa and during the 90 s plateau it decreases down to 450 MPa. Dish filling and hoop stress decrease appear to be correlated in time since they are related to the same phenomenon, fuel creep. Dish filling reaches a maximum of 65% at the end of the holding period.

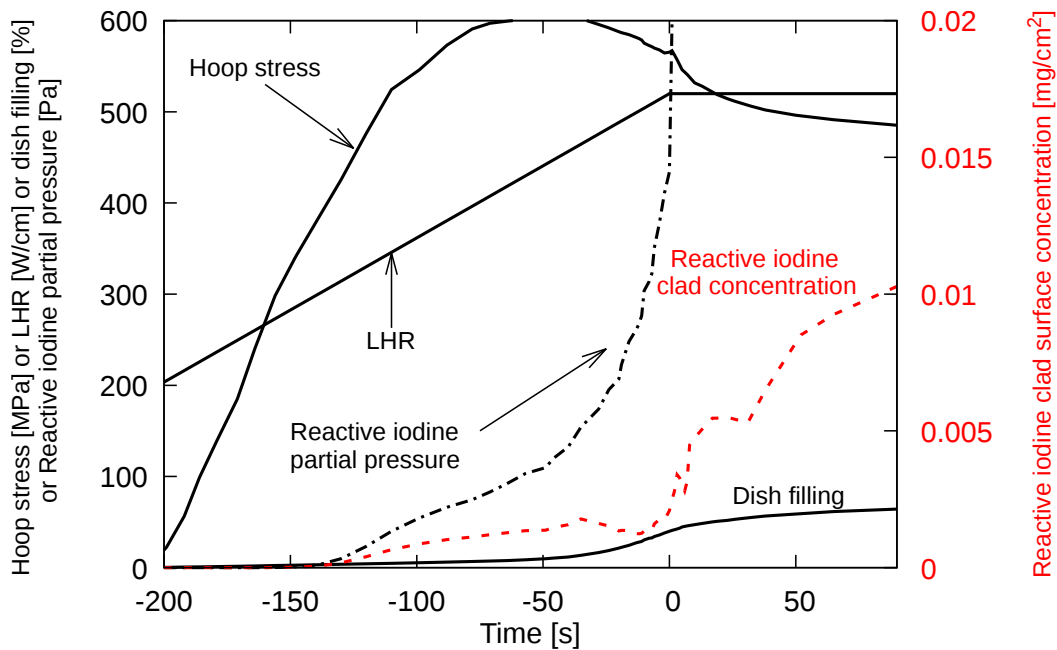


Figure 5.51: Time evolution of the maximum hoop stress at IP level (MPa), of dish filling (%), of the cladding surface concentration of 'reactive' iodine ( $\text{mg}/\text{cm}^2$ ) and of the 'reactive' iodine partial pressure (Pa) during PR5. 'Reactive' iodine takes into account the iodine species  $\text{TeI}_{2(g)}$ ,  $\text{I}_{(g)}$  and  $\text{I}_{2(g)}$ . Hoop stress at IP level (Mpa), LHR (W/cm), dish filling (%) and 'Reactive' iodine partial pressure (Pa) refer to the left vertical axis. 'Reactive' iodine clad surface concentration refers to the right vertical axis.

The hoop stress being far above the minimum stress levels required to initiate I-SCC in laboratory tests on irradiated Zy-4 cladding ( $\sim 150$  MPa) [201], the other criterion needed is related to the partial pressure of iodine in the free volume in contact with the cladding inner wall. The "reactive" iodine partial pressure curve has a shape similar to the one obtained by Baurens. A non zero iodine pressure is detected 130 seconds before the end of the transient. It increases first almost linearly with time till approximately -50 s where it exceeds the critical iodine pressure of 120 Pa (60 Pa diiodine pressure) identified in the mandrel tests from the SCIP project, see Section 2.3.2. It then increases sharply to reach more than 600 Pa at the beginning of the holding period ( $t=0$ ). The sharp increase is a consequence of the fast fission gas release from the pellet center.

The "reactive" iodine clad concentration is also shown in Figure 5.51 but not used to define I-SCC initiation because of the high scatter in experimental thresholds, see section 2.3.2. The calculated iodine clad concentration is around 10 times lower than Baurens' estimate. This difference is caused by a lower quantity of released iodine in our simulation. Nevertheless, the "reactive" iodine clad concentration calculated in this work is above all the I-SCC thresholds from the open literature.

Another condition that is usually considered by authors for I-SCC initiation is the necessary breaking of the protective zirconia layer that forms at the pellet clad interface during normal reactor operations. Generally discontinuous up to fuel average burnups of around 45 GWd/tHM, the rupture of the zirconia layer is associated in many models to the cladding strain. Le Boulch et al. indicated that strains as low as 0.5% can break the zirconia layer. I-SCC initiation is also generally associated to the reaching of a sufficient clad hoop strain at the inner wall, with part of it leading to plastic irreversible strains that are thought to facilitate the penetration of iodine in Zy-4 grain boundaries. A threshold of 0.4-0.5% has been suggested by Lewis based on simulations of an extensive database of power ramps [144]. In this work, an 0.5% minimum strain will be considered as a necessary condition for I-SCC to initiate. The cladding strain at the triple point is calculated as follows:

$$\text{Strain} = \frac{|R_{triple}^t - R_{triple}^{BI}|}{R_{triple}^{BI}} \times 100\% \quad (5.12)$$

where  $R_{triple}^{BI}$  is the radius of the cladding at the triple point at the end of base irradiation and  $R_{triple}^t$  is the radius at the same point at time  $t$ . Only the strain generated during the power ramp is thus taken into account. Figure 5.52 presents the cladding strain at the triple point as a function of time. Time  $t=0$  on the x axis corresponds to the beginning of the holding period ("t0 HP"). It can be seen that the strain increases almost linearly until the beginning of the holding period where it reaches its maximum value of 1.2%. The strain crosses the threshold around 140 s before "t0 HP". During the holding period it decreases by less than 0.1%. After 90 s, at the end of the holding period, the strain decreases rapidly below the threshold value.

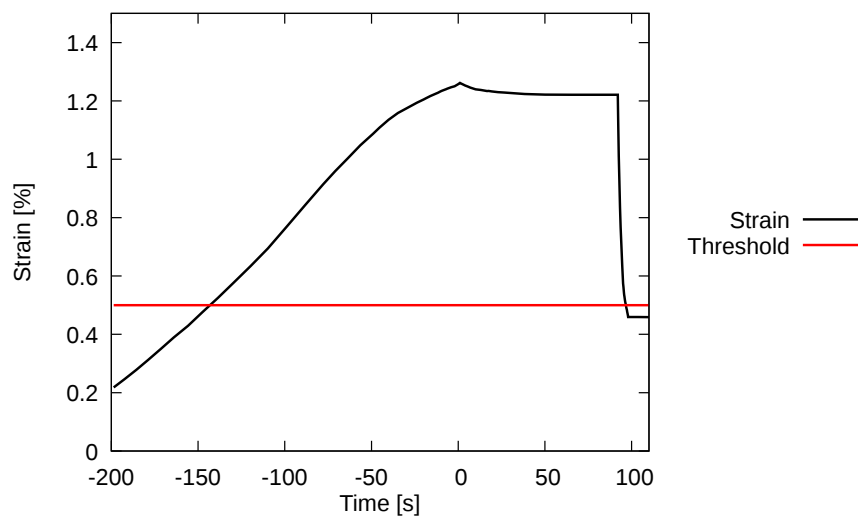


Figure 5.52: Cladding strain at the triple point (black line) and the zirconia layer crack threshold (red line) of PR5.

Among the three conditions considered for I-SCC initiation (stress, strain, iodine partial pressure), the limiting factor appears to be the iodine partial pressure which reaches the threshold 50 seconds before the end of the transient.

### 5.2.8.2 Crack propagation model

PR5 is particularly interesting for an I-SCC analysis since the post-ramp examinations have shown the presence of radial cracks starting from the clad inner surface and extending in the thickness of the cladding to a maximum depth of 100  $\mu\text{m}$ . The cladding crack propagation model described in Section 2.3.4.1 has been applied in post-processing of the PR5 simulation to estimate the crack depth and compare it to the experimental measures.

Apart from the clad hoop stress at the triple point and the iodine partial pressure, the third quantity of importance in the crack propagation model is the clad inner wall temperature. The temperature evolution calculated at the triple point is shown in Figure 5.53. It increases from 350 till nearly 420  $^{\circ}\text{C}$  during the power ramp. It is elevated when compared to those of the tests performed by Le Boulch to identify the activation energy of the mechanisms (320 to 390  $^{\circ}\text{C}$ ).

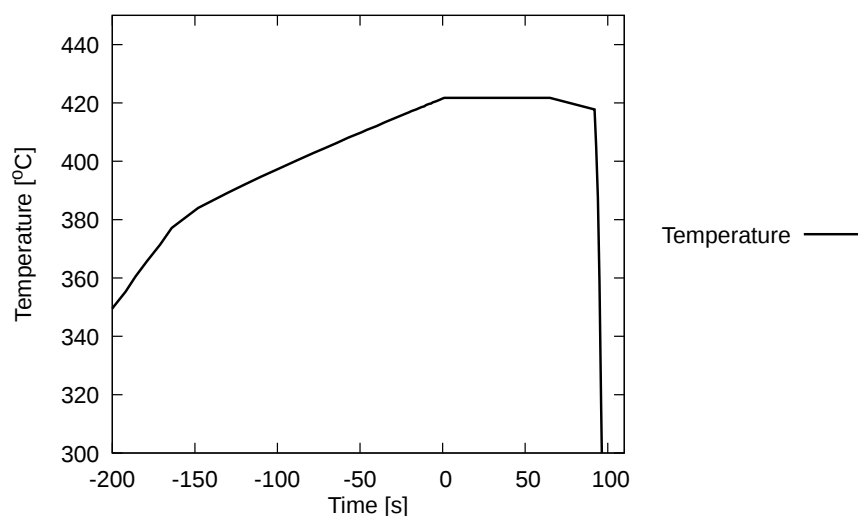


Figure 5.53: Cladding temperature at the triple point during PR5.

The crack initial depth is also a parameter required in the crack propagation model. In this study, an initial crack depth of  $8 \mu\text{m}$  is considered to be consistent with the thickness of the zirconia layer in a fuel of this burnup range [58]. Figure 5.54 shows the crack depth calculated with the model. Corrosion starts 50 s before the beginning of the holding period when the reactive iodine partial pressure exceeds the threshold (120 Pa). The crack propagation is linear in time till approximately 50 s and then a change of slope can be observed when the critical crack depth is reached. Transgranular crack propagation leads in fact to a much faster crack propagation rate. The crack depth calculated at the end of the holding period is around  $200 \mu\text{m}$ , which is twice deeper than measured.

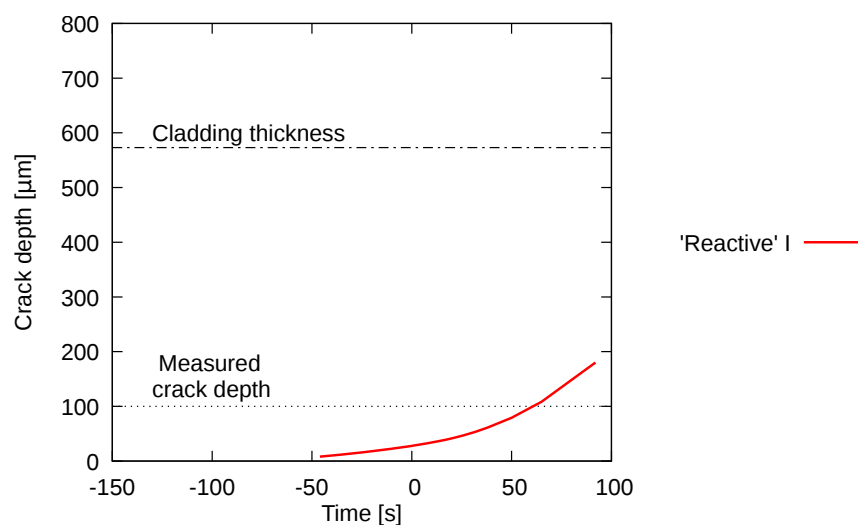


Figure 5.54: Cladding crack depth calculated at the triple point during PR5.

## 5.2.9 Sensitivity studies on the I-SCC model

### 5.2.9.1 Initial crack depth

The I-SCC model used in this work requires an initial crack depth. The value  $8 \mu\text{m}$  was used in the previous section. Sensitivity studies have been carried out to evaluate the impact of this parameter on the crack depth. It is assumed that crack propagation starts when the partial pressure of "reactive iodine" exceeds the threshold value  $120 \text{ Pa}$  ( $\sim -50 \text{ s}$ ). Four different initial crack depths have been tested. The calculated crack depth evolutions are shown in Figure 5.55.

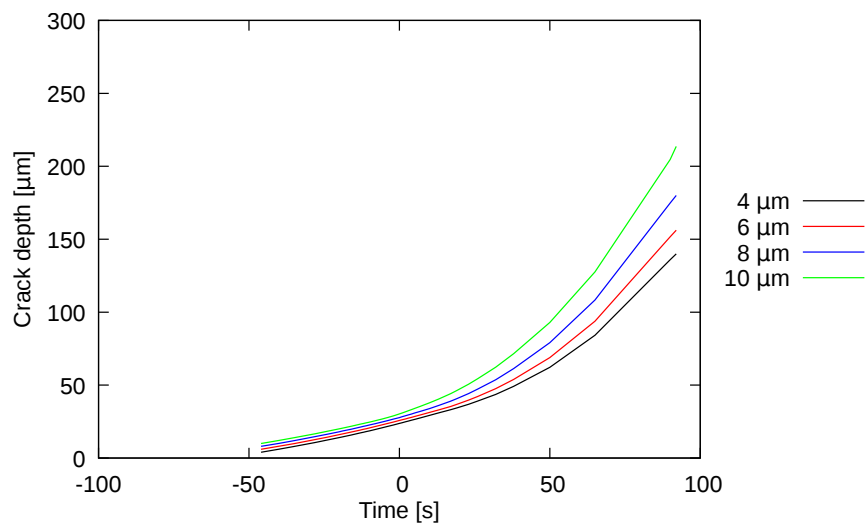


Figure 5.55: Cladding crack depth calculated at the triple point during PR5 with different initial crack depths.

As can be seen in Figure 5.55, the initial crack depth has a strong influence on the crack depth evolution. This is related to the small crack propagation kinetics during the incubation phase of I-SCC that last until a critical crack depth is reached (stress dependent). The final penetration with the initial value  $4 \mu\text{m}$  is  $130 \mu\text{m}$  whereas the initial value  $10 \mu\text{m}$  results in a final penetration of  $210 \mu\text{m}$ . The difference of  $80 \mu\text{m}$  is around 15% of the cladding thickness. This difference was built up in around 90 s since all the curves show similar crack penetration at "t0 HP" (0 on the x axis). The change of crack propagation rate is related to the change of crack propagation mechanism. It must be emphasized that usually, I-SCC leads to a failure within the first minutes at high power so it means that the initial crack depth is a very sensitive parameter and it has a significant impact on predicting I-SCC failure.

### 5.2.9.2 Iodine partial pressure threshold

Even a low partial pressure of "reactive" iodine is sufficient to induce SCC. Additionally, a continuous iodine supply is not required to maintain crack propagation. In the Van Arkel reaction (see Section 2.3.1.3), which is considered responsible for I-SCC crack propagation, iodine can be regenerated. Theoretically, even a one-time delivery of a sufficient amount of "reactive" iodine to the crack surface could provoke failure. In this parametric study, the impact of the iodine partial pressure threshold is studied by changing the time at which the I-SCC model is activated from -70 s to -30 s by steps of 10 s. These times correspond to diiodine partial pressure threshold varying between 40 and 100 Pa, instead of the 60 Pa used in the reference calculation. The time evolutions of the crack depth are shown in Figure 5.56.

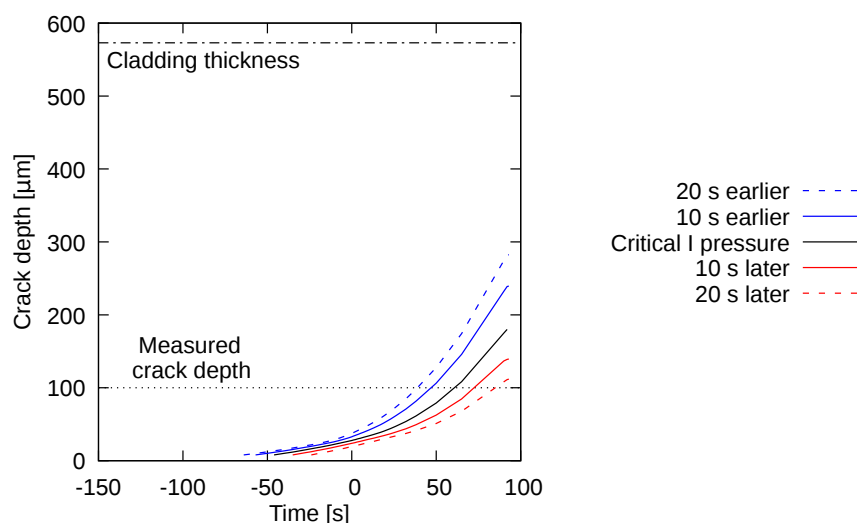


Figure 5.56: Cladding crack depth calculated at the triple point during PR5. Different curves correspond to different activation times for the I-SCC model.

The black curve gives the reference calculation. As can be seen, the impact is negligible during the transient (till  $t=0$ s) but important during the holding period. If I-SCC initiation is 20 s later than in the reference calculation, the final crack depth is around 100  $\mu\text{m}$  and half the crack depth from the reference calculation. On the contrary, if I-SCC starts 20 seconds earlier, the crack depth reaches 300  $\mu\text{m}$ . These results show that changing the crack initiation time by only 20 s strongly influences the final crack depth. Such a time variation is not unrealistic since the iodine partial pressure is calculated from several quantities that change significantly during the power ramp, i.e., the pellet crack volume and pellet dish volumes, and can hardly be measured. Only the residual dish volume can be estimated with a precision of  $\pm 20\%$ .

### 5.2.9.3 Iodine from CsI radiolysis

In the estimation of the iodine partial pressure, the possible contribution of CsI radiolysis [115, 132] (released from the pellet as  $\text{CsI}_{(g)}$  and condensed on the fuel pellet cracks' surfaces as  $\text{CsI}_{(s)}$ ) to the "reactive" iodine might be considered. Frégonèse et al. quantified  $\text{CsI}_{(s)}$  radiolysis in the inter-pellet zone and in the fuel pellet radial cracks [202], assuming that  $\text{CsI}_{(s)}$  decomposition was likely in the first  $5 \mu\text{m}$  at the fuel pellet surface. They used the model proposed by Konashi et al. [133] to estimate a potential for dissociation of 20%. Figure 5.57 shows calculations of the iodine partial pressure considering different fractions of CsI decomposed by radiolysis (10, 20 and 30%).

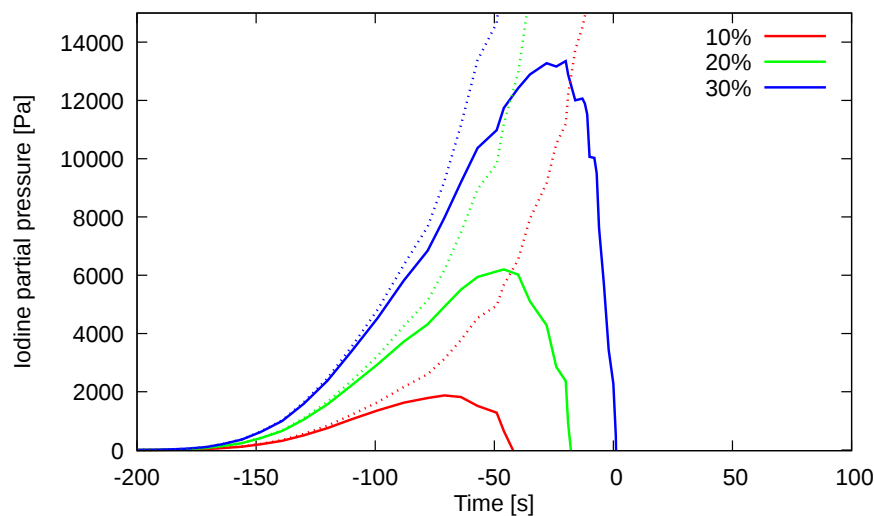


Figure 5.57: Solid lines correspond to the iodine partial pressure taking into account interactions of the "reactive" iodine with the free cesium and radiolysis of CsI. Dotted lines correspond to the iodine partial pressure of the 'reactive' iodine and radiolysis of CsI. Different colors correspond to different fractions of CsI that undergo decomposition by radiolysis.

The three dotted curves reach the threshold iodine partial pressure (120 Pa) at almost the same time around "t<sub>0</sub> HP" -171 s, that is to say much earlier than in the reference calculation. This result is due to the fact that the bulk of iodine released from the fuel pellet is mostly in the chemical compound  $\text{CsI}_{(g)}$ . The iodine partial pressure increases then rapidly to reach very high values.

Calculation of crack propagation in the cladding thickness with iodine partial pressure including CsI radiolysis (20%) is illustrated in Figure 5.58 by the black solid line. The reference calculation is recalled by the red curve. With CsI radiolysis included, the limiting factor for I-SCC initiation is the clad strain criterion. It exceeds the threshold value of 0.5% 140 s before "t<sub>0</sub> HP", see Figure 5.52.

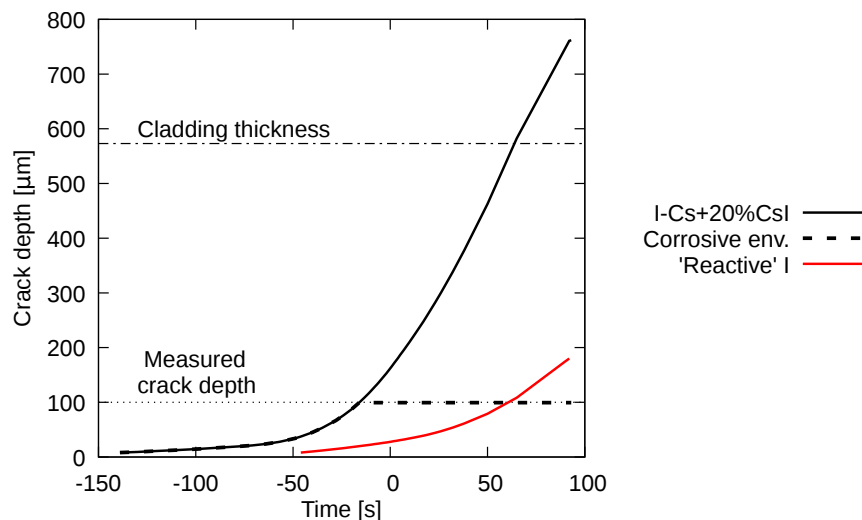


Figure 5.58: Cladding crack depth calculated at the triple point during PR5.

The crack propagation starts sooner and is faster in the calculation with CsI radiolysis and should have led to clad failure within the first minute at maximum LHR. This is a general result that is obtained in any simulation of a PWR power ramp on irradiated fuel where the iodine partial pressure includes a contribution from CsI radiolysis. In consequence of this conclusion, Baurens proposed to correct the partial iodine pressure by accounting for the possible recombination of iodine with the cesium released from the fuel pellet, according to the following equation:

$$p_I = \frac{(n_I - n_{Cs})RT_{clad}}{V_{dish} + V_{crack}} \quad (5.13)$$

where  $n_{Cs}$  is the number of moles of Cs released from the fuel pellet in gaseous form ( $Cs_{(g)}$  and  $Cs_{2(g)}$ ). The resulting iodine partial pressure curves are plotted with solid lines in Figure 5.57. Release of gaseous cesium in great quantities leads to a limitation and a decrease of the partial iodine pressure that occurs during the transient. Independent of the % of CsI considered in the partial iodine pressure, all free iodine reacts with cesium before the beginning of the holding period at  $t=0$  s, meaning that the corrosion process should stop if continuous iodine supply is necessary. The crack depth calculated with this hypothesis is shown in Figure 5.58 by the black dashed line "Corrosive env." The maximum reached is consistent with the post-irradiation examinations (around  $100 \mu\text{m}$ ).

This parametric study has shown that iodine coming from the radiolysis of CsI has a major impact on the iodine partial pressure. Accounting for the recombination of iodine with the cesium released from the fuel pellet changes completely the picture. In this respect, oxygen redistribution is at the origin of the significant cesium release and could be of major importance to define the time lapse where I-SCC is possible.

### 5.2.9.4 Crack opening

Another factor that may influence I-SCC is the crack opening. Chemical species are released mostly from the pellet center and migrate through the pellet radial cracks towards the cladding. Theoretically, when the radial cracks are partially closed, the released gas compounds cannot reach the cladding, most of them should be found as solid deposits on the crack lips, an observation often recorded in post-irradiation examinations of samples taken close to pellet ends. The crack closure at the inter-pellet plane takes place during the transient (see Figure 5.50) in consequence of fuel creep activated at high temperature. Figure 5.59 presents the crack depth calculation shown previously in Figure 5.54. The vertical dashed line indicates the moment of the pellet radial crack closure at inter-pellet plane. Crack closure occurs 24 s before "t<sub>0</sub> HP".

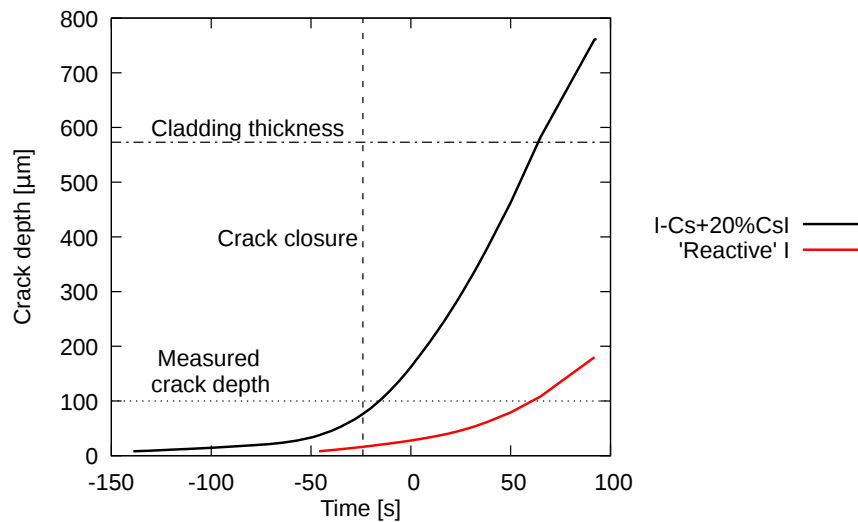


Figure 5.59: As Figure 5.54 but with the vertical, dashed line marking the pellet radial crack closure at "t<sub>0</sub> HP"-24 s.

Assuming that the corrosion stops at this moment because no more corrosive iodine can reach the cladding, the calculated crack depths are low and do not cross the horizontal dotted line showing the experimentally observed crack depth. With consideration of CsI radiolysis, the crack depth reaches 76  $\mu\text{m}$  for 16  $\mu\text{m}$  without. This phenomenon could also explain why the clad crack depth did not exceed 100  $\mu\text{m}$ .

## 5.3 Summary

The coupling between oxygen thermal diffusion and irradiated fuel thermochemistry has been presented in this chapter. The 1D Finite Volume OXITRAN solution and

the 2D/3D CAST3M Finite Element solutions developed in chapter 4 have been implemented in the fuel performance code ALCYONE. The coupling with thermochemistry relies on an additional constraint in the thermochemical solver ANGE, which allows performing thermochemical computations at prescribed O/M ratio in the fluorite solid solution. Thanks to this condition, ANGE returns thermodynamic equilibrium states consistent with the O/M ratios calculated from the oxygen redistribution model. This coupling methodology is fast and efficient. To guaranty in the simulations the simultaneous conservation of the total oxygen content and of the O/M ratio in the fuel pellet, linear relations between these two quantities have been established for irradiated  $\text{UO}_2$  fuels with or without Cr dopants.

Simulations of power ramps have been performed to check the proposed coupling strategy in ALCYONE. At first, a 1D simulation of a power ramp on an irradiated  $\text{UO}_2$  fuel with post-ramp measures of oxygen potential has been carried out. The radial profile of oxygen potential obtained in the simulation was found in good agreement with the experimental values reported by Adamson et al. [73]. Also, the computed O/M ratios were satisfying when compared to Adamson's estimations. This 1D simulation has shown that the 1D oxygen transport model proposed in this work as well as its parameters can be used to predict the thermochemical state of irradiated and power ramped  $\text{UO}_2$  fuels.

A 3D simulation of the PR2 power ramp performed on a Cr-doped  $\text{UO}_2$  fuel has been carried out to check extensively the behavior of the proposed coupling strategy. The impact of oxygen redistribution on the thermochemistry of fission products was the focus of this test case. It was verified that oxygen thermal diffusion led to the reduction of Cr and Mo oxides at the pellet center, as inferred from EPMA measurements. The consequences on FGR were furthermore investigated. While Xe and I release were not modified by oxygen redistribution, Cs release was found enhanced by this phenomenon. In fact, oxygen redistribution from the pellet center to the pellet periphery leads to a reduction of condensed cesium molybdate and to the formation of gaseous Cs that is then released in great quantity from the pellet center, in agreement with post-ramp EPMA measurements.

The potential importance of oxygen redistribution as regards to PCI failure by I-SCC was then investigated by the 3D simulation of a short power ramp analyzed previously by Baurens et al. [14]. It has been shown that oxygen thermal diffusion has some non negligible impact on the results even if the duration of the power ramp plateau at 520 W/cm did not last more than 90 s. In particular, it was found an increased Cs release from the fuel pellet more consistent with the post-ramp SIMS measurements. PCI-SCC initiation criteria related to both mechanical and chemical factors have been established and estimated based on the 3D fields calculated: temperature, hoop stress and hoop strain at the triple point, partial iodine pressure from iodine release from the fuel pellet fragment and from the radial crack and dish volumes. Finally, the I-SCC crack propagation model proposed by Le Boulch et al. [114] has been applied to estimate the

crack depth in the cladding at the end of the power ramp. It was shown by sensitivity analysis that the model could lead to consistent predictions of the I-SCC crack depth with small variations of either the initial crack depth or the critical iodine partial pressure.

## Chapter 6

# Conclusions and perspectives

The main purpose of this thesis was to study the impact of oxygen thermal diffusion on the chemical state of fission products in a PWR fuel rod during a power ramp and to analyze its impact on PCI failure propensity. The main conclusions and the prospective work are discussed in four sections.

### 6.1 Irradiated fuel thermochemistry

The first step in thermochemical modeling of irradiated fuel was to predict the fission products content. In this work, the neutronics model PRODHEL has been used and successfully validated by comparison to the evolution code CESAR and to fission products measurements in medium to high burnup fuels.

The thermochemical calculations performed with the solver ANGE on irradiated fuel compositions obtained with PRODHEL have then been detailed with a particular emphasis on the description available in the thermodynamic database of ANGE of the fluorite solid solution phase. Systematic comparison with available experimental data on a number of U-O-FP systems have been presented to check the validity of the thermodynamic representation adopted in this work. Thermochemical simulations of irradiated  $\text{UO}_2$  fuels have shown that the experimental measurements of oxygen potential ( $RT \ln p_{\text{O}_2}$ ) can be satisfactorily predicted with ANGE and its thermodynamic database, at least within the critical burnup range for PCI failure (20-45 GWd/tHM). Calculations on high burnup fuels showed more deviation with experimental measures but this conclusion may be tempered by the important scatter of measures in the open literature, with no clear explanations. One important result that was obtained in this work is the apparent decrease of the O/M ratio with irradiation in  $\text{UO}_2$  fuels.

Improvement of the thermochemical modeling of irradiated fuel could come from the use of a more complex description for the fluorite solid solution phase such as the one proposed in the TAF-ID [100], following the recent implementation of the thermochemical solver OpenCalphad [203] in ALCYONE fuel performance code [152]. Recent thermochemical simulations of the high burnup fuel analyzed by Walker with the TAF-ID has shown the capacity of the database to reproduce the measured increase of the oxygen potential along the fuel pellet radius [156], one of the trend that could not be obtained with ANGE database. It is however important to point out that high burnup fuels (over 45 GWd/tHM) are usually less prone to PCI failure. For this reason, the modeling of high burnup fuels thermochemistry was not the primary goal of this work.

A chromium solubility model has been implemented in ANGE thermodynamic database. The thermochemical description of the U-Cr-O system was essential to perform simulations of Cr-doped  $\text{UO}_2$  fuels. The temperature range where experimental data are available to check the model is however limited ( $< 1800^\circ\text{C}$ ) and some efforts should be put in its extension to higher temperatures (experiments and modeling). An original approach, which consists in using chromium in Cr-doped nuclear fuels as an in-situ redox indicator, has been developed in this work. The method allows estimating indirectly from the experimental Cr solubility profile, the  $\text{O}_2$  partial pressure profile of irradiated fuels, for which no direct measurement is accessible or available. This profile can be further used to deduce the oxygen potential or oxygen redistribution magnitude. Simulations of irradiated fuels have proven that their oxidation states can be predicted correctly with this method. To the best of this author's knowledge, a similar approach has never been used before.

## 6.2 Oxygen thermal diffusion

Oxygen thermal diffusion describes oxygen transport in the solid solution phase of  $\text{UO}_2$  under concentration and temperature gradients. Its experimental characterization dates back to the research made in the 70's on SFR's mixed oxide fuels. In hypostoichiometric fuels ( $\text{O}/\text{M} < 2$ ), oxygen was found to migrate from the hot to the cold part of the pellet. In PWR's, due to the lower temperatures at hand, thermal diffusion is usually not considered in fuel performance simulations. The code ALCYONE that has been used in this work to perform fuel simulations is characterized by the multi-dimensional representation available of the fuel pellet and cladding. Three different schemes allow one to model either the complete fuel rod with a 1D radial axisymmetric description of the fuel pellet, or a fuel pellet fragment in 2D generalized plane strain or in 3D. In consequence, two different numerical solutions for the oxygen thermal diffusion equation have been developed during this work and implemented in ALCYONE. For the 1D radial scheme of ALCYONE, a fast and robust finite volume based solution called OXITRAN has been proposed. In 2D and 3D, to be consistent with the thermal solver of the Finite

element code Cast3M used in ALCYONE, a finite element solution has been developed for oxygen thermal diffusion. Convergence of these numerical solutions has been analyzed with strongly nonlinear parameters leading constraints on the time steps. The 2D and 3D finite element solutions have been furthermore validated by comparison with the results of a coupled thermal - oxygen diffusion problem from the open literature [81]: a case study treated with the COMSOL software involving a strong coupling between thermal diffusion and oxygen transport with fast change of power density in the fuel pellet. The results obtained with the developed finite element solutions in 2D and 3D were very close to those of COMSOL.

The main difficulty in the development of the oxygen thermal diffusion model concerned the derivation of the material parameters, i.e., the heat of oxygen transport and the chemical diffusion of oxygen. Very limited experimental data are available and they concern only non irradiated mixed oxide fuels. To determine the heat of oxygen transport in irradiated  $\text{UO}_2$  fuels, an inverse analysis has been proposed in this work, considering the chromium dopant as an oxido-reductive tracer. EPMA measurements of Cr after power ramps, simulations of the radial temperature profiles with ALCYONE and of the fuel thermochemistry with ANGE have been used to estimate the oxygen potential and O/M evolution in the fuel pellet due to oxygen thermal diffusion. The heat of oxygen transport was then fitted to reproduce these evolutions at the pellet center. Obviously, this identification by inverse analysis limits the applicability to irradiated  $\text{UO}_2$ . Only two EPMA measurements of Cr after power ramps were used to derive the heat of oxygen transport, assuming furthermore that steady-state was reached. A negative heat of transport was identified, consequence of the O/M decrease at the pellet center (fuel becomes hypostoichiometric) leading to a thermal diffusion of oxygen towards the cold pellet periphery.

Future work could consist in extending the identification of the heat of oxygen transport to other power ramps. To this end, the Cr solubility model need to be extended to higher temperatures. Kinetics of the process could furthermore be studied if power ramps with short periods at maximum linear heat rates are available. To complete, in view of the potential importance of oxygen thermal diffusion, out-of-pile thermal diffusion experiments ought to be developed on non irradiated fuel. Care should be taken to avoid electrical interference as shown by Janek [108].

The derivation of the chemical diffusion coefficient of oxygen has been based on the work of Berthinier et al. [91]. It relies first on the definition of a defect model in non stoichiometric  $\text{UO}_{2\pm x}$  (Breitung's model) describing the evolution of oxygen vacancies and interstitials with stoichiometry deviation and temperature. The self-diffusion coefficient of oxygen is then expressed as a function of the defects concentrations and of temperature. The chemical diffusion coefficient is finally obtained from the self-diffusion coefficient and from the derivation of the oxygen partial pressure in equilibrium with  $\text{UO}_{2\pm x}$  with respect to the stoichiometry deviation. This complex procedure has been completely

reconsidered in this work since the apparent discontinuity of the derivative in Bertinier's work stemmed from the precision used in the thermodynamic equilibrium calculations. The obtained chemical diffusion coefficient has been validated in the hyperstoichiometric domain by comparison to a limited set of experimental measures. It must be emphasized that the experimental measurements from different authors are not consistent with each other thus making it difficult to conclude if the chemical diffusion coefficient derived in this work predicts oxygen transport kinetics properly. The hypostoichiometric domain, which is of greater interest in this work, has not been validated since absolutely no experimental data is available. This derivation led to a chemical diffusion coefficient valid only for  $\text{UO}_2$  fuels. It should be furthermore emphasized that this derivation relies on distinct models for the defects and the oxygen partial pressure derivative in  $\text{UO}_{2\pm x}$ , in spite of the fact that the thermodynamic model used for the later includes a description of defects which is not consistent with Breitung's model.

Great progress could certainly be achieved by using a set of consistent models to derive the heat of oxygen transport and the chemical diffusion coefficient. In this respect, the use of the TAF-ID in ALCYONE should solve the problem. The explicit calculation of point defects (vacancies and oxygen interstitials) in  $\text{UO}_{2\pm x}$  and possibly in the different phases considered in the database could help improve the modeling of oxygen transport and lead to self-consistent estimations of the chemical diffusion coefficient. In this respect, the expressions identified by Moore et al. [89] could be used since they are derived from the vacancy and interstitial concentrations calculated directly from the thermodynamic equilibrium calculations with the  $\text{UPuO}_{2\pm x}$  model included in the TAF-ID database. The extension to irradiated fuels remains still not straightforward and could possibly differ from the approach proposed in this work since the calculated defects concentrations might be totally different. Experimental characterizations of oxygen diffusion kinetics in SIMFUELS could help assess the chemical diffusion coefficient in irradiated materials.

### 6.3 Fuel performance simulations including oxygen transport

To study the impact of oxygen transport on the chemical speciation of fission products, thermo-chemical-mechanical simulations of power ramps have been carried out with the fuel performance code ALCYONE including local thermochemical equilibrium calculations and oxygen transport at the pellet fragment scale. The coupling of these two phenomena is a complex topic that required some modifications in the thermochemical solver ANGE to prescribe the O/M ratios from the oxygen thermal diffusion solution. The proposed methodology ensures the simultaneous conservation of oxygen content and oxygen defects in the fuel pellet and leads to fast calculations that allow one to perform 3D simulations. The coupling procedure was applied to three power ramps.

First, to a 1D simulation of a power ramp with measures of oxygen potential in the fuel sample [73]. The simulation results have confirmed that oxygen thermal diffusion is necessary to recover the radial profile of oxygen potential in the fuel pellet, which showed a marked decrease at the pellet center. Second, a 3D simulation of one of the power ramp used to fit the heat of oxygen transport has been detailed. It was shown that several post-irradiation examinations were recovered in the simulation in consequence of oxygen thermal diffusion. The reduction of Cr and Mo oxides into metallic precipitates were calculated at the pellet center, in agreement with measured EPMA profiles. Among the Mo oxides, the reduction of cesium molybdate lead to the formation of great quantities of gaseous cesium that were then released from the fuel pellet core, in agreement with experimental measurements.

In spite of these interesting results, the current coupling procedure is limited to irradiation periods where the temperature distribution and the fission products inventory do not evolve, as in the case of holding periods during power ramp experiments. It would be interesting to extend this work to calculations where these quantities evolve, such as during base irradiations or power transients. It must be recalled that the goal of this work was PCI modeling which has been reached by considering only thermal diffusion during the holding period of the power ramps. The kinetics of oxygen redistribution are however fast and usually lead to some marked oxygen migration within a few minutes. Compared to the duration of the power transient, it is possible that partial redistribution takes place during this loading sequence. This might also be the case during the return to zero power following a power ramp at high linear heat rates. Preliminary simulations, not included in this report, have been carried out to study oxygen transport during power transients. The main difficulty encountered in those simulations stems from the fact that the solubility of fission products increases with temperature. This phenomenon decreases the O/M ratio, an input in the oxygen transport model where conservation of the average O/M ratio in the fuel pellet is assumed. A partial decoupling of fuel thermochemistry and oxygen transport as proposed in this work is no longer possible. The recent publication of Simunovic et al. [157] seems promising in solving this issue. The authors proposed a formulation of oxygen and heat transport that can be used during power transient, in which the driving force for oxygen transport is the Planck potential of oxygen ( $\mu_O/T$ ) instead of the traditional stoichiometry deviation. In this method, the oxygen transport equation is independent of the O/M ratio and can be more easily coupled with fuel thermochemistry since the oxygen chemical potential can be prescribed in the thermodynamic equilibrium computation. A first coupling between fuel thermochemistry and oxygen diffusion has been proposed at the Oak Ridge National Laboratory using the TAF-ID database and the chemical diffusion coefficient derived by Moore [89, 158].

The fuel studied by Walker et al. [7] is another example where the inclusion of oxygen thermal diffusion in a transient calculation could possibly improve the results. The

linear heat rate during the first cycle was 340 W/cm, which could have initiated oxygen redistribution. The thermochemical simulation of Walker's fuel with ANGE has led to nearly flat radial profiles of oxygen potential whereas the measured values increase with radius. This oxygen potential gradient could be explained by oxygen transport from the pellet center towards the periphery. Preliminary simulations of Walker's fuel including oxygen transport during the base irradiation have been performed. The steady state redistribution model OXIREC, described in Section 4.1.2, has been applied. The heat of oxygen transport from Janek and Timm [108] has been used because the expression derived in this work is not applicable to fresh fuel. The obtained results have shown that, under certain conditions, the increasing oxygen potential with the radius can be well reproduced thanks to oxygen redistribution. However, simulating base irradiation with oxygen transport is associated with numerous assumptions and uncertainties and requires more work.

## 6.4 PCI-SCC

To study the impact of oxygen redistribution on PCI failure by I-SCC in more details, a 3D simulation of a power ramp with a short holding period has been performed. It was shown that oxygen thermal diffusion affects thermochemistry of fission products even during a 90 s long holding period. The reduction of cesium molybdate increased the release of gaseous Cs, which is consistent with post-ramp SIMS measurements. In this respect, the simulation was improved compared to the same calculation by Baurens where oxygen redistribution was not considered [14]. The Cs release was very small in this calculation.

The 3D simulation was used to discuss I-SCC initiation criteria, based on the 3D fields calculated: temperature, hoop stress and strain at the triple point, partial iodine pressure from the release of "reactive" iodine ( $I_{(g)}$ ,  $I_{2(g)}$ ,  $TeI_{2(g)}$ , all chemical compounds that will react with bare Zr to form  $ZrI_{4(g)}$ ) from the fuel pellet and the pellet radial crack/dish volumes. The limiting factor for I-SCC initiation was found to be the iodine partial pressure which exceeded the threshold identified from laboratory tests, 50 seconds before reaching the maximum linear heat rate. The I-SCC crack propagation model of Le Boulch, based on laboratory tests performed on irradiated clad samples, has been applied to predict the crack depth at the end of the power ramp. The calculated crack depth was comparable to the experimental estimate based on post-ramp observations of the fuel rod ( $\sim 100 \mu\text{m}$ ). The iodine partial pressure calculated did not consider iodine from CsI radiolysis. Inclusion of the latter phenomenon based on the model of Lewis could probably help improve the evolution of iodine partial pressure during power ramps. The topic is however difficult because deposition of CsI on the fuel surfaces, a first order factor, is not very well documented.

The application of the proposed PCI-SCC approach accounting for fuel thermochemistry and oxygen redistribution to a larger database of power ramps such as the one detailed in reference [24] is part of the possible perspectives to this work. The simulation of the power ramps performed by Davies on hyperstoichiometric fuels could also help understand the origin of PCI mitigation in this case, whether related to a specific fission products speciation in the fuel that would inhibit I-SCC or to the formation of zirconia in the clad inner wall during the transient.

Recently, Loukusa et al. [204] has presented a thermochemical analysis of irradiated fuel taking into account the kinetics of certain chemical reactions involving iodine species. The authors have obtained unexpected results suggesting that hydrogen iodide can play a role in I-SCC. The inclusion of chemical reaction kinetics required constrained Gibbs energy minimization calculations. The consideration of reaction kinetics related to adsorption at the I-SCC crack tip in our calculations could possibly lead to a more detailed description of the crack propagation in the clad thickness during the incubation phase.

## Appendix A

# Theoretical derivation of the oxygen transport equation

This appendix details the theoretical derivation of the oxygen transport equation. For the sake of simplicity the cylindrical coordinate system is used.

Diffusion describes the movement of atoms from a region of high concentration to a region of low concentration [97]. In the cylindrical coordinate system, the flux of particles is given by:

$$J = -D^* \frac{\partial c}{\partial r} \quad (\text{A.1})$$

where

$J$  - flux [mol/m<sup>2</sup>/s]

$D^*$  - self-diffusion coefficient [m<sup>2</sup>/s]

$c$  - concentration [mol]

If one considers a binary system composed of a dilute solution of an isotope  $A^*$  in atoms  $A$  of the same chemical element, the diffusion of an isotope  $A^*$  is given as:

$$J_{A^*} = -D_{A^*}^* \frac{\partial c_{A^*}}{\partial r} \quad (\text{A.2})$$

The system is isolated and no matter exchange with surroundings occurs. Therefore:

$$\frac{\partial c_A}{\partial r} = - \frac{\partial c_{A^*}}{\partial r} \quad (\text{A.3})$$

The chemical potential of species  $A^*$  assuming ideal behavior is:

$$\mu_{A^*} = \mu_{A^*}^p + RT \ln x_{A^*} \quad (\text{A.4})$$

$$\mu_{A^*} = \mu_{A^*}^p + RT \ln \frac{c_{A^*}}{c_A} \quad (\text{A.5})$$

Where  $x_{A^*}$  is the atomic fraction,  $\mu_{A^*}^p$  is the chemical potential at standard pressure,  $R$  is the gas constant and  $T$  is temperature. Derivation of above equation is as follows:

$$\frac{\partial \mu_{A^*}}{\partial r} = \frac{RT}{c_{A^*}} \frac{\partial c_A}{\partial r} \quad (\text{A.6})$$

By using Equation A.6 and Equation A.2 one gets the flux of an isotope  $A^*$  as a function of the chemical potential gradient:

$$J_{A^*} = -D_{A^*}^* \frac{c_{A^*}}{RT} \frac{\partial \mu_{A^*}}{\partial r} \quad (\text{A.7})$$

One may write in a similar way the general equations describing the flux of components  $A$  and  $B$  in a binary system:

$$J_A = -D_A^* \frac{c_A}{RT} \frac{\partial \mu_A}{\partial r} \quad (\text{A.8})$$

$$J_B = -D_B^* \frac{c_B}{RT} \frac{\partial \mu_B}{\partial r} \quad (\text{A.9})$$

In order to find the chemical diffusion coefficient of species  $A$ , Equation A.8 can be written as a function of the concentration gradient:

$$J_A = -D_A^* \frac{c_A}{RT} \frac{\partial \mu_A}{\partial x_A} \frac{\partial x_A}{\partial c_A} \frac{\partial c_A}{\partial r} \quad (\text{A.10})$$

with

$$\mu_A = \mu_A^p + RT \ln (\gamma_A x_A) \quad (\text{A.11})$$

Where  $\gamma_A$  is the activity coefficient of species  $A$ . The individual elements of Equation A.10 (assuming this time a non-ideal mixture of atoms):

$$\frac{\partial \mu_A}{\partial x_A} = \frac{\partial \mu_A}{\partial \ln x_A} \frac{\partial \ln x_A}{\partial x_A} = \frac{RT}{x_A} \left( 1 + \frac{\partial \ln \gamma_A}{\partial \ln x_A} \right) \quad (\text{A.12})$$

$$\frac{\partial x_A}{\partial c_A} = \frac{1}{c_A + c_B} \quad (\text{A.13})$$

Equation A.11 combined with Equations A.12 and A.13 gives:

$$J_A = -D_A^* \left( 1 + \frac{\partial \ln \gamma_A}{\partial \ln x_A} \right) \frac{\partial c_A}{\partial r} = -D_A^c \frac{\partial c_A}{\partial r} \quad (\text{A.14})$$

$$D_A^c = D_A^* \left( 1 + \frac{\partial \ln \gamma_A}{\partial \ln x_A} \right) \quad (\text{A.15})$$

Where  $D_A^c$  is the chemical diffusion coefficient of species  $A$ .

The flux  $J_B$  and the chemical diffusion coefficient of species  $B$  can be obtained in a similar way:

$$J_B = -D_B^c \frac{\partial c_B}{\partial r} \quad (\text{A.16})$$

$$D_B^c = D_B^* \left( 1 + \frac{\partial \ln \gamma_B}{\partial \ln x_B} \right) \quad (\text{A.17})$$

## Diffusion in solid solution (Darken's equation)

To estimate the inter-diffusion coefficient of a binary system of atoms in a solid solution from the chemical diffusion coefficients of the independent components Fick's first law can be used. The fluxes of components  $A$  and  $B$  are as follows:

$$J_A = -D_A^c \left\{ \frac{\partial c_A}{\partial r} \right\} \quad (\text{A.18})$$

$$J_B = -D_B^c \left\{ \frac{\partial c_B}{\partial r} \right\} \quad (\text{A.19})$$

Total amount of atoms per unit volume is:

$$c_A + c_B = c_0 \quad (\text{A.20})$$

If the number of atoms in the system is conserved, the sum of concentration gradients is null:

$$\frac{\partial c_A}{\partial r} + \frac{\partial c_B}{\partial r} = 0 \quad (\text{A.21})$$

Equation A.21 can be used to express  $\frac{\partial c_B}{\partial r}$  in Equation A.19 as a function of  $\frac{\partial c_A}{\partial r}$ :

$$J_B = -D_B^c \left\{ \frac{\partial c_A}{\partial r} \right\} \quad (\text{A.22})$$

In general, in a solid, the movement of atoms requires a simultaneous flux of vacancies  $J_v$ :

$$J_v = -(J_B + J_A) = (D_A^c - D_B^c) \left\{ \frac{\partial c_A}{\partial r} \right\} \quad (\text{A.23})$$

It can be assumed that the area  $S$ , moving with the velocity  $v$  sweeps out the volume  $Svdt$  in the time step  $dt$ . The total number of atoms in this volume is  $Svdtc_0$ .

$$J_v S dt = Sv dt c_0 \quad (\text{A.24})$$

$$J_v = v c_0 \quad (\text{A.25})$$

Employing Equation A.23 the velocity of the lattice drift (Equation A.26) is obtained in the form:

$$v = \frac{1}{c_0} (D_A^c - D_B^c) \left\{ \frac{\partial c_A}{\partial r} \right\} \quad (\text{A.26})$$

The lattice drift has impact on the diffusion of species  $A$  and  $B$ . The net flux of species  $A$ ,  $J'_A$ , is increased by the lattice flux such that:

$$J'_A = J_A + J_{lattice} \quad (\text{A.27})$$

$$J_{\text{lattice}} = v c_A \quad (\text{A.28})$$

$$J'_A = -D_A^c \left\{ \frac{\partial c_A}{\partial r} \right\} + v c_A \quad (\text{A.29})$$

Using previous correlations and the velocity of the lattice drift (Equation A.26), the flux of species  $A$  dependent on the diffusion coefficients  $D_A^c$  and  $D_B^c$  can be found:

$$J'_A = -D_A^c \left\{ \frac{\partial c_A}{\partial r} \right\} + \frac{1}{c_0} (D_A^c - D_B^c) \left\{ \frac{\partial c_A}{\partial r} \right\} c_A \quad (\text{A.30})$$

$$J'_A = -D_A^c \left\{ \frac{\partial c_A}{\partial r} \right\} + x_A (D_A^c - D_B^c) \left\{ \frac{\partial c_A}{\partial r} \right\} \quad (\text{A.31})$$

$$J'_A = (x_A D_A^c - x_A D_B^c - D_A^c) \left\{ \frac{\partial c_A}{\partial r} \right\} \quad (\text{A.32})$$

$$J'_A = [(1 - x_B) D_A^c - x_A D_B^c - D_A^c] \left\{ \frac{\partial c_A}{\partial r} \right\} \quad (\text{A.33})$$

$$J'_A = (-x_B D_A^c - x_A D_B^c - D_A^c + D_A^c) \left\{ \frac{\partial c_A}{\partial r} \right\} \quad (\text{A.34})$$

$$J'_A = -(x_B D_A^c + x_A D_B^c) \left\{ \frac{\partial c_A}{\partial r} \right\} \quad (\text{A.35})$$

$$J'_A = -\tilde{D} \left\{ \frac{\partial c_A}{\partial r} \right\} \quad (\text{A.36})$$

Where  $\tilde{D}$  is the inter-diffusion coefficient.

$$\tilde{D} = (x_B D_A^c + x_A D_B^c) \quad (\text{A.37})$$

$x_A$  and  $x_B$  are atomic fractions of species  $A$  and  $B$ .

$$x_A = \frac{c_A}{c_0} \quad (\text{A.38})$$

$$x_B = \frac{c_B}{c_0} \quad (\text{A.39})$$

Simultaneously to Equation A.36, the flux  $J'_B$  can be expressed as:

$$J'_B = -\tilde{D} \left\{ \frac{\partial c_B}{\partial r} \right\} \quad (\text{A.40})$$

such that

$$J'_A + J'_B = 0 \quad (\text{A.41})$$

## Application to $\text{UO}_{2\pm x}$

The inter-diffusion coefficient for the uranium-oxygen system is defined as follows:

$$\tilde{D} = (x_O D_U^c + x_U D_O^c) \quad (\text{A.42})$$

Mole fractions of oxygen and uranium in  $UO_{2\pm x}$  are given by:

$$x_O = \frac{2+x}{3+x} = \frac{c_O}{c_{tot}} \quad (\text{A.43})$$

$$x_U = \frac{1}{3+x} = \frac{c_U}{c_{tot}} \quad (\text{A.44})$$

Where  $x$  is the stoichiometry deviation and  $c_{tot}$  is the total amount of atoms per unit volume.

Chemical potential of oxygen is associated with the presence of a certain oxygen pressure that is in equilibrium with the solid. To get an expression for the oxygen potential one may write the following equilibria between gaseous oxygen  $O_{2(g)}$  and oxygen in solid solution  $O_{2(ss)}$ .



For above equilibria, the chemical potential may be written:

$$\frac{1}{2}\mu_{O_{2(g)}} = \mu_{O_{(g)}} = \mu_{O_{(ss)}} \quad (\text{A.47})$$

$$\mu_{O_{(ss)}} = \mu_{O_{(g)}} = \frac{1}{2}\mu_{O_{2(g)}}^p + RT \ln(\gamma_O x_O) = \frac{1}{2}\mu_{O_{2(g)}}^p + RT \ln p_{O_2}^{1/2} \quad (\text{A.48})$$

$$\ln(\gamma_O x_O) = \frac{1}{2} \ln p_{O_2} \quad (\text{A.49})$$

$$\frac{\partial \ln \gamma_O}{\partial \ln x_O} = -1 + \frac{1}{2} \frac{\partial \ln p_{O_2}}{\partial \ln x_O} \quad (\text{A.50})$$

Equation A.50 employed in Equation A.15 gives the chemical diffusion coefficient of oxygen as follows:

$$D_O^c = D_O^* \left( 1 - 1 + \frac{1}{2} \frac{\partial \ln p_{O_2}}{\partial \ln x_O} \right) = D_O^* \frac{1}{2} \frac{\partial \ln p_{O_2}}{\partial \ln x_O} = D_O^* \frac{1}{2} \frac{\partial \ln p_{O_2}}{\partial x} \frac{\partial x}{\partial \ln x_O} \quad (\text{A.51})$$

with

$$\frac{\partial \ln x_O}{\partial x} = \frac{\partial}{\partial x} \left( \ln \frac{2+x}{3+x} \right) = \frac{1}{3+x} \frac{1}{2+x} \quad (\text{A.52})$$

The chemical diffusion coefficient of oxygen is a few orders of magnitude greater than the one of uranium. Due to this fact,  $D_U^c$  can be neglected in Equation A.42, which gives:

$$\tilde{D}_O \approx x_U D_O^c = \frac{1}{3+x} D_O^* \frac{1}{2} \frac{\partial \ln p_{O_2}}{\partial \ln x} \quad (\text{A.53})$$

Using Equations A.51 and A.52, the inter-diffusion coefficient of  $UO_{2+x}$  can be expressed as follows:

$$\tilde{D}_O = D_O^* \frac{2+x}{2} \frac{\partial \ln p_{O_2}}{\partial \ln x} \quad (\text{A.54})$$

Simultaneously, Equation A.54 applied to  $\text{UO}_{2-x}$  becomes:

$$\tilde{D}_O = D_O^* \frac{2-x}{2} \frac{\partial \ln p_{O_2}}{\partial \ln x} \quad (\text{A.55})$$

## Theory of thermodiffusion

Thermodiffusion can be described using the theory of irreversible processes. According to this theory, transport processes occurring simultaneously in the same system can influence each other [205]. In the case of nuclear fuel, these fluxes are the flux of heat  $J_q$  and the flux of matter  $J_k$ . For the binary system of  $A$  and  $B$ , one may express these fluxes in the following way:

$$J_A = a_{AA}X_A + a_{AB}X_B + a_{Aq}X_q \quad (\text{A.56})$$

$$J_B = a_{BA}X_A + a_{BB}X_B + a_{Bq}X_q \quad (\text{A.57})$$

$$J_q = a_{qA}X_A + a_{qB}X_B + a_{qq}X_q \quad (\text{A.58})$$

Where  $X_q$  is the thermodynamic force that drives heat flux while  $X_A$  and  $X_B$  are related to the flux of elements  $A$  and  $B$ . Referring to “Reciprocal relations in irreversible processes” written by L. Onsager [205], it is possible to simplify the set of Equations A.56 - A.58 by using the following relations between the  $a_{i,j}$  coefficients:

$$a_{AB} = a_{BA} \quad (\text{A.59})$$

$$a_{qA} = a_{Aq} \quad (\text{A.60})$$

$$a_{qB} = a_{Bq} \quad (\text{A.61})$$

Moreover, de Groot [206] introduced more relations between the coefficients:

$$a_{AB} = -a_{AA} \quad (\text{A.62})$$

$$a_{qA} = -a_{qB} \quad (\text{A.63})$$

$$a_{qA} = a_{AA}Q_A^* \quad (\text{A.64})$$

It is important to say that the quantity of mass is conserved in the isolated system. Thus  $J_A + J_B = 0$ . Using this conservation, Bober and Schumacher have combined the fluxes A.56 - A.58 and obtained:

$$J_A = a_{AA}(X_A - X_B + Q_A^*X_q) = -J_B \quad (\text{A.65})$$

$$J_q = a_{AA}Q_A^*(X_A - X_B) + a_{qq}X_q \quad (\text{A.66})$$

$Q^*$  is the parameter linking fluxes of heat and matter. Writz has defined this factor in his Kinetic Theory [207, 208]. The author describes the energy of activation of an atom as the sum of three elements:

$$q = q_0 + q_s + q_f \quad (\text{A.67})$$

Where  $q_0$  is the energy that needs to be given to the atom before the jump,  $q_s$  is the energy needed to create the saddle point between initial and final positions of the jumping atom,  $q_f$  is the energy given to atoms surrounding the final position that need to be displaced. The heat of transport of the atom can be expressed as the difference between the energy  $q_0$  that the atom carries and the energy  $q_f$  transferred from the initial to the final position.

$$Q^* = q_0 - q_f \quad (\text{A.68})$$

Forces driving diffusion of species  $A$  and  $B$  and the heat conduction  $X_q$  can be expressed as:

$$X_A = -\frac{\partial \mu_A}{\partial r} \quad (\text{A.69})$$

$$X_B = -\frac{\partial \mu_B}{\partial r} \quad (\text{A.70})$$

$$X_q = -\frac{1}{T} \frac{\partial T}{\partial r} \quad (\text{A.71})$$

Thus, equations describing the flux of the element  $A$  in the 2-element system is given by combining equations A.65 and A.69 - A.71:

$$J_A = a_{AA} \left( \frac{\partial \mu_A}{\partial r} - \frac{\partial \mu_B}{\partial r} + \frac{Q_A^*}{T} \frac{\partial T}{\partial r} \right) \quad (\text{A.72})$$

By assuming that the element  $B$  is immobile (in the case of uranium for example), the impact of the flux  $J_B$  can be neglected and Equation A.72 becomes:

$$J_A = a_{AA} \left( \frac{\partial \mu_A}{\partial r} + \frac{Q_A^*}{T} \frac{\partial T}{\partial r} \right) \quad (\text{A.73})$$

If  $\frac{\partial T}{\partial r} = 0$ , analogy with Equation A.8 gives the coefficient  $a_{AA}$  as:

$$a_{AA} = D_A^* \frac{c_A}{RT} \quad (\text{A.74})$$

From Equations A.8 and A.14 can be deduced that:

$$\frac{\partial \mu_A}{\partial r} = \frac{RT}{c_A} \left( 1 + \frac{\partial \ln \gamma_A}{\partial \ln x_A} \right) \frac{\partial c_A}{\partial r} \quad (\text{A.75})$$

Equations A.74 and A.75 employed in Equation A.73 gives:

$$J_A = -\frac{D_A^* c_A}{RT} \left( \frac{RT}{c_A} \left[ 1 + \frac{\partial \ln \gamma_A}{\partial \ln x_A} \right] \frac{\partial c_A}{\partial r} + \frac{Q_A^*}{T} \frac{\partial T}{\partial r} \right) \quad (\text{A.76})$$

$$J_A = -D_A^c \left( \frac{\partial c_A}{\partial r} + \frac{c_A}{RT \left(1 + \frac{\partial \ln \gamma_A}{\partial \ln x_A}\right)} \frac{Q_A^*}{T} \frac{\partial T}{\partial r} \right) \quad (\text{A.77})$$

Simultaneously, the flux  $J_B$  is as follows:

$$J_B = -D_B^c \left( \frac{\partial c_B}{\partial r} + \frac{c_B}{RT \left(1 + \frac{\partial \ln \gamma_B}{\partial \ln x_B}\right)} \frac{Q_B^*}{T} \frac{\partial T}{\partial r} \right) \quad (\text{A.78})$$

According to the Gibbs-Duhem relation [78]:

$$\frac{\partial \ln \gamma_A}{\partial \ln x_A} = \frac{\partial \ln \gamma_B}{\partial \ln x_B} \quad (\text{A.79})$$

## Thermo-diffusion with the vacancy flux

In solids, the flux of vacancies must be considered. It links Equations A.77 and A.78 as follows:

$$J_v = -(J_B - J_A) \quad (\text{A.80})$$

$$J_v = (D_A^c - D_B^c) \frac{\partial c_A}{\partial r} + \frac{D_A^c Q_A^* c_A - D_B^c Q_B^* c_B}{RT \left(1 + \frac{\partial \ln \gamma_A}{\partial \ln x_A}\right)} \frac{\partial T}{\partial r} \quad (\text{A.81})$$

By analogy with Equations A.24 - A.28, the net flux of species  $A$  relative to the vacancy flux can be defined as:

$$J'_A = J_A + J_{lattice} = J_A + v c_A \quad (\text{A.82})$$

$$J'_A = \tilde{D} \frac{\partial c_A}{\partial r} + \frac{D_B^c Q_B^* c_B x_A - D_A^c Q_A^* c_A x_B}{RT \left(1 + \frac{\partial \ln \gamma_A}{\partial \ln x_A}\right)} \frac{\partial T}{\partial r} \quad (\text{A.83})$$

Equation A.83 can be simplified by using Equation A.84, as proposed by Howard and Lidiard [209]:

$$Q_{ACB}^* = -Q_{BCB}^* \quad (\text{A.84})$$

$$J'_A = -(x_A D_B^c - x_B D_A^c) \left[ \frac{\partial c_A}{\partial r} - \frac{Q_{ACB}^* c_A}{RT^2 \left(1 + \frac{\partial \ln \gamma_A}{\partial \ln x_A}\right)} \frac{\partial T}{\partial r} \right] \quad (\text{A.85})$$

## Application to $\text{UO}_2$

It can be assumed that:

$$D_O^c \gg D_U^c \quad (\text{A.86})$$

$$\tilde{D}_O = x_U D_O^c \quad (\text{A.87})$$

$$J'_O = -x_U D_O^c \left[ \frac{\partial c_O}{\partial r} + \frac{Q_O^* c_O}{RT^2 \left(1 + \frac{\partial \ln \gamma_O}{\partial \ln x_O}\right)} \frac{\partial T}{\partial r} \right] \quad (\text{A.88})$$

Applying Fick's second law:

$$\frac{\partial c_O}{\partial t} = \frac{1}{r} \frac{\partial}{\partial r} \left[ r x_U D_O^c \left( \frac{\partial c_O}{\partial r} + \frac{Q_O^* c_O}{RT^2 \left(1 + \frac{\partial \ln \gamma_O}{\partial \ln x_O}\right)} \frac{\partial T}{\partial r} \right) \right] \quad (\text{A.89})$$

If one assumes that the system is a dilute solution of oxygen interstitials or vacancies, the factor  $\partial \ln \gamma_O / \partial \ln x_O$  disappears.

$$\frac{\partial c_O}{\partial t} = \frac{1}{r} \frac{\partial}{\partial r} \left[ r x_U D_O^c \left( \frac{\partial c_O}{\partial r} + \frac{Q_O^* c_O}{RT^2} \frac{\partial T}{\partial r} \right) \right] \quad (\text{A.90})$$

In literature, one may find the thermodiffusion equation expressed as a function of the stoichiometry deviation gradient. Since the relation between the stoichiometry deviation  $x$  and the oxygen concentration  $c_O$  in fresh  $\text{UO}_{2\pm x}$  is as follows:

$$c_O = 2 \pm x [\text{mol O} / \text{mol UO}_2] \quad (\text{A.91})$$

By using the stoichiometry deviation instead of the oxygen concentration Equation A.89 can be rewritten as:

$$\frac{\partial x}{\partial t} = \frac{1}{r} \frac{\partial}{\partial r} \left[ r \tilde{D}_O \left( \frac{\partial x}{\partial r} + \frac{Q_O^* x}{RT^2} \frac{\partial T}{\partial r} \right) \right] \quad (\text{A.92})$$

Equation A.92 in a more generic form is given by:

$$\frac{\partial x}{\partial t} = \text{div.} \left[ \tilde{D}_O \left( \underline{\text{grad}}(x) + \frac{Q_O^* x}{RT^2} \underline{\text{grad}}(T) \right) \right] \quad (\text{A.93})$$

where grad and div are the gradient and divergence operators.

## Appendix B

# Concentration of point defects in $\text{UO}_2$

The main defects present in  $\text{UO}_{2\pm x}$  fuel are oxygen Frenkel defects. The reaction of defects formation is:



where

$[O_O]$ -concentration of oxygen sites

$[V_O]$ -concentration of oxygen vacancies

$[O_i]$ -concentration of oxygen interstitial atoms

The equilibrium constant of Equation B.1 is equal to:

$$K_{FO} = \frac{[V_O][O_i]}{[O_O]} \quad (\text{B.2})$$

The balance of the electrical charge is:

$$x = -[V_O] + [O_i] \quad (\text{B.3})$$

where  $x$  is the stoichiometry deviation.

The concentration of the regular oxygen sites is equal to  $[O_O] + [V_O]$ . In order to simplify the model, it can be assumed that the concentration of oxygen sites is constant and equal to 1. Thus:

$$[O_O] + [V_O] = 1 \quad (\text{B.4})$$

In order to get concentrations of oxygen vacancies and oxygen interstitials, it is necessary to do the following transformations:

$$[O_O] = 1 - [V_O] \quad (\text{B.5})$$

$$[O_O] = \frac{[V_O][O_i]}{K_{FO}} \quad (\text{B.6})$$

$$1 - [V_O] = \frac{[V_O][O_i]}{K_{FO}} \quad (\text{B.7})$$

Equation B.3 can be used to remove  $V_O$  from Equation B.7.

$$1 - ([O_i] - x) = \frac{([O_i] - x)[O_i]}{K_{FO}} \quad (\text{B.8})$$

$$[O_i]^2 + [O_i](K_{FO} - x) - K_{FO}(1 + x) = 0 \quad (\text{B.9})$$

Equation B.9 has the form of a quadratic equation in which:

Coefficient	Value
a	1
b	$K_{FO} - x$
c	$-K_{FO}(1 + x)$

Solution of the quadratic equation is:

$$[O_i] = \frac{-(K_{FO} - x) \pm \sqrt{(K_{FO} - x)^2 + 4K_{FO}(1 + x)}}{2} \quad (\text{B.10})$$

Solution gives two values of  $[O_i]$ . However,  $[O_i]$  cannot be negative. Thus, the only correct answer is:

$$[O_i] = \frac{x - K_{FO} + \sqrt{(K_{FO} + x)^2 + 4K_{FO}}}{2} \quad (\text{B.11})$$

$[V_O]$  can be treated in a similar way.

$$[V_O] = \frac{-x - K_{FO} + \sqrt{(K_{FO} + x)^2 + 4K_{FO}}}{2} \quad (\text{B.12})$$

## Appendix C

# Isotopic composition after 3 months

This appendix contains isotopic compositions of fuel irradiated up to burnups of 20, 40 and 60 GWd/tHM. Compositions were calculated with PRODHEL as a stand-alone model. It was assumed that the initial enrichment of the fuel was 3.5% and the pellet radius was 4.1 mm. Linear heat rate used in the calculations was 200 W/cm. Results are presented in the table below. Columns 'Before' and 'After' refer to isotopic compositions at the end of base irradiation and after 3 months of cooling at zero power. Composition of the 'after' columns consists mostly of long-lived and stable isotopes. The concentrations of isotopes are given in units of mol/mol UO<sub>2</sub>.

Isotope	20 GWd/tHM		40 GWd/tHM		60 GWd/tHM	
	Before	After	Before	After	Before	After
HE4	9.91E-05	9.96E-05	3.60E-04	3.70E-04	1.21E-03	1.24E-03
C13	5.61E-05	5.61E-05	1.75E-04	1.75E-04	4.04E-04	4.04E-04
O16	2.00E+00	2.00E+00	2.00E+00	2.00E+00	2.00E+00	2.00E+00
GE77	5.70E-10	0.00E+00	3.35E-10	0.00E+00	1.99E-10	4.06E-16
AS75	2.18E-07	2.18E-07	5.66E-07	5.66E-07	9.73E-07	9.73E-07
AS76	1.15E-11	1.03E-17	2.92E-11	0.00E+00	4.98E-11	2.37E-15
AS77	6.42E-09	9.33E-14	3.50E-09	1.94E-14	1.87E-09	1.58E-13
SE76	2.30E-09	2.31E-09	1.87E-08	1.87E-08	7.27E-08	7.28E-08
SE77	1.92E-06	1.93E-06	4.38E-06	4.38E-06	6.28E-06	6.29E-06
SE78	5.02E-06	5.02E-06	1.28E-05	1.28E-05	2.21E-05	2.21E-05
SE79	1.12E-05	1.12E-05	2.60E-05	2.60E-05	3.78E-05	3.78E-05
SE80	2.93E-05	2.93E-05	7.04E-05	7.04E-05	1.14E-04	1.14E-04
SE81	6.68E-13	9.67E-28	1.60E-12	2.37E-27	2.60E-12	5.71E-27
SE82	7.48E-05	7.48E-05	1.76E-04	1.76E-04	2.73E-04	2.73E-04
BR81	4.53E-05	4.53E-05	1.06E-04	1.06E-04	1.61E-04	1.61E-04

BR82	3.08E-09	3.31E-14	6.66E-09	2.60E-14	9.89E-09	7.30E-13
BR82M	7.25E-12	6.84E-30	1.70E-11	1.72E-29	2.58E-11	4.20E-29
KR82	5.10E-07	5.13E-07	3.50E-06	3.50E-06	1.20E-05	1.20E-05
KR83	1.15E-04	1.15E-04	2.15E-04	2.15E-04	2.15E-04	2.15E-04
KR84	2.39E-04	2.39E-04	5.93E-04	5.93E-04	1.00E-03	1.00E-03
KR85	6.03E-05	5.94E-05	1.21E-04	1.19E-04	1.37E-04	1.35E-04
KR86	4.42E-04	4.42E-04	9.97E-04	9.97E-04	1.47E-03	1.47E-03
RB85	2.31E-04	2.32E-04	5.42E-04	5.43E-04	8.50E-04	8.52E-04
RB86	2.62E-08	7.56E-10	6.02E-08	2.25E-09	9.36E-08	4.22E-09
RB87	5.76E-04	5.76E-04	1.30E-03	1.30E-03	1.91E-03	1.91E-03
SR86	3.20E-07	3.45E-07	2.51E-06	2.57E-06	9.85E-06	9.94E-06
SR87	3.56E-10	3.56E-10	9.19E-09	9.19E-09	8.77E-08	8.77E-08
SR88	8.03E-04	8.03E-04	1.80E-03	1.80E-03	2.64E-03	2.64E-03
SR89	1.05E-04	3.02E-05	5.07E-05	1.51E-05	2.11E-05	6.42E-06
SR90	1.23E-03	1.22E-03	2.60E-03	2.58E-03	3.36E-03	3.34E-03
SR91	1.01E-06	0.00E+00	5.08E-07	0.00E+00	2.31E-07	2.08E-13
Y89	9.27E-04	1.00E-03	2.26E-03	2.29E-03	3.35E-03	3.36E-03
Y90	3.16E-07	3.10E-07	6.74E-07	6.56E-07	8.74E-07	8.48E-07
Y91	1.55E-04	5.30E-05	7.71E-05	2.71E-05	3.42E-05	1.22E-05
Y92	7.04E-11	0.00E+00	3.51E-11	0.00E+00	1.55E-11	2.42E-20
Y93	1.24E-06	0.00E+00	6.72E-07	0.00E+00	3.52E-07	4.24E-13
ZR90	2.70E-05	3.43E-05	2.05E-04	2.21E-04	7.31E-04	7.52E-04
ZR91	1.14E-03	1.24E-03	2.85E-03	2.91E-03	4.30E-03	4.32E-03
ZR92	1.36E-03	1.36E-03	3.13E-03	3.13E-03	4.78E-03	4.78E-03
ZR93	1.46E-03	1.46E-03	3.41E-03	3.41E-03	5.24E-03	5.24E-03
ZR94	1.47E-03	1.47E-03	3.51E-03	3.51E-03	5.61E-03	5.61E-03
ZR95	2.03E-04	7.58E-05	1.16E-04	4.41E-05	6.39E-05	2.47E-05
ZR96	1.47E-03	1.47E-03	3.55E-03	3.55E-03	5.76E-03	5.76E-03
ZR97	2.03E-06	6.46E-16	1.23E-06	0.00E+00	7.53E-07	8.81E-12
NB95	1.13E-04	6.98E-05	6.43E-05	4.00E-05	3.51E-05	2.21E-05
NB96	4.33E-09	2.97E-16	2.47E-09	0.00E+00	1.35E-09	4.79E-14
NB97	1.46E-07	4.99E-17	8.82E-08	0.00E+00	5.40E-08	6.81E-13
MO95	1.17E-03	1.34E-03	3.22E-03	3.32E-03	4.85E-03	4.90E-03
MO96	2.09E-05	2.09E-05	2.14E-04	2.14E-04	8.66E-04	8.66E-04
MO97	1.42E-03	1.42E-03	3.46E-03	3.46E-03	5.67E-03	5.68E-03
MO98	1.39E-03	1.39E-03	3.48E-03	3.48E-03	5.95E-03	5.95E-03
MO99	8.42E-06	1.68E-10	5.32E-06	0.00E+00	3.43E-06	2.77E-11
MO100	1.52E-03	1.52E-03	3.82E-03	3.82E-03	6.54E-03	6.54E-03
TC99	1.41E-03	1.42E-03	3.23E-03	3.23E-03	4.56E-03	4.56E-03
TC99M	6.76E-07	1.49E-11	4.27E-07	0.00E+00	2.75E-07	2.44E-12
TC100	4.72E-11	7.68E-29	1.08E-10	1.93E-28	1.52E-10	3.31E-28

RU100	5.78E-05	5.78E-05	4.61E-04	4.61E-04	1.73E-03	1.73E-03
RU101	1.26E-03	1.26E-03	3.12E-03	3.12E-03	5.10E-03	5.10E-03
RU102	1.11E-03	1.11E-03	3.07E-03	3.07E-03	5.99E-03	5.99E-03
RU103	7.79E-05	1.56E-05	6.38E-05	1.35E-05	5.12E-05	1.12E-05
RU104	5.93E-04	5.93E-04	1.87E-03	1.87E-03	3.97E-03	3.97E-03
RU105	1.92E-07	0.00E+00	2.10E-07	0.00E+00	1.99E-07	1.61E-15
RU106	1.38E-04	1.17E-04	2.83E-04	2.39E-04	3.02E-04	2.55E-04
RH103	6.74E-04	7.37E-04	1.51E-03	1.56E-03	1.74E-03	1.78E-03
RH103M	7.64E-08	1.53E-08	6.26E-08	1.32E-08	5.02E-08	1.10E-08
RH104	2.53E-10	5.49E-35	5.65E-10	1.33E-34	6.50E-10	2.56E-34
RH105	1.49E-06	1.72E-11	1.63E-06	7.01E-12	1.54E-06	1.29E-10
RH106	1.38E-10	1.09E-10	2.73E-10	2.23E-10	2.90E-10	2.38E-10
RH106M	2.46E-10	9.18E-21	2.69E-10	1.23E-21	2.54E-10	2.20E-21
PD104	1.06E-04	1.06E-04	9.18E-04	9.18E-04	3.15E-03	3.15E-03
PD105	3.64E-04	3.66E-04	1.29E-03	1.30E-03	2.87E-03	2.88E-03
PD106	9.83E-05	1.20E-04	7.51E-04	7.95E-04	2.54E-03	2.58E-03
PD107	1.30E-04	1.30E-04	6.27E-04	6.27E-04	1.64E-03	1.64E-03
PD108	7.48E-05	7.48E-05	4.13E-04	4.13E-04	1.18E-03	1.18E-03
PD109	1.08E-07	0.00E+00	1.93E-07	0.00E+00	2.52E-07	1.28E-12
PD110	2.46E-05	2.46E-05	1.46E-04	1.46E-04	4.32E-04	4.32E-04
PD111	9.56E-13	7.59E-27	5.65E-12	4.13E-26	1.67E-11	1.73E-25
PD112	1.64E-08	2.64E-16	2.12E-08	0.00E+00	2.11E-08	4.92E-13
SN121	1.18E-08	1.64E-11	1.25E-08	5.58E-11	1.15E-08	1.22E-10
SN121M	3.78E-07	3.77E-07	1.29E-06	1.28E-06	2.81E-06	2.80E-06
SN122	5.88E-06	5.88E-06	1.98E-05	1.98E-05	4.45E-05	4.45E-05
SN123	2.48E-07	1.52E-07	3.15E-07	1.94E-07	2.99E-07	1.85E-07
SN124	1.01E-05	1.01E-05	3.42E-05	3.42E-05	7.66E-05	7.66E-05
SN125	9.75E-08	6.05E-11	1.09E-07	0.00E+00	1.04E-07	5.55E-10
SB121	3.94E-06	3.96E-06	1.32E-05	1.32E-05	2.77E-05	2.77E-05
SB122	1.18E-09	2.97E-14	3.97E-09	0.00E+00	8.33E-09	5.77E-14
SB123	5.50E-06	5.60E-06	2.08E-05	2.09E-05	4.79E-05	4.81E-05
SB124	2.84E-08	9.96E-09	7.92E-08	2.84E-08	1.65E-07	6.02E-08
SB125	7.12E-06	6.78E-06	1.62E-05	1.53E-05	1.91E-05	1.81E-05
SB126	4.06E-08	4.55E-11	4.27E-08	2.14E-10	3.96E-08	4.98E-10
SB126M	6.03E-11	9.81E-26	6.34E-11	1.09E-25	5.89E-11	1.53E-25
SB127	3.76E-07	2.28E-11	3.64E-07	0.00E+00	3.20E-07	2.05E-11
SB128	7.66E-08	0.00E+00	6.26E-08	0.00E+00	5.00E-08	3.16E-14
TE122	8.70E-08	8.81E-08	9.18E-07	9.22E-07	4.64E-06	4.65E-06
TE123	3.62E-10	4.00E-10	7.56E-09	8.07E-09	4.95E-08	5.22E-08
TE123M	9.34E-11	5.51E-11	1.25E-09	7.44E-10	6.82E-09	4.06E-09
TE124	1.17E-07	1.36E-07	9.93E-07	1.04E-06	4.80E-06	4.91E-06

TE125	1.45E-06	1.89E-06	1.25E-05	1.35E-05	4.36E-05	4.48E-05
TE125M	8.01E-08	8.57E-08	2.04E-07	2.01E-07	2.49E-07	2.40E-07
TE126	2.60E-06	2.64E-06	9.77E-06	9.81E-06	2.34E-05	2.35E-05
TE127	3.76E-08	3.42E-09	3.68E-08	3.54E-09	3.23E-08	3.14E-09
TE127M	1.68E-06	9.79E-07	1.73E-06	1.01E-06	1.53E-06	8.99E-07
TE128	9.31E-05	9.32E-05	2.75E-04	2.75E-04	5.55E-04	5.55E-04
TE129M	4.65E-06	7.06E-07	3.63E-06	5.92E-07	2.79E-06	4.77E-07
TE130	4.54E-04	4.54E-04	1.20E-03	1.20E-03	2.17E-03	2.17E-03
TE131	2.31E-08	1.92E-22	1.52E-08	1.34E-22	1.02E-08	1.35E-22
TE132	7.13E-06	1.92E-10	4.69E-06	0.00E+00	3.12E-06	6.73E-11
I127	3.62E-05	3.73E-05	1.18E-04	1.20E-04	2.41E-04	2.42E-04
I128	6.22E-11	6.42E-25	2.03E-10	2.07E-24	4.13E-10	6.06E-24
I129	1.82E-04	1.85E-04	5.01E-04	5.04E-04	9.02E-04	9.04E-04
I130	6.17E-09	0.00E+00	1.69E-08	0.00E+00	3.03E-08	9.59E-14
I131	1.23E-05	5.67E-09	8.23E-06	0.00E+00	5.58E-06	1.48E-08
I132	2.13E-07	5.92E-12	1.40E-07	0.00E+00	9.33E-08	2.07E-12
I133	2.88E-06	6.33E-14	1.84E-06	0.00E+00	1.19E-06	3.00E-11
I135	8.71E-07	0.00E+00	5.54E-07	0.00E+00	3.56E-07	3.68E-14
XE128	6.73E-07	6.73E-07	7.21E-06	7.21E-06	3.62E-05	3.62E-05
XE129	1.42E-09	1.42E-09	4.86E-08	4.86E-08	5.92E-07	5.92E-07
XE130	2.56E-06	2.57E-06	2.35E-05	2.35E-05	1.04E-04	1.04E-04
XE131	6.19E-04	6.31E-04	1.20E-03	1.21E-03	1.23E-03	1.24E-03
XE131M	2.00E-07	7.04E-10	1.34E-07	2.03E-09	9.03E-08	2.60E-09
XE132	1.15E-03	1.15E-03	3.38E-03	3.38E-03	6.84E-03	6.84E-03
XE133	1.75E-05	4.03E-09	1.12E-05	0.00E+00	7.21E-06	3.18E-09
XE133M	2.12E-07	7.76E-12	1.37E-07	8.10E-13	9.00E-08	3.32E-12
XE134	1.84E-03	1.84E-03	4.55E-03	4.55E-03	7.63E-03	7.63E-03
XE135	5.20E-07	0.00E+00	3.38E-07	0.00E+00	2.22E-07	8.89E-13
XE136	2.55E-03	2.55E-03	6.45E-03	6.45E-03	1.11E-02	1.11E-02
CS133	1.49E-03	1.51E-03	3.35E-03	3.36E-03	4.48E-03	4.48E-03
CS134	6.66E-05	6.13E-05	3.48E-04	3.20E-04	6.55E-04	6.03E-04
CS135	6.49E-04	6.50E-04	1.65E-03	1.65E-03	2.91E-03	2.91E-03
CS136	4.88E-07	8.78E-10	1.08E-06	7.50E-09	1.81E-06	2.63E-08
CS137	1.47E-03	1.46E-03	3.54E-03	3.52E-03	5.51E-03	5.48E-03
BA134	1.35E-05	1.88E-05	2.62E-04	2.90E-04	1.47E-03	1.52E-03
BA135	3.06E-08	3.06E-08	1.99E-06	1.99E-06	2.88E-05	2.88E-05
BA136	9.79E-06	1.03E-05	6.86E-05	6.97E-05	2.72E-04	2.73E-04
BA137	3.01E-05	3.85E-05	2.46E-04	2.66E-04	9.81E-04	1.01E-03
BA138	1.59E-03	1.59E-03	3.95E-03	3.95E-03	6.64E-03	6.64E-03
BA140	3.91E-05	4.79E-08	2.37E-05	1.47E-07	1.44E-05	2.00E-07
LA139	1.51E-03	1.51E-03	3.70E-03	3.70E-03	6.11E-03	6.11E-03

LA140	5.20E-06	7.24E-09	3.24E-06	2.22E-08	2.09E-06	3.03E-08
LA141	4.06E-11	0.00E+00	2.53E-11	0.00E+00	1.63E-11	5.49E-20
CE140	1.45E-03	1.49E-03	3.68E-03	3.71E-03	6.29E-03	6.31E-03
CE141	9.41E-05	1.34E-05	5.70E-05	8.77E-06	3.46E-05	5.59E-06
CE142	1.39E-03	1.39E-03	3.40E-03	3.40E-03	5.65E-03	5.65E-03
CE143	3.84E-06	2.60E-11	2.23E-06	5.53E-12	1.29E-06	8.84E-11
CE144	6.29E-04	5.04E-04	4.88E-04	3.91E-04	2.51E-04	2.01E-04
PR141	1.28E-03	1.36E-03	3.29E-03	3.33E-03	5.38E-03	5.40E-03
PR142	2.79E-08	1.86E-16	7.14E-08	0.00E+00	1.17E-07	2.25E-12
PR143	3.80E-05	1.40E-07	2.21E-05	2.18E-07	1.26E-05	2.35E-07
PR144	2.66E-08	2.12E-08	2.06E-08	1.65E-08	1.06E-08	8.47E-09
PR145	4.67E-07	0.00E+00	2.76E-07	0.00E+00	1.63E-07	9.48E-15
ND142	7.24E-06	7.27E-06	6.56E-05	6.56E-05	2.70E-04	2.70E-04
ND143	1.20E-03	1.24E-03	2.28E-03	2.30E-03	2.25E-03	2.26E-03
ND144	7.75E-04	9.00E-04	3.54E-03	3.64E-03	7.67E-03	7.72E-03
ND145	8.86E-04	8.86E-04	1.96E-03	1.96E-03	2.67E-03	2.67E-03
ND146	7.49E-04	7.49E-04	2.04E-03	2.04E-03	3.99E-03	3.99E-03
ND147	1.21E-05	7.87E-09	7.66E-06	1.15E-08	4.95E-06	4.23E-08
ND148	4.13E-04	4.13E-04	1.03E-03	1.03E-03	1.75E-03	1.75E-03
ND149	5.20E-10	1.04E-20	1.30E-09	1.56E-20	2.20E-09	3.25E-20
ND150	1.71E-04	1.71E-04	4.61E-04	4.61E-04	8.51E-04	8.51E-04
ND151	1.86E-11	2.10E-27	5.01E-11	5.94E-27	9.25E-11	1.66E-26
PM147	3.30E-04	3.20E-04	3.56E-04	3.41E-04	2.17E-04	2.08E-04
PM148	1.13E-06	2.83E-09	1.23E-06	2.73E-09	7.45E-07	2.69E-09
PM148M	2.40E-06	5.15E-07	2.64E-06	5.95E-07	1.60E-06	3.73E-07
PM149	1.54E-06	3.49E-11	1.20E-06	3.19E-12	8.47E-07	2.51E-11
PM150	4.02E-10	0.00E+00	3.14E-10	0.00E+00	2.21E-10	2.86E-20
PM151	3.04E-07	7.46E-13	2.41E-07	6.90E-14	1.93E-07	1.07E-11
SM147	8.08E-05	1.03E-04	3.33E-04	3.56E-04	4.43E-04	4.57E-04
SM148	7.29E-05	7.59E-05	4.51E-04	4.55E-04	1.20E-03	1.20E-03
SM149	5.48E-06	7.02E-06	4.36E-06	5.57E-06	3.23E-06	4.08E-06
SM150	2.79E-04	2.79E-04	7.56E-04	7.56E-04	1.20E-03	1.20E-03
SM151	2.26E-05	2.29E-05	2.65E-05	2.67E-05	3.05E-05	3.06E-05
SM152	1.25E-04	1.25E-04	2.38E-04	2.38E-04	2.74E-04	2.74E-04
SM153	6.55E-07	1.44E-11	1.04E-06	5.97E-12	1.14E-06	6.77E-11
SM154	2.49E-05	2.49E-05	8.24E-05	8.24E-05	1.79E-04	1.79E-04
SM155	1.31E-11	6.67E-26	4.33E-11	2.20E-25	9.42E-11	7.01E-25
EU151	4.85E-08	9.25E-08	5.87E-08	1.10E-07	6.77E-08	1.27E-07
EU152	3.51E-08	3.47E-08	4.63E-08	4.57E-08	5.37E-08	5.30E-08
EU152M	8.49E-11	0.00E+00	1.03E-10	0.00E+00	1.19E-10	8.94E-17
EU153	7.81E-05	7.88E-05	2.98E-04	2.99E-04	4.72E-04	4.73E-04

EU154	9.60E-06	9.40E-06	5.88E-05	5.76E-05	1.06E-04	1.04E-04
EU155	3.99E-06	3.85E-06	1.80E-05	1.73E-05	3.20E-05	3.09E-05
EU156	1.20E-06	1.18E-08	4.65E-06	7.44E-08	8.09E-06	1.85E-07
EU157	8.72E-09	0.00E+00	1.50E-08	0.00E+00	1.82E-08	1.44E-13
EU158	2.60E-13	1.17E-25	4.46E-13	1.68E-25	5.41E-13	2.80E-25
GD152	3.33E-08	3.35E-08	8.55E-08	8.57E-08	1.12E-07	1.13E-07
GD153	1.33E-09	1.03E-09	3.64E-09	2.80E-09	4.81E-09	3.71E-09
GD154	4.39E-07	6.30E-07	9.44E-06	1.06E-05	4.62E-05	4.83E-05
GD155	5.42E-08	1.97E-07	3.04E-07	9.46E-07	7.42E-07	1.89E-06
GD156	1.95E-05	2.06E-05	1.94E-04	1.99E-04	9.50E-04	9.58E-04
GD157	8.52E-08	9.39E-08	2.09E-07	2.24E-07	5.34E-07	5.52E-07
GD158	6.15E-06	6.15E-06	3.72E-05	3.72E-05	1.63E-04	1.63E-04
GD159	3.10E-09	1.08E-17	6.76E-09	0.00E+00	1.13E-08	1.94E-13
GD160	4.92E-07	4.92E-07	3.96E-06	3.96E-06	1.30E-05	1.30E-05
U235	4.33E-02	4.33E-02	1.64E-02	1.64E-02	2.55E-03	2.55E-03
U236	4.50E-03	4.50E-03	8.30E-03	8.30E-03	7.99E-03	7.99E-03
U237	6.23E-06	2.52E-09	1.10E-05	0.00E+00	1.06E-05	1.34E-08
U238	9.23E-01	9.23E-01	9.05E-01	9.05E-01	8.71E-01	8.71E-01
U239	2.91E-07	1.66E-21	2.85E-07	1.77E-21	2.75E-07	2.52E-21
NP237	2.07E-04	2.13E-04	1.03E-03	1.04E-03	1.89E-03	1.90E-03
NP238	3.21E-07	8.84E-12	1.61E-06	7.02E-12	2.94E-06	1.20E-10
NP239	4.21E-05	9.13E-10	4.13E-05	4.40E-11	3.97E-05	1.14E-09
PU238	2.35E-05	2.42E-05	3.93E-04	4.02E-04	1.56E-03	1.58E-03
PU239	3.85E-03	3.89E-03	4.76E-03	4.80E-03	4.81E-03	4.85E-03
PU240	7.18E-04	7.18E-04	1.32E-03	1.32E-03	1.38E-03	1.39E-03
PU241	4.59E-04	4.54E-04	1.69E-03	1.67E-03	1.93E-03	1.90E-03
PU242	5.27E-05	5.27E-05	7.90E-04	7.90E-04	1.97E-03	1.97E-03
PU243	7.23E-09	0.00E+00	1.07E-07	0.00E+00	2.67E-07	4.61E-15
AM241	9.29E-06	1.48E-05	8.83E-05	1.09E-04	1.26E-04	1.49E-04
AM242	1.56E-08	1.89E-12	1.47E-07	2.58E-11	2.09E-07	4.12E-11
AM242M	1.50E-07	1.50E-07	2.02E-06	2.02E-06	3.04E-06	3.04E-06
AM243	3.35E-06	3.35E-06	1.68E-04	1.68E-04	8.56E-04	8.56E-04
AM244	9.96E-11	0.00E+00	4.95E-09	0.00E+00	2.50E-08	2.94E-14
AM244M	6.42E-11	2.05E-24	3.18E-09	5.35E-23	1.61E-08	3.17E-22
CM242	1.33E-06	9.09E-07	2.50E-05	1.71E-05	4.12E-05	2.82E-05
CM243	9.25E-09	9.20E-09	5.69E-07	5.65E-07	1.63E-06	1.62E-06
CM244	3.08E-07	3.05E-07	5.55E-05	5.50E-05	7.48E-04	7.41E-04

## Appendix D

# Thomas algorithm for solving tridiagonal systems of equations

Thomas algorithm is a simplified form of the Gaussian elimination method that can be applied to solve tridiagonal systems of equations. It can be used to solve the system with  $n$  unknowns, which has the following form:

$$[A][x] = [B] \quad (\text{D.1})$$

where  $[A] = (a_{ij}), 1 \leq i, j \leq n$  is a matrix of  $n \times n$  real numbers.  $[b] = (b_i), 1 \leq i \leq n$  is a column vector of  $n$  real numbers and  $[x] = (x_i), 1 \leq i \leq n$  is the vector of  $n$  unknowns. The matrix form in Equation D.1 is equivalent to:

$$\sum_{j=1}^n a_{ij}x_j = b_i, \quad i = 1, \dots, n \quad (\text{D.2})$$

To solve the system  $[A][x] = [b]$  it is necessary to write the system  $[A] = [L][U]$  where  $[L]$  is a lower triangular matrix with 1 in the main diagonal and  $[U]$  is an upper triangular matrix. The solution of  $[A][x] = [b]$  is achieved by solving successively the systems  $[L][y] = [b]$  and  $[U][x] = [y]$ .

The tridiagonal matrix  $[A]$  is given by:

$$\begin{bmatrix} d_1 & h_1 & 0 & 0 \\ s_2 & d_2 & \ddots & 0 \\ 0 & \ddots & \ddots & h_{n-1} \\ 0 & 0 & s_n & d_n \end{bmatrix} \quad (\text{D.3})$$

and the triangular matrices  $[L]$  and  $[U]$  are as follows:

$$[L] = \begin{bmatrix} 1 & 0 & \dots & 0 \\ \beta_2 & 1 & \ddots & \vdots \\ 0 & \ddots & \ddots & 0 \\ 0 & 0 & \beta_n & 1 \end{bmatrix}, \quad [U] = \begin{bmatrix} \alpha_1 & h_1 & 0 & 0 \\ 0 & \alpha_2 & \ddots & 0 \\ \vdots & \ddots & \ddots & h_{n-1} \\ 0 & \dots & 0 & \alpha_n \end{bmatrix} \quad (\text{D.4})$$

The coefficients  $\alpha_i$  and  $\beta_i$  can be calculated with the following equations:

$$\alpha_1 = d_1, \beta_i = \frac{s_i}{\alpha_{i-1}}, \alpha_i = d_i - \beta_i h_{i-1}, \quad i = 2, \dots, n \quad (\text{D.5})$$

The systems  $[L][y] = [b]$  and  $[U][x] = [y]$  can be solved in the following way:

$$[L][y] = [b] \iff y_1 = b_1, y_i = b_i - \beta_i y_{i-1}, \quad i = 1, \dots, n \quad (\text{D.6})$$

$$[U][x] = [y] \iff x_n = \frac{y_n}{\alpha_n}, x_i = \frac{y_i - h_i x_{i+1}}{\alpha_i}, \quad i = n-1, \dots, 1 \quad (\text{D.7})$$

The number of operations needed to find the unknowns  $[x]$  is not greater than  $8n - 7$ .

## Appendix E

# Thermal diffusion problem solved by the finite element method

A general transient thermal diffusion problem in the domain  $\Omega$  is governed by the heat transport equation and Fourier's law:

$$\begin{cases} \rho c_p \frac{\partial T}{\partial t} + \text{div}(\underline{q}) = f \\ \underline{q} = -\lambda \underline{\text{grad}}(T) \end{cases} \quad (\text{E.1})$$

in every point of  $\Omega$  with

- $T$ —temperature
- $\underline{q}$ —heat flux density
- $t$ —time
- $f$ —volumetric calorific power provided by the heat source
- $\rho$ —volumetric mass density
- $c_p$ —thermal mass capacity
- $\lambda$ —thermal conductivity
- $\underline{\text{grad}}$ —gradient operator
- $\text{div}$ —divergence operator.

To solve these equations by the method of Galerkin, the first equation is multiplied by an arbitrary function  $\Theta^*$  and integrated over the entire domain  $\Omega$ :

$$\int_{\Omega} \rho c_p \frac{\partial T}{\partial t} \Theta^* dV + \int_{\Omega} \text{div}(\underline{q}) \Theta^* dV = \int_{\Omega} f \Theta^* dV. \quad (\text{E.2})$$

By integrating the second integral by parts and introducing the vector  $\underline{n}$ , which is normal to the surface  $\partial\Omega$ , the following expression is obtained:

$$\int_{\Omega} \rho c_p \frac{\partial T}{\partial t} \Theta^* dV - \int_{\Omega} \underline{q} \cdot \underline{\text{grad}}(\Theta^*) dV + \int_{\partial\Omega} \underline{q} \cdot \underline{n} \Theta^* dS = \int_{\Omega} f \Theta^* dV \quad (\text{E.3})$$

Integration on the surface  $\partial\Omega$  can be expressed as the sum of several terms:

$$\begin{aligned} \int_{\partial\Omega} \underline{q} \cdot \underline{n} \Theta^* dS &= \underbrace{\int_{\partial\Omega_T} -\lambda \underline{\text{grad}}(T) \cdot \underline{n} \Theta^* dS}_{\text{imposed temperature}} + \underbrace{\int_{\partial\Omega_C} h (T_{ec} - T) \Theta^* dS}_{\text{convection}} \\ &+ \underbrace{\int_{\partial\Omega_R} \epsilon \sigma (T_{er}^4 - T^4) \Theta^* dS}_{\text{radiation}} + \underbrace{\int_{\partial\Omega_Q} q_0 \Theta^* dS}_{\text{imposed flux}}. \end{aligned} \quad (\text{E.4})$$

The surface  $\partial\Omega_T$  corresponds to the boundary condition with imposed temperature  $T$ . The surface  $\partial\Omega_C$  corresponds to the boundary condition with heat convection with the external temperature  $T_{ec}$  and the heat exchange coefficient  $h$ . The surface  $\partial\Omega_R$  corresponds to the boundary condition with radiation with the external temperature  $T_{ec}$ , the emissivity coefficient  $\epsilon$  and the Stefan-Boltzman constant  $\sigma$ . The surface  $\partial\Omega_Q$  corresponds to the boundary condition with the imposed heat flux  $q_0$ . Also, the term  $(T_{er}^4 - T^4)$  can be written as:

$$T_{er}^4 - T^4 = (T_{er} - T) \underbrace{(T^3 + T^2 T_{er} + T T_{er}^2 + T_{er}^3)}_{\tilde{T}^3}. \quad (\text{E.5})$$

By choosing The expression of the integral on the surface E.4 becomes:

$$\int_{\partial\Omega} \underline{q} \cdot \underline{n} \Theta^* dS = \int_{\partial\Omega_C} h (T_{ec} - T) \Theta^* dS + \int_{\partial\Omega_R} \epsilon \sigma \tilde{T}^3 (T_{er} - T) \Theta^* dS + \int_{\partial\Omega_Q} q_0 \Theta^* dS. \quad (\text{E.6})$$

By employing Equation E.6 and Fourier's law in Equation E.4 the following expression is obtained:

$$\begin{aligned} \int_{\Omega} \rho c_p \frac{\partial T}{\partial t} \Theta^* dV + \int_{\Omega} \lambda \underline{\text{grad}}(T) \cdot \underline{\text{grad}}(\Theta^*) dV - \int_{\partial\Omega_C} h T \Theta^* dS - \int_{\partial\Omega_R} \epsilon \sigma \tilde{T}^3 T \Theta^* dS = \\ = \int_{\Omega} f \Theta^* dV - \int_{\partial\Omega_C} h T_{ec} \Theta^* dS - \int_{\partial\Omega_R} \epsilon \sigma \tilde{T}^3 T_{er} \Theta^* dS - \int_{\partial\Omega_Q} q_0 \Theta^* dS. \end{aligned} \quad (\text{E.7})$$

The spatial discretization allows to find unknowns at each spacial point by interpolation from the nodal values. The temperature  $T(\underline{u})$  and the function  $\Theta^*(\underline{u})$  at the spatial point  $\underline{u}$  of the finite element  $\Omega^e$  with  $N_e$  nodes can be interpolated from nodal values  $T_i$  and  $\Theta_j^*$ :

$$\begin{aligned} T(\underline{u}) &= \sum_{i=1}^{N_e} T_i N_i(\underline{u}) = T_i N_i(\underline{u}) \\ \Theta^*(\underline{u}) &= \sum_{j=1}^{N_e} \Theta_j^* N_j(\underline{u}) = \Theta_j^* N_j(\underline{u}) \end{aligned} \quad (\text{E.8})$$

where  $N_i(\underline{u})$  is the shape function associated to the node  $i$ . Equation E.7 with employed Equation E.8 becomes:

$$\begin{aligned} & \Theta_j^* \left( \left[ \int_{\Omega^e} \rho c_p N_i N_j dV \right] \frac{\partial T_i}{\partial t} + \right. \\ & \left. + \left[ \int_{\Omega^e} \lambda \underline{\text{grad}}(N_i) \cdot \underline{\text{grad}}(N_j) dV - \int_{\partial\Omega_C^e} h N_i N_j dS - \int_{\partial\Omega_R^e} \epsilon \sigma \tilde{T}^3 N_i N_j dS \right] T_i \right) = \quad (\text{E.9}) \\ & = \Theta_j^* \left[ \int_{\Omega^e} f N_j dV - \int_{\Omega_C^e} h T_{ec} N_j dS - \int_{\Omega_R^e} \epsilon \sigma \tilde{T}^3 T_{er} N_j dS - \int_{\Omega_Q^e} q_0 N_j dS \right] \end{aligned}$$

where  $\partial\Omega_C^e$ ,  $\partial\Omega_R^e$  and  $\partial\Omega_Q^e$  refer respectively to the surfaces of the element  $\Omega^e$  where the boundary conditions of convection, radiation and imposed flux are applied. The system of equations that needs to be solved for the element  $\Omega^e$  is as follows:

$$\underline{\underline{C}} \cdot \dot{\underline{T}} + \underline{\underline{K}} \cdot \underline{T} = \underline{Q}. \quad (\text{E.10})$$

with:

$\underline{T}$ -vector of temperatures at nodes

$\dot{\underline{T}}$ -vector of time derivatives of temperatures at nodes

$\underline{\underline{C}}$ -capacity matrix:

$$C_{ij} = \int_{\Omega^e} \rho c_p N_i N_j dV \quad (\text{E.11})$$

$\underline{\underline{K}}$ -conductivity matrix:

$$K_{ij} = \int_{\Omega^e} \lambda \underline{\text{grad}}(N_i) \cdot \underline{\text{grad}}(N_j) dV - \int_{\partial\Omega_C^e} h N_i N_j dS - \int_{\partial\Omega_R^e} \epsilon \sigma \tilde{T}^3 N_i N_j dS \quad (\text{E.12})$$

$\underline{Q}$ -vector of nodal flux:

$$Q_i = \int_{\Omega^e} f N_i dV - \int_{\partial\Omega_C^e} h T_{ec} N_i dS - \int_{\partial\Omega_R^e} \epsilon \sigma \tilde{T}^3 T_{er} N_i dS - \int_{\partial\Omega_Q^e} q_0 N_i dS. \quad (\text{E.13})$$

# Bibliography

- [1] <https://www.iaea.org/pris/>.
- [2] <http://web.archive.org/web/20080207010024/http://www.808multimedia.com/winnt/kernel.htm>.
- [3] D. Baron and L. Hallstadius, “2.19 - Fuel Performance of Light Water Reactors (Uranium Oxide and MOX),” in *Comprehensive Nuclear Materials* (R. J. Konings, ed.), pp. 481 – 514, Oxford: Elsevier, 2012.
- [4] <http://www.deltami.edu.pl>.
- [5] P. S. Sidky, “Iodine stress corrosion cracking of Zircaloy reactor cladding: iodine chemistry (a review),” *Journal of nuclear materials*, vol. 256, no. 1, pp. 1–17, 1998.
- [6] W. Martin, “Nuclear power,” *Britannica*, 2016.
- [7] C. Walker, V. Rondinella, D. Papaioannou, S. Van Winckel, W. Goll, and R. Manzel, “On the oxidation state of UO<sub>2</sub> nuclear fuel at a burn-up of around 100 MWd/kgHM,” *Journal of nuclear materials*, vol. 345, no. 2-3, pp. 192–205, 2005.
- [8] <https://www.oecd-nea.org/science/pubs/2006/nea6224-burn-up.pdf>.
- [9] K. Dayman, S. Biegalski, and D. Haas, “Determination of short-lived fission product yields with gamma spectrometry,” *Journal of Radioanalytical and Nuclear Chemistry*, vol. 305, pp. 213–223, Jul 2015.
- [10] [https://en.wikipedia.org/wiki/Fission\\_product\\_yield](https://en.wikipedia.org/wiki/Fission_product_yield).
- [11] R. W. Gauld, O. Hermann, “ORIGEN scale system module to calculate fuel depletion, actinide transmutation, fission product buildup and decay, and associated radiation terms,” tech. rep., Oak Ridge National Laboratory, ORNL/TM-2005/39, Version 6, Vol. II, Sect. F7, 2005.
- [12] M. Piro, J. Banfield, K. T. Clarno, S. Simunovic, T. M. Besmann, B. Lewis, and W. Thompson, “Coupled thermochemical, isotopic evolution and heat transfer simulations in highly irradiated UO<sub>2</sub> nuclear fuel,” *Journal of Nuclear Materials*, vol. 441, no. 1-3, pp. 240–251, 2013.

- [13] M. Vidal, R. Eschbach, A. Launay, C. Binet, and J.-F. Thro, “CESAR 5.3: An industrial tool for nuclear fuel and waste characterization with associated qualification,” in *Waste Management, Phoenix, Arizona, USA*, 2012.
- [14] B. Baurens, J. Sercombe, C. Riglet-Martial, L. Desgranges, L. Trotignon, and P. Maugis, “3D thermo-chemical-mechanical simulation of power ramps with ALCYONE fuel code,” *Journal of Nuclear Materials*, vol. 452, no. 1-3, pp. 578–594, 2014.
- [15] H. Bailly, D. Ménessier, and C. Prunier, “Le combustible nucléaire des réacteurs à eau sous pression et des réacteurs à neutrons rapides,” *Conception et comportement*, 1996.
- [16] L. Bray, L. Burger, L. Morgan, and D. Baldwin, “Thermal release of volatile fission products from irradiated nuclear fuel,” tech. rep., Pacific Northwest Lab., Richland, WA (USA), 1983.
- [17] <http://www.hhallberg.com/?feed=rss2&tag=grain-boundaries>.
- [18] P. Brohan, “Grain boundary swelling and gas release in UO<sub>2</sub>,” *ANS-2000 Meeting*, 2000.
- [19] B. Lewis, W. Thompson, and F. Iglesias, “2.20 - fission product chemistry in oxide fuels,” in *Comprehensive Nuclear Materials* (R. J. Konings, ed.), pp. 515 – 546, Oxford: Elsevier, 2012.
- [20] R. White, “Equi-axed and columnar grain growth in UO<sub>2</sub>,” *Water reactor fuel element modelling at high burnup and its experimental support*, p. 419, 1997.
- [21] J. Turnbull, C. Friskney, J. Findlay, F. Johnson, and A. Walter, “The diffusion coefficients of gaseous and volatile species during the irradiation of uranium dioxide,” *Journal of Nuclear Materials*, vol. 107, no. 2-3, pp. 168–184, 1982.
- [22] S. Cole, C. Delafoy, R. Graebert, P.-H. Louf, and N. Teboul, “AREVA optimized fuel rods for LWRs,” in *TopFuel, Manchester, UK*, 2012.
- [23] B. Cox, “Pellet-clad interaction (PCI) failures of zirconium alloy fuel cladding—a review,” *Journal of Nuclear Materials*, vol. 172, no. 3, pp. 249–292, 1990.
- [24] C. Mougel, B. Verhaeghe, C. Verdeau, S. Lansart, S. Beguin, and B. Julien, “Power ramping in the Osiris reactor: database analysis for standard UO<sub>2</sub> fuel with Zy-4 cladding,” in *Proc. Symp. on Pellet-clad Interaction in Water Reactor Fuels, Aix-en-Provence, France*, 2005.
- [25] “INZA-6 special report,” tech. rep., ANT International, 2006.
- [26] H. Rosenbaum, J. Davies, and J. Pon, “EURAEK report,” 1966.

- [27] H. Rosenbaum, “The interaction of iodine with Zircaloy-2,” *Electrochemical Technology (US) Absorbed by J. Electrochem. Soc.*, vol. 4, 1966.
- [28] S. Beguin, “PCI-related constraints on EDF PWRs and associated challenges,” in *Pellet-clad Interaction in Water Reactor Fuels, Aix-en-Provence, France*, 2004.
- [29] P. V. Uffelen and M. Suzuki, “3.19 - oxide fuel performance modeling and simulations,” in *Comprehensive Nuclear Materials* (R. J. Konings, ed.), pp. 535 – 577, Oxford: Elsevier, 2012.
- [30] B. Michel, J. Sercombe, C. Nonon, and O. Fandeur, “3.22 - Modeling of Pellet Cladding Interaction,” in *Comprehensive Nuclear Materials* (R. J. Konings, ed.), pp. 677 – 712, Oxford: Elsevier, 2012.
- [31] J. T. Goorley, M. R. James, T. E. Booth, F. B. Brown, J. S. Bull, L. J. Cox, J. W. Durkee Jr, J. S. Elson, M. L. Fensin, R. A. Forster III, *et al.*, “Initial MCNP6 release overview-MCNP6 version 1.0,” tech. rep., Los Alamos National Laboratory (LANL), 2013.
- [32] J. Leppänen, M. Pusa, T. Viitanen, V. Valtavirta, and T. Kaltiaisenaho, “The Serpent Monte Carlo code: Status, development and applications in 2013,” *Annals of Nuclear Energy*, vol. 82, pp. 142–150, 2015.
- [33] H. Golfier, R. Lenain, C. Calvin, J.-J. Lautard, A.-M. Baudron, P. Fougeras, P. Magat, E. Martinolli, and Y. Dutheillet in *Int. Conf. on Mathematics, Computational Methods and Reactor Physics*, 2009.
- [34] V. Marelle, “Validation of PLEIADES/ALCYONE 2.0 fuel performance code,” in *Water Reactor Fuel Performance Meeting, Jeju Island, Korea*, 2017.
- [35] P. J. Palmer, K. Hesketh, “A model for predicting the radial power profile in a fuel pin,” in *IAEA Specialists’ Meeting on Water Reactor Fuel Element Performance*, 1992.
- [36] K. Lassmann, C. Ronchi, and G. Small, “The development of fuel performance models at the european institute for transuranium elements,” *Journal of Nuclear Materials*, vol. 166, no. 1, pp. 112 – 119, 1989.
- [37] L. Noirot, “MARGARET: A comprehensive code for the description of fission gas behavior,” *Nuclear Engineering and Design*, vol. 241, no. 6, pp. 2099–2118, 2011.
- [38] J. Sercombe, I. Aubrun, and C. Nonon, “Power ramped cladding stresses and strains in 3D simulations with burnup-dependent pellet–clad friction,” *Nuclear Engineering and Design*, vol. 242, pp. 164–181, 2012.
- [39] J. Sercombe, M. Agard, C. Struzik, B. Michel, G. Thouvenin, C. Poussard, and K. Kallstrom, “1D and 3D analyses of the Zy2 SCIP BWR ramp tests with the fuel

- codes METEOR and ALCYONE,” *Nuclear Engineering and Technology*, vol. 41, no. 2, pp. 187–198, 2009.
- [40] C. Guéneau, M. Baichi, D. Labroche, C. Chatillon, and B. Sundman, “Thermodynamic assessment of the uranium–oxygen system,” *Journal of Nuclear Materials*, vol. 304, no. 2, pp. 161 – 175, 2002.
- [41] H. Kleykamp, “The solubility of selected fission products in  $\text{UO}_2$  and  $(\text{U}, \text{Pu})\text{O}_2$ ,” *Journal of Nuclear Materials*, vol. 206, no. 1, pp. 82–86, 1993.
- [42] H. Haug and F. Weigel, “Mischoxidsysteme von lanthaniden- und actinidenelementen: I. röntgen-untersuchungen im system uranoxid-europiumoxid,” *Journal of Nuclear Materials*, vol. 9, no. 3, pp. 355 – 359, 1963.
- [43] T. Fujino, “Thermodynamics of fluorite type solid solutions containing plutonium, lanthanide elements or alkaline earth metals in uranium dioxide host lattices,” *Journal of Nuclear Materials*, vol. 154, no. 1, pp. 14 – 24, 1988.
- [44] D. Carroll, “The system  $\text{PuO}_2\text{-ZrO}_2$ ,” *Journal of the American Ceramic Society*, vol. 46, no. 4, pp. 194–195, 1963.
- [45] K. Une and M. Oguma, “Oxygen potential of  $\text{U}_{0.85}\text{Zr}_{0.15}\text{O}_{2+x}$  solid solutions at 1500 °C,” *Journal of the American Ceramic Society*, vol. 66, no. 10, pp. 179–180.
- [46] K. Romberger, C. Baes, and H. Stone, “Phase equilibrium studies in the  $\text{UO}_2\text{-ZrO}_2$  system,” *Journal of Inorganic and Nuclear Chemistry*, vol. 29, no. 7, pp. 1619 – 1630, 1967.
- [47] F. Schleifer, A. Naoumidis, and H. Nickel, “Thermodynamics on  $\text{UO}_2\text{-ZrO}_2\text{-LnO}_{2-x}$  solid solutions,” *Journal of Nuclear Materials*, vol. 115, no. 2, pp. 143 – 158, 1983.
- [48] H. Kleykamp, “The chemical state of the fission products in oxide fuels,” *Journal of Nuclear Materials*, vol. 131, no. 2-3, pp. 221–246, 1985.
- [49] Y. Guerin, J. Noirot, and D. Parrat, “Nuclear fuels for light water reactors and fast reactors,” *International school in nuclear engineering*, CEA Cadarache, 2017.
- [50] L. Desgranges, J. Lamontagne, C. Riglet-Martial, and T. Blay, “Experimental evidence of the formation of a new chemical phase in a power ramped  $\text{UO}_2$  nuclear fuel,” *Journal of Nuclear Materials*, vol. 457, pp. 246 – 251, 2015.
- [51] H. Kleykamp, “The chemical state of LWR high-power rods under irradiation,” *Journal of Nuclear Materials*, vol. 84, no. 1, pp. 109 – 117, 1979.
- [52] C. Riglet-Martial, J. Sercombe, J. Lamontagne, J. Noirot, I. Roure, T. Blay, and L. Desgranges, “Experimental evidence of oxygen thermo-migration in PWR  $\text{UO}_2$  fuels during power ramps using in-situ oxido-reduction indicators,” *Journal of Nuclear Materials*, vol. 480, pp. 32–39, 2016.

- [53] C. Riglet-Martial, P. Martin, D. Testemale, C. Sabathier-Devals, G. Carlot, P. Matheron, X. Iltis, U. Pasquet, C. Valot, C. Delafoy, *et al.*, “Thermodynamics of chromium in  $\text{UO}_2$  fuel: A solubility model,” *Journal of Nuclear Materials*, vol. 447, no. 1-3, pp. 63–72, 2014.
- [54] L. Bourgeois. PhD thesis, Institut National Polytechnique de Grenoble, 1992.
- [55] A. Leenaers, L. De Tollenaere, C. Delafoy, and S. Van den Berghe, “On the solubility of chromium sesquioxide in uranium dioxide fuel,” *Journal of nuclear materials*, vol. 317, no. 1, pp. 62–68, 2003.
- [56] L. Desgranges, T. Blay, J. Lamontagne, I. Roure, and P. Bienvenu, “Fission products behaviour during a power transient: Their inventory in an intragranular bubble,” *Journal of Nuclear Materials*, vol. 493, pp. 225 – 229, 2017.
- [57] C. Ciszak, M. Mermoux, S. Miro, G. Gutierrez, F. Lepretre, I. Popa, K. Hanifi, I. Zacharie-Aubrun, L. Fayette, and S. Chevalier, “Micro-Raman analysis of the fuel-cladding interface in a high burnup PWR fuel rod,” *Journal of Nuclear Materials*, vol. 495, pp. 392 – 404, 2017.
- [58] L. Desgranges, “Internal corrosion layer in PWR fuel,” *Thermal Performance of High Burn-Up LWR Fuel*, p. 187, 1998.
- [59] J. Minne, *Contribution a la modelisation du couplage mecanique/chimique de l'evolution de l'interface pastille-gaine sous irradiation*. PhD thesis, Université de Bourgogne, 2009.
- [60] J. Lamontagne, C. Eysseric, L. Desgranges, C. Valot, J. Noirot, T. Blay, I. Roure, and B. Pasquet, “Study of structural material resulting from the nuclear fuel cycle using SEM-WDX, EPMA and SIMS techniques,” *Microchimica Acta*, vol. 161, pp. 355–362, 06 2008.
- [61] L. Desgranges, C. Riglet-Martial, I. Aubrun, B. Pasquet, I. Roure, J. Lamontagne, and T. Blay, “Evidence of tellurium iodide compounds in a power-ramped irradiated  $\text{UO}_2$  fuel rod,” *Journal of Nuclear Materials*, vol. 437, no. 1-3, pp. 409–414, 2013.
- [62] B. Baurens, *Couplages thermo-chimie-mécaniques dans le dioxyde d'uranium : application à l'interaction pastille-gaine*. PhD thesis, Université Aix-Marseille, 2014.
- [63] J. Gittus, J. Matthews, and P. Potter, “Safety aspects of fuel behaviour during faults and accidents in pressurised water reactors and in liquid sodium cooled fast breeder reactors,” *Journal of Nuclear Materials*, vol. 166, no. 1-2, pp. 132–159, 1989.

- [64] K. Une and M. Oguma, "Oxygen potentials of  $\text{UO}_2$  fuel simulating high burnup," *Journal of Nuclear Science and Technology*, vol. 20, no. 10, pp. 844–851, 1983.
- [65] K. Une, Y. Tominaga, and S. Kashibe, "Oxygen potentials and lattice parameter of irradiated BWR fuel," *Journal of Nuclear Science and Technology*, vol. 28, no. 5, pp. 409–417, 1991.
- [66] H. Matzke, "Oxygen potential in the rim region of high burnup  $\text{UO}_2$  fuel," *Journal of nuclear materials*, vol. 208, no. 1-2, pp. 18–26, 1994.
- [67] H. Matzke, "Oxygen potential measurements in high burnup LWR  $\text{UO}_2$  fuel," *Journal of Nuclear Materials*, vol. 223, no. 1, pp. 1 – 5, 1995. Thermodynamics of Nuclear Materials.
- [68] C. Ciszak, *Etude de l'accrochage pastille/gaine des crayons combustibles des reacteurs a eau pressurisee*. PhD thesis, Université de Bourgogne-Franche-Comté, 2017.
- [69] C. Walker, T. Kameyama, S. Kitajima, and M. Kinoshita, "Concerning the microstructure changes that occur at the surface of  $\text{UO}_2$  pellets on irradiation to high burnup," *Journal of Nuclear Materials*, vol. 188, pp. 73 – 79, 1992.
- [70] T. Kameyama, T. Matsumura, and M. Kinoshita in *Proc. Int. Topical Mtg. on LWR Fuel Performance, Fuel for the 90's, Avignon, France*, 1991.
- [71] E. Corcoran, *Thermochemical modelling of advanced CANDU reactor fuel*. PhD thesis, Royal Military College of Canada, 2009.
- [72] H. Loukusa, T. Ikonen, V. Valtavirta, and V. Tulkki, "Thermochemical modeling of nuclear fuel and the effects of oxygen potential buffers," *Journal of Nuclear Materials*, vol. 481, pp. 101–110, 2016.
- [73] M. Adamson, F. Aitken, S. Evans, and J. Davies, "Oxygen redistribution and its measurement in irradiated oxide fuels," in *Proc. IAEA Symp. on thermodynamics of irradiated materials, IAEA-SM-190/54*, 1975.
- [74] C. W. Bale, P. Chartrand, S. Degterov, G. Eriksson, K. Hack, R. B. Mahfoud, J. Melançon, A. Pelton, and S. Petersen, "Factsage thermochemical software and databases," *Calphad*, vol. 26, no. 2, pp. 189–228, 2002.
- [75] C. Bale, E. Bélisle, P. Chartrand, S. Deckerov, G. Eriksson, K. Hack, I.-H. Jung, Y.-B. Kang, J. Melançon, A. Pelton, C. Robelin, and S. Petersen, "Factsage thermochemical software and databases — recent developments," *Calphad*, vol. 33, no. 2, pp. 295 – 311, 2009. Tools for Computational Thermodynamics.
- [76] K. Maeda, K. Tanaka, T. Asaga, and H. Furuya, "Distributions of volatile fission products in or near the fuel-cladding gap of the FBR MOX fuel pins irradiated to

- high burn-up,” *Journal of Nuclear Materials*, vol. 344, no. 1, pp. 274 – 280, 2005. Proceedings of the 11th International Symposium on Thermodynamics of Nuclear Materials.
- [77] T. M. Besmann, J. W. McMurray, and S. Simunovic, “Application of thermochemical modeling to assessment/evaluation of nuclear fuel behavior,” *Calphad*, vol. 55, pp. 47 – 51, 2016. Christopher W. Bale Symposium - Thermodynamic Applications, Optimizations and Simulations in High Temperature Processes.
- [78] M. Bober and G. Schumacher, “Material transport in the temperature gradient of fast reactor fuels,” in *Advances in Nuclear Science and Technology, Volume 7*, pp. 121–179, Elsevier, 1973.
- [79] M. Welland, “3.21 - matter transport in fast reactor fuels,” in *Comprehensive Nuclear Materials* (R. J. Konings, ed.), pp. 629 – 676, Oxford: Elsevier, 2012.
- [80] V. Ozrin, “A model for evolution of oxygen potential and stoichiometry deviation in irradiated  $\text{UO}_2$  fuel,” *Journal of Nuclear Materials*, vol. 419, no. 1, pp. 371 – 377, 2011.
- [81] J. Ramirez, M. Stan, and P. Cristea, “Simulations of heat and oxygen diffusion in  $\text{UO}_2$  nuclear fuel rods,” *Journal of Nuclear Materials*, vol. 359, no. 3, pp. 174–184, 2006.
- [82] B. Mihaila, M. Stan, J. Ramirez, A. Zubelewicz, and P. Cristea, “Simulations of coupled heat transport, oxygen diffusion, and thermal expansion in  $\text{UO}_2$  nuclear fuel elements,” *Journal of Nuclear Materials*, vol. 394, no. 2-3, pp. 182–189, 2009.
- [83] B. Mihaila, M. Stan, J. Crapps, and D. Yun, “Impact of thermal conductivity models on the coupling of heat transport, oxygen diffusion, and deformation in  $(\text{U, Pu})\text{O}_{2-x}$  nuclear fuel elements,” *Journal of Nuclear Materials*, vol. 433, no. 1-3, pp. 132–142, 2013.
- [84] J. Higgs, B. Lewis, W. Thompson, and Z. He, “A conceptual model for the fuel oxidation of defective fuel,” *Journal of Nuclear Materials*, vol. 366, no. 1-2, pp. 99–128, 2007.
- [85] M. Welland, W. Thompson, B. Lewis, and D. Manara, “Computer simulations of non-congruent melting of hyperstoichiometric uranium dioxide,” *Journal of Nuclear Materials*, vol. 385, no. 2, pp. 358–363, 2009.
- [86] K. Lassmann, “The oxired model for redistribution of oxygen in nonstoichiometric uranium-plutonium oxides,” *Journal of Nuclear Materials*, vol. 150, no. 1, pp. 10 – 16, 1987.
- [87] H. Matzke, “Diffusion processes and surface effects in non-stoichiometric nuclear fuel oxides  $\text{UO}_{2+x}$  and  $(\text{U, Pu})\text{O}_{2\pm x}$ ,” *Journal of Nuclear Materials*, vol. 114, no. 2, pp. 121 – 135, 1983.

- [88] W. Breitung, “Oxygen self and chemical diffusion coefficients in  $\text{UO}_{2\pm x}$ ,” *Journal of Nuclear Materials*, vol. 74, no. 1, pp. 10–18, 1978.
- [89] E. Moore, C. Guéneau, and J.-P. Crocombette, “Diffusion model of the non-stoichiometric uranium dioxide,” *Journal of Solid State Chemistry*, vol. 203, pp. 145–153, 2013.
- [90] S. A. Rice, “Dynamical theory of diffusion in crystals,” *Physical Review*, vol. 112, no. 3, p. 804, 1958.
- [91] C. Berthier, C. Rado, C. Chatillon, and F. Hodaj, “Thermodynamic assessment of oxygen diffusion in non-stoichiometric  $\text{UO}_{2\pm x}$  from experimental data and frenkel pair modeling,” *Journal of Nuclear Materials*, vol. 433, no. 1-3, pp. 265–286, 2013.
- [92] A. Auskern and J. Belle, “Self-diffusion of oxygen in uranium dioxide,” *The Journal of Chemical Physics*, vol. 28, no. 1, pp. 171–172, 1958.
- [93] A. Auskern and J. Belle, “Oxygen ion self-diffusion in uranium dioxide,” *Journal of Nuclear Materials*, vol. 3, no. 3, pp. 267–276, 1961.
- [94] K. Kim and D. Olander, “Oxygen diffusion in  $\text{UO}_{2-x}$ ,” *Journal of Nuclear Materials*, vol. 102, no. 1-2, pp. 192–199, 1981.
- [95] J. Andersson and J. Ågren, “Models for numerical treatment of multicomponent diffusion in simple phases,” *Journal of Applied Physics*, vol. 72, no. 4, pp. 1350–1355, 1992.
- [96] P. Contamin, J. Bacmann, and J. Marin, “Autodiffusion de l’oxygene dans le dioxyde d’uranium surstoichiometrique,” *Journal of Nuclear Materials*, vol. 42, no. 1, pp. 54 – 64, 1972.
- [97] J. Pelleg, *Diffusion in Ceramics*. Springer, 2016.
- [98] P. Blackburn tech. rep., Argonne National Laboratory, Report ANL-RDP-35, 1974.
- [99] M. De Franco, J. Gatesoupe, H. Blank, and R. Lindner, “Plutonium 1975 and other actinides,” *Blank, H*, p. 133, 1976.
- [100] <https://www.oecd-nea.org/science/taf-id/>.
- [101] A. S. Bayoglu. PhD thesis, Orsay, 1981.
- [102] P. Ruello, G. Chirlesan, G. Petot-Ervas, C. Petot, and L. Desgranges, “Chemical diffusion in uranium dioxide—influence of defect interactions,” *Journal of Nuclear Materials*, vol. 325, no. 2, pp. 202 – 209, 2004.

- [103] J. T. Bittel, L. H. Sjudahl, and J. F. White, "Steam oxidation kinetics and oxygen diffusion in  $\text{UO}_2$  at high temperatures," *Journal of the American Ceramic Society*, vol. 52, no. 8, pp. 446–451.
- [104] A. Taskinen and H. Kuliberg, "Oxygen chemical diffusion coefficient in hyperstoichiometric uranium dioxide," *Journal of Nuclear Materials*, vol. 83, no. 2, pp. 333 – 334, 1979.
- [105] K. W. LAY, "Oxygen chemical diffusion coefficient of uranium dioxide," *Journal of the American Ceramic Society*, vol. 53, no. 7, pp. 369–373.
- [106] C. Sari and G. Schumacher, "Oxygen redistribution in fast reactor oxide fuel," *Journal of Nuclear Materials*, vol. 61, no. 2, pp. 192–202, 1976.
- [107] S. Evans, E. Aitken, and C. Craig, "Effect of a temperature gradient on the stoichiometry of urania-plutonia fuel," *Journal of Nuclear Materials*, vol. 30, no. 1-2, pp. 57–61, 1969.
- [108] J. Janek and H. Timm, "Thermal diffusion and soret effect in  $(\text{U, Me})\text{O}_{2+\delta}$ : the heat of transport of oxygen," *Journal of Nuclear Materials*, vol. 255, no. 2-3, pp. 116–127, 1998.
- [109] S. Evans, E. Aitken, and C. Craig, "Effect of a temperature gradient on the stoichiometry of urania-plutonia fuel," *Journal of Nuclear Materials*, vol. 30, no. 1, pp. 57 – 61, 1969.
- [110] S. H. Shann and D. Olander, "Stress corrosion cracking of zircaloy by cadmium, iodine, and metal iodides," *Journal of Nuclear Materials*, vol. 113, no. 2-3, pp. 234–248, 1983.
- [111] M. Gartner and J. La Vake, "Power ramp testing and non-destructive post-irradiation examinations of high burnup PWR fuel rods," in *Proceedings of the IAEA Meeting on Pellet-Cladding Interaction in Water Reactor Fuel, Seattle*, 1983.
- [112] M. H. Piro, D. Sunderland, S. Livingstone, J. Sercombe, W. Revie, A. Quastel, K. Terrani, and C. Judge, "A Review of Pellet–Clad Interaction Behavior in Zirconium Alloy Fuel Cladding," in *Reference Module in Materials Science and Materials Engineering*, Elsevier, 2017.
- [113] A. Miller, H. Ocken, and A. Tasooji, "Iodine stress corrosion cracking of zircaloy: Laboratory data, a phenomenological model, and predictions of in-reactor behavior," *Journal of Nuclear Materials*, vol. 99, no. 2-3, pp. 254–268, 1981.
- [114] D. Le Boulch, L. Fournier, and C. Sainte-Catherine, "PCI behaviour of chromium oxide-doped fuel," in *Proc. Symp. on Pellet-clad Interaction in Water Reactor Fuels, Aix-en-Provence, France*, 2004.

- [115] B. Lewis, W. Thompson, M. Kleczek, K. Shaheen, M. Juhas, and F. Iglesias, “Modelling of iodine-induced stress corrosion cracking in CANDU fuel,” *Journal of Nuclear Materials*, vol. 408, no. 3, pp. 209 – 223, 2011.
- [116] D. Cubicciotti, R. L. Jones, and B. C. Syrett tech. rep., EPRI-NP-1329, EPRI, Palo Alto, CA, 1980.
- [117] H. S. M. Peehs, E. Steinberg in *IAEA Meeting on Pellet-Cladding Interaction in Water Reactors, Denmark*, 1980.
- [118] B. Normand, N. Pebere, C. Richard, and M. Wery, . *Prévention et lutte contre la corrosion: une approche scientifique et technique*, vol. PPUR Collection – Sciences appliquées INSA Lyon. 2004.
- [119] T.-T. Yang and C.-H. Tsai, “On the susceptibility to stress corrosion cracking of Zircaloy in an iodine containing environment,” *Journal of Nuclear Materials*, vol. 166, no. 3, pp. 252 – 264, 1989.
- [120] J. Wood, B. Surette, I. Aitchison, and W. Clendening, “Pellet cladding interaction—evaluation of lubrication by graphite,” *Journal of Nuclear Materials*, vol. 88, no. 1, pp. 81–94, 1980.
- [121] A. Garlick in *Proc. BNES Conf. on Effects of Environment on Materials Properties in Nuclear Systems*, 1971.
- [122] K. Videm, L. Lunde, T. Hollowell, K. Vilpponen, and C. Vitanza, “Cracking of cladding tubes caused by power ramping and by laboratory stress corrosion experiments,” *Journal of Nuclear Materials*, vol. 87, no. 2-3, pp. 259–267, 1979.
- [123] G. Roberts, “An analysis of the permissible upratings in water reactor systems,” tech. rep., Central Electricity Generating Board, UK, Report RD/B/N4379, 1979.
- [124] D. Hardy, J. Wood, and A. Bain in *Proc. 18th Annual. Conf. CNA, Ottawa*, 1978.
- [125] A. Tasooji, R. E. Einziger, and A. K. Miller in *Sixth International Symposium, ASTM STP 824, American Society of Testing and Materials*, 1984.
- [126] C. C. Busby, R. Tucker, and J. McCauley, “Halogen stress corrosion cracking of zircaloy-4 tubing,” *Journal of Nuclear Materials*, vol. 55, no. 1, pp. 64–82, 1975.
- [127] C. Anghel, A.-M. Holston, G. Lysell, S. Karlsson, R. Jakobsson, E. Sund, and S. T. Mahmood, “Experimental and finite element modeling parametric study for iodine-induced stress corrosion cracking of irradiated cladding,” *TopFuel conference, Paris, France*, 2010.
- [128] C. Anghel, A.-M. Holston, G. Lysell, S. Karlsson, R. Jakobsson, J. Flygare, S. Mahmood, D. Le Boulch, and I. Arimescu, “Experimental and finite element modeling parametric study for iodine-induced stress corrosion cracking of irradiated cladding,” *TopFuel conference, Orlando, US*, 2010.

- [129] M. Peehs and G. Kaspar, "Experimental investigations of caesium and iodine release from irradiated  $\text{UO}_2$ ," *High Temperatures-High Pressures*, vol. 14, no. 5, pp. 517–522, 1982.
- [130] W. Burns, E. Cordfunke, P. Johnson, P. Potter, G. Prins, and M. Rand, "Fuel rod internal chemistry and fission product behaviour," *IAEA, Vienna*, pp. 35–42, 1986.
- [131] R. Ball, W. Burns, J. Henshaw, M. Mignanelli, and P. Potter, "The chemical constitution of the fuel-clad gap in oxide fuel pins for nuclear reactors," *Journal of Nuclear Materials*, vol. 167, pp. 191 – 204, 1989.
- [132] K. Konashi, K. Kamimura, and Y. Yokouchi, "Estimation of irradiation induced iodine pressure in an LWR fuel rod," *Journal of Nuclear Materials*, vol. 125, pp. 244–247, 1984.
- [133] K. Konashi, Y. Shiokawa, and H. Kayano, "Simulation of CsI decomposition in fuel cladding gap," *Journal of nuclear materials*, vol. 232, no. 2-3, pp. 181–185, 1996.
- [134] J. Sercombe, C. Riglet-Martial, and B. Baurens, "Simulations of power ramps with ALCYONE including fission products chemistry and oxygen thermo-diffusion," in *Proceedings of the workshop PCI in Water-Cooled Reactors, Lucca, IT*, 2016.
- [135] CAST3M. <http://www-cast3m.cea.fr/>.
- [136] COMSOL Multiphysics®, COMSOL AB, Stockholm, Sweden. [www.comsol.com](http://www.comsol.com).
- [137] B. Lewis, C. Hunt, and F. Iglesias, "Source term of iodine and noble gas fission products in the fuel-to-sheath gap of intact operating nuclear fuel elements," *Journal of Nuclear Materials*, vol. 172, no. 2, pp. 197 – 205, 1990.
- [138] B. Lewis, A. El-Jaby, J. Higgs, W. Thompson, F. Iglesias, R. Laidler, J. Armstrong, R. Stone, and R. Oduntan, "A model for predicting coolant activity behaviour for fuel-failure monitoring analysis," *Journal of Nuclear Materials*, vol. 366, no. 1, pp. 37 – 51, 2007.
- [139] A. Booth, "A suggested method for calculating the diffusion of radioactive rare gas fission products from  $\text{UO}_2$  fuel elements and a discussion of proposed in-reactor experiments that may be used to test its validity,"
- [140] S. Chapman, T. Cowling, D. Burnett, and C. Cercignani, *The Mathematical Theory of Non-uniform Gases: An Account of the Kinetic Theory of Viscosity, Thermal Conduction and Diffusion in Gases*. Cambridge Mathematical Library, Cambridge University Press, 1990.
- [141] L. O. Jernkvist, "A model for predicting pellet-cladding interaction-induced fuel rod failure," *Nuclear Engineering and Design*, vol. 156, no. 3, pp. 393 – 399, 1995.

- [142] A. Prudil, B. Lewis, P. Chan, and J. Baschuk, “Development and testing of the FAST fuel performance code: Normal operating conditions (Part 1),” *Nuclear Engineering and Design*, vol. 282, pp. 158 – 168, 2015.
- [143] A. Prudil, B. Lewis, P. Chan, J. Baschuk, and D. Wowk, “Development and testing of the FAST fuel performance code: Transient conditions (Part 2),” *Nuclear Engineering and Design*, vol. 282, pp. 169 – 177, 2015.
- [144] A. Oussoren, *Towards a mechanistic model for stress corrosion cracking in nuclear fuel elements*. PhD thesis, Royal Military College of Canada, 2015.
- [145] G. Eriksson, “Thermodynamic studies of high-temperature equilibria. 12. SOLGASMIX, a computer-program for calculation of equilibrium compositions in multiphase systems,” *Chemica Scripta*, vol. 8, no. 3, pp. 100–103, 1975.
- [146] J.-O. Andersson, T. Helander, L. Höglund, P. Shi, and B. Sundman, “ThermoCalc & DICTRA, computational tools for materials science,” *Calphad*, vol. 26, no. 2, pp. 273 – 312, 2002.
- [147] M. Piro, *Computation of Thermodynamic Equilibria Pertinent to Nuclear Materials in Multi-Physics Codes*. PhD thesis, Royal Military College of Canada, 2011.
- [148] H. Loukusa, “Computation module for the calculation of thermochemical equilibria in nuclear fuel,” Master’s thesis, 2014.
- [149] W. Thompson, B. Lewis, E. Corcoran, M. Kaye, S. White, F. Akbari, Z. He, R. Verrall, J. Higgs, D. Thompson, *et al.*, “Thermodynamic treatment of uranium dioxide based nuclear fuel,” *International Journal of Materials Research*, vol. 98, no. 10, pp. 1004–1011, 2007.
- [150] P. Garcia, J. P. Piron, and D. Baron, “A model for the oxygen potential of oxide fuels at high burnup,” in *Proc. Symp. on Water reactor fuel element modelling at high burnup and its Experimental Support*, Windermere, UK, 1994.
- [151] J.-C. Dumas, *Etude des conditions de formation du joint oxyde-gaine dans les combustibles des réacteurs à neutrons rapides : observations et proposition d’un modèle de comportement des produits de fission volatils*. PhD thesis, Institut National Polytechnique, Grenoble, France, 1995.
- [152] C. Introini, “Title to add, in preparation,” *Journal of Nuclear Materials*, 2018.
- [153] M. S. Veshchunov, V. D. Ozrin, V. E. Shestak, V. I. Tarasov, R. Dubourg, and G. Nicaise, “Development of the mechanistic code MFPR for modelling fission-product release from irradiated UO<sub>2</sub> fuel,” *Nuclear Engineering and Design*, vol. 236, no. 2, pp. 179–200, 2006.

- [154] M. Veshchunov, A. Boldyrev, V. Ozrin, V. Shestak, and V. Tarasov, “A new mechanistic code SFPR for modeling of single fuel rod performance under various regimes of LWR operation,” *Nuclear Engineering and Design*, vol. 241, no. 8, pp. 2822 – 2830, 2011.
- [155] K. Geelhood and W. Luscher, “FRAPCON-4.0: Integral assessment,” *Pacific Northwest National Laboratory, PNNL-19418*, vol. 2, 2015.
- [156] T. M. Besmann, J. W. McMurray, B. G. Gaston, S. Simunovic, and M. A. Piro, “Modeling thermochemistry of fuel and coupling to fuel performance codes,” in *Top Fuel conference, Boise, Idaho, USA*, 2016.
- [157] S. Simunovic, J. McMurray, T. Besmann, E. Moore, and M. Piro, “Coupled mass and heat transport models for nuclear fuels using thermodynamic calculations,” tech. rep., Oak Ridge National Laboratory, ORNL/TM-2018/2, 2017.
- [158] E. Moore, C. Guéneau, and J.-P. Crocombette, “Oxygen diffusion model of the mixed (U, Pu)O<sub>2±x</sub>: Assessment and application,” *Journal of Nuclear Materials*, vol. 485, pp. 216–230, 2017.
- [159] OCDE/NEA, “JANIS 4.0 Java-based Nuclear Data Information System.” <https://www.oecd-nea.org/janis/>.
- [160] A. Santamarina, D. Bernard, P. Blaise, P. Leconte, R. Le Tellier, C. Vaglio-Gaudard, and J.-F. Vidal, “APOLLO 2.8: a validated code package for PWR neutronics calculations,” in *4th Topical Meeting on Advances in Nuclear Fuel Management*, vol. 2, 2009.
- [161] K. Lassmann, C. O’Carroll, J. van de Laar, and C. Walker, “The radial distribution of plutonium in high burnup UO<sub>2</sub> fuels,” *Journal of Nuclear Materials*, vol. 208, no. 3, pp. 223 – 231, 1994.
- [162] T. W. May and R. H. Wiedmeyer, “A table of polyatomic interferences in icp-ms,” 1998.
- [163] G. Eriksson, “Thermodynamic studies of high temperature equilibria. SOLGAS, a computer program for calculating the composition and heat condition of an equilibrium mixture,” *Acta Chemica Scandinavica*, vol. 25, pp. 2651 – 2658, 1971.
- [164] T. N. PHAM THI, *Caractérisation et modélisation du comportement thermodynamique du combustible RNR-Na sous irradiation*. PhD thesis, Université Aix-Marseille, 2014.
- [165] M. Yamawaki, Y. Nagai, T. Kogai, and M. Kanno, “Thermodynamic studies on molybdenum/noble-metal alloys,” in *Advances in Nuclear Science and Technology, Volume 7*, pp. 249–261, International Atomic Energy Agency, 1980.

- [166] T. B. Lindemer and T. M. Besmann, "Chemical thermodynamic representation of  $\text{UO}_{2\pm x}$ ," *Journal of Nuclear Materials*, vol. 130, pp. 473 – 488, 1985.
- [167] B. Lindemer and J. Brynstad, "Review and chemical thermodynamic representation of  $\text{U}_{1-z}\text{Ce}_z\text{O}_{2\pm x}$  and  $\text{U}_{1-z}\text{Ln}_z\text{O}_{2\pm x}$ ; Ln = Y, La, Nd, Gd," *Journal of the American Ceramic Society*, vol. 69, no. 12, pp. 867–876, 1986.
- [168] R. Woodley, "Oxygen potentials of plutonia and urania-plutonia solid solutions," *Journal of Nuclear Materials*, vol. 96, no. 1, pp. 5 – 14, 1981.
- [169] T. L. Markin and E. J. Mc Iver, *Plutonium 1965*. Chapman and Hall, London, 1979.
- [170] "Oxygen potential and thermal conductivity of (U,Pu) mixed oxides," *Journal of Nuclear Materials*, vol. 348, no. 3, pp. 329 – 334, 2006.
- [171] T. B. Lindemer and A. L. Sutton Jr, "Study of nonstoichiometry of solid  $\text{U}_{1-z}\text{Gd}_z\text{O}_{2\pm x}$ ," *Journal of the American Ceramic Society*, vol. 71, no. 7, pp. 553–561, 1988.
- [172] K. Une and M. Oguma, "Oxygen potentials of (U, Gd) $\text{O}_{2\pm x}$  solid solutions in the temperature range 1000-1500 °C," *Journal of Nuclear Materials*, vol. 115, no. 1, pp. 84–90, 1983.
- [173] J. H. Yang, K. S. Kim, K. W. Kang, K. W. Song, and Y. H. Jung, "Electrical conductivity and non-stoichiometry in the (U,Gd) $\text{O}_{2\pm x}$  system," *Journal of Nuclear Materials*, vol. 340, no. 2, pp. 171 – 178, 2005.
- [174] K. Hagemark and M. Broli, "Equilibrium oxygen pressures over solid solutions of urania-yttria and urania-lanthana at 1100 to 1400 °C," *Journal of the American Ceramic Society*, vol. 50, no. 11, pp. 563–567.
- [175] E. Stadlbauer, U. Wichmann, U. Lott, and C. Keller, "Thermodynamics and phase relationships of the ternary lanthanum-uranium-oxygen system," *Journal of Solid State Chemistry*, vol. 10, no. 4, pp. 341 – 350, 1974.
- [176] K. Yoshida, T. Arima, Y. Inagaki, K. Idemitsu, M. Osaka, and S. Miwa, "Oxygen potential of hypo-stoichiometric La-doped  $\text{UO}_2$ ," *Journal of Nuclear Materials*, vol. 418, no. 1, pp. 22 – 26, 2011.
- [177] J. McMurray, S. Hirooka, T. Murakami, K. Suzuki, J. White, S. Voit, A. Nelson, B. Slone, T. Besmann, K. McClellan, and M. Kato, "Thermodynamic assessment of the oxygen rich U–Ce–O system," *Journal of Nuclear Materials*, vol. 467, pp. 588 – 600, 2015.
- [178] R. Ducroux and P. Baptiste, "Mesure du potentiel d'oxygène dans le système  $\text{U}_{0.7}\text{C}_{0.3}\text{O}_{2\pm x}$  à l'aide d'une minisonde à électrolyte solide," *Journal of Nuclear Materials*, vol. 97, no. 3, pp. 333 – 336, 1981.

- [179] D. Norris and P. Kay, "Oxygen potential and lattice parameter measurements in (U, Ce)O<sub>2-x</sub>," *Journal of Nuclear Materials*, vol. 116, no. 2, pp. 184 – 194, 1983.
- [180] L. Bourgeois tech. rep., CEA, Report CEA-R-5621, 1993.
- [181] D. R. Olander, "Fundamental aspects of nuclear reactor fuel elements," tech. rep., California Univ., Berkeley (USA). Dept. of Nuclear Engineering, 1976.
- [182] S. R. Dharwadkar, "Standard free energy of formation of umoo6 by thermogravimetry," *Journal of Materials Science Letters*, vol. 5, pp. 1003–1006, Oct 1986.
- [183] R. Courant, K. Friedrichs, and H. Lewy, "Über die partiellen Differenzgleichungen der mathematischen Physik," *Mathematische Annalen*, vol. 100, pp. 32–74, 1928.
- [184] A. Iserles, *A First Course in the Numerical Analysis of Differential Equations*. New York, NY, USA: Cambridge University Press, 2nd ed., 2008.
- [185] J. Fink, "Thermophysical properties of uranium dioxide," *Journal of Nuclear Materials*, vol. 279, no. 1, pp. 1 – 18, 2000.
- [186] M. Amaya, T. Kubo, and Y. Korei, "Thermal conductivity measurements on UO<sub>2+x</sub> from 300 to 1.400 K," *Journal of Nuclear Science and Technology*, vol. 33, no. 8, pp. 636–640, 1996.
- [187] A. Bejan, *Heat transfer*, vol. New York, John Wiley and Sons. 1993.
- [188] J. Sercombe, F. J. Ulm, and H. A. Mang, "Numerical solutions for chemoplastic models with internal couplings," 04 1999.
- [189] Frontline Systems. <http://www.solver.com/>.
- [190] B. Sundman, B. Jansson, and J.-O. Andersson, "The Thermo-Calc databank system," *Calphad*, vol. 9, no. 2, pp. 153 – 190, 1985.
- [191] C. Guéneau, N. Dupin, B. Sundman, C. Martial, J.-C. Dumas, S. Gossé, S. Chatain, F. D. Bruycker, D. Manara, and R. J. Konings, "Thermodynamic modelling of advanced oxide and carbide nuclear fuels: Description of the U–Pu–O–C systems," *Journal of Nuclear Materials*, vol. 419, no. 1, pp. 145 – 167, 2011.
- [192] Roberts et al., *cited by Belle*. 1969.
- [193] Z. Hadari, M. Kroupp, and Y. Wolfson, "Self-diffusion measurement of oxygen in UO<sub>2</sub> by the nuclear reaction 18O(p,  $\gamma$ )19F," *Journal of Applied Physics*, vol. 42, no. 2, pp. 534–535, 1971.
- [194] A. Bayoğlu and R. Lorenzelli, "Oxygen diffusion in fcc fluorite type nonstoichiometric nuclear oxides MO<sub>2±x</sub>," *Solid State Ionics*, vol. 12, pp. 53 – 66, 1984.

- [195] V. Marelle, P. Goldbronn, C. Introini, S. Bernaud, A. Bouloré, M. Casella, C. Filiaux, J. Julien, K. Mer-Nkonga, and L. Noirot, “Validation of PLEIADES/ALCYONE 2.0 fuel performance code,”
- [196] P. Koukkari, R. Pajarre, and K. Hack, “Constrained Gibbs energy minimisation,” *International journal of materials research*, vol. 98, no. 10, pp. 926–934, 2007.
- [197] J.-B. Minne, L. Desgranges, V. Optasanu, N. Largenton, L. Raceanu, and T. Montesin, “Specific aspects of internal corrosion of nuclear clad made of Zircaloy,” in *Defect and Diffusion Forum*, vol. 323, pp. 227–232, Trans Tech Publ, 2012.
- [198] J. Davies, E. Hoshi, and D. Zimmerman, “Ramp test behavior of high O/U fuel,” *Journal of nuclear materials*, vol. 270, no. 1-2, pp. 87–95, 1999.
- [199] D. Le Boulch, L. Fournier, and C. Sainte-Catherine, “Testing and modelling iodine-induced stress corrosion cracking in stress-relieved Zircaloy-4,” in *Pellet-clad Interaction in Water Reactor Fuels, Aix-en-Provence, France, 2004*.
- [200] L. Desgranges, B. Pasquet, I. Roure, S. Portier, S. Brémier, C.T.Walker, R. Hasnaoui, D. Gavillet, M. Martin, and L. Raimbault, “Assessment of the Nd/U ratio for the quantification of neodymium in  $\text{UO}_2$ ,” *Applied Surface Science*, vol. 255, no. 4, pp. 863 – 865, 2008. Proceedings of the Sixteenth International Conference on Secondary Ion Mass Spectrometry, SIMS XVI.
- [201] D. Le Boulch, M. Bono, E. Federici, M. Mozzani, M. Rautenberg, and V. Chabretou, “Testing and modelling iodine-induced stress corrosion cracking (I-SCC) in zircaloy alloys,” in *Proceedings of the workshop PCI in Water-Cooled Reactors, Lucca, IT, 2016*.
- [202] M. Frégonèse, G. Delette, G. Ducros, and F. Lefebvre, “Amount of iodine responsible for I-SCC of Zircaloy-4 in PCI-conditions: recoil-implanted and thermally released iodine,” *Nuclear Engineering and Design*, vol. 186, no. 3, pp. 307 – 322, 1998.
- [203] B. Sundman, U. Kattner, M. Palumbo, and S. Fries, “OpenCalphad - a free thermodynamic software,” *Integrating Materials and Manufacturing Innovation*, vol. 4, no. 1, pp. 1–15, 2015.
- [204] H. Loukusa, “Application of constrained Gibbs energy minimization to nuclear fuel thermochemistry,” in *TopFuel, Prague, CZ, 2018*.
- [205] L. Onsager, “Reciprocal relations in irreversible processes. I.,” *Physical review*, vol. 37, no. 4, p. 405, 1931.
- [206] S. De Groot and P. Mazur, “Non-equilibrium thermodynamics, northholland, amsterdam, 1962,”

- [207] K. Writz, "Zur kinetischen theorie der thermodiffusion im kristallgitter," *Zeitschrift für Physik*, vol. 44, 1943.
- [208] K. Writz, "Thermodiffusion and überführungswärmen in kondensierten phasen," *Zeitschrift für Physik*, vol. 482, 1948.
- [209] R. Howard and A. Lidiard, "Matter transport in solids," *Reports on progress in Physics*, vol. 27, no. 1, p. 161, 1964.



## FOLIO ADMINISTRATIF

### THESE DE L'UNIVERSITE DE LYON OPEREE AU SEIN DE L'INSA LYON

NOM : KONARSKI

DATE de SOUTENANCE : 10 Octobre 2019

Prénoms : PIOTR

TITRE : THERMO-CHEMICAL-MECHANICAL MODELING OF NUCLEAR FUEL BEHAVIOR. IMPACT OF OXYGEN TRANSPORT IN THE FUEL ON PELLETT CLADDING INTERACTION

NATURE : Doctorat

Numéro d'ordre : 2019LYSEI080

Ecole doctorale : ED34

Spécialité : Matériaux

RESUME : The goal of this thesis is to study the impact of oxygen transport on thermochemistry of nuclear fuel and pellet cladding interaction. During power ramps, nuclear fuel is exposed to high temperature gradients. It undergoes chemical and structural changes. The fuel swelling leads to a mechanical contact with the cladding causing high mechanical stresses in the cladding. Simultaneously, chemically reactive gas species are released from the hot pellet center and can interact with the cladding. The combination of these chemical and mechanical factors may lead to the cladding failure by iodine stress corrosion cracking. It has been proven that oxygen transport under high temperature gradients affects irradiated fuel thermochemistry, a phenomenon which may be of importance for stress corrosion cracking. This thesis presents 3D simulations of power ramps in pressurized water reactors with the fuel performance code ALCYONE, which is part of the computing environment PLEIADES. The code has been upgraded to couple the description of irradiated fuel thermochemistry already available with oxygen transport taking into account oxygen thermal diffusion. The impact of oxygen redistribution during a power transient on irradiated fuel thermochemistry in the fuel and on chemically reactive gas release from the fuel (consisting of I(g), I<sub>2</sub>(g), CsI(g), TeI<sub>2</sub>(g), Cs(g) and Cs<sub>2</sub>(g), mainly) is studied. The simulations show that oxygen redistribution, even if moderate in magnitude, leads to the reduction of metallic oxides (molybdenum dioxide, cesium molybdate, chromium oxide) at the fuel pellet center and consequently to the release of a much greater quantity of gaseous cesium, in agreement with post-irradiation examinations. The three-dimensional calculations of the quantities of importance for iodine stress corrosion cracking (hoop stress, hoop strain, iodine partial pressure at the clad inner wall) are then used in simulations of clad crack propagation.

MOTS-CLÉS : Combustible nucléaire, thermochimie, modélisation, rampe de puissance, corrosion sous contraintes, interaction pastille gaine, relâchement de produits de fission, transport de l'oxygène

Laboratoire (s) de recherche :

MATEIS (INSA), Laboratoire d'Expertises et de Validation des Applications combustibles multi-filières (CEA)

Directrice de thèse: Professeur Marion Frégonèse

Composition du jury :

PIRO, Markus	Prof.	Ontario Tech University	Rapporteur
GALLIERO, Guillaume	Prof.	Université de Pau	Rapporteur
SERCOMBE, Jérôme	Dr.	CEA Cadarache	Examineur
LUZZI, Leilo	Prof.	Politecnico di Milano	Examineur
FREGONESE, Marion	Prof.	INSA de Lyon	Directrice de thèse
CHANTRENNE, Patrice	Prof.	INSA de Lyon	Co-directeur de thèse
BAURENS, Bertrand	Dr.	EDF	Invité
RIGLET-MARTIAL, Chantal	Dr.	CEA Cadarache	Invitée
GARNIER, Christophe	Dr.	Framatome	Invité